Dynamical Modelling of Power Systems with Power Electronic Controllers using Individual Channel Analysis and Design

by

Carlos Ernesto Ugalde-Loo

A Thesis submitted to the

Department of Electronics and Electrical Engineering

of

The University of Glasgow

for the degree of Doctor of Philosophy

October 2009

To my family

Abstract

Global demand for electrical energy is at an all time high. In industrialised societies consumers have come to expect an interruption-free, high-quality electricity supply and environmentally aware consumers and pressure groups have been very successful in encouraging the electricity supply industry towards incorporating, as part of the generation mix, sources of electricity that are benign to the environment. In some European countries great progress has been made in the integration of wind generation and photo-voltaics. Moreover, the industry has gone through major privatisation and deregulation programmes worldwide; and there is the notion in some quarters that deregulation and widespread cross-border interconnections may have exacerbated the incidence of wide-area break-downs in electricity supply.

The challenges facing today's electricity supply industry are many, and the technology to deliver the necessary grid control is still underdeveloped. A major research thrust is required to make a power network flexible, resilient and responsive to the consumer's wishes of being supplied with environmentally sound electricity. Renewable generation such as wind and marine turbines and photo-voltaic cells need power electronics and effective controllers if they are to be successfully integrated into the electricity grid without reduction of supply quality. The dynamical interaction of multi-machine networks, power electronics and large penetration of intermittent generation are highly complex phenomena and a better understanding of their dynamical behaviour is mandatory before larger increases of intermittent generation are added to it, to avoid widespread black-outs and thwarted energy transactions.

The impact of successful integration of FACTS equipment into power systems networks worldwide is affecting all sectors of the market: power generation, transmission, distribution, utilisation and equipment manufacturers. However, further progress requires investigating further the dynamic performance of the FACTS technology in order to continue acquiring leading-edge, relevant knowledge. Devices used to enhance the stability of power systems such as the Static VAr Compensator (SVC) and the Thyristor-Controlled Series Compensator (TCSC) are prime candidates for investigation owing to their popularity. Both FACTS controllers are comprehensively investigated in this research.

The main aims of this research project are to develop and evaluate dynamic high-order multi-machine models, dynamic models of FACTS devices, such as the SVC and the TCSC, with particular emphasis in their electromechanical oscillations damping capabilities; to carry out fundamental analyses and control system designs of synchronous generators and FACTS controllers; and to investigate their dynamic effects and interactions with the power network. Individual Channel Analysis and Design (ICAD), a classical oriented multivariable control systems framework is used in this research project. ICAD has shown its suitability for carrying out small-signal stability assessments, with which it has been possible to evaluate the potential robustness and performance of the control system design, affording physical insight.

Acknowledgements

First and foremost I would like to express my deepest gratitude to Prof Enrique Acha for his guidance and criticism in this thesis and during my research project. His valuable direction, suggestions, thoughtful support, advice and patience were fundamental in order to carry out successfully this research work.

Likewise, I would like to deeply thank Dr Eduardo Licéaga–Castro for having motivated me to undertake this research project. His supervision, criticism, encouragement, support and advice were key for the development of this thesis.

I also would like to thank Dr Jesús Licéaga–Castro, with whom I had very helpful discussions related to this work. I am grateful to my colleagues Damián, Enrique, Rodrigo, Pedro, Behzad, Piotr and Luigi for the time spent at the Power Systems research group and for their friendships. Thanks are also due to the staff members of the Department of Electronics and Electrical Engineering for providing me with a great environment for study and research.

Many thanks to the valuable people that I had the opportunity to meet in Glasgow, in particular to José, Rafael, Christian, Jonny, Frizzi, Meiko and Sylvia, who have been my friends since the very beginning of this journey, to my fellow teammates in Kelvinbridge AFC, to the Psychology/Engineering football crew, to my fellow committee members of the International Society, and to all the friends with whom I spent unforgettable time – this space is not enough to mention all of you. Thanks as well to my friends back home and abroad who have always been close despite the miles away – you know who you are.

I owe my deepest and sincere gratitude to Silvia for her love, patience, encouragement, invaluable support, for being my inspiration, and for being always there, no matter what.

I would like to thank my mother Irene, my father Ernesto and my sister Adriana not only for their strong encouragement and understanding throughout this time, but also for their love and unconditional support, for being my best example and for giving me the motivation to reach all my goals.

This research work was funded by CONACyT (Consejo Nacional de Ciencia y Tecnología, Mexico). I gratefully acknowledge the scholarship given to me during my PhD studies.

Table of Contents

List of Figures

List of Tables

Abbreviations

Synchronous generator and power systems

3-ϕ	Three-phase
AC	Alternating current
AVR	Automatic voltage regulator
B_{ii}	Driving point susceptance for node *i*
B_{ik}	Susceptance between nodes *i* and *k*
B_{Li}	Load susceptance at node *i*
δ	Internal rotor or load angle
D	Damping coefficient
DC	Direct current
EMF, emf	Electromotive force
$E_d^{'}$	*d*-axis component of the transient internal emf proportional to the total flux linkage in the *q*-axis damper winding
$E_q^{'}$	*q*-axis component of the transient internal emf proportional to the field winding flux linkage
$E_d^{''}$, $E_q^{''}$	*d*-axis (*q*-axis) component of the sub-transient internal emf proportional to the total flux linkage in the *q*-axis (*d*-axis) damper winding
$E_q^{'}$	*q*-axis component of the transient internal emf proportional to the field winding flux linkage
E_{fd}	Generator field voltage
e_t	Generator terminal voltage in *dq*-axis reference frame
E_t	Generator terminal voltage in *DQ*-axis reference frame
e_{td}, e_{tq}	Generator armature current *dq* components
E_{tD}, E_{tQ}	Generator armature current *DQ* components
ϕ	Power factor angle

f	Electrical frequency
G_{ii}	Driving point conductance for node *i*
G_{ik}	Conductance between nodes *i* and *k*
G_{Li}	Load conductance at node *i*
FACTS	Flexible AC transmission systems
H	Intertia constant
i_a , i_b , i_c	Armature currents in real coordinates
I_{Li}	Load current at node *i*
i_t	Generator armature current in *dq*-axis reference frame
I_t	Generator armature current in *DQ*-axis reference frame
i_{td} , i_{tq}	Generator armature current *dq* components
I_{tD} , I_{tQ}	Generator armature current *DQ* components
I_∞	Current injected at the infinite bus
$I_{\infty d}$, $I_{\infty q}$	Current *dq* component injected at the infinite bus
HVDC	High-voltage direct-current
MMF, mmf	Magnetomotive force
OMIB	One-machine infinite bus
P_e	Electrical power injected into the grid system
P_{Li}	Load active power at node *i*
P_m	Mechanical power supplied to the generator
P_t	Terminal active power
PSS	Power system stabiliser
θ_{ii}	Driving point admittance phase angle for node *i*
θ_{ik}	Admittance phase angle between nodes *i* and *k*
θ_r	Rotor position relative to the stator
Q_{Li}	Load reactive power at node *i*
Q_t	Terminal reactive power
R_a	Stator resistance
S_t	Terminal apparent power
SSR	Sub-synchronous resonance
STATCOM	Static synchronous compensator
SVC	Static VAr compensator

$\tau_{d0}^{'}$, $\tau_{q0}^{'}$	Open circuit *d*- and *q*-axis transient time constant, respectively
$\tau_{d0}^{''}$, $\tau_{q0}^{''}$	Open circuit *d*- and *q*-axis sub-transient time constant, respectively
TCSC	Thyristor-controlled series compensator
TCR	Thyristor-controlled reactor
UPFC	Unified power flow controller
V_{Li}	Load voltage at node *i*
VFT	Variable frequency transformer
VSC	Voltage source converter
V_{∞}	Infinite bus voltage
$V_{\infty d}$, $V_{\infty q}$	Infinite bus voltage *dq* components
X_d , X_q	Synchronous reactance in *d*- and *q*-axis, respectively
$X_d^{'}$, $X_q^{'}$	Transient synchronous reactance in *d*- and *q*-axis, respectively
$X_d^{''}$, $X_q^{''}$	Sub-transient synchronous reactance in *d*- and *q*-axis, respectively
X_t	Tie-line reactance
$\overline{\mathbf{Y}}$	Nodal admittance matrix
ω	Rotor speed
ω_0	Nominal rotor speed

SVC and TCSC

α	SVC or TCSC firing angle
B_C	SVC capacitive susceptance
$B_L(\alpha)$	SVC varying inductive susceptace as a function of the firing angle
B_{SVC}	SVC total susceptance
I_{SVC}	SVC output current
I_{SVCd} , I_{SVCq}	SVC output current components
I_{TCSC}	Current flowing through the TCSC
V_{SVC}	SVC terminal voltage
V_{SVCd} , V_{SVCq}	SVC terminal voltage components
X_C , X_L	Capacitive, inductive reactances
X_{t1}, X_{t2}	Tie-line reactance subjected to $X_t = X_{t1} + X_{t2}$
X_{TCSC}	TCSC total reactance

ICAD and control systems

$\mathbf{0}_{i\times k}$	$i\times k$ matrix of zero entries
2×2	2-input 2-output multivariable system
3×3	3-input 3-output multivariable system
4×4	4-input 4-output multivariable system
A	System matrix of a state-space representation
B	Input matrix of a state-space representation
BW	Bandwidth
C	Output matrix of a state-space representation
$C_i(s)$	*i*-th individual channel from input $u_i(s)$ to output $y_i(s)$
d	External disturbance vector in a multivariable system
d_i	*i*-th external disturbance in a multivariable system
D	Feed-forward matrix of a state-space representation
e	Error vector in a closed-loop multivariable system
e_i	*i*-th error in a closed-loop multivariable system
$\mathbf{G}(s)$	Transfer function matrix of a multivariable system
$\gamma_i(s)$	*i*-th multivariable structure function
$\Gamma_i(s)$	*i*-th multivariable structure function (potential performance and coupling assessment)
$g_{ik}(s)$	*ik*-th element of a transfer function matrix
GM	Gain margin
$h_i(s)$	*i*-th closed-loop subsystem in a multivariable system
ICAD	Individual channel analysis and design
$\mathbf{I}_{n\times n}$	Identity matrix of order *n*
$\mathbf{K}(s)$	Multivariable controller matrix, ICAD controller
$k_{ik}(s)$	*ik*-th element of a multivariable controller matrix
LHPP	Left hand plane pole
LHPZ	Left hand plane zero
λ	Eigenvalue
m×*m*	*m*-input *m*-output multivariable system
$\mathbf{M}_{ik}(s)$	Multiple channel with individual channels *ik*
MIMO	Multiple-input multiple-output
MSF	Multivariable structure function
n	Order of a multivariable system
N	Number of clockwise encirclements to the $(1,0)$ point in the Nyquist plot of $\gamma_i(s)$

PM	Phase margin
r	Reference vector in a closed-loop multivariable system
r_i	*i*-th reference in a closed-loop multivariable system
RGA	Relative gain array
RHPP	Right hand plane pole
RHPZ	Right hand plane zero
SISO	Single-input single-output
σ	Real part of complex conjugate roots
P	Number of RHPPs of $\gamma_i(s)$
Q	Number of eigenvalues in the right hand plane of the state-space representation
u	Input vector of a state-space representation
u_i	*i*-th input of a multivariable system
ω_d	Damped natural frequency
ω_n	Natural frequency
x	State vector of a state-space representation
x_i	*i*-th state of the state vector
y	Output vector of a state-space representation
y_i	*i*-th output of a multivariable system
Z	Number of RHPZs of $(1-\gamma_i)$
ζ	Damping ratio of complex conjugate roots

Operators and functions

$\lvert\ \rvert$	Magnitude
$\sum$	Summation
∞	Infinite
cos	Cosine trigonometric function
$\frac{\partial}{\partial \mathbf{x}}$	Partial derivative with respect to vector **x**
$\frac{d}{dt}$	Time derivative
diag	Matrix with diagonal elements
Δ	Incremental change; linearised variable
j	Complex operator
lim	Limit function

s	Laplace operator
sin	Sine trigonometric function
t	Time
^{T}	Transpose of a vector or matrix
tan	Tangent trigonometric function
x_0	Initial value or operating condition of variable x
$\dot{x}$	Time derivative of variable x
$\vec{x}$	Phasor of variable x
$\overline{x}$	Complex variable x
x^*	Complex conjugate of variable x

Chapter 1

INTRODUCTION

1.1. Justification and motivation

Global demand for electrical energy is at an all time high. In industrialised societies consumers have come to expect an interruption-free, high-quality electricity supply and environmentally aware consumers and pressure groups have been very successful in encouraging the electricity supply industry towards incorporating, as part of the generation mix, sources of electricity that are benign to the environment in the form of gas emissions reduction. This has created many new business opportunities in the electrical energy sector but also some of the greatest operational challenges in the history of electricity supply – the power engineering community has met this challenge head-on and great progress has been made concerning the operation of power systems with a high penetration of wind generation. Nevertheless, the industry has gone through major privatisation and deregulation programmes in all corners of the world; and there is the notion that deregulation may have exacerbated the incidence of wide-area break-downs in electricity supply. The inter-state blackouts in the USA and Canada in the last decade are well documented and so are the more recent ones in Europe, involving several countries. Blackouts are all too common in other parts of the world but only a few of them are as devastating as the one that took place in Colombia, on 26th April 2007.

Due to greater commercial and environmental pressures, compounded with higher demands, power transmission engineers are being left with no option but to push systems towards their emergency limits – the construction of new generation and transmission facilities suffers long delays due to a tightening of the legislation caused by a more environmentally aware society. Moreover, electrical utilities worldwide have to contend with increased consumer lead pressures to improve the security and quality of electrical supply and the generation of electricity with primary energy sources that are benign to the environment. Industry's response to the conflicting requirements imposed by higher energy demands, long delays in the construction of new infrastructure and higher penetration of intermittent generation, has been the interconnection of wide-area systems to form truly continental systems and the use of power electronics-based equipment to enable submarine interconnections and higher through-puts in existing

transmission corridors constrained by angular stability. At the distribution level, there are demands from large industrial users to count with improved security and quality of supply in the face of lost production time running into millions of pounds per annum.

The challenges facing today's electricity supply industry are many, and the technology to deliver the necessary electricity grid control required is still underdeveloped. A major research thrust is required to make the power network flexible, resilient and responsive to the consumer's wishes of being supplied with environmentally sound electricity; with a warranted high-level of security of supply. Renewable generation such as wind and marine turbines and photo-voltaic cells need power electronics and effective control techniques if they are to be successfully integrated into the electricity grid without reduction of supply quality. There is widespread agreement among power system engineers that a better understanding of the dynamical behaviour of the power network is mandatory before large increases of intermittent generation is added to it, to avoid widespread "black-outs" and thwarted energy transactions between power brokers. In view of the forecasted large-scale deployment of such interconnections, it is most desirable to go on with the current programmes of research on the dynamic aspects of FACTS (Flexible AC Transmission Systems) equipment [1–5], in order to continue acquiring leading-edge, relevant knowledge.

The impact of successful integration of FACTS equipment into power systems networks worldwide will affect all sectors of the market: power generation, transmission, distribution, utilisation and equipment manufacturers. An initial step to tackle this issue is to investigate the dynamic performance of the already installed and mature members of the FACTS technology. The Static VAr Compensator (SVC) and the Thyristor-Controlled Series Compensator (TCSC), as devices used to enhance the stability of power systems, are prime candidates for investigation. Afterwards, the dynamic performance of the newest FACTS devices, namely the High-Voltage Direct-Current based on Voltage Source Converters (HVDC-VSC) and the Variable Frequency Transformer (VFT), should be evaluated.

To contribute towards achieving such aims, the research work reported in this thesis uses a classical oriented framework [6–12] for multivariable systems, Individual Channel Analysis and Design (ICAD). It is suitable for small-signal stability assessments in which is possible to evaluate the potential robustness and performance of the control design, allowing analysis and synthesis of multivariable control design by applying techniques based on Bode/Nyquist plots. The design process involves individual input-output channels definition in terms of the Multivariable Structure Function (MSF), an information rich variable with which it is possible to assess the robustness and performance of the multivariable control design. ICAD has been successfully used for integrated control. Due to its characteristics, it represents an ideal framework for analysis and control system design since it does not suffer from lack of physical transparency and may be still applicable to large-scale systems.

Particularly, the research project is set to investigate the dynamic response of FACTS equipment. Key objectives of the research are to develop high-order single- and multi-machine mathematical models, to develop dynamic models of mature FACTS devices such as the SVC and the TCSC with particular emphasis in their electromechanical oscillations damping capabilities and to investigate their dynamic effects on the power network.

The research work is aimed at the global electricity supply industry; it is a synergy of knowledge from a variety of enabling backgrounds, namely power electronics, power systems and control engineering. The current research project sums up preliminary research efforts in the area, providing a spring board upon which practical solutions to a very real and timely engineering problem can be made. The overall contribution will be on improving the operating characteristics of FACTS equipment, with the long-term goal of making electrical power systems with a large penetration of renewable generation, less brittle; diminishing the multi-million pound loss in revenue derived from supply interruption.

1.2. Flexible AC Transmission Systems (FACTS)

Two kinds of emerging power electronics applications in power systems are already well defined [1]: (1) bulk active and reactive power flow control and (2) power quality improvement. The first application area is known as FACTS [1,4,5], where the latest power electronic devices are used to control the high-voltage side of the network. The second application area is Custom Power, which focuses on low-voltage distribution. FACTS and Custom Power concepts were envisioned by Hingorani [2,3,13].

Custom Power was created in response to reports of poor power quality and reliability of supply affecting factories, offices and homes [1]. When widespread deployment of the technology takes place, tighter voltage regulation, minimum power interruptions, low harmonic voltages, and acceptance of rapidly fluctuating and other nonlinear loads in the vicinity are expected [13].

FACTS is based on the incorporation of power electronics devices into the high-voltage side of the power network to make it *electronically-controllable* [1,4,5]. As an integrated philosophy, it is a novel concept that was brought to fruition at the Electric Power Research Institute (EPRI) during the 1980s [4]. Operationally, it concerns the ability to control the path of the power flows throughout the network during both steady-state and transient conditions. These devices have the ability to control the line impedance and the nodal voltage magnitudes and angles at both the sending and receiving end of key transmission corridors of the network whilst enhancing considerably the security of the system [1,4]. High-voltage transmission networks have been usually meshed to provide redundant paths for reliability. Under certain operating conditions, redundant paths may give rise to circulating power and extra losses. FACTS controllers should be able to eliminate circulating currents in meshed networks [5].

A number of FACTS equipment have been commissioned [1–5,14–29], being of special interest for this research project the following controllers:

- *Thyristor-Controlled Reactor (TCR):* this is a shunt-connected reactor where its effective reactance is varied in a continuous manner by partial conduction control of the thyristor valve.

- *Thyristor-Controlled Series Compensator (TCSC):* it consists of a series capacitor paralleled by a thyristor-controlled reactor in order to provide smooth variable series compensation.

- *Static Synchronous Compensator (STATCOM):* this is a solid-state synchronous condenser connected in shunt with the AC system. The output current is adjusted to control either the nodal voltage magnitude or the reactive power injected at the bus.

- *Static VAr Compensator (SVC):* this is a shunt-connected static source or sink of reactive power compensation.

- *High-Voltage Direct-Current using Voltage Source Converters (HVDC-VSC):* this is a two-converter system connected in series in its DC side and in shunt in its AC side.

- *Variable Frequency Transformer (VFT):* it can be considered to be an induction machine that consumes reactive power to maintain the required magnetic field in its rotor that would enable the machine to operate. The phase-shifting action of the rotor to regulate a specified amount of power flowing from rotor to stator or vice-versa, also demands reactive power – one power system is connected to the VFT stator and the other to the VFT rotor.

1.3. Individual Channel Analysis and Design (ICAD)

In a typical control design task the performance is specified in terms of an output response to a given input reference [30,31]. Nevertheless, the multivariable control design problem is inherently interactive in nature with an interplay between plant attributes, customer specification, and the design process itself [12]. For clarity of both performance specification and design, it remains desirable to consider inputs and outputs in pairs, with an individual pairing of an input to a given output being called a channel [12]. When the plant cross–coupling is weak, the design task reduces to a set of SISO design tasks and a scalar controller can be designed separately for each channel [30]. In such context, the most appropriate methodology is the classical Nyquist/Bode analysis and design.

Individual Channel Analysis and Design (ICAD) [6–12] is a framework in which Bode/Nyquist techniques can be applied directly to the channels not only when cross-coupling is weak but in all

circumstances including when cross-coupling is strong. The multivariable system is decomposed into an equivalent set of SISO systems. What is particular to ICAD is that the SISO channel transmittances are reformulated to make explicit the role of the plant structure. Scalar multivariable structure functions (MSFs), to which the individual channel transmittances are simply related, encapsulate the significant aspects of the plant structure. The multivariable nature of the original plant is maintained in the equivalent SISO systems through the multivariable structure functions with no loss of information. In other words, ICAD seeks to provide the potential user with a design framework for multivariable feedback control systems that is transparent and flexible, is no more complex than necessary, is capable of validation against observed plant data, builds confidence in the arrived-at design, and is well-suited to the specific engineering context.

So far, ICAD has been reported in several control strategies, such as in OMIB systems and other contrived power systems dynamics problems [32–35], submarines [36,37], aerospace industry [38–45], induction motors [46–48], and combustion processes [49]. With ICAD it is possible to reach simple and effective control system designs. See for instance [50,51].

1.4. Main aims of the PhD research project

The research is primarily concerned with small-signal stability modelling and control system design of power systems using the multivariable control system framework of ICAD [6–12]. The incorporation of electronically-controlled shunt and series compensation is also considered. The motivation arises since various FACTS equipments are currently being installed in electrical power systems. Although several power system tools have been developed, it is necessary to be able to understand the full aspects of dynamic interactions between synchronous generators and between synchronous generators and FACTS devices. On the one hand, eigenvalues techniques, commonly deployed in the industry, lack of physical insight and transparency; on the other hand, block-diagram based methodologies become complicated for multi-machine representations and the information they provide might not be useful for control system design. The use of ICAD fits the gap between state-space based analysis and block-diagrams methodologies, in the sense that physical insight is not lost, it is possible to obtain formal proofs as to why some operating characteristics occur in practice, and control system design following a complete multivariable analysis can be carried out. It should be pointed out that in this thesis the frequency domain is investigated, rather than the time domain, due to two main reasons: (*i*) within the ICAD framework, it is essential to obtain a frequency domain representation of the system to be studied; and (*ii*) as the studies are limited to small-signal stability, a linear representation of the systems can be obtained, amenable to frequency domain analysis. Nevertheless, time domain simulations are also included for completeness.

The objectives of this research project are as follows:

- *To develop comprehensive power system models for single-machine dynamic analysis and control system design*. Synchronous generator models range from models with no damper windings to models where damper windings are included in the *d*- and *q*-axis. Transfer function matrix representations are employed to represent the systems under study and compared to the physical-oriented block-diagram methodology. From a modelling point of view, the single machine is a 2×2 system amenable to small-signal stability studies under the ICAD framework. Development, testing and simulation will be carried out in MATLAB.
- *To develop comprehensive power system models including different FACTS devices for small-signal dynamic analysis and control system design*. Transfer function matrix representations are employed to represent the systems under study and compared to the physical-oriented block-diagram methodology. Initially, the SVC and the TCSC are considered, with particular emphasis on the electromechanical oscillation damping capability offered by both devices. The SVC [1,2,4,52–54] is a mature piece of technology, which has become very popular for providing fast-acting reactive power support. The primary application of the SVC is the provision of dynamic voltage control to improve transient stability. However, an additional damping control loop can be injected to provide system damping capabilities [27–29,55–57]. On the other hand, the TCSC [1,54,58–61] is the electronically-controlled counterpart of the conventional series bank of capacitors. It is able to rapidly control line compensation over a continuous range resulting in increased flexibility. Active power across the compensated transmission line can be maintained at a specified level under a wide range of operating conditions. From the modelling point of view, both the SVC and TCSC are 3×3 systems which can be studied within the ICAD framework. Development, testing and simulation will be carried out in MATLAB.
- *To develop comprehensive power system models for multi-machine small-signal dynamic analysis*. The multi-machine system is constructed in such a way that any of the *n* machines may have a different representation (each generator model ranges from representations with no damper windings to models where damper windings are included in the *d*- and *q*-axis). Therefore, models with the same kind of machine representation or multi-order systems should be available. State-space representations are employed to compare the mathematical model with results obtained using commercial industry-grade software. Development and testing will be carried out in MATLAB.
- *To develop comprehensive power system models for multi-machine small-signal dynamic analysis and control system design*. Transfer function matrix representations are employed. From a modelling point of view, the multi-machine system, where *n* is a number of machines, is a $2n \times 2n$ system amenable to small-signal stability studies under the ICAD framework. Development, testing and simulation will be carried out in MATLAB.

1.5. Main contributions

The main contributions of this research work are summarised below:

- Thorough evaluation of various synchronous machine mathematical models, ranging from low order (3^{rd} order) to high order (6^{th} order) representations.

- Mathematical models of power systems containing FACTS devices (electronically-controlled compensation). The models are derived from first principles for small-signal stability analysis. Both a state-space and a frequency domain representation in the form of transfer function matrix are arrived at. SVC and TCSC models have been developed for one-machine infinite-bus systems.

- Multi-machine, multi-order models of power systems for an arbitrary number of machines. The evaluation of the mathematical models has been carried out through direct comparison against results obtained with commercial industry-grade software. Considerations for the construction of multi-order models and a complete example of a three-machine multi-order system are also presented.

- The use of a multivariable control oriented framework based on the application of the classical Bode/Nyquist analysis, ICAD, for the study of single-machine systems, multi-machine systems and FACTS devices.

- Through the use of the ICAD framework, formal proofs as to why some operating system characteristics occur in practical power systems.

- Through the use of the ICAD framework, formal proofs on the ability of FACTS devices to improve the dynamic performance of the system due to the contribution of additional system damping (SVC) and as a function of series compensation levels (TCSC).

- Computational software for small-signal stability assessments using the ICAD framework.

1.6. Transaction-grade and conference publications

The following publications were generated during the course of the present research work:

- Ugalde–Loo CE, Olguín-Salinas D, Licéaga–Castro E, Licéaga–Castro J. *Individual Channel Design for Synchronous Generators*. International Journal of Emerging Electric Power Systems, **4**, no.2, art. 4, 2005 (http://www.bepress.com/ijeeps/vol4/iss2/art4).

- Licéaga–Castro E, Ugalde–Loo CE, Licéaga–Castro J, Ponce P. *An Efficient Controller for SV–PWM VSI Based on the Multivariable Structure Function*. Proceedings of the Joint 44th IEEE Conference on Decision and Control and European Control Conference, pp. 4754–4759, 2005.

- Licéaga–Castro E, Licéaga–Castro J, Ugalde–Loo CE. *Beyond the existence of diagonal controllers: from the relative gain array to the multivariable structure function*. Proceedings of the Joint 44th IEEE Conference on Decision and Control - European Control Conference, pp.7150–7156, 2005.

- Ugalde–Loo CE, Licéaga–Castro E, Licéaga–Castro J. 2×2 *Individual Channel Design MATLAB® Toolbox*. Proceedings of the Joint 44th IEEE Conference on Decision and Control and European Control Conference, pp. 7603–7608, 2005.

- Licéaga–Castro E, Ugalde–Loo CE, Licéaga–Castro J. *Induction Motor Control by Individual Channel Analysis and Design*. Proceedings of the International Conference Control 2006 (UK-ACC), Glasgow, Scotland, UK, 2006.

- Ugalde–Loo CE, Vanfretti L, Licéaga–Castro E, Acha E. *Synchronous Generators Control: From the Traditional Perspective to the ICAD Framework*. Proceedings of the International Conference Control 2006 (UK-ACC), Glasgow, Scotland, UK, 2006.

- Ugalde–Loo CE, Acha E, Licéaga–Castro E, Licéaga–Castro J. *Individual Channel Analysis of the Static VAr Compensator Performance*. Postgraduate Conference 2007, University of Glasgow, Scotland, UK, 2007.

- Ugalde–Loo CE, Vanfretti L, Licéaga–Castro E, Acha E. *Synchronous Generators Modeling and Control Using the Framework of Individual Channel Analysis and Design. Part* 1. International Journal of Emerging Electric Power Systems, **8**, no.5, art. 4, 2007 (http://www.bepress.com/ijeeps/vol8/iss5/art4).

- Ugalde–Loo CE, Acha E, Licéaga–Castro E, Liceaga–Castro J. *Fundamental Analysis of the Static VAr Compensator Performance Using Individual Channel Analysis and Design.* International Journal of Emerging Electric Power Systems, **9**, no.2, art. 6, 2008 (http://www.bepress.com/ijeeps/vol9/iss2/art6).

- Ugalde–Loo CE, Acha E, Licéaga–Castro E, Vanfretti L. *Fundamental Analysis of the Synchronous Generator – TCSC System Using the ICAD Framework.* Proceedings of the 16th Power Systems Computation Conference (PSCC), Scotland, UK, 2008.

- Ugalde–Loo CE, Acha E, Licéaga–Castro E, Vanfretti L. *Individual Channel Analysis of the Thyristor-Controlled Series Compensator Performance.* Submitted to: International Journal of Emerging Electric Power Systems, 2009.

- Ugalde–Loo CE, Acha E, Licéaga–Castro E. *Fundamental Analysis of the Elecromechanical Oscillation Damping Control Loop of the Static VAr Compensator using Individual Channel Analysis and Design.* Submitted to: IEEE Transactions on Power Delivery, 2009.

- Ugalde–Loo CE, Acha E, Licéaga–Castro E. *Individual Channel Analysis and Design of Multi-machine Power Systems.* Submitted to: IEEE Transactions on Power Systems, 2009.

1.7. Outline of the thesis

The thesis is organised as follows: Chapter 2 reviews key aspects of the synchronous machine as a building block of modern power systems. The mathematical modelling of the synchronous generator, together with the representation of the power system network, is addressed. Also, an overview of relevant FACTS devices is presented. The presence of electromechanical oscillations in a power system and the dynamical damping provided by members of the FACTS technology is critically discussed. The chapter closes with an overview of the ICAD framework, where essential derivations and procedures are provided in Appendix A.

Chapter 3 presents the individual channel analysis and design of a one-machine infinite-bus system. The transfer function matrix representation for different order synchronous generator representations is discussed and critically examined, where related mathematical derivations are carried out in Appendix C. For completeness, the state-space representation and its equivalence to the frequency domain transfer function matrix representation is discussed. A comparison with block diagram models is carried out. A comprehensive analysis of the multivariable structure function associated to different operating conditions is made. Excitation and turbine-governor controllers of the synchronous generator are briefly addressed. A control system design, together with its performance and robustness assessment is presented. A discussion on the use of high-order models closes the chapter.

Chapter 4 assesses the individual channel analysis and design of systems including a synchronous generator and FACTS devices capable of providing damping of electromechanical oscillations. The state-space and transfer function matrix representations of the synchronous generator – SVC system are presented, with associated mathematical derivations included in Appendix D. A multivariable analysis and control system design, with performance and robustness assessment is provided. The action of both voltage and damping control loops is examined and the dynamic interactions existing between the SVC and the synchronous generator are shown. In a similar manner, the synchronous machine – TCSC system is studied, where its associated mathematical modelling is given in Appendix E. Multivariable analysis and control system design are provided. Study cases include the traditional capacitive region of operation, some extreme conditions of series compensation and the inductive region of operation. For completeness, the capabilities of the TCSC and the SVC to improve the system dynamic performance are compared against each other and with the PSS – a non-member of the FACTS technology designed for the damping of oscillations.

Chapter 5 derives the transfer function matrix representation of multi-machine systems consisting of n generating sources. A generic multi-order, multi-machine state-space representation is deduced.

Reductions to lower order models and considerations for multi-order models are discussed. The model is evaluated through three-machine and four-machine test systems reported in the open literature.

Chapter 6 addresses the individual channel analysis and design of multi-machine systems. A comprehensive multivariable analysis of a two-machine system is presented, where the dynamic interactions taking place between the two synchronous generators are clearly discussed. The influence of the transmission line length and system loading is critically examined. A control system design together with its performance and robustness assessment closes the chapter.

Chapter 7 presents the major conclusions of the research project and discusses opportunity areas to carry out further research.

1.8. References

[1] Acha E, Fuerte-Esquivel CR, Ambriz-Perez H, Angeles-Camacho C. *FACTS Modelling and Simulation in Power Networks*. UK: John Wiley & Sons; 2004.

[2] Hingorani NG. *FACTS – Flexible AC Transmission Systems*. IEE International Conference on AC and DC Power Transmission, pp. 1–7, 1991.

[3] Hingorani NG. *Flexible AC Transmission*. IEEE Spectrum, **30**, no. 4, pp. 40–45, April 1993.

[4] Hingorani NG, Gyugyi L. *Understanding FACTS: Concepts and Technology of Flexible AC Transmission Systems*. USA: IEEE Press; 2000.

[5] IEEE/CIGRE (Institute of Electrical and Electronic Engineers/Conseil International des Grands Reseaux Electriques). *FACTS Overview*, special issue, 95TP108, USA: IEEE Service Centre; 1995.

[6] Leithead WE, O'Reilly J. *Investigation of the ICD structure of systems defined by state space models.* International Journal of Control, **60**, no. 1, pp. 71–89, 1994.

[7] Leithead WE, O'Reilly J. *M-input m-output feedback control by individual channel design. Part 1. Structural Issues.* International Journal of Control, **56**, no. 6. pp. 1347–1397, 1992.

[8] Leithead WE, O'Reilly J. *Performance issues in the individual channel 2–input 2–output systems. Part 1: Structural issues.* International Journal of Control, **54**, no. 1, pp. 47–82, 1991.

[9] Leithead WE, O'Reilly J. *Performance issues in the individual channel 2–input 2–output systems. Part 2: Robustness issues.* International Journal of Control, **55**, pp. 3–47, 1992.

[10] Leithead WE, O'Reilly J. *Performance issues in the individual channel 2–input 2–output systems. Part 3: Non-diagonal control and related issues.* International Journal of Control, **55**, no 2, pp. 265–312, 1992.

[11] Leithead WE, O'Reilly J. *New roles for feedforward in multivariable control by individual channel design*. International Journal of Control, **57**, no. 6, pp. 1357–1386, 1993.

[12] O'Reilly J, Leithead WE. *Multivariable control by individual channel design*. International Journal of Control, **54**, no. 1, pp. 1–46, 1991.

[13] Hingorani NG. *Introducing Custom Power*. IEEE Spectrum, **32**(6), pp. 41–48, June 1995.

[14] ABB Power Technologies. *Eagle Pass / Piedras Negras BtB Light*. http://search.abb.com/library/.

[15] Angeles-Camacho C, Tortelli OL, Acha E, Fuerte-Esquivel CR. *Inclusion of a high voltage DC-voltage source converter model in a Newton-Raphson power flow algorithm*. IEE Proceedings in Generation, Transmission, and Distribution, **150**, no. 6, pp. 691–696, 2003.

[16] Arrillaga, J, Watson NR. *Computer Modelling of Electrical Power Systems*. UK: John Wiley & Sons; 2001.

[17] Chan KH, Parle JA, Johnson N, Acha E. *Real Time Implementation of a HVDC-VSC Model for Application in a scaled-down Wind Energy Conversion System (WECS)*. IEE AC-DC Power Transmission, pp. 599–604, 2001.

[18] Song R, Zheng C, Li R, Zhou X. *VSCs Based HVDC and its Control Strategy*. IEEE/PES Transmission and Distribution Conference and Exhibition: Asia and Pacific, pp. 1–6, 2005.

[19] Chen G, Zhou X. *Digital Simulation of Variable Frequency Transformers for Asynchronous Interconnection in Power System*. IEEE/PES Transmission and Distribution Conference and Exhibition: Asia and Pacific, pp. 169–174, 2005.

[20] Fujita H, Ihara S, Larsen EV, Pratico ER, Price WW. *Modeling and Dynamic Performance of a Rotary Power Flow Controller*. IEEE Power Engineering Society Winter Meeting, **2**, pp. 599–604, 2001.

[21] GE Energy. *Variable Frequency Transformers – Grid Inter-tie*. www.gepower.com/

[22] GE Energy. *GE's New Interconnection Technology Completes Commissioning Tests*. News release. www.gepower.com/

[23] Larsen E. *A Classical Approach to Constructing a Power Flow Controller*. IEEE Power Engineering Society Summer Meeting, **2**, pp. 1192–1195, 1999.

[24] Larsen E, Piwko R, McLaren D, McNabb D, Gragner M, Dusseault M, Rollin LP, Primeau J. *Variable Frequency Transformer – A New Alternative For Asynchronous Power Transfer*. GE Energy and Hydro-Quebec TransEnergie, 2004.

[25] McNabb D, Nadeau D, Nantel A, Pratico E, Larsen E, Sybille G, Van QD, Pare D. Transient and Dynamic *Modeling of the New Langlois VFT Asynchronous Tie and Validation with Commissioning Tests*. International Conference on Power Systems Transients, Canada, 2005.

[26] Piwko RJ, Larsen EV, Wegner CA. *Variable Frequency Transformer – A New Alternative for Asynchronous Power Transfer*. Proceedings of the IEEE PES 2005 Conference and Exposition in Africa, pp. 393–398, 2005.

[27] Angquist L, Lundin B, Samuelson J. *Power Oscillation Damping Using Controlled Reactive Power Compensation: A Comparison between Series and Shunt Approaches*. IEEE Transactions on Power Systems, **8**, no. 2, pp. 687–699, 1993.

[28] Martins N, Lima LTG. *Determination of Suitable Locations for Power System Stabilizers and Static VAr Compensators for Damping Electromechanical Oscillations in Large Scale Power Systems*. IEEE Transactions on Power Systems, **5**, no. 4, pp. 1455–1469, 1990.

[29] Mithulananthan N, Canizares CA, Reeve J, Rogers GJ. *Comparison of PSS, SVC, and STATCOM Controllers for Damping Power System Oscillations.* IEEE Transactions on Power Systems, **18**, no. 2, pp. 786–792, 2003.

[30] Goodwin G, Graebe SF, Salgado ME. *Control System Design*. USA: Prentice–Hall; 2001.

[31] Skogestad S, Postlethwaite I. *Multivariable feedback control. Analysis and design*. UK: John Wiley & Sons; 1996.

[32] Dudgeon GJW, Leithead WE, O'Reilly J, McDonald JR. *Prospects for the decentralized control of small-scale power networks with embedded generation*. IEEE Power Engineering Society Summer Meeting, **2**, pp. 1399–1404, 2000.

[33] Edwards FV, Dudgeon GJW, McDonald JR, Leithead WE. *Dynamics of distribution networks with distributed generation*. *IEEE* Power Engineering Society Summer Meeting, **2**, pp. 1032–1037, 2000.

[34] Fadlalmoula Z, Robertson SS, O'Reilly J, Leithead WE. *Individual channel analysis of the turbogenerator with a power system stabilizer*. International Journal of Control, **69**, no. 2, pp. 175–202, 1998.

[35] Fadlalmoula Z. *An Investigation of Turbogenerator Dynamics and Control*. PhD Thesis. Department of Electronics and Electrical Engineering, University of Glasgow, Scotland, UK, 1998.

[36] Licéaga–Castro E, Licéaga–Castro J. *Submarine depth control by individual channel design*. Proceedings of the 37th IEEE Conference on Decision and Control, **3**, pp. 3183–3188, 1998.

[37] Licéaga–Castro E, Licéaga–Castro J, Ugalde–Loo CE, Navarro–López EM. *Efficient Multivariable Submarine Depth-Control System Design*. Ocean Engineering, **35**, no. 17–18, pp. 1747–1758, 2008.

[38] Akbar MA, Leithead WE, O'Reilly J. *Design of robust controllers for a fighter aircraft using individual channel design.* Proceedings of the 32nd IEEE Conference on Decision and Control, **1**, pp. 430–435, 1993.

[39] Akbar MA, Leithead WE, O'Reilly J, Robertson SS. *Design of robust controllers for 3–input 3–output supersonic aircraft power plant using ICD*. Proceedings of the 3rd IEEE Conference on Control Applications, **1**, pp. 95–99, 1994.

[40] Dudgeon GJW, Gribble JJ. *Helicopter translational rate command using individual channel design.* UKACC International Conference on Control '96, **1**, pp. 632–637, 1996.

[41] Licéaga J, Licéaga E, Amézquita L. *Multivariable Gyroscope Control by Individual Channel Design*. Proceedings of the 2005 IEEE Conference on Control Applications, pp. 785–790, 2005.

[42] Licéaga–Castro J, Verde C, O'Reilly J, Leithead WE. *Helicopter control using individual channel design.* IEE Proceedings – Control Theory and Applications, **142,** pp. 58–72, 1995.

[43] Robertson SS, Leithead WE, O'Reilly J. *Design of controller for GVAM aircraft model using ICAD software.* UKACC International Conference on Control '96, **1**, pp. 533–538, 1996.

[44] Dudgeon GJW. *Individual Channel Analysis and Design and its Application to Helicopter Flight Control*. PhD Thesis. Department of Electronics and Electrical Engineering, University of Glasgow, Scotland, UK, 1996.

[45] Licéaga–Castro J. *Helicopter Flight Control by Individual Channel Design*. PhD Thesis. Department of Electronics and Electrical Engineering, University of Glasgow, Scotland, UK, 1995.

[46] Licéaga–Castro E, Ugalde–Loo CE, Licéaga–Castro J, Ponce P. *An Efficient Controller for SV–PWM VSI Based on the Multivariable Structure Function.* Proceedings of the Joint 44th IEEE Conference on Decision and Control and European Control Conference, pp. 4754–4759, Sevilla, Spain, 2005.

[47] Licéaga–Castro E, Ugalde–Loo CE, Licéaga–Castro J. *Induction Motor Control by Individual Channel Analysis and Design*. Proceedings of the International Conference Control 2006 (UK-ACC), Glasgow, Scotland, UK, 2006.

[48] Licéaga–Castro J, Amezquita–Brooks L, Licéaga–Castro E. *Induction Motor Currente Controller for Field Oriented Control Using Individual Channel Design*. Proceedings of the 34th Annual Conference of the IEEE Industrial Electronics Society (IECON 2008), pp. 235–240, Orlando, Florida, USA, 2008.

[49] Kocijan J, O'Reilly JO. *An example of multivariable combustion, control design within individual channel design framework.* Proceedings of the 3rd IEEE Conference on Control Applications, **1**, pp. 741–746, 1994.

[50] Licéaga–Castro E, Licéaga–Castro J, Ugalde–Loo CE. *Beyond the existence of diagonal controllers: from the relative gain array to the multivariable structure function*. Proceedings of the Joint 44th IEEE Conference on Decision and Control and European Control Conference, pp. 7150–7156, 2005.

[51] Ugalde–Loo CE, Licéaga–Castro E, Licéaga–Castro J. *2x2 Individual Channel Design MATLAB® Toolbox*. Proceedings of the Joint 44th IEEE Conference on Decision and Control and European Control Conference, pp. 7603–7608, Sevilla, Spain, 2005.

[52] Aree P, Acha E. *Block diagram model for fundamental studies of a synchronous generator – static VAR compensator system*. IEE Proceedings on Generation, Transmission and Distribution, **146**, no. 5, pp. 507–514, 1999.

[53] Kapoor SC. *Dynamic Stability of Static Compensator – Synchronous Generator Combination*. IEEE Transactions on Power Apparatus and Systems, **100**, no. 4, pp. 1694–1702, 1981.

[54] Aree P. *Small Signal Stability Modelling and Analysis of Power Systems with Electronically Controlled Compensation*. PhD Thesis. Department of Electronics and Electrical Engineering, University of Glasgow, Scotland, UK, 2000.

[55] Chen J, Milanovic JV, Hughes FM. *Comparison of the Effectiveness of PSS and SVC in Damping of Power System Oscillations.* Proceedings of the International Conference on Electric Power Engineering, pp. 103, 1999.

[56] Chen J, Milanovic JV, Hughes FM. *Selection of Auxiliary Input Signal and Location of a SVC for Damping Electromechanical Oscillations.* Proceedings of the IEEE Power Engineering Society Winter Meeting, **2**, pp. 623–627, 2001.

[57] Hammad AE, El-Sadek M. *Application of a Thyristor Controlled VAr Compensator for Damping Subsynchronous Oscillations in Power Systems*. IEEE Transactions on Power Apparatus and Systems, **103**, no. 1, pp. 198–212, 1984.

[58] Chen XR, Pahalawaththa NC, Annakkage UD, Kumble CS. *Output Feedback TCSC Controllers to Improve Damping of Meshed Multi-machine Power Systems.* IEE Proceedings on Generation, Transmission and Distribution, **144**, Part C, no. 3, pp. 243–248, 1997.

[59] Helbing SG, Karady GG. *Investigations of an Advanced Form of Series Compensation.* IEEE Transactions on Power Delivery, **9**, no. 2, pp. 939–947, 1994.

[60] Larsen EV, Clark K, Miske SS, Urbanek J. *Characteristic and Rating Considerations of Thyristor Controlled Series Compensation.* IEEE Transactions on Power Delivery, **9**, no. 2, pp. 883–841, 1994.

[61] Zhou X, Liang J. *Overview of Control Schemes for TCSC to Enhance the Stability of Power System.* IEE Proceedings on Generation, Transmission and Distribution, **146**, C, no. 2, pp. 125–130, 1999.

Chapter 2

STATE OF ART

2.1. Introduction

The synchronous generator is an essential component of a conventional power system. It is the main source of electrical energy, which is sent to the points of consumption using a mesh of high voltage transmission lines and into low voltage distribution systems [1]. From the operational point of view, the quality of power supply should meet stringent standards of frequency and voltage levels; therefore, several control structures exist in order to maintain key variables within adequate operating limits. For instance, in the generating plant itself, turbine-governor systems and excitation control systems, respectively, regulate frequency and output voltage magnitude at the terminals of the generating plant [2]. Meanwhile, in the high-voltage transmission network, devices such as synchronous condensers and tap-changing transformers control voltage magnitude and phase-shifting transformers may be used to regulate active power flow [3]. Moreover, many technological advances in power electronics have taken place and a wide range of advanced power plant controllers have become available. Such controllers, generically known as Flexible AC Transmission System (FACTS) devices, enhance the power transfer capacity of existing transmission corridors by making them electronically controllable [4]. These controllers have been developed to provide almost instantaneous power flow regulation and voltage magnitude control at key points of the transmission network, decreasing line losses and generation costs and improving the overall stability and security of the power system [5].

The accurate and adequate modelling of emerging and established power plant components is mandatory in order to carry out meaningful dynamic studies of modern interconnected power systems. Once a satisfactory representation exists, its performance can be assessed by using a wide variety of existing methods; among them are the synchronising and damping coefficients method, frequency response methods, root-locus plots, state-space analysis by eigenvalues and eigenvectors, and block diagrams [1]. Some of these techniques, such as block diagrams, yield great physical insight into how system variables interact with each other [6]; however, such benefits become blurred when conducting studies of more than one machine. On the other hand, the use of eigenvalue and eigenvector analysis,

although popular in the study of large-scale systems, relies exclusively on mathematical abstraction and physical insight is almost non-existent. Hence, it is of great interest to develop analysis tools and methods which do not suffer unduly from the lack of physical transparency and that would also be applicable to large-scale systems. The introduction of the Individual Channel Analysis and Design (ICAD) framework [7] in the early 90s looks like a suitable alternative to existing methods and techniques, with which to carry out small-signal stability studies of modern power systems.

In this chapter, the mathematical models of power system components suitable for small-signal stability studies are addressed. Emphasis is placed on the mathematical modelling of synchronous generators and electronically controlled shunt and series compensation. The chapter starts by reviewing the basic theory and classification of synchronous generator models. An overview of the main characteristics of relevant FACTS devices is then presented. Particular attention is paid to FACTS devices that are able to provide dynamic damping and that have shown to be the most popular in practice, such as the Static VAr Compensator (SVC) and the Thyristor-Controlled Series Compensator (TCSC). The importance of power system oscillations and damping is highlighted. The chapter closes with a brief description of the ICAD framework and the representation of multivariable systems in individual channels.

2.2. The synchronous machine

An electrical power system comprises thousands of individual elements of various kinds. When connected together, they form large complex systems capable of generating, transmitting and distributing electrical energy over large geographical areas. Synchronous machines are essential components of such systems: synchronous generators are the main source of electrical energy, while many large loads are driven by synchronous motors [1]. In fact, most stability issues in power system operation are concerned with studying the behaviour of synchronous generators following a perturbation [2,8].

Detailed modelling and analysis of the synchronous generator has been a subject of study for over fifty years. Its theory and performance have been covered in a vast number of books [1,3,9–16]. In system stability studies, the basic approach to generator modelling is to consider the machine as an arrangement of three armature windings, 120 electrical degrees apart, mounted on the stator and a rotating structure (or rotor) with a field winding and one or more damper windings. The synchronous machine is basically an AC rotating machine whose speed under steady-state condition is proportional to the frequency of the current in its armature. The magnetic field created by the armature currents rotates at the same speed as that created by the field current on the rotor, which is rotating at the synchronous speed, and a steady

torque results. During steady-state operation this winding arrangement is amenable to a DC magnetic field rotating at synchronous speed.

Figure 2.1 shows the schematic diagram of an elementary three-phase synchronous machine with one pair of field poles [1]. It illustrates the two essential elements of the three-phase synchronous machine: the field and the armature. The field winding gives rise to poles *N* (north) and *S* (south), as marked in the figure. The axis of the field poles is called the direct axis or simply *d*-axis, and it is centred along the centreline of the south-north pole; the centreline of the inter-polar space is called the quadrature axis or simply the *q*-axis. The position of the rotor relative to the stator is measured by the angle θ_r between the *d*-axis and the magnetic axis of phase *a* winding. The selection of the *q*-axis as leading the *d*-axis is an arbitrary one. This widely used convention is based on the IEEE standard definition [17] and it will be the one adopted in this work. Alternatively, the *q*-axis could be chosen to lag the *d*-axis by 90° [1,2,3,14,15].

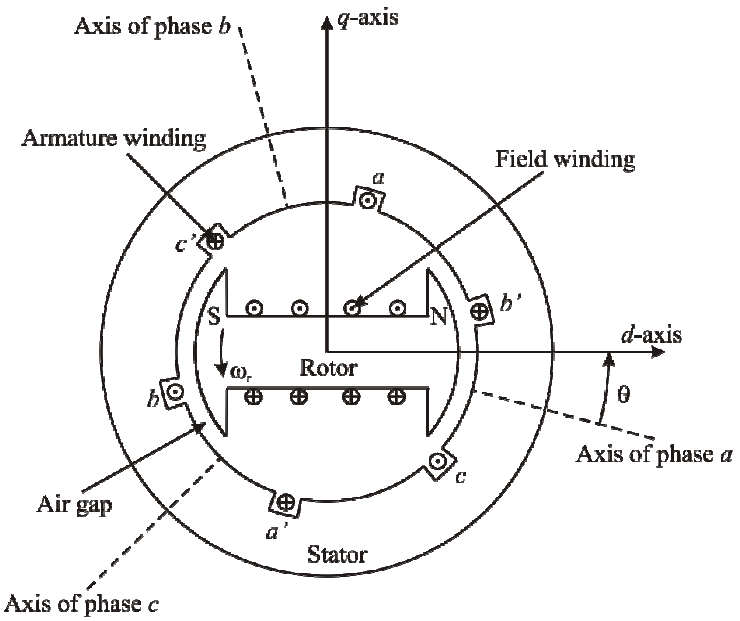

Figure 2.1. Schematic diagram of an elementary three-phase synchronous machine

2.2.1. Synchronous machine description and operation

Consider the synchronous machine representation shown in Figure 2.1. When excited, the rotating field winding carries direct current, which produces a rotating magnetic field that revolves with the rotor. When carrying balanced three-phase currents, the armature will produce a magnetic field rotating at synchronous speed in the air-gap. That is, the mmf (magnetomotive force) wave due to stator currents is stationary with respect to the rotor. The high mmf produced by the field current in the field winding combines with the mmf produced by the currents in the armature windings. The resultant flux across the air gap between the stator and rotor induces alternating voltages in the coils of the armature windings and provides the electromagnetic torque between the stator and the rotor. The three-phase windings of the

armature are distributed 120° apart (in space) so that, with uniform rotation of the magnetic fields, voltages displaced by 120° (in time phase) will be produced in the windings. The production of torque in the machine results from the natural tendency of the two magnetic fields (stator and rotor) to align themselves. For production of steady torque, the fields of stator and rotor must rotate at the same speed. Therefore, the rotor must run at precisely the synchronous speed, dictated by the number of field poles in the rotor and the electric frequency of stator currents [1,3,10,11,15,16].

Figure 2.2 shows the schematic diagram of a typical generating unit [6]. The machine's rotor is driven by a prime mover, which is usually a steam or a hydraulic turbine. The electromagnetic torque developed by the generator when delivering power opposes the torque of the prime mover. Differences resulting between these two torques are due to losses in the iron core and friction. The turbine is equipped with a governor to control the generator's speed according to a pre-set power-frequency characteristic [18]. The generated power is fed into the transmission network via a step-up transformer. Concerning the motor operation of a synchronous machine, the developed electromagnetic torque is converted to the shaft torque which drives the mechanical load [3].

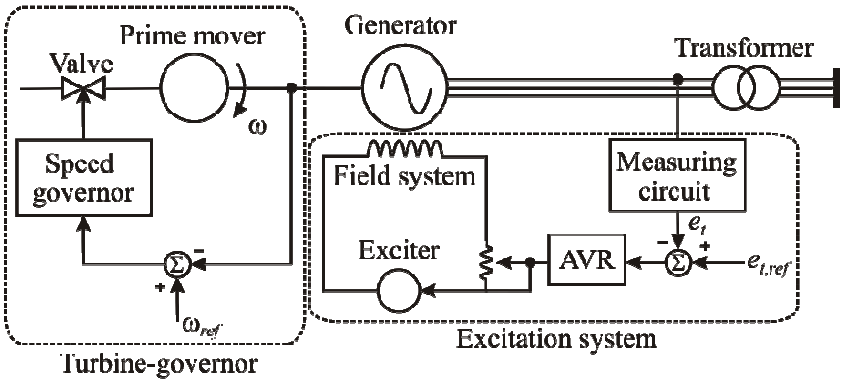

Figure 2.2. Generating unit

The direct current is supplied to the field winding by an exciter, which may be a generator mounted on the same shaft (self-excitation) or a separately source connected to the field winding through brushes bearing on slip rings (external excitation). Large generators usually have exciters consisting of an AC source with solid-state rectifiers. Otherwise, the external source can be a shaft-driven DC generator or a separately excited DC generator [3]. In Figure 2.2, the generator output voltage is regulated by an Automatic Voltage Regulator (AVR). Both the turbine-governor and the excitation systems will be given particular attention in Chapter 3.

The number of field poles in the rotor is determined by the mechanical speed of the rotor and electric frequency of stator currents. The synchronous speed is given by [3]

$$n = \frac{120\,f}{p_f} \tag{2.1}$$

where n is the speed in *rev/min*, f is the frequency in *Hz*, and p_f is the number of poles.

In practice, two basic rotor structures are used depending on speed. Hydraulic turbines operate at low speeds; therefore, a relatively large number of poles are required to produce the rated frequency. A rotor with salient poles and concentrated windings is better suited mechanically to this situation. Such rotors often have damper windings or amortisseurs (continuous or discontinuous), which are intended to damp out speed oscillations around synchronous speed. On the other hand, steam and gas turbines operate at high speeds. Their generators have round or cylindrical rotors featuring two or four field poles, formed by distributed windings. They often do not have damper windings, but the solid steel rotor offers paths for eddy currents which have effects equivalent to amortisseur windings [1].

2.2.2. Synchronous machine modelling

Figure 2.3 shows the schematic representation of the circuits involved in the analysis of the synchronous machine. The stator circuits consist of three-phase armature windings carrying alternating currents. The rotor circuits comprise the field and one or more damper windings. The field is connected to a source of direct current. For the purpose of analysis, the currents in the damper winding may be assumed to flow in two sets of closed circuits: one set whose flux is in line with that of the field axis or along the *d*-axis and the other set whose flux is at right angles to the field axis or along the *q*-axis [1]. Subscript *k* stands for the *k*-th damper circuit in the *d*- and *q*-axis (with $k = 1,2,\ldots,n$ and *n* is the number of damper windings). Notice that the *q*-axis leads the *d*-axis by 90° in accordance with the IEEE standard definition [17].

Differential and algebraic equations (not shown) associated with the stator and rotor circuits of Figure 2.3 completely describe the electrical performance of a synchronous machine [1]. However, such equations contain inductance terms which vary with angle θ_r which in turn varies with time. This introduces considerable complexity in solving machine and power system problems.

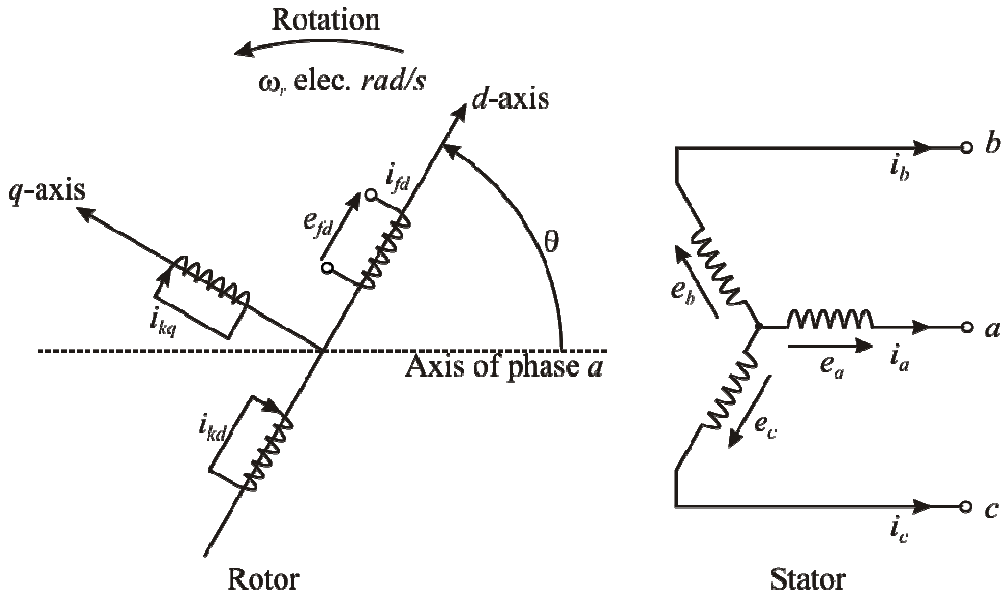

Figure 2.3. Stator and rotor circuits of a synchronous machine

The equations describing the physical behaviour of the synchronous machine can be expressed in a simpler form by transforming the *a*, *b*, *c* variables of the stator into corresponding sets of new variables, called the direct-axis, quadrature-axis and zero-sequence quantities, which are distinguished by the subscripts *d*, *q*, and 0, respectively [3]. To this end, the mathematical tool called Park's transformation is used [19,20], which defines a set of currents, voltages and flux linkages for three fictitious coils (the stationary 0-coil and the *d*-coil and *q*-coil, which rotate in synchronism with the rotor). Mathematically, all time varying three-phase voltages, currents and flux linkages are transformed into time invariant direct and quadrature axes quantities. In the transformed framework, deviations in speed of the rotor structure are easily accounted for as a function of the stator direct and quadrature axes flux linkages and voltages relationships. The circuit representation of the equivalent synchronous generator is shown in Figure 2.4.

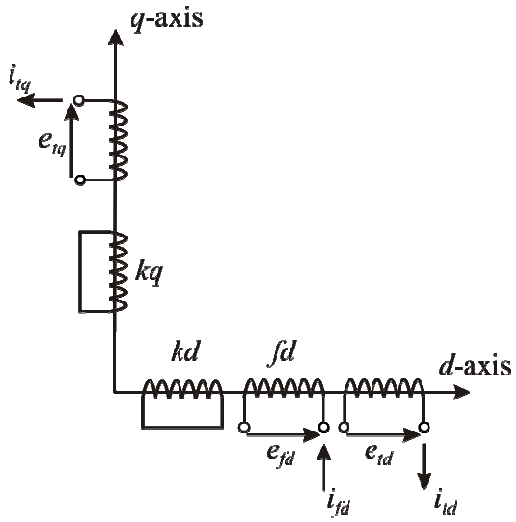

Figure 2.4. Machine equivalent circuit after applying Park's transformation

The *dq*0 transformation may be viewed as a means of referring the stator quantities to the rotor side in an analogous way as the secondary side quantities of a transformer are referred to the primary side by means of the turns ratio [1]. The analysis of the synchronous machine equations in *dq*0 variables is simpler than in terms of phase quantities since

- the dynamic performance equations have constant inductances;
- zero sequence quantities disappear for balanced conditions; and
- parameters associated with *d*- and *q*-axis may be directly measured from terminal tests.

For transient analysis, it is suitable to consider a *two-axis model*. The model shown in Figure 2.4 represents the best known configuration of the generator model, in which the order is defined by the number of rotor circuits in both the *d*- and *q*-axis. Theoretically, rotor circuits may explicitly contain an arbitrary number of circuits. However, in reality this choice might be restricted since lack of standard data inhibits the use of highly elaborated rotor models except for very specialised studies [21].

For the purpose of power system stability studies, the most complex model that has appeared in the open literature is model (3*d*.3*q*), which comprises the field winding and two damper windings in the *d*-axis and three damper windings in the *q*-axis [21]. Based on this model, twelve circuit combinations are available, but according to some of the most authoritative material published in the field, it appears that only seven model structures are serious candidates for inclusion in large power system stability studies: (1*d*.0*q*), (1*d*.1*q*), (2*d*.1*q*), (2*d*.2*q*), (2*d*.3*q*), (3*d*.3*q*) and the constant voltage behind reactance model (or classical model) [21,22]. Five out of the seven model structures are key to this research work and their mathematical representations are given in the section below.

2.2.3. Synchronous generator mathematical representation

Assuming balanced conditions, the three-phase synchronous generator voltages, fluxes and currents are well defined in the two-dimensional *dq* reference frame using Park's transformation. The *dq* components may be expressed as phasors in a complex plane having *d*- and *q*-axis as coordinates, as shown in Figure 2.5, which is similar to the phasor representation of alternating quantities varying sinusoidally with respect to time. Phasor representations can be used to understand the relationships that exist between the various synchronous machine quantities in steady-state, transient and sub-transient conditions. For instance, Figure 2.6 shows the phasor diagram for the transient model of the synchronous generator [1,6].

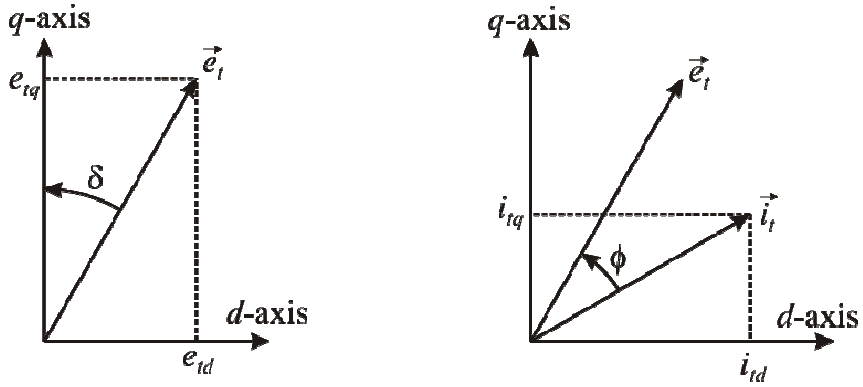

Figure 2.5. Representation of *dq* components of armature voltage and current as phasors

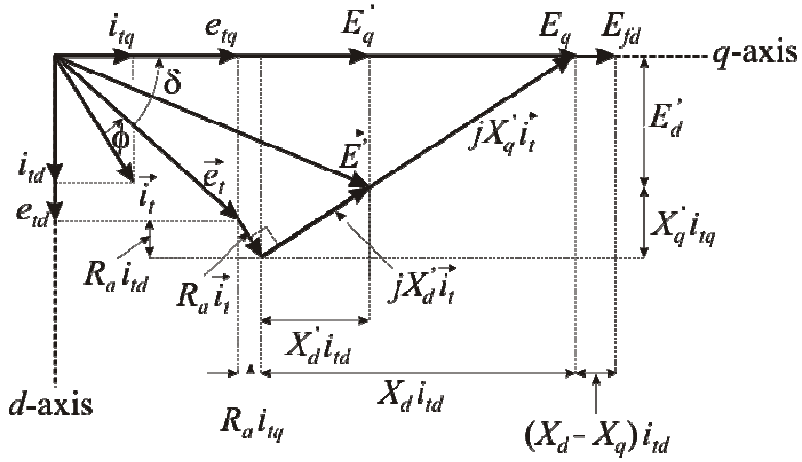

Figure 2.6. Synchronous generator phasor diagram for transient operation

From Figure 2.5, each phasor quantity can be represented in terms of its components as

$$\vec{i}_t = i_{td} + ji_{tq} \tag{2.2}$$

$$\vec{e}_t = e_{td} + je_{tq} \tag{2.3}$$

The algebraic equations for the synchronous machine transient model in Figure 2.6 can be written as [1]

$$E_d^{'} - e_{td} = R_a i_{td} - X_q^{'} i_{tq} \tag{2.4}$$

$$E_q^{'} - e_{tq} = R_a i_{tq} + X_d^{'} i_{td} \tag{2.5}$$

Equations (2.4) and (2.5) lead to the formulation of the following transient differential equations [23]:

$$\frac{dE_d^{'}}{dt} = \frac{1}{\tau_{q0}^{'}}\left[i_{td}\left(X_q - X_q^{'}\right) - E_d^{'} \right] \tag{2.6}$$

$$\frac{dE_q^{'}}{dt} = \frac{1}{\tau_{d0}^{'}}\left[E_{fd} - i_{tq}\left(X_d - X_d^{'}\right) - E_q^{'} \right] \tag{2.7}$$

The sub-transient algebraic [1] and differential [23] equations are developed similarly,

$$E_d^{''} - e_{td} = R_a i_{td} - X_q^{''} i_{tq} \tag{2.8}$$

$$E_q^{''} - e_{tq} = R_a i_{tq} + X_d^{''} i_{td} \tag{2.9}$$

$$\frac{dE_d^{''}}{dt} = \frac{1}{\tau_{q0}^{''}}\left[i_{td}\left(X_q^{'} - X_q^{''}\right) - E_d^{''} \right] \tag{2.10}$$

$$\frac{dE_q^{''}}{dt} = \frac{1}{\tau_{d0}^{''}}\left[E_q^{'} - i_{tq}\left(X_d^{'} - X_d^{''}\right) - E_q^{''} \right] + \frac{dE_q^{'}}{dt} \tag{2.11}$$

By means of Park's transformation, power relationships of the synchronous generator can be written in terms of *dq* components as [2]

$$\begin{aligned} S &= P_t + jQ_t \\ &= \vec{e}_t \vec{i}_t^{\,*} \end{aligned} \tag{2.12}$$

$$S = \left(e_{td} i_{td} + e_{tq} i_{tq}\right) + j\left(e_{tq} i_{td} + e_{td} i_{tq}\right) \tag{2.13}$$

Thus,

$$P_t = e_{td} i_{td} + e_{tq} i_{tq} \tag{2.14}$$

$$Q_t = e_{tq} i_{td} + e_{td} i_{tq} \tag{2.15}$$

The dynamic equation of motion, commonly known as swing equation since it represents swings in rotor angle δ during disturbances, is given by [1]

$$\frac{2H}{\omega_0}\frac{d^2\delta}{dt^2} = \left[P_m - P_e - D\Delta\omega\right] \tag{2.16}$$

which expressed as two first order differential equations becomes

$$\frac{d\Delta\omega}{dt} = \frac{1}{2H}\left[P_m - P_e - D\Delta\omega\right] \tag{2.17}$$

$$\frac{d\delta}{dt} = \omega_0 \Delta\omega \tag{2.18}$$

The rotational inertia equations (2.17) and (2.18) describe the electrical and mechanical power mismatches for the synchronous machine.

Suitable combination of (2.6), (2.7), (2.10) and (2.11), together with (2.17) and (2.18), provides different mathematical models of the synchronous generator of varying complexity and accuracy [1,6,21]:

- Model (2*d*.2*q*): For most practical purposes, this model is the most elaborated structure used in stability studies. It considers two windings in each axis (two damper circuits in the *q*-axis and a field circuit plus one damper circuit in the *d*-axis). The synchronous generator is represented by the sub-transient voltages $E_d^{"}$ and $E_q^{"}$ behind the sub-transient reactances $X_d^{"}$ and $X_q^{"}$, as defined by (2.8) and (2.9). The changes in $E_d^{"}$ and $E_q^{"}$ as the fluxes linking the rotor circuits decay are described by (2.6), (2.7), (2.10) and (2.11). Parameter values for this model are normally supplied by manufacturers. Two time constants and two rotor reactances and resistances are employed to describe the response of the model in each of the *d*- and *q*-axis. The model is applicable to round rotor generators. Overall, model (2*d*.2*q*) is of 6th order when the dynamic equation of motion described by (2.17) and (2.18) is considered.
- Model (2*d*.1*q*): With a single *q*-axis damper circuit, it is used to represent salient pole structures such as hydro-generators. In this model, no distinction is made, in the *q*-axis, between transient and synchronous (steady-state) conditions and only one *q*-axis rotor circuit is used for representing the rapidly decaying sub-transient effects. In other words, $X_q^{'} = X_q$ and $E_d^{'} = 0$; hence, equation (2.6) is eliminated from the set of equations associated with model (2*d*.2*q*). Model (2*d*.1*q*) is a 5th order model.
- Model (1*d*.1*q*): This model arises from a simplification to model (2*d*.2*q*), where the effects of the damper windings present in a round-rotor generator are neglected. Only two rotor windings are considered, the field winding in the *d*-axis and one damper winding in the *q*-axis. The synchronous generator is represented by the transient voltages $E_d^{'}$ and $E_q^{'}$ behind the transient reactances $X_d^{'}$ and $X_q^{'}$ as defined by (2.4) and (2.5). The changes in $E_d^{'}$ and $E_q^{'}$ are determined by (2.6) and (2.7), producing a 4th order model when considering the swing equation. Some variations can be made to produce other 4th order models, as it will be discussed in Chapter 3.
- Model (1*d*.0*q*): A further simplified structure of model (2*d*.2*q*), in model (1*d*.0*q*) all damper winding effects are neglected and only changes in the field flux linkages can be determined. The *d*-axis transient voltage is assumed to remain constant; therefore, $E_d^{'} = 0$ and $X_q^{'} = X_q$. This

model is of 3rd order, as the generator dynamics are only described by equations (2.7), (2.17) and (2.18). Although it was widely used until recently, its limitations are far too many to continue being used in small-signal stability studies.

- Classical representation: A 2nd order model, this representation assumes a constant voltage E' behind the transient reactance X'_d. The rotor flux linkages are assumed to be constant and no transient saliency exists. The voltages and currents are not resolved into *d*- and *q*-axis components. The existence of this model was justified in the past on the grounds that the time constant τ'_{d0} in equation (2.7) is relatively long. Under this assumption, E'_q is assumed to remain constant because changes in E_{fd} and i_{td} are small. An advantage of this model is that the interfacing of the generator and network equations is carried out with ease during step-by-step calculations, and a minimum amount of data is required; therefore, this model may be used for simplified analysis of power system transient stability. Similar models can be made for sub-transient and steady-state conditions.

2.2.4. Initial operation conditions

For stability analysis, it is necessary to obtain the initial steady-state operating conditions of the synchronous machine as a function of specified system loading [1], which can be found by applying a simple procedure. Starting from a power flow analysis – also termed load flow analysis [5] – and using machine parameters information, the steady-state operating point can be determined [2].

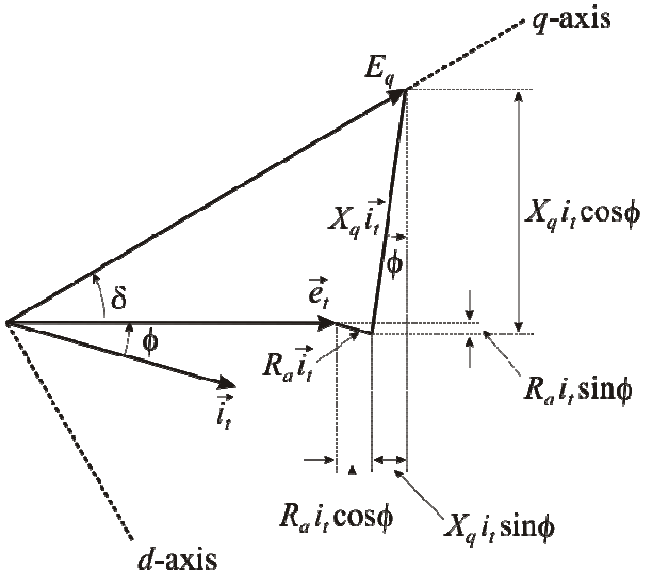

Figure 2.7. Steady-state phasor diagram

Consider the steady-state phasor diagram of Figure 2.7, where the terminal active power P_t, reactive power Q_t and magnitude of voltage e_t are specified using a power flow solution. The corresponding current i_t and power factor angle ϕ are given by

$$i_t = \frac{\sqrt{P_t^2 + Q_t^2}}{e_t} \tag{2.19}$$

$$\phi = \cos^{-1}\left(\frac{P_t}{e_t i_t}\right) \tag{2.20}$$

The internal rotor or load angle δ, which represents the angle by which the *q*-axis leads the stator terminal voltage phasor $\vec{e}_t$, is given by

$$\delta = \tan^{-1}\left(\frac{X_q i_t \cos\phi - R_a i_t \sin\phi}{e_t + R_a i_t \cos\phi + X_q i_t \sin\phi}\right) \tag{2.21}$$

Considering that the angle β of terminal voltage $\vec{e}_t$ is different from zero, that is, $\vec{e}_t = e_t \angle \beta$, where β accounts for the angular displacement from the *d*-axis with the axis of phase *a*, equation (2.21) becomes

$$\delta = \tan^{-1}\left(\frac{e_t \sin\beta + X_q i_t \cos\phi - R_a i_t \sin\phi}{e_t \cos\beta + R_a i_t \cos\phi + X_q i_t \sin\phi}\right) \tag{2.22}$$

With δ known, the *dq* components of stator voltage and current are given by

$$e_{td} = e_t \sin\delta \tag{2.23}$$

$$e_{tq} = e_t \cos\delta \tag{2.24}$$

$$i_{td} = i_t \sin(\delta + \phi) \tag{2.25}$$

$$i_{td} = i_t \cos(\delta + \phi) \tag{2.26}$$

From Figure 2.6, field voltage and voltages behind synchronous and transient reactances are given by

$$E_q = e_{tq} + R_a i_{tq} + X_d i_{td} \tag{2.27}$$

$$E_{fd} = E_q + (X_d - X_q) i_{td} \tag{2.28}$$

$$E_d' = e_{td} + R_a i_{td} - X_q' i_{tq} \tag{2.29}$$

$$E_q' = e_{tq} + R_a i_{tq} + X_d' i_{td} \tag{2.30}$$

In a similar way, voltages behind sub-transient reactances are expressed as

$$E_d'' = e_{td} + R_a i_{td} - X_q'' i_{tq} \tag{2.31}$$

$$E_q'' = e_{tq} + R_a i_{tq} + X_d'' i_{td} \tag{2.32}$$

Notice that (2.29)–(2.32) can be also obtained from (2.4), (2.5), (2.8) and (2.9).

2.2.5. Network reference frame

The previously synchronous generator equations are given in the machine's own *dq* reference frame. In a power system comprising different machines, each one has its own reference frame and rotates independently from the others in the network. Therefore, studies of interactions between machines

through the network are difficult unless the individual machine's reference frames are converted to a common reference frame. It makes sense to consider a network reference frame which rotates at synchronous speed [2]. Such a situation is reflected in Figure 2.7, which shows the terminal voltage of a machine both in its *dq* reference frame and in the network *DQ* reference frame.

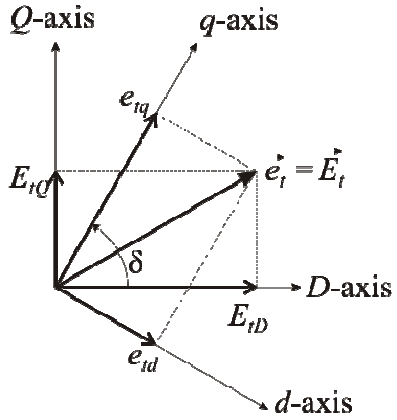

Figure 2.8. Two frames of reference for terminal voltage

The terminal voltage, in phasor notation, is given by (2.3). Let the same voltage, expressed in the new notation, be

$$\vec{E}_t = E_{tD} + jE_{tQ} \tag{2.33}$$

By inspection of Figure 2.8,

$$\begin{aligned} E_{tD} + jE_{tQ} &= \left[e_{tq}\cos\delta + e_{td}\cos\left(\pi/2 - \delta\right)\right] + j\left[e_{tq}\sin\delta - e_{td}\sin\left(\pi/2 - \delta\right)\right] \\ &= \left[e_{tq}\sin\left(\pi/2 - \delta\right) + e_{td}\cos\left(\pi/2 - \delta\right)\right] + j\left[e_{tq}\cos\left(\pi/2 - \delta\right) - e_{td}\sin\left(\pi/2 - \delta\right)\right] \\ &= \left[-e_{tq}\sin\left(\delta - \pi/2\right) + e_{td}\cos\left(\delta - \pi/2\right)\right] + j\left[e_{tq}\cos\left(\delta - \pi/2\right) + e_{td}\sin\left(\delta - \pi/2\right)\right] \\ &= \left(e_{td} + je_{tq}\right)\cos\left(\delta - \pi/2\right) + \left(-e_{tq} + je_{td}\right)\sin\left(\delta - \pi/2\right) \\ &= \left(e_{td} + je_{tq}\right)\left[\cos\left(\delta - \pi/2\right) + j\sin\left(\delta - \pi/2\right)\right] \end{aligned} \tag{2.34}$$

or

$$\vec{E}_t = e^{j\left(\delta - \pi/2\right)}\vec{e}_t \tag{2.35}$$

The previous expression has the following interpretation in matrix form,

$$\begin{bmatrix} E_{tD} \\ E_{tQ} \end{bmatrix} = \begin{bmatrix} \sin\delta & \cos\delta \\ -\cos\delta & \sin\delta \end{bmatrix} \begin{bmatrix} e_{td} \\ e_{tq} \end{bmatrix} \tag{2.36}$$

Similarly, for the currents

$$\vec{I}_t = e^{j\left(\delta - \pi/2\right)}\vec{i}_t \tag{2.37}$$

where the terminal current $\vec{i}_t$ is given by (2.2) and

$$\vec{I}_t = I_{tD} + jI_{tQ} \tag{2.38}$$

2.2.6. Electrical network

The previous equations of the synchronous machine are given in the form of a Thévenin voltage behind an impedance. On the other hand, the relationships between network bus (nodal) voltages and currents may be represented by either loop equations or nodal equations. However, the latter are normally preferred because the number of independent nodal equations is smaller than the number of independent loop equations [1]. For a nodal representation of the network equations, the machine's Thévenin equivalent is converted into a Norton equivalent [2]. The network current injection vector then includes the Norton equivalent current of each synchronous machine and the machine's admittance is added to the system admittance at the machine's busbar.

The matrix form of the network in terms of the nodal admittance matrix including *n* nodes can be written as [1]

$$\begin{bmatrix} \vec{I}_1 \\ \vec{I}_2 \\ \vdots \\ \vec{I}_n \end{bmatrix} = \begin{bmatrix} \bar{Y}_{11} & \bar{Y}_{12} & \cdots & \bar{Y}_{1n} \\ \bar{Y}_{21} & \bar{Y}_{22} & \cdots & \bar{Y}_{2n} \\ \vdots & \vdots & \ddots & \vdots \\ \bar{Y}_{n1} & \bar{Y}_{n2} & \cdots & \bar{Y}_{nn} \end{bmatrix} \begin{bmatrix} \vec{V}_1 \\ \vec{V}_2 \\ \vdots \\ \vec{V}_n \end{bmatrix} \qquad \bar{\mathbf{I}} = \bar{\mathbf{Y}}\bar{\mathbf{V}} \tag{2.39}$$

where $\bar{\mathbf{Y}}$ is the nodal admittance matrix, $\vec{V}_i$ is the phasor voltage to ground at node *i* and $\vec{I}_i$ is the phasor current flowing into the network at node *i*. The nodal admittance matrix $\bar{\mathbf{Y}}$ is formed by elements [2]

$$\begin{aligned} \bar{Y}_{ii} &= Y_{ii}\angle\theta_{ii} = \text{driving point admittance for node } i \\ &= G_{ii} + jB_{ii} \\ \bar{Y}_{ik} &= Y_{ik}\angle\theta_{ik} = \text{negative of the transfer admittance between nodes } i \text{ and } k \\ &= G_{ik} + jB_{ik} \end{aligned} \tag{2.40}$$

The nodal admittance matrix $\bar{\mathbf{Y}}$ in (2.39) has the following characteristics [1]:

- It is sparse, with the degree of sparsity increasing with the network size,
- It is singular if there are no shunt branches to the ground,
- It is symmetrical if there are no phase-shifting transformers,
- It has weak diagonal dominance, *i.e.*, $\left|\bar{Y}_{ii}\right| \geq \sum_{k\neq i}\left|\bar{Y}_{ik}\right|$

Static loads are converted to equivalent impedances or admittances, using nodal voltages obtained from a power flow solution [2]. If a load bus of voltage $\vec{V}_L$, active power P_L, reactive power Q_L, and current $\vec{I}_L$ flowing into an admittance $\bar{Y}_L = G_L + jB_L$, then

$$P_L + jQ_L = \vec{V}_L\vec{I}_L^{\,*} = \vec{V}_L\left[\vec{V}_L^{\,*}\left(G_L - jB_L\right)\right] = V_L^2\left(G_L - jB_L\right) \tag{2.41}$$

Hence, the equivalent shunt admittance at the bus is

$$\bar{Y}_L = \left(\frac{P_L}{V_L^2}\right) - j\left(\frac{Q_L}{V_L^2}\right) \tag{2.42}$$

The size of the network can be reduced by elimination of the passive nodes by applying Kron's reduction [1,2], which can be achieved by matrix operation. If loads are assumed to be static, then all nodes have zero current injection except for the internal generation nodes. The matrix form of the network including *n* machines and *r* loads can be written as

$$\begin{bmatrix} \vec{I}_{t1} \\ \vdots \\ \vec{I}_{tn} \\ 0 \\ \vdots \\ 0 \end{bmatrix} = \begin{bmatrix} \bar{Y}_{11} & \cdots & \bar{Y}_{1n} & \bar{Y}_{1(n+1)} & \cdots & \bar{Y}_{1r} \\ \vdots & \ddots & \vdots & \vdots & \ddots & \vdots \\ \bar{Y}_{n1} & \cdots & \bar{Y}_{nn} & \bar{Y}_{n(n+1)} & \cdots & \bar{Y}_{nr} \\ \bar{Y}_{(n+1)1} & \cdots & \bar{Y}_{(n+1)n} & \bar{Y}_{(n+1)(n+1)} & \cdots & \bar{Y}_{(n+1)r} \\ \vdots & \ddots & \vdots & \vdots & \ddots & \vdots \\ \bar{Y}_{r1} & \cdots & \bar{Y}_{rn} & \bar{Y}_{r(n+1)} & \cdots & \bar{Y}_{rr} \end{bmatrix} \begin{bmatrix} \vec{E}_{t1} \\ \vdots \\ \vec{E}_{tn} \\ \vec{V}_{(n+1)} \\ \vdots \\ \vec{V}_r \end{bmatrix} \tag{2.43}$$

or more compactly, as

$$\begin{bmatrix} \bar{\mathbf{I}}_t \\ \cdots \\ \mathbf{0} \end{bmatrix} = \begin{bmatrix} \bar{\mathbf{Y}}_{nn} & \vdots & \bar{\mathbf{Y}}_{nr} \\ \cdots\cdots & \vdots & \cdots\cdots \\ \bar{\mathbf{Y}}_{rn} & \vdots & \bar{\mathbf{Y}}_{rr} \end{bmatrix} \begin{bmatrix} \bar{\mathbf{E}}_t \\ \cdots \\ \bar{\mathbf{V}}_r \end{bmatrix} \tag{2.44}$$

Expressing (2.44) in equation form:

$$\bar{\mathbf{I}}_t = \bar{\mathbf{Y}}_{nn}\bar{\mathbf{E}}_t + \bar{\mathbf{Y}}_{nr}\bar{\mathbf{V}}_r \tag{2.45}$$

$$\mathbf{0} = \bar{\mathbf{Y}}_{rn}\bar{\mathbf{E}}_t + \bar{\mathbf{Y}}_{rr}\bar{\mathbf{V}}_r \tag{2.46}$$

Solving for $\bar{\mathbf{V}}_r$ in (2.46) and substitution in (2.45) provides

$$\bar{\mathbf{I}}_t = \left(\bar{\mathbf{Y}}_{nn} - \bar{\mathbf{Y}}_{nr}\bar{\mathbf{Y}}_{rr}^{-1}\bar{\mathbf{Y}}_{rn}\right)\bar{\mathbf{E}}_t \tag{2.47}$$

or

$$\bar{\mathbf{I}}_t = \bar{\mathbf{Y}}_n\bar{\mathbf{E}}_t \tag{2.48}$$

Matrix $\bar{\mathbf{Y}}_n$, with dimensions ($n \times n$), is the desired reduced admittance matrix.

2.3. An overview of FACTS devices

Flexible AC Transmission Systems (FACTS) is a recent technological development in electrical power systems. It builds on the great many advances achieved in high-current, high-power semiconductor device technology, digital control and signals conditioning [5]. The FACTS concept is based on the substantial incorporation of modern power electronics devices and methods into the high-voltage side of the power

network, to make it *electronically-controllable* [4,24,25,26]. FACTS devices are deployed at key locations of the high-voltage transmission system in order to control and adjust one or more of the main parameters in the transmission system. By introducing flexible and rapid control of key AC transmission parameters, the FACTS technology enhances the power transfer capacity of existing transmission corridors, decreases line losses and generation costs, and improves the stability and security of the power system [4,5].

It should be mentioned that the ability of the transmission system to transmit power becomes impaired by the following (steady-state and dynamic) limitations [5]:

- *Angular stability*: Ability of synchronous machines of an interconnected power system to remain in synchronism after being subjected to a disturbance [27].
- *Transient stability*: Ability of the power system to maintain synchronism when subjected to a severe disturbance, such as a short circuit on a transmission line [27].
- *Voltage stability* (*regulation*): Ability of a power system to maintain steady voltages at all buses in the system after being subjected to a disturbance from a given initial operating condition [27].
- *Frequency stability*: Ability of a power system to maintain steady frequency following a severe system upset resulting in a significant imbalance between generation and load [27].
- Thermal limits.

These limits define the maximum amount of electrical power that can be transmitted without damaging the transmission lines and the equipment. Such limitations may be relieved by the addition of new transmission and generation facilities. Nevertheless, FACTS controllers can meet the same objectives with no major alterations of the system layout [4,5].

Within the basic system security guidelines, FACTS controllers enable transmission owners to obtain, on a case-by-case basis, one or more of the following potential benefits [4,5,24–26]:

- Control of power flows, including reductions of loop flows and of reactive power flows, thus allowing the lines to carry more active power.
- Increase the loading capability of lines to their thermal capabilities.
- Increase the system security and reliability through raising the transient stability limit, limiting short-circuit currents and overloads, managing cascading blackouts and damping electromechanical oscillations of power systems and machines.
- Provide secure tie-line connections to neighbouring utilities and regions thereby decreasing overall generation reserve requirements on both sides.
- Provide greater flexibility in siting new generation.
- Upgrade of lines.
- Increase utilisation of lowest cost generation through cost-effective enhancement of capacity.

- Overall enhancement of the quality of the electric energy delivered to consumers.

Due to the great many advances of modern power electronic technology, a wide range of FACTS devices has emerged in recent years. This section outlines the main operating characteristics of some relevant FACTS devices.

2.3.1. Static VAr Compensator (SVC)

Power electronic circuits using conventional thyristors, such as the SVC, have been widely used in power transmission applications since the mid-70s, long before the concept of FACTS had been formulated [28,29]. The SVC was first demonstrated in Nebraska and commercialised by GE in 1974 and Westinghouse in 1975 [4]. The primary role of the SVC is to adjust the amount of reactive power compensation at the point of connection to the AC network. It behaves like a shunt-connected variable reactance, which either generates or absorbs reactive power in order to regulate voltage magnitude. The firing angle control of the thyristor enables the SVC to have an almost *instantaneous* speed of response; hence, providing fast reactive power and voltage regulation support with no moving parts involved in contrast to mechanically-controlled shunt elements. In its simplest form, it consists of fast thyristor switches controlling a Thyristor-Controlled Reactor (TCR) in parallel with a bank of capacitors (FC) [5,6].

The TCR can be defined as a shunt-connected thyristor-controlled inductor whose effective reactance is varied in a continuous manner by partial-conduction control of the thyristor valve [4]. It is usually connected in delta configuration to cancel out the third harmonic currents [5]. The *controllable* element is the anti-parallel thyristor pair, which conducts on alternate half-cycles of the supply frequency. The thyristors may be switched on at any point of the voltage wave (from 90 to 180 electrical degrees) to provide fully adjustable control over the range of rated reactive power absorption, at the expense of generating harmonic distortion except for the condition of full conduction [5]. The other component is the linear inductor. The overall action of the thyristor controller on the reactor is to enable it to act as a variable susceptance, which is a function of the firing angle.

Figure 2.9 shows a schematic representation of the SVC, where a three-pulse, three-winding transformer is used to interface the SVC to a high-voltage bus. The transformer has two identical secondary windings, one of which is used for the delta-connected six-pulse TCR and the other for the star-connected, three-phase bank of capacitors. It is observed that the three transformer windings are star-connected.

A simplified form of the FC-TCR, suitable for analysis, is shown in Figure 2.10 [6]. The fixed capacitor provides a permanently connected source of reactive power. The variable shunt reactance is adjusted in order to control voltage magnitude at the network point of connection.

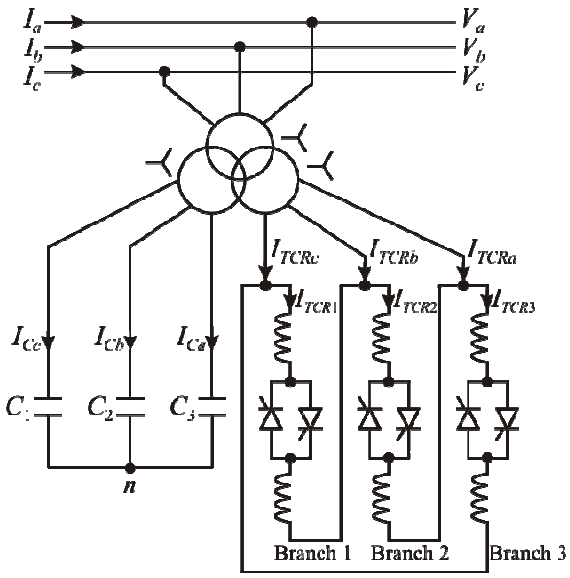

Figure 2.9. Representation of a three-phase FC-TCRs structure of the SVC

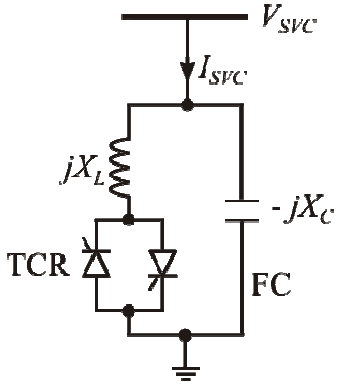

Figure 2.10. Simplified representation of the FC-TCRs structure of the SVC

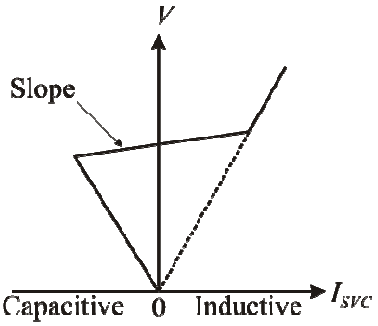

Figure 2.11. Voltage-current composite characteristic of the SVC

The SVC voltage-current (V/I) characteristic for the FC-TCR structure is shown in Figure 2.11 [6]. Depending on the SVC's equivalent reactance, *i.e.*, capacitive or inductive, Figure 2.11 indicates that the SVC is capable of drawing capacitive or inductive current from the power system. Suitable control of the equivalent reactance allows continuous voltage regulation at the node where the SVC is connected. The range of the slope is determined by the capacitive and inductive susceptance limits. These susceptances represent the total SVC susceptance required to maintain the voltage magnitude at the specified value. The expression for the total susceptance value is given by [30]

$$B_{SVC} = B_C - B_L(\alpha) \tag{2.49}$$

where

$$B_C = 2\pi fC \tag{2.50}$$

$$B_L(\alpha) = \frac{2}{\pi X_L}\left\{(\pi - \alpha) + \frac{1}{2}\sin 2\alpha\right\} \tag{2.51}$$

The general SVC control scheme shown in Figure 2.12 is normally used for stability studies [1,6]. The conventional control block of the SVC voltage regulator consists of the gain K_r and the time constant τ_r. The next block in line is the thyristor susceptance control block, which represents the variation of reactor susceptance as a function of firing angle. The parameter τ_d is a gating transport delay of typical values of around 1 *ms*; hence, it is normally neglected. Similarly, the time constant τ_b associated with the thyristor firing sequence control, of values of around 5 *ms*, can be also neglected in most studies. Thus, under such simplifying assumptions, this block may be represented by a unity gain with no time delay. The SVC control system takes the feedback voltage from the high-voltage side of the connecting node. The time delay, τ_m, represents the lagging time constant of the measuring circuit, which is also neglected in most studies. Conventional and optional additional signals, such as the speed signal, can also be injected at the summing points to improve the overall system dynamic performance. The operation and control of the SVC will be investigated in Chapter 4.

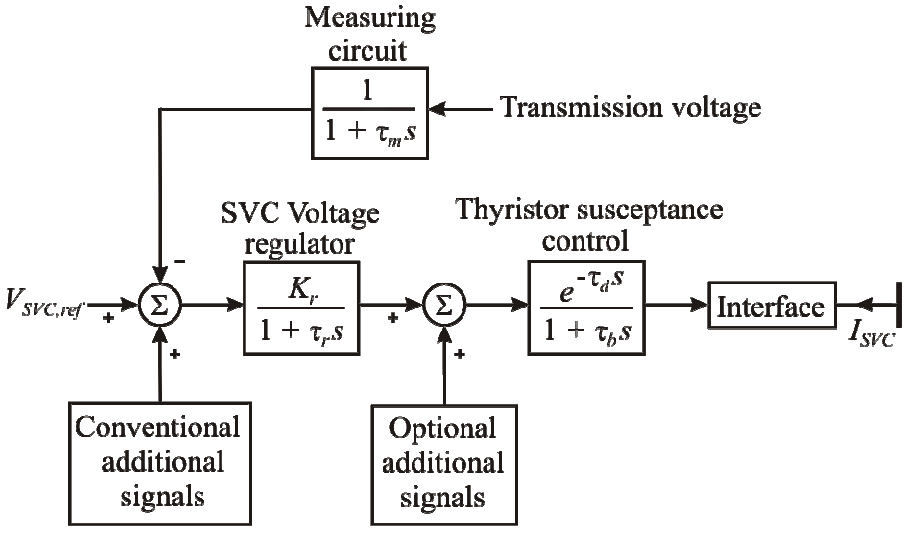

Figure 2.12. SVC block diagram model

2.3.2. Thyristor-Controlled Series Compensator (TCSC)

The TCSC is the electronically-controlled counterpart of the conventional series banks of capacitors. Series capacitive compensation schemes are used in order to increase the transmission lines power transmission capability by reducing the electrical length of the line. In these conventional schemes the series capacitive modules are either permanently connected or actioned by electromechanical switches

[26]. However, electromechanical devices have a relatively slow response. On the other hand, the TCSC is able to rapidly control the line compensation over a continuous range with little delay, resulting in increased flexibility. This characteristic enables the TCSC to be used to provide fast active power flow regulation along the compensated line and to rapidly modulate the effective impedance of the line in response to dynamic events in the vicinity of the line. It also increases the stability margin of the system and has proved very effective in damping sustained oscillations at sub-synchronous frequencies, a phenomenon termed sub-synchronous resonance (SSR), and power oscillations [4,26,28,29,31,32].

The basic TCSC module comprises a TCR in parallel with a fixed capacitor, and an actual TCSC installation may comprise several modules or only one or two controllable modules in series with fix capacitor modules. For the purpose of positive sequence application studies, such as power flows and small-signal stability, the TCSC may be adequately represented by an equivalent reactance, which is a function of the thyristor gating signals. This equivalent representation, shown in Figure 2.18, enables a straightforward representation of the TCSC in the form of a nodal transfer matrix. In three-phase installations, three independent TCSC modules may be used, one for each phase [5].

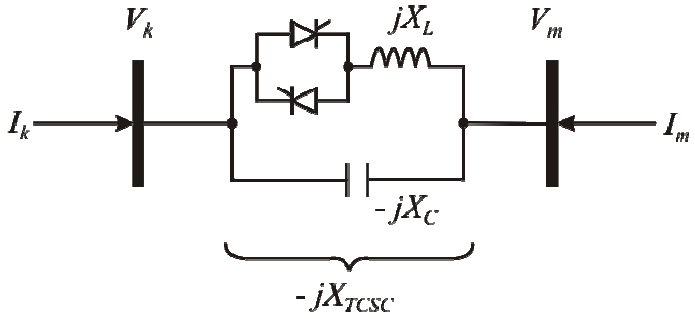

Figure 2.18. Physical structure of one phase of a TCSC comprising an equivalent capacitor and a TCR

The TCR achieves its fundamental frequency operating state at the expense of generating harmonic currents, which are a function of the thyristor conduction angle. Nevertheless, in the TCSC application the TCR harmonic currents are trapped inside the TCSC because of the low impedance of the capacitor compared with the network equivalent impedance [5]. It should be mentioned that normally the TCSC does not operate in inductive mode as this would increase the electrical length of the compensated transmission line, with adverse consequences on stability margins and extra losses. However, both the capacitive and inductive modes of operation will be investigated in detail in Chapter 4.

The expression for the fundamental frequency of the TCSC impedance, as a function of the thyristor's firing angle is given as [33]

$$\begin{aligned} X_{TCSC} = &-X_C + C_1\left\{2(\pi-\alpha)+\sin\left[2(\pi-\alpha)\right]\right\}+ \\ &-C_2\cos^2(\pi-\alpha)\left\{\lambda\tan\left[\lambda(\pi-\alpha)\right]-\tan(\pi-\alpha)\right\} \end{aligned} \tag{2.52}$$

where

$$C_1 = \frac{X_C + X_{LC}}{\pi} \tag{2.53}$$

$$C_2 = \frac{4X_{LC}^2}{\pi X_L} \tag{2.54}$$

$$\lambda = \frac{\omega_0}{\omega} = \sqrt{\frac{X_C}{X_L}} \tag{2.55}$$

$$X_{LC} = \frac{X_C X_L}{X_C - X_L} \tag{2.56}$$

$$\omega_0^2 = \frac{1}{LC} = \omega^2 \frac{X_C}{X_L} \tag{2.57}$$

In power system operation and control, the TCSC has two key roles to play: to schedule active power flow and to enhance dynamic performance. In the latter application area, the control system becomes a matter of great importance, and a distinction is drawn between the transient stability control loop and the power damping control loop [34–37]. The former is a pre-programmed open-loop control used to improve first swing stability. The control allows for maximum compensation level just after the occurrence of a fault in the power network and it remains so for a pre-specified period of time. The control is then transferred to the damping control loop to mitigate the ensuing power oscillations [38]. For small-signal stability purposes, only the damping control loop is of practical relevance. Figure 2.19 shows a generic block diagram of the TCSC control which is well suited for small-signal stability studies [39].

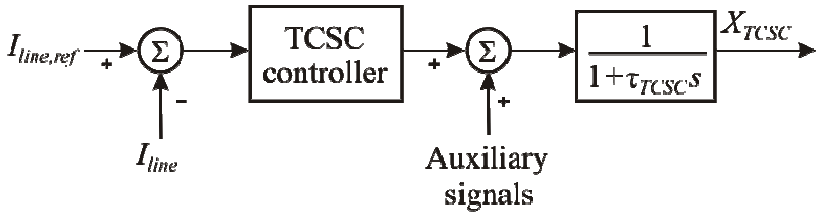

Figure 2.19. TCSC control block diagram

Figure 2.19 shows a TCSC block diagram consisting of a control module and a first-order lag transfer function representing the time delay τ_{TCSC} associated with the thyristor's firing angle control. However, since the value of τ_{TCSC} varies from 15 to 30 *ms*, it is normally neglected in small-signal stability studies [39]. For the TCSC control block, a simple control scheme such as a PI controller is normally used to schedule power [6]. The current signal derived from the network (I_{line}) is compared with the reference signal ($I_{line\text{-}ref}$) in order to control active power flow, which is achieved by adjusting the TCSC reactance (X_{TCSC}). The auxiliary signal can be used for the purpose of damping system oscillations with the input coming from an additional damping control loop.

2.3.3. Voltage Source Converter-based FACTS equipment

2.3.3.1. Static Compensator (STATCOM)

The STATCOM is a static synchronous condenser whose capacitive or inductive output current can be controlled independently of the AC system voltage [4,5,26,29]. It generates/absorbs reactive power at a faster rate either than a synchronous generator or condenser because no moving parts are involved. It performs the same voltage regulation function as the SVC but in a more robust manner since its operation is not impaired by the presence of low voltages [5].

The STATCOM can be based on the Voltage Source Converter (VSC) or the Current Source Converter (CSC) principle, although the former seems to be the preferred alternative owing to costs considerations [4]. Figure 2.20 shows a schematic representation of the STATCOM and its equivalent circuit. It consists of a VSC [40–43] and an associated shunt-connected transformer. The equivalent circuit corresponds to the Thévenin equivalent as seen from bus *k*, with the voltage source E_{vR} being the fundamental frequency component of the VSC output voltage, resulting from the product of V_{DC} and the amplitude modulation ratio m_a.

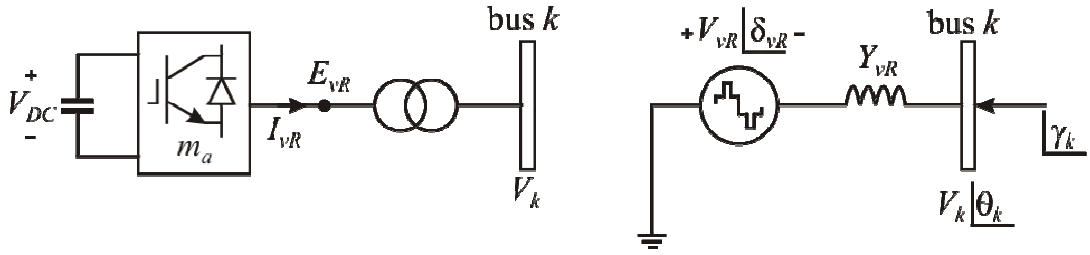

(*a*) (*b*)

Figure 2.20. STATCOM system: (*a*) VSC connected to the AC network via a shunt-connected transformer; (*b*) equivalent circuit in the form of a shunt solid-state voltage source

In steady-state fundamental frequency studies, the STATCOM may be represented in the same way as a rotating synchronous condenser, which in most cases is modelled as a synchronous generator with zero active power generation. A more flexible model represents the STATCOM as a variable voltage source for which the magnitude and phase angle may be adjusted to satisfy a specified voltage magnitude at the point of connection with the AC network. The per-phase shunt voltage source of the STATCOM may be given by [5]

$$\begin{aligned} E_{vR} &= V_{vR} e^{j\delta_{vR}} \\ &= V_{vR}\left(\cos\delta_{vR} + j\sin\delta_{vR}\right) \end{aligned} \tag{2.58}$$

The voltage magnitude V_{vR} is given maximum and minimum limits, which are a function of the STATCOM capacitor rating. However, δ_{vR} may take any value between 0 and 2π radians. With reference to the equivalent circuit of Figure 2.20, a transfer admittance equation can be written [5].

As the STATCOM comprises a VSC, it should include a switching strategy in order to control the switching sequence of the various semiconductor devices in the VSC, aiming at producing an output voltage waveform, that is as near to a sinusoidal waveform as possible. VSC switching strategies may be classified in two main categories: (1) fundamental frequency switching and (2) pulse-width modulation (PWM). Both of them are fully documented in literature [40–46]. In either case, in fundamental frequency application studies it is assumed that perfect filters exist at the AC side of the STATCOM.

2.3.3.2. Unified Power Flow Controller (UPFC)

The UPFC is a combination of a STATCOM and a Static Synchronous Series Compensator (SSSC), which are coupled via a common DC link, to allow bidirectional flow of active power between the series output terminals of the SSSC and the shunt output terminals of the STATCOM [4].

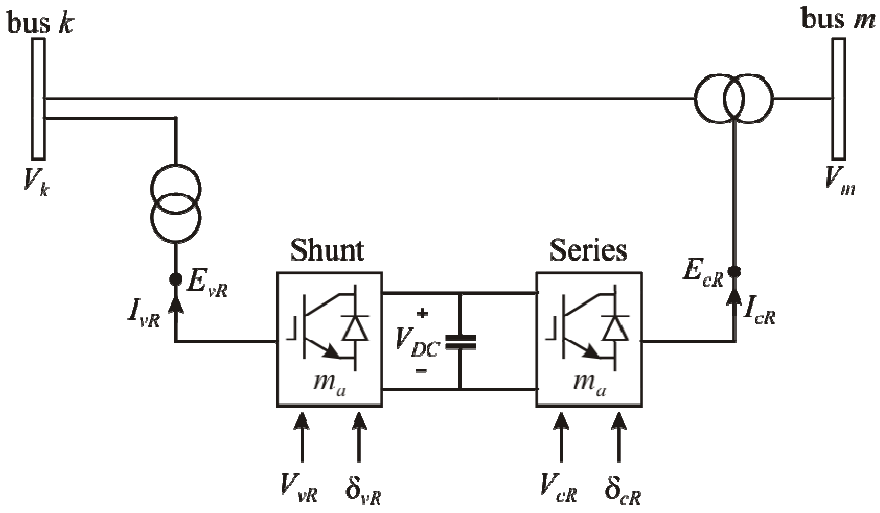

Figure 2.21. Schematic representation of the UPFC system

Figure 2.21 shows a UPFC system, representation showing the two back-to-back VSCs, with one VSC connected to the AC network using a shunt transformer and the SSSC connected to the AC network using a series transformer [5,47]. The active power demanded by the series converter is drawn by the shunt converter from the AC network and supplied to bus *m* through the DC link. The output voltage of the series converter is added to the nodal voltage, at say bus *k*, to boost the nodal voltage at bus *m*. The voltage magnitude of the output voltage V_{cR} provides voltage regulation, and the phase angle δ_{cR} determines the mode of power flow control [4,5].

The UPFC allows simultaneous control of active power flow, reactive power flow, and voltage magnitude at the UPFC terminals; however, it may be set to control one or more of these parameters in any combination or to control none of them [48]. For instance, in addition to providing a supporting role in the active power exchange between the series converter and the AC system, the shunt converter may also generate or absorb reactive power in order to provide independent voltage magnitude regulation at its point of connection with the AC system [5].

2.3.3.3. High-Voltage Direct-Current (HVDC)

High-Voltage Direct-Current (HVDC) power transmission using thyristor valves is a significant technology used to transmit power in a more economic manner over long distances, to connect two asynchronous networks and to link systems separated by the sea. The idea was developed in the early 1920s, with the first commercial HVDC installation built in 1954 between the island of Götland and the mainland of Sweden [28].

In simple terms, HVDC converts AC power into DC power using a phase-controlled converter with thyristors; power is transferred in DC using either an overhead line or a cable to the inverter station, where power is converted from DC into AC form [32,49–51]. HVDC using VSC technology is a newer alternative of DC transmission. Figure 2.22 shows a schematic representation of the HVDC-VSC. It comprises two VSCs, one operating as a rectifier and the other as an inverter. The two converters are connected either back-to-back or joined together by a DC cable, depending on the application. Its main function is to transmit constant DC power from the rectifier to the inverter station, with high *controllability*. Among the power system control capabilities of the HVDC-VSC, it can be mentioned its ability to regulate either nodal voltage magnitude or injection of reactive power at the AC side of one of its converters, and active power flow on the DC side of the other converter.

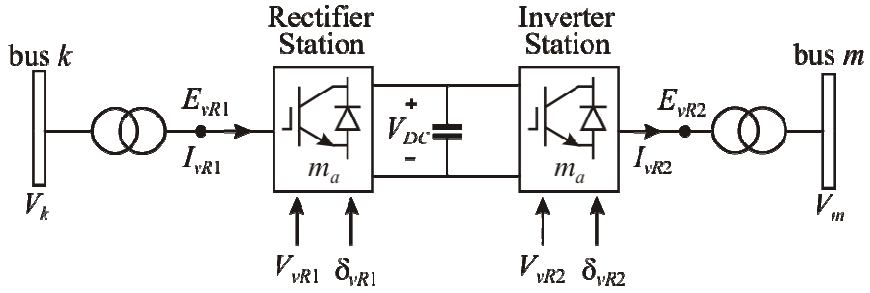

Figure 2.22. Schematic representation of the HVDC-VSC system

2.3.3.4. Variable Frequency Transformer (VFT)

The Variable Frequency Transformer (VFT) is a new alternative in the flexible control of active power flow in AC circuits [52]. The VFT is a bidirectional power transmission device that can transfer power between asynchronous networks. It provides a means to continuously control power flow between two grids. The VFT produces no harmonics and avoids undesirable interactions with neighbouring generators or equipment in the grid. From the operational perspective, it is very similar to a back-to-back HVDC converter station, but it is essentially a continuously variable phase shifting transformer [52–57].

Figure 2.23 shows a one-line diagram of the VFT installed in Langlois, Quebec [56–58]. The core technology of the VFT is a rotary transformer with three-phase windings on both rotor and stator, having the stator windings connected to one power grid and the rotor windings connected to another power grid.

The power systems may have different operating frequencies; however, this can be naturally accommodated by the speed of rotation of the machine.

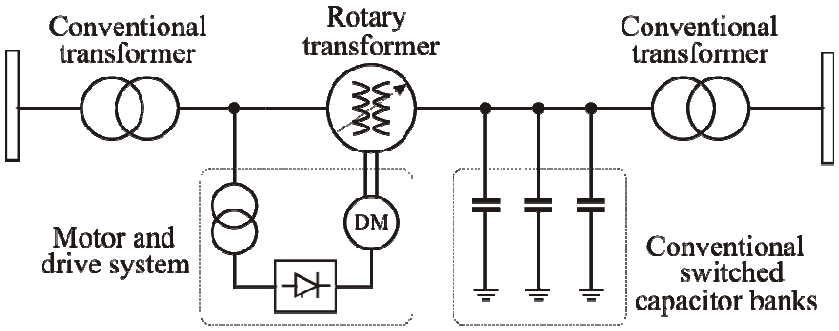

Figure 2.23. One-line diagram of Langlois VFT

The difference in alignment between the stator and the rotor produces a phase shift between the two systems. The power flow through the rotary transformer is proportional to this angle and a function of the torque applied to the rotor. The impedance of the rotary transformer and the AC grid determine the magnitude of phase shift required for a given power transfer. Reactive power flow through the VFT is determined by the series impedance of the rotary transformer and the difference in magnitude of voltages on both sides. However, it should be noticed that the control action is not the phase displacement between the rotor and the stator, but the mechanical torque [52,55–60]. Figure 2.24 shows a generic block diagram illustrating the VFT control strategy.

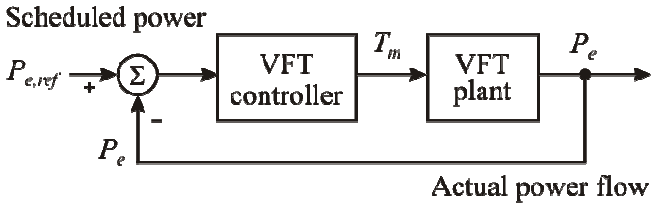

Figure 2.24. VFT control block diagram

Torque is applied to the rotor by a motor, which is controlled by a variable speed drive system [52]. By adjusting motor torque on the shaft as a function of power error, the rotational position of the rotor relative to the stator can be modified. That way, the magnitude and direction of the power flowing through the VFT is controlled – power flow is proportional to the magnitude and direction of the applied torque. If torque is applied in one direction, then power flows from the stator winding to the rotor winding, and vice-versa. When the VFT is used to interconnect two power grids at the same frequency, its normal operating speed is zero – although torque is produced. With no torque, there is no power flow through the rotary transformer [52,55,59,60]. Regardless of power flow, the rotor inherently orients itself to follow the phase angle difference imposed by the two asynchronous systems, and will rotate continuously if the grids are at different frequencies. If one power grid experiences a frequency excursion, the VFT will rotate at a speed proportional to the difference of frequency of both grids, but power flow is maintained [59,60].

2.4. Power system oscillations, damping and FACTS devices

An electrical power system can be seen as the interconnection of generating sources and customer loads through a network of transmission lines, transformers, and ancillary equipment. However, its structure is subjected to many variations which are the result of different decisions, ranging from economical, political, engineering and environmental [5]. With no doubt, the majority of the world's electric power supply systems are widely interconnected. This is done, firstly, to reduce the cost of electricity and secondly, to improve reliability of power supply. As the system becomes more complex, stability assessments become more complicated.

Early power system stability studies, in the 1920s and 1930s, emphasised the network configuration and assumed the generators to be voltage sources behind fix reactances, with loads being modelled as constant impedances. When faster-fault clearing and continuous-acting voltage regulators appeared in the early 1920s, a good step towards the limitation of first-swing transient stability and increased steady-state power transfer limits was made. Such technology rapidly became widely adopted by most utilities. The downside of fast-responding excitation was that it decreased damping of power swings, and therefore, oscillatory instability became a cause of concern. The main limitation in stability assessment studies was computational – the available tools were well suited for the solution of algebraic equations but not so for differential equations [1].

The introduction of digital computers in the 1950s facilitated the use of more detailed mathematical models for power system stability analysis. As power systems evolved and interconnections brought economically attractive scenarios, the complexity of stability problems substantially increased – and the consequences of instability became more apparent. Moreover, it was envisioned that digital computer programs would be key to the effective study of stability phenomena between formerly separated power systems [1,4].

During the 1960s, most of the research effort was deviated to transient stability performance of power systems undergoing large disturbances. The breakthroughs made in computer technology and in numerical methods, together with more sophisticated modelling of synchronous machines, excitation systems and loads, made possible the development of very powerful packages with which to study these kinds of phenomena. However, the growth of power systems was accompanied with an increased tendency of oscillatory instability. A dramatic consequence of this issue occurred in 1965, when a blackout hit the largely interconnected system of United States and Canada. Although some devices such as higher-response exciters improved transient stability, an adverse effect in small-signal stability proved to be a disadvantage as local plant modes of oscillation arose due to the introduction of negative damping. Another important source of the oscillatory instability problem is directly related to the increase in the

number of interconnections within a power system. As the system grows, large numbers of closely coupled machines connected by weak links are created. Under a heavy power transfer such systems exhibit inter-area modes of oscillation [1].

There is little doubt that as power transfers grow, the power system becomes more complex to operate and less secure [4]. Financial and regulatory conditions have caused electric utilities to build power systems with less redundancy and to operate them closer to their transient stability limits, significantly changing the dynamic characteristics of the system. Instability modes are becoming more complex and require an in-depth understanding of low-frequency inter-area oscillations [1].

In order to maximise existing transmission assets while keeping high reliability levels and stability, the smart solution has been the inclusion of power electronics equipment and methods. There is a general agreement that novel power electronics equipment and techniques are potential substitutes for conventional solutions, which are normally based on electromechanical technologies that have slow response times and high maintenance costs [4]. Traditionally, an important part of the job of system operators and transmission planners has been to try to achieve power flow distribution throughout the transmission system, with a limited amount of success. Operating problems arise whenever unregulated active and reactive power flows occur, such as loss of system stability, power flow loops, high transmission losses, voltage limit violations, an inability to utilise transmission line capability up to the thermal limit and cascade tripping [5]. The proponents of the FACTS technology argue that the full potential of transmission interconnections cannot be realised unless FACTS solutions are employed more widely, without which the operability of the interconnected power system itself can be compromised.

In general, the FACTS technology has equipped transmission planners with alternatives for controlling power flows and enhancing the usable capacity of the transmission grid. The collection of FACTS devices enables the smooth control of different interrelated parameters that govern the operation of transmission systems, such as series impedance, shunt impedance, current, voltage, phase angle, and damping of sub-synchronous oscillations [4].

A well-chosen FACTS controller should be able to overcome a specific limitation of a designated transmission corridor [4]. For example, the Advanced Series Capacitor (ASC) at the Kayenta 230 *kV* Substation in the Western Area Power Administration in Northeast Arizona, USA, was installed to increase the transmission capacity of a 230 *kV* line between Glen Canyon and Shiprock. It was originally designed for an initial power transfer capability of 300 *MW*, but the line's effectiveness to carry schedule power was diminished in the late 1960s due to the addition of parallel 345 *kV* and 500 *kV* paths. Adding series compensation became an attractive alternative to improve the line's power scheduling and transfer capability [4].

The latest member of the FACTS technology is a device termed VFT. In 2004, a VFT, constructed by General Electric, entered into commercial service at the Langlois Substation. The device provides a controlled power exchange between two electrical grids involving Ontario and New York – exchanges that had been thwarted because of technical constraints, such as asynchronous boundaries or congestion. The aim was for the VFT to transfer up to 200 *MW* of power between grids. Hence, an additional 100 *MW* was installed soon afterwards [55].

The successful integration of FACTS equipment into interconnected power systems networks worldwide is benefiting all sectors of the market: generation, transmission, distribution, utilisation and equipment manufacturers. However, further progress is dependent upon investigation of the dynamic impact of FACTS equipment in the network.

2.5. An overview of Individual Channel Analysis and Design

2.5.1. Multivariable control system design

In practice, the great majority of real systems are multiple-input multiple-output (MIMO). There are some occasions in which such systems are decoupled and the inputs and outputs can be paired. Thus, the control system design and analysis can be treated as a number of single-input single-output (SISO) problems. Nevertheless, almost every real system has several variables interacting with one another. Obviously, such type of interactions is hard to understand and as a consequence the control system design is non-trivial and challenging. In this case, there is no choice but to treat the design task as a genuine multivariable problem [61].

Great advances in techniques and methods have been developed in multivariable control. The Optimal Control, based on the work of Wiener (optimum filtering) in the 40s reached maturity during the 60s in what is currently known as Linear Quadratic Gaussian Control (LQG) [62]. Its development coincided with research programs carried out both in United States and the ex-Soviet Union. The control problems in which a cost function was intended to be minimised (for example, the time that a process lasts, the error, loses, among others) could be clearly defined as optimisation problems [63]. However, due to the lack of precise models the designs were not robust enough to be used in practice [62]. Several texts document very well such control theory [62,64–66].

Motivated by the results obtained with the LQG control, during the 80s a turning point towards the H_∞ optimisation to achieve robust controllers occurred [62]. Such development was originated from the work of Zames [67], although Helton previously used an H_∞ optimisation in an engineering context [68]. Zames argued that the poor robustness properties of LQG could be allocated to the integral criteria

in terms of the H_2 norm. He also criticised that the representation of uncertain disturbances throughout white noise processes was normally unreal [67]. In 1981, the *IEEE Transactions on Automatic Control* journal published a special issue focusing in Linear Multivariable Control Systems. The article of Doyle and Stein [69], in particular, was of great importance. Basically, an explanation about how to achieve the benefits of feedback in the presence of non-structured uncertainty is provided. The use of singular values for multivariable control design is introduced. Also, the authors propose that the traditional *loop-shaping* could be performed by means of a controller that would guarantee stability in advance. For such a task, a LQG controller could be used if the regulation part was designed using the "*sensitivity recovery*" procedure of Kwakernaak [70] to provide adequate robustness properties (in terms of gain and phase margins).

While the H_∞ theory (or Robust Control Theory) was developed several similarities were found with the H_2 control (or LQG), specifically in the solution process [71,72]. In fact, this theory opened new options to achieve better designs and it is fully documented in the literature [62,66,73–78]. A key step of this methodology is the weighting functions selection. Such functions are chosen in order to reflect the design objectives and the influence of disturbances and noise over the system [76]; however, a clear and appropriate manner to select an adequate set of weighting functions is still lacking [66]. In addition, if several performance objectives in some signals exist, the problem formulation is so complex that the designer has very little influence in the design [62].

Although the Modern Control Theory provides powerful tools for control system design, there are some issues associated to it. It could be thought that in practice the controllers forming a closed-loop control are able to tolerate *certain* uncertainty in their coefficients (since the controller implementation is subject to inherent inaccuracies of the analogue-to-digital and the digital-to-analogue conversion and to the finite resolution of the measuring instruments) [61]. This means that any useful design process must provide a controller with an enough range for coefficient adjustment. However, some cases have been reported in which the parametric stability margins of the controllers are so small that even extremely small disturbances in the controller coefficients (such a gain reduction of one thousandth) are sufficient to make the control loop unstable [79–81]. Such situation is unacceptable in a real system, since not only the controller is *fragile* but also the control system. This fragility is associated to poor robustness margins. Moreover, the designs normally correspond to high-order controllers (and therefore, hard to implement) [79,80]. In this case, the stability regions in the parameters' space of this kind of systems have "*instability holes*". Also, the optimisation algorithm can produce a controller with parameters near such holes since there is no margin with respect to the controller in the design process itself. Therefore, the design transfers sensitivity from the plant to the controller [79,80]. It should be mentioned that the results of [79] were obtained from fully documented designs available in the open literature [75,82–84].

Another issue related to the Modern Control Theory arises when high frequency effects are considered [85]. If certain techniques are directly applied it is possible to obtain a complex system and sensitive to parametric variations of the plant, to noise in control signals, and to random disturbances in outputs [85]. These kind of problems have been faced whenever the designs are used in practice, as in [63,64,86], but there is no general solution that allows to deal with such difficulties in a systematic way [85]. In fact, some designs for complex systems such as automatic pilots found in airplanes that apparently hold adequate stability characteristics can easily become unstable [85,86].

More recently, an alternative for multivariable control systems called Individual Channel Analysis and Design (ICAD) emerged [7,87–93]. It is based on the analysis of the Multivariable Structure Function (MSF), enabling a clear and transparent design process that allows robust multivariable control designs. So far, ICAD has been reported in several control strategies, such as in OMIB systems and other contrived power systems dynamics problems [94–97], submarines [98,99], aerospace industry [100–107], induction motors control strategies [108–110], and combustion processes [111]. The ICAD process involves the investigation of system capabilities and the minimum requirements to accomplish them, achieving design specifications (robustness and performance) and avoiding the use of unnecessary sophisticated controllers [87,112]. Additionally, the dynamical characteristics of the plant structure are clarified [7,89]. In fact, it provides simple and highly effective control system designs [112,113].

2.5.2. Justifying the use of ICAD

The performance in a typical control task is normally specified in terms of an output response to a given input. Meanwhile, in the multivariable control there are a determined number of inputs and outputs, and, although it is not very clear which inputs should specifically drive determined outputs, the design process task can be jeopardised due to the inherent coupling of the plant dynamics [87]. However, it is useful to consider the inputs and outputs in pairings to clarify the performance and design specifications [61]. This situation is shown in Figure 2.25, where **G** is the plant and **K** is the controller. Input u_i is paired with output y_i accordingly with the specifications. In this way, an individual pairing is called *channel*. Then, channel C_i is the pairing between u_i and y_i [7], where the closed-loop reference for the individual channel is provided by r_i.

As discussed by Leithead in [87], when the plant cross-coupling is weak, the design task is reduced to a set of single-input single-output (SISO) design tasks and a scalar controller can be designed separately for each channel. In this context, the most appropriate methodology is the Nyquist/Bode analysis and design for each channel. The Nyquist/Bode methodology for SISO systems is highly attractive due to [61,87,114,115]:

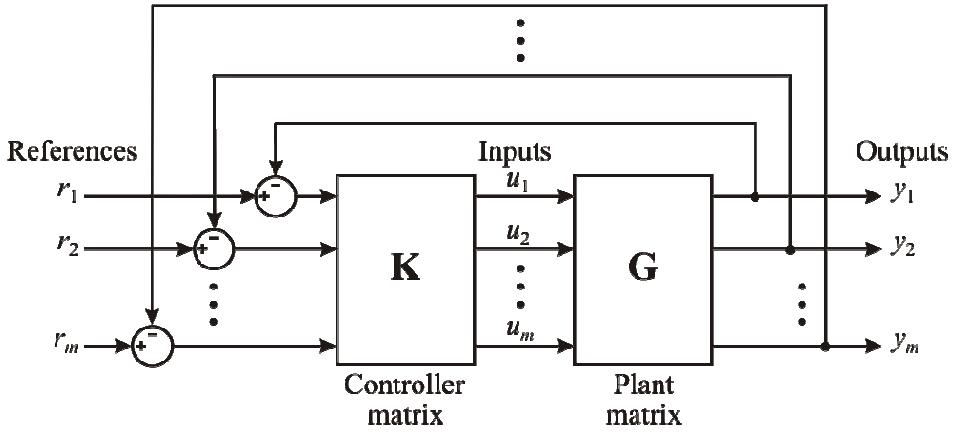

Figure 2.25. Channel definition in a standard *m*×*m* multivariable system

- Its simplicity, since the dynamical characteristics of the plant, physical constraints, and performance requirements are included in the methodology;
- It can be used to analyse a system;
- For a plant, the attainable performance potential by the feedback control system can be evaluated;
- For a plant and a controller independently of the control design method, the closed-loop performance can be directly inferred from the open loop system;
- For a plant and a controller independently of the control design method, it can be determined if the performance is restricted due to the specific controller design or to the dynamical characteristics of the plant;
- It can be used to design controllers;
- For a plant and given design specifications, a balance between the design objectives can be directly assessed, the design specifications can be achieved, and the possible compromises between the objectives can be evaluated;
- The design objectives include: steady-state and transient response, disturbance rejection, actuator protection, closed-loop system stability, and robustness;
- Acceptable robustness indicators are available and measurable *in-situ* in the form of gain and phase margins.

In summary, the Nyquist/Bode methodology is transparent, flexible, measurable, and highly applicable in an engineering context. It should be mentioned that several dynamic characteristics of a system dominate its dynamical behaviour. Such characteristics are known as the system structure. In SISO systems the plant structure is defined by its poles and zeros in the right hand plane (RHPP and RHPZ). The influence of the plant structure in the controller is easily understood and the controller design for closed-loop stabilisation of the plant is straightforward [7,87].

It would be highly attractive to apply the Nyquist/Bode methodology directly to the channels of the multivariable system not only when the coupling is weak but under any circumstance, even when the coupling is strong. Nevertheless, this involves some important issues, pointed out by Leithead in [87]:

1. The determination of the controller structure influence on the plant;
2. The application of gain and phase margins to multiple-input multiple-output (MIMO) systems;
3. The large number of individual transfer functions in the controller matrix, **K**;
4. The determination of an appropriate role for each transfer function in **K**;
5. The design of each individual control element although it depends on all other elements of the control matrix.

Moreover, it should be noticed that in multivariable systems the structure is defined not only by the RHPPs and RHPZs of the plant but also by the RHPZs of the individual elements of the transfer function matrix, the system coupling nature, and the asymptotic behaviour (at low and high frequency) of the plant [7,62,77,89,116].

Individual Channel Analysis and Design (ICAD), developed by O'Reilly and Leithead, is a framework inspired in Classical Control Theory that allows the application of the Nyquist/Bode analysis and design to multivariable systems irrespective of any coupling circumstance [7,87–93]. The multivariable system is represented by an equivalent set of SISO systems. Each system is the open loop channel transmittance between the reference r_i and the output y_i with the feedback loop between y_i and r_i opened but with all the other feedback loops closed for a given value of i. Although such a representation for multivariable systems has been previously considered in several occasions, what is particular to ICAD is that the transmittances of the SISO channels are reformulated to highlight the role of the plant structure. The significant aspects of such structure are encapsulated in scalar *Multivariable Structure Functions* (MSF) to which the channel transmittances are simply related. The multivariable nature of the original plant is preserved in the SISO equivalent systems through the MSFs with *no loss of information* [7,87,89].

As stated by Leithead in [87], if a diagonal controller is assumed, problems 3 and 4 can be avoided. If the Nyquist paths of the MSFs are far from the point (1,0), problem 2 is also eliminated; that is, gain and phase margins are closed-loop robustness measures. An adequate analysis of the MSFs allows the circumvention of problem 1. When the plant uncertainty causes a variable structure, some nominal plants for each possible structure should satisfy some simple low frequency conditions. The insight provided by ICAD allows the elimination of issue 5 for several plants. The fact that simple diagonal controllers are able to satisfy design specifications is in function of the plant structure [7]. Plants are said to have a *benign* structure if diagonal controllers can be designed to meet specifications – otherwise, they have a *poor* structure. The poor structure plants can be identified by means of the MSFs. By itself ICAD is not a specific design technique but a set of techniques previously investigated and appropriate within

the context. For example, when a plant has a poor structure, it is possible to use *feed-forward* control to amend it. Considering all the previous arguments, the initial restrictions are eliminated and ICAD can be applied to any multivariable plant [7,87,89].

Therefore, ICAD is an analytical framework with the help of which it is possible to investigate the potential and limitations for feedback control design of any linear and time invariant multivariable system. Although ICAD is in principle a feedback structure based on diagonal controllers, it can be applied to any cross-coupled multivariable system regardless of the coupling strength [112]. In this context, the control design under ICAD is an interactive process involving the required specifications, the plant characteristics, and the multivariable feedback design process itself. In general, the input-output channels arise from the design specifications. Once they are defined it is possible to form a feedback loop with a specifically designed controller to meet specifications. In this way the multivariable control problem is reduced to the design of SISO controllers for each channel. Another important aspect of ICAD is that the influence of transmission zeros in the control design and in the closed-loop performance is clearly revealed [7,87,89].

Several previous attempts to extend the classical control methods to multivariable control exist, *i.e.*, Sequential Return Difference [119], Direct/Inverse Nyquist Array [120], and Quantitative Feedback Theory [121]. In addition to constitute a general analysis and design framework and not a design method, the aspects that distinguish ICAD from the former are the emphasis on the structure and the development of simple scalar functions that provide the structural aspects of the plant. Likewise, the conditions for which gain and phase margins provide robustness measures have been established [87].

ICAD seeks to provide the potential user with a design framework for multivariable feedback control systems that is transparent, flexible and capable of validation against observed plant data, building confidence in the arrived-at design, and being well-suited to the specific engineering context [7]. Some useful ICAD theoretical formulations for 2×2 and $m \times m$ systems can be found in Appendix A.

2.6. Conclusions

This chapter has introduced generic aspects of power systems, synchronous generators and power electronic controllers. The modelling of synchronous generators aimed at small-signal stability assessments is addressed in detail. Several mathematical models, ranging in complexity, are presented. The many benefits that the application of FACTS controllers can bring into power systems operation are highlighted. Some relevant members of the FACTS technology are particularly addressed. The effects of oscillations arising within an interconnected power system and its contribution to instability are discussed. In connection to this, the FACTS technology is proposed as a practical solution to enable a

smooth control of key parameters that govern the operation of transmission systems and to obtain full potential of active power transmission.

In the last part of the chapter, the ICAD framework is presented. The basic theory and individual channel representation of multivariable systems is discussed, with comprehensive mathematical formulations found in Appendix A. The aim of this chapter is to provide the reader with a working understanding of the mathematical modelling associated with power plant components and its analysis under ICAD. As follows efforts are made to apply ICAD to power systems including FACTS devices.

2.7. References

[1] Kundur P. *Power System Stability and Control*. USA: McGraw-Hill; 1994.

[2] Anderson PM, Fouad AA. *Power System Control and Stability*. USA: IEEE Press; 1994.

[3] Grainger JJ, Stevenson WD. *Power System Analysis*. Singapore: McGraw-Hill; 1994.

[4] Hingorani NG, Gyugyi L. *Understanding FACTS: Concepts and Technology of Flexible AC Transmission Systems.* USA: IEEE Press; 2000.

[5] Acha E, Fuerte-Esquivel C, Ambriz-Perez H, Angeles-Camacho C. *FACTS. Modelling and Simulation in Power Networks.* UK: John Wiley & Sons Ltd; 2004.

[6] Aree P. *Small Signal Stability Modelling and Analysis of Power Systems with Electronically Controlled Compensation*. PhD Thesis. Department of Electronics and Electrical Engineering, University of Glasgow, Scotland, UK, 2000.

[7] O'Reilly J, Leithead WE. *Multivariable Control by Individual Channel Design*. International Journal of Control, **54**, no. 1, pp. 1–46, 1991.

[8] Padiyar KR. *Power System Dynamics: Stability and Contro*l. USA: John Wiley & Sons; 1995.

[9] Concordia C. *Synchronous Machines*. USA: John Wiley & Sons; 1951.

[10] Adkins B. *The General Theory of Electrical Machines*. UK: Chapman and Hall; 1964.

[11] Fitzgerald AE, Kingsley C. *Electric Machinery*. USA: McGraw-Hill; 1961.

[12] Chapman SJ. *Electric Machinery Fundamentals.* USA: McGraw-Hill; 1998.

[13] Kimbark EW. *Power System Stability I, II, III*. USA: IEEE Press; 1995.

[14] Krause PC. *Analysis of Electric Machinery*. Singapore: McGraw-Hill; 1987.

[15] O'Kelly D, Simmons S. *Introduction to Generalised Electrical Machine Theory*. UK: McGraw-Hill; 1968.

[16] Sen PC. *Principles of Electric Machines and Power Electronics*. USA: John Wiley & Sons; 1997.

[17] ANSI/IEEE Standard 100-1997. *IEEE Standard Dictionary of Electrical and Electronic Terms,* 1997.

[18] Kundur P, Rogers GJ, Wong DY, Wang L, Lauby MG. *A Comprehensive Computer Program Package for Small Signal Stability Analysis of Power Systems*. IEEE Transactions on Power Systems, **5**, no. 4, pp. 1076–1083, 1990.

[19] Park RH. *Two-Reaction Theory of Synchronous Machines. Part I.* AIEE Transactions, **48**, pp. 716–730, 1929.

[20] Park RH. *Two-Reaction Theory of Synchronous Machines. Part II.* AIEE Transactions, **52**, pp. 352–355, 1933.

[21] IEEE Standard 1110-1991. *IEEE Guide for Synchronous Generator Modelling Practices in Stability Analyses*, 1991.

[22] IEEE Task Force on Definitions and Procedures. *Current Usage and Suggested Practices in Power System Stability Simulations for Synchronous Machines*. IEEE Transactions on Energy Conversion, **1**, no. 1, pp. 77–93, 1986.

[23] Hammons TJ, Winning DJ. *Comparisons of Synchronous-Machine Models in the Study of the Transient Behaviour of Electrical Power Systems*. IEE Proceedings, **118**, no. 10, pp. 1442–1458, 1971.

[24] Hingorani NG. *FACTS – Flexible AC Transmission Systems*. IEE International Conference on AC and DC Power Transmission, pp. 1–7, 1991.

[25] Hingorani NG. *Flexible AC Transmission*. IEEE Spectrum, **30**, no. 4, pp. 40–45, April 1993.

[26] IEEE/CIGRE (Institute of Electrical and Electronic Engineers/Conseil International des Grands Reseaux Electriques). *FACTS Overview*, special issue, 95TP108, USA: IEEE Service Centre; 1995.

[27] Kundur P, Paserba J, Ajjarapu V, Andersson G, Bose A, Canizares C, Hatziargyriou N, Hill D, Stankovic A, Taylor C, Van Cutsem T, Vittal V (IEEE/CIGRE Joint Task Force on Stability Terms and Definitions). *Definition and Classification of Power System Stability*. IEEE Transactions on Power Systems, **19**, no. 2, pp. 1387–1401, 2004.

[28] Acha E, Agelidis VG, Anaya-Lara O, Miller TJE. *Power Electronic Control in Electrical Systems*. UK: Newnes Power Engineering Series; 2002.

[29] Arrillaga J, Watson NR. *Computing Modelling of Electrical Power Systems*. UK: John Wiley & Sons; 2001.

[30] Miller TJE. *Reactive Power Control in Electric Systems*. UK: John Wiley Interscience; 1982.

[31] Larsen EV, Sanchez-Gasca JJ, Chow JH. *Concept for Design of FACTS Controllers to Damp Power Swings*. IEEE Transactions on Power Systems, **10**, no. 2, pp. 984–955, 1995.

[32] Arrillaga, J. *High Voltage Direct Current Transmission*. UK: Institution of Electrical Engineers; 1998.

[33] Helbing SG, Karady GG. *Investigations of an Advanced Form of Series Compensation.* IEEE Transactions on Power Delivery, **9**, no. 2, pp. 939–947, 1994.

[34] Noroozian M, Andersson G. *Power Flow Control by Use of Controllable Series Components.* IEEE Transactions on Power Delivery, **9**, no. 2, pp. 12–18, 1993.

[35] Wang HF, Swift FJ. *A Unified Model for the Analysis of FACTS Devices in Damping Power System Oscillation. Part I: Single-machine Infinite-Bus Power System.* IEEE Transactions on Power Delivery, **12**, no. 12, pp. 941–946, 1997.

[36] Wang HF, Swift FJ. *A Unified Model for the Analysis of FACTS Devices in Damping Power System Oscillation. Part II: Single-machine Power System.* IEEE Transactions on Power Delivery, **13**, no. 4, pp. 1355–1360, 1998.

[37] Wang HF, Swift FJ. *Application of the Controllable Series Compensator in Damping Power System Oscillation.* IEE Proceedings on Generation, Transmission and Distribution, **143**, Part C, no. 4, pp. 359–364, 1996.

[38] Zhou X, Liang J. *Overview of Control Schemes for TCSC to Enhance the Stability of Power System.* IEE Proceedings on Generation, Transmission and Distribution, **146**, Part C, no. 2, pp. 125–130, 1999.

[39] Padiyar KR. *Analysis of Subsynchronous Resonance in Power Systems*. UK: Kluwer Academic Publisher; 1999.

[40] Bose BK. *Modern Power Electronics and AC Drives*. India: Pearson Education; 2002.

[41] Holtz J. *Pulsewidth Modulation for Electronic Power Conversion*. Proceedings of the IEEE, **82**, no. 8, pp. 1194–1214, August 1994.

[42] Mohan N, Undeland TM, Robbins WP. *Power Electronics, Converters, Applications and Design*. USA: John Wiley & Sons; 2003.

[43] Kazmierkowski MP, Krishnan R, Blaabjerg F. *Control in Power Electronics. Selected Problems.* USA: Academic Press; 2002.

[44] Mohan N. *Advanced Electric Drives: Analysis, Control and Modeling using Simulink*. USA: Mnpere; 2001.

[45] Ong CM. *Dynamic Simulation of Electric Machinery using MATLAB®/ SIMULINK*. USA: Prentice–Hall; 1998.

[46] Van der Broeck H, Skudelny HC, Stanke G. *Analysis and Realization of a Pulsewidth Modulator Based on Voltage Space Vectors*. IEEE Transactions on Industrial Applications, **24**, No. 1, pp. 142–150, Jan/Feb. 1988.

[47] Nabaki-Niaki A, Iravani MR. *Steady-state and Dynamic Models of Unified Power Flow Controller (UPFC) for Power System Studies*. IEEE Transactions on Power Systems, **11**, No. 4, pp. 1937–1943, 1996.

[48] Fuerte-Esquivel CR, Acha E, Ambriz Perez H. A Comprehensive UPFC Model for the Quadratic Load Flow Solution of Power Networks. IEEE Transactions on Power Systems, **15**, No. 1, pp. 102–109, 2000.

[49] Angeles-Camacho C, Tortelli OL, Acha E, Fuerte-Esquivel CR. *Inclusion of a high voltage DC-voltage source converter model in a Newton-Raphson power flow algorithm*. IEE Proceedings in Generation, Transmission, and Distribution, **150**:6, pp. 691-696, 2003.

[50] Chan KH, Parle JA, Johnson N, Acha E. *Real Time Implementation of a HVDC-VSC Model for Application in a scaled-down Wind Energy Conversion System (WECS)*. IEE AC-DC Power Transmission pp. 599-604, 2001.

[51] Song R, Zheng C, Li R, Zhou X. *VSCs Based HVDC and its Control Strategy*. IEEE/PES Transmission and Distribution Conference and Exhibition: Asia and Pacific, pp. 1–6, 2005.

[52] GE Energy. *Variable Frequency Transformers – Grid Inter-tie*. http://www.gepower.com/

[53] Fujita H, Ihara S, Larsen EV, Pratico ER, Price WW. *Modeling and Dynamic Performance of a Rotary Power Flow Controller*. IEEE Power Engineering Society Winter Meeting, **2**, pp. 599–604, 2001.

[54] Chen G, Zhou X. *Digital Simulation of Variable Frequency Transformers for Asynchronous Interconnection in Power System*. IEEE/PES Transmission and Distribution Conference and Exhibition: Asia and Pacific, pp. 169–174, 2005.

[55] GE Energy. *GE's New Interconnection Technology Completes Commissioning Tests*. News release. http://www.gepower.com/

[56] Larsen E, Piwko R, McLaren D, McNabb D, Gragner M, Dusseault M, Rollin LP, Primeau J. *Variable Frequency Transformer – A New Alternative For Asynchronous Power Transfer*. GE Energy and Hydro-Quebec TransEnergie, 2004.

[57] McNabb D, Nadeau D, Nantel A, Pratico E, Larsen E, Sybille G, Van QD, Pare D. *Transient and Dynamic Modeling of the New Langlois VFT Asynchronous Tie and Validation with Commissioning Tests*. International Conference on Power Systems Transients, Canada, 2005.

[58] Piwko RJ, Larsen EV, Wegner CA. *Variable Frequency Transformer – A New Alternative for Asynchronous Power Transfer*. Proceedings of the IEEE PES 2005 Conference and Exposition in Africa, pp. 393–398, 2005.

[59] Molinas M. *Power System Stability Control Based on Phase Angle Regulation*. PhD Thesis. Department of Electrical Engineering, Tokyo Institute of Technology, Japan, 2000.

[60] Molinas M, Nakamura H, Koyanagi A, Shimada R. *Analytical and Experimental Study of a Rotary Phase Shifter for Power System Applications*. Transactions IEE Japan, **120-B**, no. 10, pp. 1336–1342, 2000.

[61] Goodwin G, Graebe SF, Salgado ME. *Control System Design*. USA: Prentice–Hall; 2001.

[62] Skogestad S, Postlethwaite I. *Multivariable feedback control. Analysis and design*. UK: John Wiley & Sons; 1996.

[63] Kalman RE. *When is a Linear Control System Optimal?* Transactions of the ASME Journal of Basic Engineering, **86D**, pp 51–60, 1964.

[64] Anderson BDO, Moore JB. *Optimal Control: Linear Quadratic Methods.* USA: Prentice–Hall; 1989.

[65] Kwakernaak H, Sivan R. *Linear Optimal Control Systems.* USA: Wiley Interscience; 1972.

[66] Zhou K, Doyle J. *Essentials of Robust Control*. USA: Prentice–Hall; 1998.

[67] Zames G. *Feedback and Optimal Sensitivity: Model Reference Transformations, Multiplicative Seminorms, and Approximate Inverse*. IEEE Transactions on Automatic Control, **AC–26**, pp. 301–320, 1981.

[68] Helton JW. *Operator Theory and Broadband Matching.* Proceedings of the 11th Annual Allerton Conference on Communications, Control and Computing, 1976.

[69] Doyle JC, Stein G. *Multivariable Feedback Design: Concepts for a Classical/Modern Synthesis*. IEEE Transactions on Automatic Control, **AC26**, pp. 4–16, 1981.

[70] Kwakernaak H. *Optimal Low–Sensitivity Linear Feedback Systems.* Automatica, **5(3)**, pp. 279–286, 1969.

[71] Doyle JC, Glover K, Khargonekar PP, Francis BA. *State Space Solutions to Standard H_2 and H_∞ Control Problems*. IEEE Transactions on Automatic Control, **34**, pp. 831–347, 1989.

[72] Glover K, Doyle JC. *State–Space Formulae for all Stabilizing Controller that Satisfy an H_∞ Norm Bound and Relations to Risk Sensitivity.* System and Control Letters, **11**, pp. 167–172, 1988.

[73] Chiang RY, Safonov MG. *MATLAB® Robust Control Toolbox*. USA: The MathWorks Inc.; 1998.

[74] Dailey RL, Glover K, Green M, Limebeer D. *Lecture Notes for the Workshop on H_∞ and μ Methods for Robust Control*. IEEE Conference on Decision and Control, Brighton, England, 1991.

[75] Doyle JC, Francis BA, Tannenbaum A. *Modern Control Systems*. USA: Macmillan Publishing; 1990.

[76] Helton JW, Merino O. *Classical Control using H_∞ Methods. Theory, Optimization, and Design*. USA: SIAM; 1998.

[77] Maciejowski JM. *Multivariable Feedback Design*. UK: Addison–Wesley; 1989.

[78] Morari M, Zafiriou M. *Robust Process Control*. USA: Prentice–Hall; 1989.

[79] Keel LH, Bhattacharyya SP. *Robust, Fragile, or Optimal?* IEEE Transactions on Automatic Control, **42**, No. 8, 1997.

[80] Keel LH, Bhattacharyya SP. *Authors' Reply to "Comments on Robust, Fragile, or Optimal?"* IEEE Transactions on Automatic Control, **43**, No. 9, 1998.

[81] Mäkilä PM. *Comments on "Robust, Fragile, or Optimal?"* IEEE Transactions on Automatic Control, **43**, No. 9, 1998.

[82] Bhattacharyya SP, Chapellat H, Keel LH. *Robust Control: The Parametric Approach*. USA: Prentice–Hall; 1995.

[83] Dahleh MA, Diaz–Bobillo IJ. *Control of Uncertain Systems: A Linear Programming Approach*. USA: Prentice–Hall; 1995.

[84] Fujita M, Namerikawa T, Matsumura F, Uchida K. *μ–Synthesis of an Electromagnetic Suspension System.* IEEE Transactions on Automatic Control, **40**, pp. 530–536, 1989.

[85] Nesline FW, Zarchan P. *Why Modern Controllers can go Unstable in Practice*. AIAA Guidance and Control Conference, San Diego, USA, 1982.

[86] Nesline FW, Wells BH, Zarchan P. *A Combined Optimal/Classical Approach to Robust Missile Autopilot Design*. Proceedings of the AIAA Guidance and Control Conference, pp. 265–280, 1979.

[87] Leithead WE. *What is Individual Channel Analysis and Design?* Department of Electronic and Electrical Engineering, University of Strathclyde, Scotland; University of Glasgow, Scotland, 1993.

[88] Leithead WE, O'Reilly J. *Investigation of the ICD Structure of Systems Defined by State Space Models.* International Journal of Control, **60**, no.1, pp. 71–89, 1994.

[89] Leithead WE, O'Reilly J. *M-input m-output Feedback Control by Individual Channel Design. Part 1. Structural Issues.* International Journal of Control, **56**, no. 6. pp. 1347–1397, 1992.

[90] Leithead WE, O'Reilly J. *Performance Issues in the Individual Channel 2–input 2–output Systems. Part 1: Structural issues.* International Journal of Control, **54**, no. 1, pp. 47–82, 1991.

[91] Leithead WE, O'Reilly J. *Performance Issues in the Individual Channel 2–input 2–output Systems. Part 2: Robustness issues.* International Journal of Control, **55**, no.1, pp. 3–47, 1992.

[92] Leithead WE, O'Reilly J. *Performance Issues in the Individual Channel 2–input 2–output Systems. Part 3: Non-diagonal control and related issues.* International Journal of Control, **55**, no 2, pp. 265–312, 1992.

[93] Leithead WE, O'Reilly J. *New Roles for Feedforward in Multivariable Control by Individual Channel Design*. International Journal of Control, **57**, no. 6, pp. 1357–1386, 1993.

[94] Dudgeon GJW, Leithead WE, O'Reilly J, McDonald JR. *Prospects for the Decentralized Control of Small-Scale Power Networks with Embedded Generation*. IEEE Power Engineering Society Summer Meeting, **2**, pp. 1399–1404, 2000.

[95] Edwards FV, Dudgeon GJW, McDonald JR, Leithead WE. *Dynamics of Distribution Networks with Distributed Generation*. *IEEE* Power Engineering Society Summer Meeting, **2**, pp. 1032–1037, 2000.

[96] Fadlalmoula Z, Robertson SS, O'Reilly J, Leithead WE. *Individual Channel Analysis of the Turbogenerator with a Power System Stabilizer*. International Journal of Control, **69**, no.2, pp. 175–202, 1998.

[97] Fadlalmoula Z. *An Investigation of Turbogenerator Dynamics and Control*. PhD Thesis. Department of Electronics and Electrical Engineering, University of Glasgow, Scotland, UK, 1998.

[98] Licéaga–Castro E, Licéaga–Castro J. *Submarine Depth Control by Individual Channel Design*. Proceedings of the 37th IEEE Conference on Decision and Control, **3**, pp. 3183–3188, 1998.

[99] Licéaga–Castro E, Licéaga–Castro J, Ugalde–Loo CE, Navarro–López EM. *Efficient Multivariable Submarine Depth-Control System Design*. Ocean Engineering, **35**, no. 17–18, pp. 1747–1758, 2008.

[100] Akbar MA, Leithead WE, O'Reilly J. *Design of Robust Controllers for a Fighter Aircraft using Individual Channel Design.* Proceedings of the 32nd IEEE Conference on Decision and Control, **1**, pp. 430–435, 1993.

[101] Akbar MA, Leithead WE, O'Reilly J, Robertson SS. *Design of Robust Controllers for 3–input 3–output Supersonic Aircraft Power Plant using ICD*. Proceedings of the 3rd IEEE Conference on Control Applications, **1**, pp. 95–99, 1994.

[102] Dudgeon GJW, Gribble JJ. *Helicopter Translational Rate Command using Individual Channel Design.* UKACC International Conference on Control '96, **1**, pp. 632–637, 1996.

[103] Licéaga J, Licéaga E, Amézquita L. *Multivariable Gyroscope Control by Individual Channel Design*. Proceedings of the 2005 IEEE Conference on Control Applications, pp. 785–790, 2005.

[104] Licéaga–Castro J, Verde C, O'Reilly J, Leithead WE. *Helicopter Control using Individual Channel Design.* IEE Proceedings – Control Theory and Applications, **142,** pp. 58–72, 1995.

[105] Robertson SS, Leithead WE, O'Reilly J. *Design of Controller for GVAM Aircraft Model using ICAD Software*. UKACC International Conference on Control '96, **1**, pp. 533–538, 1996.

[106] Dudgeon GJW. *Individual Channel Analysis and Design and its Application to Helicopter Flight Control*. PhD Thesis. Department of Electronics and Electrical Engineering, University of Glasgow, Scotland, UK, 1996.

[107] Licéaga–Castro J. *Helicopter Flight Control by Individual Channel Design*. PhD Thesis. Department of Electronics and Electrical Engineering, University of Glasgow, Scotland, UK, 1995.

[108] Licéaga–Castro E, Ugalde–Loo CE, Licéaga–Castro J, Ponce P. *An Efficient Controller for SV–PWM VSI Based on the Multivariable Structure Function.* Proceedings of the Joint 44th IEEE Conference on Decision and Control and European Control Conference, pp. 4754–4759, 2005.

[109] Licéaga–Castro E, Ugalde–Loo CE, Licéaga–Castro J. *Induction Motor Control by Individual Channel Analysis and Design*. Proceedings of the International Conference Control 2006 (UK-ACC), Glasgow, Scotland, UK, 2006.

[110] Licéaga–Castro J, Amezquita–Brooks L, Licéaga–Castro E. *Induction Motor Currente Controller for Field Oriented Control Using Individual Channel Design*. Proceedings of the 34th Annual Conference of the IEEE Industrial Electronics Society (IECON 2008), pp. 235–240, Orlando, Florida, USA, 2008.

[111] Kocijan J, O'Reilly J. *An Example of Multivariable Combustion, Control Design within Individual Channel Design Framework.* Proceedings of the 3rd IEEE Conference on Control Applications, **1**, pp. 741–746, 1994.

[112] Licéaga–Castro E, Licéaga–Castro J, Ugalde–Loo CE. *Beyond the Existence of Diagonal Controllers: from the Relative Gain Array to the Multivariable Structure Function*. Proceedings of the Joint 44th IEEE Conference on Decision and Control and European Control Conference, pp. 7150–7156, 2005.

[113] Ugalde–Loo CE, Licéaga–Castro E, Licéaga–Castro J. *2x2 Individual Channel Design MATLAB® Toolbox*. Proceedings of the Joint 44th IEEE Conference on Decision and Control and European Control Conference, pp. 7603–7608, 2005.

[114] Dorf RC, Bishop RH. *Modern Control Systems*. USA: Addison–Wesley; 1998.

[115] Ogata K. *Modern Control Engineering*. USA: Prentice–Hall; 1997.

[116] Patel RV, Munro N. *Multivariable System Theory and Design*. UK: Pergamon Press, International Series on Systems and Control; 1982.

[117] Hovd M, Skogestad S. *Sequential Design of Decentralized Controllers.* Automatica, **30**, no. 10, pp. 1601–1607, 1994.

[118] Rosenbrock HH. *Computer–Aided Control System Design*. USA: Academic Press; 1974.

[119] Horowitz I. *Survey of Quantitative Feedback Theory (QFT)*. International Journal of Control, **53**, no. 2, pp. 255–291, 1991.

Chapter 3

INDIVIDUAL CHANNEL ANALYSIS AND DESIGN OF THE SYNCHRONOUS MACHINE

3.1. Introduction

Owing to the physical insight afforded by the Heffron-Phillips representation of the synchronous generator – initially introduced in [1] and then explored further in [2,3], the model has been widely used and applied to One-Machine – Infinite Bus (OMIB) systems. Extensions have been made to include Power System Stabilisers (PSS), sub-transient effects of damper windings and *electronically-controlled* compensation [4]. A major asset of the Heffron-Phillips block diagram model is that it lends itself to the use of classical and robust control techniques [5]. However, a drawback of the block diagram representation is that the visual simplicity of this approach is lost when applied to cases of even two machines. On the other hand, eigenanalysis remains the industry's preferred approach for assessing small-signal stability owing to its large-scale applicability [6]; although it may be argued that the great physical insight afforded by the Heffron-Phillips model is not apparent in the eigenanalysis-based solutions.

On the quest for an alternative analysis tool which does not suffer from lack of physical transparency but which would still be applicable to large-scale systems, the classical oriented framework for multivariable systems, termed Individual Channel Analysis and Design (ICAD) [7], has been applied to different contrived power systems dynamic problems [8–10]. It has also been used for an induction motor control scheme [11–13], and with particular reference to OMIB systems, it has been reported in [8,14]. Furthermore, a flux model of the synchronous generator is considered in reference [14].

Fundamental studies of OMIB systems using block diagrams have shown to be very useful in understanding key aspects of synchronous machine modelling and the impact of power electronics controllers on the generator dynamic performance. Building on this positive experience, and in the quest for a truly multi-machine, multi-controller environment which yields physical insight, a comprehensive dynamical assessment of synchronous generator representations under the ICAD framework is carried out in this chapter. Moreover, the adequacy of several generator order models is critically examined.

ICAD enables the analysis and synthesis of multivariable control design by applying techniques based on Bode/Nyquist plots. The design process involves individual input-output channels definition in terms of a Multivariable Structure Function (MSF), an information rich function with which it is possible to assess the structural and stability robustness and performance of multivariable control designs. ICAD's MSF provides an elegant framework for the analysis and control system design of synchronous generators. Furthermore, it helps to formally explain why some generator operating conditions are more critical than others. Throughout this chapter it is shown that an appropriate examination of the MSF and its correct interpretation are amenable to simple, straightforward, stable and robust control system designs. The OMIB system performance is studied for different operating conditions. One study is carried out to assess the operation under various power factor conditions and a second study deals with the impact of different tie-line reactance values.

ICAD analysis of the dynamical structure of the system is presented and compared with that obtained using the long-time honoured block diagram representations. Furthermore, the great benefits that ICAD brings to small-signal stability assessment when compared to both the block diagram representations and eigenanalysis are outlined. Moreover, the great advantages of carrying out control system analysis and design with higher order generator models are revealed. For completeness, results obtained under the ICAD framework are compared with those arising from conventional controllers. Their characteristics are discussed thoroughly, with the emphasis being on closed-loop performance and robustness of the system.

3.2. Block diagram modelling of synchronous generators

The synchronous machine dynamic representation used to derive all the models presented in this chapter is based on the work of Hammons and Winning [15]. The small-signal model is developed from first principles by using the non-linear differential and algebraic equations (2.2)–(2.18), which represent the synchronous generator (introduced in Chapter 2, section 2.2.3). Suitable manipulation of those dynamic equations yields a series of mathematical models of the synchronous generator of a varying degree of complexity and accuracy. Following a linearisation exercise and by expressing the resultant equations in the frequency domain, several transfer function block diagram models are obtained. It should be mentioned that for this model construction the stator resistance is assumed to be negligible. Further details and the full mathematical modelling procedure can be found in Appendix C.

The test system in Figure 3.1 is used to study the synchronous generator dynamic characteristics. It consists of a synchronous generator feeding into a large system represented as an infinite bus via a reactive tie-line system.

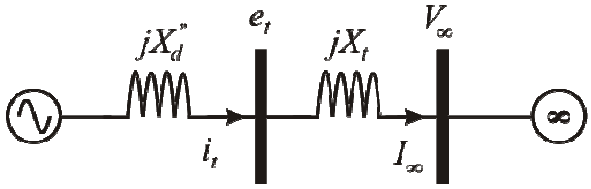

Figure 3.1. Synchronous generator connected to an infinite bus via a tie-line reactance

3.2.1. Model 1 (2*d*.1*q*, 5th order, two-axis)

The following equations in the *s*-domain characterise Model 1 [3].

$$\Delta P_e(s) = K_1\Delta\delta(s) + K_2\Delta E_q''(s) - K_{2d}\Delta E_d''(s) \tag{3.1}$$

$$\Delta e_t(s) = K_5\Delta\delta(s) + K_6\Delta E_q''(s) + K_{6d}\Delta E_d''(s) \tag{3.2}$$

$$\Delta E_q''(s) = K_3(s)\Delta E_{fd}(s) - K_4(s)\Delta\delta(s) \tag{3.3}$$

$$\Delta E_d''(s) = K_{4d}(s)\Delta\delta(s) \tag{3.4}$$

$$\Delta\omega(s) = \frac{1}{2Hs}\left[\Delta P_m(s) - \Delta P_e(s) - D\Delta\omega(s)\right] \tag{3.5}$$

$$\Delta\delta(s) = \frac{\omega_0}{s}\Delta\omega(s) \tag{3.6}$$

where the parameters and transfer functions of equations (3.1)–(3.4) are given in Appendix C. Equations (3.1)–(3.6) are used to form the block diagram representation for this model, which is shown in Figure 3.2. Notice that the controllers for terminal voltage and speed are included in the block diagram.

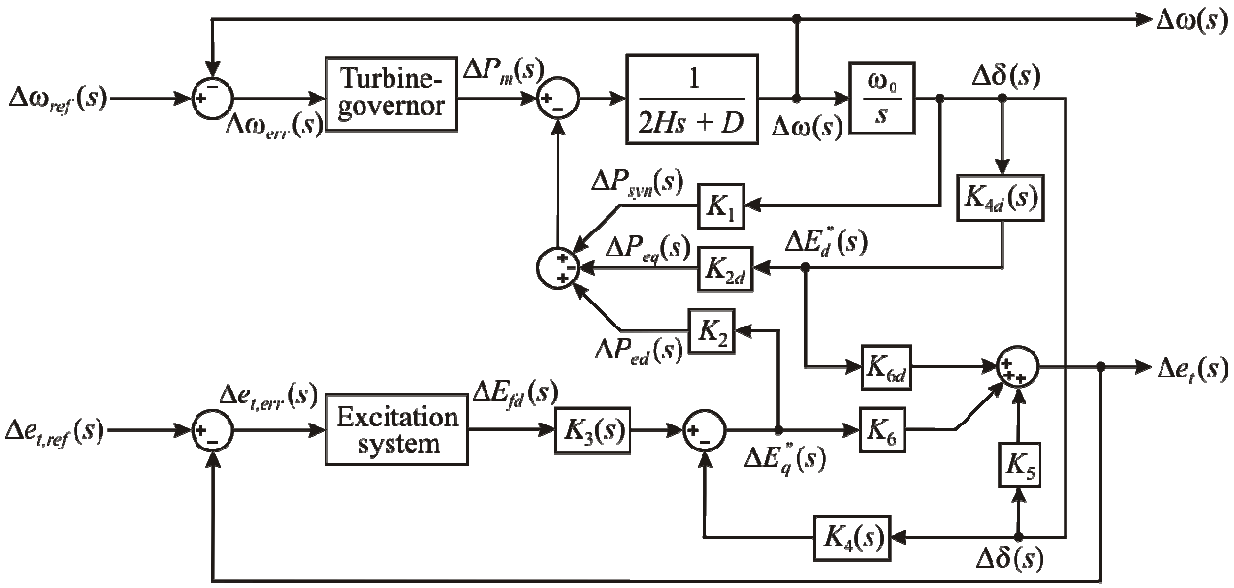

Figure 3.2. Block diagram for the OMIB system with synchronous generator Model 1

3.2.2. Model 2A (1*d*.1*q*, 4th order, two-axis)

Simplifications may be made in Model 1 in an attempt to reduce modelling complexity and computing overheads while still retaining key generator dynamics effects. To this end, the sub-transient effects that produce a demagnetising effect due to a change in the rotor are neglected in this model. However, the transient effects of the damping windings are retained. The following simplifying assumptions are made in Model 1:

$$\tau_{d0}^{"} \to 0, X_d^{"} = X_d^{'}, E_q^{"} = E_q^{'}$$

to yield the synchronous machine Model 2A. Similarly to Model 1, this is a two-axis generator representation but considers no damper winding in the *d*-axis. The block diagram representation (not shown) is a particular case of the one given in Figure 3.2.

3.2.3. Model 2B (2*d*.0*q*, 4th order, one-axis)

With reference to Model 1, the following simplifying assumptions are made to yield Model 2B:

$$\tau_{q0}^{"} \to 0, X_q^{"} = X_q, E_d^{"} = 0$$

This 4th order model is essentially a one-axis model with the field winding and one damping winding in the *d*-axis, *i.e.*, no *q*-axis exists. The block diagram representation (not shown) is a particular case of the one given in Figure 3.2.

3.2.4. Model 3 (1*d*.0*q*, 3rd order, one-axis)

This is the classical model presented by DeMello and Concordia [2], where the dynamic effects of damping windings are all but neglected. This model may be arrived at by making the following simplifying assumptions in Model 2A

$$\tau_{q0}^{"} \to 0, X_q^{"} = X_q, E_d^{"} = 0$$

In this case too, the block diagram representation is a particular case of the one given in Figure 3.2.

3.2.5. Additional models: Model 0 (2*d*.2*q*) and Model 2C (1*d*.1*q*)

In addition to these mathematical models, other more complex structures do exist. Among them, a 6th order model is of particular interest, having a two-axis representation with the field and one damping winding in the *d*-axis and two damping windings in the *q*-axis. This is model 2*d*.2*q* (called from now on Model 0), in which the synchronous generator is represented by the sub-transient voltages behind the sub-transient reactances.

Moreover, if the following simplifying assumptions,

$$\tau_{q0}^{"} \to 0, X_q^{"} = X_q^{'}, E_d^{"} = 0$$

$$\tau_{d0}^{''} \to 0, X_d^{''} = X_d^{'}, E_q^{''} = 0$$

are made in Model 0, an additional model termed Model 2C, is realised. This is a 4th order two-axis model with the field winding in the *d*-axis and one damper winding in the *q*-axis. Although both Models 2A and 2C are 4th order, two-axis representations, Model 2C is described by transient voltages behind the transient reactances, whereas Model 2A considers sub-transient information in one axis.

3.2.6. Comparison of models

It is a matter of paramount interest in ICAD synchronous generator research to determine what should be the correct synchronous generator model to use in order to exact a realistic response of the plant in generator control design tasks, without unduly increasing the overall mathematical complexity. It is reasonable to argue that the higher the model order is, *i.e.*, amount of damping winding representation, the closer the model should be to the real machine, but this premise would need to be investigated in detail.

In work related to block diagram representation of OMIB systems, it has already been established that higher order models are most desirable [3]. This may be corroborated by assessing the dynamic characteristics of the system using frequency responses. The impact of the simplifying assumptions in Models 2A, 2B, and 3 on the dynamic behaviour of the synchronous generator is shown by comparing the Bode plots of their transfer functions $K_3(s)$ and $K_4(s)$ with those of Model 1. The transfer functions $K_3(s)$ and $K_4(s)$ for all models can be found in Appendix C and the generator parameters are given in Appendix B. The generator operating condition corresponds to the lagging power factor operation given in [3], and reproduced in Table 3.1. The Bode diagrams of the transfer functions $K_3(s)$ and $K_4(s)$ are shown in Figure 3.3.

Table 3.1. System operating condition for Study 1

	Value		
Variable	**Case I: Lagging PF**	**Case II: Unit PF**	**Case III: Leading PF**
P_g	0.736 *p.u.*	0.832 *p.u.*	0.912 *p.u.*
Q_g	0.7518 *p.u.*	0.1277 *p.u.*	–0.3921 *p.u.*
PF	0.69956	0.98843	0.91869 (lead)
δ_0	29.85 °	41.72 °	58.85 °
$\lvert V_{\infty 0}\rvert$	0.92 *p.u.*	1.04 *p.u.*	1.14 *p.u.*
$\angle V_{\infty 0}$	60.15 °	48.28 °	31.15 °
$\lvert e_{t0}\rvert$	1.0522 *p.u.*	1.0522 *p.u.*	1.0522 *p.u.*
$\angle e_{t0}$	68.89 °	57.03 °	39.91 °
$\lvert i_{t0}\rvert / \lvert I_{\infty 0}\rvert$	1 *p.u.*	0.8 *p.u.*	0.94347 *p.u.*
$\angle i_{t0} / \angle I_{\infty 0}$	23.282 °	48.305 °	63.175 °
E_{fd0}	2.3088 *p.u.*	1.6517 *p.u.*	1.2903 *p.u.*
X_t	0.2 *p.u.*	0.2 *p.u.*	0.2 *p.u.*

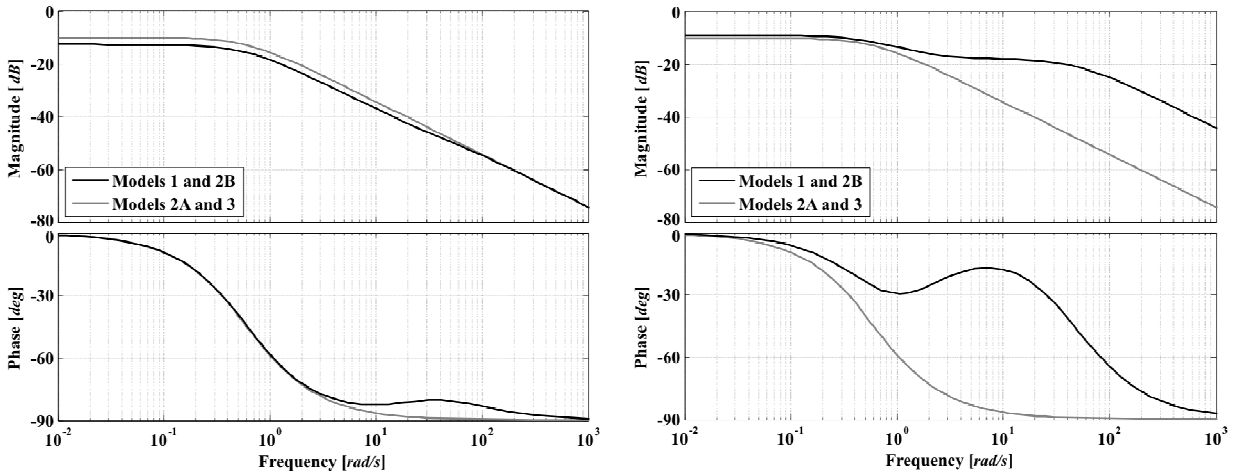

Figure 3.3. Frequency response characteristics for different generator models: (*a*) $K_3(s)$; (*b*) $K_4(s)$

It should be noticed that this assessment is for Models 1, 2A, 2B and 3. Since the value of the transient reactance $X_q^{'}$ is not available for the machine used in this study, Models 0 and 2C are not realisable at this point. Both models will be examined later in the chapter using a different synchronous generator for which full data is available.

The frequency response characteristics can be interpreted as the interaction of one variable upon another, such as $\Delta E_q^{''}$ on ΔE_{fd} through $K_3(s)$ (or $\Delta E_q^{'}$ on ΔE_{fd}, depending on the model used), $\Delta E_q^{''}$ on $\Delta\delta$ (or $\Delta E_q^{'}$ on $\Delta\delta$) through $K_4(s)$, and $\Delta E_d^{''}$ on $\Delta\delta$ through $K_{4d}(s)$. From the Bode plots of the transfer functions $K_3(s)$ and $K_4(s)$ (Figure 3.3), it can be seen that Models 1 and 2B exhibit the same behaviour, an expected result since their transfer functions are exactly the same – and similarly for Models 2A and 3. From these results it can be seen that the response provided by Models 2A and 3, resulting from simplifications made to Model 1, has a higher magnitude and phase lag when compared to the response given by Model 1. Also, a significant difference can be observed in magnitude and a phase lag in $K_4(s)$, especially at higher frequency values.

The block diagram representation yields physical insight and understanding of the machine's inner behaviour; with the representation enabling a transparent analysis of the interaction between internal machine variables in terms of constants and transfer functions that encapsulate fully all key dynamic parameters of the system. However, caution needs to be exercised since not all interactions between the various variables may be useful for control system design purposes. Equally important, and based on the previous assessment of the block diagram transfer function models, it is not clear which model should be used for control system design purposes, since the frequency response plots of Models 1 (two-axis model) and 2B (one-axis) are similar (except for the transfer function $K_{4d}(s)$ which does not appear in Model 2B). The same is true for Models 2A (two-axis) and 3 (one-axis). Such uncertainties can be resolved by working with ICAD, a powerful analysis and control system design framework which is well suited to the

task of carrying out small-signal stability assessments of OMIB systems. It will be shown in later sections of this chapter that through the analysis of Multivariable Structure Functions (MSF), the dynamical behaviour and structure of the system can be described in a global context in which the characteristics of the individual transfer functions do not mask the relevant dynamics which are key to a robust multivariable control system design.

3.3. Transfer function matrix representation

The transfer function matrix representation of the various block-diagram models presented in Section 3.2 can be obtained by suitable manipulation of the relevant equations. Such a representation is essential for analysis of the synchronous generator plant dynamics under the ICAD framework.

The synchronous generator connected to an infinite bus via a tie-line reactance, irrespective of the block diagram model under consideration, has the following generic representation in frequency domain

$$\begin{bmatrix} \Delta\omega(s) \\ \Delta e_t(s) \end{bmatrix} = \begin{bmatrix} g_{11}(s) & g_{12}(s) \\ g_{21}(s) & g_{22}(s) \end{bmatrix} \begin{bmatrix} \Delta P_m(s) \\ \Delta E_{fd}(s) \end{bmatrix} \tag{3.7}$$

$$\mathbf{y}(s) = \mathbf{G}(s)\mathbf{u}(s) \tag{3.8}$$

where $\mathbf{G}(s)$ is the transfer function matrix of the linearised models of the synchronous generator connected to an infinite bus via a tie-line reactance. The individual elements of $\mathbf{G}(s)$ will vary depending on the selected model. The full derivation and form of these terms are shown in Appendix C.

3.3.1. Model 1

This model is defined by equations (3.1)–(3.6). Following some algebraic manipulations, the transfer function matrix (3.7) is obtained, where

$$\begin{aligned}
g_{11}(s) &= \frac{\left(1+\tau_q^{"}s\right)\left(Es^2+Fs+G\right)s}{\Pi(s)} \\
g_{12}(s) &= -\frac{K_2A\left(1+\tau_{d0}^{"}s\right)\left(1+\tau_q^{"}s\right)s}{\Pi(s)} \\
g_{21}(s) &= \omega_0\left[\frac{K_5\left(Es^2+Fs+G\right)\left(1+\tau_q^{"}s\right)-K_6\left(B+Cs\right)\left(1+\tau_q^{"}s\right)+K_{6d}C_{4d}\left(Es^2+Fs+G\right)}{\Pi(s)}\right] \\
g_{22}(s) &= \frac{A\left(1+\tau_{d0}^{"}s\right)}{\Pi(s)}\cdot\left[K_6\left(1+\tau_q^{"}s\right)\left(2Hs+D\right)s\right]+ \\
&\quad +\frac{A\left(1+\tau_{d0}^{"}s\right)}{\Pi(s)}\cdot\left(K_6\left[\left(1+\tau_q^{"}s\right)K_1-K_{2d}C_{4d}\right]-K_2\left[\left(1+\tau_q^{"}s\right)K_5+K_{6d}C_{4d}\right]\right)\omega_0
\end{aligned} \tag{3.9}$$

and

$$\Pi(s) = (2Hs + D)\left(Es^2 + Fs + G\right)\left(1 + \tau_q^{"}s\right)s + K_1\left(Es^2 + Fs + G\right)\left(1 + \tau_q^{"}s\right)\omega_0 +$$
$$-K_2\left(B + Cs\right)\left(1 + \tau_q^{"}s\right)\omega_0 - K_{2d}C_{4d}\left(Es^2 + Fs + G\right)\omega_0$$

The various constant terms of the transfer function matrix (3.9), for this model, are given in Appendix C.

3.3.2. Models 2A, 2B and 3

Following a similar line of algebraic manipulations as for Model 1, the corresponding transfer function matrix representation is arrived at for the rest of the models. Refer to Appendix C for full details.

3.3.3. Transfer function matrix obtained through state-space representations

It is also possible to arrive at the transfer function matrix representation (3.7) of the OMIB system using an alternative route, avoiding algebraic manipulations of equations (3.1)–(3.6). This involves the state-space representation of the algebraic and differential set of equations (2.2)–(2.18). Following linearisation of these equations, the state-space representation is:

$$\begin{aligned} \dot{\Delta\mathbf{x}} &= \mathbf{A}\Delta\mathbf{x} + \mathbf{B}\Delta\mathbf{u} \\ \Delta\mathbf{y} &= \mathbf{C}\Delta\mathbf{x} + \mathbf{D}\Delta\mathbf{u} \end{aligned} \tag{3.10}$$

where

$$\Delta\mathbf{y} = \left[\Delta\omega \quad \Delta e_t\right]^T \tag{3.11}$$

$$\Delta\mathbf{u} = \left[\Delta P_m \quad \Delta E_{fd}\right]^T \tag{3.12}$$

$$\Delta\mathbf{x} = \left[\Delta\omega \quad \Delta\mathbf{E} \quad \Delta\delta\right]^T \tag{3.13}$$

The size and form of vector $\Delta\mathbf{E}$ in (3.13) vary depending on the synchronous generator model used. For example, for Model 1, the state vector $\Delta\mathbf{x}$ (3.13) becomes

$$\Delta\mathbf{x} = \left[\Delta\omega \quad \Delta E_q^{'} \quad \Delta E_q^{"} \quad \Delta E_d^{"} \quad \Delta\delta\right]^T \tag{3.14}$$

The output and input vectors $\Delta\mathbf{y}$ and $\Delta\mathbf{u}$ remain the same regardless of the model used.

The system, control and output matrices **A**, **B** and **C** in (3.10) will vary depending on the model, while feed-forward matrix **D** will be a (2×2) matrix with zero entries for all cases. For Model 1, the **A**, **B,** **C** and **D** matrices are:

$$\mathbf{A} = \begin{bmatrix} -\frac{D}{2H} & 0 & -\frac{K_2}{2H} & \frac{K_{2d}}{2H} & -\frac{K_1}{2H_i} \\ 0 & -\frac{1}{\tau_{d0}^{'}} & a_{23} & 0 & a_{25} \\ 0 & \frac{1}{\tau_{d0}^{"}} - \frac{1}{\tau_{d0}^{'}} & a_{33} & 0 & a_{35} \\ 0 & 0 & 0 & a_{44} & a_{45} \\ \omega_0 & 0 & 0 & 0 & 0 \end{bmatrix} \tag{3.15}$$

$$\mathbf{B} = \begin{bmatrix} \dfrac{1}{2H} & 0 & 0 & 0 & 0 \\ 0 & \dfrac{1}{\tau'_{d0}} & \dfrac{1}{\tau'_{d0}} & 0 & 0 \end{bmatrix}^T \tag{3.16}$$

$$\mathbf{C} = \begin{bmatrix} 1 & 0 & 0 & 0 & 0 \\ 0 & 0 & K_6 & K_{6d} & K_5 \end{bmatrix} \tag{3.17}$$

$$\mathbf{D} = \mathbf{0}_{2\times 2} = \begin{bmatrix} 0 & 0 \\ 0 & 0 \end{bmatrix} \tag{3.18}$$

with the parameters of (3.15) and (3.17) given in Appendix C. The procedure for obtaining the state-space representations is shown in Appendix C.

In order to obtain the transfer function matrix representation, starting from the state-space representation (3.10), and assuming linearity, its Laplace transform is given by

$$s\Delta\mathbf{x}(s) - \Delta\mathbf{x}(0) = \mathbf{A}\Delta\mathbf{x}(s) + \mathbf{B}\Delta\mathbf{u}(s) \tag{3.19}$$

$$\Delta\mathbf{y}(s) = \mathbf{C}\Delta\mathbf{x}(s) + \mathbf{D}\Delta\mathbf{u}(s) \tag{3.20}$$

Solving for $\Delta\mathbf{x}(s)$ in the state equation (3.19),

$$\Delta\mathbf{x}(s) = (s\mathbf{I} - \mathbf{A})^{-1}\Delta\mathbf{x}(0) + (s\mathbf{I} - \mathbf{A})^{-1}\mathbf{B}\Delta\mathbf{u}(s) \tag{3.21}$$

Substituting (3.21) into the output equation (3.20) yields

$$\Delta\mathbf{y}(s) = \mathbf{C}(s\mathbf{I} - \mathbf{A})^{-1}\Delta\mathbf{x}(0) + \left[\mathbf{C}(s\mathbf{I} - \mathbf{A})^{-1}\mathbf{B} + \mathbf{D}\right]\Delta\mathbf{u}(s) \tag{3.22}$$

Assuming an initial condition $\Delta\mathbf{x}(0) = 0$ in (3.22) gives

$$\Delta\mathbf{y}(s) = \mathbf{G}(s)\Delta\mathbf{u}(s) \tag{3.23}$$

where

$$\mathbf{G}(s) = \mathbf{C}(s\mathbf{I} - \mathbf{A})^{-1}\mathbf{B} + \mathbf{D} \tag{3.24}$$

which is the transfer function matrix of the system. Notice that equations (3.23) and (3.8) are fully equivalent.

It is quite clear that the algebraic procedure to obtain an explicit representation of elements $g_{ij}(s)$ of transfer function matrix $\mathbf{G}(s)$, such as the ones provided for Model 1 in (3.9), is a rather cumbersome procedure for OMIB systems, as shown in Appendix C. However, it has the advantage that as individual elements are fully expressed by system parameters, parametric studies are feasible and very useful. Nevertheless, whenever considering more complex systems, such as those involving more than one synchronous machine, the algebraic procedure becomes unyielding. For such cases, covered in Chapters 5 and 6, transfer function matrices obtained through state-space representations may be the only practical alternative.

The analysis of the MSFs of the transfer function matrix models presented in this section enables an effective basis on which to design controllers for synchronous generators. They also provide for a transparent and straightforward framework with which to assess the dynamical characteristics of the system. Furthermore, their appropriate interpretation provides a formal explanation as to why some operating conditions are more critical than others. Such insight is not afforded by the block diagram approach.

3.4. Multivariable structure function analysis

In the framework afforded by ICAD, discussed in Appendix A, the dynamical structure of the plant (3.7) is determined by the input-output channels resulting from pairing each input to each output by means of diagonal controllers. For instance in the case of the OMIB system, we have

$$\mathbf{K_a}(s)=\begin{bmatrix} k_{11}(s) & 0 \\ 0 & k_{22}(s) \end{bmatrix} \Rightarrow \begin{cases} C_1(s):\Delta P_m(s)\rightarrow\Delta\omega(s) \\ C_2(s):\Delta E_{fd}(s)\rightarrow\Delta e_t(s) \end{cases} \Rightarrow \gamma_a(s)=\frac{g_{12}(s)g_{21}(s)}{g_{11}(s)g_{22}(s)} \tag{3.25}$$

$$\mathbf{K_b}(s)=\begin{bmatrix} 0 & k_{12}(s) \\ k_{21}(s) & 0 \end{bmatrix} \Rightarrow \begin{cases} C_1(s):\Delta P_m(s)\rightarrow\Delta e_t(s) \\ C_2(s):\Delta E_{fd}(s)\rightarrow\Delta\omega(s) \end{cases} \Rightarrow \gamma_b(s)=\frac{g_{11}(s)g_{22}(s)}{g_{12}(s)g_{21}(s)}=\gamma_a^{-1}(s) \tag{3.26}$$

The diagonal controller given in (3.25), which considers pairings as $\Delta P_m(s)\rightarrow\Delta\omega(s)$ and $\Delta E_{fd}(s)\rightarrow\Delta e_t(s)$, agrees with that used for conventional controllers, *i.e.*, the turbine-governor control corresponds to $k_{11}(s)$ and the excitation system corresponds to $k_{22}(s)$. In practice, a loop-by-loop design is normally carried out based on the bandwidth separation between the mechanical and electrical subsystems of the synchronous generator (represented by $C_1(s)$ and $C_2(s)$, respectively, in (3.25)). A more detailed description of the turbine-governor and the excitation system is given at a later stage of this chapter. For control system analysis purposes, the closed-loop diagram of the system when considering the controller given in (3.25) is shown in Figure 3.4. Figure 3.5 shows an equivalent individual channel representation of the system.

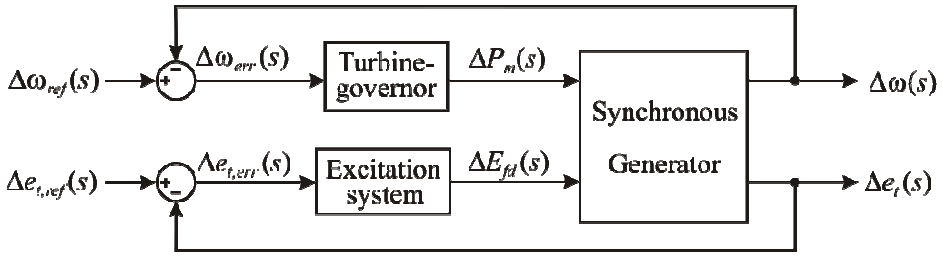

Figure 3.4. Block diagram for control system analysis considering (3.25)

From Figure 3.5, it can be seen observed that the multivariable system can be re-formulated as two SISO channels, where each channel comprises a feedback loop and its controller. Each channel is subject to a disturbance $d_i(s)$; therefore, the behaviour of an individual channel will be affected both by its controller and by the other individual channel. The representation of Figure 3.5 is fully equivalent to the

system of Figure 3.4, with no loss of information. The multivariable character of the plant is suitably contained and quantified, in the frequency domain, by the MSF $\gamma_a(s)$.

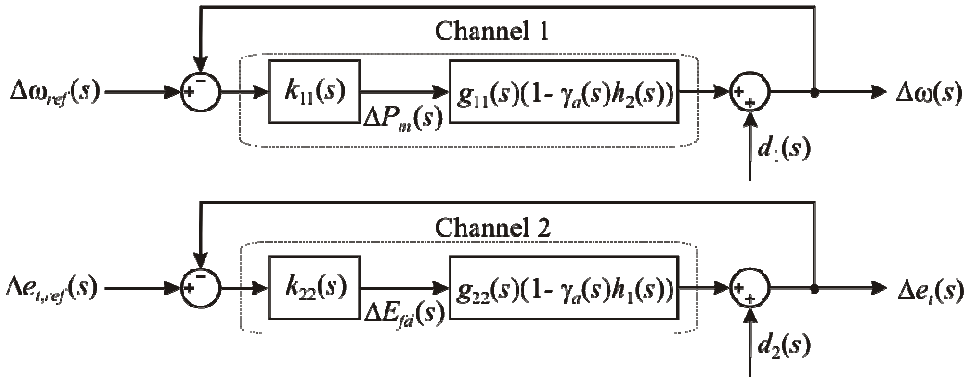

Figure 3.5. Individual channel representation considering (3.25)

It is also possible to design a controller associated to (3.26), where the inputs are swapped. Such configuration is examined in reference [8], where two practical disadvantages are discussed: (*i*) an integrity problem due to an unstable subsystem, where should the exciter loop fail, the whole system would go unstable; and (*ii*) the subjection of the governor to high-frequency signals. In the analysis presented in this chapter, the configuration described by (3.25) will be the only case here considered. No further discussion is warranted for the swapped input-output pairing configuration given by (3.26).

Coupling between the two individual channels given in (3.25) is determined by $\gamma_a(s)$, their associated MSF. A small magnitude of MSF is amenable to a low signal interaction between the governor and exciter loops and vice-versa. It should be noticed from (3.25) that the MSF $\gamma_a(s)$ has an explicit parametric form which is dependent on the model being used, which is extremely useful in assessing the impact of system parameters changes on system performance [8]. For instance, for Model 1 it is given by

$$\gamma_a(s) = \frac{-K_2\left[K_5\left(Es^2+Fs+G\right)\left(1+\tau_q^{''}s\right)-K_6\left(B+Cs\right)\left(1+\tau_q^{''}s\right)+K_{6d}C_{4d}\left(Es^2+Fs+G\right)\right]\omega_0}{\left(Es^2+Fs+G\right)\left\{K_6\left(1+\tau_q^{''}s\right)\left(2Hs+D\right)s+\left(K_6\left[\left(1+\tau_q^{''}s\right)K_1-K_{2d}C_{4d}\right]-K_2\left[\left(1+\tau_q^{''}s\right)K_5+K_{6d}C_{4d}\right]\right)\omega_0\right\}} \quad (3.27)$$

Two quite different kinds of studies are presented next. The first study assesses the behaviour of the plant at different power factors (Table 3.1) with a fix value of tie-line reactance. The second study assesses the impact of a varying tie-line reactance value on system performance and its effect on reactive power requirements. The parameters associated to those operating conditions are found in Table 3.2.

3.4.1. Study 1. Operation under different power factors

Three cases of power factor values are presented here, which correspond to previously studied cases using the block diagram approach in [3]. Lagging, near-unit, and leading power factor operations of the synchronous generator are considered for analysis while keeping a constant tie-line reactance of X_t = 0.2

p.u. It should be noticed that a zero mechanical damping term *D* is used as a system parameter in order to assess a more critical condition. Parameter information corresponding to such operating conditions is given in Table 3.1.

3.4.1.1. Case 1. Lagging power factor

Using the operating condition given in Table 3.1 for the case of lagging power factor, the transfer function matrices and MSFs of all models are obtained (not shown). The Nyquist and Bode diagrams of the MSFs corresponding to the four models are shown in Figure 3.6.

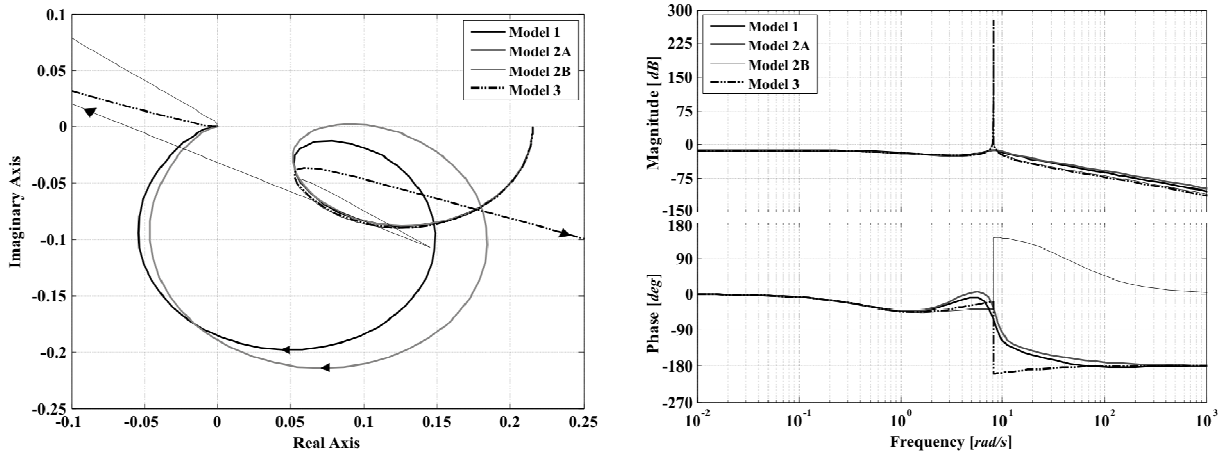

(*a*) (*b*)

Figure 3.6. Assessment of $\gamma_a(s)$ (Case 1): (*a*) Nyquist plots; (*b*) Bode plots

As evidenced by the set of results, Models 2B and 3 do not yield suitable information for analysis, owing to the absence of a damping winding in the *q*-axis. Moreover, a switch-back characteristic manifests in all four models due to the presence of a resonance (lightly damped LHPP pair) closely followed by an inverted resonance (lightly damped LHPZ pair). Such feature is exacerbated in Models 2B and 3 due to the lack of damping in the *q*-axis, yielding incorrect information in the Bode plots. This also explains the differences shown when comparing the Nyquist plots of Models 3 and 2B with those of Models 1 and 2A. Therefore, analysis for the input-output pairing configurations carried out below is restricted to Models 1 and 2A.

The existence and design of stabilising compensators $k_{11}(s)$ and $k_{22}(s)$ for individual channels (3.25) (refer to equations (A.6) and (A.11) in Appendix A) can be determined from the characteristics of $\gamma_a(s)$, revealed by its Nyquist/Bode plots shown in Figure 3.6. The following analysis is carried out as in [11]:

(a.1) The value of $\gamma_a(s)$ as $s \rightarrow \infty$ is less than one (in fact, it is zero), so

$$1 - \lim_{s \to \infty} \gamma_a(s) > 0$$

and the Nyquist plot of $\gamma_a(s)$ lies on the left of the point (1,0) for all frequency values.

(a.2) From (3.25) and the calculation of the individual elements of **G**(*s*) given in (3.9), it can be seen that $\gamma_a(s)$ contains no RHPPs and its Nyquist plot does not encircle the point (1,0). Therefore, using the Nyquist Stability Criterion, $(1-\gamma_a(s))$ contains no RHPZs.

(a.3) As a result of **(a.1)** and **(a.2)**, $h_i(s)$ do not influence the channel structure at high frequency values. The number of encirclements to (1,0) by $\gamma_a(s)h_i(s)$ and $\gamma_a(s)$ coincide (in this case, zero).

(a.4) For this control configuration, transfer functions $g_{ii}(s)$ are stable and minimum phase. Thus, no cancellation of RHPPs of $\gamma_a(s)$ with the RHPZs of $h_i(s)$ occur in the following product

$$\gamma_a(s)h_i(s) = \frac{g_{ij}(s)g_{ji}(s)}{g_{ii}(s)g_{jj}(s)} \cdot \frac{k_{ii}(s)g_{ii}(s)}{1+k_{ii}(s)g_{ii}(s)}$$

Therefore, the structure of $(1-\gamma_a(s))$ is preserved by $(1-\gamma_a(s)h_i(s))$ provided that $h_i(s)$ do not have RHPPs. To achieve this, $k_{ii}(s)$ must be designed as a stabilising controller of $g_{ii}(s)$ – facilitated by the fact that the $g_{ii}(s)$ are stable and minimum-phase.

It can be concluded that the existence of a stabilising controller for channels (3.25) –see equations (A.6) and (A.11)– reduces to the existence of controllers $k_{ii}(s)$ which, simultaneously, stabilise both $g_{ii}(s)(1-\gamma_a(s)h_i(s))$ and $g_{ii}(s)$, with $i,j = 1,2$, $i \neq j$. In other words, controllers $k_{ii}(s)$ should stabilise both the channels and the diagonal elements of the transfer function matrix.

Besides the necessary characteristics that the controllers ought to possess to achieve a closed-loop stable system, assessed by the analysis of the MSFs, an analysis of the system models should be carried out in order to identify a suitable model for small-signal stability studies. Models 1 and 2A offer similar structural characteristics but the latter gives a slightly higher coupling if the pairing associated to conventional controllers is used, as shown in the previous Nyquist/Bode diagrams of the MSFs. Nevertheless, in the absence of static damping, the behaviour of Models 2B and 3 is rather different when compared to that of Models 1 and 2A. This point is shown all the more clearly when the switch-back characteristic is looked at in the Nyquist/Bode diagrams of MSFs $\gamma_a(s)$. Such features may reflect a poor performance and poor robustness measures of Models 2B and 3 and not due to a bad controller design in itself.

3.4.1.2. Cases 2 and 3. Near-unit and leading power factor

Similarly to Case 1, in these cases too the Models 2B and 3 have quite different characteristics from those of Models 1 and 2A. Therefore, only Model 1 is analysed. Figure 3.7 shows the Nyquist and Bode diagrams of the MSFs for the cases of near-unit and leading power factor operations. For comparison purposes, the case of lagging power factor is also plotted in this figure. Borrowing from the discussion in Case 1, the existence and design of stabilising compensators $k_{11}(s)$ and $k_{22}(s)$ can be determined from the characteristics of $\gamma_a(s)$, revealed by its Nyquist/Bode plots shown in Figure 3.7. The analysis for the cases

of near-unit and leading power factors does not differ significantly from that of lagging power factor; hence, no further discussion is warranted.

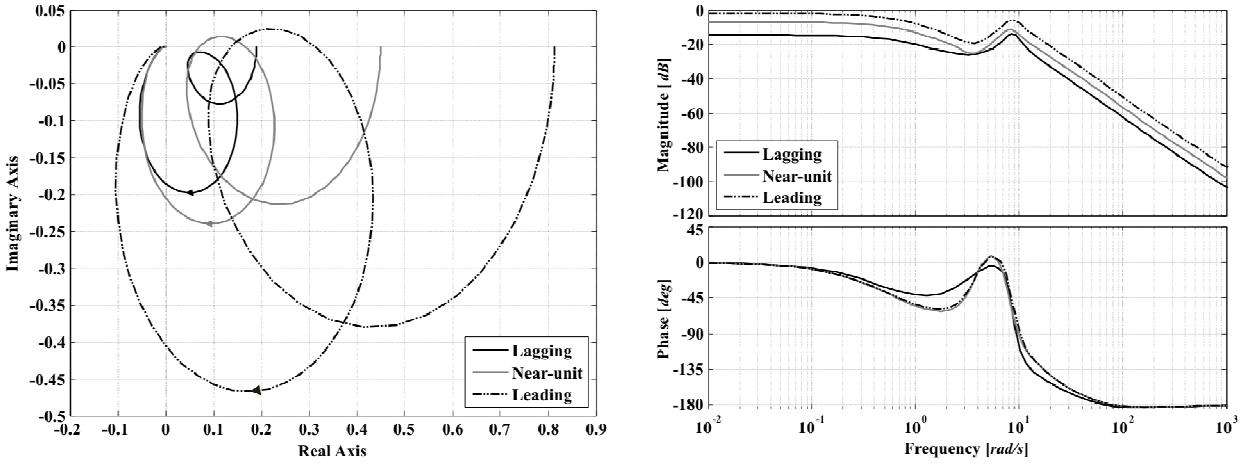

(*a*) (*b*)

Figure 3.7. Assessment of $\gamma_a(s)$ of Model 1 at different power factor conditions: (*a*) Nyquist plots; (*b*) Bode plots

Figure 3.7 shows the Nyquist and Bode plots of $\gamma_a(s)$ of Model 1 for all operating conditions assessed in Study 1. Notice that the phase margin is infinite for all cases. If conventional controllers are used the most critical operating condition is when the generator works at a leading power factor because $\gamma_a(0)$ approaches the point (1,0). As seen, the coupling between channels in this case starts to be considerable (just below 0 *dB*). Similarly, an increase in active power is associated with a decrease in stability robustness. Such characteristics are consistent with what has been observed in practice. Moreover, the Nyquist plot always starts to the left of the point (1,0) – an important fact, since the structural characteristics are preserved for all the cases here presented. In other words, it can be stated that the system is minimum phase and stable for all operating conditions.

It is a well known fact in ICAD that robustness decreases as the Nyquist plot of $\gamma_a(s)$ moves toward (1,0). In general, whenever a plant exhibits poor structural characteristics, the system will become very sensitive to uncertainty [7]. If that is the case, robustness measures (in terms of gain and phase margins) are no longer valid. Therefore, it can be said that the MSF $\gamma_a(s)$ clarifies the possibilities to meet design specifications while satisfying robustness conditions [16].

Notice that the polar plots of $\gamma_a(s)$ (Figure 3.4, lagging power factor condition) clearly show that Models 2B and 3 contain no damping at the natural oscillation frequency and, as a result of that, a high switch-back characteristic is present. By addition of the *q*-axis damper in the models, as in Models 1 and 2A, system damping is introduced over the frequency range of concern. It can be concluded that models 2B and 3, including only winding representation in the *d*-axis, do not yield sufficient system damping representation and are not recommended for analysis and control system design. Models 1 and 2A offer similar structural characteristics to one another; however, Model 1 exhibits a higher level of damping.

Whenever computational burden is not an issue, Model 1 should be used because of its increased accuracy.

As a corollary of the previous analysis, it may be stated, in quite broad terms, that independently of the operating points at which the synchronous generator finds itself, the existence of a stabilising controller for channels (3.25) (considering pairings: $\Delta P_m(s) \rightarrow \Delta\omega(s)$ and $\Delta E_{fd}(s) \rightarrow \Delta e_t(s)$) reduces to the existence of controllers $k_{ii}(s)$ which stabilise simultaneously $g_{ii}(s)(1 - \gamma_d(s)h_j(s))$ and $g_{ii}(s)$, with $i,j = 1,2$, $i \neq j$; that is, a controller that stabilises both the channels and the diagonal elements of the transfer function matrix. In terms of control system design, this is the simplest case scenario [16], further facilitated by the fact that all elements $g_{ij}(s)$ are stable and minimum phase. In other words, if a multivariable controller is obtained in which the characteristics of the MSFs are addressed correctly, such fixed controller should guarantee stability and robustness for all operating conditions.

3.4.2. Study 2. Operation with different tie-line reactance values

An assessment of the synchronous generator performance is carried out under different values of tie-line reactance at lagging power factor conditions. Such study is carried out as in [3] (where X_t = 0.2, 0.4, 0.6, 0.8 *p.u.*). Model 1 is the only one considered in this study. Information corresponding to such operating conditions is given in Table 3.2.

Table 3.2. System operating condition for Study 2

	Value					
Variable	**Case 1**	**Case 2**	**Case 3**	**Case 4**	**Case 5**	**Case 6**
	X_t = 0.2 *p.u.*	X_t = 0.3 *p.u.*	X_t = 0.4 *p.u.*	X_t = 0.5 *p.u.*	X_t = 0.6 *p.u.*	X_t = 0.8 *p.u.*
P_g	0.736 *p.u.*	0.736 *p.u.*	0.736 *p.u.*	0.736 *p.u.*	0.736 *p.u.*	0.736 *p.u.*
Q_g	0.128 *p.u.*	0.193 *p.u.*	0.256 *p.u.*	0.323 *p.u.*	0.384 *p.u.*	0.512 *p.u.*
PF	0.98521	0.9673	0.9445	0.9157	0.88658	0.82091
δ_0	45.22 °	47.558 °	49.76 °	51.873 °	53.58 °	56.82 °
$\lvert V_{\infty 0}\rvert$	0.92 *p.u.*	0.92 *p.u.*	0.92 *p.u.*	0.92 *p.u.*	0.92 *p.u.*	0.92 *p.u.*
$\angle V_{\infty 0}$	44.78 °	42.442 °	40.24 °	38.127 °	36.42 °	33.18 °
$\lvert e_{t0}\rvert$	0.9338 *p.u.*	0.934 *p.u.*	0.9741 *p.u.*	0.974 *p.u.*	1.0377 *p.u.*	1.1207 *p.u.*
$\angle e_{t0}$	54.64°	57.332 °	59.42 °	62.451 °	63.97 °	68 °
$\lvert i_{t0}\rvert$ / $\lvert I_{\infty 0}\rvert$	0.8 *p.u.*	0.81465 *p.u.*	0.8 *p.u.*	0.82521 *p.u.*	0.8 *p.u.*	0.8 *p.u.*
$\angle i_{t0}$ / $\angle I_{\infty 0}$	44.778 °	42.638 °	40.241 °	38.756 °	36.417 °	33.176 °
E_{fd0}	1.5822 *p.u.*	1.6522 *p.u.*	1.721 *p.u.*	1.7934 *p.u.*	1.8627 *p.u.*	2.0067 *p.u.*
X_t	0.2 *p.u.*	0.3 *p.u.*	0.4 *p.u.*	0.5 *p.u.*	0.6 *p.u.*	0.8 *p.u.*

The Nyquist and Bode plots of the associated MSFs for the four tie-line reactances are shown in Figure 3.8. As previously discussed, the existence of stabilising controllers is determined by the

characteristics of the MSF. The analysis in all cases is carried out in a similar manner as in Case 1 of Study 1, since the structural characteristics under varying tie-line reactance are preserved. In fact, $\gamma_a(s)$ offers a gain margin of around 5.9 *dB* for all values of the tie-line reactance and the Nyquist plot always starts to the left of (1,0). It should be noticed that the coupling between channels increases if the value of the tie-line reactance grows. For the cases when X_t = 0.6 *p.u.* and X_t = 0.8 *p.u.* coupling over 0 *dB* is present for a range of frequencies, as evidenced by the Bode diagram. This is consistent with the fact that for long-distance transmission, with no compensation, system operation becomes impaired because of the long electrical distances involved. One other key observation elucidated from this analysis is that the larger the amount of reactive power flow in the tie-line reactance (while keeping active power constant), the higher the coupling between channels – with the plant becoming difficult to control.

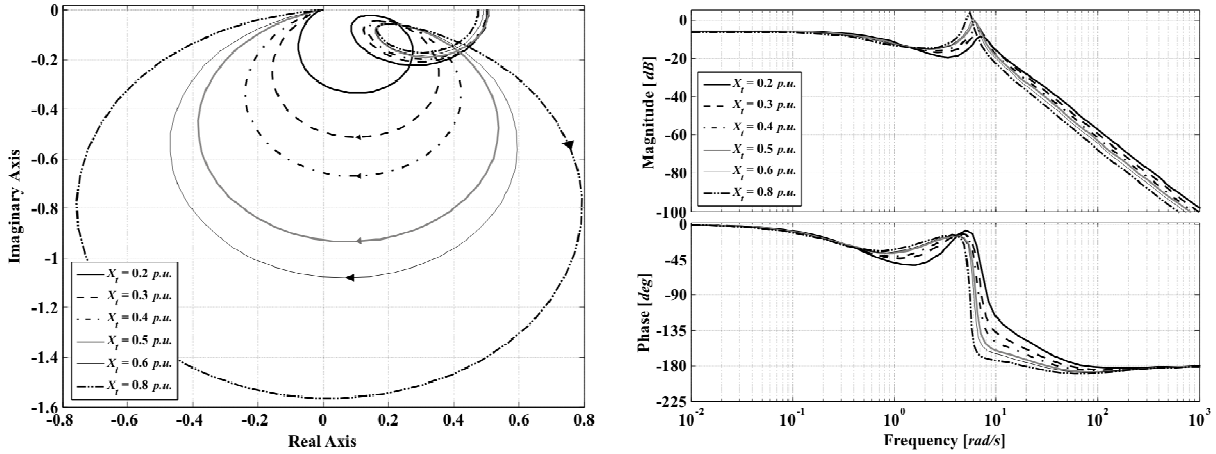

(*a*) (*b*)

Figure 3.8. Assessment of $\gamma_a(s)$ at different tie-line reactance values: (*a*) Nyquist plots; (*b*) Bode plots.

It is argued that the block diagram representation provides a useful basis for the analysis of the generator dynamic performance [3]. It should be noticed, however, that the frequency response plots of the individual transfer functions (*i.e.*, $K_3(s)$, $K_4(s)$ and $K_{4d}(s)$) offer little information about the structure and characteristics that the controllers should possess in order to have a stable and robust control system. In contrast, an appropriate analysis (at low and high frequencies) of the MSF gives an effective and complete framework for designing multivariable control systems. In fact, the MSF analysis dictates what characteristics the controllers should have in order to assure closed-loop stability and robustness. It also provides a measurable coupling quantification between the input-output channels, information which is available in the frequency domain. Moreover, the MSFs show in a clear and simple manner why some operating conditions are more critical than others.

Remark: When analysing the MSF $\gamma(s)$, it is useful to include its Bode diagram alongside its Nyquist diagram for a complete assessment. The Nyquist plot is only shown for the frequency values $s = j\omega$ ranging from $\omega = 0$ to $\omega = \infty$ for a clearer visual understanding – with the *complete* plot being obtained by mirroring the positive frequency plot along the real axis in order to build a symmetric

trajectory for the negative frequencies. Although the Nyquist and the Bode plots offer equivalent information, the main difference lies in the way that it is presented. Each frequency response diagram offers distinctive information not so apparent on the other plot: on the one hand, the Bode diagram shows the phase and the magnitude of $\gamma(j\omega)$ versus ω, which is desirable to evaluate the coupling between individual channels (or multiple channels) and the frequencies where such a coupling is stronger or weaker; on the other hand, the Nyquist plot shows the position of the MSF in the complex plane, which is useful for assessing (*i*) the dynamical structure of the system by using the Nyquist Stability Criterion and (*ii*) the structural robustness of the system. For more details the reader is referred to Appendix A.

3.4.3. The static damping term and its influence on the models

It has been concluded, following a detailed MSF study, that only Models 1 and 2A are suitable for control system design. In reaching such a conclusion, a zero static damping term *D* was used as a system parameter, with the aim of assessing the most critical condition. Nevertheless, it may be argued that there is always some mechanical damping present in a physical machine and that the differences between Models 3 and 2B and Models 1 and 2A may be exaggerated if such an effect is not taken into account.

Hence, in order to examine the effect of static damping, consider the transfer function matrix representation (3.24), rewritten as

$$\mathbf{G}(s) = \frac{1}{\det(s\mathbf{I} - \mathbf{A})}\mathbf{C}\mathrm{Adj}(s\mathbf{I} - \mathbf{A})\mathbf{B} + \mathbf{D} \tag{3.28}$$

Assuming that the feed-forward matrix **D** is zero (which is the case for the state-space representation of OMIB systems, as shown in Appendix C), transfer function matrix (3.28) can be expressed as

$$\mathbf{G}(s) = \frac{\mathbf{R}(s)}{\det(s\mathbf{I} - \mathbf{A})} \tag{3.29}$$

where **R**(*s*) is a polynomial matrix in *s*. Therefore,

$$\Pi(s) = \det(s\mathbf{I} - \mathbf{A}) \tag{3.30}$$

is the characteristic polynomial of transfer function matrix **G**(*s*). The roots of

$$\det(s\mathbf{I} - \mathbf{A}) = 0 \tag{3.31}$$

are the poles of the individual transfer functions in **G**(*s*), which are identical to the eigenvalues of system matrix **A** [17]:

$$\det(\mathbf{A} - \lambda\mathbf{I}) = 0 \tag{3.32}$$

The *n* solutions of $\lambda = \lambda_1, \lambda_2, \ldots, \lambda_n$ are eigenvalues of **A**. Complex pairs of eigenvalues are given as:

$$\lambda = \sigma \pm j\omega \tag{3.33}$$

where the frequency of oscillation (in *Hz*) is given by

$$f = \frac{\omega}{2\pi} \tag{3.34}$$

which represents the actual or damped frequency. The damping ratio is given by

$$\zeta = \frac{-\sigma}{\sqrt{\sigma^2 + \omega^2}} \tag{3.35}$$

which determines the rate of decay of the amplitude of the oscillation. This will be furthered in Chapter 5 in connection with the state-space representation of multi-machine models. For instance, the characteristic polynomial of Model 3 is given by (C.138) in Appendix C,

$$\Pi(s) = (2Hs + D)\left(G + A\tau_{d0}^{'}s\right)s + K_1\omega_0\left(G + A\tau_{d0}^{'}s\right) - K_2B\omega_0 \tag{C.138}$$

Notice that the value of the damping term *D* will clearly affect the location of the eigenvalues. In order to assess the pole trajectories as a function of the damping term *D*, the Evans root locus [18] is used. The characteristic polynomial (C.138) of Model 3 can be expressed explicitly as a function of *D* as

$$\Pi(s) = \left(b_3s^3 + b_2s^2 + b_1s + b_0\right) + D\left(a_2s^2 + a_1s\right) \tag{3.36}$$

or

$$\Pi(s) = d(s) + Dn(s) \tag{3.37}$$

where

$$\begin{aligned} d(s) &= b_3s^3 + b_2s^2 + b_1s + b_0 \\ n(s) &= a_2s^2 + a_1s \end{aligned} \tag{3.38}$$

and

$$\begin{aligned} a_2 &= A\tau_{d0}^{'} & b_3 &= 2HA\tau_{d0}^{'} & b_1 &= K_1\omega_0A\tau_{d0}^{'} \\ a_1 &= G & b_2 &= 2HG & b_0 &= \omega_0\left(K_1G - K_2B\right) \end{aligned} \tag{3.39}$$

Let an auxiliary SISO open loop model be defined by transfer function

$$h(s) = \frac{n(s)}{d(s)} \tag{3.40}$$

Consider the closed-loop of (3.40) with a feedback gain *D* (that is, the damping term) as shown in Figure 3.9. Its transfer function will be given as

$$T = \frac{Dh(s)}{1 + Dh(s)} = \frac{Dn(s)}{d(s) + Dn(s)} = \frac{Dn(s)}{\Pi(s)} \tag{3.41}$$

Therefore, the closed-loop poles of the system in Figure 3.9 are the roots of

$$d(s) + Dn(s) = 0 \tag{3.42}$$

which are also the roots of the characteristic equation (3.37).

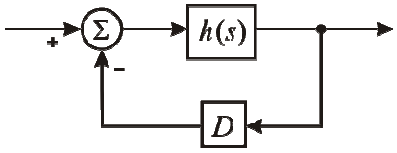

Figure 3.9. Feedback loop to examine static damping in OMIB systems

The Evans root locus of system $h(s)$ in (3.40) will provide the closed-loop pole trajectories of Model 3 as a function of the feedback gain D (with reference to Figure 3.9, provided a negative feedback). In general, the root loci are used to study the effects of varying feedback gains on the closed-loop pole locations, which in turn provide indirect information on time and frequency responses [18]. However, provided the previous procedure, the root locus can be used to study the eigenvalue locations and trajectories of the OMIB system described by (3.7) as a function of the damping term D. Similar steps can be followed to assess the pole trajectories associated to Models 1, 2A and 2B by considering their corresponding characteristic polynomial given by (C.81), (C.103) and (C.121) in Appendix C.

Figure 3.10 presents the pole trajectories associated to Models 1, 2A, 2B and 3 as a function of damping term D, at the lagging power factor condition described by Table 3.1. The pole locations at particular values of D are highlighted for each model as shown in the legend. The information associated to Figure 3.10 is summarised in Table 3.3, with the damping ratio and oscillation frequency of the complex conjugate poles included in Table 3.4.

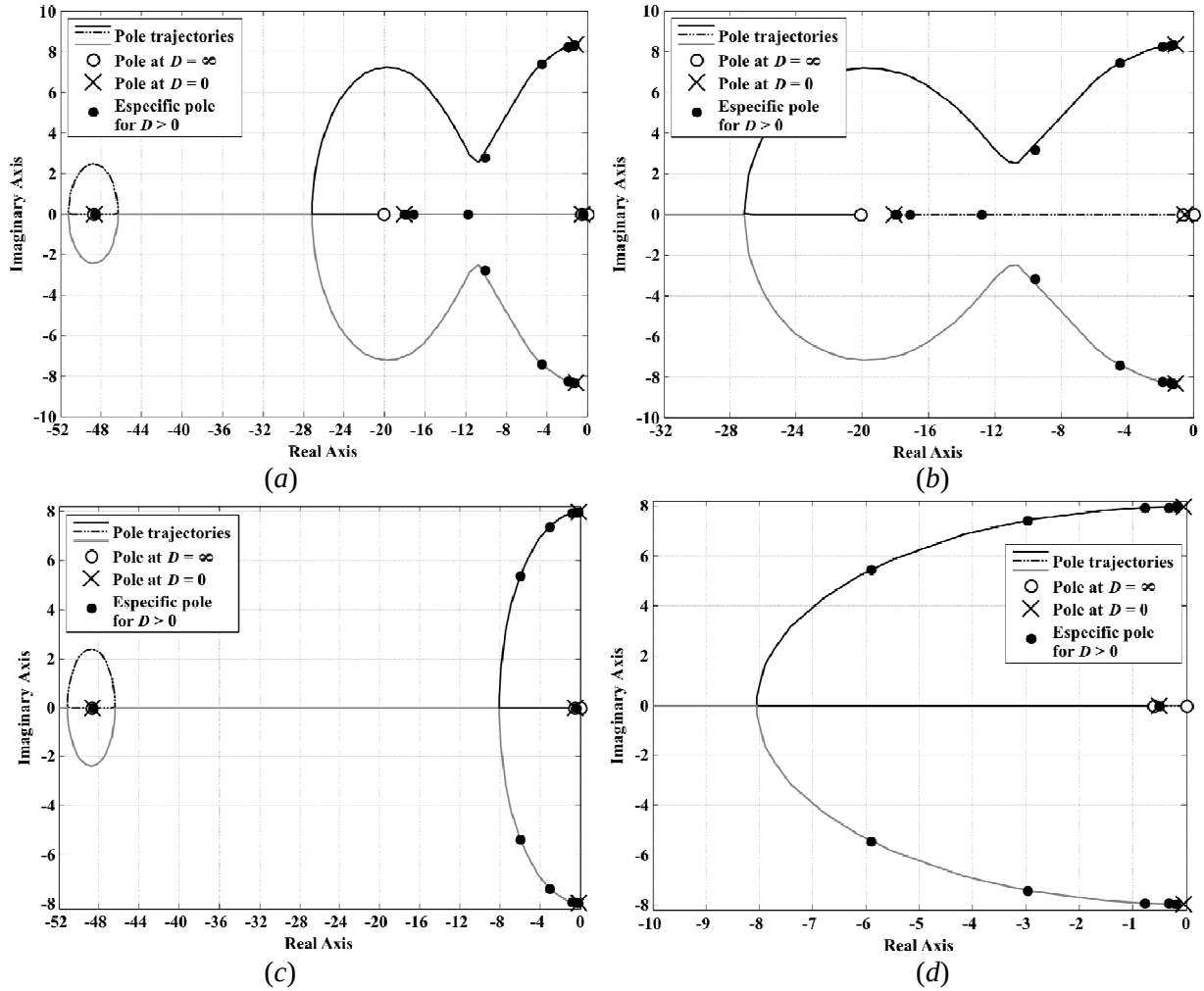

Figure 3.10. Assessment of eigenvalues locations as a function of static damping term D: (*a*) Model 1; (*b*) Model 2A; (*c*) Model 2B; (*d*) Model 3

Table 3.3. Eigenvalues as a function of static damping

Static damping	Eigenvalue	Machine representation			
		Model 1	Model 2A	Model 2B	Model 3
D = 0 *p.u.*	λ_1	–0.50542	–0.50633	–0.5072	–0.50813
	λ_2	–1.14263 + *j*8.33434	–1.08015 + *j*8.33449	–0.1035 + *j*7.95156	–0.04897 + *j*7.94827
	λ_3	–1.14263 + –*j*8.33434	–1.08015 + –*j*8.33449	–0.1035 + –*j*7.95156	–0.04897 + –*j*7.94827
	λ_4	–18.0564	–18.07565	–48.66644	
	λ_5	–48.66977			
D = 2.5 *p.u.*	λ_1	–0.50518	–0.50609	–0.50698	–0.50790
	λ_2	–1.30511 + *j*8.31989	–1.24202 + *j*8.32114	–0.25031 + *j*7.95014	–0.19546 + *j*7.94782
	λ_3	–1.30511 + –*j*8.31989	–1.24202 + –*j*8.32114	–0.25031 + –*j*7.95014	–0.19546 + –*j*7.94782
	λ_4	–18.02504	–18.0449	–48.66579	
	λ_5	–48.66916			
D = 5 *p.u.*	λ_1	–0.50494	–0.50585	–0.50675	–0.50767
	λ_2	–1.4681 + *j*8.30243	–1.40439 + *j*8.3048	–0.39712 + *j*7.94601	–0.34194 + *j*7.94467
	λ_3	–1.4681 + –*j*8.30243	–1.40439 + –*j*8.3048	–0.39712 + –*j*7.94601	–0.34194 + –*j*7.94467
	λ_4	–17.99264	–18.01314	–48.66513	
	λ_5	–48.66854			
D = 12.5 *p.u.*	λ_1	–0.50423	–0.50513	–0.50606	–0.50697
	λ_2	–1.96055 + *j*8.23161	–1.89481 + *j*8.23754	–0.83759 + *j*7.91735	–0.78140 + *j*7.91905
	λ_3	–1.96055 + –*j*8.23161	–1.89481 + –*j*8.23754	–0.83759 + –*j*7.91735	–0.78140 + –*j*7.91905
	λ_4	–17.88858	–17.91123	–48.63311	
	λ_5	–48.66665			
D = 50 *p.u.*	λ_1	–0.50054	–0.50141	–0.50247	–0.50336
	λ_2	–4.54156 + *j*7.39643	–4.46061 + *j*7.42756	–3.04059 + *j*7.3897	–2.97876 + *j*7.40971
	λ_3	–4.54156 + –*j*7.39643	–4.46061 + –*j*7.42756	–3.04059 + –*j*7.3897	–2.97876 + –*j*7.40971
	λ_4	–17.13192	–17.17446	–48.65179	
	λ_5	–48.65606			
D = 100 *p.u.*	λ_1	–0.49528	–0.4961	–0.49737	–0.4982
	λ_2	–10.14144 + *j*2.7626	–9.56695 + *j*3.17756	–5.98012 + *j*5.36395	–5.90874 + *j*5.43354
	λ_3	–10.14144 + –*j*2.7626	–9.56695 + –*j*3.17756	–5.98012 + –*j*5.36395	–5.90874 + –*j*5.43354
	λ_4	–11.80998	–12.82189	–48.63264	
	λ_5	–48.6383			

Table 3.4. Frequencies and damping ratios of the complex eigenvalues

Static damping	**Machine representation** Model 1	Model 2A	Model 2B	Model 3
D = 0 *p.u.*	f = 1.3265 *Hz* ζ = 0.1358	f = 1.3265 *Hz* ζ = 0.1285	f = 1.2655 *Hz* ζ = 0.013	f = 1.265 *Hz* ζ = 0.00616
D = 2.5 *p.u.*	f = 1.3242 *Hz* ζ = 0.155	f = 1.3243 *Hz* ζ = 0.1476	f = 1.2653 *Hz* ζ = 0.0315	f = 1.2649 *Hz* ζ = 0.02458
D = 5 *p.u.*	f = 1.3214 *Hz* ζ = 0.1741	f = 1.3218 *Hz* ζ = 0.1667	f = 1.2646 *Hz* ζ = 0.0499	f = 1.2644 *Hz* ζ = 0.043
D = 12.5 *p.u.*	f = 1.3101 *Hz* ζ = 0.2317	f = 1.311 *Hz* ζ = 0.2242	f = 1.26 *Hz* ζ = 0.1052	f = 1.2604 *Hz* ζ = 0.0982
D = 50 *p.u.*	f = 1.1772 *Hz* ζ = 0.5233	f = 1.1821 *Hz* ζ = 0.5148	f = 1.1761 *Hz* ζ = 0.3805	f = 1.1793 *Hz* ζ = 0.3730
D = 100 *p.u.*	f = 0.4397 *Hz* ζ = 0.9648	f = 0.5057 *Hz* ζ = 0.9490	f = 0.8537 *Hz* ζ = 0.7444	f = 0.8447 *Hz* ζ = 0.7361

From the complex conjugated pole information presented in Figure 3.10 and Tables 3.3 and 3.4 for the four models under consideration, it is clear that an increase in the value of the damping term D induces an increase in the damping ratio of the pole pair. For any value of D, Models 1 and 2A provide a complex pair with a higher damping ratio than those of Models 2B and 3. For small values of D, in the range 0–5 *p.u.*, the real part of the complex pair of Models 2B and 3 is small, providing a rather lightly damped pair ($\zeta < 0.05$). This is a result of the lack of dynamic damping in the one-axis models, which will be reflected in a more pronounced switch-back characteristic and internal coupling in the synchronous generator. This situation tends to reverse with an increase in the value of D but it is far from satisfactory. For instance, take the value D = 12.5 *p.u.*, where the ratios for the complex pair of Models 2B and 3 increase, but they have only half the value of those of Models 1 and 2A. In contrast, the damping ratio of the complex pairs of Models 1 and 2A varies little for values of D in the range 0–12.5 *p.u*. Even for large values of D, such as 50 *p.u.* and 100 *p.u.*, Models 1 and 2A exhibit a higher damping ratio in their complex pairs than Models 2B and 3.

Figure 3.11(*a*) compares the MSFs of Model 1 with D = 0 *p.u.* and with D = 2.5 *p.u.*, at a lagging power factor condition. The Bode plot reveals no major differences between them. The effect of not including the static damping in this model, which already incorporates dynamic damping by virtue of the damping windings, is practically negligible. Moreover, Figure 3.11(*b*) shows the MSFs of the four models when a static damping of D = 2.5 *p.u.* is employed. Models 1 and 2A agree on well throughout the frequency range. In contrast, the frequency response characteristics obtained with Models 2B and 3 (one-axis models) only coincide with those of the two-axis models at low frequencies, up to about 6 *rad/s*. It should also be noticed that the inclusion of damping, with a value of D = 2.5 *p.u.*, does not dent the switch-back characteristic in models 2B and 3.

Figure 3.11(*c*) shows the MSF using Model 1 with zero mechanical damping and those of Model 3 with five damping terms *D*, for a lagging power factor operation. The difference between the two models is significant even for cases when a large value of *D* is used, such as 50 *p.u.* or 100 *p.u.* These differences apply to both the magnitudes and phases of the Bode plots. In fact, for values of *D* in the range 2–5 *p.u.*, the MSFs show the presence of a high-magnitude peak around the frequencies of the switch-back characteristic when Model 3 is used. As the MSF provides a measure of coupling, one may think that a high coupling would exist between the channels if the analysis were to be conducted using Model 3, which clearly is not the case. Use of Model 3, unless an unrealistic value of artificial high damping *D* is considered, would lead to a poor performance due to an intrinsically inaccurate model.

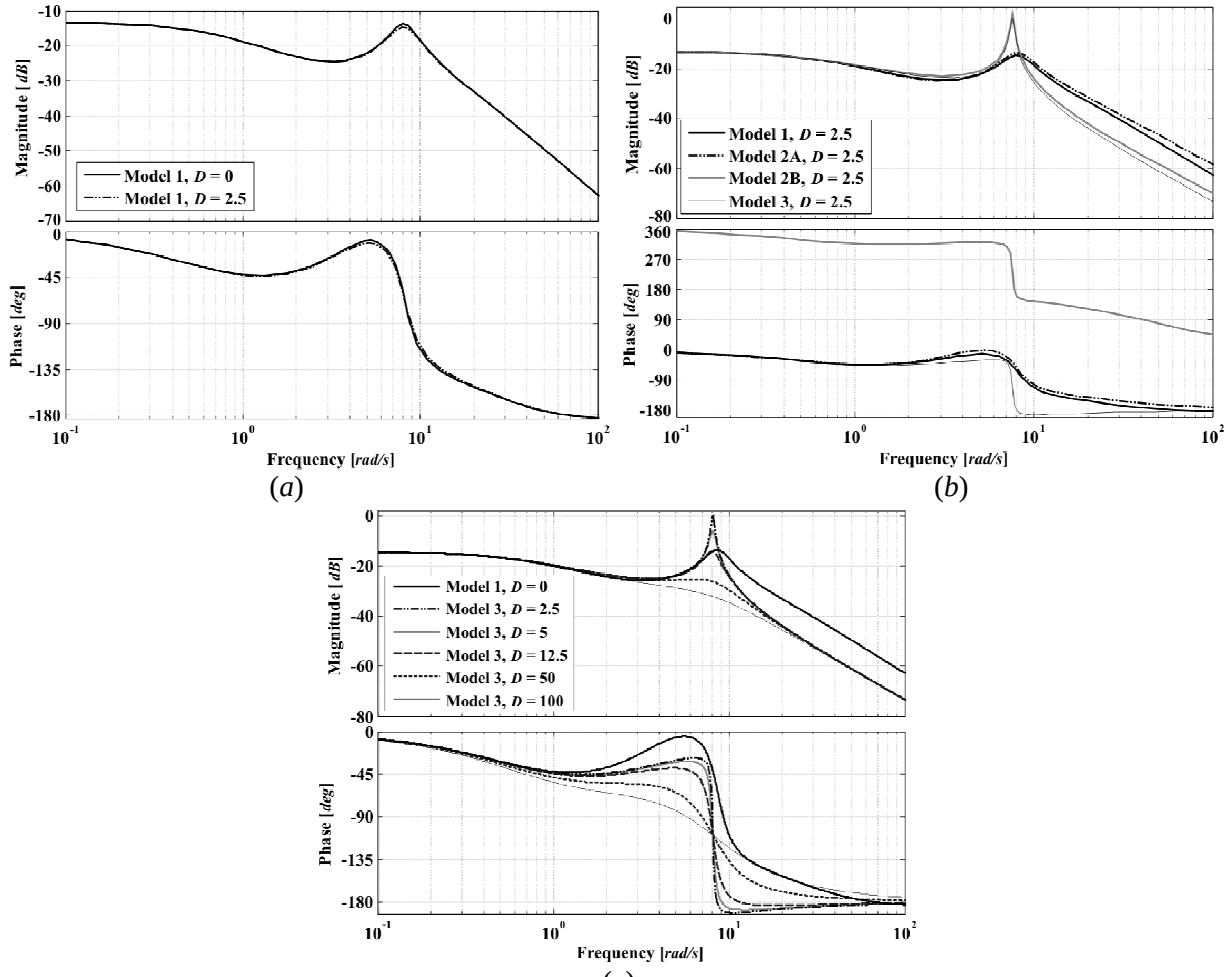

Figure 3.11. Assessment of the static damping term *D*. Bode plots of $\gamma_a(s)$:
(*a*) Model 1 for $D = 0$ *p.u.* and 2.5 *p.u.*; (*b*) all models with $D = 2.5$ *p.u.*;
(*c*) Model 3 at different values of *D* vs Model 1 with $D = 0$ *p.u.*

It may be said that Models 2B and 3, whose winding representation is confined to the *d*-axis, do not yield enough system damping. Therefore, the use of such a model for small-signal stability studies may also lead to inaccurate analysis. Whenever it is required that a model exhibits a realistic dynamic behaviour throughout the frequency range, one-axis models should be avoided. Although Model 2A can be used for small-signal stability studies, Model 1 provides a higher level of reliability.

3.5. A brief description of conventional controllers

Control and stability issues of synchronous machines have received much research attention in the past. Therefore, the characteristics and modelling of different types of synchronous generator turbine-governor and excitation systems have been extensively studied [17,19–24]. The schematic diagram of Figure 2.2 in Chapter 2 illustrates a typical generating unit with both control systems, which for analysis purposes will be called conventional controllers.

A comprehensive list of standard excitation system models can be found in [17,19–21]. In rotating structures, the excitation current is supplied by either a DC generator or an AC generator fitted with a rectifier. Although DC generators have almost been replaced by alternators, they require the use of slip rings in order to feed the rectified excitation current to the rotating field winding. Moreover, the exciter itself is quite bulky. Static exciters have been introduced to enable more reliable and smaller footprint excitation systems. A generic structure of modern excitation systems usually comprises an exciter, an automatic voltage regulator (AVR) and a stabiliser loop [19].

In connection with the description of the generating unit given in Chapter 2, the exciter provides the direct current to the synchronous machine field winding. The AVR controls the output of the exciter: it processes and amplifies input control signals to an appropriate level and form for control of the exciter. The feedback stabiliser loop, in the form of a derivative feedback system, is employed to improve the dynamic performance of the control system by minimising the phase shift introduced by the time delays over a selected frequency range [17,19]. Other elements are essential parts of the excitation systems such as limiters and protective circuits to ensure that the capability limits of the exciter and the synchronous generator are not exceeded. From the various possible excitation system models, Type 1 systems considering a continuously acting regulator and an exciter are considered for analysis. In this work the block diagram for this representation is given in Figure 3.12 [19,20].

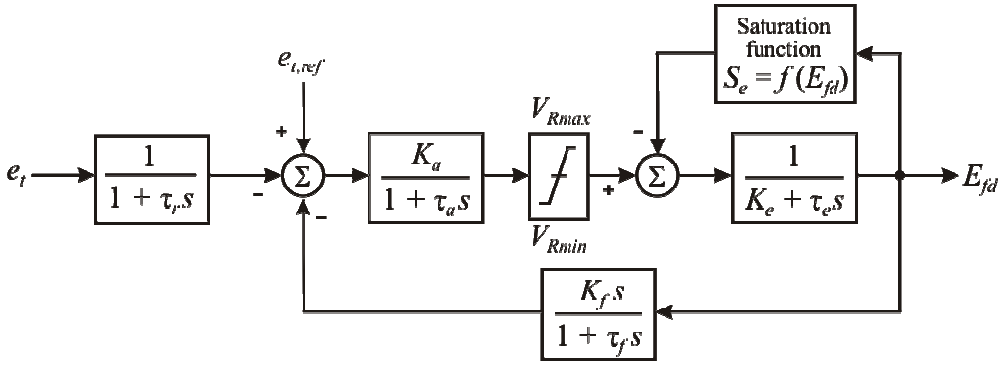

Figure 3.12. IEEE type 1 excitation system

In Figure 3.12 the terminal voltage e_t is filtered through a first-order filter having a time constant τ_r which is usually very small and often taken to be zero. The AVR is represented by a first-order linear system with time constant τ_a and a gain K_a, with its output limited by V_{Rmax} and V_{Rmin}. The exciter itself is represented as a first-order linear system with time constant τ_e. A provision is made to include the effect of saturation in the exciter by the saturation function S_e. The feedback stabiliser loop is represented by a transfer function with a gain constant K_f and a time constant τ_f. In addition, it introduces a derivative feedback [19].

If in Type 1 systems the excitation is obtained through rectification of the terminal voltage, the maximum voltage output is not a constant but proportional to e_t , *i.e.*, $V_{Rmax} = K_p e_t$. Such a representation, called Type 1S systems and shown in Figure 3.13, has an almost instantaneous response, so that $K_e = 1$, $\tau_e = 0$ and $S_e = 0$, and the exciter representation may be dropped from Figure 3.12 [19,20]. As in Type 1 systems, the time constant τ_r is usually very small.

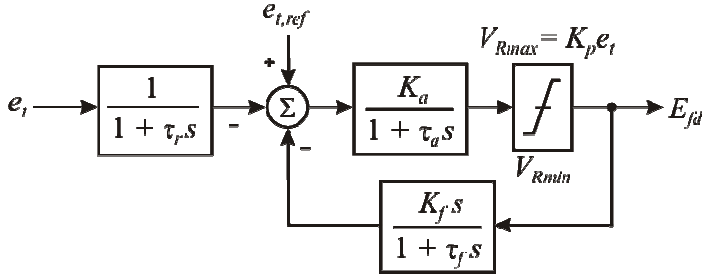

Figure 3.13. IEEE type 1S excitation system

In conventional power systems, steam turbines, hydro turbines and diesel engines are normally used to drive the synchronous generators. Standard turbine configurations and their dynamic models are fully documented in the literature [17,22–24]. The generator speed is controlled by the governor, which adjusts the gate valve positions to increase or decrease the amount of mechanical power to the input turbine by using a servomotor mechanism. Figure 3.14 shows a simple turbine-governor model comprising the turbine and a speed governor with speed regulation R [25].

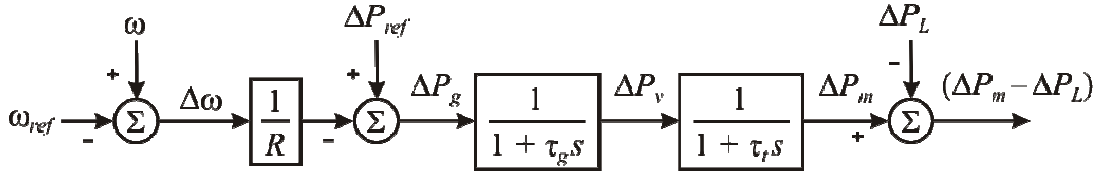

Figure 3.14. Turbine-governor

The model of the turbine in Figure 3.14 relates changes in mechanical power output ΔP_m to changes in steam valve position ΔP_v. The simplest prime mover model for the non-reheat steam turbine can be approximated by a single time constant τ_t, which is in the range of 0.2 to 2 *s*. On the other hand, governors have a speed regulation of 5–6 % from zero to full load. The speed governor mechanisms acts as a comparator whose output ΔP_g is the difference between the reference set power ΔP_{ref} and the power

$(1/R)\cdot\Delta\omega$ as given from the governor speed characteristics. The command ΔP_g is transformed through the hydraulic amplifier to the steam valve position command ΔP_v, which by assuming a linear relationship is represented as a first-order linear filter with time constant τ_g. The load change ΔP_L, considered as an input to the system, completes the block diagram model to be used [25].

For the study presented in the following section, the Type 1S excitation system of Figure 3.13 and the turbine-governor of Figure 3.14 are employed. In terms of ICAD, the pairing associated to $\gamma_a(s)$ given by (3.25) is considered and, therefore,

$$\mathbf{K}_1(s)=\begin{bmatrix} k_{11}(s) & 0 \\ 0 & k_{22}(s) \end{bmatrix}=\begin{bmatrix} \dfrac{1}{R(1+\tau_g s)(1+\tau_t s)} & 0 \\ 0 & \dfrac{K_a(1+\tau_f s)}{\left[1+(\tau_a+\tau_f+K_aK_f)s+\tau_a\tau_f s^2\right]} \end{bmatrix} \tag{3.43}$$

in which the expression for $k_{22}(s)$ is arrived at after some block diagram manipulation. Gains and time constants in (3.43) correspond to typical values provided in [19,25] and are given as follows: $\tau_r \rightarrow 0$, τ_a = 0.03 *s*, K_a = 198, τ_f = 0.03 *s* and K_f = 0.01 for the excitation system; and τ_g = 0.5 *s*, τ_t = 0.2 *s* and R = 0.05 for the turbine-governor. Hence,

$$\mathbf{K}_1(s)=\begin{bmatrix} k_{11}(s) & 0 \\ 0 & k_{22}(s) \end{bmatrix}=\begin{bmatrix} \dfrac{200}{(s+5)(s+2)} & 0 \\ 0 & \dfrac{6600(s+2.695)}{(s+213.5)(s+0.4208)} \end{bmatrix} \tag{3.44}$$

3.6. Control system design

According to (3.25), the turbine-governor control and the excitation control correspond to $k_{11}(s)$ and $k_{22}(s)$, respectively. Within the ICAD context, the turbine-governor control $k_{11}(s)$ is applied to achieve the set point regulation of the shaft speed; that is, the loop is closed round the turbine-governor subsystem $k_{11}g_{11}(s)$ to yield a closed-loop subsystem $h_1(s)$. Speed regulation is typically required to be effective over a frequency range of 0–1 *rad/s* [17], blinding the governor to interaction with higher-frequency signals. On the other hand, the excitation system $k_{22}(s)$ is used to achieve the set point regulation of the machine terminal voltage. Its performance is given by the frequency response of the excitation channel $C_2(s)$. Typically, voltage regulation over a frequency range of 0–10 *rad/s* is required [17]. However, since the turbine-governor channel is relatively slow, the frequency response of the turbine-governor subsystem $h_1(s)$ will have rolled-off in the frequency range of interest to the faster excitation channel $C_2(s)$; that is, the excitation channel $C_2(s)$ can be approximated by $k_{22}g_{22}(s)$ in the typical excitation channel frequency range [8].

The previous discussion, originally presented in [8], is an explanation, from the ICAD vantage, of the observed fact that the slow governor loop has little effect on the faster exciter loop response. Hence, the performance of the overall generator system is largely determined by that of the electrical subsystem transfer function $g_{22}(s)$ – featuring the problematic switch-back characteristic due to the presence of a resonance (lightly damped LHPP pair) closely followed by an inverted resonance (lightly damped LHPZ pair). Any attempt to apply direct excitation control, active over the frequency range that includes the switch-back characteristic, would be problematic because it implies an unrealistically precise knowledge of the dynamics and variations arising depending on system loading conditions [8], not to mention those due to the chosen model and operating conditions (as addressed in previous sections of this chapter). The close proximity of such lightly damped pairs of zeros and poles [8,26] in addition to the lack of system damping (as discussed in [2]) pose the fundamental problems of the synchronous generator control. If traditional controllers are to be used, the obvious solution is to restrict the bandwidth of the excitation channel below the frequencies where the switch-back characteristic is present. However, this is at the expense of a slower step response.

3.6.1. Study 1 using conventional controllers

The traditional controller structure given in [19,20] is widely used in academic studies of power systems dynamics; however, it is not difficult to figure out that it will incur problems in its operation. The control system performance of the test system of Figure 3.1, at different power factors, using controller (3.44) is presented in Figures 3.15 and 3.16.

Channel 1 performance, as reflected by Figures 3.15 and 3.16, is rather poor. The controller itself is unable to perform compensation actions. Notice that the element $g_{11}(s)$ given in (3.9) contains a pure differentiating term and that the element of the controller $k_{11}(s)$ in (3.44) is not able to counteract such effect. Consequently, Channel 1 does not reach its step reference.

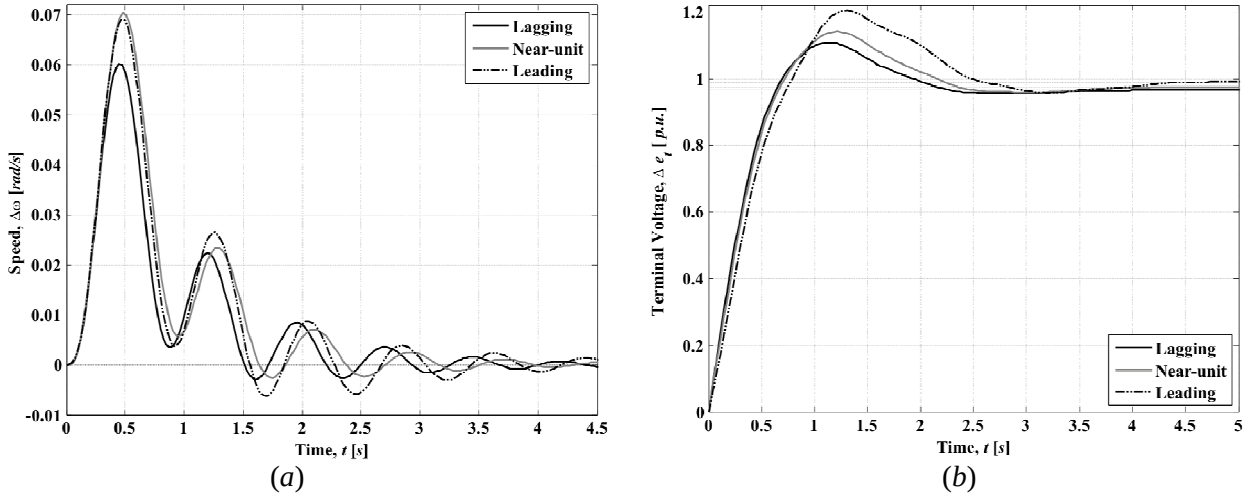

(*a*) (*b*)

Figure 3.15. Step response (conventional controller $\mathbf{K}_1(s)$): (*a*) Channel 1 ($T_{c1}(s)$); (*b*) Channel 2 ($T_{c2}(s)$)

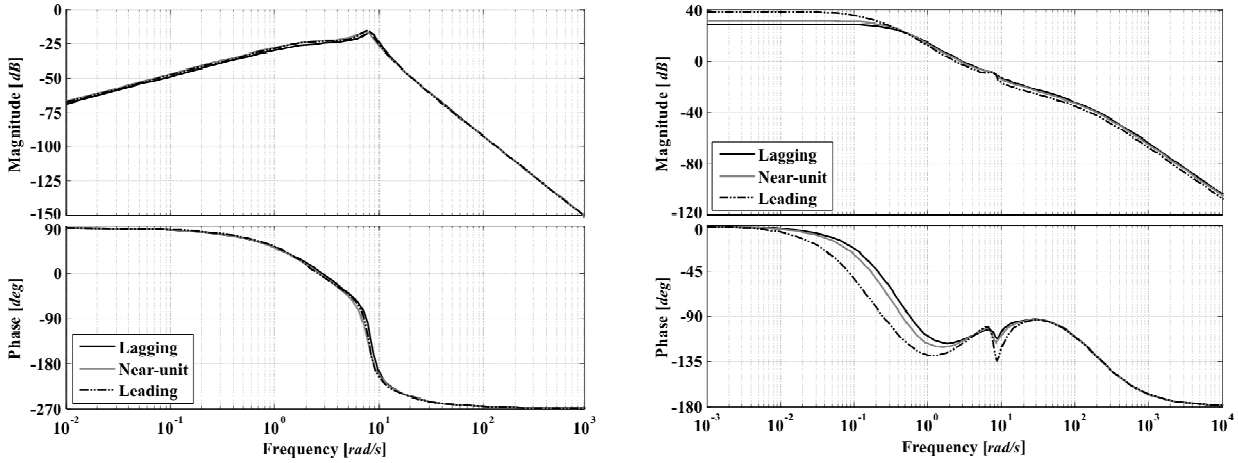

(*a*) (*b*)

Figure 3.16. Bode diagram (conventional controller $\mathbf{K}_1(s)$): (*a*) Channel 1 ($C_1(s)$); (*b*) Channel 2 ($C_2(s)$)

To eliminate the steady state error in Channel 1, but without drastically changing the expression given in (3.44), the following controller is proposed

$$\mathbf{K}_2(s) = \begin{bmatrix} \dfrac{5285}{s^2(s+5)(s+2)} & 0 \\ 0 & \dfrac{6600(s+2.695)}{(s+213.5)(s+0.4208)} \end{bmatrix} \tag{3.45}$$

which complies with the necessary requirements stated in the analysis of $\gamma_a(s)$ provided by conditions **(a.1)**–**(a.4)** of Section 3.4.1.1. The control system performance using (3.45) is observed in Figures 3.17 and 3.18. The conventional speed controller was modified by adding two integrators and tuning the gain.

Figure 3.17(*a*) illustrates the step response of Channel 1 (speed). It can be seen that all three responses have a similar behaviour, with the near-unit power factor operation presenting the highest overshoot. Also, the lagging power factor operation response features a slightly longer settling time compared to the leading and near-unit power factor operation responses. Figure 3.17(*b*) shows the step response of the terminal voltage channel (Channel 2). Notice that none of the step responses reach the unit reference. Nevertheless, the best performance is achieved during lagging power factor operation. Such characteristics are in agreement with the MSF analysis presented previously and with what is known to be the case in practice.

Figure 3.18 presents the Bode plots of the open-loop transmission channels. It can be seen that for all the operating conditions the speed channel has a bandwidth of 1 *rad/s*, whereas for the terminal voltage channel it is 3 *rad/s* for lagging power factor operation, 2.75 *rad/s* for near-unit and it drops to almost 2.4 *rad/s* for the leading condition. Stability margins for both channels are acceptable, *i.e.*, gain and phase margins over 6 *dB* and 40 *deg*, respectively, according to reference [17].

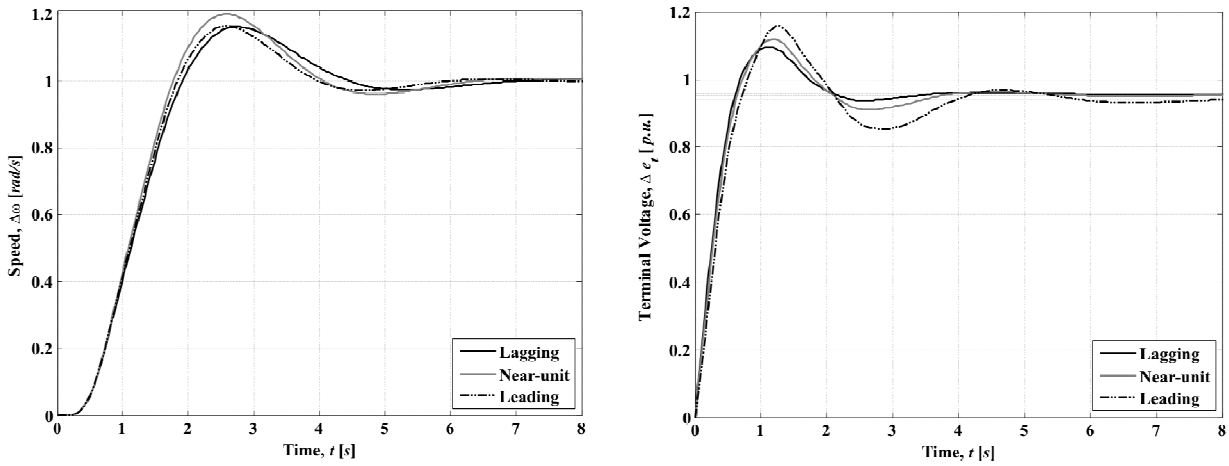

(*a*) (*b*)

Figure 3.17. Step response (amended conventional controller $\mathbf{K}_2(s)$):
(*a*) Channel 1 ($T_{c1}(s)$); (*b*) Channel 2 ($T_{c2}(s)$)

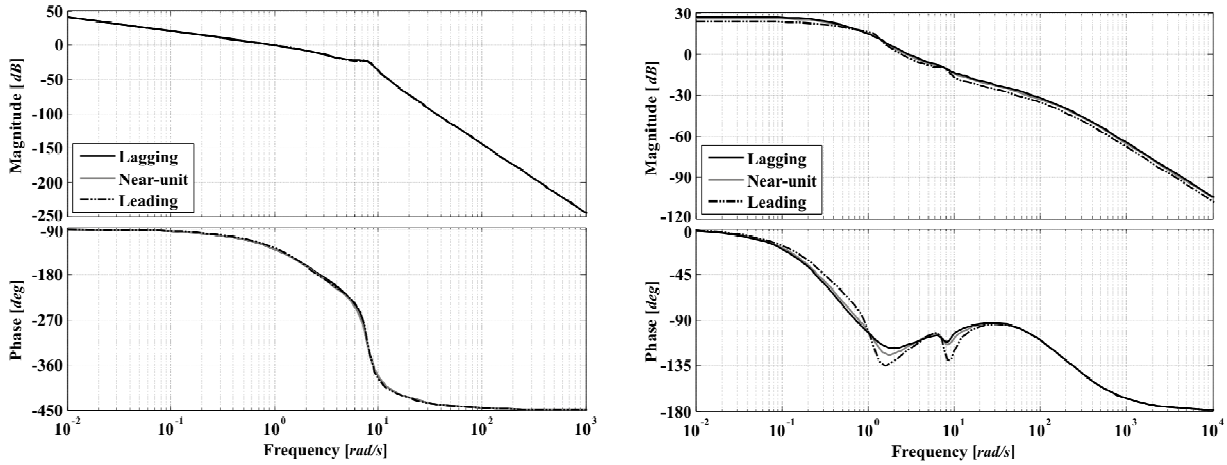

(*a*) (*b*)

Figure 3.18. Bode diagram (amended conventional controller $\mathbf{K}_2(s)$):
(*a*) Channel 1 ($C_1(s)$); (*b*) Channel 2 ($C_2(s)$)

The overall performance of the control system is enhanced with controller (3.45). However, the response of Channel 2 has an associated steady-state error. In an attempt to eliminate it, an integrator may be included in element $k_{22}(s)$ of the controller. However, adding an integrator to the controller of Channel 2 results in an unstable response, as shown in the Bode plot in Figure 3.19 for the case of lagging power factor. Notice that 90 *deg* are lost in the phase plot. Such a problem could be corrected if a suitable zero is introduced to increase the phase near the cut-off frequency and a lead-lag term to improve stability margins. Nevertheless, such a controller structure would be very different from the one given by (3.44) corresponding to the conventional controller. Alternatively, a simpler design may be carried out by appealing to the use of the MSF described previously. This will be addressed in the following sub-section.

Remark: It should be pointed out that the previous discussion and the controller performance assessment are easily analysed under the framework of ICAD. It is not as straightforward to reach such conclusions by eigenanalysis as such method does not yield the same physical insight as that provided by ICAD.

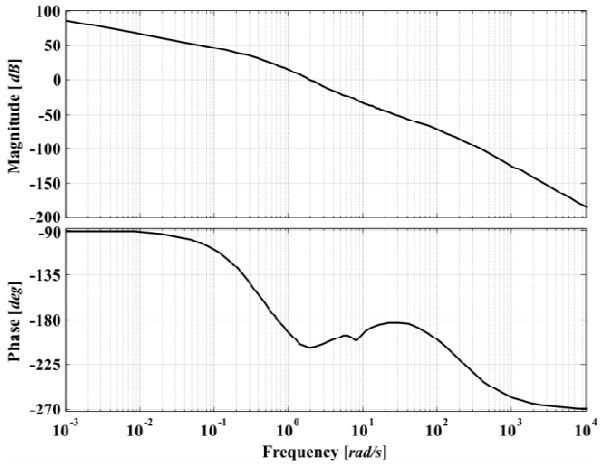

Figure 3.19. Bode diagram (amended conventional controller $\mathbf{K}_2(s)$ with an integrator in $k_{22}(s)$): Channel 2 ($C_2(s)$)

3.6.2. Study 1 using the proposed controllers

Study 1 is carried out under the same conditions as for the previous case but this time using the controller obtained after analysing the MSF. For instance

$$\mathbf{K}_3(s)=\begin{bmatrix} \dfrac{640(s+5)}{s^2(s+6)(s+1)} & 0 \\ 0 & \dfrac{102(s+0.5)}{s(s+3)} \end{bmatrix} \tag{3.46}$$

complies with the necessary requirements stated in the analysis of $\gamma_a(s)$ provided by conditions **(a.1)**–**(a.4)** of Section 3.4.1.1. The control system performance and stability and structural robustness measures for the OMIB system, at three different power factors (lagging, near-unit, and leading) are presented in Figures 3.20–3.23. Relevant information associated to these figures is summarised in Table 3.5.

Figure 3.20 illustrates the step response of both channels. The responses for Channel 1 (Figure 3.20(*a*)) are quite similar to the ones obtained with the amended conventional controller; this is an expected result since both controller structures are similar (only the time constants are different). Nevertheless, the settling time is slightly higher since a lower bandwidth was chosen the latter case. The step responses for Channel 2 are shown in Figure 3.20(*b*). It should be noted that the outputs do reach their unit references – an indication of a much improved performance aided by the presence of an integrating term in the controller for this channel. It should be remarked that the proposed controller structure is simpler than the conventional design. Moreover, the overshoots are lower compared to the performance exhibited with conventional controllers. The best dynamic performance is achieved under a lagging power factor.

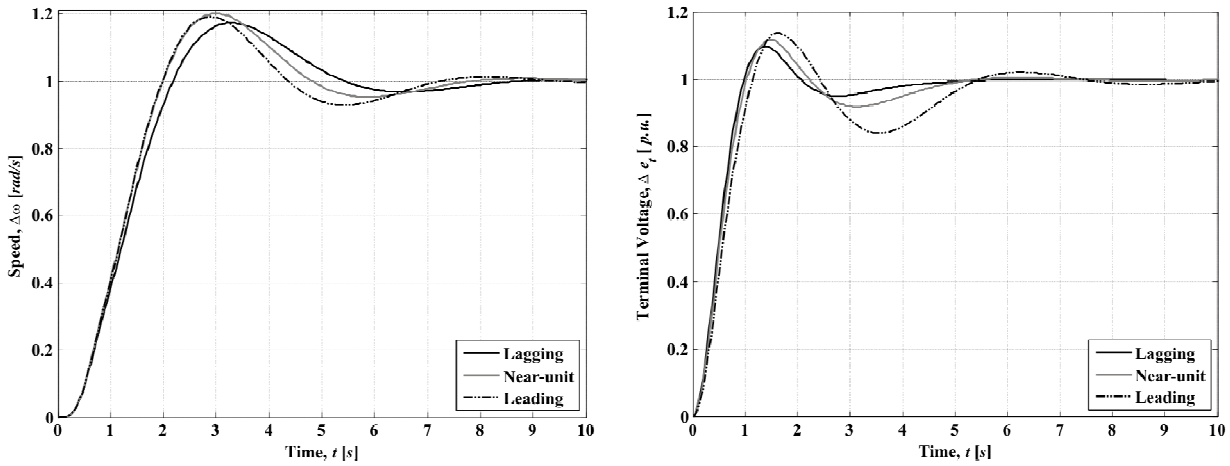

(*a*) (*b*)

Figure 3.20. Step response (designed controller $\mathbf{K}_3(s)$): (*a*) Channel 1 ($T_{c1}(s)$); (*b*) Channel 2 ($T_{c2}(s)$)

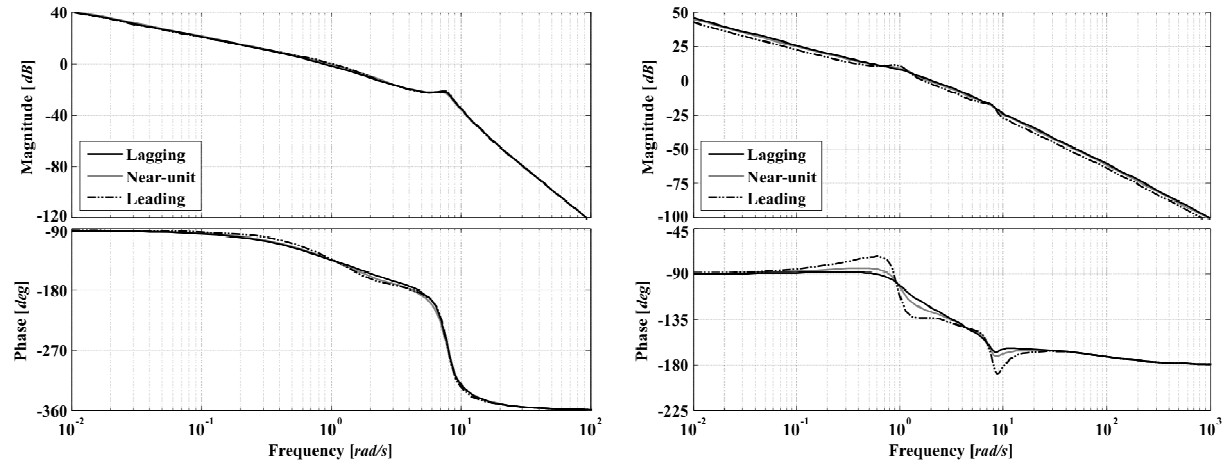

(*a*) (*b*)

Figure 3.21. Bode diagram (designed controller $\mathbf{K}_3(s)$): (*a*) Channel 1 ($C_1(s)$); (*b*) Channel 2 ($C_2(s)$)

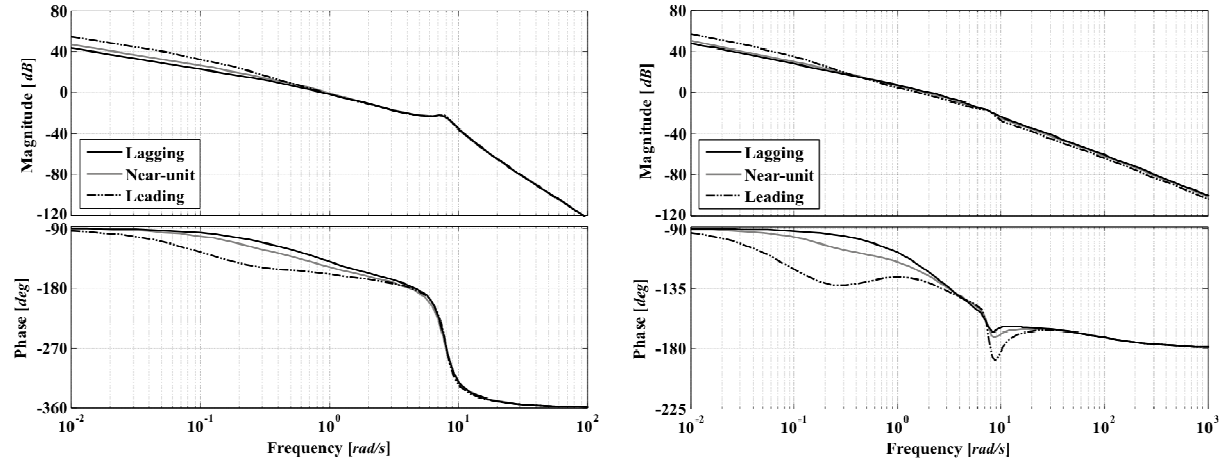

(*a*) (*b*)

Figure 3.22. Bode diagram (designed controller $\mathbf{K}_3(s)$): (*a*) $k_{11}g_{11}(s)$; (*b*) $k_{22}g_{22}(s)$

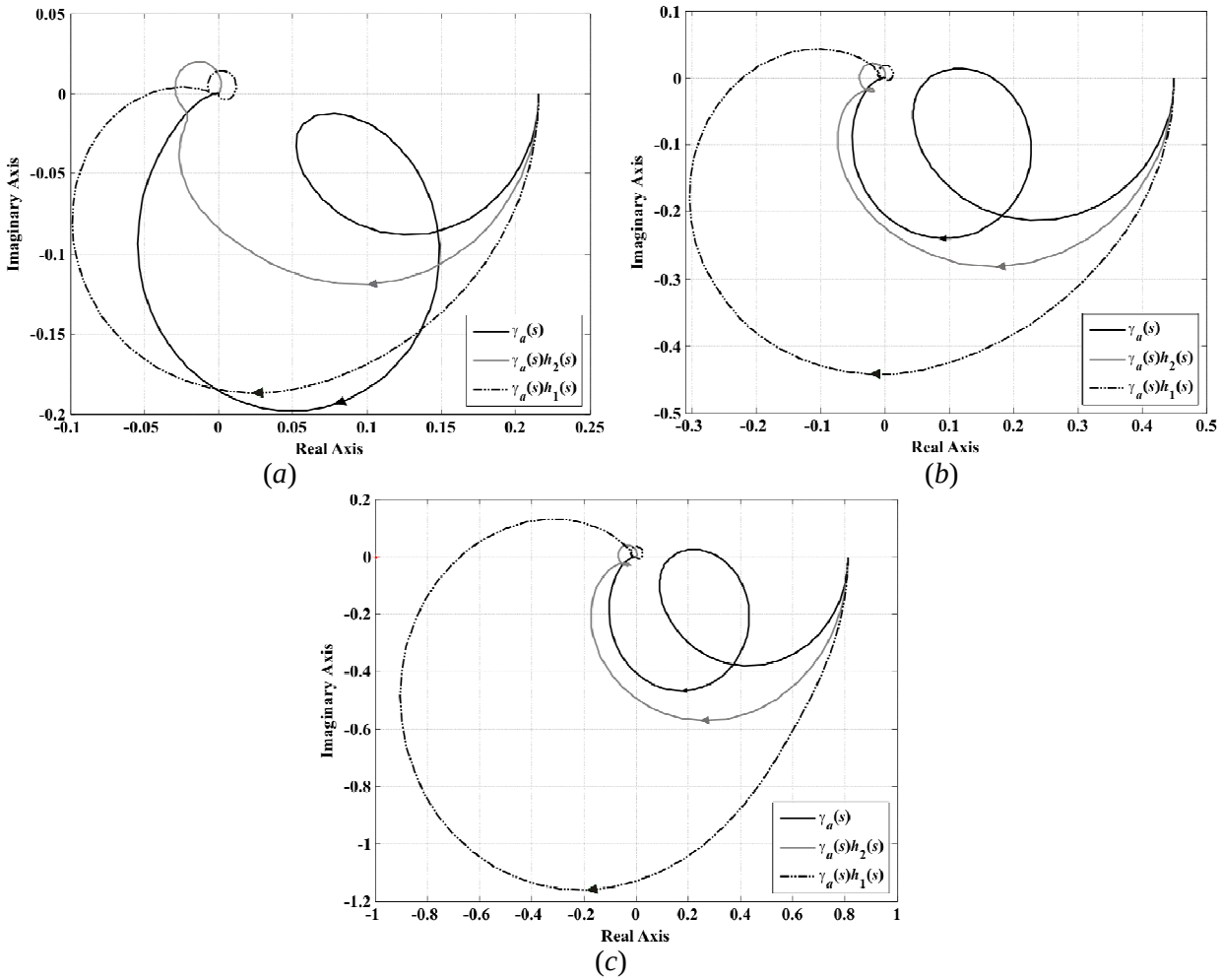

Figure 3.23. Nyquist diagram (designed controller $\mathbf{K}_3(s)$). $\gamma_a(s)$ vs $\gamma_1(s) = \gamma_a(s)h_2(s)$ vs $\gamma_2(s) = \gamma_a(s)h_1(s)$ with (*a*) Lagging power factor; (*b*) near-unit power factor; (*c*) leading power factor

Table 3.5. Structural and stability robustness of the channels and control system. Study 1: different power factors

Condition	Measure	$C_1(s)$	$k_{11}g_{11}(s)$	$\gamma_1(s)$	$C_2(s)$	$k_{22}g_{22}(s)$	$\gamma_2(s)$
Lagging PF	**Bandwidth** (*rad/s*)	1.1	1.12	–	2.62	2.6	–
	Gain margin (*dB*)	21.7	21.7	13.33	∞	∞	13.33
	Phase margin (*deg*)	50.2	42.2	∞	56.4	57.1	∞
Near-unit PF	**Bandwidth** (*rad/s*)	1.21	1.18	–	2.43	2.39	–
	Gain margin (*dB*)	20.4	20.3	6.95	∞	∞	6.95
	Phase margin (*deg*)	47.3	32.4	∞	53.4	55.7	∞
Leading PF	**Bandwidth** (*rad/s*)	1.26	1.15	–	2.1	2.03	–
	Gain margin (*dB*)	21.4	21.1	1.81	18.8	19	1.81
	Phase margin (*deg*)	47.4	20.9	∞	46.7	51.8	70.71

Figure 3.21 presents the Bode diagrams of the open-loop transmission channels to assess the control system performance and the stability robustness, summarised in Table 3.5. As shown in Figure 3.21(*a*), the speed controller was designed to provide a bandwidth of 1.1 *rad/s* for the speed channel in a lagging power factor operation. Similarly, the bandwidth for the voltage channel is 2.62 *rad/s*, as shown

by Figure 3.21(*b*). The stability margins (*i.e.*, phase and gain margins) of Channel 1 are adequate. Although phase margins in Channel 2 are slightly lower than with the conventional controller, they are still satisfactory.

The structural robustness of the control system is assessed in Figure 3.22 and 3.23. Figure 3.22 shows the Bode diagrams of subsystems $h_1(s)$ and $h_2(s)$. The gain and phase margins for subsystems $h_1(s)$ and $h_2(s)$ with the proposed controllers are adequate, as evidenced by the information given in Table 3.5. Figure 3.23 illustrates the Nyquist diagrams of $\gamma_a(s)$, $\gamma_1(s) = \gamma_a(s)h_2(s)$ and $\gamma_2(s) = \gamma_a(s)h_1(s)$ for a lagging, near-unit, and leading power factor. Notice that functions $\gamma_i(s)$ (i = 1,2) have the following gain margins: 13.33 *dB* for a lagging power factor, 6.95 *dB* for a near-unit power factor, and 1.81 *dB* for a leading power factor. It could be argued that a gain margin of 1.81 *dB* is not high enough to guarantee robustness. Nevertheless, it should be pointed out that operation under a leading power factor represents a critical condition. In fact, the synchronous machine becomes stressed under such operating conditions. This result is in a way, a formal demonstration of leading power factor operation being undesirable for synchronous machines and should be avoided whenever possible.

In summary, the proposed controller (3.46) has improved the dynamical performance of the control system. The control system provides adequate stability margins and unit references are successfully reached in both channels. The latter characteristic contrasts with the performance exhibited by conventional controllers. It should be noted that the structure of $k_{22}(s)$ in the proposed controller is much simpler than that of the conventional controller and it exhibits a better dynamical performance.

3.6.3. Study 2 using conventional controllers

The control system performance of the OMIB system at X_t = 0.2, 0.3, 0.4, 0.5 *p.u.* values of tie-line reactance is presented in Figures 3.24 and 3.25, using the conventional controller given by (3.44).

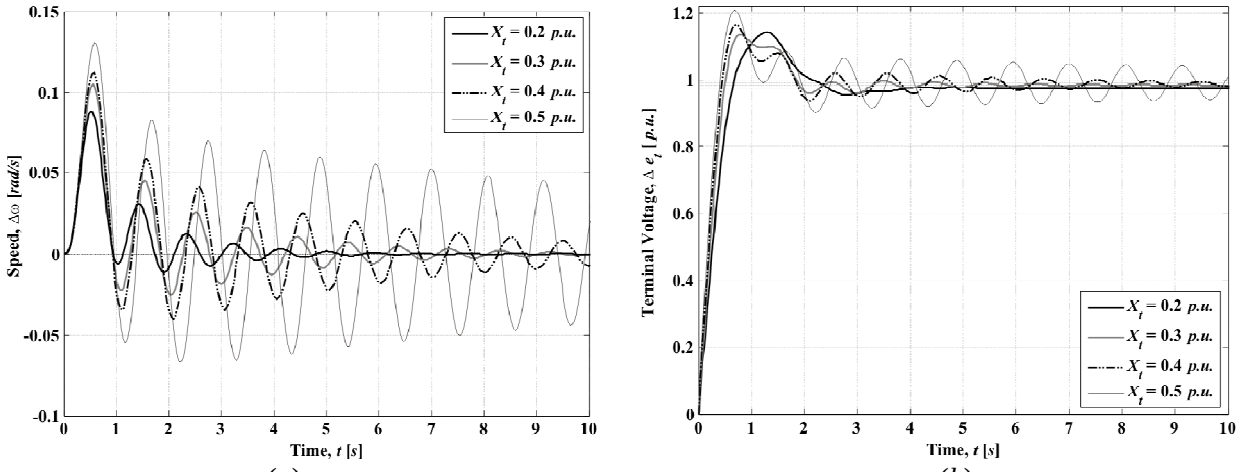

(*a*) (*b*)

Figure 3.24. Step response (conventional controller $\mathbf{K}_1(s)$): (*a*) Channel 1 ($T_{c1}(s)$); (*b*) Channel 2 ($T_{c2}(s)$)

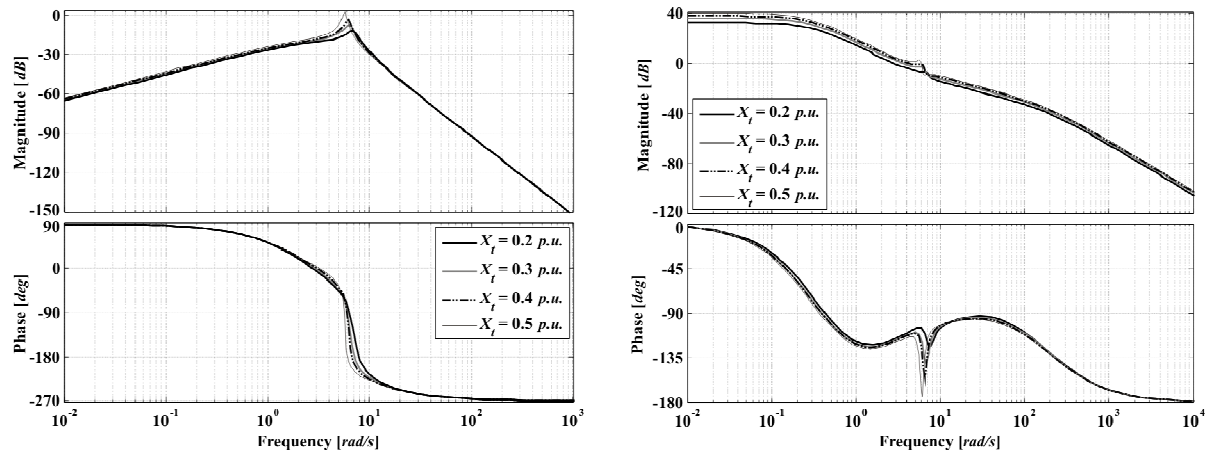

(*a*) (*b*)

Figure 3.25. Bode diagram (conventional controller $\mathbf{K}_1(s)$): (*a*) Channel 1 ($C_1(s)$); (*b*) Channel 2 ($C_2(s)$)

As in Study 1, the performance of Channel 1 using the conventional controller is very poor. Notice that in Channel 2 the unit reference is not reached and that the behaviour is a rather oscillatory one. A clear pattern emerges from these results: the larger the electrical distance is, the more oscillatory the response becomes. As evidenced by Figure 3.25(*a*), the conventional speed controller is unable to perform any control action at all in Channel 1. With respect to Channel 2, notice that the switch-back characteristic is present around the cut-off frequency, offering poor stability margins and an almost unstable response whenever the transmission line length increases.

3.6.4. Study 2 using the proposed controllers

The proposed controller (3.46) is used in this section to carry out an assessment of the OMIB system under the same conditions as with the conventional controllers in Study 1. The control system performance and robustness measures for the OMIB system at different values of the tie-line reactance (X_t = 0.2, 0.3, 0.4 *p.u.*) are presented in Figures 3.26–3.29 and Table 3.6.

Table 3.6. Structural and stability robustness of the channels and control system. Study 2: different tie-line reactances (X_t = 0.2, 0.3, 0.4 *p.u.*)

Condition	Measure	$C_1(s)$	$k_{11}g_{11}(s)$	$\gamma_1(s)$	$C_2(s)$	$k_{22}g_{22}(s)$	$\gamma_2(s)$
	Bandwidth (*rad/s*)	1.37	1.34	–	2.48	2.41	–
X_t = 0.2 *p.u.*	**Gain margin** (*dB*)	17.5	17.4	5.96	∞	∞	5.96
	Phase margin (*deg*)	44.6	28.8	∞	51.7	54.5	∞
	Bandwidth (*rad/s*)	1.46	1.49	–	3.13	3.03	–
X_t = 0.3 *p.u.*	**Gain margin** (*dB*)	14.5	15	5.49	11.6	12.3	5.49
	Phase margin (*deg*)	44.4	27.8	∞	46.2	48	∞
	Bandwidth (*rad/s*)	1.46	1.54	–	3.56	3.44	–
X_t = 0.4 *p.u.*	**Gain margin** (*dB*)	12.9	14.2	6	7.97	8.84	6
	Phase margin (*deg*)	44.4	29.4	∞	43.3	44.6	∞

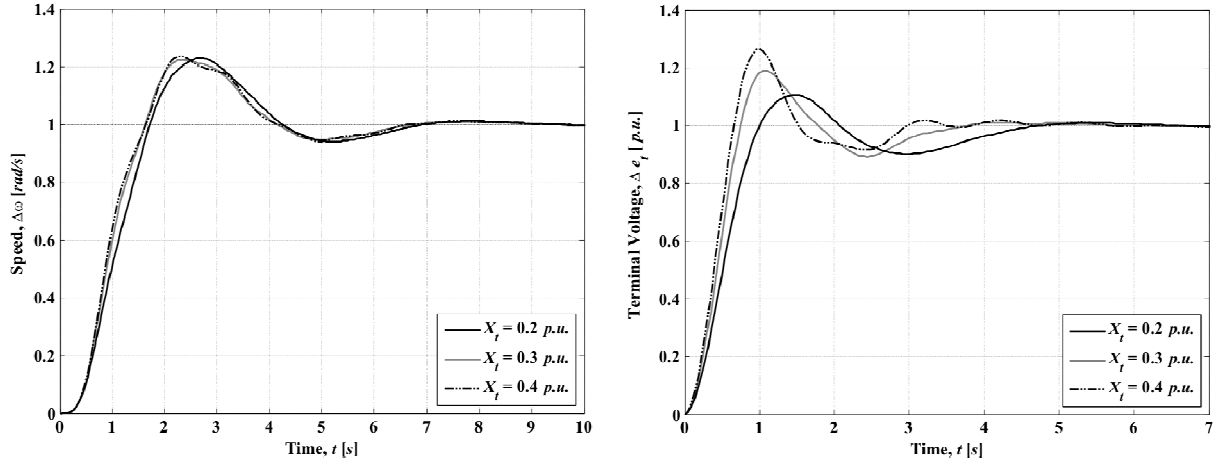

(*a*) (*b*)

Figure 3.26. Step response (designed controller $\mathbf{K}_3(s)$): (*a*) Channel 1 ($T_{c1}(s)$); (*b*) Channel 2 ($T_{c2}(s)$)

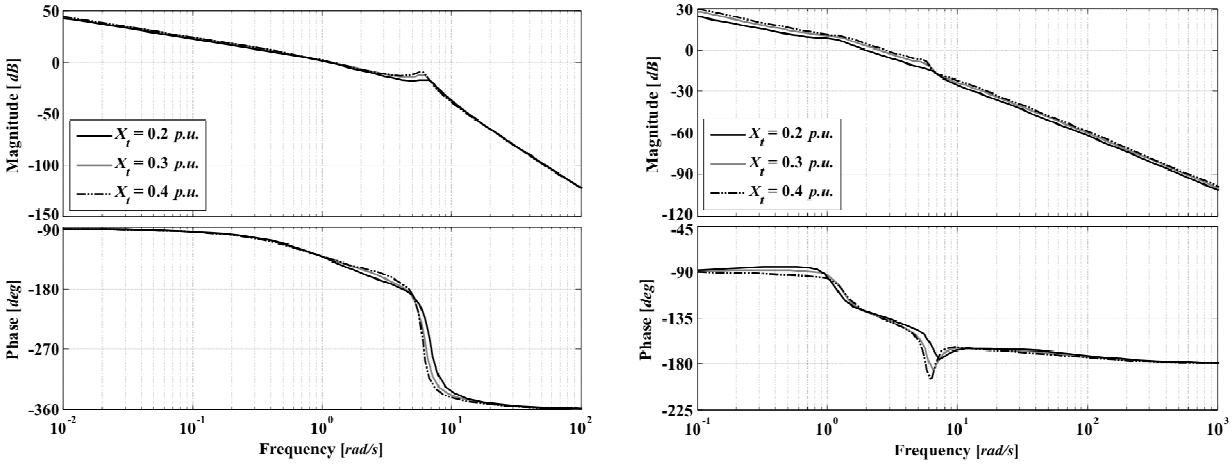

(*a*) (*b*)

Figure 3.27. Bode diagram (designed controller $\mathbf{K}_3(s)$): (*a*) Channel 1 ($C_1(s)$); (*b*) Channel 2 ($C_2(s)$)

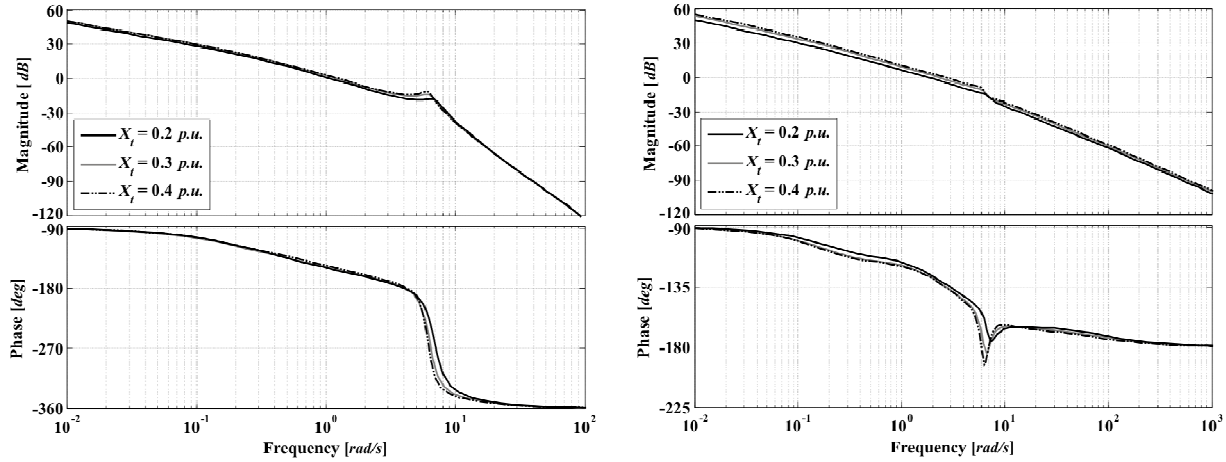

(*a*) (*b*)

Figure 3.28. Bode diagram (designed controller $\mathbf{K}_3(s)$): (*a*) $k_{11}g_{11}(s)$; (*b*) $k_{22}g_{22}(s)$

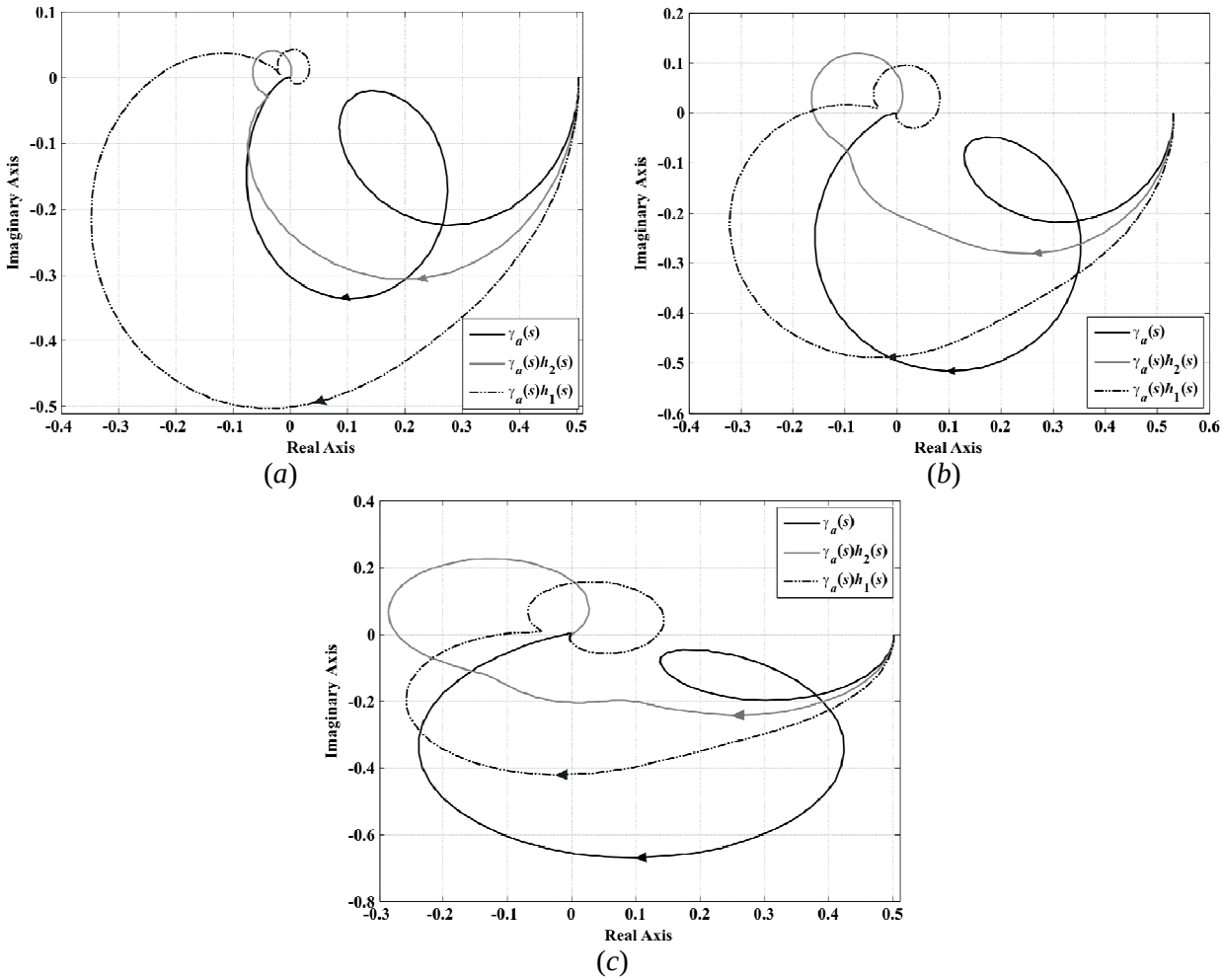

Figure 3.29. Nyquist diagram (designed controller $\mathbf{K}_3(s)$): $\gamma_a(s)$ vs $\gamma_1(s) = \gamma_a(s)h_2(s)$ vs $\gamma_2(s) = \gamma_a(s)h_1(s)$ with (*a*) $X_t = 0.2$ *p.u.*; (*b*) $X_t = 0.3$ *p.u.*; (c) $X_t = 0.4$ *p.u.*

The control system performance is assessed in Figure 3.26. Figure 3.26(*a*) illustrates the step responses of Channel 1 (speed). All three responses exhibit a similar behaviour, but increases in the tie-line reactance tend to dent the smoothness of the characteristic. The same situation arises in the step responses of Channel 2, as shown in Figure 3.26(*b*). It can be seen that the overshoot increases with increasing values of tie-line reactance.

Stability robustness and control system performances are evaluated in Figure 3.27, which depicts the Bode diagrams of the open-loop transmission channels. As the electrical distance (tie-line reactance) increases, an undesirable peak appears in the magnitude of the speed channel after the cut-off frequency. The larger the tie-line reactance value, the sooner the frequency at which the peak appears. Such a phenomenon impacts directly on the disturbance rejection capability. At frequencies where the peak presents itself, any signal having such frequency values will be amplified and, as a consequence of this, the system is likely to become unstable. As for the terminal voltage channel, shown in Figure 3.27(*b*), it can be observed that an increase in tie-line reactance is amenable to an increase of the channel bandwidth. Near the cut-off frequency values, the phase presents undesirable curly trajectories due to the presence of

the switch-back characteristic. As the electrical distance increases, this characteristic becomes more pronounced and the phase margins decrease, as shown in the Bode plot and Table 3.6.

Figures 3.28 and 3.29 are used to assess the structural robustness of the control system. Figure 3.28 shows the Bode diagrams of subsystems $h_1(s)$ and $h_2(s)$. The discussion of Figure 3.27 also applies here. It should be pointed out, following the analysis of the MSF in previous sections, that both subsystems are required to be stable for the overall system to be stable. Figure 3.29 illustrates the Nyquist diagrams of $\gamma_a(s)$, $\gamma_1(s) = \gamma_a(s)h_2(s)$ and $\gamma_2(s) = \gamma_a(s)h_1(s)$. It can be seen that functions $\gamma_i(s)$ (i = 1,2) have adequate stability margins.

An improved performance of the control system covering any of the four tie-lines considered in this study may be achieved if the bandwidths of both channels are reduced so that the undesirable magnitude and phase characteristics are pushed into higher frequencies – and therefore posing no harm as they would become attenuated. For instance, the performance with tie-line reactance values higher than X_t = 0.4 *p.u.* can be improved if the following controller is used:

$$\mathbf{K}_4(s) = \begin{bmatrix} \dfrac{315(s+5)}{s^2(s+6)(s+1)} & 0 \\ 0 & \dfrac{15(s+3)(s+0.5)}{s(s+5)(s+1)} \end{bmatrix} \tag{3.47}$$

Notice that the structure of (3.47) is quite similar to that of (3.46). Element $k_{11}(s)$ only differs in the gain and element $k_{22}(s)$ includes an extra lag-lead term and a slight modification in the poles and zeros in order to lower the bandwidth of both channels while still preserving adequate phase margins.

The control system performance and robustness measures for the OMIB system, with the new controllers, at different values of the tie-line reactance (X_t = 0.4, 0.5, 0.6, 0.8 *p.u.*) are presented in Figures 3.30–3.33 and Table 3.7.

Table 3.7. Structural and stability robustness of the channels and control system. Study 2: different tie-line reactances, bandwidth reduction

Condition	Measure	$C_1(s)$	$k_{11}g_{11}(s)$	$\gamma_1(s)$	$C_2(s)$	$k_{22}g_{22}(s)$	$\gamma_2(s)$
X_t = 0.4 *p.u.*	**Bandwidth** (*rad/s*)	1.09	0.982	–	1.14	1.01	–
	Gain margin (*dB*)	20.2	20.4	6	25.2	25.6	6
	Phase margin (*deg*)	50.7	38.9	∞	52.4	44.1	∞
X_t = 0.5 *p.u.*	**Bandwidth** (*rad/s*)	1.22	1.09	–	1.26	1.12	–
	Gain margin (*dB*)	17.2	17.5	5.44	21.4	22	5.44
	Phase margin (*deg*)	49.4	36.9	∞	49.9	40.7	∞
X_t = 0.6 *p.u.*	**Bandwidth** (*rad/s*)	1.21	1.1	–	1.3	1.18	–
	Gain margin (*dB*)	16.4	16.7	6.18	20.1	20.8	6.18
	Phase margin (*deg*)	53.1	38.8	∞	48.6	40.3	∞
X_t = 0.8 *p.u.*	**Bandwidth** (*rad/s*)	1.34	1.22	–	1.4	1.28	–
	Gain margin (*dB*)	12.5	13	6.45	16.5	17.7	6.45
	Phase margin (*deg*)	52.2	38.2	∞	47.9	38.2	∞

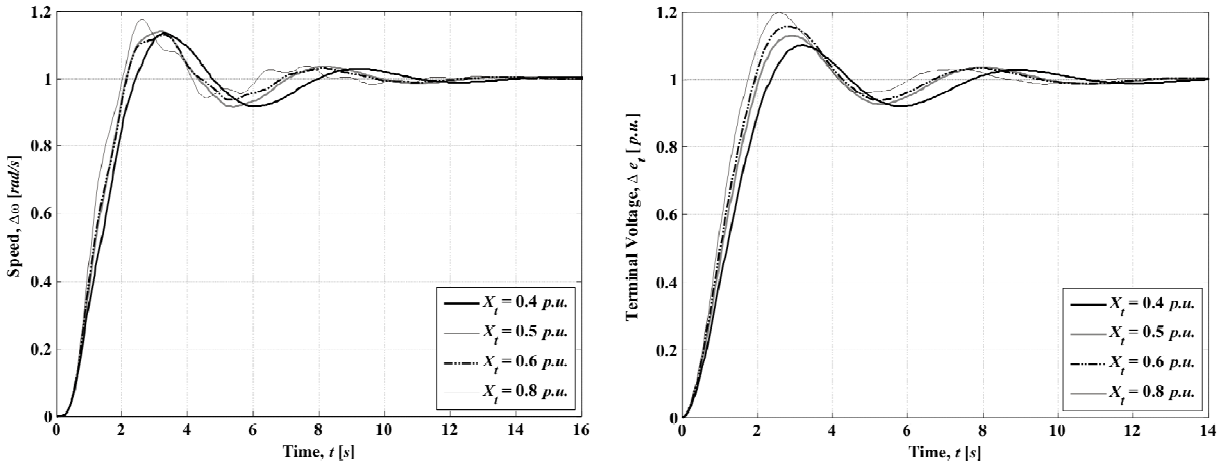

(*a*) (*b*)

Figure 3.30. Step response (designed controller $\mathbf{K}_4(s)$): (*a*) Channel 1 ($T_{c1}(s)$); (*b*) Channel 2 ($T_{c2}(s)$)

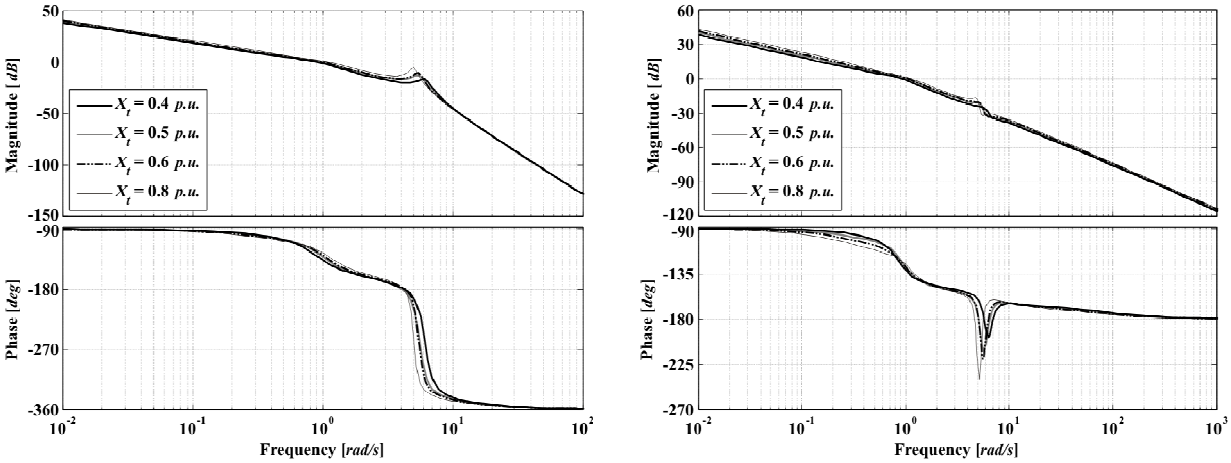

(*a*) (*b*)

Figure 3.31. Bode diagram (designed controller $\mathbf{K}_4(s)$): (*a*) Channel 1 ($C_1(s)$); (*b*) Channel 2 ($C_2(s)$)

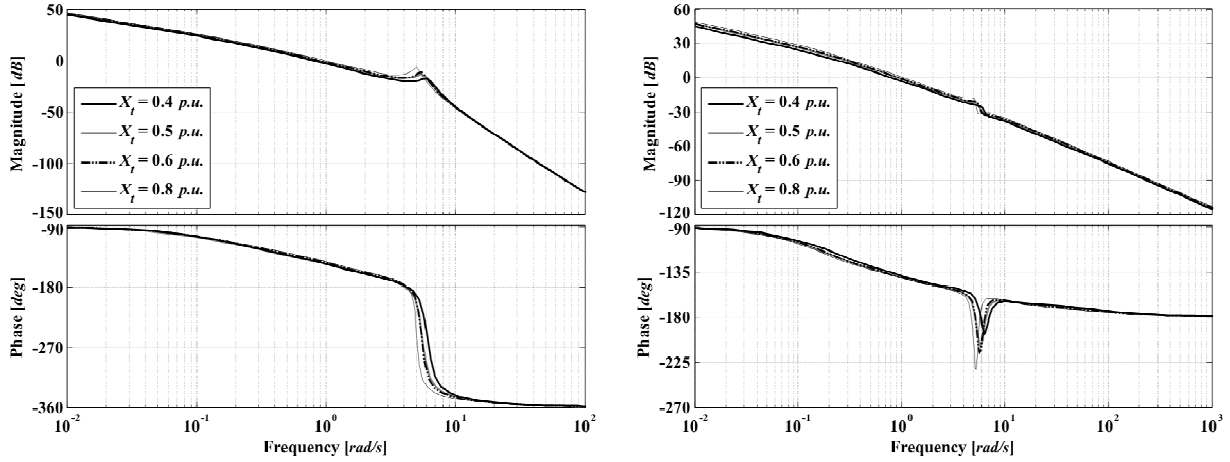

(*a*) (*b*)

Figure 3.32. Bode diagram (designed controller $\mathbf{K}_4(s)$): (*a*) $k_{11}g_{11}(s)$; (*b*) $k_{22}g_{22}(s)$

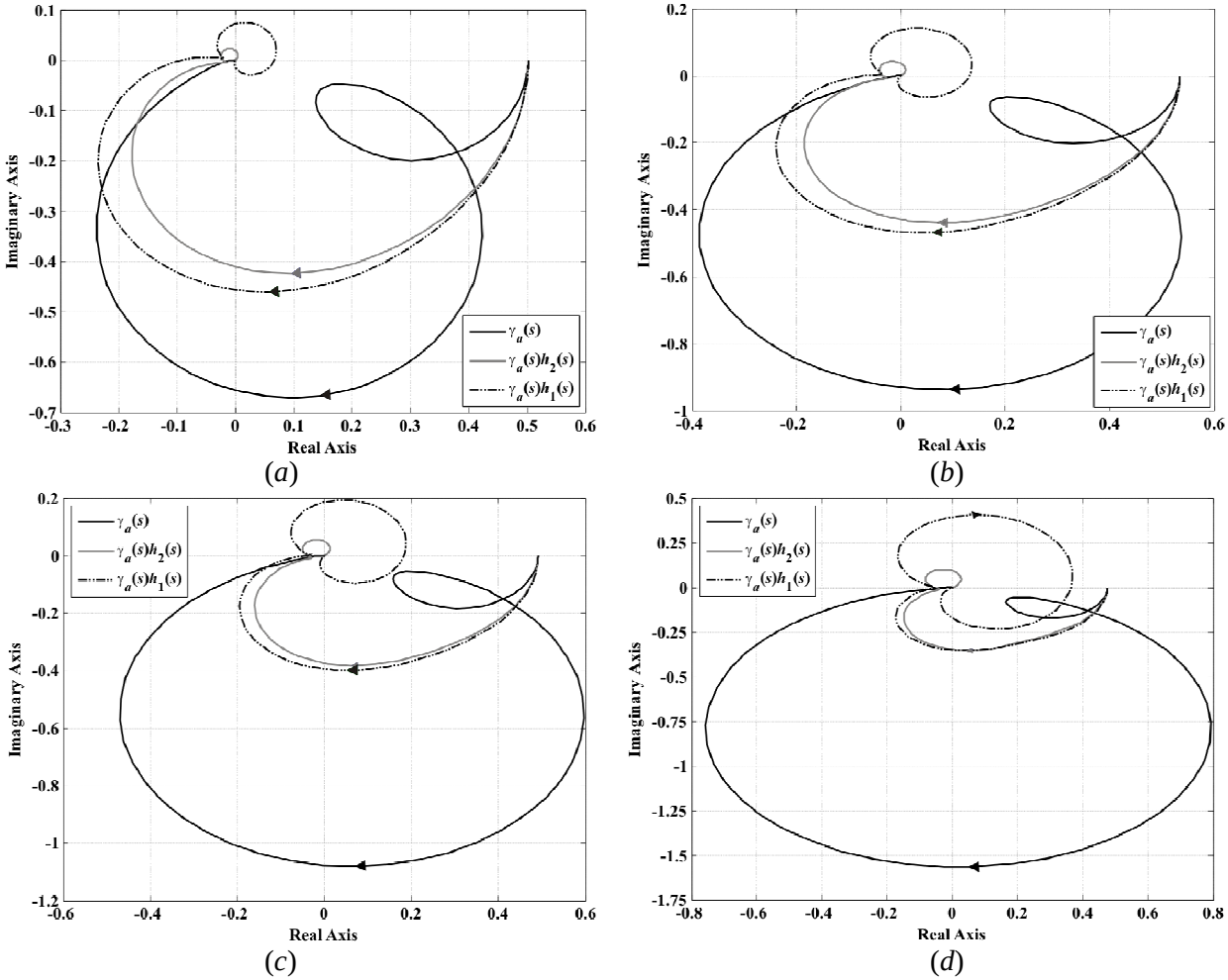

Figure 3.33. Nyquist diagram (designed controller $\mathbf{K}_4(s)$): $\gamma_a(s)$ vs $\gamma_1(s) = \gamma_a(s)h_2(s)$ vs $\gamma_2(s) = \gamma_a(s)h_1(s)$ with (*a*) $X_t = 0.4$ *p.u.*; (*b*) $X_t = 0.5$ *p.u.*; (*c*) $X_t = 0.6$ *p.u.*; (*d*) $X_t = 0.8$ *p.u.*

It is observed in Figures 3.30 and 3.31 that an adequate performance is exhibited for electrical distances of $X_t = 0.4$ and $X_t = 0.5$ *p.u.* and it is acceptable even for higher values ($X_t = 0.6$ and $X_t = 0.8$ *p.u.*). The achieved bandwidth reduction with controller (3.47) (Table 3.7) yields a better dynamical performance as the tie-line reactance increases, with adequate robustness measures, as it can be seen in Figures 3.32 and 3.33. The trade-off is a slower response for both channels.

Remark: The multivariable analysis carried out in this section, previously discussed in [8], provides a formal justification for the validity of the loop-by-loop design practice used for synchronous generator control.

3.6.5. A note on the models

It has been established, following a detailed MSF study, that Models 1 and 2A are to be used for control system design purposes. This is further qualified by assessing the performance of all four models. Figure 3.34 shows the control system performance using the controller $\mathbf{K}_2(s)$ (given by (3.45)) for lagging power factor operation and a tie-line reactance of $X_t = 0.5$ *p.u.*

Results in Figure 3.34 pertaining to Models 2B and 3, for lagging power factor, could mislead one in thinking that the control system design is unsatisfactory, when in fact, for this operating condition, it turns out not to be the case at all, as evidenced by the performance achieved with Models 1 and 2A. In fact, when the performance is evaluated for a tie-line reactance X_t = 0.5 *p.u.* using Models 2B and 3, the closed-loop system, using traditional controllers, turns out to be unstable, as shown in Figure 3.35. In contrast, if Models 1 and 2A are used, the control system is still stable, even though the system performance may not be the most desirable.

This further qualifies the point that Models 2B and 3, whose winding representation is confined to the *d*-axis, do not yield enough system damping. The use of such models for small-signal stability studies may lead to inaccurate analysis due to a poor performance arising from inherent modelling short-comings in such models and not due to a bad control system design at all. Although Model 2A can be used for small-signal stability studies, Model 1 is preferred since it provides a higher level of reliability.

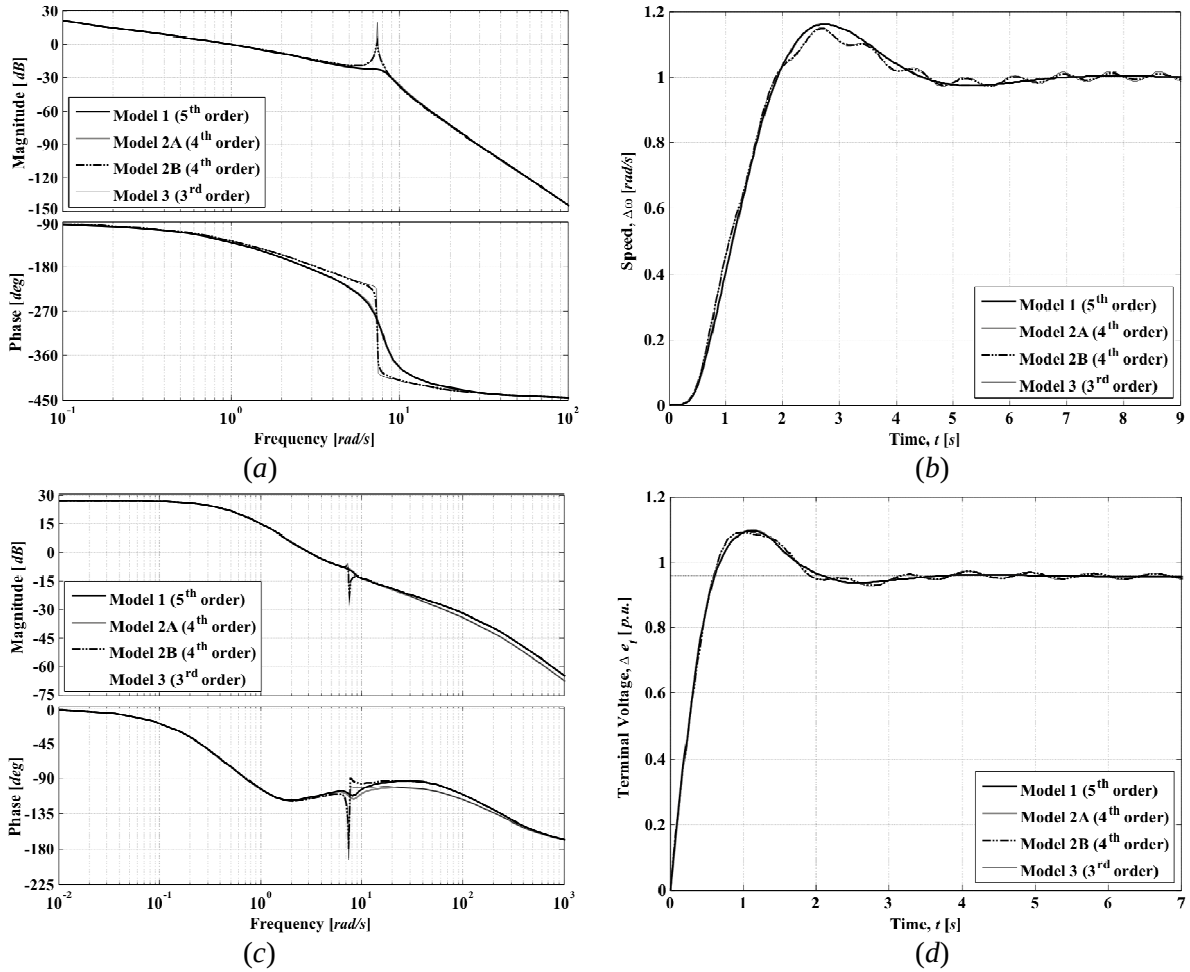

Figure 3.34. Model assessment using controller $\mathbf{K}_2(s)$ in lagging power factor operation. Channel 1: (*a*) Bode diagram; (*b*) Step response. Channel 2: (*c*) Bode diagram; (*d*) Step response;

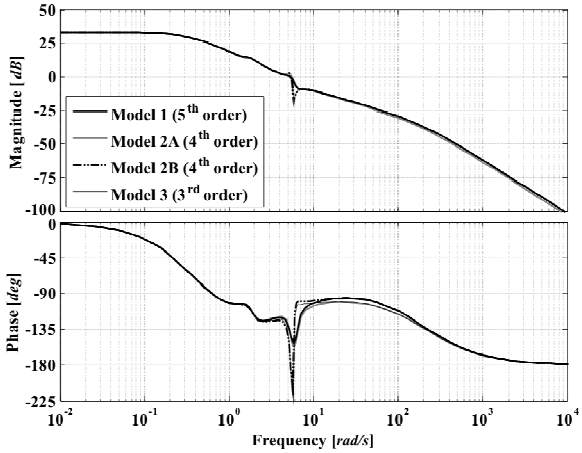

Figure 3.35. Model assessment of synchronous generator under traditional controllers with a tie-line reactance of X_t = 0.5 *p.u.* Channel 2 Bode diagram

3.6.6. When to use higher order models?

Throughout this chapter, an extensive study of the OMIB system has been carried out, focusing on the performance of Model 1 and its comparison with that of lower order models 2A, 2B and 3. However, two additional representations for the synchronous generator, namely Model 0 (6^{th} order, 2*d*.2*q*) and Model 2C (4^{th} order, 1*d*.1*q*) were also presented, but so far they have received no attention in this work since the parameters of the chosen generator are not suitable for these models. Hence, there is still the open question as to how convenient is it to use a more complex representation whenever machine parameters are available.

Table 3.8. System operating condition for higher order models

Variable	Value
P_g	0.9 *p.u.*
Q_g	0. 28487 *p.u.*
PF	0.98521
δ_0	60.0 °
$\lvert V_{\infty 0}\rvert$	1.0 *p.u.*
$\angle V_{\infty 0}$	30.0 °
$\lvert e_{t0}\rvert$	0.995 *p.u.*
$\angle e_{t0}$	66.011°
$\lvert i_{t0}\rvert$ / $\lvert I_{\infty 0}\rvert$	0.94875 *p.u.*
$\angle i_{t0}$ / $\angle I_{\infty 0}$	48.447 °
E_{fd0}	2.0481 *p.u.*
X_t	0.65 *p.u.*

Consider a system representation applicable to a thermal generating station consisting of four 555 *MVA*, 24 *kV*, 60 *Hz* units connected to an infinite bus via a tie-line reactance [17]. It is standard practice to model the station as a single equivalent generator with parameters expressed in per unit on a 2220 *MVA*,

24 *kV* base. These parameters are given in Appendix B, and they represent a full set of machine data that allow the assessment of all the generator models discussed in Sections 3.2.1–3.2.5. The system operating conditions are provided in Table 3.8.

Figure 3.36 shows the Nyquist and Bode plots of $\gamma_a(s)$ using Models 0, 1 and 2C. A damping coefficient $D = 0$ *p.u.* is used for all the models. From the figure it can be seen that Model 2C exhibits an unrealistic coupling near the resonant point, even though it features a *q*-axis damping winding, which does not exist in Models 2B and 3. As for Models 1 and 0, although both are two-axis representations, they do feature relevant differences. Even though their phases in the Bode plot agree on reasonably well, the peak magnitude is larger and moves on to higher frequencies when using the 6th order model. As shown by the Nyquist and Bode plots of Model 0, the system is actually more coupled than what it is apparent with Model 1.

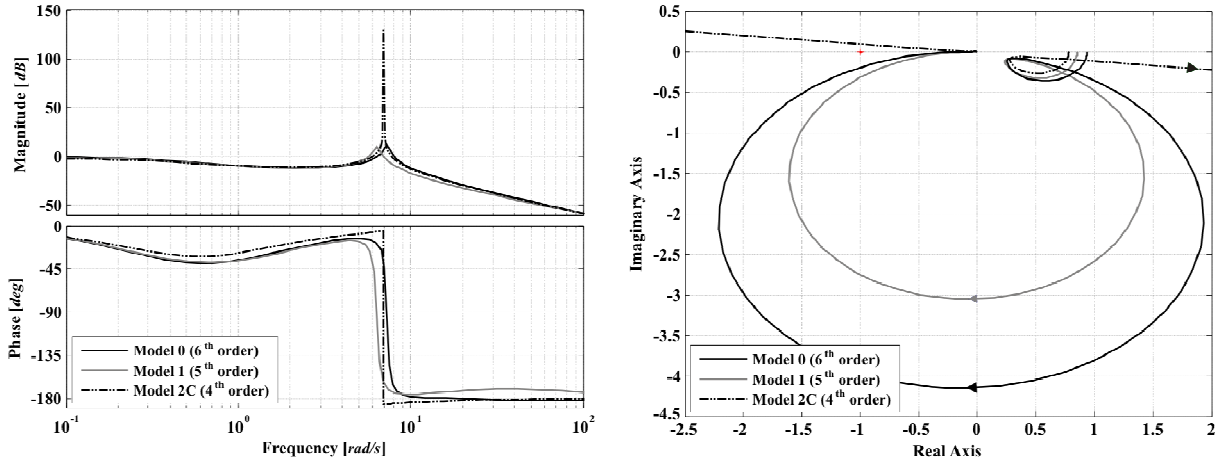

(*a*) (*b*)

Figure 3.36. Assessment of $\gamma_a(s)$ with Models 0, 1 and 2C: (*a*) Bode diagrams; (*b*) Nyquist diagrams

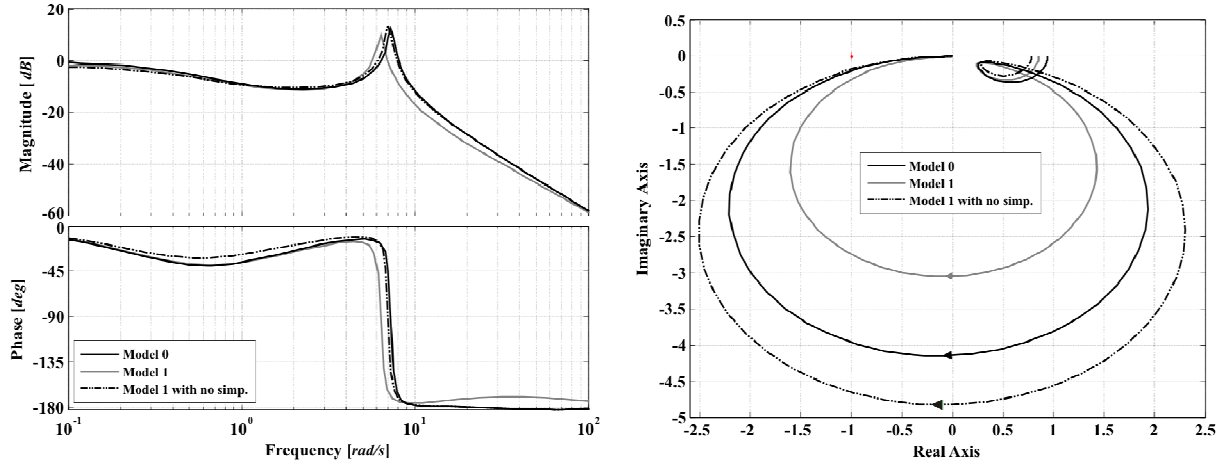

(*a*) (*b*)

Figure 3.37. A further assessment of $\gamma_a(s)$ with Models 0 and 1: (*a*) Bode diagrams; (*b*) Nyquist diagrams

Focusing on Models 0 and 1, an important difference arises from the assumption that $X_q^{'} = X_q$ in Model 0 in order to obtain Model 1. For instance, Figure 3.37 shows the Bode and Nyquist plots of $\gamma_a(s)$ for both models and a special case of Model 1, with no such simplification ($X_q^{'} \neq X_q$). It can be seen that both the magnitude and phase of Model 1 with no simplification on the transient impedance tend to agree on better with those of Model 0 particularly at frequencies around the resonance.

As evidenced by the previous results, special care should be taken when choosing the generator models to carry out small-signal stability studies. As shown, there are not insignificant differences even when two high-order models are used. Whenever computational burden is not a problem, Model 0 can exact an even more realistic response than that of Model 1. However, an important limitation for the use of higher order models arises whenever machine parameters are not available for the analysis. This situation will be discussed further in Chapter 5 when dealing with multi-machine systems.

Remark: A not so obvious issue associated to OMIB systems is that their behaviour in small-signal stability studies may be influenced by the initial conditions. In a power system, active power transfer between two adjacent nodes is determined by the absolute rotor angular difference between them. The initial values are provided by a power flow study, in which one of the nodes is selected as a reference. Common practice is to associate an angle of 0 *deg* to the slack node. If a different value is chosen, an angular offset in every node should appear, but the absolute angular difference between the voltages of two arbitrary nodes will remain be the same. It would be expected that regardless of the initial infinite bus and machine terminal voltage angles, the behaviour of the system remains the same as long as the angular difference between the buses is the preserved. Nevertheless, care should be exercised when choosing the initial values, as several constants in the models could become zero for particular choices of angles (0, 90 *deg*, and multiples). As a consequence, the system may exhibit an unexpected performance and the advantages of employing a higher order model might not be apparent.

3.7. Conclusions

In this chapter, the analysis and control system design of a high order synchronous generator plant is carried out using an established but contemporary control engineering framework referred to as Individual Channel Analysis and Design (ICAD). It provides an alternative, very insightful framework with which to carry out small-signal stability assessments of OMIB systems. It shows analytical advantages over the physically-oriented block-diagram method. Also, a suitable analysis of the MSF, at low and high frequencies, is amenable to a complete multivariable control system design. Moreover, its correct interpretation provides simple and straightforward designs. In addition, a quantification of the coupling

between input and output transmission channels becomes readily available and it provides a formal explanation as to why some operating conditions are more critical than others.

AVRs and turbine-governors are standard control features in large synchronous generators. In this chapter their performance has been revisited using ICAD. The system's dynamical characteristics, encapsulated in MSFs, are analysed in a transparent manner in the frequency domain. It is concluded that two-axis synchronous generator models should be preferred over one-axis models, since the latter have been found to be system damping deficient – a conclusion reached after having performed comprehensive studies using ICAD. As shown, one-axis models may lead to inaccurate analysis and a poor control system performance due to the inferior quality of the model used and not to a bad controller in itself. Nevertheless, it should be mentioned that most of the results assumed an idealised damping coefficient $D = 0$ *p.u.* In practice, the value of D will be small, but non-zero. The methods and analyses presented in this chapter are of course valid for any value of D. Among the two-axis models, Models 0 and 1 should be preferred over Models 2A and 2C, owing to their superior reliability and performance at high frequencies. However, availability of machine parameters may dictate the choice of a particular mathematical model.

Simulation results obtained are in agreement with system behaviour observed in practice. It was shown that the most critical operating condition occurs at leading power factor. Coupling between channels is higher during leading power factor operation than under lagging or near-unit power factor operation, resulting in a considerable loss of robustness. It was also noticed that channel coupling increases with electrical distance, decreasing stability robustness. Similarly, the larger the amount of reactive power that flows from the generating plant to the infinite bus (while keeping active power constant), the higher the coupling between channels is, becoming more difficult to control the plant. The control system designs generated under the ICAD framework offer a better performance, with suitable stability and structural robustness measures, than the conventional controllers. In the following chapters machine models including FACTS devices and a generalised multi-machine model suitable for ICAD are addressed.

3.8. References

[1] Heffron WG, Phillips RA. *Effects of modern Amplidyne voltage regulator in under excited operation of large turbine generators*. Transactions AIEE, **71**, pp. 692–697, 1952.

[2] DeMello FP, Concordia C. *Concepts of synchronous machine stability as affected by excitation control*. IEEE Transactions on Power Apparatus and Systems, **88**, no. 4, pp. 316–329, 1969.

[3] Saidy M, Hughes FM. *Block diagram transfer function model of a generator including damper windings*. IEE Proceedings on Generation, Transmission and Distribution, **141**, no. 6, pp. 599–608, 1994.

[4] Aree P, Acha E. *Block diagram model for fundamental studies of a synchronous generator – static VAR compensator system*. IEE Proceedings on Generation, Transmission and Distribution, **146**, no. 5, pp. 507–514, 1999.

[5] Rogers G. *Power System Oscillations*. USA: Kluwer Academic Publishers; 2000.

[6] Kundur P, Rogers GJ, Wong DY, Wang L, Lauby MG. *A comprehensive computer program package for small signal stability analysis of power systems*. IEEE Transactions on Power Systems, **5**, no. 4, pp. 1076–1083, 1990.

[7] O'Reilly J, Leithead WE. *Multivariable control by individual channel design*. International Journal of Control, **54**, no. 1, pp. 1–46, 1991.

[8] Fadlalmoula Z, Robertson SS, O'Reilly J, Leithead WE. *Individual channel analysis of the turbogenerator with a power system stabilizer*. International Journal of Control, **69**, no.2, pp. 175–202, 1998.

[9] Edwards FV, Dudgeon GJW, McDonald JR, Leithead WE. *Dynamics of distribution networks with distributed generation*. *IEEE* Power Engineering Society Summer Meeting, **2**, pp. 1032–1037, 2000.

[10] Dudgeon GJW, Leithead WE, O'Reilly J, McDonald JR. *Prospects for the decentralized control of small-scale power networks with embedded generation*. IEEE Power Engineering Society Summer Meeting, **2**, pp. 1399–1404, 2000.

[11] Licéaga-Castro E, Ugalde–Loo CE, Licéaga-Castro J, Ponce P. *An Efficient Controller for SV–PWM VSI Based on the Multivariable Structure Function.* Proceedings of the Joint 44th IEEE Conference on Decision and Control and European Control Conference, pp. 4754–4759, Sevilla, Spain, 2005.

[12] Licéaga–Castro E, Ugalde–Loo CE, Licéaga–Castro J. *Induction Motor Control by Individual Channel Analysis and Design*. Proceedings of the International Conference Control 2006 (UK-ACC), Glasgow, Scotland, UK, 2006.

[13] Licéaga–Castro J, Amezquita–Brooks L, Licéaga–Castro E. *Induction Motor Currente Controller for Field Oriented Control Using Individual Channel Design*. Proceedings of the 34th Annual Conference of the IEEE Industrial Electronics Society (IECON 2008), pp. 235–240, Orlando, Florida, USA, 2008.

[14] Ugalde–Loo CE, Olguín–Salinas D, Licéaga–Castro E, Licéaga–Castro J. *Individual Channel Design for Synchronous Generators*. International Journal of Emerging Electric Power Systems, **4**, no.2, art. 4, 2005 (http://www.bepress.com/ijeeps/vol4/iss2/art4).

[15] Hammons TJ, Winning DJ. *Comparisons of synchronous – machine models in the study of the transient behaviour of electrical power systems*. IEE Proceedings, **118**, no. 10, pp. 1442–1458, 1971.

[16] Licéaga–Castro E, Licéaga–Castro J, Ugalde–Loo CE. *Beyond the Existence of Diagonal Controllers: from the Relative Gain Array to the Multivariable Structure Function*. Proceedings of the Joint 44th IEEE Conference on Decision and Control and the European Control Conference, pp. 7150–7156, Sevilla, Spain, 2005.

[17] Kundur P. *Power System Stability and Control*. USA: McGraw-Hill; 1994.

[18] Ogata K. *Modern Control Engineering*. USA: Prentice–Hall; 1997.

[19] Anderson PM, Fouad AA. *Power system control and stability*. IEEE Press, USA; 1994.

[20] IEEE Committee Report. *Computer Representation of Excitation Systems*. IEEE Transactions on Power Apparatus and Systems, **87**, pp. 1460–1464, 1968.

[21] IEEE Committee Report. *Excitation System Models for Power System Stability Studies*. IEEE Transactions on Power Apparatus and Systems, **100**, pp. 494–509, 1981.

[22] IEEE Committee Report. *Dynamic Models for Steam and Hydro Turbines in Power System Studies*. IEEE Transactions on Power Apparatus and Systems, **92**, pp. 1904–1915, 1973.

[23] IEEE Working Group Report. *Dynamic Models for Fossil Fueled Steam Units in Power Systems Studies*. IEEE Transactions on Power Systems, **6**, no. 2, pp. 753–761, 1991.

[24] IEEE Working Group Report. *Hydraulic Turbine and Turbine Control Models for System Dynamic Studies*. IEEE Transactions on Power Systems, **7**, no. 1, pp. 167–179, 1992.

[25] Saadat H. *Power System Analysis*. USA: McGraw-Hill; 2002.

[26] Hamdan AM, Hughes FM. *Analysis and design of power system stabiliser*. International Journal of Control, **26**, pp. 769–782, 1977.

Chapter 4

INDIVIDUAL CHANNEL ANALYSIS AND DESIGN OF SYNCHRONOUS MACHINE – FACTS SYSTEMS FEATURING ELECTROMECHANICAL OSCILLATION DAMPING

4.1. Introduction

The Heffron-Phillips representations have been popular tools for studying the dynamic behaviour of synchronous generators [1–3], as amply detailed in Chapter 3. More recently, this work has been extended to include the *electronically-controlled* compensation provided by FACTS devices in higher-order machine models [4]. As an extension of single machine systems, these transfer function block-diagram models are used to carry out transparent analyses of the interaction between internal machine variables and FACTS controllers in terms of constants and transfer functions that fully encapsulate all key dynamic parameters of the combined system. They yield physical insight and aid to the understanding of system behaviour, including the impact that FACTS devices have on the generator dynamic characteristic [4]. However, since not all interactions between the various variables are useful for control system design purposes, caution needs to be exercised with the use of Heffron-Phillips-type analysis.

A successful integration of FACTS devices into power systems networks is of great importance for all sectors of the electrical industry: power generation, transmission, distribution, and high-voltage power electronics equipment manufacturers. A proper and detailed understanding of the dynamic behaviour of FACTS controllers will positively contribute to this task. Nevertheless, further research is required since the existing analysis tools, although applicable to large-scale systems, lack physical transparency [5] and may not facilitate effective control designs. Such shortcoming in the analysis tools available for dynamic power system design has provided the motivation for carrying out fundamental studies using alternative options.

ICAD, as shown in the case of the synchronous generator plant, is a powerful analysis and control system design tool that provides an alternative and very insightful control-oriented framework with which

to carry out small-signal stability assessments of systems that include FACTS devices. With ICAD, the redundant interactions presented by the block diagram approach can be avoided. Throughout the analysis of Multivariable Structure Functions (MSF), the dynamical behaviour and structure of the system can be described in a global context in which the characteristics of the individual transfer functions do not have explicit relevance. Moreover, a multivariable control system design is possible provided such characteristics are addressed properly, where robustness and performance can be evaluated [6].

In this chapter, a comprehensive assessment of the dynamic interaction of a high-order synchronous generator and FACTS controllers is carried out using Individual Channel Analysis and Design. Owing to their electromechanical oscillation damping capabilities, the Static VAr Compensator (SVC) with a damping control loop and the Thyristor-Controlled Series Compensator (TCSC) are considered. Fundamental analyses are carried out explaining the generator dynamic behaviour as affected by the SVC and the TCSC. Transfer function matrix representations are obtained, which are suitable for the analysis and design within the ICAD framework. Multivariable control system designs are presented, with particular emphasis in closed loop performances and robustness assessments. Reflecting in the insight provided by ICAD, some operational characteristics exhibited by systems featuring such FACTS devices are formally explained, and some interesting conclusions are arrived at.

4.2. Synchronous Generator – SVC System

Major breakthroughs in high-current, high-power electronic technology led to the development of the Static VAr Compensator (SVC), an earlier member of the Flexible AC Transmission Systems family [7–10]. The SVC is already a mature piece of technology, which has become very popular for providing fast-acting reactive power support. The primary application of the SVC is the provision of dynamic voltage regulation to improve *transient stability* [4]. A general description of this FACTS device has been presented in Chapter 2.

In this section the performance of a synchronous generator – SVC system connected to an infinite bus via a tie-line reactance is studied. A transfer function matrix representation of the system is obtained, which is suitable for the analysis and design within the ICAD framework. The system performance is assessed for cases of a strong and a weak connection. Moreover, the performance of the system with SVC is compared to the case when no SVC is used.

4.2.1. System under study

The synchronous machine dynamic representation model to be used is based on the work of Hammons and Winning [11]. The system under study, as reported by Aree and Acha [4], is shown in Figure 4.1.

The test system in Figure 4.1 is used to study the influence that the SVC exerts on the generator dynamic characteristic. It consists of a synchronous generator feeding into an infinite bus via a tie-line system, which includes a shunt compensator in the form of a SVC. In order to conduct a more general study of the dynamic interactions between the generator and the SVC, the latter is placed at an arbitrary point along the tie-line system, between reactances X_{t1} and X_{t2}.

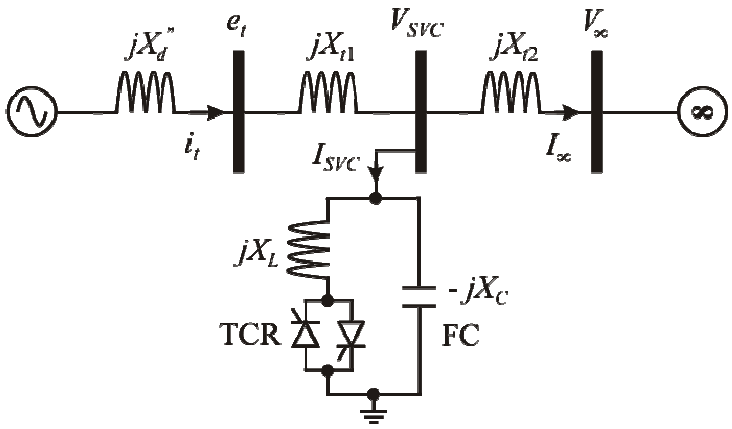

Figure 4.1. Synchronous generator – SVC system

4.2.1.1. Block diagram representation

The small-signal model that represents the system is developed from first principles, by using the non-linear and algebraic equations that represent the synchronous generator and the SVC. A straightforward but cumbersome linearisation exercise of the dynamic equations, which can be found in Appendix D, produces the following expressions in the *s*-domain [4]:

$$\Delta P_e(s) = K_1\Delta\delta(s) + K_2\Delta E_q''(s) - K_{2d}\Delta E_d''(s) + K_{SVC1}\Delta\alpha(s) \tag{4.1}$$

$$\Delta e_t(s) = K_5\Delta\delta(s) + K_6\Delta E_q''(s) + K_{6d}\Delta E_d''(s) + K_{SVC3}\Delta\alpha(s) \tag{4.2}$$

$$\Delta V_{SVC}(s) = K_{5n}\Delta\delta(s) + K_{6n}\Delta E_q''(s) + K_{6dn}\Delta E_d''(s) + K_{SVC3n}\Delta\alpha(s) \tag{4.3}$$

$$\Delta E_q''(s) = K_3(s)\Delta E_{fd}(s) - K_4(s)\Delta\delta(s) + K_{SVC2}(s)\Delta\alpha(s) \tag{4.4}$$

$$\Delta E_d''(s) = K_{4d}(s)\Delta\delta(s) + K_{SVC2d}(s)\Delta\alpha(s) \tag{4.5}$$

$$\Delta\omega(s) = \frac{1}{2Hs}\left[\Delta P_m(s) - \Delta P_e(s) - D\Delta\omega(s)\right] \tag{4.6}$$

$$\Delta\delta(s) = \frac{\omega_0}{s}\Delta\omega(s) \tag{4.7}$$

where the coefficients and transfer functions of equations (4.1)–(4.7) are also given in Appendix D.

It should be noticed that the generator model corresponds to the 5th order synchronous generator model presented in Chapter 3. The previous equations are used to form the block diagram representation for the model, which is shown in Figure 4.2 [4].

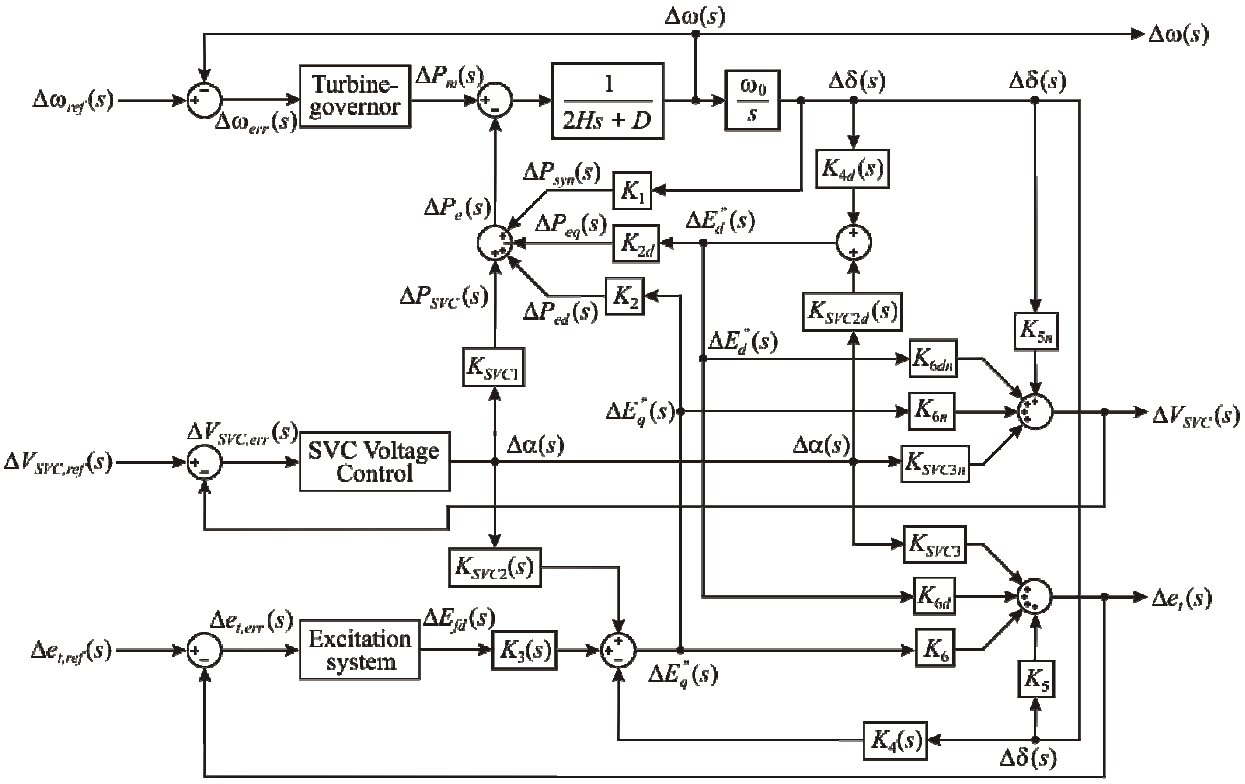

Figure 4.2. Block diagram: synchronous generator – SVC system

The overall structure of the system is shown in Figure 4.2. It comprises three subsystems, *i.e.*, excitation control, turbine-governor control and SVC voltage control loops. These are in addition to the generator – SVC system. The outputs of interest are: generator speed ($\Delta\omega$), generator output voltage (Δe_t) and SVC output voltage (ΔV_{SVC}). The first channel corresponds to the turbine-governor control, which regulates the generator rotor speed by controlling the generator electrical power. The second channel is the excitation control, which regulates the generator output voltage by controlling the generator field voltage (ΔE_{fd}). In the third channel, the SVC control voltage loop is designed to control output voltage by changing the firing angle ($\Delta\alpha$). The feedback control voltage is directly taken from the SVC terminal voltage [12]. It should be noted that the response of the turbine-governor is much slower than the response of the terminal voltage channels.

The block diagram of Figure 4.2 gives a detailed account of the many dynamic interactions that may exist in the generator – SVC system. Such effects can be also presented in terms of a generator output power loop, where incremental changes in the generator's electrical output power (ΔP_e) and the rotor angle ($\Delta\delta$) are taken to be output and input signals, respectively. A change in $\Delta\delta$ is directly fed into the flux linkage in the direct axis via the transfer function $K_4(s)$ and into the flux linkage in the quadrature axis via the transfer function $K_{4d}(s)$. Also, $\Delta\delta$ is passed on to the SVC voltage control loop via the coefficient K_{5n} to make an incremental change in the firing angle ($\Delta\alpha$). A variation in $\Delta\alpha$ may lead to change in voltage proportional to *d*-axis flux linkage ($\Delta E'_q$) directly through the transfer function $K_{SVC2}(s)$

and indirectly through the coefficient K_{SVC3}; it will also induce a change in voltage proportional to the q-axis flux linkage $\Delta E_d^{"}$ through the transfer function $K_{SVC2d}(s)$; and a change in electrical power ΔP_{SVC} through the coefficient K_{SVC1}. ΔP_{SVC} is a portion of the generator's output power that changes due to a change in the SVC susceptance (ΔB_{SVC}) induced by a change in the firing angle. Hence, it can be seen that the generator's electrical power ΔP_e is influenced by the SVC directly through a variation in ΔP_{SVC} and indirectly through variations in ΔP_{ed} and ΔP_{eq}, which are due to d- and q-axis flux linkages, respectively [12].

When the SVC is incorporated into the system, it impacts the electrical performance of the generator in various ways. The SVC susceptance (B_{SVC0}) and location along the tie-line have a major impact on the generator performance. All coefficients and transfer functions making up the generator – SVC system are function of B_{SVC0} and X_{t1} to X_{t2}. The generator performance is also greatly affected by the SVC firing angle. Once a small perturbation in the firing angle takes place, its effect is delivered to the generator through coefficients and transfer functions K_{SVC1}, K_{SVC3}, $K_{SVC2}(s)$ and $K_{SVC2d}(s)$. The extent of such an effect can be assessed by examining the variation of electrical power in the power loop, *i.e.*, ΔP_{ed}, ΔP_{eq} and ΔP_{SVC}.

The SVC interacts electrically with the generator through coefficients K_{SVC1}, K_{SVC3} and transfer functions $K_{SVC2}(s)$ and $K_{SVC2d}(s)$. On the other hand, changes in the generator rotor angle, and changes in the d- and q-axis flux linkages will affect the SVC through coefficients K_{5n}, K_{6n} and K_{6dn}, respectively, via the SVC terminal voltage ΔV_{SVC}.

The block diagram of the synchronous generator – SVC system yields unique physical insight as to how the SVC dynamically affects the generator. It enables a transparent analysis of the interaction between internal machine variables and the SVC in terms of constants and transfer functions that fully encapsulate all key dynamic parameters of the system. However, caution needs to be exercised since not all interactions between the various variables may be useful for control system design purposes.

4.2.1.2. Transfer function matrix representation

The transfer function matrix representation of the system is not only desirable but essential for the analysis of the synchronous generator – SVC plant dynamics under the ICAD framework. After some arduous algebra, described in Appendix D, such a representation can be obtained, given by

$$\begin{bmatrix} \Delta\omega(s) \\ \Delta e_t(s) \\ \Delta V_{SVC}(s) \end{bmatrix} = \begin{bmatrix} g_{11}(s) & g_{12}(s) & g_{13}(s) \\ g_{21}(s) & g_{22}(s) & g_{23}(s) \\ g_{31}(s) & g_{32}(s) & g_{33}(s) \end{bmatrix} \begin{bmatrix} \Delta P_m(s) \\ \Delta E_{fd}(s) \\ \Delta\alpha(s) \end{bmatrix} \tag{4.8}$$

or in a more compact form

$$\mathbf{y}(s) = \mathbf{G}(s)\mathbf{u}(s) \tag{4.9}$$

where **G**(*s*) is the transfer function matrix of the 3×3 linearised model of the synchronous generator – SVC system. The individual elements of **G**(*s*) are also given in Appendix D. For control system analysis, the closed-loop diagram of the system is shown in Figure 4.3. The parameters of the synchronous machine and the Static VAr compensator are listed in Appendix B.

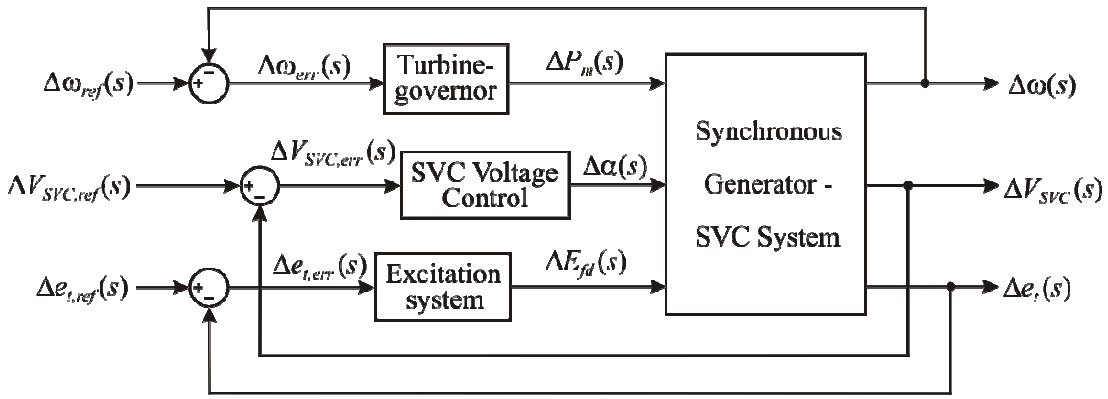

Figure 4.3. Block diagram for control system analysis

Two different studies are carried out. The first one assesses the influence that the SVC exerts on the generator dynamic characteristic when it is connected to a strong transmission system. The second study evaluates the SVC performance in a weak tie-line system. The operating conditions are given as in the work of Aree [12] and shown in Tables 4.1 and 4.2. In each case, the aim is to increase the voltage magnitude at the point of connection of the SVC with the network, enhancing *voltage regulation*. It should be noticed that all the individual transfer functions $g_{jj}(s)$ of **G**(*s*) for both operating conditions (not shown) are stable and minimum-phase.

Table 4.1. System operating conditions. Strong connection

Parameter	Value with no SVC	Value with SVC	Parameter	Value with no SVC	Value with SVC
P_g	0.736 *p.u.*	0.736 *p.u.*	B_{SVC0}	-	0.37734 *p.u.*
Q_g	0.7518 *p.u.*	0.5514 *p.u.*	E_{fd0}	2.3088 *p.u.*	2.0623 *p.u.*
PF	0.7	0.8	$\lvert V_{\infty 0}\rvert$	0.92 *p.u.*	0.92 *p.u.*
P_{SVC}	-	0 *p.u.*	$\angle V_{\infty 0}$	60.15 °	58.08196 °
Q_{SVC}	-	0.378 *p.u.*	$\lvert I_{\infty 0}\rvert$	1 *p.u.*	1.1243 *p.u.*
Q_t	0.552 *p.u.*	0.727 *p.u.*	$\angle I_{\infty 0}$	23.282 °	13.442 °
X_t	0.2 *p.u.*	0.2 *p.u.*	$\lvert e_{t0}\rvert$	1.0522 *p.u.*	1.0522 *p.u.*
X_{t1}	-	0.1 *p.u.*	$\angle e_{t0}$	68.89 °	66.66269 °
δ_0	29.85 °	31.918 °	$\lvert V_{mid}\rvert / \lvert V_{SVC0}\rvert$	0.9832 *p.u.*	1.0022 *p.u.*
α_0	-	150 °	$\angle V_{mid} / \angle V_{SVC0}$	62.742 °	62.66044 °

Table 4.2. System operating conditions. Weak connection

Parameter	Value with no SVC	Value with SVC	Parameter	Value with no SVC	Value with SVC
P_g	0.736 *p.u.*	0.736 *p.u.*	B_{SVC0}	-	0.37734 *p.u.*
Q_g	0.512 *p.u.*	0.258 *p.u.*	E_{fd0}	2.0067 *p.u.*	1.7179 *p.u.*
PF	0.82091	0.94375	$\|V_{\infty 0}\|$	0.92 *p.u.*	0.92 *p.u.*
P_{SVC}	-	0 *p.u.*	$\angle V_{\infty 0}$	33.18 °	32.98226 °
Q_{SVC}	-	0.425 *p.u.*	$\|I_{\infty 0}\|$	0.8 *p.u.*	0.833 *p.u.*
Q_t	0 *p.u.*	0.212 *p.u.*	$\angle I_{\infty 0}$	33.17 °	16.849 °
X_t	0.8 *p.u.*	0.8 *p.u.*	$\|e_{t0}\|$	1.1207 *p.u.*	1.1207 *p.u.*
X_{t1}	-	0.4 *p.u.*	$\angle e_{t0}$	68 °	64.854 °
δ_0	56.82 °	57.018 °	$\|V_{mid}\| / \|V_{SVC0}\|$	0.974 *p.u.*	1.062 *p.u.*
α_0	-	150 °	$\angle V_{mid} / \angle V_{SVC0}$	52.1523 °	50.5264 °

Remark: Overhead transmission lines are usually classified according to length, based on the approximations justified in their modelling [13]. Short lines (shorter than about 80 km) are represented only by their series impedance since they have a negligible shunt capacitance. Medium-length and long lines are usually represented by their nominal π equivalent circuits, which feature a series impedance with shunt admittances. In general, a strong transmission system is associated to short transmission lines, whereas a weak transmission system is related to long lines. In the studies carried out in this chapter, a transmission system is said to be *strong* if its series impedance has a small magnitude. On the other hand, a transmission system is said to be *weak* if its series impedance has a large magnitude; however, the shunt capacitive effects of long transmission lines will not be taken into consideration.

4.2.2. Multivariable analysis

In the framework afforded by ICAD, the dynamical structure of plant (4.8) is determined by input-output channels resulting from pairing each input to each output by means of diagonal controllers. In fact, a key benefit of ICAD is that it enables the use of simple controllers, irrespectively of the degree of coupling exhibited by the multivariable system to be controlled. This situation is extensively discussed in the work of Licéaga-Castro, *et al.* [14], where a family of plants ranging from decoupled to highly coupled is controlled by simple, diagonal and low-order controllers. For the case of the synchronous generator – SVC system, the traditional pairing of inputs to outputs is given as

$$\mathbf{K}(s)=\begin{bmatrix} k_{11}(s) & 0 & 0 \\ 0 & k_{22}(s) & 0 \\ 0 & 0 & k_{33}(s) \end{bmatrix} \Rightarrow \begin{cases} C_1(s):\Delta P_m(s)\rightarrow\Delta\omega(s) \\ C_2(s):\Delta E_{fd}(s)\rightarrow\Delta e_t(s) \\ C_3(s):\Delta\alpha(s)\rightarrow\Delta V_{SVC}(s) \end{cases} \tag{4.10}$$

The diagonal controller given in (4.10), which considers pairings as $\Delta P_m(s)\rightarrow\Delta\omega(s)$, $\Delta E_{fd}(s)\rightarrow$

$\Delta e_t(s)$ and $\Delta\alpha(s) \rightarrow \Delta V_{SVC}(s)$, agrees with that used for conventional controllers and this would be the only case here considered. Notice that the Individual Channels $C_1(s)$ and $C_2(s)$ correspond to the pairing of inputs and outputs associated to the synchronous generator whereas $C_3(s)$ is associated to the SVC voltage control loop. Figure 4.4 shows the individual channel representation for the synchronous generator – SVC system.

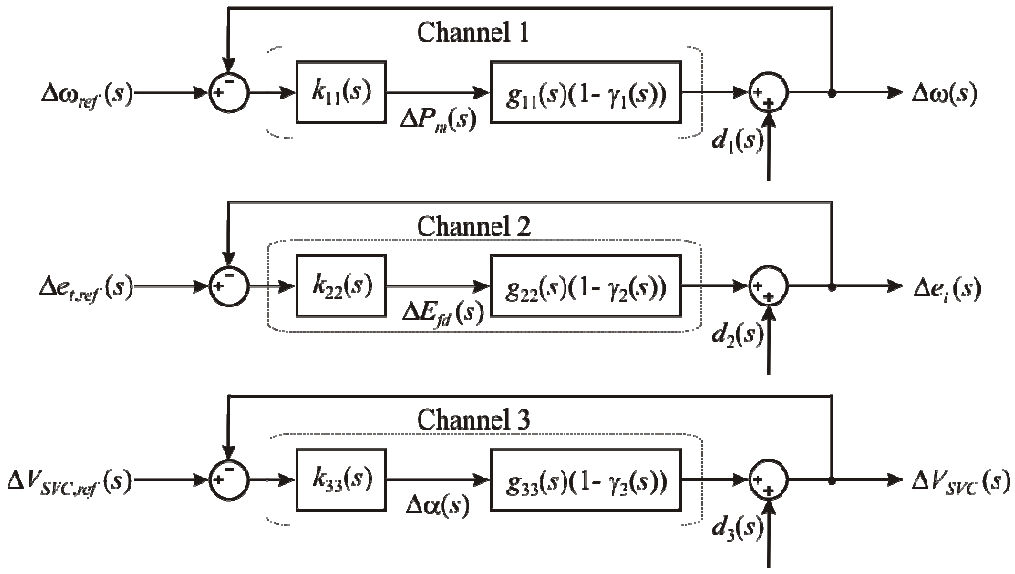

Figure 4.4. Synchronous generator – SVC system represented in individual channels

From Figure 4.4, it can be seen that the 3×3 multivariable system can be re-formulated as three SISO channels, where each channel includes a feedback loop and its controller. Each controller can be designed to comply with the specifications associated to each individual channel. Notice that every channel is subject to a disturbance $d_i(s)$ – representing the effects of other channel references. Therefore, the behaviour of an individual channel will be affected both by its controller and by the other individual channels. Moreover, the representation of Figure 4.4 is fully equivalent to the original synchronous generator – SVC system of Figure 4.3, with no loss of information. The multivariable character of the plant is suitably quantified, in the frequency domain, by the Multivariable Structure Functions (MSF) $\gamma_i(s)$.

Coupling between channels can be determined by MSFs $\Gamma_i(s)$ [6,15], as discussed in Appendix A. These functions are indicators of the potential performance of feedback control. A small magnitude of MSF is amenable to a low signal interaction between channels. As defined in Appendix A, the MSFs $\Gamma_i(s)$ (i = 1,2 and Γ_3 = 0 for 3×3 systems) are:

$$\Gamma_i(s) = -\left|\mathbf{G}_i^{12\ldots(i-1)}\right| / \left(g_{ii}\left|\mathbf{G}^{12\ldots(i-1)i}\right|\right) \tag{A.58}$$

where

$$\begin{aligned}\Gamma_1(s) &= -\left|\mathbf{G}_1\right| / \left(g_{11}\left|\mathbf{G}^1\right|\right) \\ &= -\begin{vmatrix} 0 & g_{12} & g_{13} \\ g_{21} & g_{22} & g_{23} \\ g_{31} & g_{32} & g_{33} \end{vmatrix} / \left(g_{11}\begin{vmatrix} g_{22} & g_{23} \\ g_{32} & g_{33} \end{vmatrix}\right) \\ &= \frac{-\left[-g_{12}\left(g_{21}g_{33} - g_{23}g_{31}\right) + g_{13}\left(g_{21}g_{32} - g_{22}g_{31}\right)\right]}{g_{11}\left(g_{22}g_{33} - g_{23}g_{32}\right)}\end{aligned} \tag{4.11}$$

and

$$\begin{aligned}\Gamma_2(s) &= -\left|\mathbf{G}_2^1\right| / \left(g_{22}\left|\mathbf{G}^{12}\right|\right) \\ &= -\begin{vmatrix} 0 & g_{23} \\ g_{32} & g_{33} \end{vmatrix} / \left(g_{22}\left|g_{33}\right|\right) \\ &= \frac{g_{23}g_{32}}{g_{22}g_{33}}\end{aligned} \tag{4.12}$$

In order to assess the MSFs $\Gamma_i(s)$ of the synchronous generator – SVC system, it is convenient to introduce a new notation. The transfer function matrix in (4.8) will be called $\mathbf{G}_{123}$, where the subscripts indicate that individual transfer functions associated to the output of $C_1(s)$ occupy the first row, those of $C_2(s)$ the second row, and those of $C_3(s)$ the third row. When analysing $\mathbf{G}_{123}$, $\Gamma_1(s)$ in (4.11) provides a measure of coupling between Individual Channel $C_1(s)$ and Multiple Channel $\mathbf{M}_{23}(s)$. On the other hand, $\Gamma_2(s)$ in (4.12) quantifies the coupling between Individual Channels $C_2(s)$ and $C_3(s)$. For instance, for a system $\mathbf{G}_{321}$ where the first and third rows and columns are swapped in relation to the original transfer function matrix $\mathbf{G}_{123}$, MSF $\Gamma_1(s)$ provides a measure of coupling between Individual Channel $C_3(s)$ and Multiple Channel $\mathbf{M}_{12}(s)$ – or $\mathbf{M}_{21}(s)$; on the other hand, $\Gamma_2(s)$ provides a measure of coupling between Individual Channels $C_1(s)$ and $C_2(s)$. Notice that expressions (4.11) and (4.12) will not hold for $\mathbf{G}_{321}$; that is, $\Gamma_1(s)$ and $\Gamma_2(s)$ should be obtained accordingly with the new transfer function matrix. Other combinations for transfer function matrices are available for analysis; however, notice that the associated MSFs to some transfer function matrices offer identical information, *e.g.*, $\mathbf{G}_{123}$ and $\mathbf{G}_{132}$, $\mathbf{G}_{213}$ and $\mathbf{G}_{231}$, and $\mathbf{G}_{312}$ and $\mathbf{G}_{321}$. The reader is referred to Appendix A for individual and multiple channel definitions.

It is important to state that the MSFs of the system given the operating conditions of Tables 4.1 and 4.2, shown in Figures 4.5–4.10, share common characteristics. Their numerical evaluation shows that they are stable and minimum-phase. Moreover, they have an infinite phase margin and their Nyquist plots start to the left of the point (1,0). Such features ease the design process. After suitable analysis of the MSFs of the 3×3 system, the following remarks can be made:

- When considering transfer function matrix $\mathbf{G}_{123}$ (Figures 4.5 and 4.6), $\Gamma_1(s)$ shows that Multiple Channel $\mathbf{M}_{23}(s)$ is decoupled from Individual Channel $C_1(s)$ for the case of a strong transmission system (less than –10 *dB*), but an increase in electrical distance (tie-line reactance) increases their

coupling. From $\Gamma_2(s)$ it can be noticed that Individual Channels $C_2(s)$ and $C_3(s)$ are slightly coupled for a strong transmission system, but an increase in electrical distance increases their coupling considerably.

- When considering transfer function matrix $\mathbf{G}_{213}$ (Figures 4.7 and 4.8), $\Gamma_1(s)$ shows that Multiple Channel $\mathbf{M}_{13}(s)$ is slightly coupled with Individual Channel $C_2(s)$, but an increase in electrical distance increases their coupling. From $\Gamma_2(s)$ is noticed that Individual Channels $C_1(s)$ and $C_3(s)$ are totally decoupled (less than –25 *dB* for all frequencies) – an increase in electrical distances increases their coupling considerably.

- When considering transfer function matrix $\mathbf{G}_{312}$ (Figures 4.9 and 4.10), $\Gamma_1(s)$ shows that Multiple Channel $\mathbf{M}_{12}(s)$ is slightly coupled with Individual Channel $C_3(s)$, but an increase in electrical distance slightly increases their coupling. From $\Gamma_2(s)$ is noticed that Individual Channels $C_1(s)$ and $C_2(s)$ are weakly coupled, but an increase in electrical distance increases their coupling quite considerably (above 0 *dB* in the frequency range of 4–8 *rad/s*).

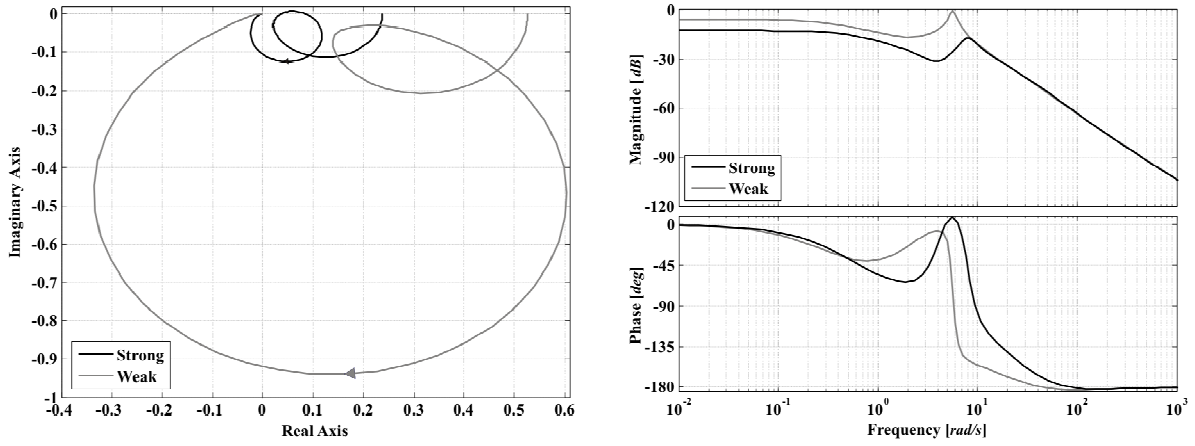

(*a*) (*b*)

Figure 4.5. Assessment of $\Gamma_1(s)$ (transfer function matrix $\mathbf{G}_{123}$) for an SVC-upgraded system with different transmission systems: (*a*) Nyquist plot; (*b*) Bode plot

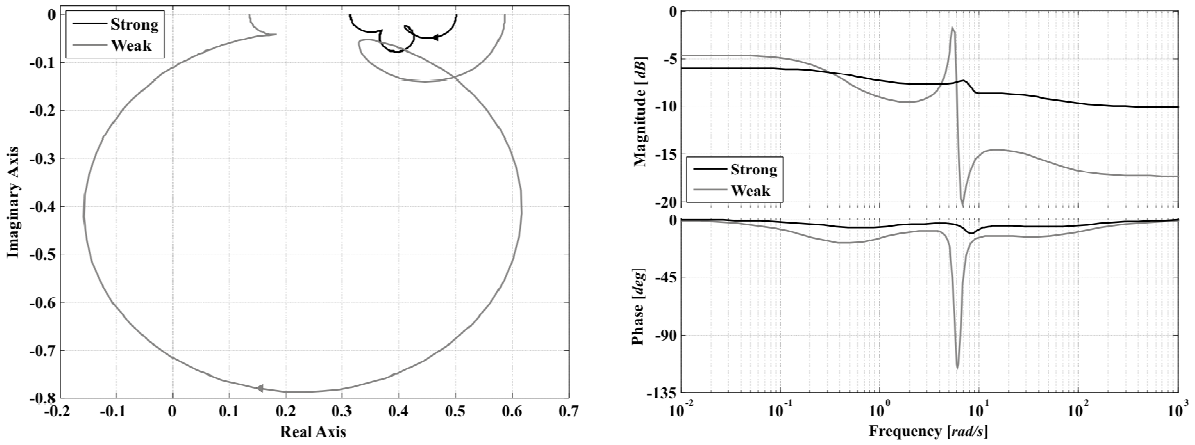

(*a*) (*b*)

Figure 4.6. Assessment of $\Gamma_2(s)$ (transfer function matrix $\mathbf{G}_{123}$) for an SVC-upgraded system with different transmission systems: (*a*) Nyquist plot; (*b*) Bode plot

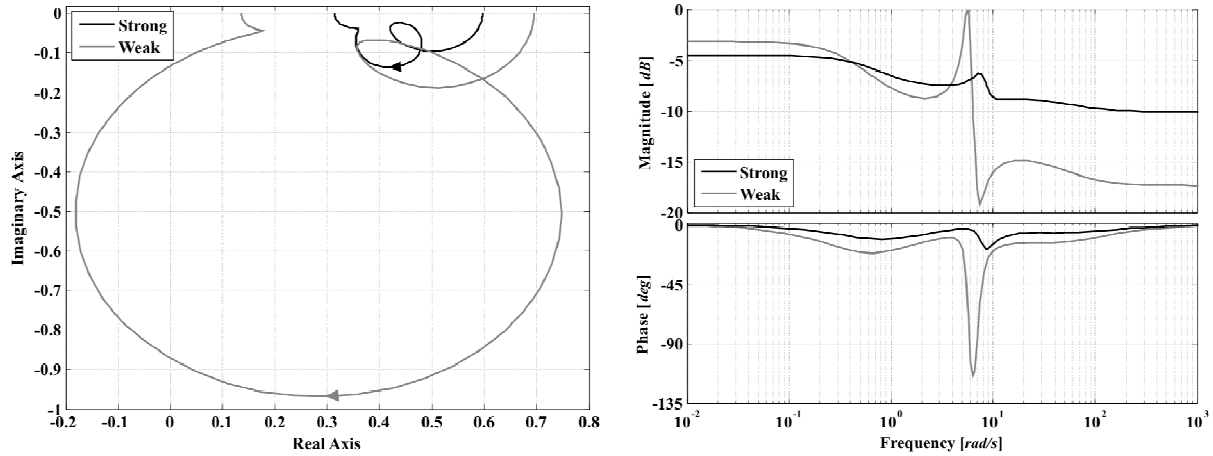

(*a*) (*b*)

Figure 4.7. Assessment of $\Gamma_1(s)$ (transfer function matrix $\mathbf{G}_{213}$) for an SVC-upgraded system with different transmission systems: (*a*) Nyquist plot; (*b*) Bode plot

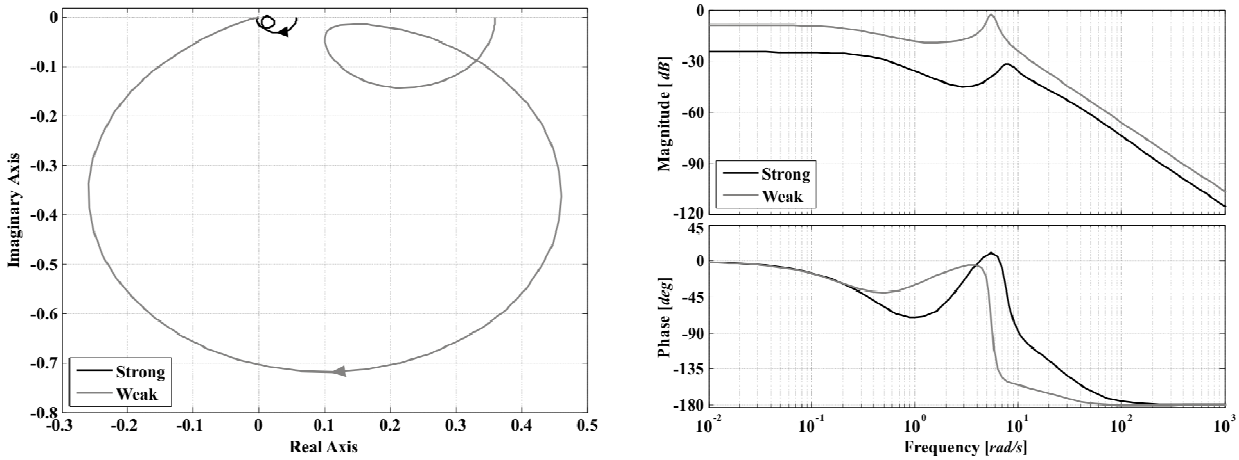

(*a*) (*b*)

Figure 4.8. Assessment of $\Gamma_2(s)$ (transfer function matrix $\mathbf{G}_{213}$) for an SVC-upgraded system with different transmission systems: (*a*) Nyquist plot; (*b*) Bode plot

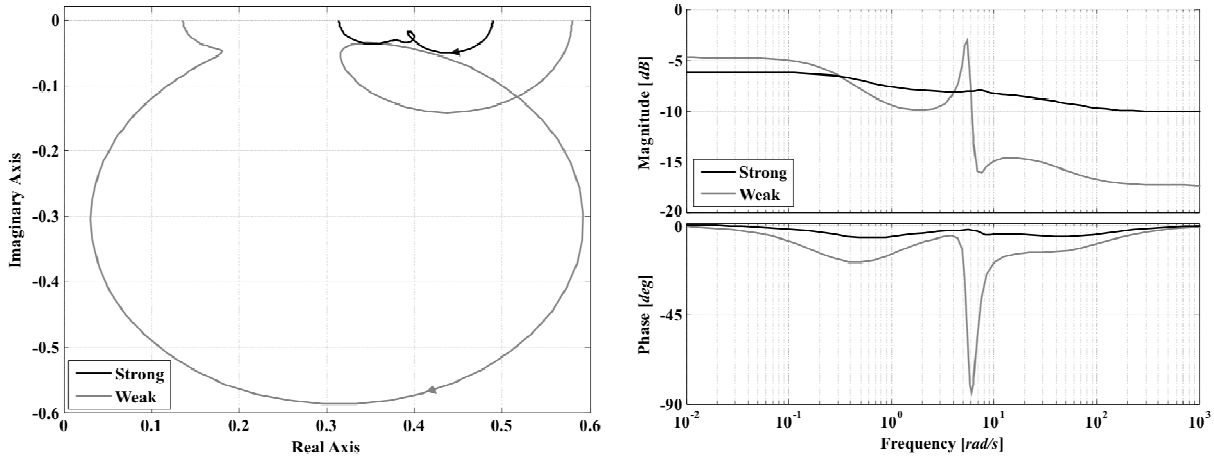

(*a*) (*b*)

Figure 4.9. Assessment of $\Gamma_1(s)$ (transfer function matrix $\mathbf{G}_{312}$) for an SVC-upgraded system with different transmission systems: (*a*) Nyquist plot; (*b*) Bode plot

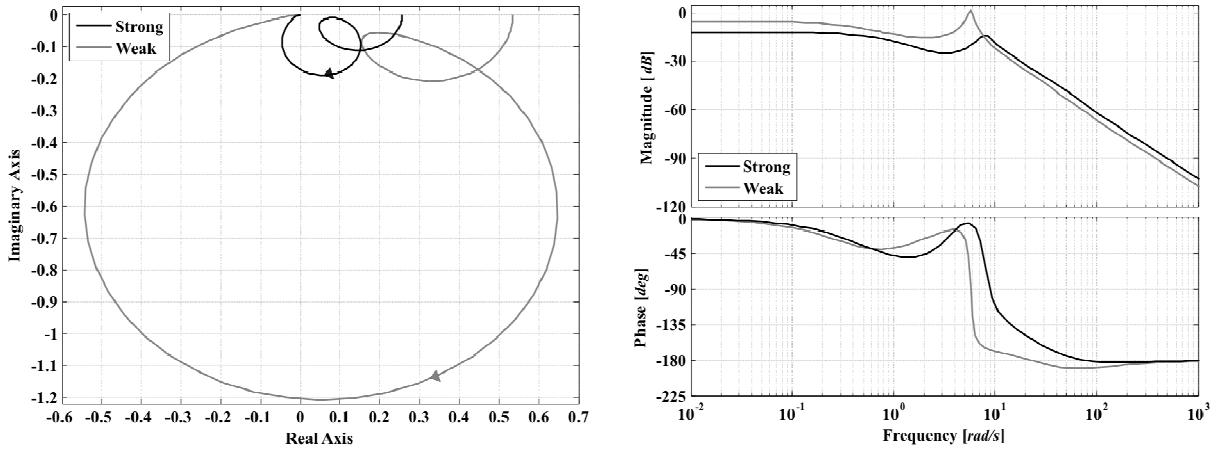

(*a*) (*b*)

Figure 4.10. Assessment of $\Gamma_2(s)$ (transfer function matrix $\mathbf{G}_{312}$) for an SVC-upgraded system with different transmission systems: (*a*) Nyquist plot; (*b*) Bode plot

From the previous analysis, it can be observed that the SVC and the synchronous machine, regardless of the value of tie-line reactance, constitute a slightly coupled multivariable system – particularly at low frequencies over the range of interest of 1–10 *rad/s*. In general, coupling is higher for weak transmission systems and decreases for strong transmission systems. It should be noted that the SVC voltage control loop, represented by $C_3(s)$, tends to slightly couple with the terminal voltage channel of the synchronous generator.

Within the ICAD context, the actual dynamics of the synchronous generator under the influence of the SVC are represented by Multiple Channel $\mathbf{M}_{12}(s)$. The Nyquist and Bode plots of MSF $\Gamma_2(s)$ for a transfer function matrix $\mathbf{G}_{312}$ given the operating conditions in Tables 4.1 and 4.2 are shown in Figure 4.10. These plots confirm that Individual Channels $C_1(s)$ and $C_2(s)$ for a strong transmission system are lowly coupled. An increase in the tie-line reactance value will increase coupling.

In Chapter 3, it has been formally proven that operation of long-distance transmission systems is less robust than in transmission systems involving short distances. Previous results obtained while considering a synchronous generator with no SVC show that coupling within the machine is low under a lagging power factor operation and relatively short tie-lines; however, coupling increases with electrical distance, decreasing robustness. Moreover, it was shown that the larger the amount of reactive power flow in the tie-line reactance, the higher the coupling between channels – making it difficult to control the plant. The previous results are important since they may dictate a control design strategy. For instance, Multiple Channel $\mathbf{M}_{12}(s)$ can be designed independently of Individual Channel $C_3(s)$. Consider the synchronous generator – SVC system with a rearranged transfer function matrix $\mathbf{G}_{312}$, or

$$\begin{bmatrix} \Delta V_{SVC}(s) \\ \Delta\omega(s) \\ \Delta e_t(s) \end{bmatrix} = \begin{bmatrix} g_{33}(s) & g_{31}(s) & g_{32}(s) \\ g_{13}(s) & g_{11}(s) & g_{12}(s) \\ g_{23}(s) & g_{21}(s) & g_{22}(s) \end{bmatrix} \begin{bmatrix} \Delta\alpha(s) \\ \Delta P_m(s) \\ \Delta E_{fd}(s) \end{bmatrix} \tag{4.13}$$

The partitioned system given by (A.30) and (A.31) in Appendix A is used for design, which with the new notation becomes:

$$\mathbf{G}_{312}(s)=\begin{bmatrix}\mathbf{G}_{11}(s) & \mathbf{G}_{12}(s)\\ \mathbf{G}_{21}(s) & \mathbf{G}_{22}(s)\end{bmatrix} \qquad \mathbf{K}_{312}(s)=\begin{bmatrix}\mathbf{K}_{1}(s) & \mathbf{0}\\ \mathbf{0} & \mathbf{K}_{2}(s)\end{bmatrix} \tag{4.14}$$

$$\mathbf{r}_{312}(s)=\begin{bmatrix}\mathbf{r}_{1}(s)\\ \mathbf{r}_{2}(s)\end{bmatrix} \qquad \mathbf{y}_{312}(s)=\begin{bmatrix}\mathbf{y}_{1}(s)\\ \mathbf{y}_{2}(s)\end{bmatrix} \tag{4.15}$$

where

$$\mathbf{G}_{11}(s)=g_{33}(s) \qquad \mathbf{G}_{12}(s)=\begin{bmatrix}g_{31}(s) & g_{32}(s)\end{bmatrix}$$

$$\mathbf{G}_{21}(s)=\begin{bmatrix}g_{13}(s)\\ g_{23}(s)\end{bmatrix} \qquad \mathbf{G}_{22}(s)=\begin{bmatrix}g_{11}(s) & g_{12}(s)\\ g_{21}(s) & g_{22}(s)\end{bmatrix}$$

$$\mathbf{K}_{1}(s)=k_{33}(s) \qquad \mathbf{K}_{2}(s)=\begin{bmatrix}k_{11}(s) & 0\\ 0 & k_{22}(s)\end{bmatrix}$$

$$\mathbf{r}_{1}(s)=r_{3}(s) \qquad \mathbf{r}_{2}(s)=\begin{bmatrix}r_{1}(s)\\ r_{2}(s)\end{bmatrix}$$

$$\mathbf{y}_{1}(s)=y_{3},(s) \qquad \mathbf{y}_{2}(s)=\begin{bmatrix}y_{1}(s)\\ y_{2}(s)\end{bmatrix}$$

and r_i and y_i represent the i-th reference and the i-th output of the closed-loop system, respectively. Recalling equation (A.32), Individual Channel $C_3(s)$ is expressed by

$$\begin{aligned}\mathbf{M}_{1}(s)=C_{3}(s)&=\left[\mathbf{I}-\mathbf{G}_{12}(s)\mathbf{G}_{22}^{-1}(s)\mathbf{H}_{2}(s)\mathbf{G}_{21}(s)\mathbf{G}_{11}^{-1}(s)\right]\mathbf{G}_{11}(s)\mathbf{K}_{1}(s)\\ &=k_{33}(s)g_{33}(s)\left[1-\mathbf{G}_{12}(s)\mathbf{G}_{22}^{-1}(s)\mathbf{H}_{2}(s)\mathbf{G}_{21}(s)g_{33}^{-1}(s)\right]\end{aligned} \tag{4.16}$$

where the multiple subsystem transfer function matrix $\mathbf{H}_2(s)$ is given by

$$\mathbf{H}_{2}(s)=\mathbf{G}_{22}(s)\mathbf{K}_{2}(s)\left[\mathbf{I}+\mathbf{G}_{22}(s)\mathbf{K}_{2}(s)\right]^{-1} \tag{A.33}$$

and is subjected to the cross-reference disturbance

$$\mathbf{D}_{1}(s)=\mathbf{G}_{12}(s)\mathbf{G}_{22}^{-1}(s)\mathbf{H}_{2}(s) \tag{A.34}$$

From (A.35), Multiple Channel $\mathbf{M}_{12}(s)$ is expressed by

$$\begin{aligned}\mathbf{M}_{2}(s)=\mathbf{M}_{12}(s)&=\left[\mathbf{I}_{2\times2}-\mathbf{G}_{21}(s)\mathbf{G}_{11}^{-1}(s)\mathbf{H}_{1}(s)\mathbf{G}_{12}(s)\mathbf{G}_{22}^{-1}(s)\right]\mathbf{G}_{22}(s)\mathbf{K}_{2}(s)\\ &=\left[\mathbf{I}_{2\times2}-g_{33}^{-1}(s)h_{1}(s)\mathbf{G}_{21}(s)\mathbf{G}_{12}(s)\mathbf{G}_{22}^{-1}(s)\right]\mathbf{G}_{22}(s)\mathbf{K}_{2}(s)\end{aligned} \tag{4.17}$$

where the multiple subsystem transfer function matrix $\mathbf{H}_1(s)$ in (A.36) is given by

$$\mathbf{H}_{1}(s)=h_{1}(s)=k_{33}(s)g_{33}(s)\left[1+k_{33}(s)g_{33}(s)\right]^{-1} \tag{4.18}$$

and is subjected to the cross-reference disturbance $\mathbf{D}_2(s)$ in (A.37) by

$$\mathbf{D}_{2}(s)=g_{33}^{-1}(s)h_{1}(s)\mathbf{G}_{21}(s) \tag{4.19}$$

Assuming $h_1(s) = 1$, Multiple Channel $\mathbf{M}_{12}(s)$ is designed as a separate 2×2 system. Once controllers $k_{11}(s)$ and $k_{22}(s)$ are obtained, $\mathbf{H}_2(s)$ can be defined (that is, the interaction of $\mathbf{M}_{12}(s)$ with $C_3(s)$) and a controller $k_{33}(s)$ for Individual Channel $C_3(s)$, as indicated in (4.16), can be designed. This is followed by the calculation of $h_1(s)$ (interaction with $\mathbf{M}_{12}(s)$) and controllers $k_{11}(s)$ and $k_{22}(s)$ are re-designed. The process is repeated until a successful multivariable controller is achieved for all channels and robustness is assured in each individual channel, subsystems $\mathbf{H}_i(s)$, and multivariable structure functions $\gamma_i(s)$.

Corollary: In general, recall from Appendix A that the i-th Individual Channel $C_i(s)$ in an $m \times m$ system has the open-loop SISO transmittance

$$C_i(s) = k_{ii} g_{ii} (1 - \gamma_i) \tag{A.55}$$

and

$$\gamma_i(s) = -\left|\bar{\mathbf{G}}_i\right| / g_{ii} \left|\bar{\mathbf{G}}^i\right| \tag{A.56}$$

subjected to disturbances

$$d_i(s) = -\left|\mathbf{R}_i\right| / \left|\bar{\mathbf{G}}^i\right| \tag{A.57}$$

where $i = 1,\ldots,m$. For the construction of matrices $\bar{\mathbf{G}}$, $\bar{\mathbf{G}}^{i_1 i_2 \ldots i_r}$ and $\bar{\mathbf{G}}_j^{i_1 i_2 \ldots i_r}$, refer to equations (A.38)–(A.45) and the procedure described in Section A.2.2.

The control system design specifications for the synchronous generator were discussed in Section 3.6 of Chapter 3. The analysis showed the difficulties arising when trying to apply direct control along the frequencies where the switch-back characteristic is present. The control system design problem for a weak system is faced in much the same way as for a strong system. However, an inherent constraint should be kept in mind: the unavoidable decrease of system bandwidth to overcome the switch-back characteristic.

4.2.3. Control system design example

4.2.3.1. Study 1. Strong transmission system

The operating conditions of the system are as in the work of Aree [12] and given in Table 4.1. After analysing the MSFs of the model, the following controller is obtained:

$$\begin{aligned} \mathbf{K}_1(s) &= \begin{bmatrix} k_{11}(s) & 0 & 0 \\ 0 & k_{22}(s) & 0 \\ 0 & 0 & k_{33}(s) \end{bmatrix} \\ &= \operatorname{diag}\left[\frac{5.75\left(s^2 + 2.472s + 60.43\right)}{s^2(s+5)}, \quad \frac{14(s+0.43)}{s}, \quad \frac{70}{s} \right] \end{aligned} \tag{4.20}$$

The control system performance and robustness measures with controller (4.20) for a strong system ($X_t = 0.2$ *p.u.*) are presented in Figures 4.11–4.14, with relevant information summarised in Table 4.3.

Table 4.3. Structural and stability robustness of the channels and control system.
Strong transmission system

Measure	$C_1(s)$	$k_{11}g_{11}(s)$	$\gamma_1(s)$	$C_2(s)$	$k_{22}g_{22}(s)$	$\gamma_2(s)$	$C_3(s)$	$k_{33}g_{33}(s)$	$\gamma_3(s)$
Bandwidth (*rad/s*)	0.228	0.264	—	1.06	1.38	—	2.07	2.19	—
Gain margin (*dB*)	∞	∞	12.5	∞	∞	4.48	∞	∞	6.21
Phase margin (*deg*)	90.8	82.8	∞	112	92.2	∞	99.4	86.7	∞

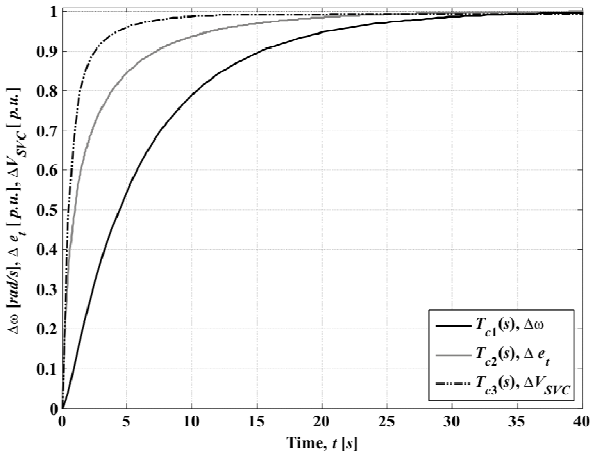

Figure 4.11. Step response: Channel 1 ($T_{c1}(s)$), Channel 2 ($T_{c2}(s)$) and Channel 3 ($T_{c3}(s)$)

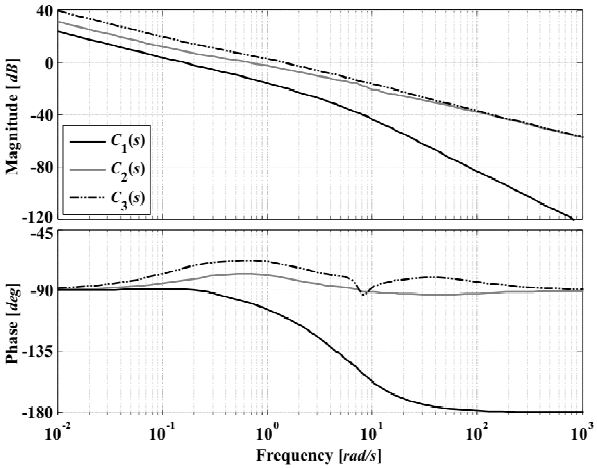

Figure 4.12. Bode diagrams: Channels $C_i(s)$

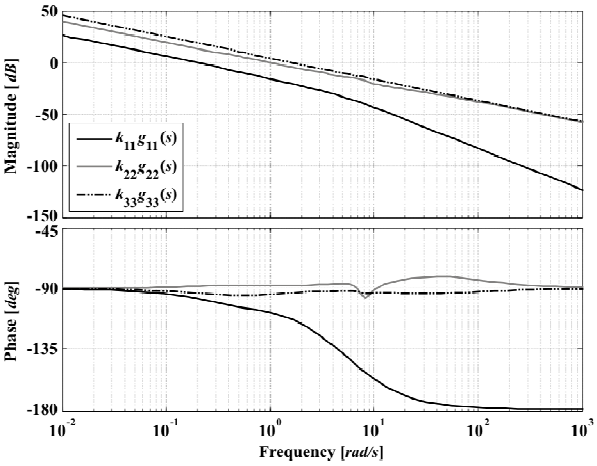

Figure 4.13. Robustness assessment. Bode diagrams of $k_{ii}g_{ii}(s)$

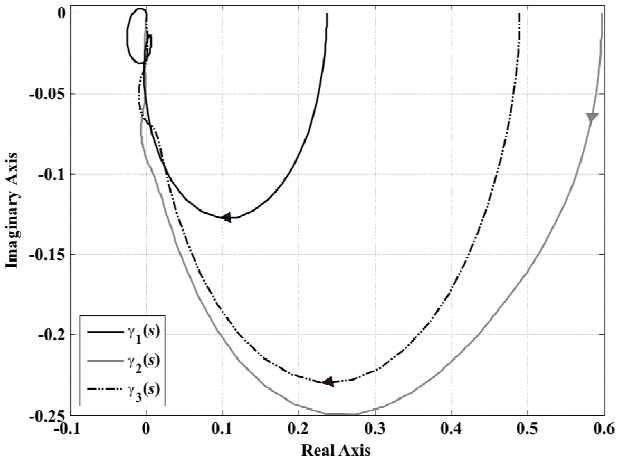

Figure 4.14. Robustness assessment of $\gamma_i(s)$. Nyquist diagrams

From Figure 4.11 it can be seen that the step response of the individual channels is adequate. The fastest channel, $C_3(s)$, corresponds to the SVC control loop, followed by the voltage control, $C_2(s)$, and then by the speed control, $C_1(s)$. This is a direct consequence of the chosen bandwidths for each channel, which can be determined from Figure 4.12 (summarised in Table 4.3). In terms of stability robustness, notice that gain and phase margins are adequate for all channels, *i.e.*, gain and phase margins over 6 *dB* and 40 *deg*, respectively, according to reference [13].

The structural robustness of the control system is assessed in Figures 4.13 and 4.14. Figure 4.13 shows the Bode diagrams of the individual channel subsystems $h_i(s)$. The gain and phase margins with the proposed controllers are adequate, as shown in Table 4.3. Figure 4.14 includes the Nyquist diagrams of $\gamma_i(s)$. Although the Nyquist plots of $\gamma_2(s)$ and $\gamma_3(s)$ start closer to (1,0) than $\gamma_1(s)$, notice that the roll-off behaviour is adequate. The use of integral action in controller (4.20) ensures high gain at low frequencies.

In summary, controller (4.20) has an overall satisfactory performance and the control system has adequate robustness margins.

4.2.3.2. Study 2. Weak transmission system

The control system performance and robustness measures for the synchronous generator – SVC system with a weak transmission system (X_t = 0.8 *p.u.*) are studied in this section. The operating condition for such a configuration is given in Table 4.2.

To enable a suitable performance in weak transmission systems the channels bandwidth should be lowered. This point has already been addressed in connection with the MSFs of weak systems. For instance, if

$$\mathbf{K}_2(s) = \mathrm{diag}\left[\frac{2.1\left(s^2+2.472s+60.43\right)}{s^2\left(s+5\right)},\quad \frac{2.15\left(s+0.43\right)}{s},\quad \frac{8}{s}\right] \tag{4.21}$$

is used, notice that the only changes when compared to controller (4.20) are in the gains of the individual transfer functions, *i.e.*, $k_{ii}(s)$. The control system performance and robustness measures with controller (4.21) are shown in Figures 4.15–4.18. Relevant information for these results is summarised in Table 4.4.

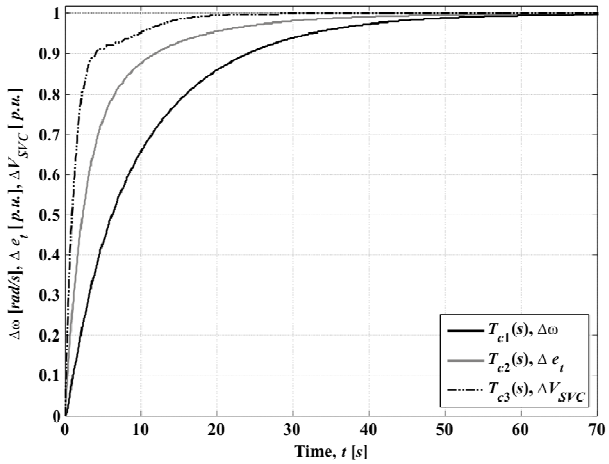

Figure 4.15. Step response: Channel 1 ($T_{c1}(s)$), Channel 2 ($T_{c2}(s)$) and Channel 3 ($T_{c3}(s)$)

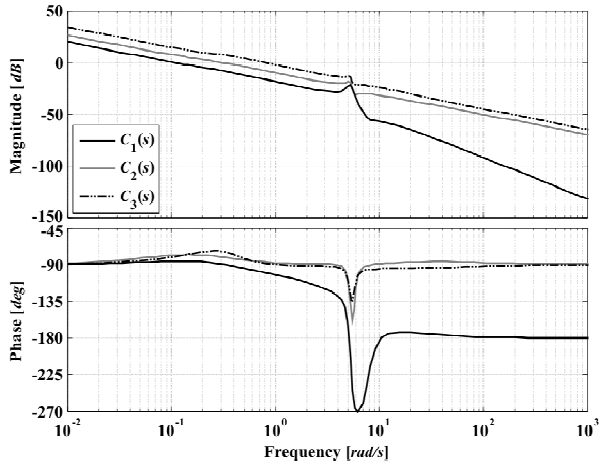

Figure 4.16. Bode diagrams: Channels $C_i(s)$

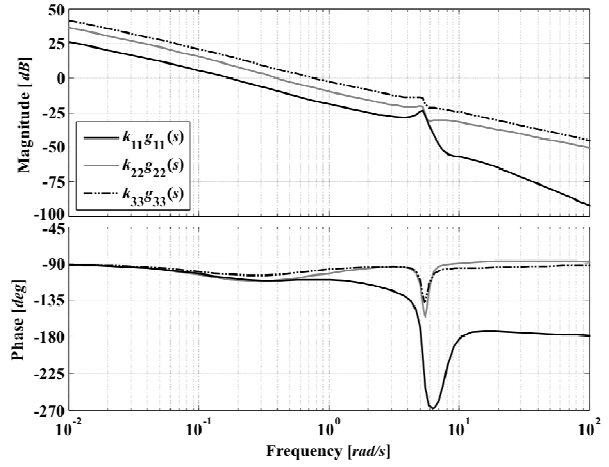

Figure 4.17. Robustness assessment. Bode diagrams of $k_{ii}g_{ii}(s)$

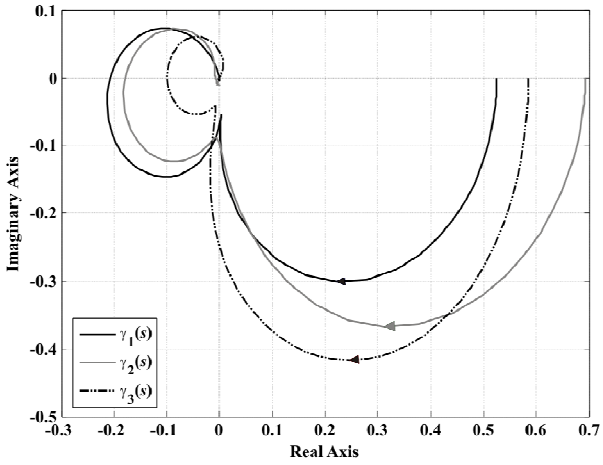

Figure 4.18. Robustness assessment of $\gamma_i(s)$. Nyquist diagrams

Table 4.4. Structural and stability robustness of the channels and control system.
Weak transmission system

Measure	$C_1(s)$	$k_{11}g_{11}(s)$	$\gamma_1(s)$	$C_2(s)$	$k_{22}g_{22}(s)$	$\gamma_2(s)$	$C_3(s)$	$k_{33}g_{33}(s)$	$\gamma_3(s)$
Bandwidth (*rad/s*)	0.156	0.228	—	0.443	0.529	—	1.1	1.08	—
Gain margin (*dB*)	22	23.5	5.597	∞	∞	3.198	∞	∞	4.657
Phase margin (*deg*)	94.2	71.8	∞	99.9	69.2	∞	91.1	80.9	∞

From this set of results it can be seen that the overall performance of the control system may be made adequate by just reducing the bandwidth of the channels. The trade-off is that the response of the control system becomes slower. In fact, the robustness measures are adequate, as it can be seen in Table 4.4. However, it is noticed that the Nyquist plots of MSFs $\gamma_i(s)$ start closer to (1,0) when compared to the case of strong transmission systems – featuring a decrease in structural robustness.

4.2.4. SVC influence on the system

4.2.4.1. Study 1. Strong transmission system

The control system characteristics are investigated to show the influence that the SVC exerts on the system. The SVC is used to increase the voltage at the mid-point of the tie-line, enhancing voltage regulation while keeping constant active power, as it can be seen in Table 4.1. Figure 4.19 shows the relevant MSFs with and with no SVC.

MSF $\Gamma_2(s)$ (considering transfer function matrix $\mathbf{G}_{312}$) provides the measure of coupling between channels of the synchronous generator $C_1(s)$ –speed– and $C_2(s)$ –voltage– in Multiple Channel $\mathbf{M}_{12}(s)$ when the SVC is in place. On the other hand, $\gamma_a(s)$ gives the coupling measure for the synchronous generator when no SVC is considered. From Figure 4.19 it can be seen that both $\Gamma_2(s)$ and $\gamma_a(s)$ have similar frequency responses. The main difference takes place at low frequencies: when the SVC is added to the system, the speed and voltage channels are slightly more coupled, although the coupling remains below –10 *dB* for both cases. However, the dynamical structure of the system is preserved.

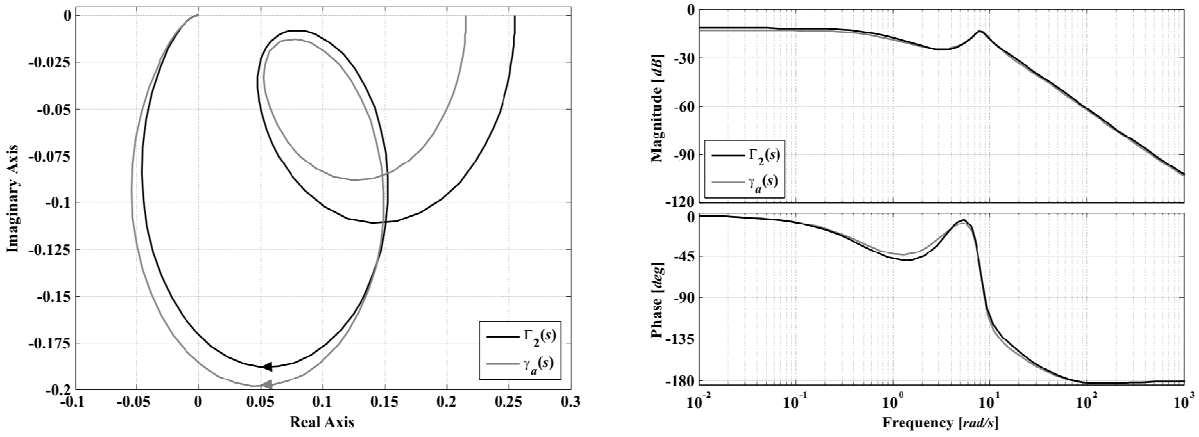

(*a*) (*b*)

Figure 4.19. Assessment of $\gamma_a(s)$ vs $\Gamma_2(s)$ (considering $\mathbf{G}_{312}$). (*a*) Nyquist plot; (*b*) Bode plot

The performance of the synchronous generator is compared to that obtained for the system with SVC. A controller for the 2×2 system with no SVC channel is

$$\begin{aligned}\mathbf{K}_{1a}(s) &= \begin{bmatrix} k_{11}(s) & 0 \\ 0 & k_{22}(s) \end{bmatrix} \\ &= \operatorname{diag}\left[\frac{5.75\left(s^2 + 2.472s + 60.43\right)}{s^2(s+5)}, \quad \frac{14(s+0.43)}{s} \right]\end{aligned} \tag{4.22}$$

Notice that controller (4.22) is exactly the same as controller (4.20) without the SVC voltage controller $k_{33}(s)$. Figures 4.20–4.23 show the performance of the closed-loop control system (terminal voltage and speed channels) and robustness assessment with and with no SVC. Information associated to these results is presented in Table 4.5.

From these results, it can be seen that the speed channel performance ($C_1(s)$) and its associated stability and structural robustness measures are quite similar regardless of whether or not an SVC is used. This can be further examined in Table 4.5. However, the voltage channel ($C_2(s)$) has a reduction of bandwidth if the SVC is used. Structural robustness decreases since $\gamma_2(s)$ starts closer to the point (1,0) and has an overall higher magnitude than $\gamma_a(s)h_1(s)$.

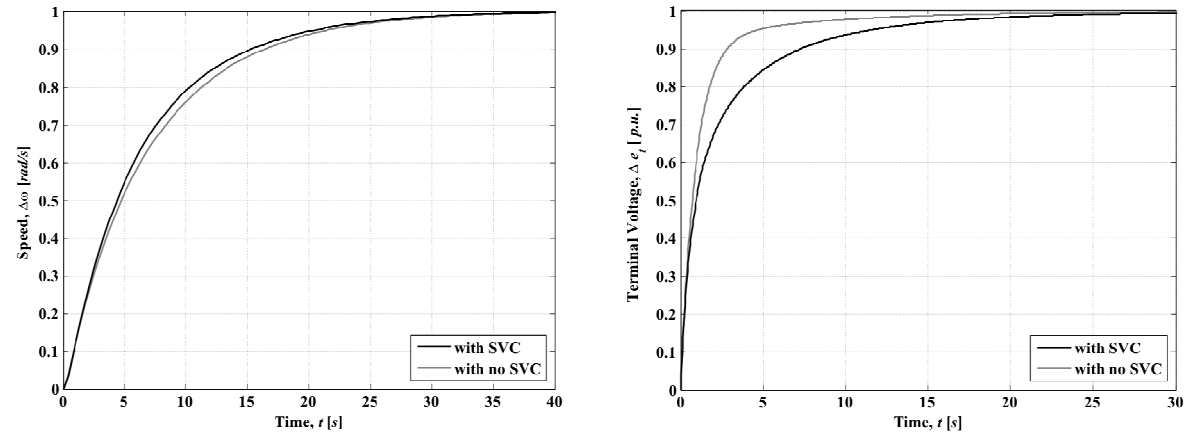

(*a*) (*b*)

Figure 4.20. Step response with and with no SVC: (*a*) Channel 1 ($T_{c1}(s)$); (*b*) Channel 2 ($T_{c2}(s)$)

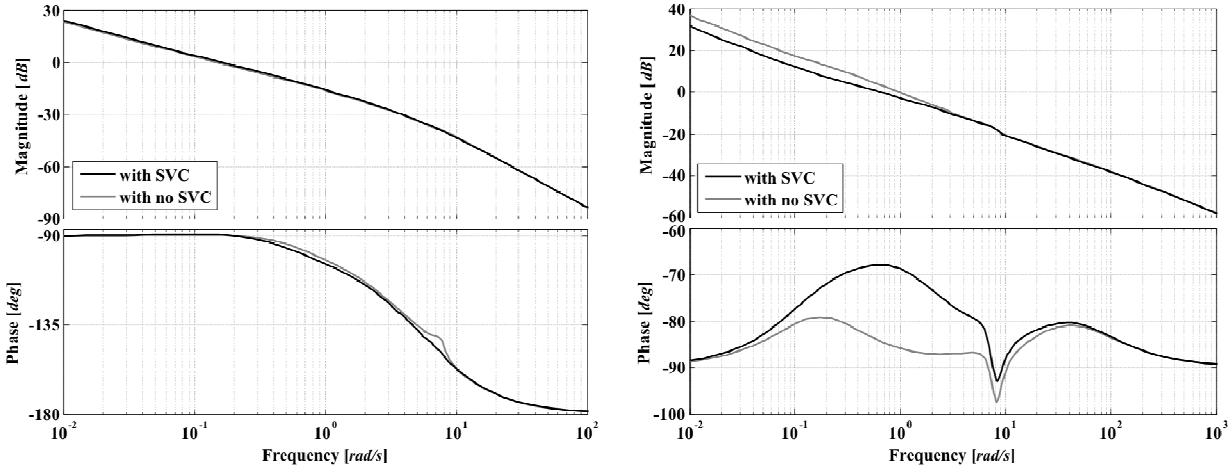

(*a*) (*b*)

Figure 4.21. Bode diagrams with and with no SVC: (*a*) Channel 1 ($C_1(s)$); (*b*) Channel 2 ($C_2(s)$)

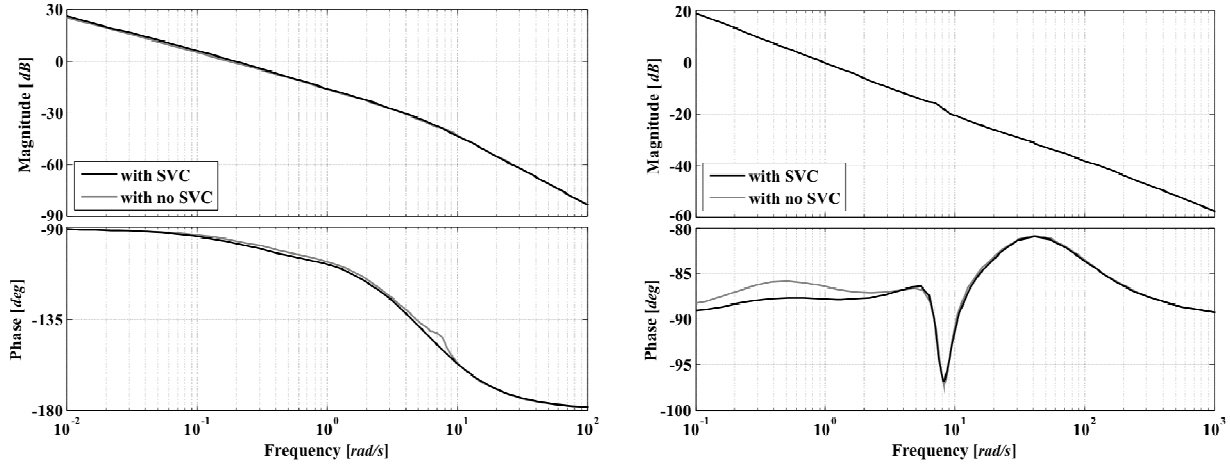

(*a*) (*b*)

Figure 4.22. Robustness assessment. Bode diagrams with and with no SVC: (*a*) $k_{11}g_{11}(s)$; (*b*) $k_{22}g_{22}(s)$

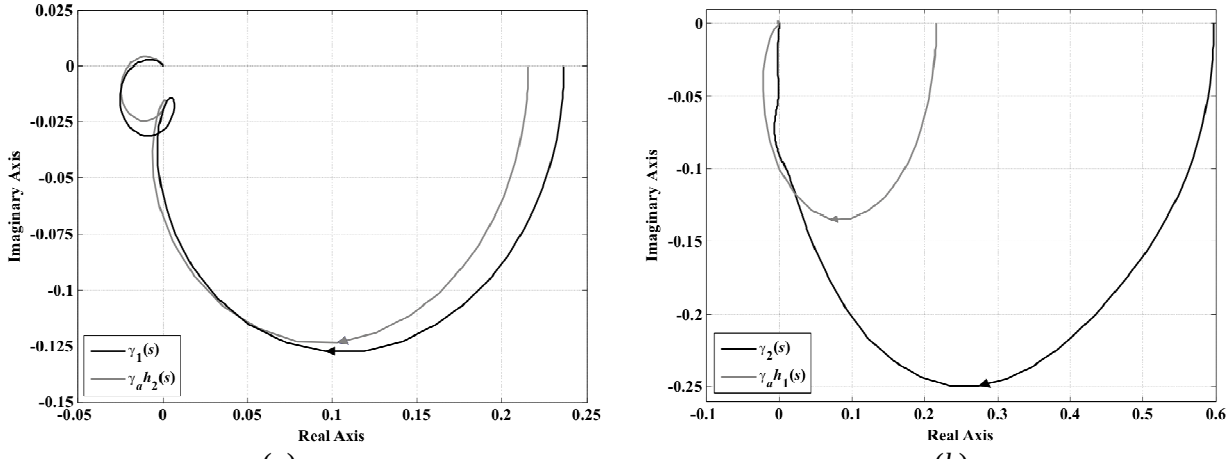

(*a*) (*b*)

Figure 4.23. Robustness assessment. Nyquist diagram of: (*a*) $\gamma_a h_2(s)$ vs $\gamma_1(s)$; (*b*) $\gamma_a h_1(s)$ vs $\gamma_2(s)$

The use of SVCs in cases of strong connections or short electrical distances is not usual practice. Although the performance of the system is not much affected by its inclusion in such cases, the results reveal that a better performance is achieved by using none.

Table 4.5. Structural and stability robustness of the channels and control system with and with no SVC. Strong transmission system

Measure	$C_1(s)$		$k_{11}g_{11}(s)$		$\gamma_1(s)$ / $\gamma_a h_2(s)$		$C_2(s)$		$k_{22}g_{22}(s)$		$\gamma_2(s)$ / $\gamma_a h_1(s)$	
	SVC	w/o	SVC	w/o	SVC	w/o	SVC	w/o	SVC	w/o	SVC	w/o
Bandwidth (*rad/s*)	0.23	0.21	0.26	0.245	—	—	1.06	1.4	1.38	1.39	—	—
Gain margin (*dB*)	∞	∞	∞	∞	12.5	13.3	∞	∞	∞	∞	4.48	13.3
Phase margin (*deg*)	90.8	90.4	82.8	84.5	∞	∞	112	94.2	92.2	93.6	∞	∞

4.2.4.2. Study 2. Weak transmission system

The control system characteristics are investigated to show the influence that the SVC exerts on weak connections. The SVC is used to increase the voltage at mid-tie-line point, enhancing voltage regulation, as shown in Table 4.2. Notice that the active power flow remains the same for both cases, the system with SVC and with no SVC. The reactive power injected to the infinite bus increases from a previous value of 0 *p.u.* to 0.212 *p.u.*

Figure 4.24 shows the MSFs of the system with and with no SVC. It can be seen that both $\Gamma_2(s)$ and $\gamma_a(s)$ have a rather similar frequency response. However, there is a higher coupling whenever the SVC is not used, as evidenced by the larger magnitude (above 0 *dB*) around the frequencies of the switch-back characteristic.

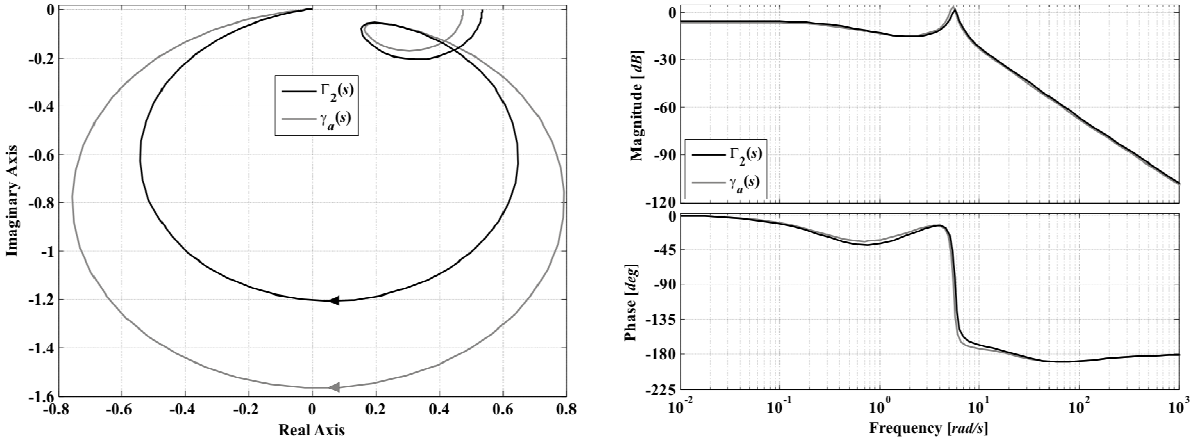

(*a*) (*b*)

Figure 4.24. Assessment of $\gamma_a(s)$ vs $\Gamma_2(s)$ (considering $\mathbf{G}_{312}$). (*a*) Nyquist plot; (*b*) Bode plot

The performance of the synchronous generator is assessed when a SVC forms part of the transmission system and with no SVC, and comparisons are drawn. Controller (4.21) for the 2×2 system with no SVC channel is given by

$$\begin{aligned}\mathbf{K}_{2a}(s) &= \begin{bmatrix} k_{11}(s) & 0 \\ 0 & k_{22}(s) \end{bmatrix} \\ &= \operatorname{diag}\left[\frac{2.1\left(s^2+2.472s+60.43\right)}{s^2(s+5)}, \quad \frac{2.15(s+0.43)}{s} \right]\end{aligned} \tag{4.23}$$

Figures 4.25–4.28 show the performance of the closed-loop control system (terminal voltage and speed channels) and robustness assessment with and with no SVC. Information associated to these results is summarised in Table 4.6.

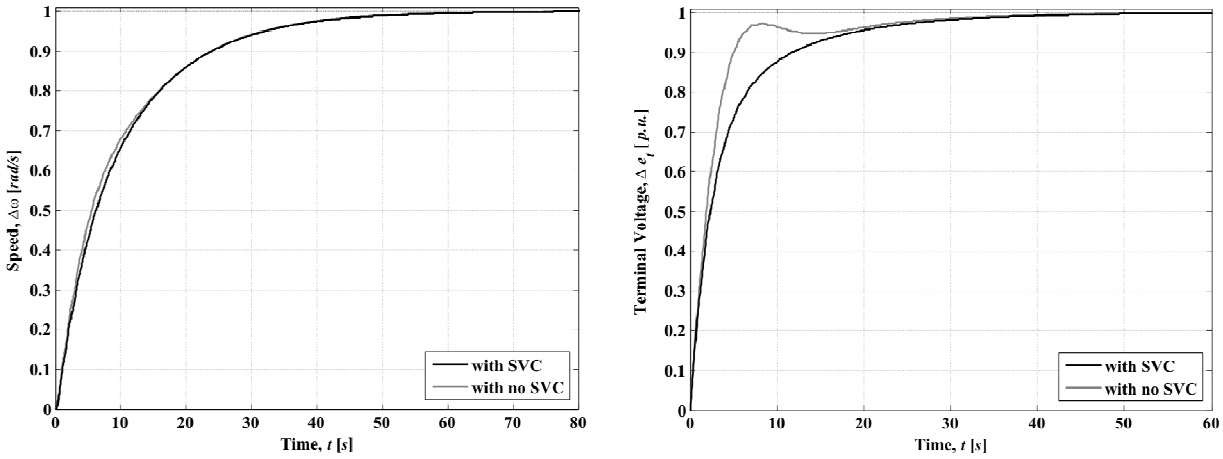

(*a*) (*b*)

Figure 4.25. Step response with and with no SVC: (*a*) Channel 1 ($T_{c1}(s)$); (*b*) Channel 2 ($T_{c2}(s)$)

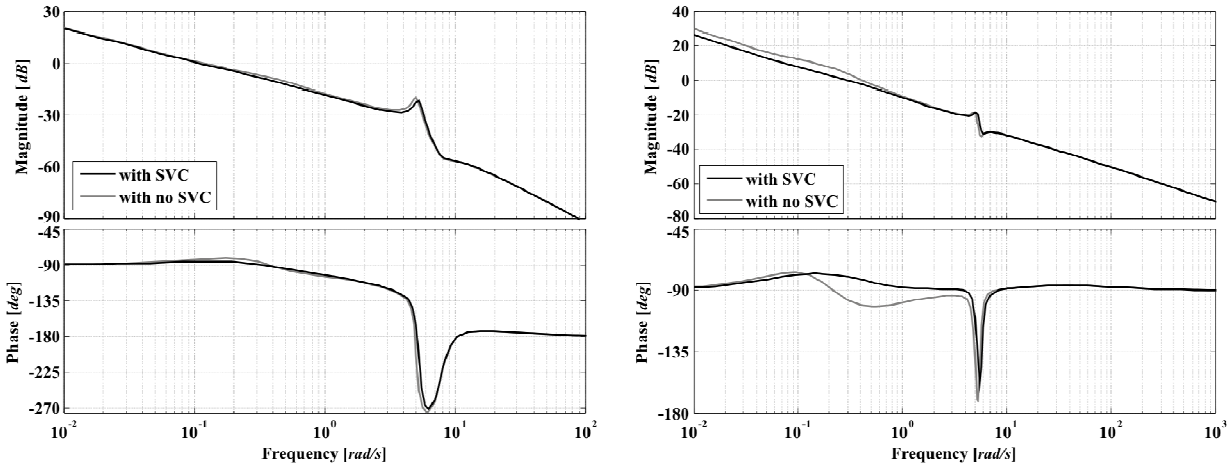

(*a*) (*b*)

Figure 4.26. Bode diagrams with and with no SVC: (*a*) Channel 1 ($C_1(s)$); (*b*) Channel 2 ($C_2(s)$)

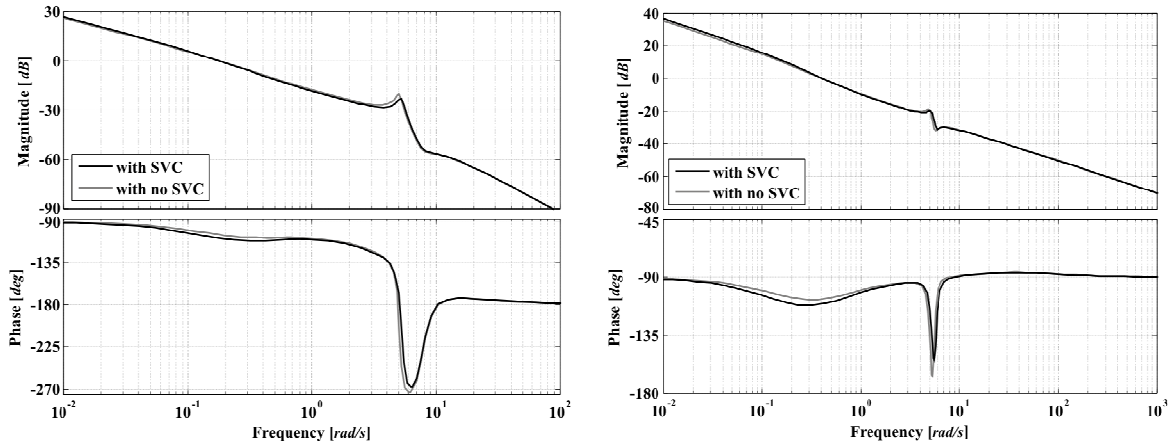

(*a*) (*b*)

Figure 4.27. Robustness assessment. Bode diagrams with and with no SVC: (*a*) $k_{11}g_{11}(s)$; (*b*) $k_{22}g_{22}(s)$

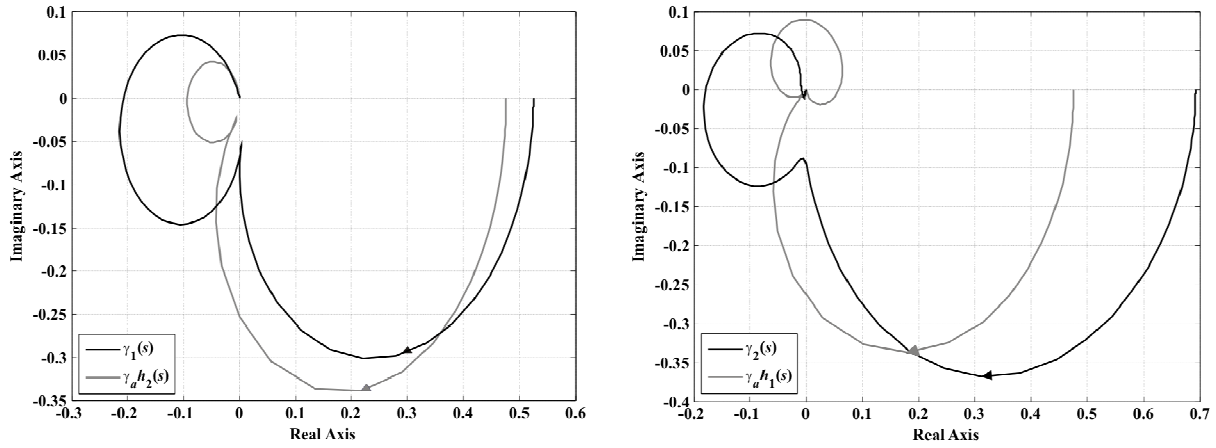

(*a*) (*b*)

Figure 4.28. Robustness assessment. Nyquist diagram of: (*a*) $\gamma_a h_2(s)$ vs $\gamma_1(s)$; (*b*) $\gamma_a h_1(s)$ vs $\gamma_2(s)$

Table 4.6. Structural and stability robustness of the channels and control system with and with no SVC. Weak transmission system

Measure	$C_1(s)$		$k_{11}g_{11}(s)$		$\gamma_1(s)$ / $\gamma_a h_2(s)$		$C_2(s)$		$k_{22}g_{22}(s)$		$\gamma_2(s)$ / $\gamma_a h_1(s)$	
	SVC	w/o	SVC	w/o	SVC	w/o	SVC	w/o	SVC	w/o	SVC	w/o
Bandwidth (*rad/s*)	0.156	0.171	0.23	0.23	—	—	0.443	0.544	0.53	0.525	—	—
Gain margin (*dB*)	22	20	23.5	20.8	5.597	6.45	∞	∞	∞	∞	3.198	6.45
Phase margin (*deg*)	94.2	97.4	71.8	75.7	∞	∞	99.9	78.8	69.2	72.9	∞	∞

It can be seen from these results that the performance of the overall system is quite similar in the case when the SVC is connected at the mid-point of a weak connection and when no SVC is used. The main differences can be noticed in the terminal voltage channel $C_2(s)$ and in the subsystem $k_{22}g_{22}(s)$. Figure 4.26(*b*) shows that there is a bandwidth reduction in $C_2(s)$ when using an SVC; however, it could be increased by adjusting the gain of the controller $k_{22}(s)$. The overshoot present in the step response of the terminal voltage with no SVC (Figure 4.25(*b*)) is a consequence of the loss of phase around the cut-off frequency, as it can be seen in Bode plot in Figure 4.26(*b*). Moreover, the use of the SVC slightly reduces the switch-back characteristic of $C_2(s)$ and of the subsystem $k_{22}g_{22}(s)$. As evidenced by Figure 4.28 and Table 4.6, the structural robustness measures when an SVC is in place are lower than when no SVC is used, since the Nyquist plots of $\gamma_i(s)$ start closer to (1,0) than those of $\gamma_a h_i(s)$.

4.2.5. SVC including damping control loop

The primary application of the SVC is the provision of dynamic reactive power support to enable an effective voltage regulation. From the results presented in Sections 4.2.2 and 4.2.3, it is clear that the SCV voltage control loop does little to dent the problematic switch-back characteristic. Moreover, in the case of a weak transmission system, a bandwidth reduction in the terminal voltage channel becomes necessary in order to avoid the frequency range where the switch-back lies. For the SVC to overcome the switch-back characteristic, a damping control loop is required [16–22].

Sub-synchronous oscillations (SSR) in power systems can be sustained and amplified due to the interaction between the electrical power system and the generator mechanical system. For instance, series compensation of transmission lines, HVDC transmission systems and DC converter loads are reported to be sources of adverse interactions [19]. It has also been reported that an adequate damping control loop in the form of a *Power System Stabiliser* (PSS) or an auxiliary damping signal in a variety of power electronic controllers can alleviate such undesirable phenomena. A case point is the damping control loop of an SVC.

The mathematical model of the synchronous machine – SVC system including a damping control loop corresponds to a 3×3 system. Figure 4.29 shows a compact block diagram representation of a synchronous generator – SVC connected to an infinite bus via a tie-line reactance, with the damping control loop [4,18]. The loop acts as a post-compensator of the speed output on the SVC voltage channel. The resulting signal, $\Delta V_{add}(s)$, is added on to the SVC voltage control channel reference. An alternative configuration is to add the auxiliary signal on to the resulting SVC voltage control signal $\Delta\alpha(s)$ [23,24]. The elements in the SVC damping control block are investigated below.

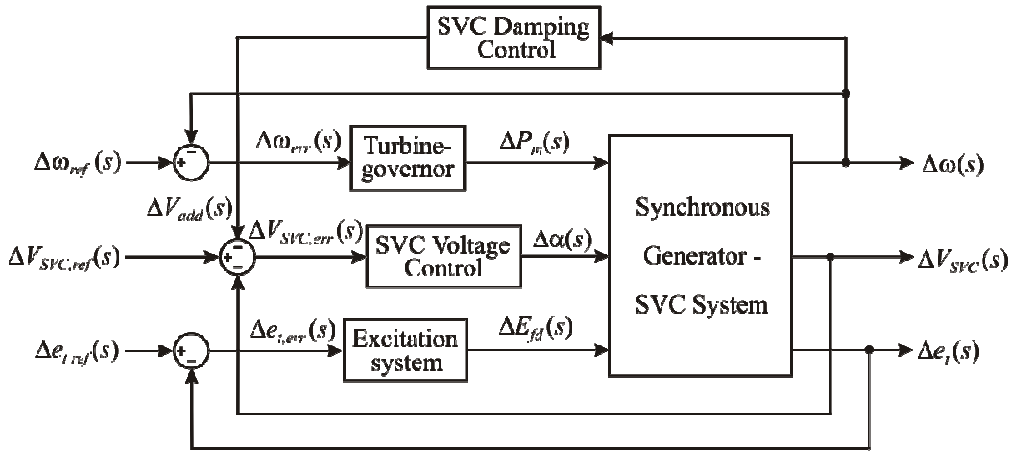

Figure 4.29. Synchronous generator – SVC system with damping capabilities for control system analysis

4.2.5.1. Damping control loop modelling

The transfer function matrix representation of the synchronous generator – SVC system is given in (4.8) and (4.9), with the individual elements of **G**(*s*) given in Appendix D. From Figure 4.29, it is observed that the system including the damping control loop assumes the post-compensated form

$$\begin{aligned}\mathbf{G}'(s) &= \mathbf{P}_{SVC}(s)\mathbf{G}(s) \\ &= \begin{bmatrix} 1 & 0 & 0 \\ 0 & 1 & 0 \\ -K_D(s) & 0 & 1 \end{bmatrix} \begin{bmatrix} g_{11}(s) & g_{12}(s) & g_{13}(s) \\ g_{21}(s) & g_{22}(s) & g_{23}(s) \\ g_{31}(s) & g_{32}(s) & g_{33}(s) \end{bmatrix}\end{aligned} \tag{4.24}$$

or

$$\mathbf{G}'(s) = \begin{bmatrix} g_{11}(s) & g_{12}(s) & g_{13}(s) \\ g_{21}(s) & g_{22}(s) & g_{23}(s) \\ g'_{31}(s) & g'_{32}(s) & g'_{33}(s) \end{bmatrix} \tag{4.25}$$

where

$$\begin{aligned} g'_{31}(s) &= g_{31}(s) - K_D(s)g_{11}(s) \\ g'_{32}(s) &= g_{32}(s) - K_D(s)g_{12}(s) \\ g'_{33}(s) &= g_{33}(s) - K_D(s)g_{13}(s) \end{aligned} \tag{4.26}$$

In the non-diagonal, post-compensator matrix $\mathbf{P}_{SVC}(s)$ in (4.24), the cross-coupling element $K_D(s)$ denotes the transfer function of the damping controller, given by

$$K_D(s) = k_d \cdot \frac{s\tau_w}{1+s\tau_w} \cdot \frac{1+s\tau_1}{1+s\tau_2} \tag{4.27}$$

where $s\tau_w/(1 + s\tau_w)$ denotes a wash-out filter, $(1 + s\tau_1)/(1 + s\tau_2)$ denotes a phase lead/lag compensator, and k_d denotes a stabiliser gain. The damping controller $K_D(s)$ has been reported in the open literature in various forms; for instance, in [22] a wash-out filter is used to provide additional damping, whereas in [23] the controller is assumed to be simply a pure gain. Controller (4.27) is a simplified version of the one proposed in [24], where two lead/lag compensators are used in addition to the stabiliser gain and the wash-out filter.

4.2.5.2. Effect of the damping control loop in a weak transmission system

Consider the synchronous generator – SVC system connected to an infinite bus via a weak tie-line as in previous sections. The operating condition is provided in Table 4.2, where X_t = 0.8 *p.u.* The following damping controller

$$K_D(s) = \frac{106.25s(s+0.2353)}{(s+2)(s+0.1)} \tag{4.28}$$

is employed, where k_d = 12.5, τ_w = 10 *s*, τ_1 = 4.25 *s* and τ_2 = 0.5 *s*.

In (4.25), the damping controller transfer function $K_D(s)$ multiplies the benign subsystem transfer functions $g_{11}(s)$, $g_{12}(s)$ and $g_{13}(s)$ which contain no lightly damped LHP zeros, and modifies the SVC's subsystem transfer functions $g_{31}(s)$, $g_{32}(s)$ and $g_{33}(s)$ to $(g_{31} - K_D\, g_{11})$, $(g_{32} - K_D\, g_{12})$ and $(g_{33} - K_D\, g_{13})$, respectively. Figure 4.30(*a*)–(*c*) shows the frequency response of the original transfer functions $g_{3i}(s)$ and the amended $g'_{3i}(s)$ (i = 1,2,3) for a weak transmission system when using controller (4.28). The Bode plot of transfer functions $g_{22}(s)$, $g_{23}(s)$, $g_{32}(s)$ and $g_{33}(s)$, all featuring the switch-back characteristic to some extent, are shown in Figure 4.30(*d*).

By comparing the frequency responses of $(g_{32} - K_D\, g_{12})$ with that of g_{32}, and $(g_{33} - K_D\, g_{13})$ with that of g_{33} in Figures 4.30(*b*) and 4.30(*c*), respectively, it is noticed that the effect of the inverted notch characteristic $K_D(s)$ of the damping controller in (4.27) multiplied by the benign system dynamics $g_{12}(s)$ and $g_{13}(s)$ dominates the problematic switch-back characteristic of elements $g_{32}(s)$ and $g_{33}(s)$. As observed in Figure 4.30(*d*), the switch-back characteristics of the transfer functions $g_{22}(s)$ and $g_{32}(s)$ (that is, those

subsystems associated to input ΔE_{fd}) are more pronounced than those of transfer functions $g_{23}(s)$ and $g_{33}(s)$ (subsystems associated to input $\Delta\alpha$) as their lightly damped pole-zero pairs are closer.

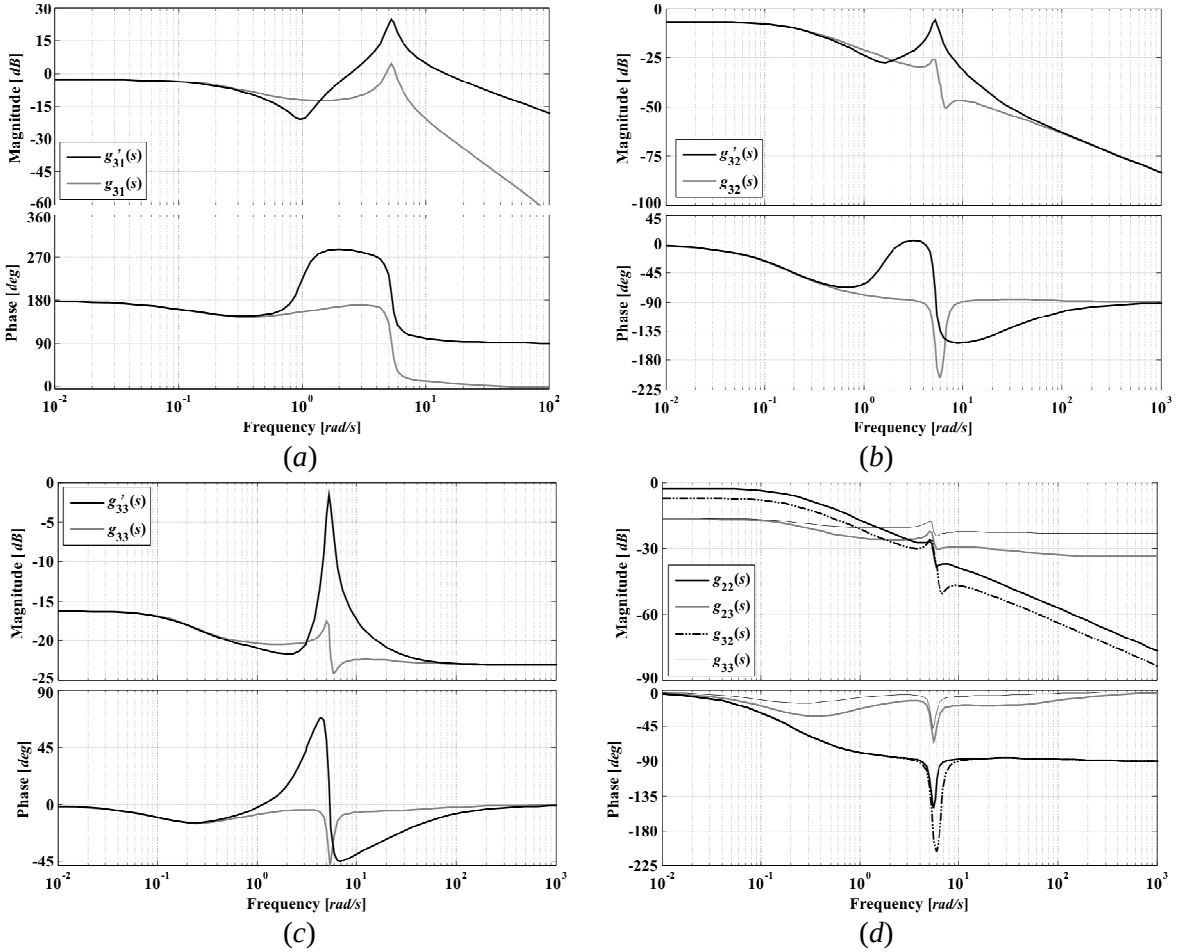

Figure 4.30. Bode diagrams of non-compensated and amended subsystems: (*a*) g_{31} vs $(g_{31} - K_D g_{11})$; (*b*) g_{32} vs $(g_{32} - K_D g_{12})$; (*c*) g_{33} vs $(g_{33} - K_D g_{13})$. (*d*) Bode diagrams of g_{22}, g_{23}, g_{32} vs g_{33}.

Figures 4.31–4.36 show the MSFs of the amended transfer function matrix (4.25) when using a damping controller (4.28) and the MSFs of the SVC system with no damping control loop.

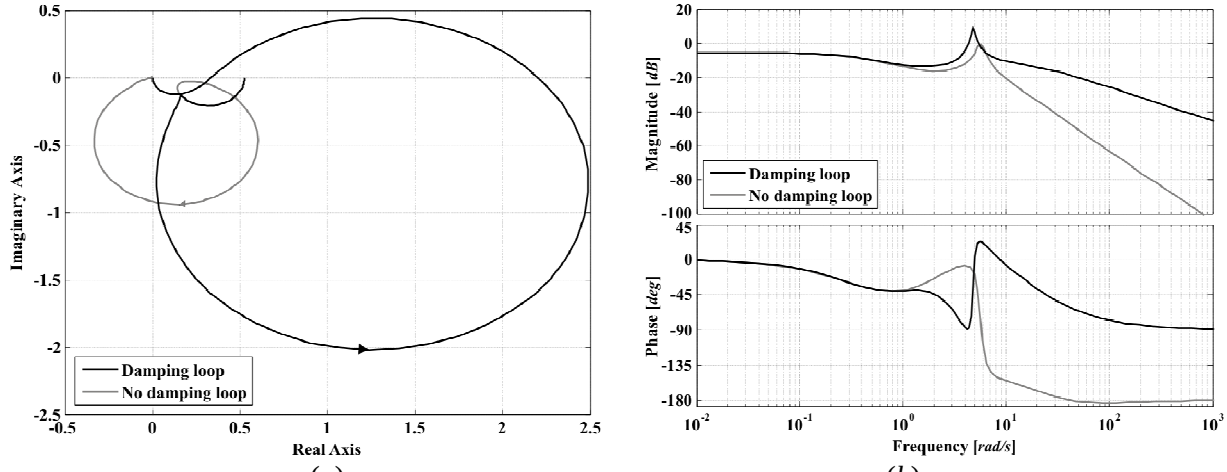

Figure 4.31. Assessment of $\Gamma_1(s)$ (transfer function matrix $\mathbf{G}_{123}$) for an SVC-upgraded system with and with no damping control loop: (*a*) Nyquist plot; (*b*) Bode plot

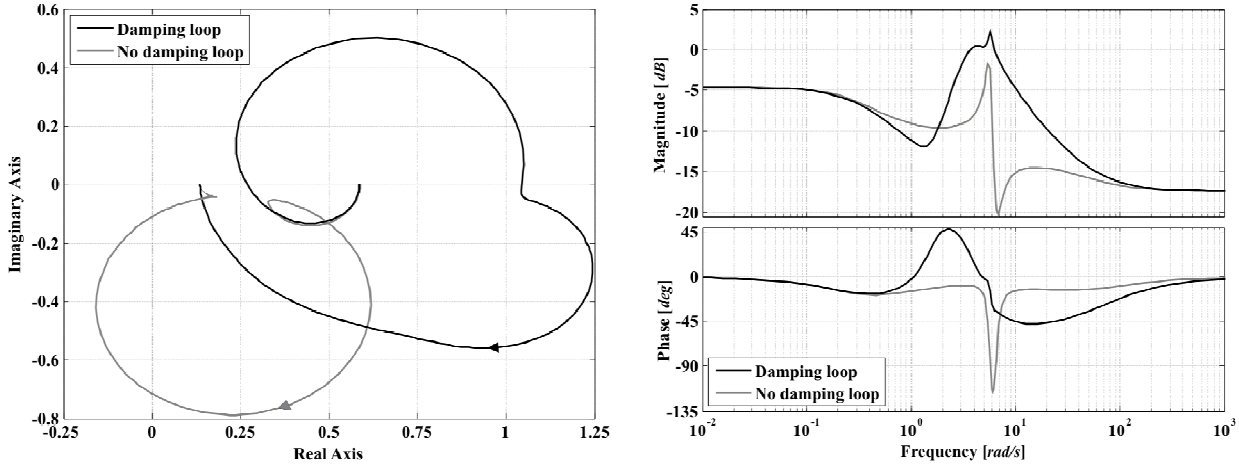

(*a*) (*b*)

Figure 4.32. Assessment of $\Gamma_2(s)$ (transfer function matrix $\mathbf{G}_{123}$) for an SVC-upgraded system with and with no damping control loop: (*a*) Nyquist plot; (*b*) Bode plot

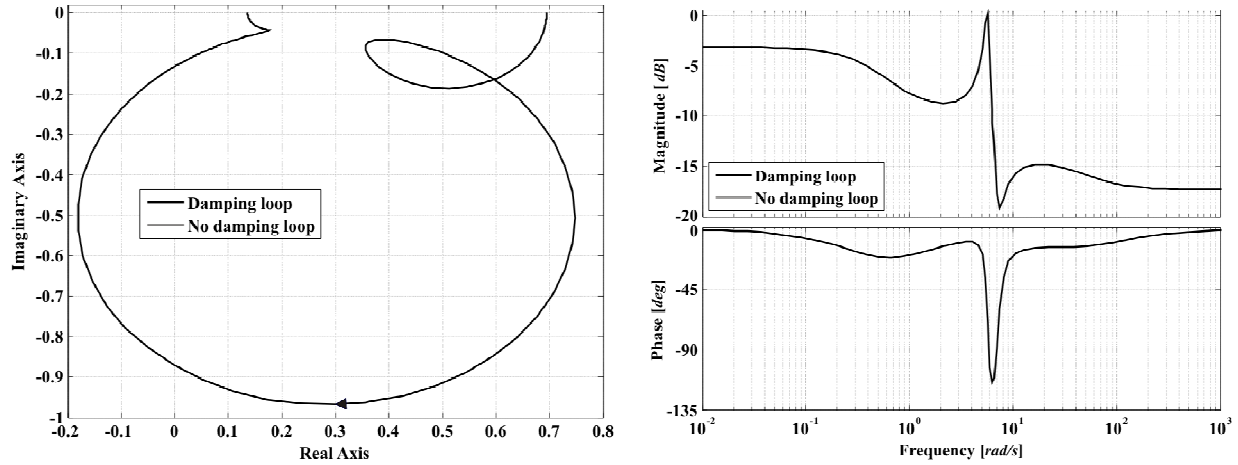

(*a*) (*b*)

Figure 4.33. Assessment of $\Gamma_1(s)$ (transfer function matrix $\mathbf{G}_{213}$) for an SVC-upgraded system with and with no damping control loop: (*a*) Nyquist plot; (*b*) Bode plot

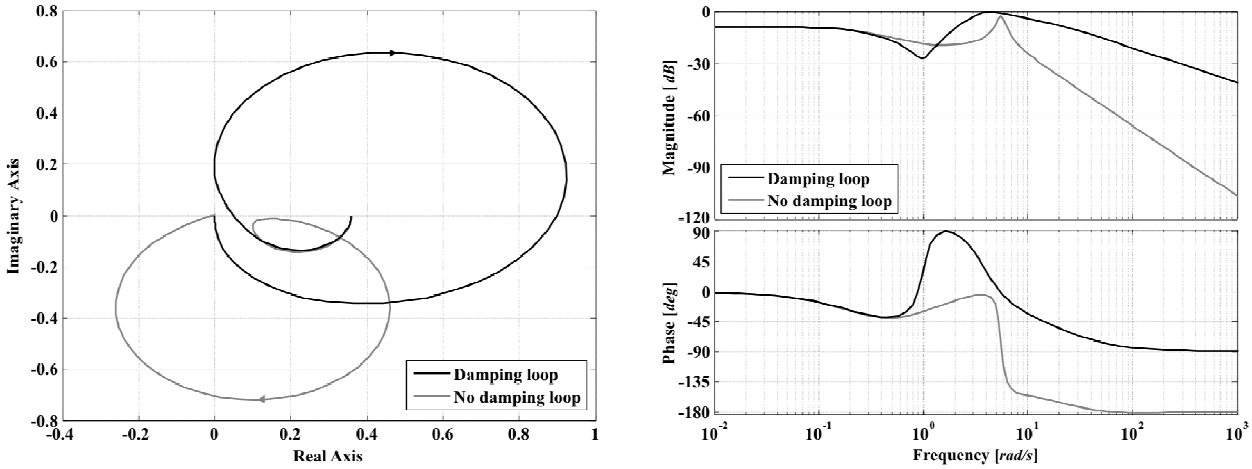

(*a*) (*b*)

Figure 4.34. Assessment of $\Gamma_2(s)$ (transfer function matrix $\mathbf{G}_{213}$) for an SVC-upgraded system with and with no damping control loop: (*a*) Nyquist plot; (*b*) Bode plot

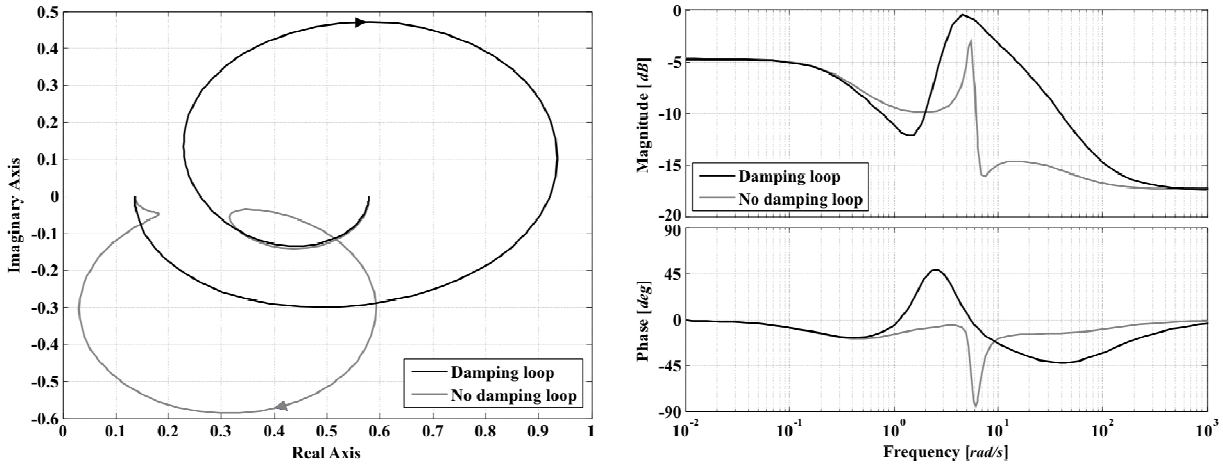

(*a*) (*b*)

Figure 4.35. Assessment of $\Gamma_1(s)$ (transfer function matrix $\mathbf{G}_{312}$) for an SVC-upgraded system with and with no damping control loop: (*a*) Nyquist plot; (*b*) Bode plot

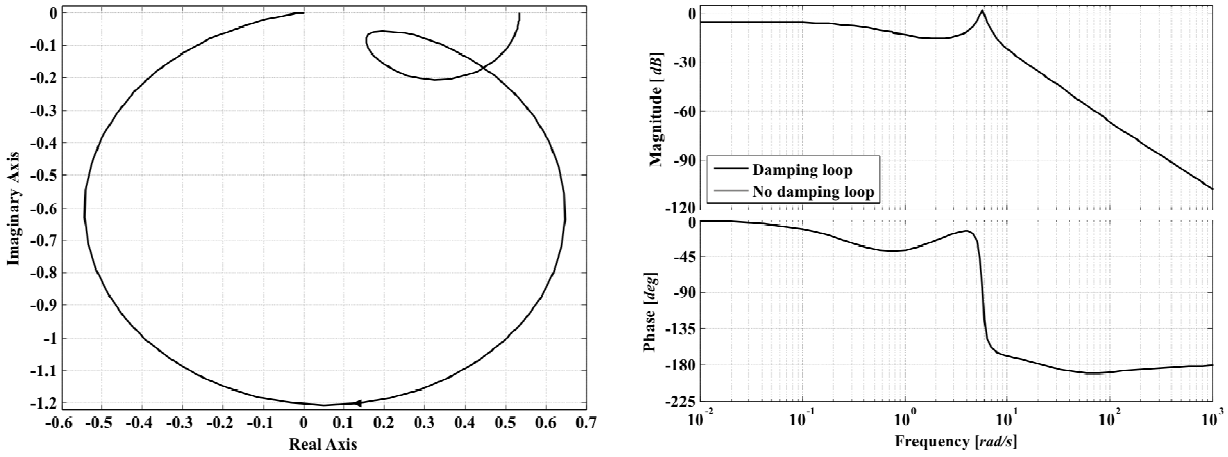

(*a*) (*b*)

Figure 4.36. Assessment of $\Gamma_2(s)$ (transfer function matrix $\mathbf{G}_{312}$) for an SVC-upgraded system with and with no damping control loop: (*a*) Nyquist plot; (*b*) Bode plot

From the results in these figures, it is noticed that the damping control loop is particularly effective at around the frequencies where the switch-back characteristic is present. The following conclusions can be made:

- With the damping loop, the Multiple Channel $\mathbf{M}_{23}(s)$ couples considerably (above 0 *dB*) with the Individual Channel $C_1(s)$ at frequencies around the switch-back, as evidenced from the plots of MSF $\Gamma_1(s)$ associated to transfer function matrix $\mathbf{G}_{123}$ in Figure 4.31. However, as seen from MSF $\Gamma_2(s)$ in Figure 4.32, the damping is provided in such a way that the coupling between Individual Channels $C_2(s)$ and $C_3(s)$, although it increases around the problematic frequency range, is smoother – that is, the inverse notch characteristic provided by the damping controller loop dominates the switch-back.

- The Multiple Channel $\mathbf{M}_{13}(s)$ is slightly coupled (near 0 *dB* at frequencies around the switch-back) with the Individual Channel $C_2(s)$ regardless of whether or not a damping control loop is used, as shown by the MSF $\Gamma_1(s)$ of transfer function matrix $\mathbf{G}_{213}$ in Figure 4.33. The Individual Channels

$C_1(s)$ and $C_3(s)$ couple considerably at frequencies around the switch-back characteristic when the damping loop is included, as evidenced by the MSF $\Gamma_2(s)$ in Figure 4.34.

- The Multiple Channel $\mathbf{M}_{12}(s)$ couples with the Individual Channel $C_3(s)$ at frequencies around the switch-back characteristic when employing the damping control loop, as shown by the MSF $\Gamma_1(s)$ of transfer function matrix $\mathbf{G}_{312}$ in Figure 4.35; however, the switch-back characteristic itself is dominated by the inverse notch characteristic of the damping controller. From the MSF $\Gamma_2(s)$ in Figure 4.36, it is noticed that the coupling between Individual Channels $C_1(s)$ and $C_2(s)$ remains unchanged regardless of whether or not the damping control loop is used.

It is clear from these results that the use of a damping control loop does not reduce the inherent coupling of the system. In fact, it is noticed that the coupling actually tends to increase. However, an immediate benefit brought about by the damping control loop lies in the elimination of the switch-back characteristic. Such an effect is introduced directly by elements associated to $C_3(s)$ – that is, $g_{23}(s)$ and $g_{33}(s)$. Due to the existent coupling between Individual Channels $C_2(s)$ and $C_3(s)$ (terminal voltage and SVC voltage), damping will be indirectly provided to $C_2(s)$ and the switch-back characteristic inherent to the synchronous generator dynamics (caused by the electrical subsystem $g_{22}(s)$) can be substantially reduced. Moreover, the synchronous generator internal coupling, that is, the coupling between $C_1(s)$ and $C_2(s)$, will remain unchanged even with the use of a damping control loop since its effect is only present in $C_3(s)$, as it can be seen from (4.24) and (4.25). These conclusions are reached only through the analysis of the MSFs provided by the ICAD framework.

A less obvious conclusion results from the examination of the block diagram in Figure 4.29 and $K_D(s)$ of the SVC damping controller (4.28). It is noticed that an additional feedback loop is introduced into the system. The main effects of this loop are to reduce the relative degree of $g'_{31}(s)$ at about 1–10 *rad/s* (shown in Figure 4.30(*a*)), while preserving the relative degree of $g'_{32}(s)$ and $g'_{33}(s)$ (Figures 4.30(*b*) and 4.30(*c*), respectively) and the negative gain of $g_{31}(s)$ in $g'_{31}(s)$ (shown in Figure 4.30(*a*)). Moreover, it can be seen that although the internal coupling of the synchronous machine does not change (Figure 4.36), the inverse notch characteristic featured by the SVC damping controller dominates the switch-back characteristic of the terminal voltage channel whenever $C_2(s)$ and $C_3(s)$ interact, as it can be observed in Figures 4.32 and 4.35. In particular, by working on an amended SVC subsystem ($g_{33} - K_D g_{13}$) instead of the original subsystem $g_{33}(s)$, the damping control loop allows the use of an arbitrary high bandwidth in the terminal voltage and the SVC voltage control channels without the presence of the switch-back characteristic.

4.2.5.3. Control system design for a weak transmission system

Following the analysis of the MSFs and the amended transfer function matrix (4.25) of the synchronous generator – SVC system with the damping control loop, it is a matter of great interest to assess the impact of the damping controller on the control system. The controller (4.21), designed for the case of a weak transmission system, is used along with the damping controller (4.28). The control system performance and robustness assessment of the system with and with no damping control loop are shown in Figures 4.37–4.40. Relevant information associated to these figures is summarised in Table 4.7.

Figure 4.37 shows the step responses of the control system. It can be seen that the performance of the synchronous machine (*i.e.*, Channels 1 and 2) is not affected by the inclusion of the damping loop. However, it produces an oscillatory response in the SVC voltage channel (Figure 4.37(*c*)), due to an increase in magnitude and a major change in the phase around the cut-off frequency of Channel 3, reflected by Figure 4.38(*c*). It is important to remark that the performance could be improved by increasing the bandwidth of the channel, as it will be shown at a later stage.

Nevertheless, inclusion of the damping control loop brings about major overall benefits to the system as evidenced by the results shown in Figure 4.38. In Figure 4.38(*b*) it is shown that the switch-back characteristic is totally eliminated from the synchronous generator terminal voltage channel. The performance of the speed channel remains unchanged when considering the damping loop, as seen in Figure 4.38(*a*).

The structural robustness of the control system is assessed in Figures 4.39 and 4.40. Figure 4.39 shows the Bode diagrams of the individual channel subsystems $h_i(s)$. Notice that for the case of the open loop subsystems $k_{11}g_{11}(s)$ and $k_{22}g_{22}(s)$ (Figures 4.39(*a*) and (*b*)), the frequency responses remain the same whether or not the damping loop is used. This is consistent with the fact that the damping controller exerts direct influence only in $g_{33}(s)$, as reflected in Figure 4.39(*c*) and consistent with (4.25). From Figure 4.40 it can be seen that the gain margins are preserved regardless of the inclusion of the damping controller: the Nyquist plots of $\gamma_1(s)$ start to the left to (1,0), at exactly the same place, and do not encircle it. However, the phase margin of $\gamma_2(s)$ decreases considerably, as shown by Figure 4.40(*b*). On the other hand, the behaviour of $\gamma_3(s)$ changes little with and with no damping loop, as shown by Figure 4.40(*c*).

Table 4.7. Structural and stability robustness of the channels and control system featuring an SVC with (D) and with no (w/o) damping control loop. Weak transmission system

	$C_1(s)$		$k_{11}g_{11}(s)$		$\gamma_1(s)$		$C_2(s)$		$k_{22}g_{22}(s)$		$\gamma_2(s)$		$C_3(s)$		$k_{33}g_{33}(s)$		$\gamma_3(s)$	
	w/o	D	w/o	D	w/o	D	w/o	D	w/o	D	w/o	D	w/o	D	w/o	D	w/o	D
BW *rad/s*	0.16	0.16	0.23	0.23	—	—	0.44	0.45	0.53	0.53	—	—	1.1	1	1.08	1	—	—
GM *dB*	22	28	23.5	23.5	5.6	5.6	∞	∞	∞	∞	3.2	3.2	∞	∞	∞	∞	4.7	4.7
PM *deg*	94	94	72	72	∞	∞	100	99	69	69	∞	56	91	93	81	70.5	∞	∞

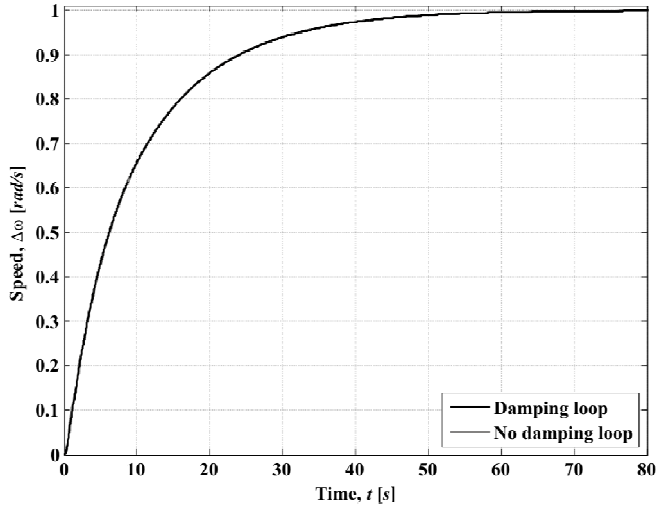

(*a*)

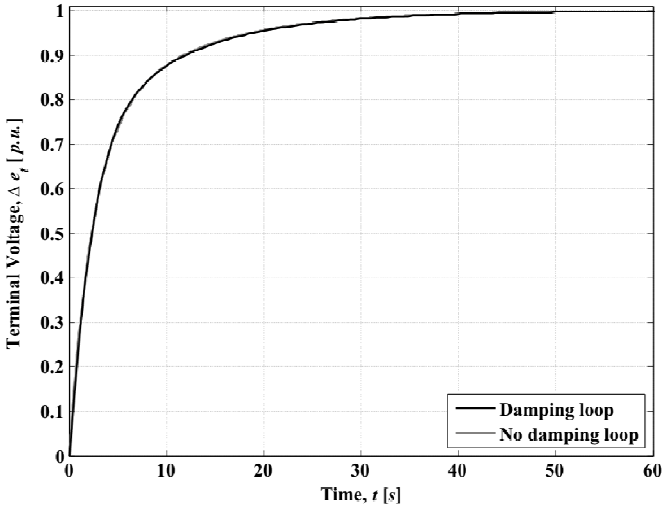

(*b*)

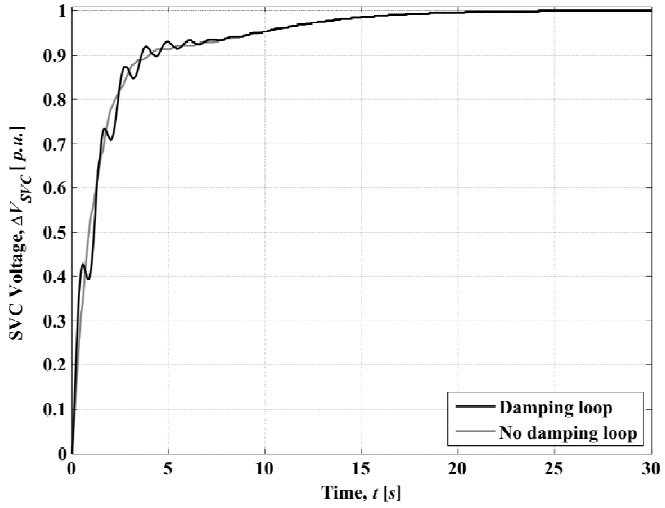

(*c*)

Figure 4.37. Step response with and with no damping control loop: (*a*) Channel 1 ($T_{c1}(s)$); (*b*) Channel 2 ($T_{c2}(s)$); (*c*) Channel 3 ($T_{c3}(s)$)

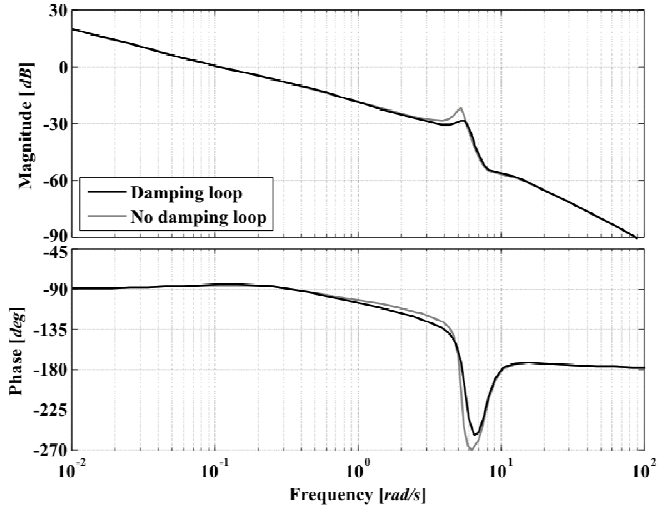

(*a*)

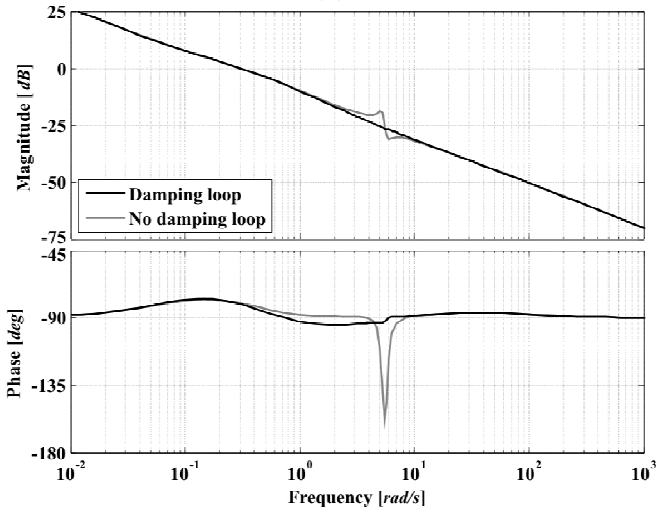

(*b*)

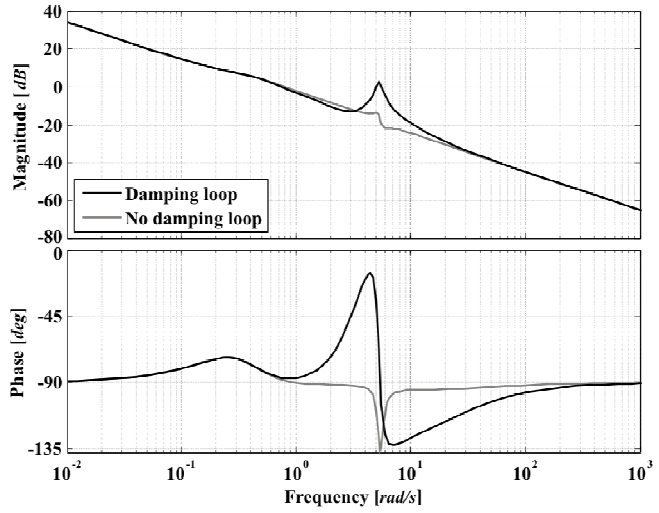

(*c*)

Figure 4.38. Bode diagrams with and with no damping control loop: (*a*) Channel 1 ($C_1(s)$); (*b*) Channel 2 ($C_2(s)$); (*c*) Channel 3 ($C_3(s)$)

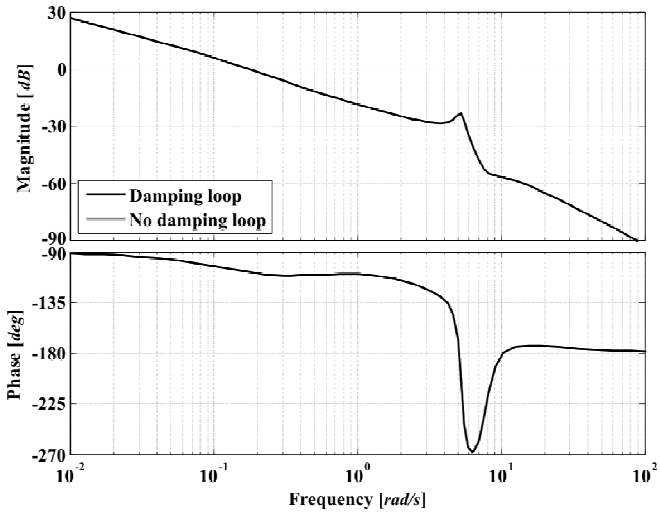

(*a*)

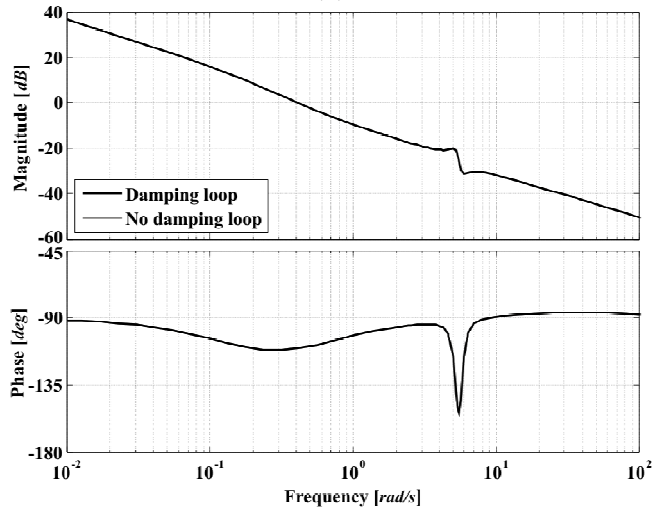

(*b*)

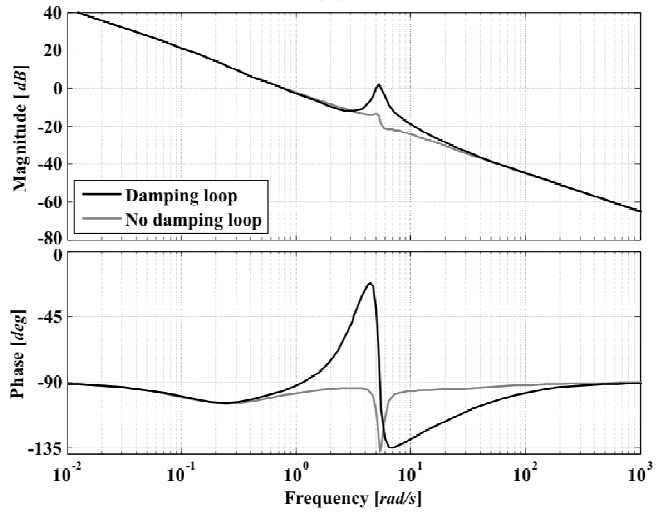

(*c*)

Figure 4.39. Robustness assessment. Bode diagrams with and with no damping control loop: (*a*) $k_{11}g_{11}(s)$; (*b*) $k_{22}g_{22}(s)$; (*c*) $k_{33}g_{33}(s)$

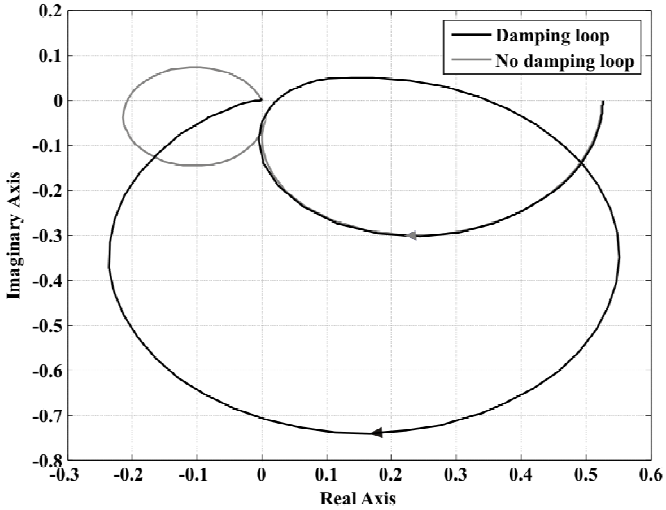

(*a*)

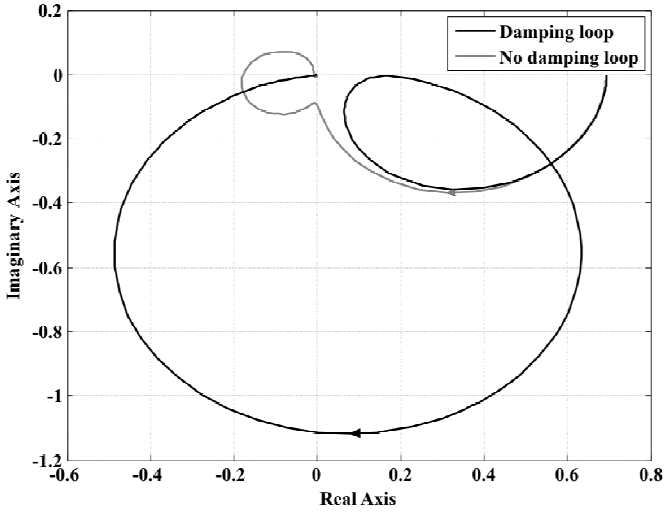

(*b*)

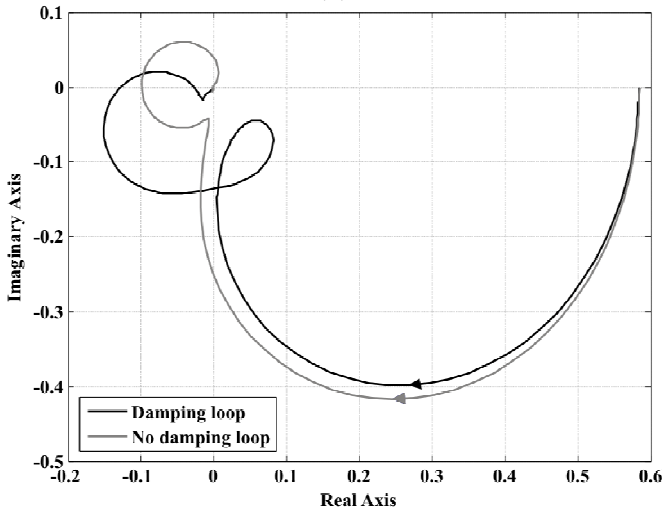

(*c*)

Figure 4.40. Robustness assessment. Nyquist diagrams with and with no damping control loop: (*a*) $\gamma_1(s)$; (*b*) $\gamma_2(s)$; (*c*) $\gamma_3(s)$

It has been reported in [24] that the response of the SVC voltage control loop channel deteriorates when using the damping control loop. In [23], a similar conclusion is reached, where it was found that reinforcement of the SVC voltage control reduces the effectiveness of its damping control. Reference [24] goes further and claims that the SVC voltage and damping controls counteract each other and points out at the limitations of using pure proportional controllers for the voltage control and a damping controller similar to the structure in (4.27) (using an extra lag/lead term). A coordination scheme based on an optimal search algorithm enabled an effective design of both the voltage and the damping controllers.

Alternatively, ICAD may be used to obtain an effective pair of SVC voltage and damping controllers. From the analysis of the MSFs, it was observed that the damping controller (4.27), through the effect of an inverted notch characteristic, provides an effective way of eliminating the switch-back characteristic. In other words, the terminal voltage response is turned off at frequencies of around the switch-back by the post-compensated speed response, which is dominant in that frequency range. It was also anticipated that an amended SVC subsystem, with an arbitrary high bandwidth in the terminal voltage and SVC voltage control channels, would be achievable. To this end, consider controller

$$\begin{aligned}\mathbf{K}_3(s) &= \begin{bmatrix} k_{11}(s) & 0 & 0 \\ 0 & k_{22}(s) & 0 \\ 0 & 0 & k_{33}(s) \end{bmatrix} \\ &= \text{diag}\left[\frac{63(s+3.5)(s^2+s+30)}{s^2(s+6)(s+5)}, \quad \frac{107.5(s+0.43)}{s}, \quad \frac{400}{s} \right]\end{aligned} \tag{4.29}$$

where $k_{33}(s)$ represents the SVC voltage control. A damping controller

$$K_D(s) = \frac{36.6s(s+3.333)}{(s+0.4)(s+0.1)} \tag{4.30}$$

will be used to modify the SVC's transfer functions $g_{3i}(s)$ to $(g_{3i} - K_D g_{1i})$. From (4.29), it can be seen that $k_{22}(s)$ and $k_{33}(s)$ have a similar structure to those in (4.21) except for the gains, which have been upped to achieve higher bandwidths in Channels 2 and 3. Element $k_{11}(s)$ has an extra pole/zero pair, a higher gain and a slightly different complex conjugate zero pair in order to increase the stability margins and bandwidth of Channel 1. Figure 4.41 shows the frequency response of the original transfer functions $g_{3i}(s)$ and the amended $g'_{3i}(s)$ (i = 1,2,3) using (4.30).

By comparing the frequency responses of $(g_{3i} - K_D g_{1i})$ with that of g_{3i} in Figure 4.41, it can be noticed that the effect of the inverted notch characteristic $K_D(s)$ of the damping controller in (4.30) multiplied by the benign system dynamics $g_{1i}(s)$ is not as dominant as the effect achieved with controller (4.28). However, its combination with controller (4.30) will provide a better performance in the SVC voltage channel as the magnitude peak is not so prominent in the amended element $g'_{33}(s)$, as evidenced by Figure 4.41(*c*).

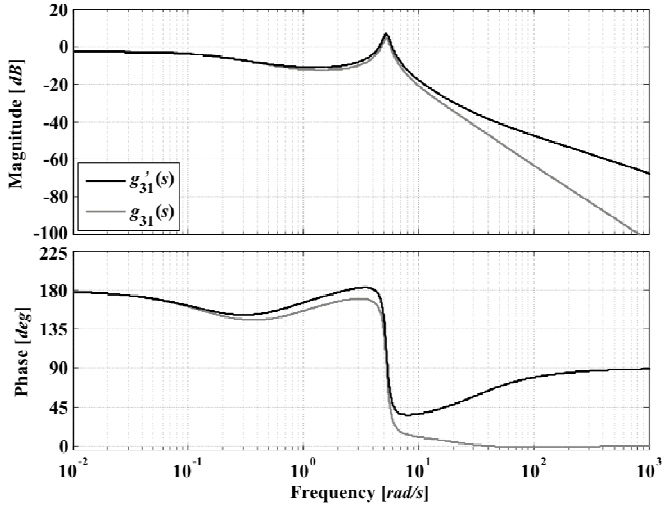

(*a*)

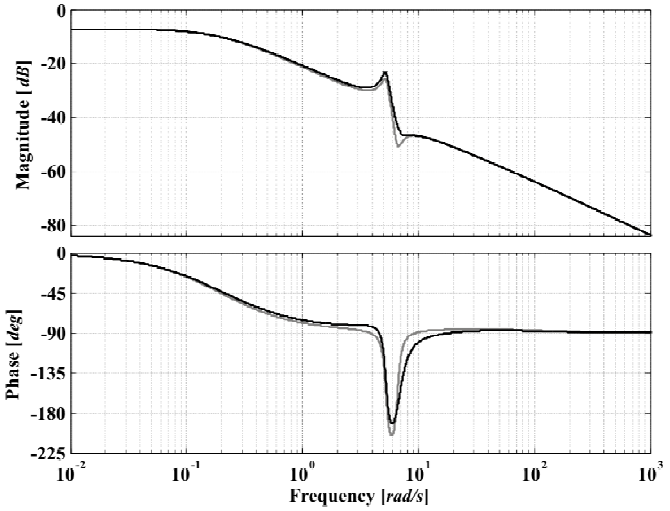

(*b*)

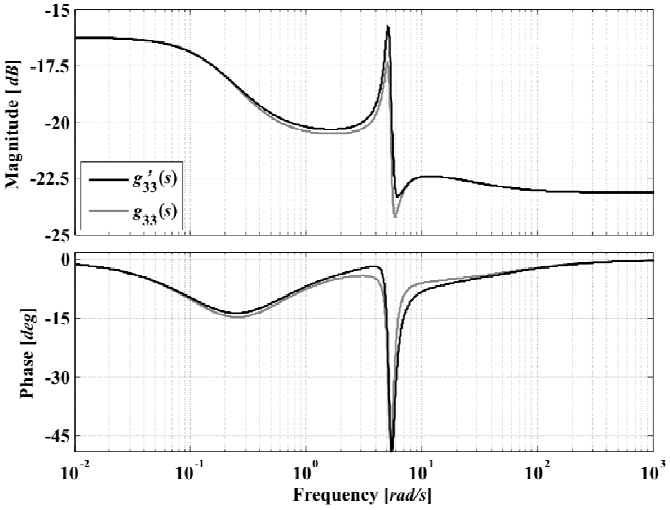

(*c*)

Figure 4.41. Bode diagrams of non-compensated and amended subsystems using controller (4.30): (*a*) g_{31} vs ($g_{31} - K_D g_{11}$); (*b*) g_{32} vs ($g_{32} - K_D g_{12}$); (*c*) g_{33} vs ($g_{33} - K_D g_{13}$)

The control system performance and robustness assessment of the system using controllers (4.29) and (4.30) are shown in Figures 4.42–4.45. Relevant information associated to these figures is summarised in Table 4.8.

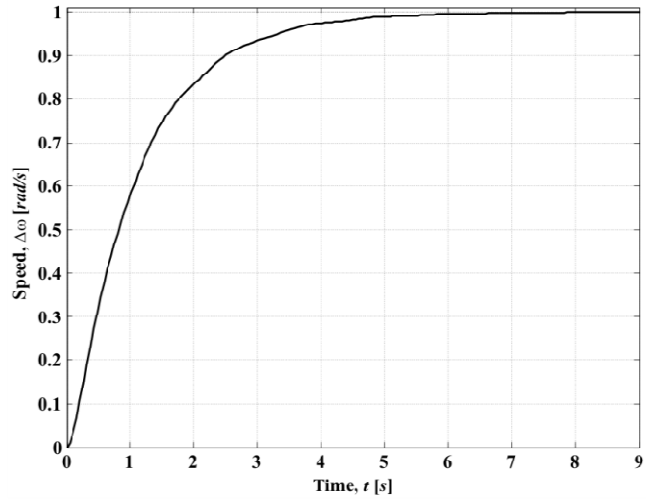

(*a*)

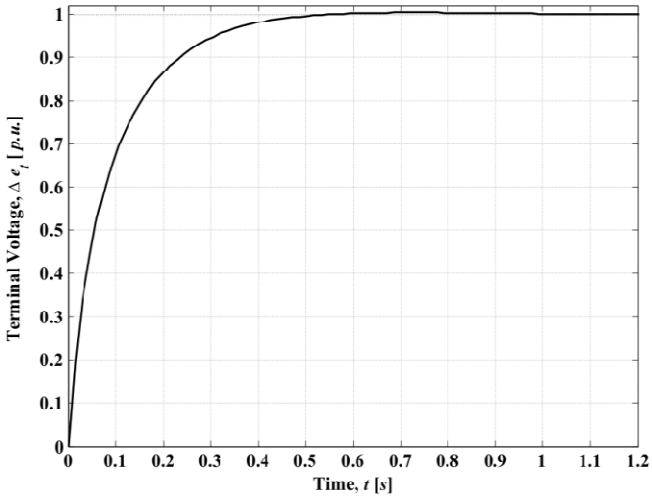

(*b*)

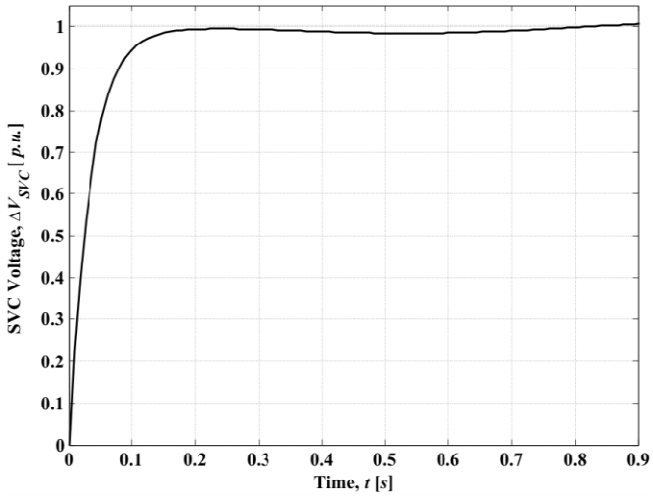

(*c*)

Figure 4.42. Step response with SVC voltage/damping control: (*a*) Channel 1 ($T_{c1}(s)$); (*b*) Channel 2 ($T_{c2}(s)$); (*c*) Channel 3 ($T_{c3}(s)$)

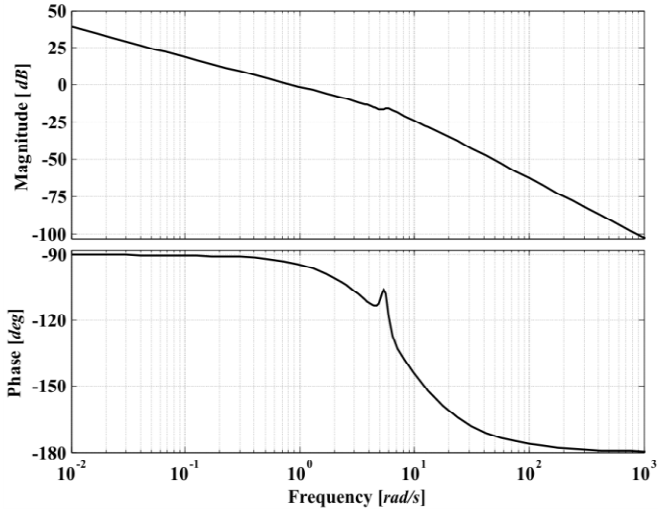

(*a*)

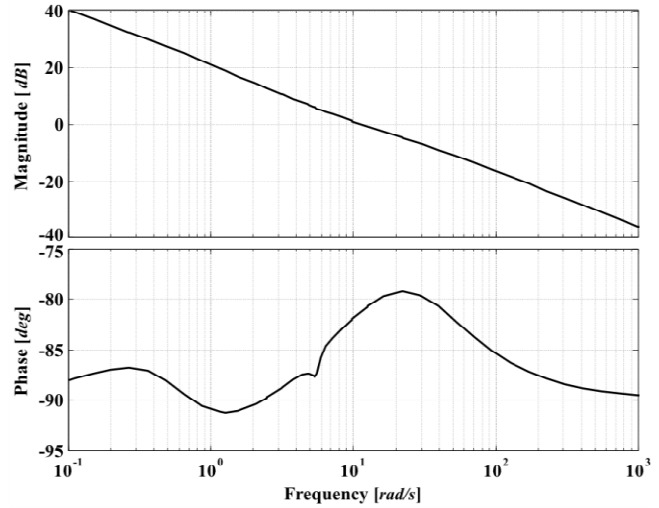

(*b*)

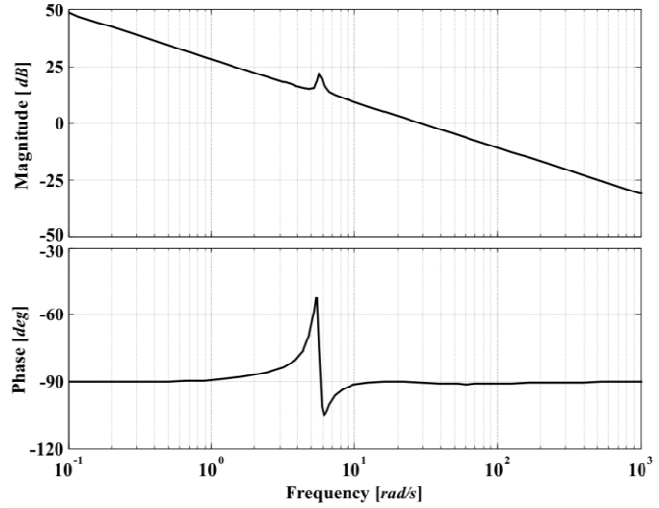

(*c*)

Figure 4.43. Bode diagrams with SVC voltage/damping control: (*a*) Channel 1 ($C_1(s)$); (*b*) Channel 2 ($C_2(s)$); (*c*) Channel 3 ($C_3(s)$);

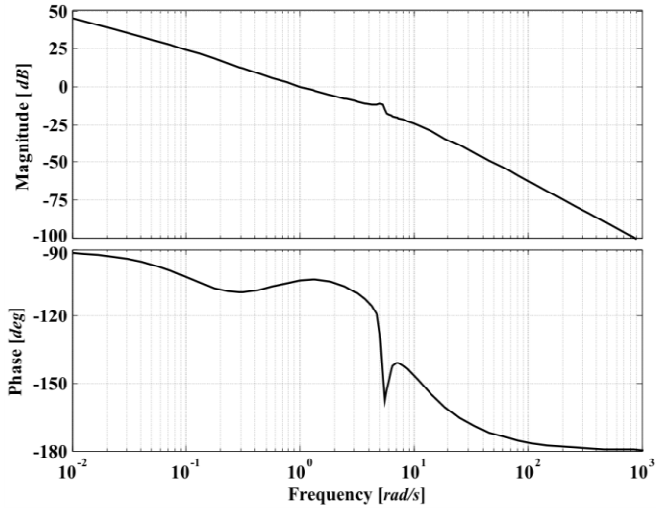

(*a*)

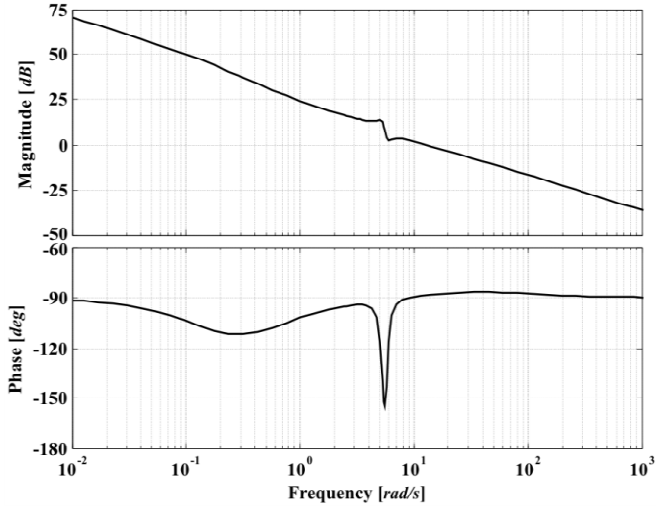

(*b*)

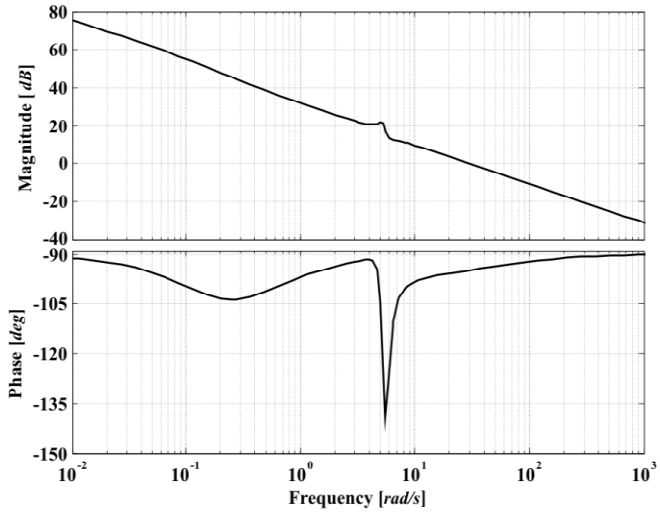

(*c*)

Figure 4.44. Robustness assessment with SVC voltage/damping control. Bode diagrams: (*a*) $k_{11}g_{11}(s)$; (*b*) $k_{22}g_{22}(s)$; (*c*) $k_{33}g_{33}(s)$

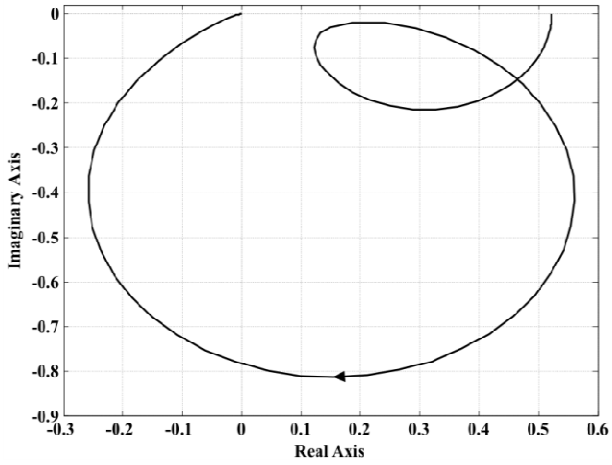

(*a*)

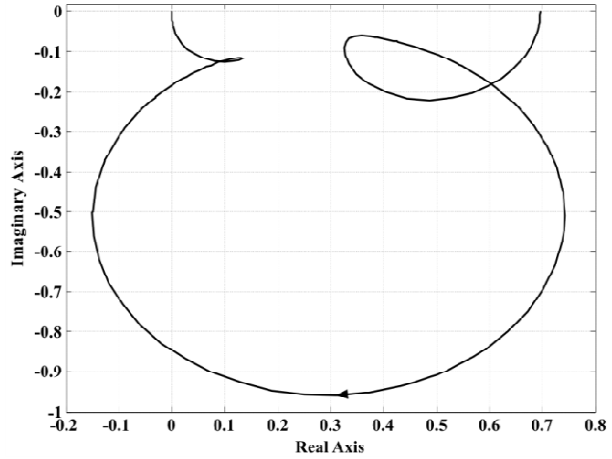

(*b*)

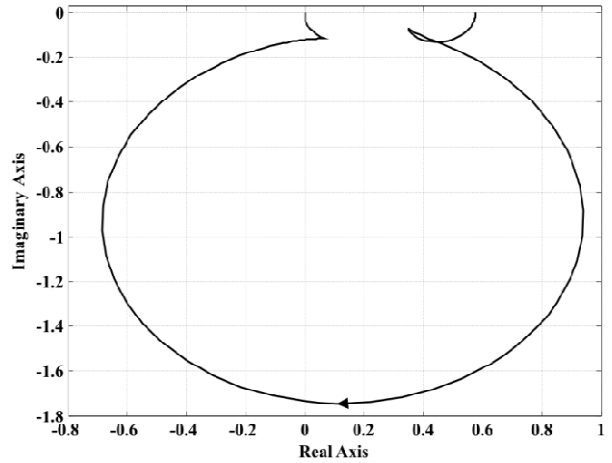

(*c*)

Figure 4.45. Robustness assessment with SVC voltage/damping control. Nyquist diagrams: (*a*) $\gamma_1(s)$; (*b*) $\gamma_2(s)$; (*c*) $\gamma_3(s)$

Table 4.8. Structural and stability robustness of the channels and control system featuring SVC voltage and damping control loops. Weak transmission system with high bandwidth

Measure	$C_1(s)$	$k_{11}g_{11}(s)$	$\gamma_1(s)$	$C_2(s)$	$k_{22}g_{22}(s)$	$\gamma_2(s)$	$C_3(s)$	$k_{33}g_{33}(s)$	$\gamma_3(s)$
Bandwidth (*rad/s*)	1.25	1.43	—	17.1	19.3	—	40.7	40.9	—
Gain margin (*dB*)	∞	∞	5.63	∞	∞	3.16	∞	∞	4.79
Phase margin (*deg*)	86	76.4	∞	98.7	91.6	∞	89.4	85.1	32

As observed in Figure 4.42, when controllers (4.29) and (4.30) are used, the step responses of the three channels reach the unit reference quicker than in the case when the control pair (4.21) and (4.28) were used. The faster step responses are a consequence of the chosen bandwidths for controller (4.29), which can be determined from Figure 4.43. It is of particular interest that the switch-back is completely eliminated from Channel 2 (Figure 4.43(*b*)). It should be emphasised that the plausibility of an arbitrary higher bandwidth was elucidated through the analysis of the MSFs of the amended system. Moreover, an effective damping control is used alongside an adequate SVC voltage control, with no negative interactions between them. In fact, notice that the individual channels possess adequate stability robustness measures, as summarised in Table 4.8.

The structural robustness is assessed through Figures 4.44 and 4.45. Figure 4.44 shows the Bode diagrams of the individual channel subsystems $h_i(s)$. Notice that the switch-back characteristic is still present in $h_2(s)$. This arises from the fact that the damping controller has no direct effect on element $g_{22}(s)$. Although the damping controller directly impacts on element $g_{33}(s)$, the switch-back characteristic appears in this subsystem. From Figure 4.45 and Table 4.8, it can be seen that the gain margins of $\gamma_i(s)$ will be quite similar to those of the previous design. In other words, the use of the new pair of controllers does not change the dynamical structure of the system – notice that the Nyquist plots of $\gamma_i(s)$ start to the left of (1,0) and do not encircle it. Therefore, the gain and phase margins provided in Table 4.8 are valid measures of robustness.

Remarks: Using the ICAD framework and careful analysis of the ensuing MSFs, a coordinated SVC voltage and damping control can be successfully achieved in a straightforward fashion. This is in marked contrast to the use of optimisation algorithms requiring iterative processes and the definition of objective and weighting functions, such as in [24]. Using ICAD the control system design is carried out through Bode shaping – such a task is a transparent one once the design objectives are established and the structural analysis is performed. The effectiveness of the SVC damping control arises from the fact that the dynamics of the generator itself are exploited: the damping controller takes the form of a non-diagonal (that is, cross-coupled) system post-compensator, which completely avoids an active direct control over the frequency range where the switch-back characteristic appears. As discussed in Chapter 3, any attempt to directly counteract the switch-back feature would be problematic; therefore, previous designs were subjected to a limitation on bandwidth. It should be emphasised that although the analysis has been directed to show the capability of the SVC to remove the switch-back characteristic due to the local plant oscillation mode of the synchronous generator in the frequency range 0.8–2 *Hz*, there should be little difficulty in extending it to damp inter-area mode oscillations in the frequency range 0.1–0.7 *Hz* [25]. In fact, the availability of a high-performance terminal voltage channel (with a high bandwidth over 10 *rad/s*) would enable a strong disturbance rejection over the frequency range 0.1–10 *rad/s*.

4.4. Synchronous generator – TCSC system

Active power transfers between areas may be substantially increased and adjusted very effectively by varying the net series impedance of the series compensated line. The Thyristor-Controlled Series Compensator (TCSC), a member of the second generation of FACTS devices, is the electronically-controlled counterpart of the conventional series bank of capacitors [26]. Its major benefits are its ability to regulate power flows along the compensated line and to rapidly modulate the effective impedance of the line in response to dynamic events in the vicinity of the line – enabling a smooth control of transmission line compensation levels. A general description of this FACTS device has been presented in Chapter 2.

Experience with the operation of TCSC installations has encouraged power system planners to look at the TCSC as a realistic solution for providing better control in the high-voltage side of the power network [16,27,28]. This provides the motivation to carry out fundamental studies of the dynamic behaviour of transmission systems with TCSCs. So far, valuable transfer function block-diagram models of the synchronous machine – TCSC system have been developed [12]. Building on this positive experience, the performance of a synchronous generator – TCSC system is evaluated using the ICAD framework.

Fundamental analysis is carried out to explain how the generator dynamic behaviour is affected by the TCSC. Moreover, a control system design for the system is presented, with particular emphasis in the closed-loop performance and robustness assessment. The percentage of series compensation is varied by changing the firing angle of the TCSC. Different study cases are considered: the effect of series compensation in weak and strong transmission systems, high levels of capacitive compensation and operation in the inductive region.

4.4.1. System under study

The test system under study, shown in Figure 4.46, is used to assess the influence that the TCSC exerts on the generator dynamic characteristic. It consists of one synchronous generator feeding into an infinite-bus system via a TCSC compensated tie-line. The synchronous machine used for this study has the parameters given in Appendix B.

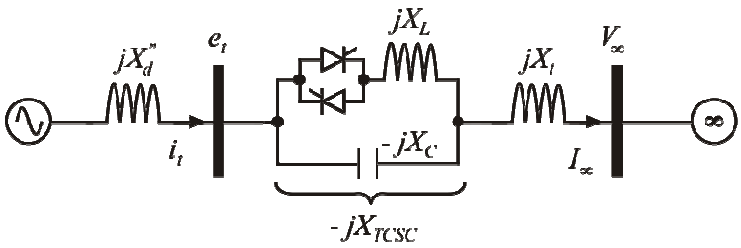

Figure 4.46. Synchronous generator – TCSC system

4.4.1.1. Block diagram representation

As in the case of the SVC, the small-signal model is developed from first principles, by using the non-linear and algebraic equations that represent the synchronous generator and the TCSC. In order to study the dynamic interaction between the generator and the TCSC, the effects of the field and damping windings in the *d*- and *q*-axis should be included. Therefore, the 5th order synchronous generator model presented in Chapter 3 is used, which accounts for the effects of the generator main field winding plus one damper winding in the *d*-axis and one in the *q*-axis. After manipulating the relevant transfer-function expressions, the following linearised equations are obtained [12]:

$$\Delta P_e(s) = K_1\Delta\delta(s) + K_2\Delta E_q^{"}(s) - K_{2d}\Delta E_d^{"}(s) + K_{TCSC1}\Delta\alpha(s) \tag{4.31}$$

$$\Delta e_t(s) = K_5\Delta\delta(s) + K_6\Delta E_q^{"}(s) + K_{6d}\Delta E_d^{"}(s) + K_{TCSC3}\Delta\alpha(s) \tag{4.32}$$

$$\Delta I_{TCSC}(s) = K_{5n}\Delta\delta(s) + K_{6n}\Delta E_q^{"}(s) - K_{6dn}\Delta E_d^{"}(s) + K_{TCSC3n}\Delta\alpha(s) \tag{4.33}$$

$$\Delta E_q^{"}(s) = K_3(s)\Delta E_{fd}(s) - K_4(s)\Delta\delta(s) - K_{TCSC2}(s)\Delta\alpha(s) \tag{4.34}$$

$$\Delta E_d^{"}(s) = K_{4d}(s)\Delta\delta(s) + K_{TCSC2d}(s)\Delta\alpha(s) \tag{4.35}$$

$$\Delta\omega(s) = \frac{1}{2Hs}\left[\Delta P_m(s) - \Delta P_e(s) - D\Delta\omega(s)\right] \tag{4.36}$$

$$\Delta\delta(s) = \frac{\omega_0}{s}\Delta\omega(s) \tag{4.37}$$

For further details about the mathematical modelling refer to Appendix E. Equations (4.31)–(4.37) are used to form the block diagram representation shown in Figure 4.47. Similarly to the case of the generator – SVC system, it can be seen that there are 3-input 3-output feedback subsystems in the synchronous generator – TCSC block diagram, *i.e.*, excitation, turbine-governor and TCSC impedance control loops. These are in addition to the generator – TCSC system, whose outputs of interest are generator speed ($\Delta\omega$), generator output voltage (Δe_t) and TCSC current (ΔI_{TCSC}) flowing through the tie-line.

The main function of the impedance control loop of the TCSC is to schedule a given amount of electrical power to be delivered through the tie-line. The feedback control signal is directly taken from the current (ΔI_{TCSC}) flowing through the TCSC. Hence, ΔI_{TCSC} brings a change from the generator's flux linkages in the *d*- and *q*-axis and rotor angle via coefficients K_{6n}, K_{6dn} and K_{5n}, which is compared with the reference $\Delta I_{TCSC,ref}$ in order to adjust the firing angle at the desired power flow level [12].

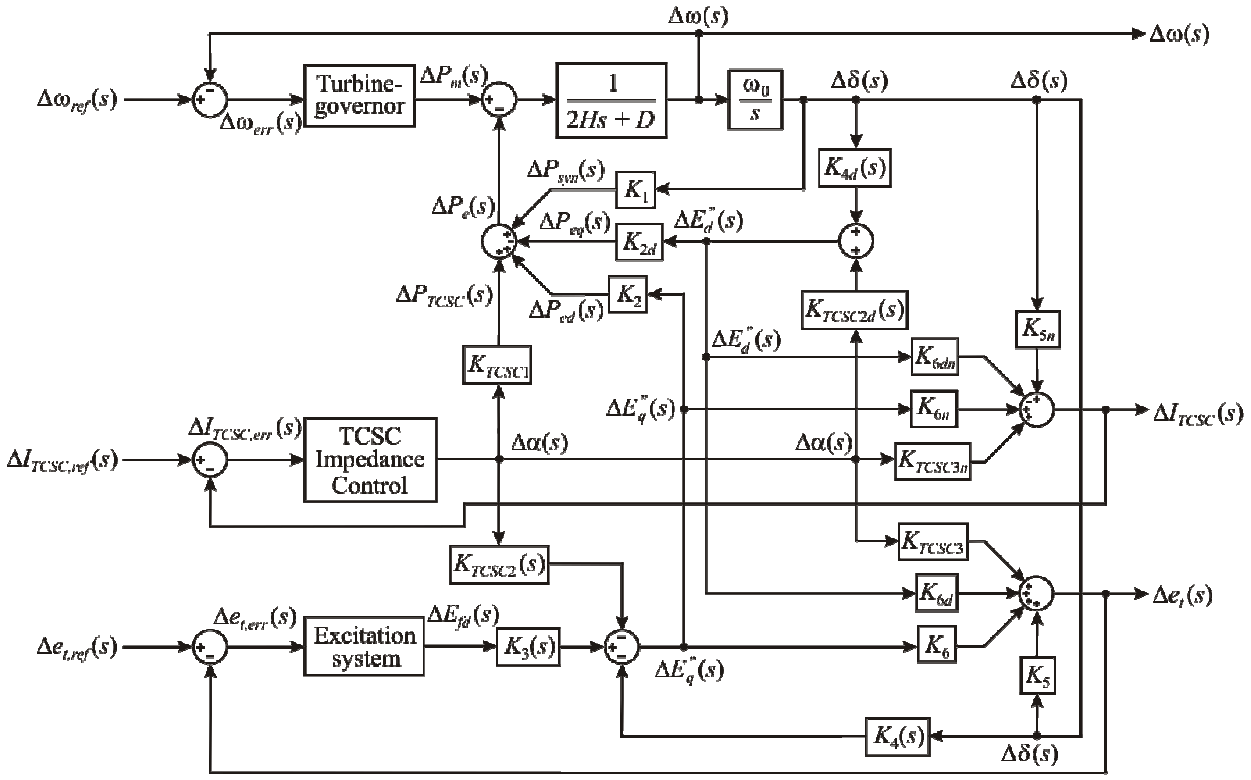

Figure 4.47. Block diagram: synchronous generator – TCSC system

Similarly to the case of the SVC, an incremental change in the electrical power of the generator is employed here to investigate the dynamic interactions between the generator and the TCSC. The TCSC branches influencing the generator's behaviour are similar to those of the SVC. An incremental change in the TCSC firing angle leads to a direct change in the output power of the generator, which is made up of three individual electrical power loops, namely ΔP_{TCSC}, ΔP_{ed}, and ΔP_{eq}. ΔP_{TCSC} is the component of the generator's output power that is directly channelled through coefficient K_{TCSC1} and it is due to a change in TCSC impedance (ΔX_{TCSC}). ΔP_{ed} and ΔP_{eq} are portions of the output power produced by the *d*- and *q*-axis flux linkages, respectively. The TCSC may influence the power produced by the flux linkages through coefficient K_{TCSC3} and the transfer functions $K_{TCSC2}(s)$ and $K_{TCSC2d}(s)$. Once the firing angle is changed to increase the TCSC contribution (in the capacitive mode of operation), all coefficients and transfer functions making up the entire system will be affected due to a reduction of the tie-line's impedance [12].

The block diagram of the generator – TCSC system yields unique physical insight as to how the TCSC dynamically affects the generator. It enables a transparent analysis of the interaction between internal machine variables and the TCSC in terms of constants and transfer functions that encapsulate fully all key dynamic parameters of the system. Nevertheless, not all interactions between various variables are required for control system design purposes. A great deal of redundancy can be avoided by working with ICAD, where the description of the dynamical behaviour and structure of the system in a global context is possible, in which the characteristics of the individual transfer functions do not have the dominant role.

4.4.1.2. TCSC characteristic

The TCSC is connected in series with the tie-line, as shown in Figure 4.48. The active power flow leaving node *n* can be adjusted by controlling the TCSC impedance (X_{TCSC}). This is achieved by suitably changing the thyristor's firing angle.

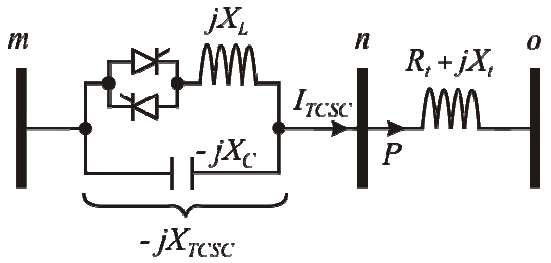

Figure 4.48. Configuration of the TCSC connected in series with a tie-line

The expression for the fundamental frequency of the TCSC impedance, as a function of the firing angle, is given as [29]:

$$\begin{aligned} X_{TCSC} = &-X_C + C_1\left\{2(\pi-\alpha)+\sin\left[2(\pi-\alpha)\right]\right\}+ \\ &-C_2\cos^2(\pi-\alpha)\left\{\lambda\tan\left[\lambda(\pi-\alpha)\right]-\tan(\pi-\alpha)\right\} \end{aligned} \tag{4.38}$$

For a small variation, the derivative value of the TCSC impedance characteristic, $F(\alpha) = \partial X_{TCSC}/\partial\alpha$, is given by

$$F(\alpha) = -2C_1(1+\cos 2\alpha) + C_2\left\{\frac{\lambda^2\cos^2(\pi-\alpha)}{\cos^2\left[\lambda(\pi-\alpha)\right]}-1\right\} + C_2\sin 2\alpha\left\{\lambda\tan\left[\lambda(\pi-\alpha)\right]-\tan(\pi-\alpha)\right\} \tag{4.39}$$

where

$$C_1 = \frac{X_C + X_{LC}}{\pi} \qquad C_2 = \frac{4X_{LC}^2}{\pi X_L} \qquad \lambda = \frac{\omega_0}{\omega} = \sqrt{\frac{X_C}{X_L}}$$

$$X_{LC} = \frac{X_C X_L}{X_C - X_L} \qquad \omega_0^2 = \frac{1}{LC} = \omega^2\frac{X_C}{X_L}$$

Consider a TCSC with inductive and capacitive reactance values corresponding to those of the fully operational Kayenta TCSC installation [30]. Figure 4.49 shows the fundamental frequency reactance as a function of α and its derivative $F(\alpha)$.

From Figure 4.49 it can be observed that the impedance characteristic has two distinctive regions of operation, one inductive and one capacitive, as the TCSC firing angle increases from 90° to 180°. The capacitive region starts at firing angles greater than 142.531°. For firing angle values near this resonant point the variations of X_{TCSC} are quite large even for a small variation in the controlling firing angle. If an increase of TCSC impedance in the capacitive mode is required then the firing angle value should move towards the resonant point. Also, $F(\alpha)$ has always positive values in the TCSC firing angle range. The effect of $F(\alpha)$ appears in many of the system coefficients of the block-diagram model.

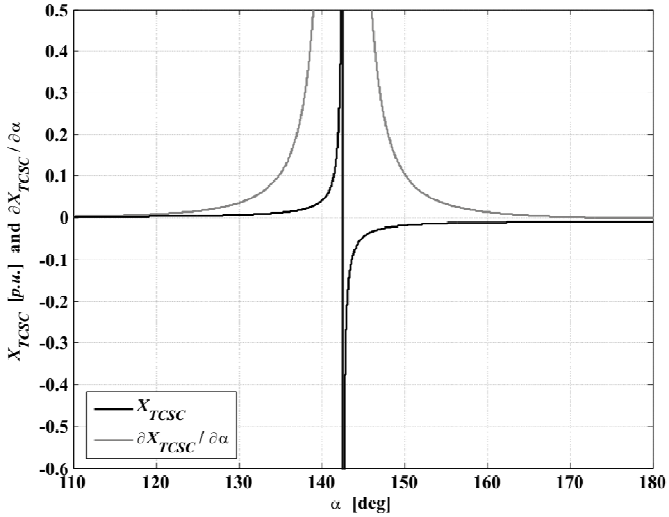

Figure 4.49. TCSC impedance characteristic (X_{TCSC}) and its derivative $F(\alpha) = \partial X_{TCSC}/\partial\alpha$ for given parameters

The usual practice is to operate the TCSC in its capacitive region for obvious reasons; it is desirable to decrease the electrical length of the transmission line in order to increase active power flows.

4.4.1.3. Transfer function matrix representation

The transfer function matrix representation of the system is not only desirable but essential for the analysis of the synchronous generator – TCSC plant dynamics under the ICAD framework. After some arduous algebra (carried out in Appendix E), such a representation is obtained and given by

$$\begin{bmatrix} \Delta\omega(s) \\ \Delta e_t(s) \\ \Delta I_{TCSC}(s) \end{bmatrix} = \begin{bmatrix} g_{11}(s) & g_{12}(s) & g_{13}(s) \\ g_{21}(s) & g_{22}(s) & g_{23}(s) \\ g_{31}(s) & g_{32}(s) & g_{33}(s) \end{bmatrix} \begin{bmatrix} \Delta P_m(s) \\ \Delta E_{fd}(s) \\ \Delta\alpha(s) \end{bmatrix} \tag{4.40}$$

or in compact form as

$$\mathbf{y}(s) = \mathbf{G}(s)\mathbf{u}(s) \tag{4.41}$$

where **G**(*s*) is the transfer function matrix of the 3×3 linearised model of the synchronous generator – TCSC system. The individual elements of **G**(*s*) can be found in Appendix E. For control system analysis, the closed-loop diagram of the system is shown in Figure 4.50.

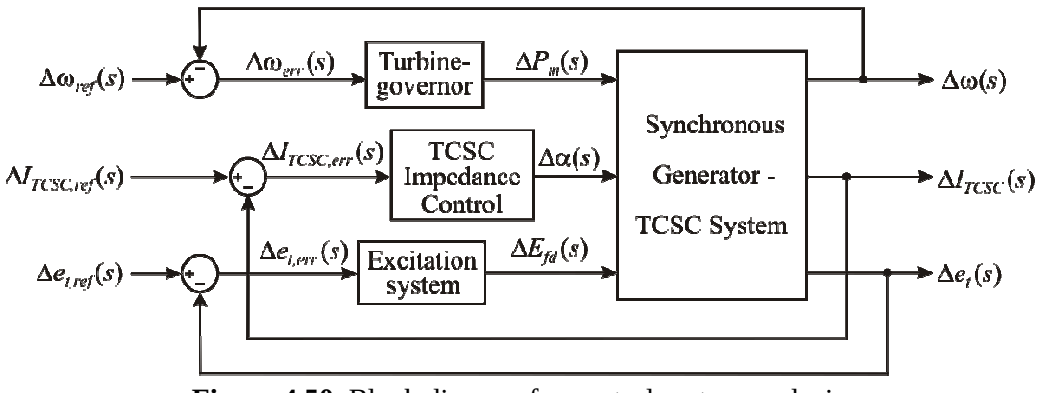

Figure 4.50. Block diagram for control system analysis

Complete study cases are carried out in this section. The first one assesses the influence that the TCSC exerts on the generator dynamic characteristic when the tie-line reactance has a fixed value (X_t = 0.4 *p.u.*) and the percentage of series compensation is varied (50, 25, 10%) by changing the firing angle α_0. A variable amount of series compensation is considered. The second study evaluates the TCSC performance considering different values of tie-line reactances (X_t = 0.4, 0.5, 0.6 *p.u.*) and a fixed compensation value (X_{TCSC} = –0.2 *p.u.*). The operating conditions are provided in Tables 4.9 and 4.10. It is important to mention that although the TCSC terminal voltage V_{TCSC0} is artificially high (above 1.05 *p.u.* in all cases), it will not impact on these studies. A practical solution involves the installation of a set of TCSC modules in series [29], causing a voltage reduction.

Another relevant aspect worth mentioning is that numerical calculation shows that for these operating conditions all individual elements $g_{ij}(s)$ in (4.40) are stable and minimum-phase (not shown). At a later stage, a performance comparison between a system with no TCSC and one with TCSC is made. Finally, extreme cases of TCSC operation are assessed: high levels of capacitive compensation and the inductive region operation.

Table 4.9. System operating condition for Study 1 (TCSC)

Variable	**Case 1** 50% comp.	**Case 2** 25% comp.	**Case 3** 10% comp.
P_g	0.736 *p.u.*	0.736 *p.u.*	0.736 *p.u.*
Q_g	0.4307 *p.u.*	0.3082 *p.u.*	0.262 *p.u.*
PF	0.91958	0.94558	0.95065
δ_0	30°	30°	30°
$\lvert V_{\infty 0}\rvert$	1 *p.u.*	1 *p.u.*	1 *p.u.*
$\angle V_{\infty 0}$	60°	60°	60°
$\lvert e_{t0}\rvert$	1.05 *p.u.*	1.05 *p.u.*	1.05 *p.u.*
$\angle e_{t0}$	68.055°	72.139°	74.615°
$\lvert i_{t0}\rvert$ / $\lvert I_{\infty 0}\rvert$	0.76225 *p.u.*	0.74129 *p.u.*	0.73734 *p.u.*
$\angle i_{t0}$ / $\angle I_{\infty 0}$	44.92°	53.151°	56.539°
$\lvert V_{TCSC0}\rvert$	1.1188 *p.u.*	1.0764 *p.u.*	1.0595 *p.u.*
$\angle V_{TCSC0}$	75.257°	75.873°	76.133°
E_{fd0}	1.7538 *p.u.*	1.6418 *p.u.*	1.5998 *p.u.*
X_{TCSC}	–0.2 *p.u.*	–0.1 *p.u.*	–0.04 *p.u.*
α_0	143.08°	143.65°	145.47°
$\partial X_{TCSC} / \partial \alpha_0$	20.431	4.9546	0.71622
X_t	0.4 *p.u.*	0.4 *p.u.*	0.4 *p.u.*
X_{total}	0.2 *p.u.*	0.3 *p.u.*	0.36 *p.u.*

Table 4.10. System operating condition for Study 2 (TCSC)

Variable	**Case 1** 50% comp.	**Case 2** 40% comp.	**Case 3** 33.3% comp.
P_g	0.736 *p.u.*	0.736 *p.u.*	0.736 *p.u.*
Q_g	0.4307 *p.u.*	0.3633 *p.u.*	0.345 *p.u.*
PF	0.91958	0.94557	0.95204
δ_0	30°	35°	40°
$\lvert V_{\infty 0}\rvert$	1 *p.u.*	1 *p.u.*	1 *p.u.*
$\angle V_{\infty 0}$	60°	55°	50°
$\lvert e_{t0}\rvert$	1.05 *p.u.*	1.05 *p.u.*	1.05 *p.u.*
$\angle e_{t0}$	68.055°	67.135°	66.278°
$\lvert i_{t0}\rvert$ / $\lvert I_{\infty 0}\rvert$	0.76225 *p.u.*	0.7413 *p.u.*	0.73626 *p.u.*
$\angle i_{t0}$ / $\angle I_{\infty 0}$	44.92°	48.144°	48.461°
$\lvert V_{TCSC0}\rvert$	1.1188 *p.u.*	1.1072 *p.u.*	1.104 *p.u.*
$\angle V_{TCSC0}$	75.257°	74.413°	73.578°
E_{fd0}	1.7538 *p.u.*	1.6823 *p.u.*	1.6668 *p.u.*
X_{TCSC}	–0.2 *p.u.*	–0.2 *p.u.*	–0.2 *p.u.*
α_0	143.08°	143.08°	143.08°
$\partial X_{TCSC} / \partial \alpha_0$	20.431	20.431	20.431
X_t	0.4 *p.u.*	0.5 *p.u.*	0.6 *p.u.*
X_{total}	0.2 *p.u.*	0.3 *p.u.*	0.4 *p.u.*

Remark: Notice from (4.40) and the block diagrams in Figures 4.47 and 4.50 that the synchronous generator – TCSC system has a similar construction as that of the synchronous generator – SVC system studied earlier in this chapter. The differences arise in the individual elements of the transfer function matrix in (4.40). Therefore, the analysis for the TCSC can be carried out in a similar manner.

4.4.2. Multivariable analysis

In the framework afforded by ICAD, the dynamical structure of plant (4.40) is determined by input-output channels resulting from pairing each input to each output by means of diagonal controllers. For the case of the synchronous generator – TCSC system, the pairing of inputs to outputs is given as [12]

$$\mathbf{K}(s)=\begin{bmatrix} k_{11}(s) & 0 & 0 \\ 0 & k_{22}(s) & 0 \\ 0 & 0 & k_{33}(s) \end{bmatrix} \Rightarrow \begin{cases} C_1(s):\Delta P_m(s)\rightarrow \Delta\omega(s) \\ C_2(s):\Delta E_{fd}(s)\rightarrow \Delta e_t(s) \\ C_3(s):\Delta\alpha(s)\rightarrow \Delta I_{TCSC}(s) \end{cases} \tag{4.42}$$

The diagonal controller given in (4.42), which considers the pairings $\Delta P_m(s) \rightarrow \Delta\omega(s)$, $\Delta E_{fd}(s) \rightarrow \Delta e_t(s)$ and $\Delta\alpha(s) \rightarrow \Delta I_{TCSC}(s)$, agrees with that used for conventional controllers. As in the synchronous generator – SVC system, notice that the Individual Channels $C_1(s)$ and $C_2(s)$ correspond to the pairing of inputs and outputs associated to the synchronous generator, whereas $C_3(s)$ is associated to the TCSC

impedance control loop. Figure 4.51 shows the individual channel representation for the synchronous generator – SVC system.

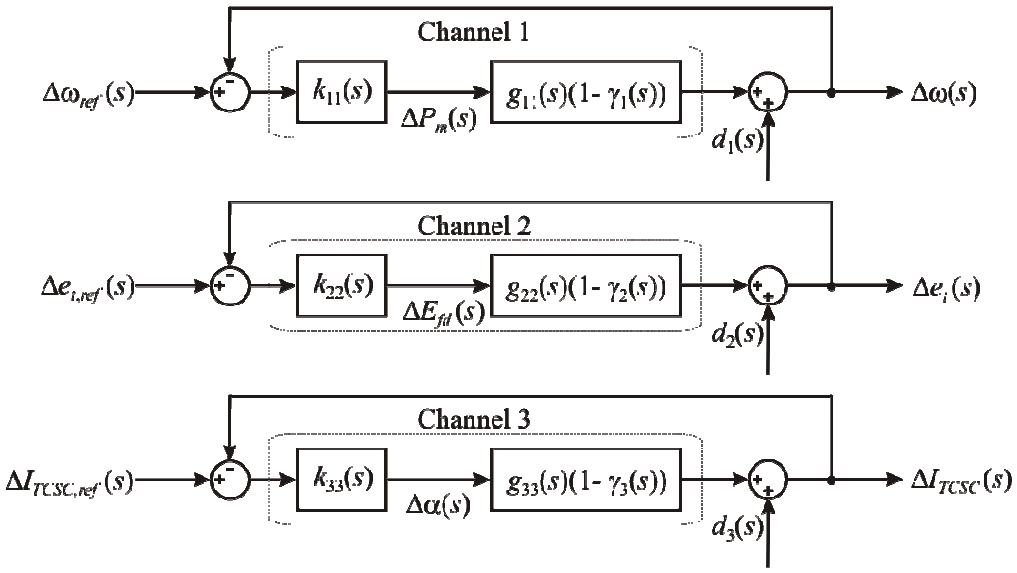

Figure 4.51. Synchronous generator – TCSC system represented in individual channels

Similarly to the case of the synchronous generator – SVC system individual channel representation (Figure 4.4), it can be seen from Figure 4.51 that the multivariable system can be re-formulated as three SISO channels, where each channel includes a feedback loop and its controller. Each controller can be designed to comply with the specifications associated to each individual channel. Notice that every channel is subject to a disturbance $d_i(s)$ – representing the effects of other channel references. Therefore, the behaviour of an individual channel will be affected both by its controller and by the other individual channels. The representation of Figure 4.51 is fully equivalent to the original synchronous generator – TCSC system of Figure 4.50, with no loss of information. The multivariable character of the plant is suitably quantified, in the frequency domain, by the MSFs $\gamma_i(s)$.

The coupling between channels is determined by the MSFs $\Gamma_i(s)$ [6,15], which are indicators of the potential performance of feedback control. The general definition of $\Gamma_i(s)$ is addressed in Appendix A by equation (A.58). For a 3×3 system, and assuming a transfer function matrix $\mathbf{G}_{123}$ (in this case, transfer function matrix in (4.40) with the notation introduced earlier in the chapter), $\Gamma_3(s) = 0$, and $\Gamma_1(s)$ and $\Gamma_2(s)$ are given by (4.11) and (4.12), respectively.

It should be noticed that all MSFs, shown in Figures 4.52–4.63, are stable and minimum-phase, and their Nyquist plots start to the left of the point (1,0) – desirable features which ease the design process. After suitable analysis of the MSFs, the following can be said about the channels:

- With reference to transfer function matrix $\mathbf{G}_{123}$ (Figures 4.52, 4.53, 4.58 and 4.59), $\Gamma_1(s)$ shows that Multiple Channel $\mathbf{M}_{23}(s)$ is highly coupled with Individual Channel $C_1(s)$ (above 0 *dB* for frequencies

below 11 *rad/s*) – however, an increase of series compensation decreases coupling. It is noticed from $\Gamma_2(s)$ that Individual Channels $C_2(s)$ and $C_3(s)$ are slightly coupled – however, an increase of series compensation increases coupling.

- With reference to transfer function matrix $\mathbf{G}_{213}$ (Figures 4.54, 4.55, 4.60 and 4.61), $\Gamma_1(s)$ shows that Multiple Channel $\mathbf{M}_{13}(s)$ is lowly coupled with $C_2(s)$ (below –10 *dB* for low compensation values) – increase of compensation increases coupling considerably. From $\Gamma_2(s)$ it can be noticed that Individual Channels $C_1(s)$ and $C_3(s)$ are highly coupled (above 0 *dB* for frequencies below 10 *rad/s*) – increase of compensation decreases coupling.

- With reference to transfer function matrix $\mathbf{G}_{312}$ (Figures 4.56, 4.57, 4.62 and 4.63), $\Gamma_1(s)$ shows that Multiple Channel $\mathbf{M}_{12}(s)$ is highly coupled with $C_3(s)$ (above 0 *dB* for frequencies below 10 *rad/s*) – increase of compensation decreases coupling. From $\Gamma_2(s)$ it can be noticed that Individual Channels $C_1(s)$ and $C_2(s)$ within Multiple Channel $\mathbf{M}_{12}(s)$ are lowly coupled (below –10 *dB*) – increase of compensation decreases coupling.

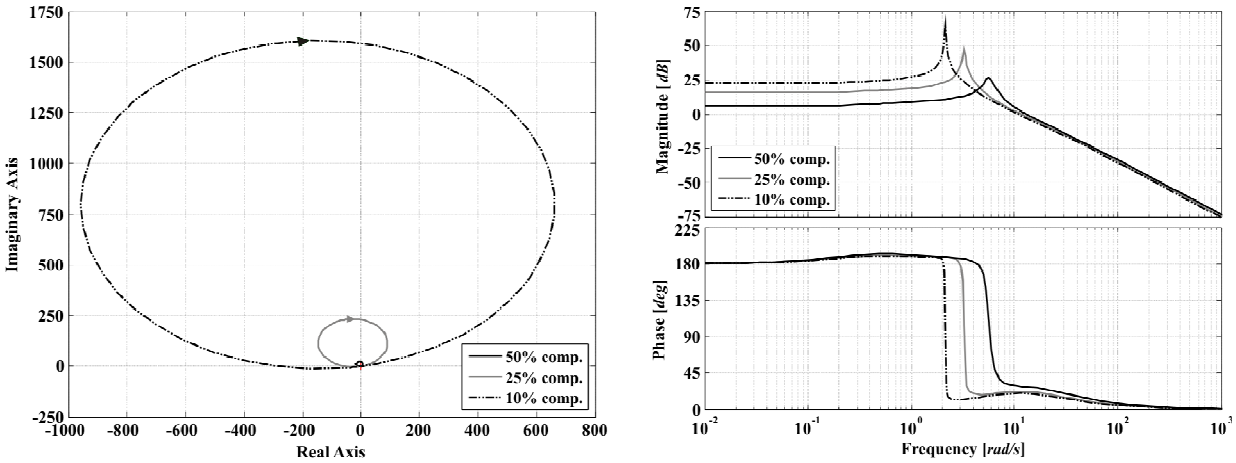

(*a*) (*b*)

Figure 4.52. Study 1. Assessment of $\Gamma_1(s)$ (transfer function matrix $\mathbf{G}_{123}$) for a TCSC-upgraded system: (*a*) Nyquist plot; (*b*) Bode plot.

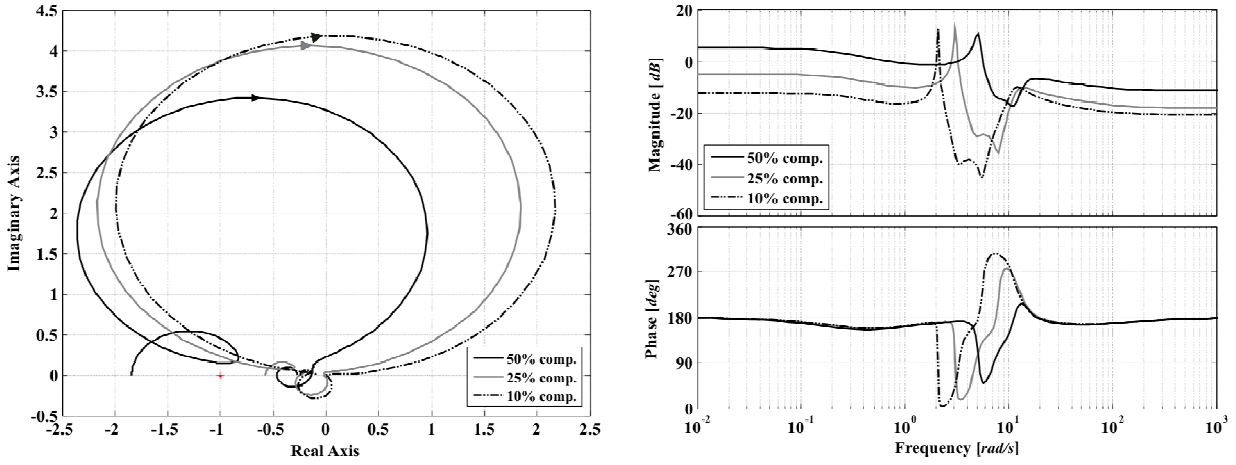

(*a*) (*b*)

Figure 4.53. Study 1. Assessment of $\Gamma_2(s)$ (transfer function matrix $\mathbf{G}_{123}$) for a TCSC-upgraded system: (*a*) Nyquist plot; (*b*) Bode plot.

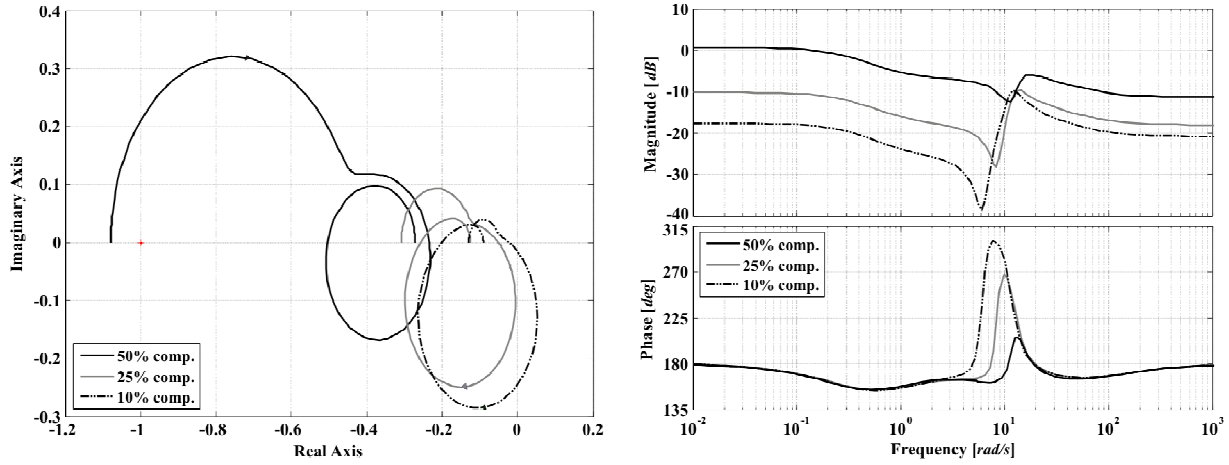

(*a*) (*b*)

Figure 4.54. Study 1. Assessment of $\Gamma_1(s)$ (transfer function matrix $\mathbf{G}_{213}$) for a TCSC-upgraded system: (*a*) Nyquist plot; (*b*) Bode plot.

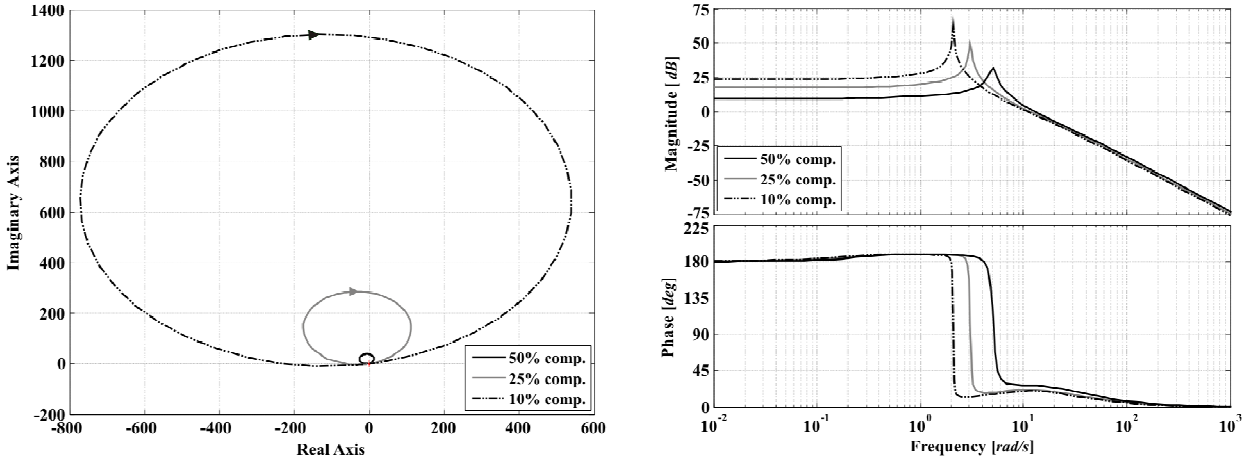

(*a*) (*b*)

Figure 4.55. Study 1. Assessment of $\Gamma_2(s)$ (transfer function matrix $\mathbf{G}_{213}$) for a TCSC-upgraded system: (*a*) Nyquist plot; (*b*) Bode plot.

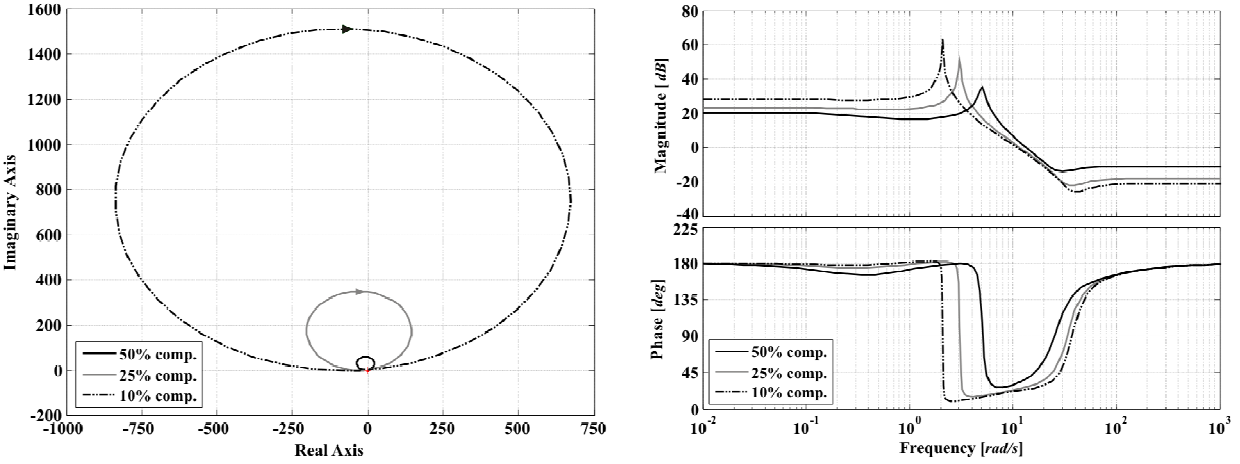

(*a*) (*b*)

Figure 4.56. Study 1. Assessment of $\Gamma_1(s)$ (transfer function matrix $\mathbf{G}_{312}$) for a TCSC-upgraded system: (*a*) Nyquist plot; (*b*) Bode plot.

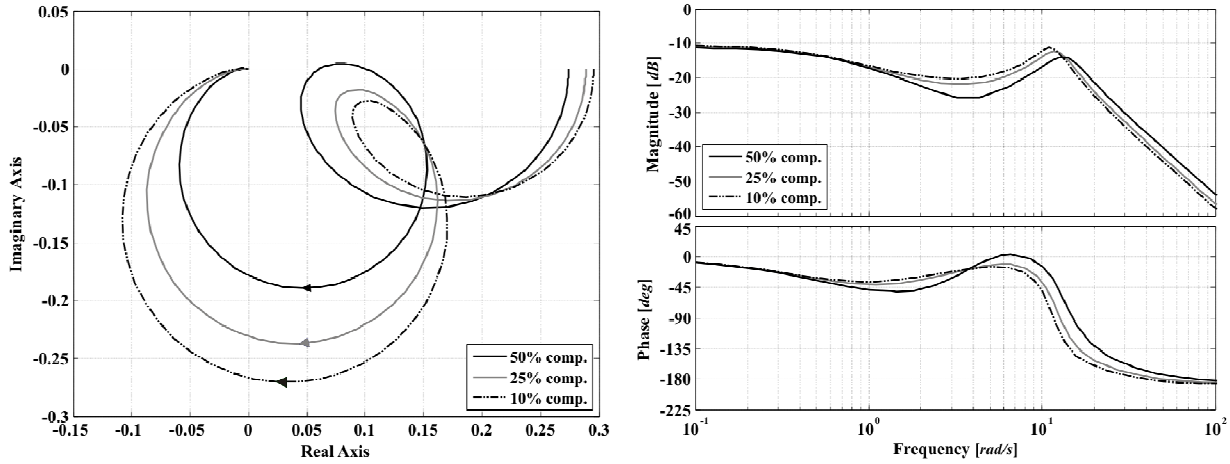

(*a*) (*b*)

Figure 4.57. Study 1. Assessment of $\Gamma_2(s)$ (transfer function matrix $\mathbf{G}_{312}$) for a TCSC-upgraded system: (*a*) Nyquist plot; (*b*) Bode plot.

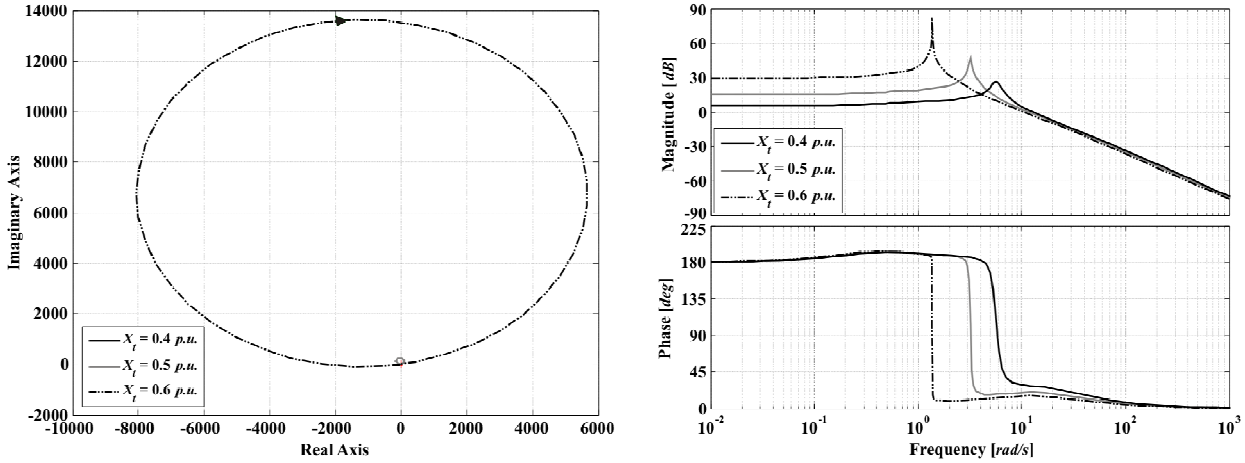

(*a*) (*b*)

Figure 4.58. Study 2. Assessment of $\Gamma_1(s)$ (transfer function matrix $\mathbf{G}_{123}$) for a TCSC-upgraded system: (*a*) Nyquist plot; (*b*) Bode plot.

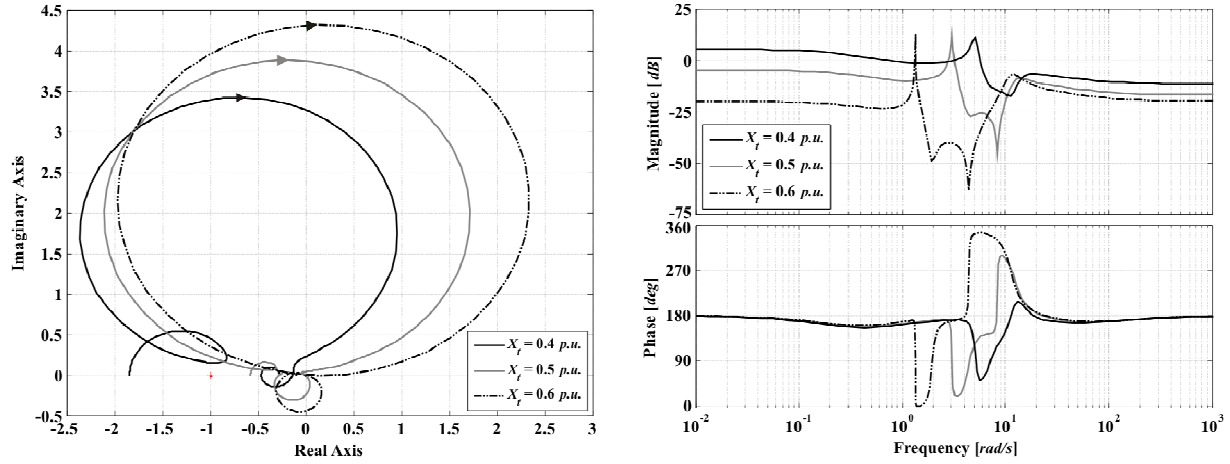

(*a*) (*b*)

Figure 4.59. Study 2. Assessment of $\Gamma_2(s)$ (transfer function matrix $\mathbf{G}_{123}$) for a TCSC-upgraded system: (*a*) Nyquist plot; (*b*) Bode plot.

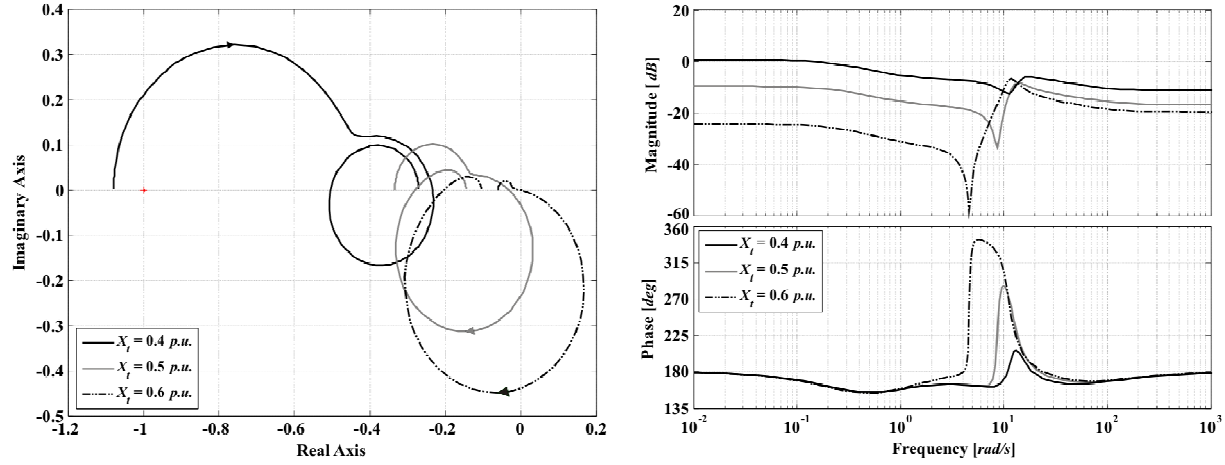

(*a*) (*b*)

Figure 4.60. Study 2. Assessment of $\Gamma_1(s)$ (transfer function matrix $\mathbf{G}_{213}$) for a TCSC-upgraded system: (*a*) Nyquist plot; (*b*) Bode plot.

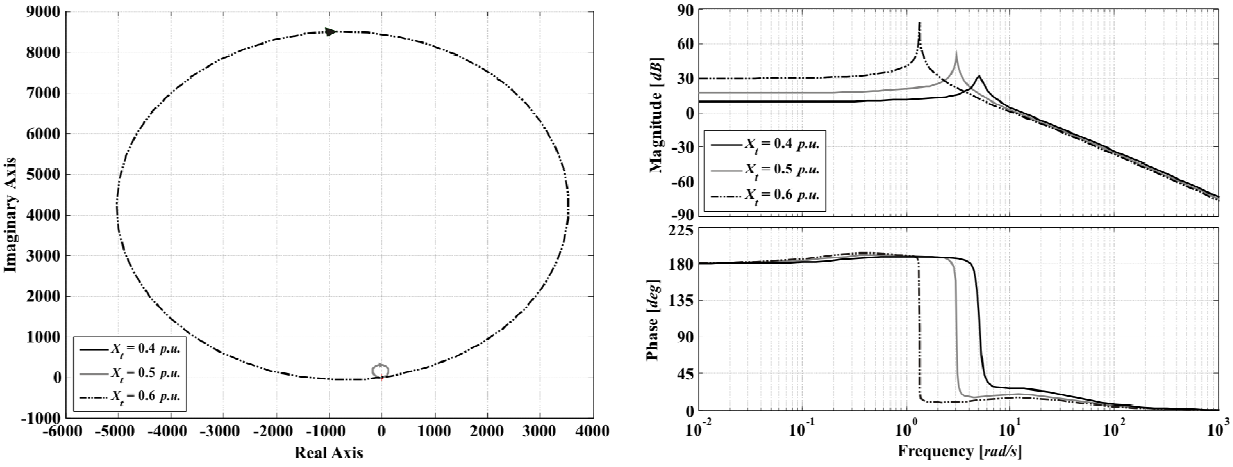

(*a*) (*b*)

Figure 4.61. Study 2. Assessment of $\Gamma_2(s)$ (transfer function matrix $\mathbf{G}_{213}$) for a TCSC-upgraded system: (*a*) Nyquist plot; (*b*) Bode plot.

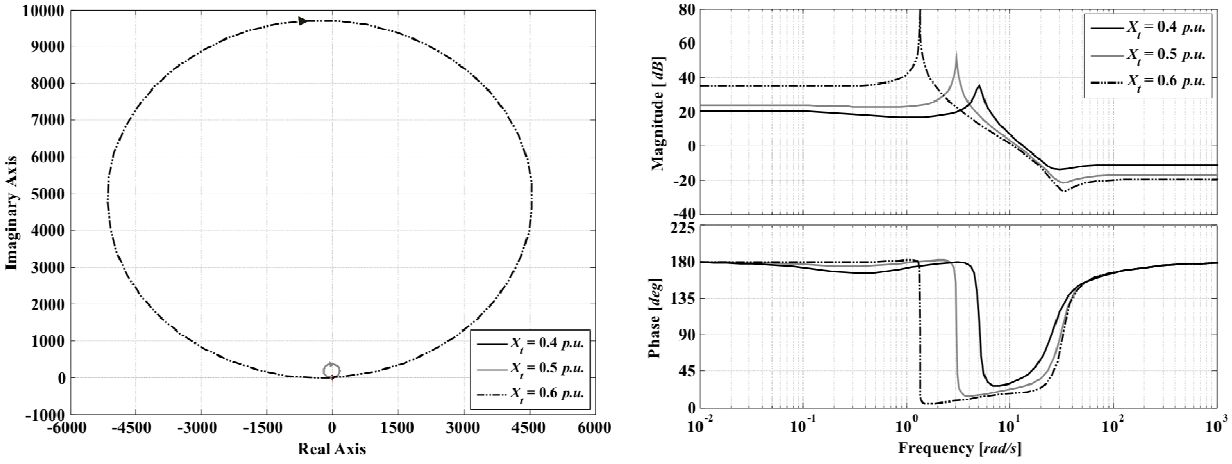

(*a*) (*b*)

Figure 4.62. Study 2. Assessment of $\Gamma_1(s)$ (transfer function matrix $\mathbf{G}_{312}$) for a TCSC-upgraded system: (*a*) Nyquist plot; (*b*) Bode plot.

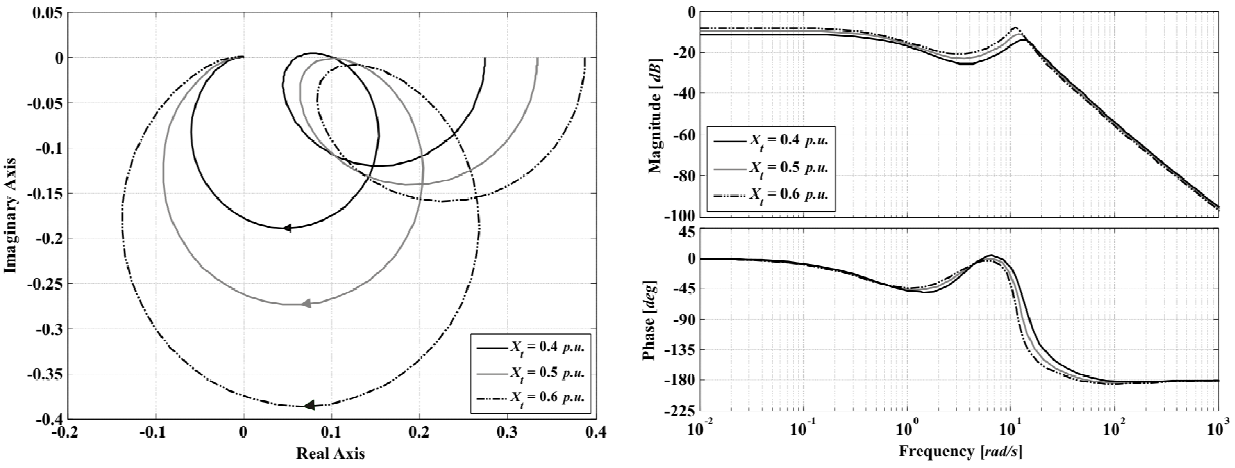

(*a*) (*b*)

Figure 4.63. Study 2. Assessment of $\Gamma_2(s)$ (transfer function matrix $\mathbf{G}_{312}$) for a TCSC-upgraded system: (*a*) Nyquist plot; (*b*) Bode plot.

From the previous analysis, it is observed that the TCSC together with the synchronous machine, regardless of the amount of series compensation and tie-line reactance value, produces a highly coupled multivariable system – particularly at low frequencies over the range of interest of 1–10 *rad/s*. It should be noticed that the TCSC impedance control loop, represented by $C_3(s)$, tends to significantly couple with the speed channel of the synchronous generator, *i.e.*, $C_1(s)$.

Multiple Channel $\mathbf{M}_{12}(s)$ represents the actual dynamics of the synchronous generator under the influence of the TCSC. The Nyquist and Bode plots of MSF $\Gamma_2(s)$ for a transfer function matrix $\mathbf{G}_{312}$ corresponding to the operating conditions in Tables 4.9 and 4.10, are shown in Figures 4.57 and 4.63. These plots confirm that Individual Channels $C_1(s)$ and $C_2(s)$ are lowly coupled (below –5 *dB* in all cases) and that an increase of series compensation decreases even more such coupling. Also, an increase in the tie-line reactance value will increase coupling, regardless of the degree of series compensation. In fact, coupling will increase with an increase in the transmission line length.

It was concluded earlier in the chapter that coupling within the machine with no FACTS device was low under a lagging power factor operation; and that channel coupling increased with electrical distance, leading to decreased robustness. These facts are helpful in elucidating a control design strategy. For instance, as the coupling in Multiple Channel $\mathbf{M}_{12}(s)$ is low, this multiple channel can be designed independently from Individual Channel $C_3(s)$. Consider the synchronous generator – TCSC system given by (4.40) with a rearranged transfer function matrix $\mathbf{G}_{312}$, or

$$\begin{bmatrix} \Delta I_{TCSC}(s) \\ \Delta\omega(s) \\ \Delta e_t(s) \end{bmatrix} = \begin{bmatrix} g_{33}(s) & g_{31}(s) & g_{32}(s) \\ g_{13}(s) & g_{11}(s) & g_{12}(s) \\ g_{23}(s) & g_{21}(s) & g_{22}(s) \end{bmatrix} \begin{bmatrix} \Delta\alpha(s) \\ \Delta P_m(s) \\ \Delta E_{fd}(s) \end{bmatrix} \tag{4.43}$$

The control system design strategy for the TCSC coincides with that of the SVC and the partitioned system used for design is provided by equations (4.14) and (4.15). Expressions for individual and

multiple channels, multiple subsystem transfer functions and cross-reference disturbances are given by (4.16)–(4.19), (A.33) and (A.34).

Assuming $h_1(s) = 1$, Multiple Channel $\mathbf{M}_{12}(s)$ is designed as a separate 2×2 system. Once controllers $k_{11}(s)$ and $k_{22}(s)$ are obtained, $\mathbf{H}_2$ can be defined (that is, the interaction of $\mathbf{M}_{12}(s)$ with $C_3(s)$) and the controller $k_{33}(s)$ for Individual Channel $C_3(s)$ as indicated in equation (4.16) can be designed. This is followed by the calculation of an expression for $h_1(s)$ (interaction with $\mathbf{M}_{12}(s)$) and controllers $k_{11}(s)$ and $k_{22}(s)$ are re-designed. This sequence is repeated until a successful multivariable controller is achieved for all channels and robustness is assured in all three individual channels, subsystems $\mathbf{H}_i(s)$, and MSFs $\gamma_i(s)$.

4.4.3. Control system design example

4.4.3.1. Study 1. Varying series compensation with a fixed tie-line reactance value

After the analysis of the MSFs and transfer function matrix corresponding to the operating conditions set out in Table 4.9, the following diagonal controller

$$\begin{aligned}\mathbf{K_1}(s) &= \begin{bmatrix} k_{11}(s) & 0 & 0 \\ 0 & k_{22}(s) & 0 \\ 0 & 0 & k_{33}(s) \end{bmatrix} \\ &= \operatorname{diag}\left[\frac{5.75\left(s^2+6.1s+165.5\right)}{s^2(s+5)}, \quad \frac{14(s+0.43)}{s}, \quad \frac{k_{TCSC}(s+0.2)}{s(s+7)(s+0.7)} \right]\end{aligned} \tag{4.44}$$

is obtained, where k_{TCSC} is a scalar gain for the TCSC impedance control loop which varies according to the level of compensation; for instance, $k_{TCSC} = -1$ for 50%, –2 for 25% and –16 for 10% compensation. Notice from Table 4.9 that the tie-line reactance is kept at a constant value of $X_t = 0.4$ *p.u.* The indicators of control system performance and robustness are presented in Figures 4.64–4.67, and all relevant information for the control system design is summarised in Table 4.11.

Table 4.11. Structural and stability robustness of the channels and control system. Study 1: Varying series compensation with a fixed tie-line reactance value

Condition	Measure	$C_1(s)$	$k_{11}g_{11}(s)$	$\gamma_1(s)$	$C_2(s)$	$k_{22}g_{22}(s)$	$\gamma_2(s)$	$C_3(s)$	$k_{33}g_{33}(s)$	$\gamma_3(s)$
X_{TCSC} = –0.2 *p.u* 50% comp.	**Bandwidth** (*rad/s*)	0.761	0.328	–	1.49	1.38	–	1.15	0.443	–
	Gain margin (*dB*)	67.1	66.3	10.86	∞	∞	55.14	40.3	∞	6.63
	Phase margin (*deg*)	64.1	80.6	98.79	73.6	91.8	163.6	62.8	124	46.6
X_{TCSC} = –0.1 *p.u* 25% comp.	**Bandwidth** (*rad/s*)	0.614	0.383	–	1.86	1.86	–	0.481	0.036	–
	Gain margin (*dB*)	41.2	39.5	15.66	∞	∞	39.41	28.2	∞	25.28
	Phase margin (*deg*)	54	79.3	134.6	89.7	89.7	∞	66.8	95.9	112
X_{TCSC} = –0.04 *p.u* 10% comp.	**Bandwidth** (*rad/s*)	0.672	0.415	–	2.12	2.1	–	0.503	0.0212	–
	Gain margin (*dB*)	37.8	36.2	14.31	∞	∞	20.62	20.6	∞	∞
	Phase margin (*deg*)	50.2	78.8	128.6	89.8	89	∞	64	93.2	113

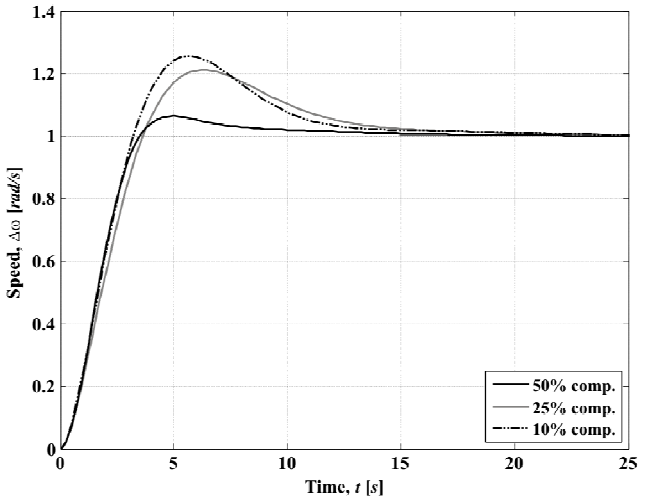

(*a*)

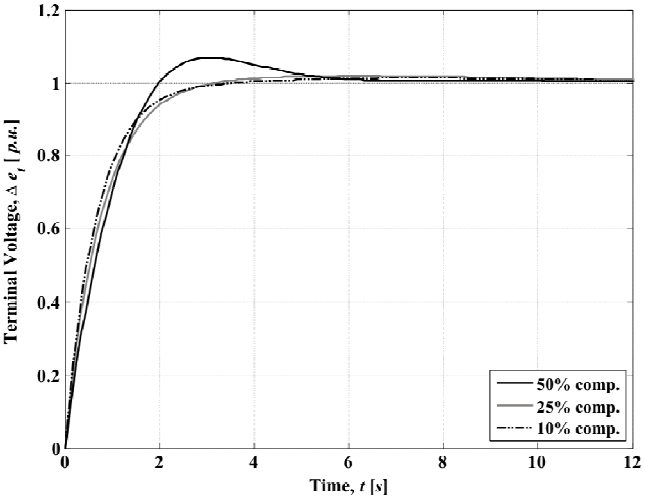

(*b*)

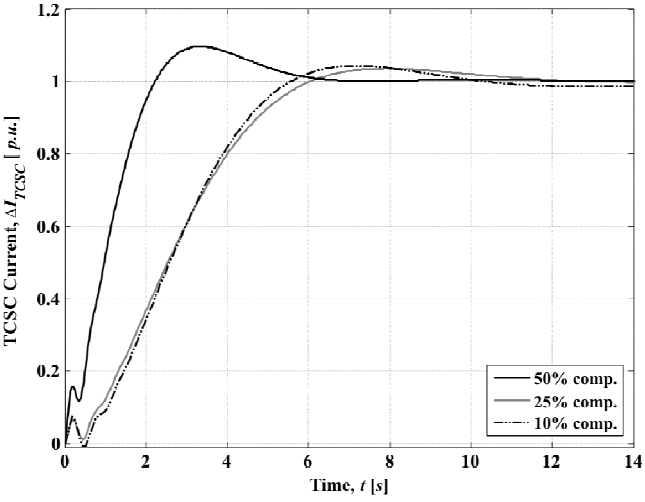

(*c*)

Figure 4.64. System performance (Study 1). Step response of: (*a*) Channel 1 ($T_{c1}(s)$); (*b*) Channel 2 ($T_{c2}(s)$); (*c*) Channel 3 ($T_{c3}(s)$)

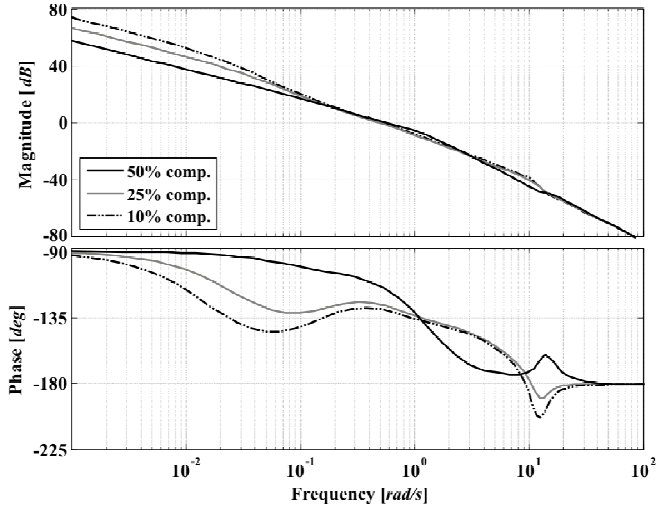

(*a*)

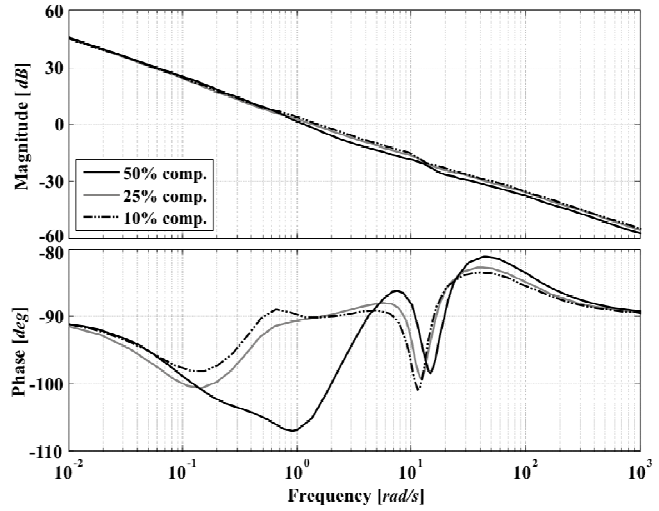

(*b*)

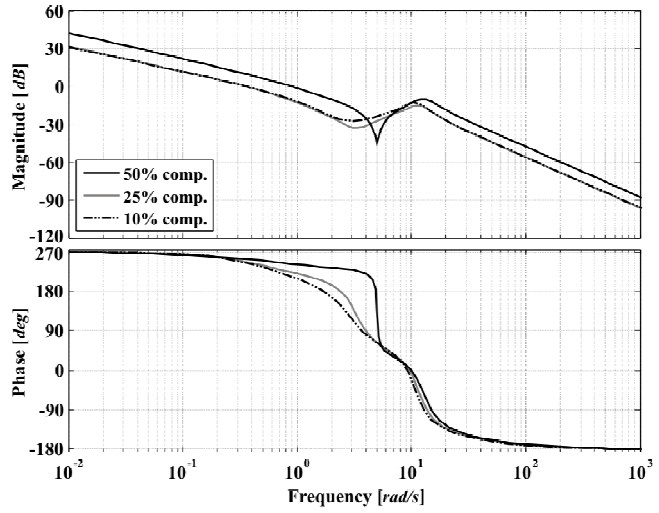

(*c*)

Figure 4.65. System performance and stability robustness assessment (Study 1). Bode diagrams: (*a*) Channel 1 ($C_1(s)$); (*b*) Channel 2 ($C_2(s)$); (*c*) Channel 3 ($C_3(s)$)

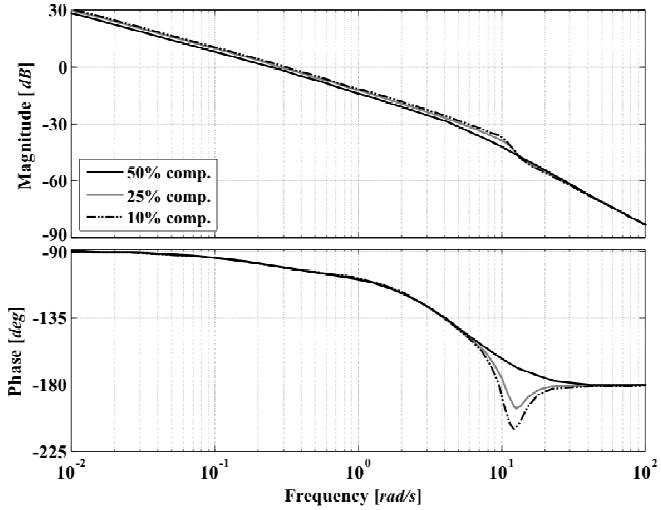

(*a*)

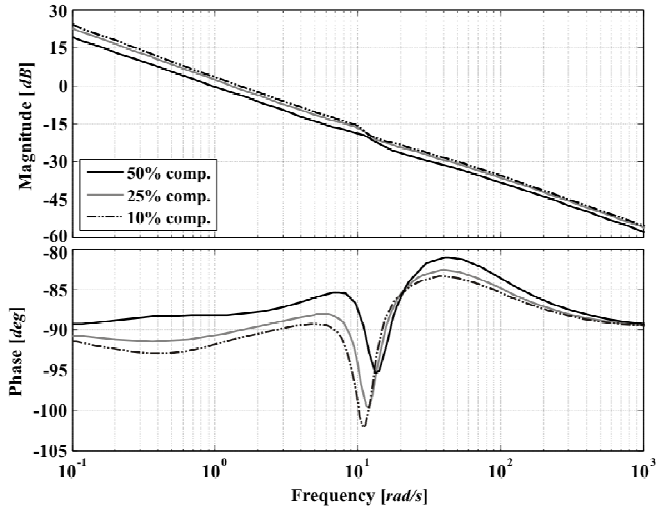

(*b*)

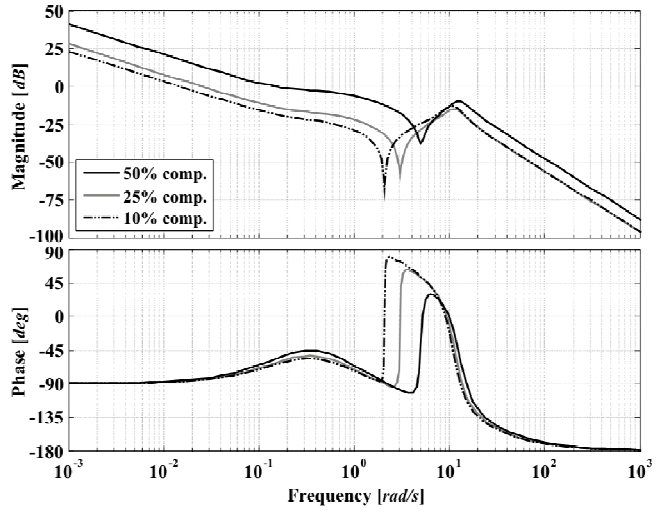

(*c*)

Figure 4.66. Stability robustness assessment (Study 1). Bode diagrams: (*a*) $k_{11}g_{11}(s)$; (*b*) $k_{22}g_{22}(s)$; (*c*) $k_{33}g_{33}(s)$

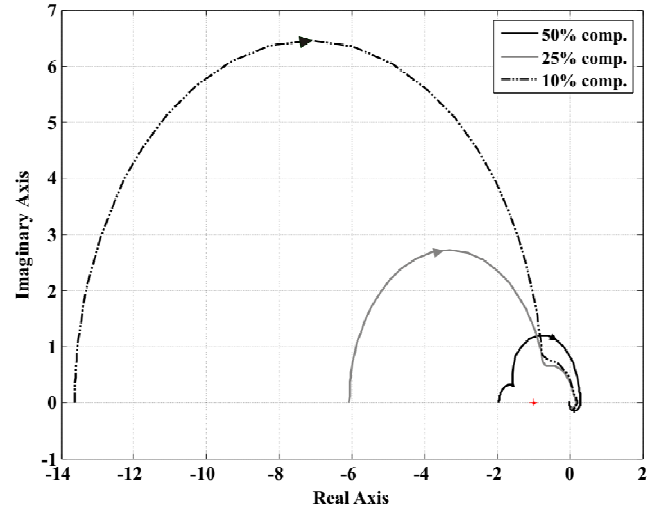

(*a*)

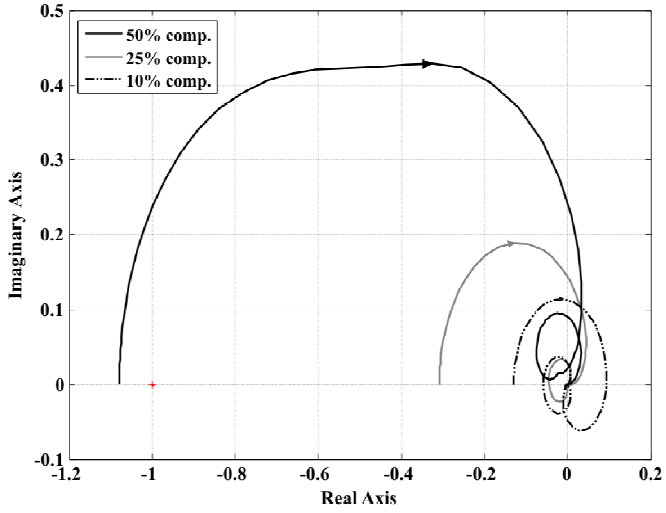

(*b*)

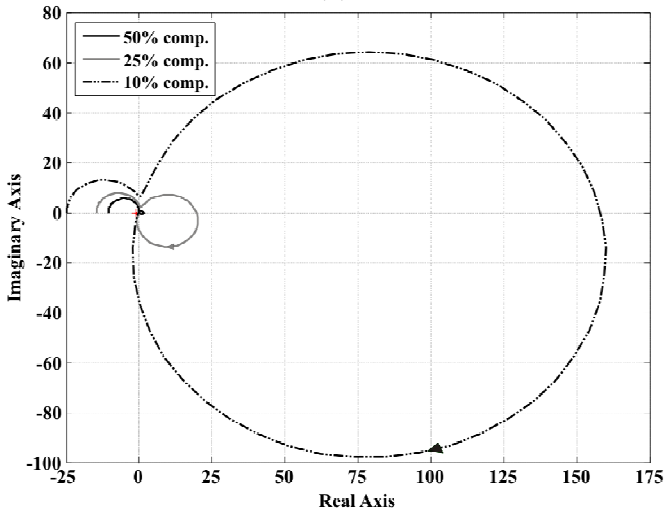

(*c*)

Figure 4.67. Structural robustness assessment (Study 1). Nyquist diagrams: (*a*) $\gamma_1(s)$; (*b*) $\gamma_2(s)$; (*c*) $\gamma_3(s)$

It is shown in Figures 4.64–4.67 and Table 4.11 that the control system performance is adequate for all operating conditions; controller (4.44) successfully decouples the generator channels and the speed regulation is effective at low frequency, blinding interactions with the higher frequency terminal voltage and TCSC impedance control channels. Moreover, the performance tends to improve with increases in the effective level of TCSC capacitive compensation. In particular, robustness measures are higher in Channels 1 and 3 with increased compensation levels. Notice that the gains k_{TCSC} in the impedance control loop in (4.44) are chosen in such a way that the bandwidths of the individual channels are maintained in Channels 1 and 2 regardless of the amount of compensation while still providing adequate robustness margins, *i.e.*, gain and phase margins over 6 *dB* and 40 *deg*, respectively [13].

Remarks: Although performance seems to be adequate, it is of great importance to notice that channel $C_3(s)$ is non-minimum phase. In fact, it can be seen from Figure 4.67(*c*) that $\gamma_3(s)$ encircles the point (1,0) twice in clockwise direction for all operating conditions. Also, the step responses in Figure 4.64(*c*) show an inverse response due to the presence of RHPZs – characteristic feature of non-minimum phase systems. Table 4.12 shows relevant information associated to the non-minimum phase characteristic of $C_3(s)$. It can be seen that for all compensation cases, $\gamma_3(s)$ and $C_3(s)$ possess an unstable complex conjugate zero pair of the form

$$\left(s^2 + 2\zeta\omega_n s + \omega_n^2\right)$$

with roots of the form

$$\begin{aligned} Z_{1,2} &= \sigma \pm j\omega_d \\ &= -\zeta\omega_n \pm j\omega_n\sqrt{1-\zeta^2} \end{aligned}$$

where ω_n is the natural frequency, ζ is damping ratio and ω_d is the damped natural frequency. The RHPZs in the TCSC channel are lightly damped; moreover, the damping ratio ζ decreases with an increase in series compensation. For instance, the considerably low damping in the case of 50% of series compensation can be assessed in Figure 4.65(*c*): the Bode magnitude plot shows a significant resonance at the natural frequency ω_n of the zero pair (≈ 5 *rad/s*), while 180 *deg* are quickly lost in the phase plot. The presence of RHPZs poses a major inconvenience for control system design and limits system performance. The bandwidth of $C_3(s)$ should be kept low and below the values of the unstable zero pair; otherwise, instability might arise. In addition, it is not possible to arbitrarily reduce sensitivity to uncertainty [31,32]. Therefore, as evidenced in Figure 4.65(*c*) and Tables 4.11–4.12, the bandwidths of the TCSC impedance control loop, for all cases, had to be reduced below the natural frequencies of the RHPZs.

It should also be mentioned that the diagonal controller (4.44), by including an integral action in each of its individual elements, guarantees a high gain at low frequencies and a zero steady-state error. The extra lead zero-pole pair in $k_3(s)$ is used to increase stability margins.

Table 4.12. $C_3(s)$ non-minimum phase assessment. Study 1.

Condition	Non-minimum phase term		RHPZs $C_3(s)$	Damped Natural Freq. ω_d (*rad/s*)	Natural Freq. ω_n (*rad/s*)	Damping Ratio ζ	Bandwidth $C_3(s)$ (*rad/s*)
	$\gamma_3(s)$	$C_3(s)$					
50% comp.	$(s^2 - 0.41s + 78.95)$	$(s^2 - 0.25s + 24.97)$	$0.12685 \pm j4.99539$	4.99539	4.997	–0.02539	1.15
25% comp.	$(s^2 - 7.82s + 79.91)$	$(s^2 - 1.645s + 10.54)$	$0.8225 \pm j3.14062$	3.14062	3.247	–0.25334	0.481
10% comp.	$(s^2 - 10.57s + 84.53)$	$(s^2 - 2.315s + 7.995)$	$1.1575 \pm j2.57977$	2.57977	2.828	–0.40937	0.503

4.4.3.2. Study 2. Effect of constant series compensation in different tie-line reactance systems

The synchronous generator – TCSC system with a range of tie-line reactance values while keeping a fixed amount of series compensation is studied. As indicated in Table 4.10, the series compensation value is kept constant, *i.e.*, $X_{TCSC} = -0.2$ *p.u.* The controller (4.44) is used in this study, where $k_{TCSC} = -1$ for $X_t = 0.4$ *p.u.*, $k_{TCSC} = -3/4$ for $X_t = 0.5$ *p.u.*, and $k_{TCSC} = -1/2$ for $X_t = 0.6$ *p.u.* The control system performance and robustness measurements are presented in Figures 4.68–4.71 and Table 4.13.

From these results, it can be seen that the control system performance is adequate for all operating conditions, even for the case of a long transmission line ($X_t = 0.6$ *p.u.*) fitted with series compensation. It can be noticed that an increase in the tie-line reactance value increases channel coupling, leading to decreasing robustness measures and performance. Similarly to the previous study case, channel $C_3(s)$ is non-minimum phase since $\gamma_3(s)$ circles the point (1,0) twice in clockwise direction for all operating conditions. As a consequence, the bandwidth of $C_3(s)$ had to be reduced below the natural frequency of the channel RHPZs. Relevant information associated to the non-minimum phase characteristic of $C_3(s)$ is given in Table 4.14. The remarks of Study 1 in Section 4.4.3.1 fully apply to Study 2.

Table 4.13. Structural and stability robustness of the channels and control system. Study 2: Effect of constant series compensation in different tie-line reactance systems

Condition	Measure	$C_1(s)$	$k_{11}g_{11}(s)$	$\gamma_1(s)$	$C_2(s)$	$k_{22}g_{22}(s)$	$\gamma_2(s)$	$C_3(s)$	$k_{33}g_{33}(s)$	$\gamma_3(s)$
$X_t = 0.4$ *p.u* 50% comp.	**Bandwidth** (*rad/s*)	0.761	0.328	–	1.49	1.38	–	1.15	0.443	–
	Gain margin (*dB*)	67.1	66.3	10.86	∞	∞	55.14	40.3	∞	6.63
	Phase margin (*deg*)	64.1	80.6	98.79	73.6	91.8	163.6	62.8	124	46.6
$X_t = 0.5$ *p.u* 40% comp.	**Bandwidth** (*rad/s*)	0.74	0.377	–	1.77	1.78	–	0.67	0.0575	–
	Gain margin (*dB*)	43.2	39.9	11.62	∞	∞	64	24.3	∞	25.2
	Phase margin (*deg*)	47.8	77.3	109.8	87.6	88.7	∞	57	99.2	112
$X_t = 0.6$ *p.u* 33% comp.	**Bandwidth** (*rad/s*)	0.645	0.42	–	2.1	2.08	–	0.452	0.0085	–
	Gain margin (*dB*)	36.7	34.6	13.68	∞	∞	15.5	18.8	∞	∞
	Phase margin (*deg*)	50.7	74.5	130	87.8	87	∞	64.7	91.2	112

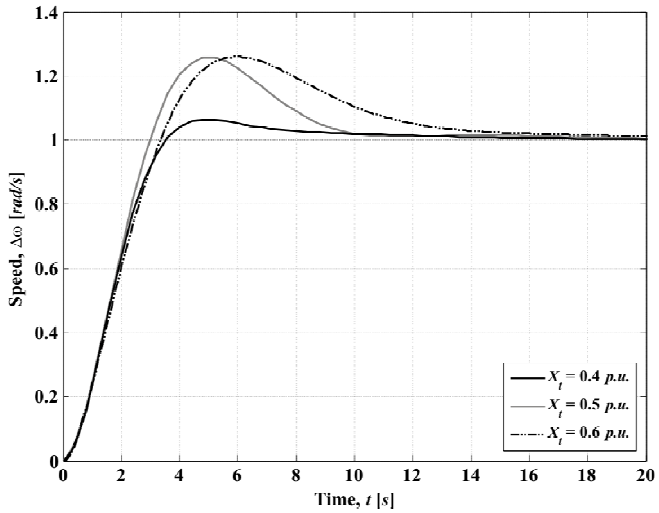

(*a*)

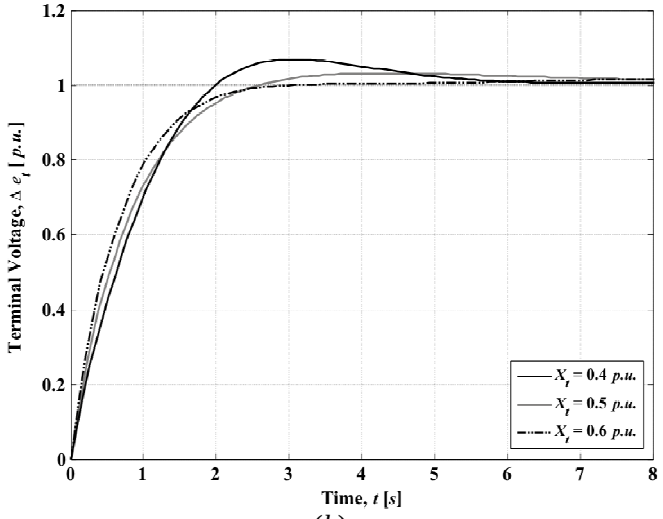

(*b*)

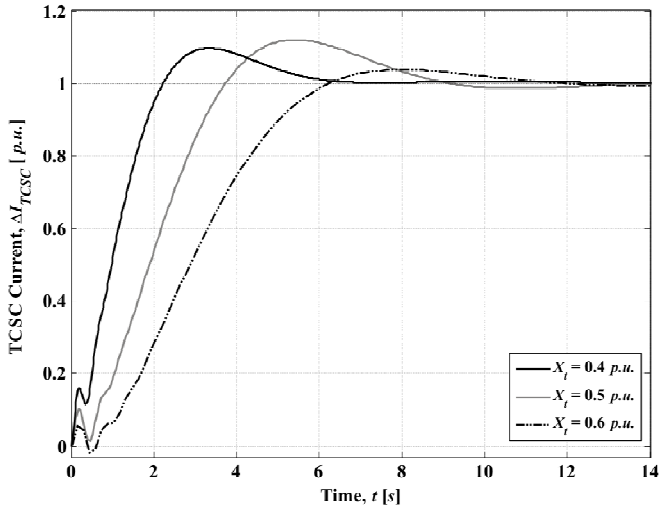

(*c*)

Figure 4.68. System performance (Study 2). Step response of: (*a*) Channel 1 ($T_{c1}(s)$); (*b*) Channel 2 ($T_{c2}(s)$); (*c*) Channel 3 ($T_{c3}(s)$)

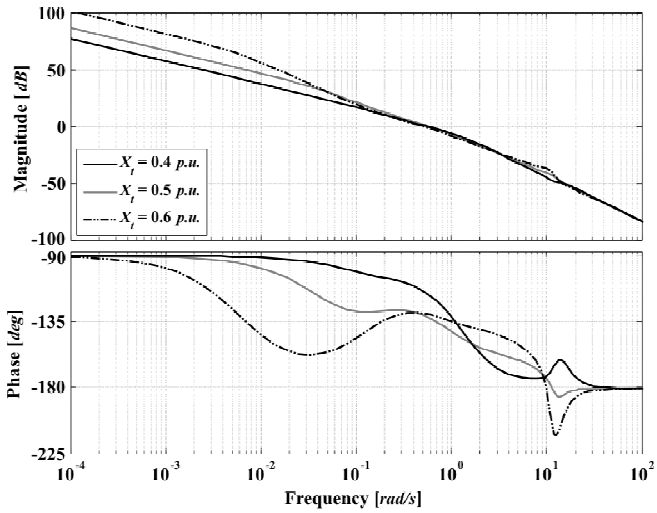

(*a*)

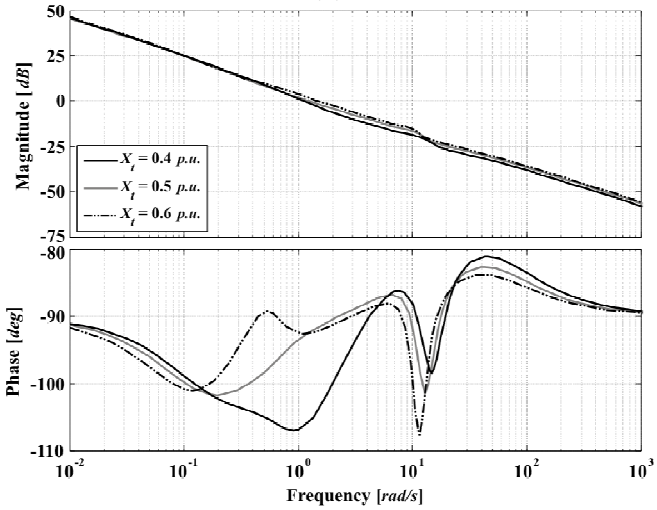

(*b*)

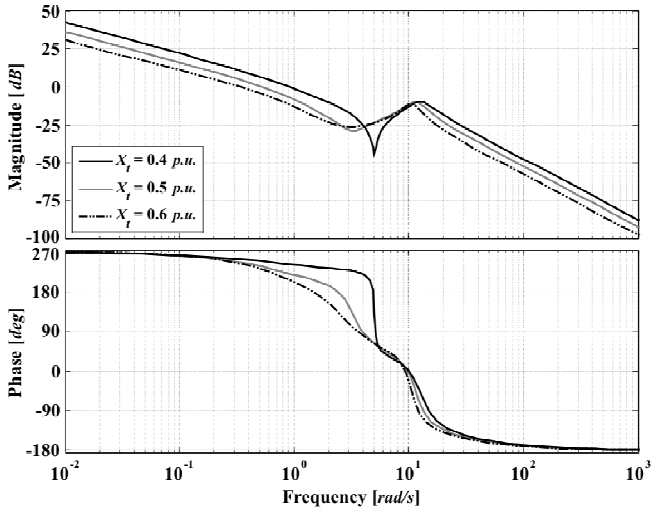

(*c*)

Figure 4.69. System performance and stability robustness assessment (Study 2). Bode diagrams: (*a*) Channel 1 ($C_1(s)$); (*b*) Channel 2 ($C_2(s)$); (*c*) Channel 3 ($C_3(s)$)

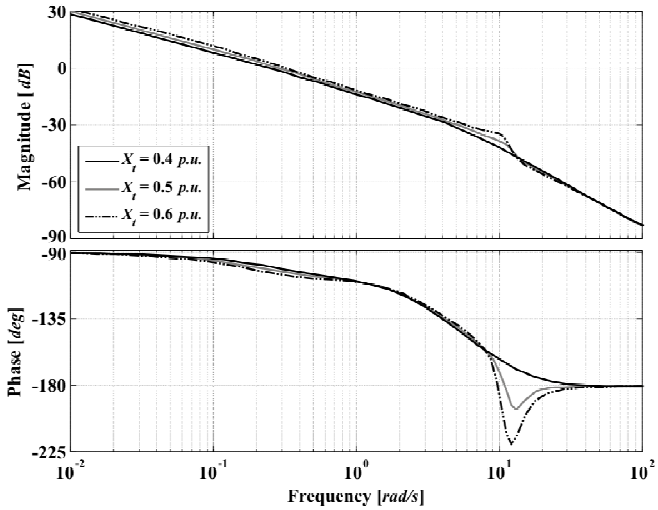

(*a*)

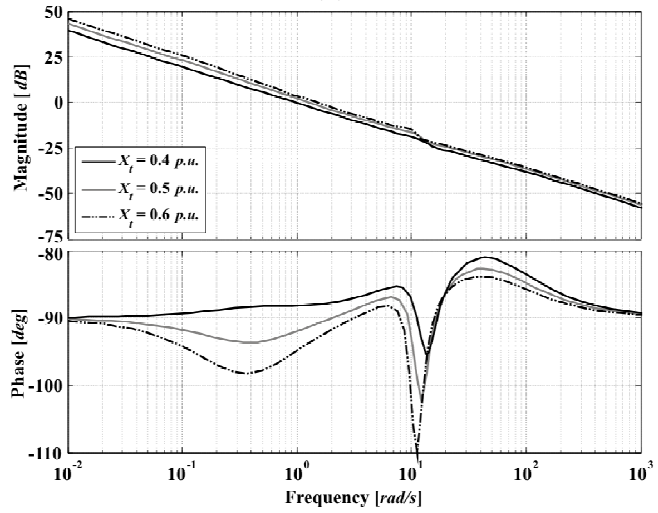

(*b*)

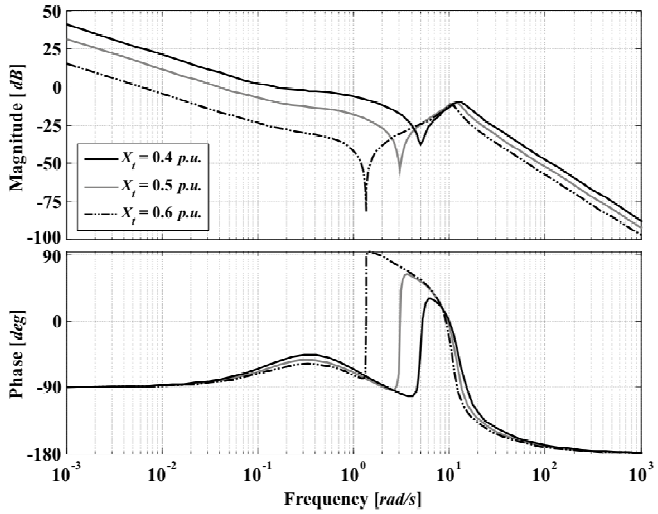

(*c*)

Figure 4.70. Stability robustness assessment (Study 2). Bode diagrams: (*a*) $k_{11}g_{11}(s)$; (*b*) $k_{22}g_{22}(s)$; (*c*) $k_{33}g_{33}(s)$

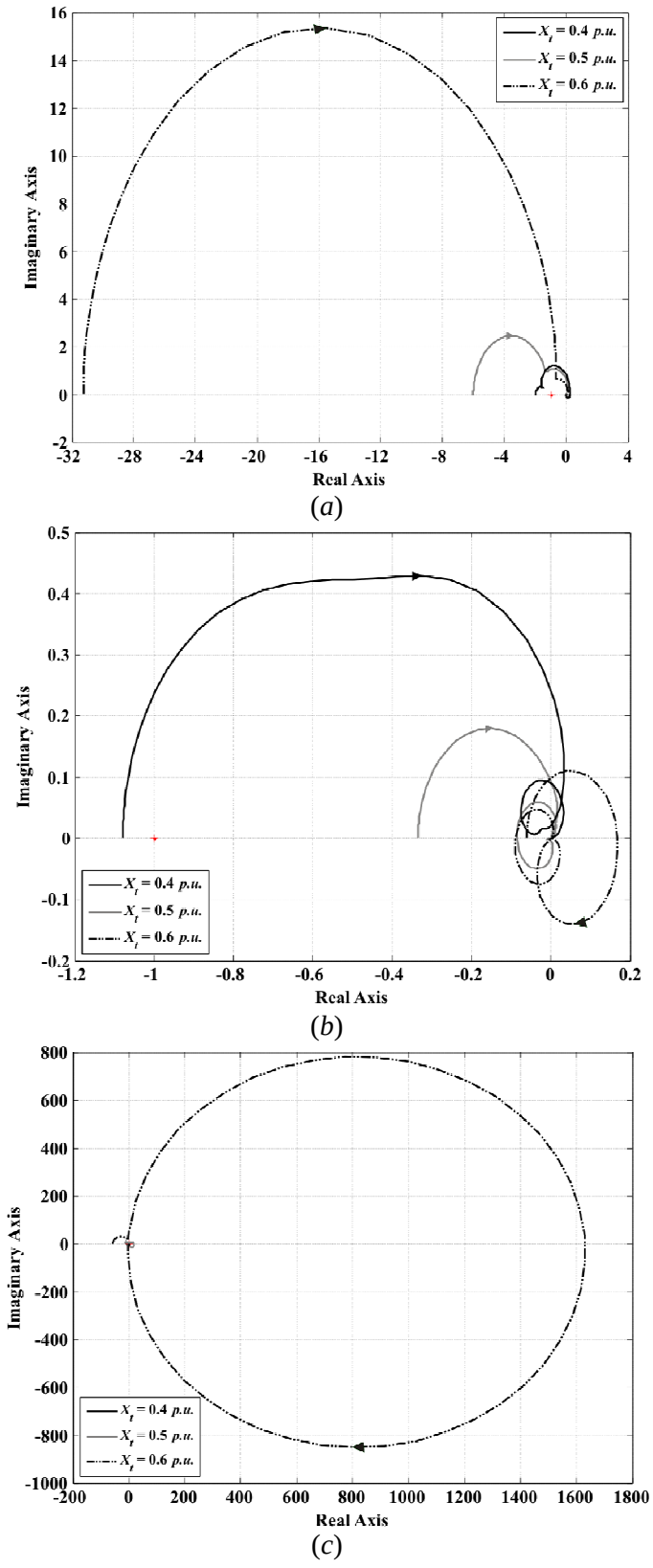

Figure 4.71. Structural robustness assessment (Study 2). Nyquist diagrams: (*a*) $\gamma_1(s)$; (*b*) $\gamma_2(s)$; (*c*) $\gamma_3(s)$

Table 4.14. $C_3(s)$ non-minimum phase assessment. Study 2.

Condition	Non-minimum phase term		RHPZs $C_3(s)$	Damped Natural Freq. ω_d (*rad/s*)	Natural Freq. ω_n (*rad/s*)	Damping Ratio ζ	Bandwidth $C_3(s)$ (*rad/s*)
	$\gamma_3(s)$	$C_3(s)$					
50% comp.	$(s^2 - 0.41s + 78.95)$	$(s^2 - 0.25s + 24.97)$	$0.12685 \pm j4.99539$	4.99539	4.997	–0.02539	1.15
40% comp.	$(s^2 - 7.907s + 79.76)$	$(s^2 - 1.649s + 10.48)$	$0.8245 \pm j3.13053$	3.13053	3.237	–0.25469	0.67
33% comp.	$(s^2 - 12.2s + 86.79)$	$(s^2 - 2.648s + 7.14)$	$1.324 \pm j2.321$	2.321	2.672	–0.49549	0.452

4.4.4. TCSC influence on the system

The control system characteristics are investigated to assess the influence that the TCSC exerts on the system. The TCSC is used to decrease the electrical length of the transmission line in order to boost active power transfer. A high value of tie-line reactance X_t = 0.6 *p.u.* is used. When in operation, the TCSC provides a 33.33% of series compensation (X_{TCSC} = –0.2 *p.u.*). Table 4.15 shows the system operating conditions used as the basis for comparison.

Figure 4.72 shows the relevant MSFs with and with no TCSC. The MSF $\Gamma_2(s)$ (considering transfer function matrix $\mathbf{G}_{312}$) gives a measure of coupling between the channels of the synchronous generator $C_1(s)$ –speed– and $C_2(s)$ –voltage– when the TCSC is used. On the other hand, $\gamma_a(s)$ provides the coupling measure for the synchronous generator when no TCSC is used. It can be observed that both $\Gamma_2(s)$ and $\gamma_a(s)$ have a similar frequency response – that is, the dynamical structure is preserved. The use of the TCSC results in lower coupling and an increase in robustness measures (in terms of gain and phase margins). Notice how the peak in the magnitude plot in Figure 4.72(*b*) is transported to higher frequencies when using the TCSC.

Table 4.15. Operating conditions for assessing TCSC influence on the system

Parameter	Value with TCSC	Value with no TCSC	Parameter	Value with TCSC	Value with no TCSC
P_g	0.736 *p.u.*	0.736 *p.u.*	$\angle i_{t0}$ / $\angle I_{\infty 0}$	48.461°	56.124°
Q_g	0.345 *p.u.*	0.2498 *p.u.*	$\lvert V_{TCSC0}\rvert$ / $\lvert V_{mid}\rvert$	1.104 *p.u.*	1.001 *p.u.*
PF	0.95204	0.94695	$\angle V_{TCSC0}$ / $\angle V_{mid}$	73.578°	62.743°
δ_0	40°	40°	E_{fd0}	1.6668 *p.u.*	1.6098 *p.u.*
$\lvert V_{\infty 0}\rvert$	1 *p.u.*	1 *p.u.*	X_{TCSC}	–0.2 *p.u.*	–
$\angle V_{\infty 0}$	50°	50°	α_0	143.08°	–
$\lvert e_{t0}\rvert$	1.05 *p.u.*	1.05 *p.u.*	$\partial X_{TCSC} / \partial \alpha_0$	20.431	–
$\angle e_{t0}$	66.278°	74.871°	X_t	0.6 *p.u.*	0.6 *p.u.*
$\lvert i_{t0}\rvert$ / $\lvert I_{\infty 0}\rvert$	0.73626 *p.u.*	0.74022 *p.u.*	X_{total}	0.4 *p.u.*	0.6 *p.u.*

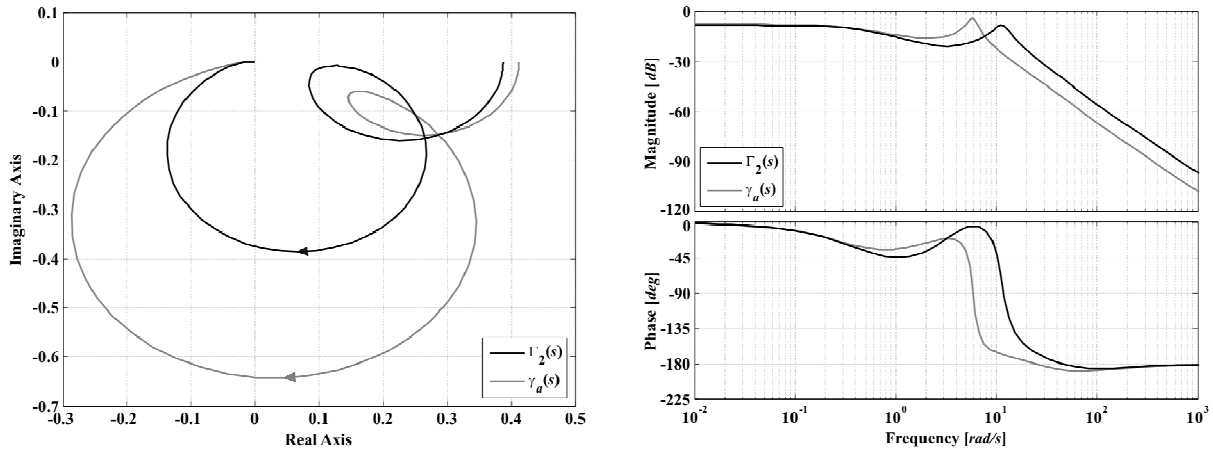

(*a*) (*b*)

Figure 4.72. Assessment of $\gamma_a(s)$ vs $\Gamma_2(s)$ (considering $\mathbf{G}_{312}$). (*a*) Nyquist plot; (*b*) Bode plot

The performance of the synchronous generator is compared to that obtained for the system including one TCSC. A controller for the 2×2 system with no TCSC impedance control loop $k_{33}(s)$ is considered,

$$\mathbf{K}_1(s) = \begin{bmatrix} k_{11}(s) & 0 \\ 0 & k_{22}(s) \end{bmatrix} = \text{diag}\left[\frac{5.75\left(s^2 + 6.1s + 165.5\right)}{s^2\left(s+5\right)} \quad \frac{14\left(s+0.43\right)}{s} \right] \tag{4.45}$$

Figures 4.73–4.76 show the performance of the control system (terminal voltage and speed channels) and robustness assessment with and with no TCSC, *i.e.*, using controllers (4.44) and (4.45), respectively, with $k_{TCSC} = -1/2$. Table 4.16 summarises key information relating to this study.

Table 4.16. Structural and stability robustness of the channels and control system with and with no TCSC. Weak transmission system

Measure	$C_1(s)$		$k_{11}g_{11}(s)$		$\gamma_1(s)$ / $\gamma_a h_2(s)$		$C_2(s)$		$k_{22}g_{22}(s)$		$\gamma_2(s)$ / $\gamma_a h_1(s)$	
	TCSC	w/o	TCSC	w/o	TCSC	w/o	TCSC	w/o	TCSC	w/o	TCSC	w/o
Bandwidth (*rad/s*)	0.645	1.12	0.42	1.19	—	—	2.1	2.97	2.08	2.83	—	—
Gain margin (*dB*)	36.7	7.1	34.6	8.54	13.68	7.7	∞	∞	∞	∞	15.5	7.68
Phase margin (*deg*)	50.7	83.9	74.5	71.6	130	∞	87.8	89.5	87	85.7	∞	∞

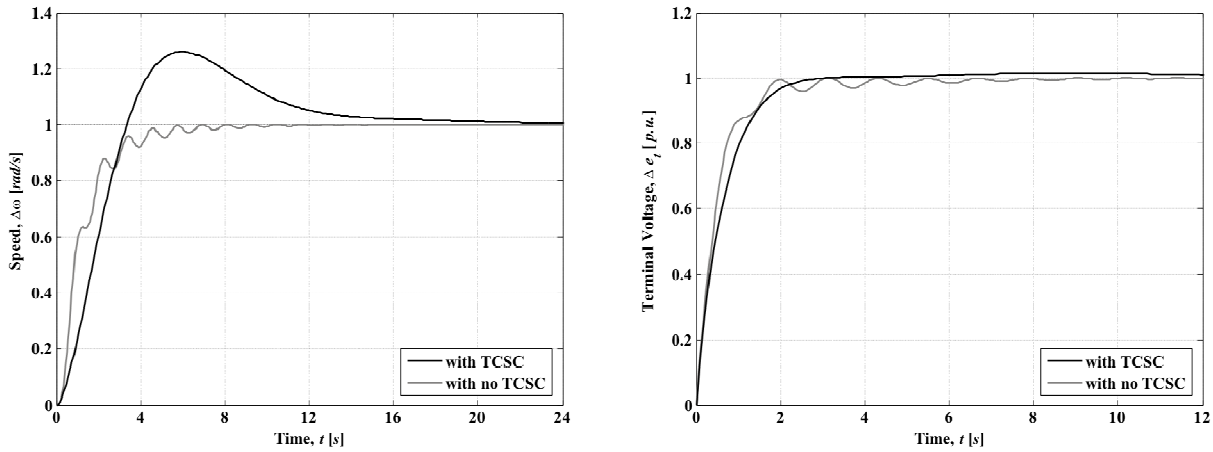

(*a*) (*b*)

Figure 4.73. System performance with and with no TCSC. Step response of: (*a*) Channel 1 ($T_{c1}(s)$); (*b*) Channel 2 ($T_{c2}(s)$)

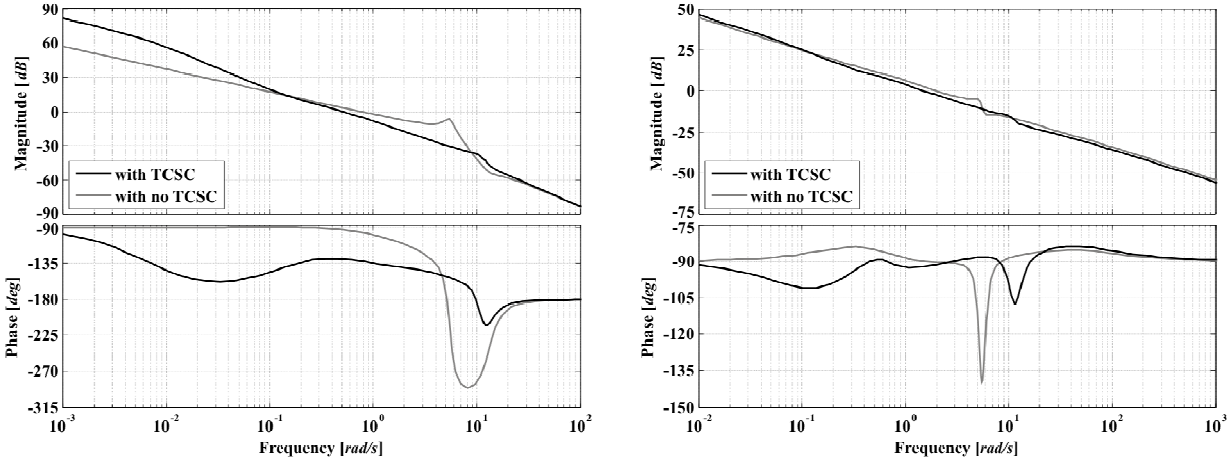

(*a*) (*b*)

Figure 4.74. System performance and stability robustness assessment with and with no TCSC. Bode diagrams: (*a*) Channel 1 ($C_1(s)$); (*b*) Channel 2 ($C_2(s)$)

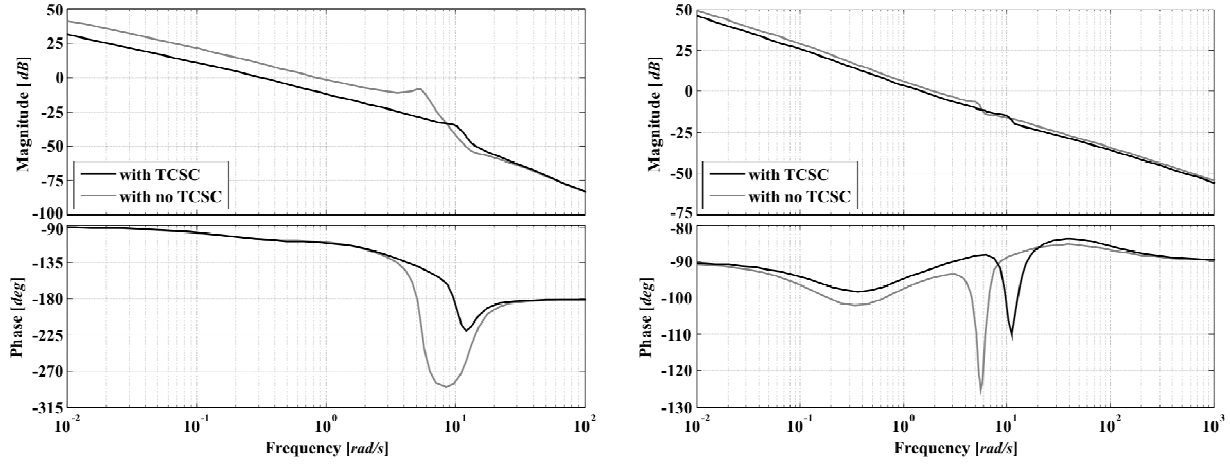

(*a*) (*b*)

Figure 4.75. Stability robustness assessment with and with no TCSC. Bode diagrams: (*a*) $k_{11}g_{11}(s)$; (*b*) $k_{22}g_{22}(s)$

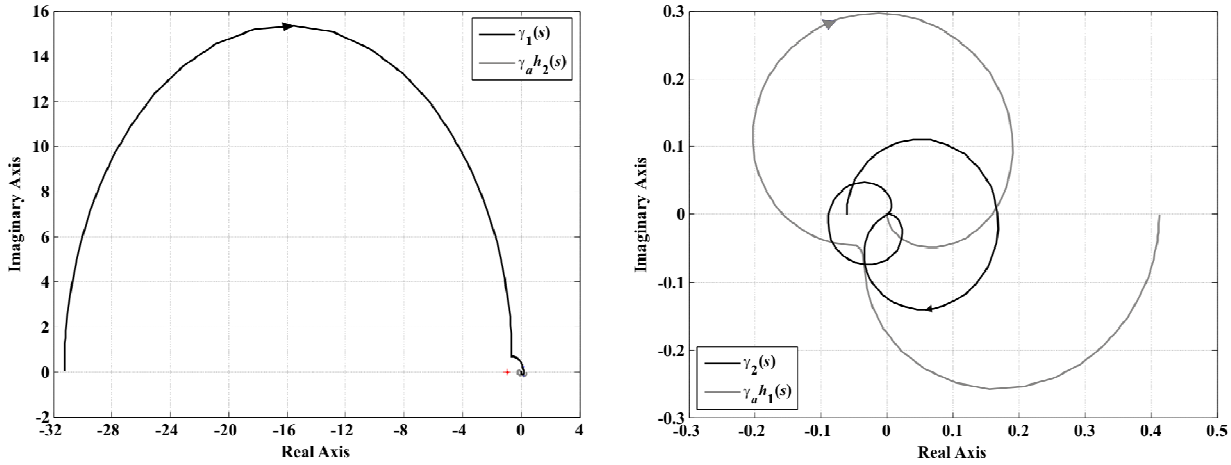

(*a*) (*b*)

Figure 4.76. Structural robustness assessment with and with no TCSC. Nyquist diagrams: (*a*) $\gamma_a h_2(s)$ vs $\gamma_1(s)$; (*b*) $\gamma_a h_1(s)$ vs $\gamma_2(s)$

From Figure 4.73, it can be seen that the system tends to be oscillatory when no TCSC is used. However, the Bode diagram of $C_1(s)$ in Figure 4.74 shows that the use of the TCSC causes a decrease in robustness in terms of phase margin, as also evidenced in Table 4.16 – which is proof that $C_3(s)$ couples very significantly with the speed channel $C_1(s)$. However, an important positive effect of the inclusion of the TCSC can be appreciated in the Bode diagram of $C_2(s)$ shown in Figure 4.74: the switch-back characteristic, which is quite prominent with no TCSC, reduces very considerably and moves on to higher frequencies. Also, the use of the TCSC does not affect structural robustness in the voltage channel $C_2(s)$, but tends to worsen the speed channel $C_1(s)$ (Figures 4.75 and 4.76).

4.4.5. Extreme cases of TCSC operation

Although the TCSC has two distinctive regions of operation, it is common practice to operate it in the capacitive region. In the case of the TCSC impedance characteristic of the Kayenta installation [30], shown in Figure 4.49, the capacitive region of operation starts at firing angles greater than 142.531°. Moreover, the closer the firing angle to the resonance is, the higher the amount of series compensation that can be achieved. However, the amount of series compensation is physically limited by the risk of a series resonance, leading to a *sub-synchronous resonance* (SSR), and the reactive power that the synchronous machine is able to supply to or absorb from the system. On the other hand, for values of firing angle smaller than the resonant point, the TCSC will operate in its inductive region. Both extreme cases of operation will be examined in detail in this section.

4.4.5.1. High values of capacitive compensation

Consider a system with the operating conditions given in Table 4.17, where a high value of tie-line reactance is taken, X_t = 0.6 *p.u.* Three cases of series compensation are examined while keeping active power constant: 70% (X_{TCSC} = –0.42 *p.u.*), 80% (X_{TCSC} = –0.48 *p.u.*) and 83.33% (X_{TCSC} = –0.5 *p.u.*). As the amount of compensation increases, the reactive power drawn from the synchronous generator increases and the power factor tends to fall. For 83.33% compensation, the reactive power is very high. Notice that the variations of X_{TCSC} are quite large even for small variations in the controlling firing angle; therefore, the value of $F(\alpha) = \partial X_{TCSC} / \partial \alpha$ (as shown in Figure 4.49) tends to increase quite considerably with increases in compensation. Such operating conditions are contrasted to the same system with no TCSC.

In order to assess the coupling between the speed and terminal voltage channels of the synchronous generator, Figure 4.77 shows the relevant MSFs relating to the operating conditions of Table 4.17 – that is, MSFs $\Gamma_2(s)$ (considering transfer function matrix $\mathbf{G}_{312}$) in the TCSC upgraded-system and $\gamma_a(s)$ for the system with no TCSC.

Table 4.17. System operating conditions for high values of compensation

Variable	**No TCSC** X_t = 0.6 *p.u.*	**Case 1** 70% comp.	**Case 2** 80% comp.	**Case 3** 83.33% comp.
P_g	0.736 *p.u.*	0.736 *p.u.*	0.736 *p.u.*	0.736 *p.u.*
Q_g	0.2498 *p.u.*	0.5884 *p.u.*	0.8 *p.u.*	0.9326 *p.u.*
PF	0.94695	0.90858	0.84348	0.80108
δ_0	30°	30°	30°	30°
$\lvert V_{\infty 0}\rvert$	1 *p.u.*	1 *p.u.*	1 *p.u.*	1 *p.u.*
$\angle V_{\infty 0}$	60°	60°	60°	60°
$\lvert e_{t0}\rvert$	1.05 *p.u.*	1.05 *p.u.*	1.05 *p.u.*	1.05 *p.u.*
$\angle e_{t0}$	84.871	67.246°	64.823°	64.027°
$\lvert i_{t0}\rvert$ / $\lvert I_{\infty 0}\rvert$	0.74022 *p.u.*	0.77148 *p.u.*	0.83102 *p.u.*	0.87501 *p.u.*
$\angle i_{t0}$ / $\angle I_{\infty 0}$	66.124°	42.556°	32.334°	27.26°
$\lvert V_{mid}\rvert$ / $\lvert V_{TCSC0}\rvert$	1.001 *p.u.*	1.2214 *p.u.*	1.3083 *p.u.*	1.3578 *p.u.*
$\angle V_{mid}$ / $\angle V_{TCSC0}$	72.743°	81.196°	79.727°	78.98°
E_{fd0}	1.4787 *p.u.*	1.7895 *p.u.*	1.9649 *p.u.*	2.0679 *p.u.*
X_{TCSC}	-	–0.42 *p.u.*	–0.48 *p.u.*	–0.5 *p.u.*
α_0	-	142.7918°	142.7589°	142.7498°
$\partial X_{TCSC} / \partial \alpha_0$	-	91.349	119.5	129.6
X_t	0.6 *p.u.*	0.6 *p.u.*	0.6 *p.u.*	0.6 *p.u.*
X_{total}	0.6 *p.u.*	0.18 *p.u.*	0.12 *p.u.*	0.1 *p.u.*

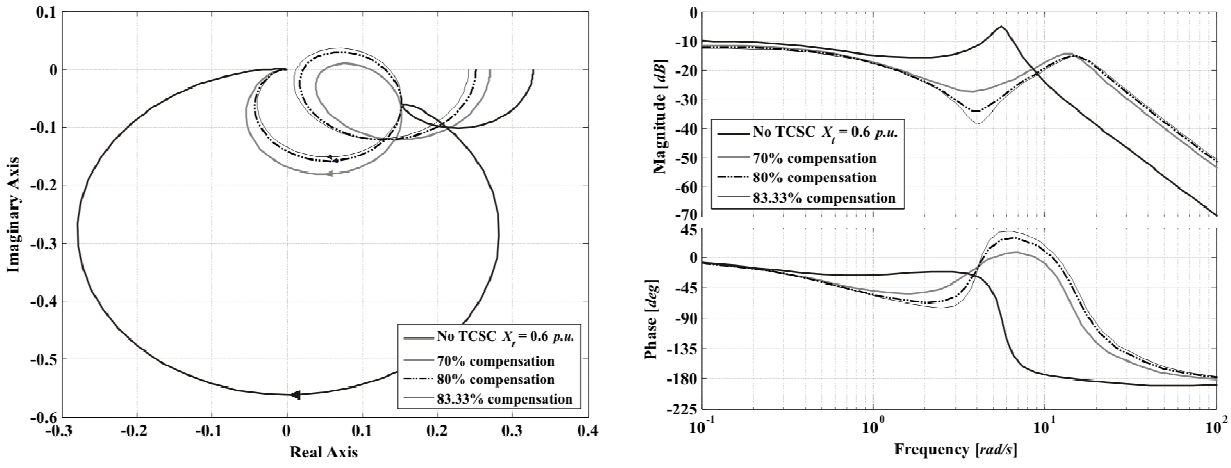

(*a*) (*b*)

Figure 4.77. Assessment of $\gamma_a(s)$ vs $\Gamma_2(s)$ (considering $\mathbf{G}_{312}$) for high compensation values. (*a*) Nyquist plot; (*b*) Bode plot

It can be seen in Figure 4.77 that the inclusion of a TCSC with high compensation values dramatically reduces the coupling between Individual Channels $C_1(s)$ and $C_2(s)$ as compared to the case when no TCSC is used. Notice how the characteristic peak of the MSFs is shifted to higher frequencies and considerably attenuated by more than 10 *dB*. As a consequence, the decrease of tie-line reactance values is reflected in the control system design by an increase in bandwidth. Revealing these features is

one of the many benefits obtained through the use of ICAD and the analysis of MSFs, not shown by other approaches.

The performance of the control system with high values of compensation is evaluated next. The values of gain k_{TCSC} in the impedance control loop in (4.44) are chosen so that a similar bandwidth is achieved for all compensation cases in $C_3(s)$: $k_{TCSC} = -0.2$ for 70% compensation, $k_{TCSC} = -0.07179$ for 80% compensation and $k_{TCSC} = -0.0468$ for 83.33% compensation. The control system performance and robustness measures are presented in Figures 4.78–4.81 and Table 4.18.

From Figures 4.78–4.81, it can be seen that the control system performance is adequate for all operating conditions. As expected, the performance is better when the amount of series compensation is higher, providing a smaller effective tie-line reactance value. Additionally, robustness measures are satisfactory, as it can be seen in Table 4.18. It should be noticed that for these operating conditions the system is minimum-phase, as shown in Figure 4.81, where the MSFs $\gamma_3(s)$ no longer encircle the point (1,0) – in fact, the gain margins tend to increase with the series compensation with the Nyquist trajectories passing farther away from the critical point. In the case of a transmission line of $X_t = 0.6$ *p.u.*, a series compensation of over 70% will ensure the system to be minimum phase. Such a condition is of great interest and relevance. An immediate benefit of the system being minimum phase is a higher bandwidth in the TCSC control loop even for high values of transmission lines and compensation levels.

It should be emphasised that an increase in series compensation modifies the structure of the MSF $\gamma_3(s)$. It turns the system from being non-minimum phase to being a minimum phase. By adjusting the amount of series compensation, the potential restrictions in performance due to non-minimum phase behaviour can be avoided. In addition, ICAD provides useful information to avoid the presence of RHPZs in Channel 3. It is well known and established that RHPZs have adverse effects in the control system performance and sensitivity [31,32].

Table 4.18. Structural and stability robustness of the channels and control system. Maximum capacitive compensation study

Condition	Measure	$C_1(s)$	$k_{11}g_{11}(s)$	$\gamma_1(s)$	$C_2(s)$	$k_{22}g_{22}(s)$	$\gamma_2(s)$	$C_3(s)$	$k_{33}g_{33}(s)$	$\gamma_3(s)$
$X_{TCSC} = -0.42$ *p.u* 70% comp.	**Bandwidth** (*rad/s*)	0.693	0.315	–	1.47	1.27	–	1.24	0.6	–
	Gain margin (*dB*)	68.6	68.2	11.76	∞	∞	55.24	∞	∞	0.72
	Phase margin (*deg*)	69	81	104.4	70.9	94.2	146.7	65.3	128	90.6
$X_{TCSC} = -0.48$ *p.u* 80% comp.	**Bandwidth** (*rad/s*)	0.442	0.272	–	1.35	0.897	–	1.29	0.461	–
	Gain margin (*dB*)	73.5	73.4	18.1	∞	∞	56.42	∞	∞	∞
	Phase margin (*deg*)	79.1	82.5	∞	63.5	95.2	118	68.7	124	92.9
$X_{TCSC} = -0.5$ *p.u* 83% comp.	**Bandwidth** (*rad/s*)	0.371	0.254	–	1.3	0.756	–	1.28	0.214	–
	Gain margin (*dB*)	75.1	75.1	21.22	∞	∞	58.56	∞	∞	∞
	Phase margin (*deg*)	81.5	83.2	∞	60.9	96.4	109.9	68	121	92.3

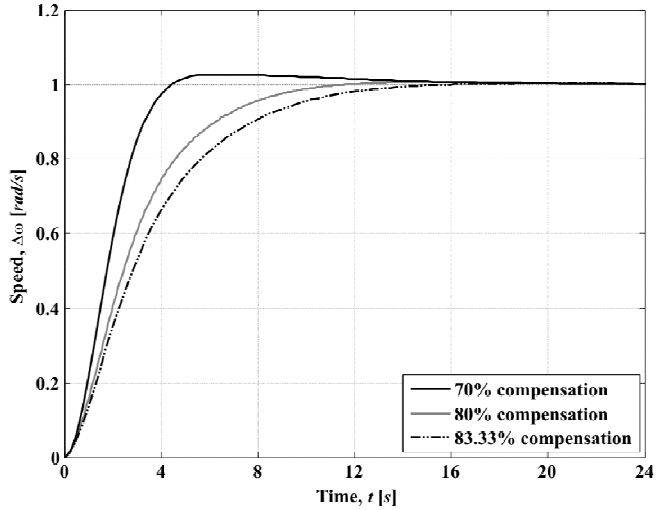

(*a*)

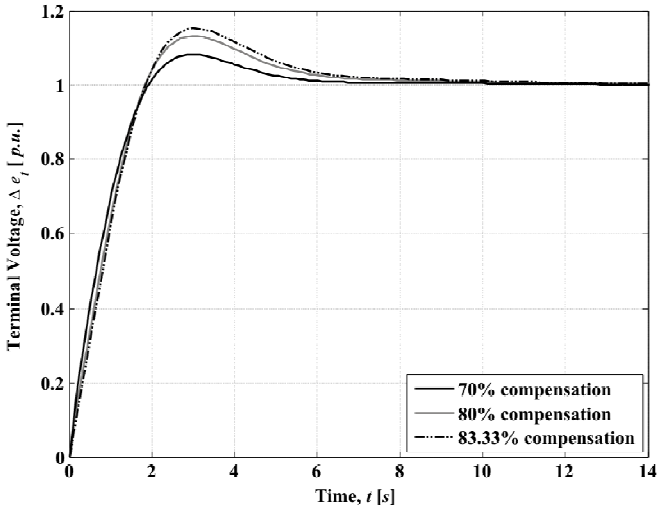

(*b*)

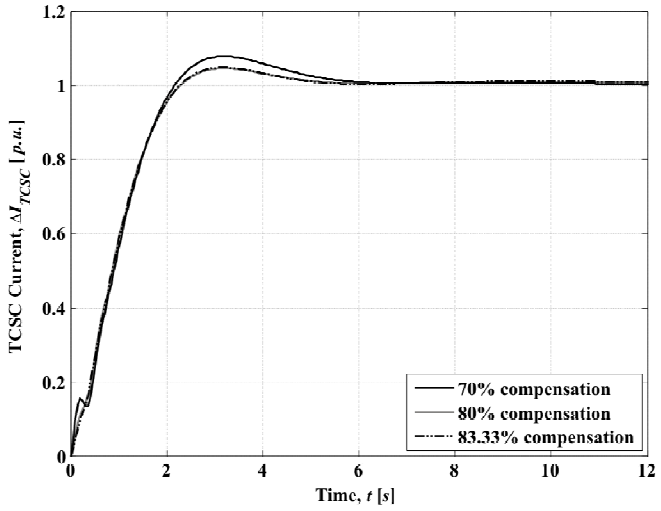

(*c*)

Figure 4.78. System performance. Step response: (*a*) Channel 1 ($T_{c1}(s)$); (*b*) Channel 2 ($T_{c2}(s)$); (*c*) Channel 3 ($T_{c3}(s)$).

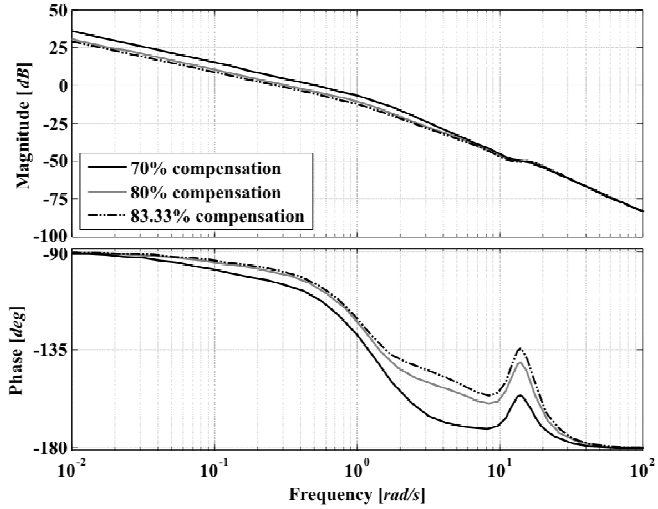

(*a*)

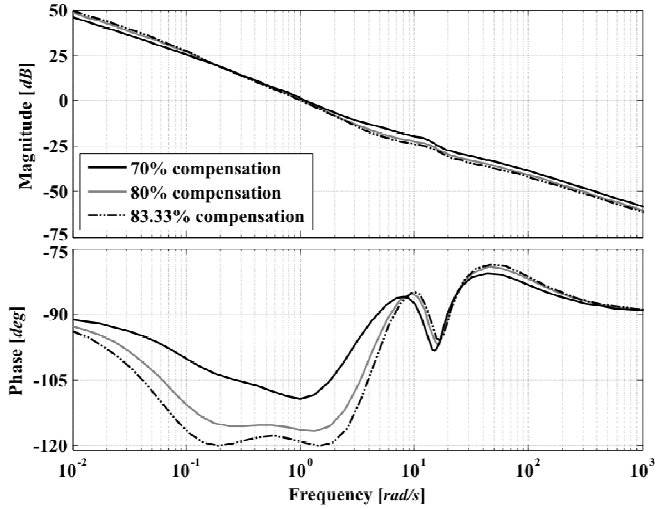

(*b*)

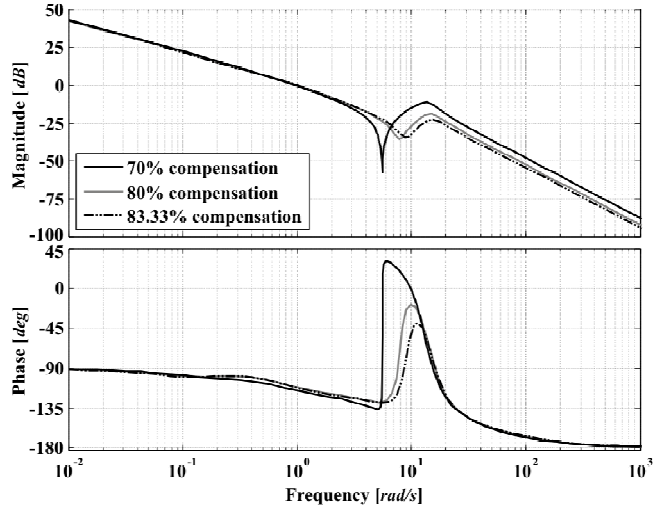

(*c*)

Figure 4.79. System performance and stability robustness assessment. Bode diagrams: (*a*) Channel 1 ($C_1(s)$); (*b*) Channel 2 ($C_2(s)$); (*c*) Channel 3 ($C_3(s)$)

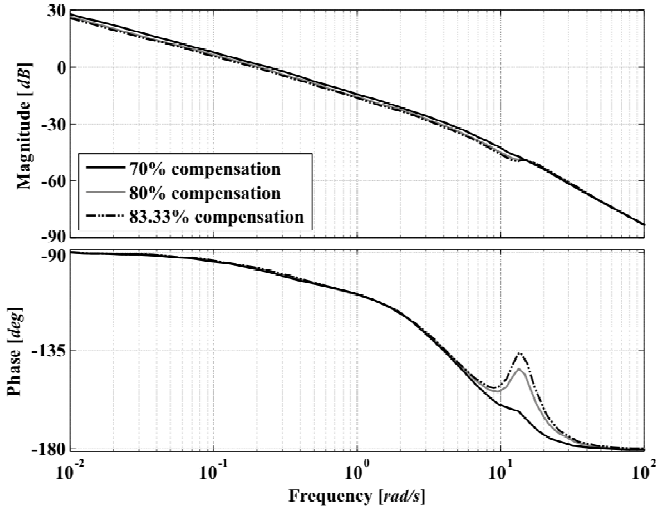

(*a*)

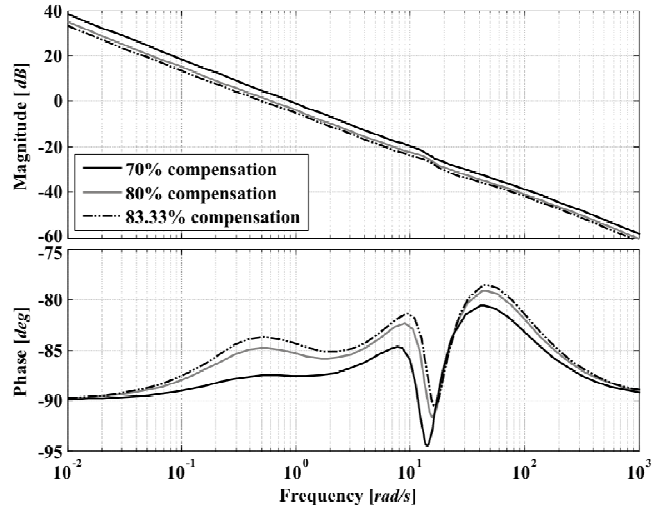

(*b*)

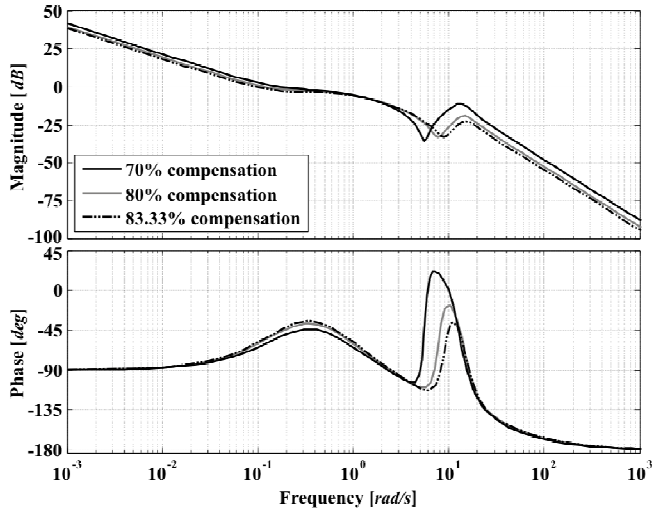

(*c*)

Figure 4.80. Stability robustness assessment. Bode diagrams: (*a*) $k_{11}g_{11}(s)$; (*b*) $k_{22}g_{22}(s)$; (*c*) $k_{33}g_{33}(s)$

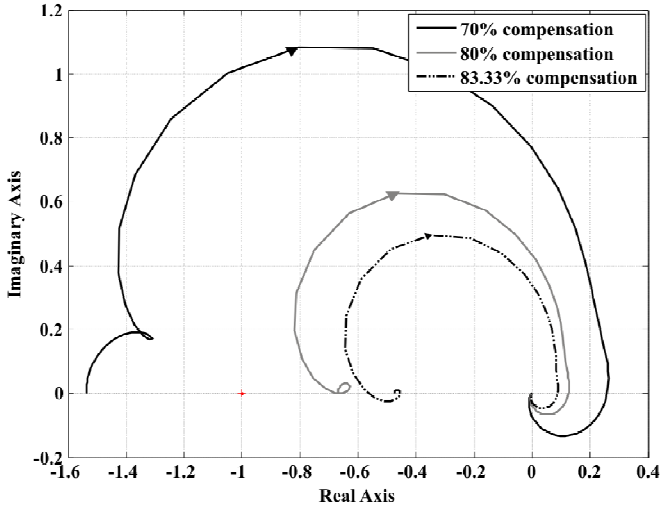

(*a*)

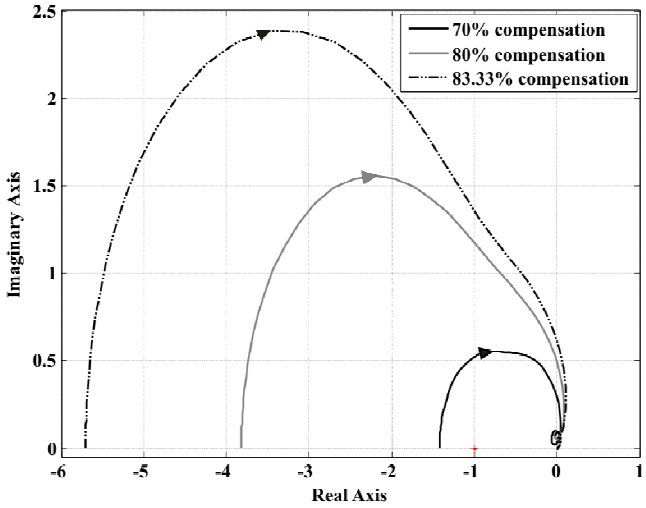

(*b*)

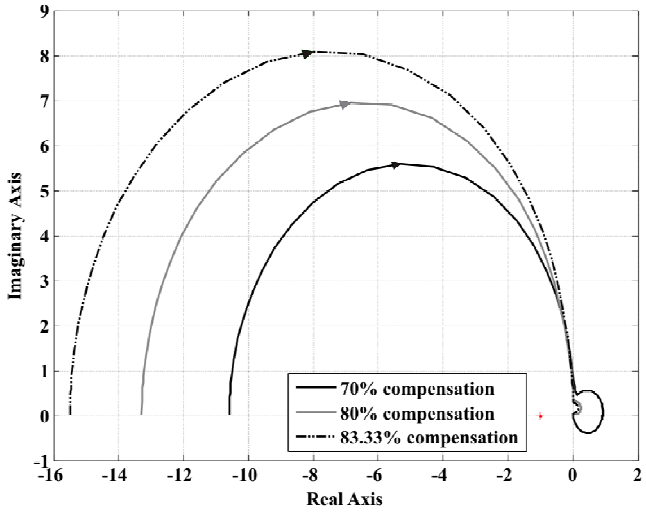

(*c*)

Figure 4.81. Structural robustness assessment. Nyquist diagrams: (*a*) $\gamma_1(s)$; (*b*) $\gamma_2(s)$; (*c*) $\gamma_3(s)$

It is a matter of interest to assess the minimum phase condition in the TCSC upgraded-system while considering different values of tie-line reactances. The operating conditions given in Table 4.19 are used for such a task. In Figure 4.82, the TCSC impedance characteristic is shown in detail for the

operating conditions being considered in this study. It is evident that the higher the amount of series compensation required, the closer the firing angle is to the resonant point – with small parametric variations capable of leading to series resonance. Extreme care should be exercised when operating in this area of the TCSC impedance characteristic. Nevertheless, the smaller the value of the tie-line reactance is, the smaller the amount of series compensation that is required to ensure a minimum phase condition.

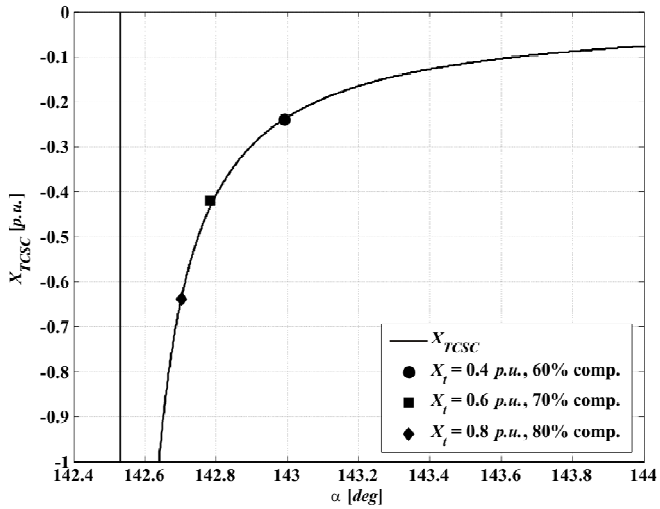

Figure 4.82. TCSC impedance characteristic (X_{TCSC}) near the resonance point

Table 4.19. Operating conditions providing minimum phase systems for different tie-lines

Variable	**Case 1** X_t = 0.4 *p.u.* 60% comp.	**Case 2** X_t = 0.6 *p.u.* 70% comp.	**Case 3** X_t = 0.8 *p.u.* 80% comp.
P_g	0.736 *p.u.*	0.736 *p.u.*	0.736 *p.u.*
Q_g	0.5171 *p.u.*	0.5884 *p.u.*	0.76275 *p.u.*
PF	0.89371	0.90858	0.89328
δ_0	30°	30°	30°
$\lvert V_{\infty 0}\rvert$	1 *p.u.*	1 *p.u.*	1 *p.u.*
$\angle V_{\infty 0}$	60°	60°	60°
$\lvert e_{t0}\rvert$	1.05 *p.u.*	1.05 *p.u.*	1.05 *p.u.*
$\angle e_{t0}$	66.441°	67.246°	66.446°
$\lvert i_{t0}\rvert$ / $\lvert I_{\infty 0}\rvert$	0.78432 *p.u.*	0.77148 *p.u.*	0.78422 *p.u.*
$\angle i_{t0}$ / $\angle I_{\infty 0}$	39.784°	42.556°	39.803°
$\lvert V_{TCSC0}\rvert$	1.1468 *p.u.*	1.2214 *p.u.*	1.3516 *p.u.*
$\angle V_{TCSC0}$	74.875°	81.196°	85.826°
E_{fd0}	1.8334 *p.u.*	1.7895 *p.u.*	1.8331 *p.u.*
X_{TCSC}	–0.24 *p.u.*	–0.42 *p.u.*	–0.64 *p.u.*
α_0	142.9905°	142.7918°	142.7015°
$\partial X_{TCSC}/\partial \alpha_0$	29.52	91.349	212.89
X_t	0.4 *p.u.*	0.6 *p.u.*	0.8 *p.u.*
X_{total}	0.16 *p.u.*	0.18 *p.u.*	0.16 *p.u.*

Figure 4.83 shows the MSF Γ_2 (s) (considering transfer function matrix $\mathbf{G}_{312}$) for different values of tie-line reactance. As expected, the Individual Channels $C_1(s)$ (speed) and $C_2(s)$ (terminal voltage) of the synchronous generator are totally decoupled by the inclusion of the TCSC – the magnitude is below –10 *dB* for all frequencies. Notice that all plots are quite similar regardless of the value of tie-line reactance and percentage of compensation.

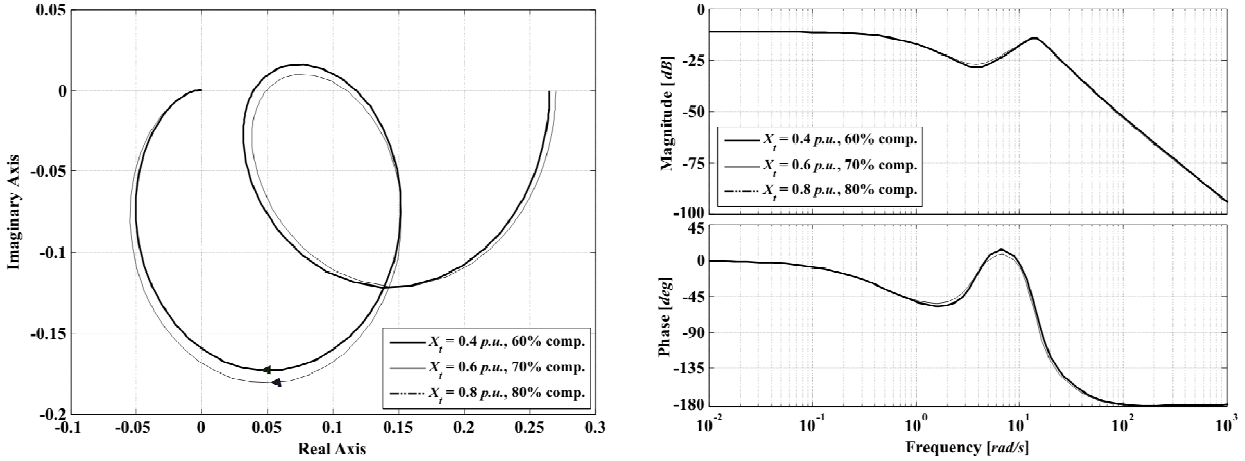

(*a*) (*b*)

Figure 4.83. Assessment of $\Gamma_2(s)$ (considering $\mathbf{G}_{312}$) for compensation values ensuring minimum phase systems: (*a*) Nyquist plot; (*b*) Bode plot

In order to evaluate the control system performance, controller (4.44) is used. The values of gain k_{TCSC} are as follows: k_{TCSC} = –0.52083 (X_t = 0.4 *p.u.*) for 60% compensation, k_{TCSC} = –0.2 (X_t = 0.6 *p.u.*) for 70% compensation and k_{TCSC} = –0.070796 (X_t = 0.8 *p.u.*) for 80% compensation. The control system performance and robustness assessment are presented in Figures 4.84–4.87 and in Table 4.20.

As evidenced by the results (Figures 4.84–4.87 and Table 4.20), it can be seen that the performance is adequate for all operating conditions: the time and frequency responses are quite similar and no encirclements to point (1,0) occur in the Nyquist plot of $\gamma_3(s)$.

Table 4.20. Structural and stability robustness of the channels and control system. High capacitive compensation ensuring minimum phase systems

Condition	Measure	$C_1(s)$	$k_{11}g_{11}(s)$	$\gamma_1(s)$	$C_2(s)$	$k_{22}g_{22}(s)$	$\gamma_2(s)$	$C_3(s)$	$k_{33}g_{33}(s)$	$\gamma_3(s)$
X_t = 0.4 *p.u* 60% comp.	**Bandwidth** (*rad/s*)	0.611	0.303	–	1.44	1.15	–	1.29	0.679	–
	Gain margin (*dB*)	70.2	70	13.16	∞	∞	55	∞	∞	4.93
	Phase margin (*deg*)	73.2	81.4	113	68.4	93.2	135.3	67	130	92
X_t = 0.6 *p.u* 70% comp.	**Bandwidth** (*rad/s*)	0.442	0.272	–	1.35	0.897	–	1.29	0.461	–
	Gain margin (*dB*)	73.5	73.4	18.1	∞	∞	56.42	∞	∞	∞
	Phase margin (*deg*)	79.1	82.5	∞	63.5	95.2	118	68.7	124	92.9
X_t = 0.8 *p.u* 80% comp.	**Bandwidth** (*rad/s*)	0.609	0.302	–	1.44	1.16	–	1.27	0.64	–
	Gain margin (*dB*)	70.2	70	13.3	∞	∞	55.24	∞	∞	4.9
	Phase margin (*deg*)	73.1	81.4	113.8	68.5	93.2	135.3	67.2	129	92

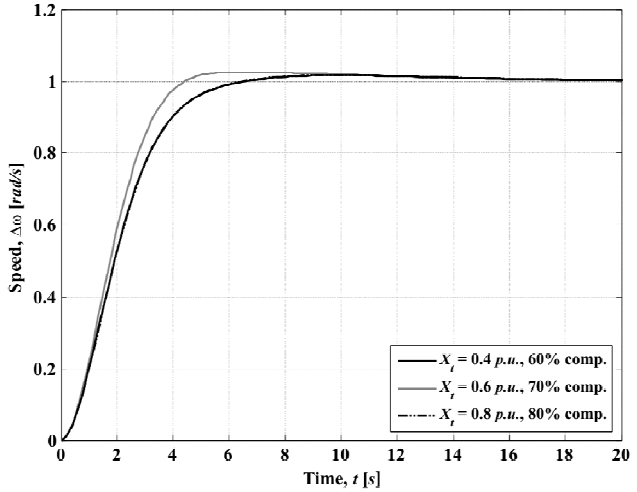

(*a*)

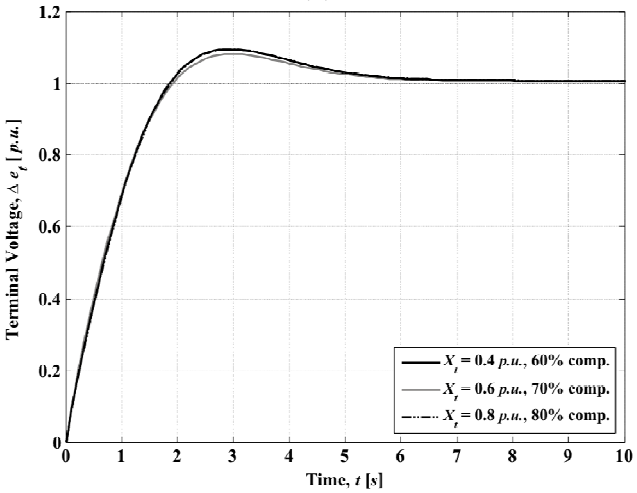

(*b*)

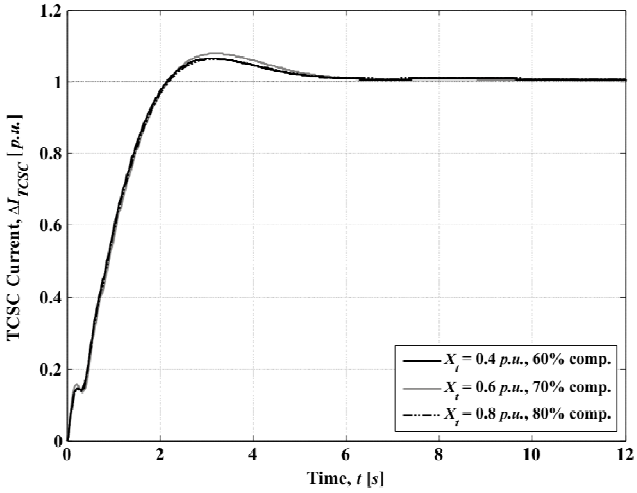

(*c*)

Figure 4.84. System performance. Step response: (*a*) Channel 1 ($T_{c1}(s)$); (*b*) Channel 2 ($T_{c2}(s)$); (*c*) Channel 3 ($T_{c3}(s)$)

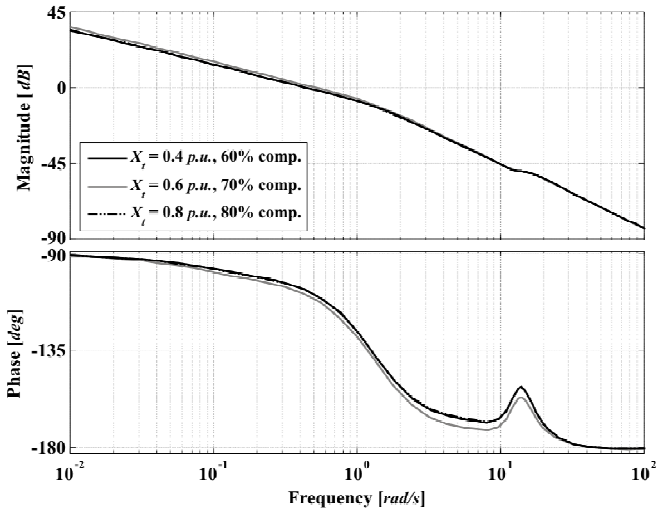

(*a*)

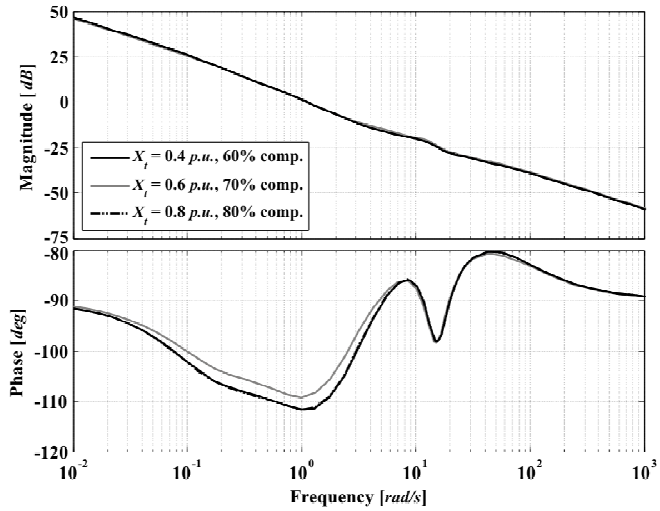

(*b*)

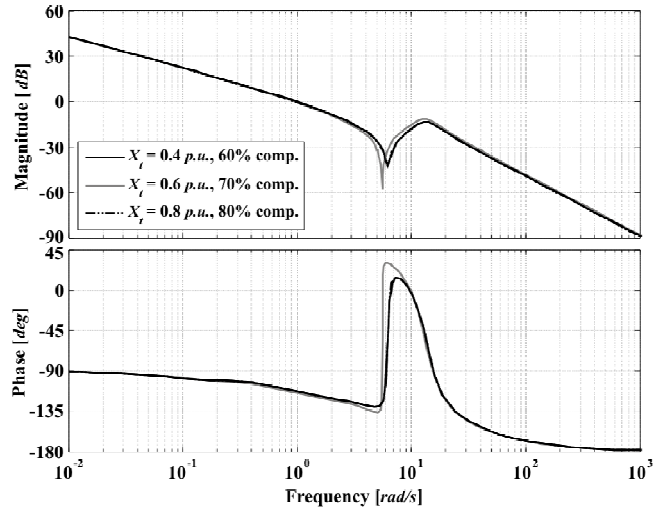

(*c*)

Figure 4.85. System performance and stability robustness assessment. Bode diagrams: (*a*) Channel 1 ($C_1(s)$); (*b*) Channel 2 ($C_2(s)$); (*c*) Channel 3 ($C_3(s)$)

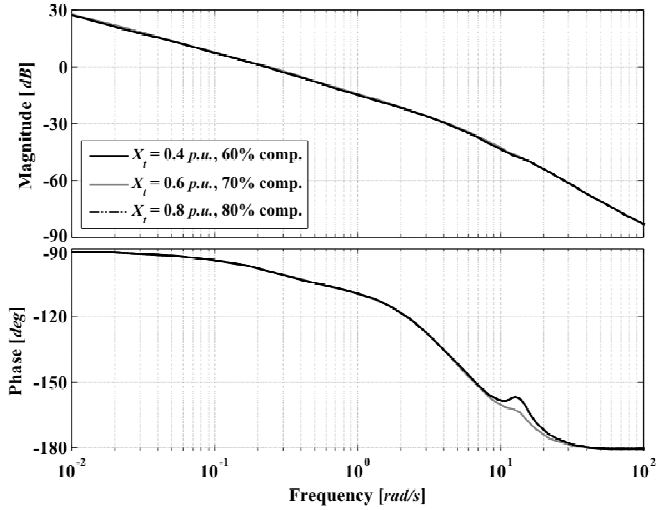

(*a*)

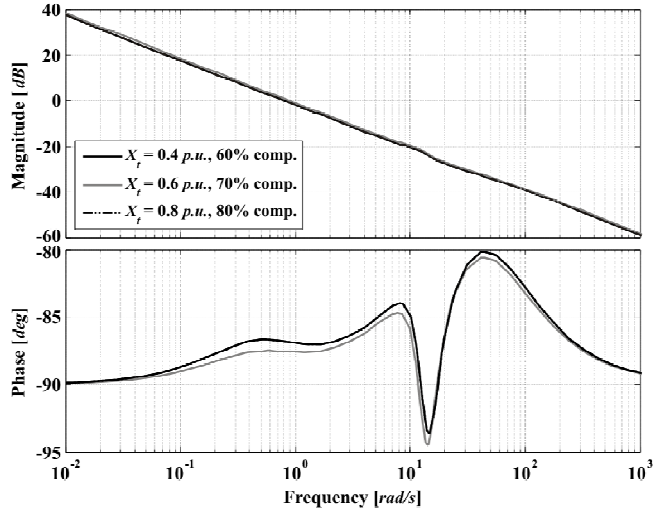

(*b*)

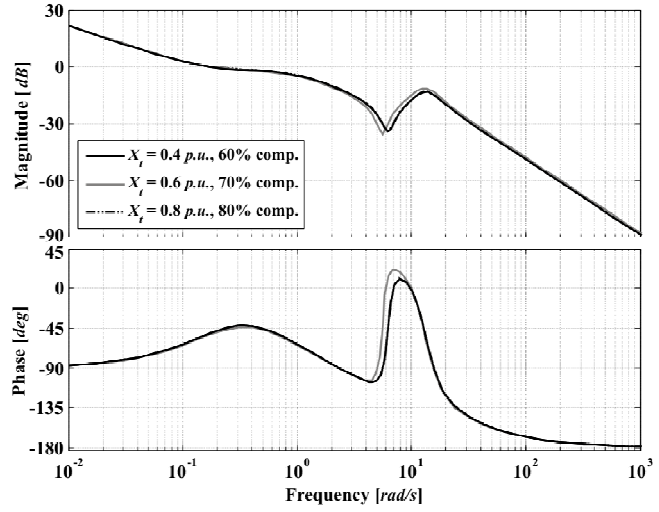

(*c*)

Figure 4.86. Stability robustness assessment. Bode diagrams: (*a*) $k_{11}g_{11}(s)$; (*b*) $k_{22}g_{22}(s)$; (*c*) $k_{33}g_{33}(s)$

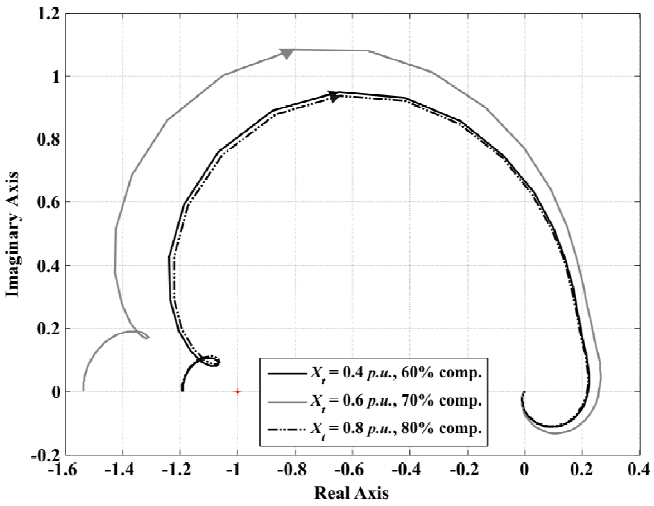

(*a*)

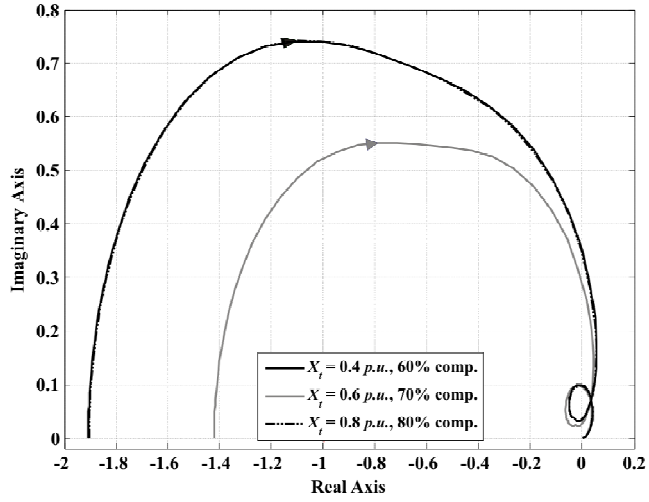

(*b*)

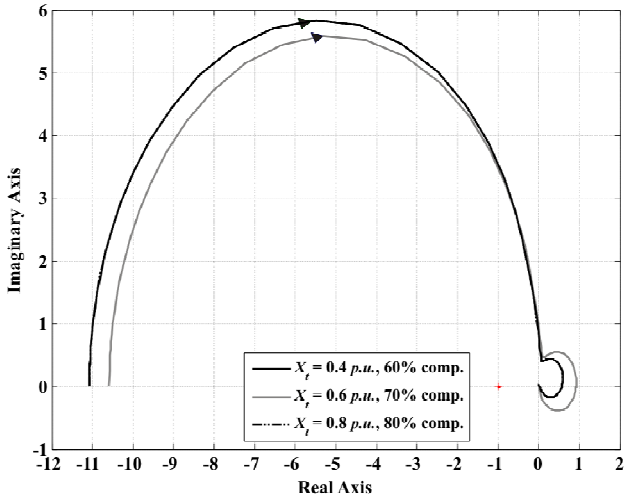

(*c*)

Figure 4.87. Structural robustness assessment. Nyquist diagrams: (*a*) $\gamma_1(s)$; (*b*) $\gamma_2(s)$; (*c*) $\gamma_3(s)$

Remark: The synchronous machine – TCSC system is minimum phase whenever high values of series compensation are considered, regardless of the transmission system tie-line reactance, producing a better performance of the overall control system. Careful analysis of the MSF $\gamma_3(s)$ gives the series compensation values that render a system with no RHPZs.

4.4.5.2. Inductive operation

Although inductive operation of the TCSC is not common practice, it is assessed here for completeness. Consider a TCSC with inductive and capacitive reactance values corresponding to those of the Kayenta TCSC installation [30], shown in Figure 4.49, with the inductive region of operation occurring at firing angles lower than 142.531°.

The operating conditions given in Table 4.21 are used to study the inductive region of operation of the TCSC, with the value of X_{TCSC} taken as positive for inductive operation. Such conditions are contrasted to transmission systems with no TCSC, with reactance values $X_t = 0.2$ *p.u.* and $X_t = 0.4$ *p.u.* The former reactance value would correspond to that of strong systems and the latter to a system of average strength. In order to assess the coupling between channels of the synchronous generator (speed and terminal voltage), Figure 4.88 shows the MSFs $\Gamma_2(s)$ (considering transfer function matrix $\mathbf{G}_{312}$) and $\gamma_a(s)$, for the system with and with no TCSC, respectively.

Table 4.21. System operating conditions for TCSC inductive operation

Variable	**No TCSC** $X_t = 0.2$ *p.u.*	**Case 1** –25% comp.	**Case 2** –50% comp.	**Case 3** –100% comp.	**No TCSC** $X_t = 0.4$ *p.u.*
P_g	0.736 *p.u.*	0.736 *p.u.*	0.736 *p.u.*	0.736 *p.u.*	0.736 *p.u.*
Q_g	0.3143 *p.u.*	0.2469 *p.u.*	0.1983 *p.u.*	0.1283 *p.u.*	0.2365 *p.u.*
PF	0.91963	0.93677	0.94558	0.95204	0.95206
δ_0	30°	32.5°	35°	40°	40°
$\lvert V_{\infty 0}\rvert$	1 *p.u.*	1 *p.u.*	1 *p.u.*	1 *p.u.*	1 *p.u.*
$\angle V_{\infty 0}$	60°	57.5°	55°	50°	50°
$\lvert e_{t0}\rvert$	1.05 *p.u.*	1.05 *p.u.*	1.05 *p.u.*	1.05 *p.u.*	1.05 *p.u.*
$\angle e_{t0}$	68.0589	67.597°	67.139°	66.273°	66.2829
$\lvert i_{t0}\rvert$ / $\lvert I_{\infty 0}\rvert$	0.76221 *p.u.*	0.74826 *p.u.*	0.74129 *p.u.*	0.73627 *p.u.*	0.73626 *p.u.*
$\angle i_{t0}$ / $\angle I_{\infty 0}$	44.932°	47.112°	48.151°	48.456°	48.466°
$\lvert V_{TCSC0}\rvert$ / $\lvert V_{mid}\rvert$	1.0225 *p.u.*	1.0375 *p.u.*	1.0283 *p.u.*	1.0147 *p.u.*	1.0147 *p.u.*
$\angle V_{TCSC0}$ / $\angle V_{mid}$	64.128°	65.657°	63.23°	58.341°	58.341°
E_{fd0}	1.7537 *p.u.*	1.7066 *p.u.*	1.6822 *p.u.*	1.6668 *p.u.*	1.6668 *p.u.*
X_{TCSC}	-	0.05 *p.u.*	0.1 *p.u.*	0.2 *p.u.*	-
α_0	-	140.45°	141.46°	141.99°	-
$\partial X_{TCSC} / \partial \alpha_0$	-	1.4418	5.5067	21.464	-
X_t	0.2 *p.u.*	0.2 *p.u.*	0.2 *p.u.*	0.2 *p.u.*	0.4 *p.u.*
X_{total}	0.2 *p.u.*	0.25 *p.u.*	0.3 *p.u.*	0.4 *p.u.*	0.4 *p.u.*

Figure 4.88 formally shows that the inclusion of the TCSC operating in its inductive region is prejudicial to the system; that is, a strong transmission system becomes weaker. The analysis of $\Gamma_2(s)$ shows categorically that whenever the TCSC is used in a strong transmission system and operated in its

inductive region, it becomes more coupled. The characteristic peak featured by the MSF $\gamma_a(s)$ appears at higher frequencies than $\Gamma_2(s)$, with an amplified magnitude. A TCSC with X_{TCSC} = 0.2 *p.u.* into a transmission tie-line of X_t = 0.2 *p.u.* is largely equivalent to having a weaker transmission system with no TCSC of X_t = 0.4 *p.u.* – the difference being the frequency at which the peak magnitude occurs.

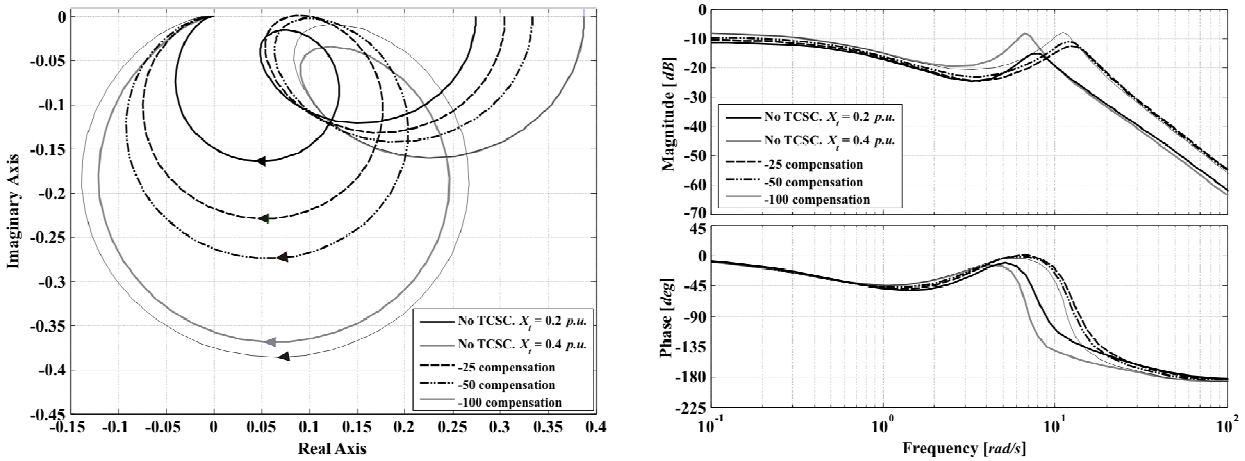

(*a*) (*b*)

Figure 4.88. Assessment of $\gamma_a(s)$ vs $\Gamma_2(s)$ (considering $\mathbf{G}_{312}$) for inductive compensation. (*a*) Nyquist plot; (*b*) Bode plot

In terms of control system design, the increase of the effective reactance of the transmission line will be reflected in a bandwidth reduction in order to obtain an adequate performance. To assess the control system performance and robustness measures, the following gains k_{TCSC} = –4.78, k_{TCSC} = –1.44375 and k_{TCSC} = –0.375 are used in controller (4.44) to achieve –25%, –50% and –100% compensation, respectively. Such values are used so that the same bandwidths are achieved for all cases of inductive operation. The control system performance and robustness measures are presented in Figures 4.89–4.92 and Table 4.22.

Table 4.22. Structural and stability robustness of the channels and control system. Inductive region of operation

Condition	Measure	$C_1(s)$	$k_{11}g_{11}(s)$	$\gamma_1(s)$	$C_2(s)$	$k_{22}g_{22}(s)$	$\gamma_2(s)$	$C_3(s)$	$k_{33}g_{33}(s)$	$\gamma_3(s)$
X_{TCSC} = 0.05 *p.u* –25% comp.	**Bandwidth** (*rad/s*)	0.521	0.354	–	1.59	1.6	–	0.406	0.0382	–
	Gain margin (*dB*)	59.4	44.2	18.44	∞	∞	68.29	38.3	∞	14.8
	Phase margin (*deg*)	59.1	78.9	130.9	88	90	∞	71.4	96.7	96.1
X_{TCSC} = 0.1 *p.u* –50% comp.	**Bandwidth** (*rad/s*)	0.562	0.377	–	1.79	1.78	–	0.408	0.0289	–
	Gain margin (*dB*)	41.7	39.9	16.71	∞	∞	25.15	29.9	∞	25.3
	Phase margin (*deg*)	56	77.3	127.8	88.7	88.7	∞	69.1	94.7	112
X_{TCSC} = 0.2 *p.u* –100% comp.	**Bandwidth** (*rad/s*)	0.587	0.42	–	2.1	2.08	–	0.368	0.00668	–
	Gain margin (*dB*)	36.3	34.6	15.7	∞	∞	14.22	20.9	∞	∞
	Phase margin (*deg*)	54.9	74.5	114.8	87.8	87	∞	70	91	111

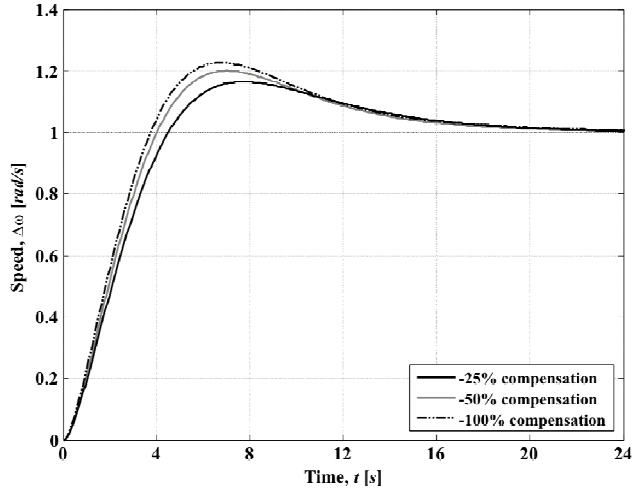

(*a*)

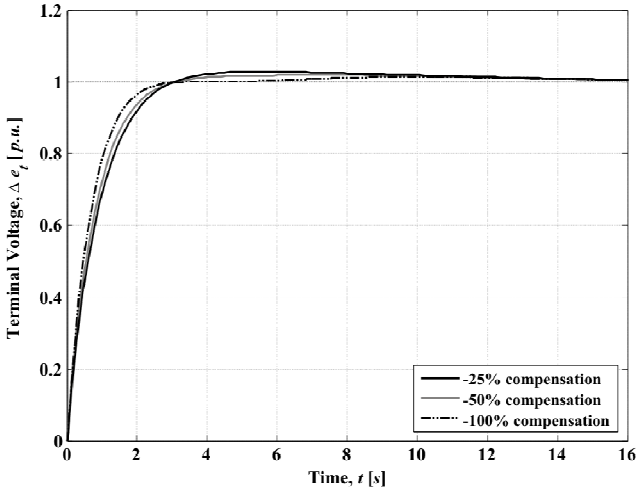

(*b*)

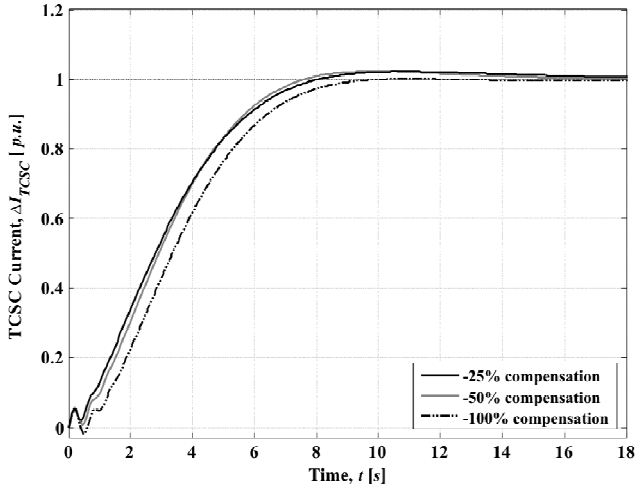

(*c*)

Figure 4.89. System performance. Step response: (*a*) Channel 1 ($T_{c1}(s)$); (*b*) Channel 2 ($T_{c2}(s)$); (*c*) Channel 3 ($T_{c3}(s)$)

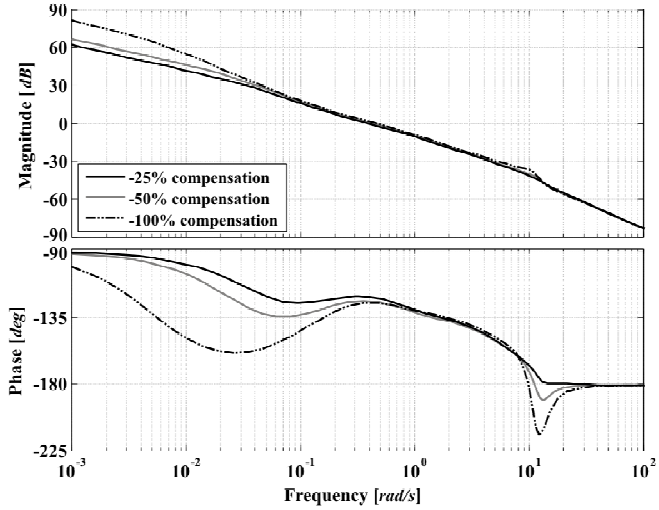

(*a*)

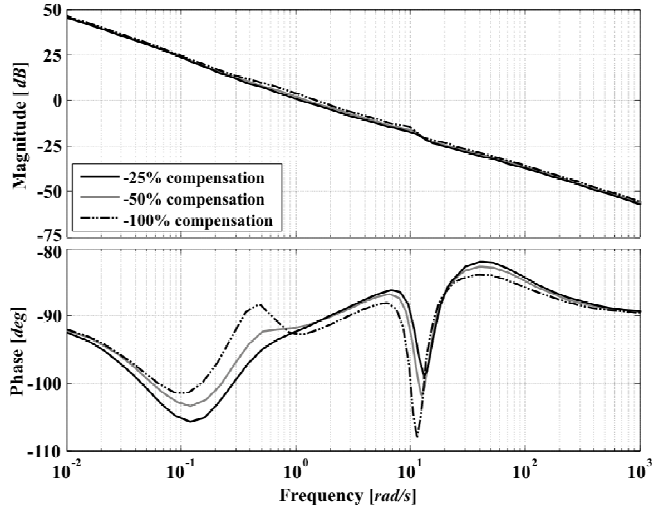

(*b*)

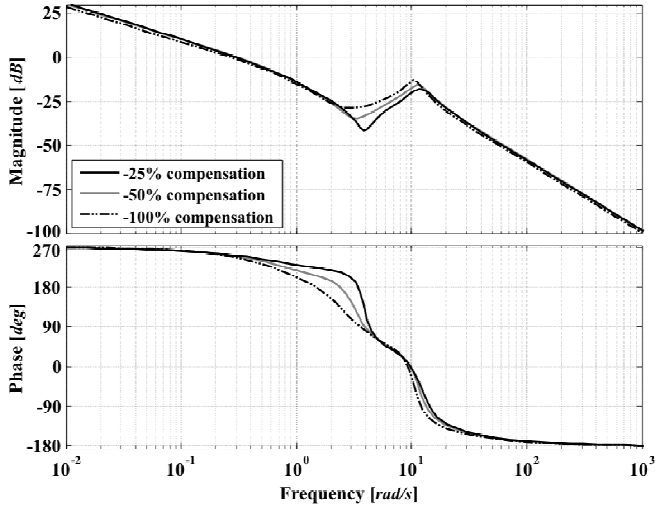

(*c*)

Figure 4.90. System performance and stability robustness assessment. Bode diagrams: (*a*) Channel 1 ($C_1(s)$); (*b*) Channel 2 ($C_2(s)$); (*c*) Channel 3 ($C_3(s)$)

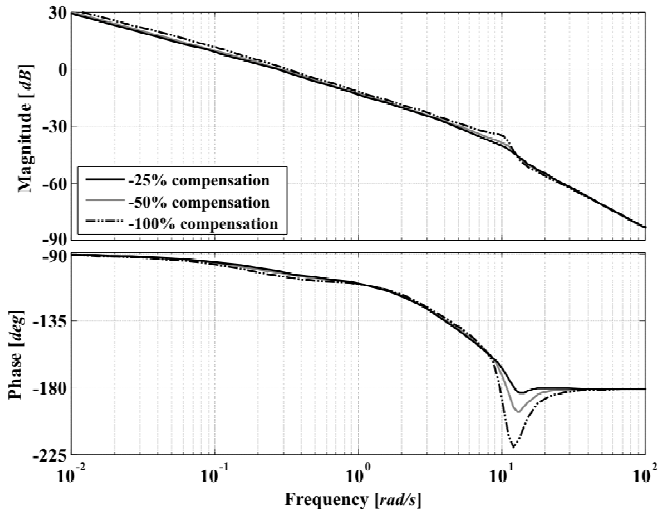

(*a*)

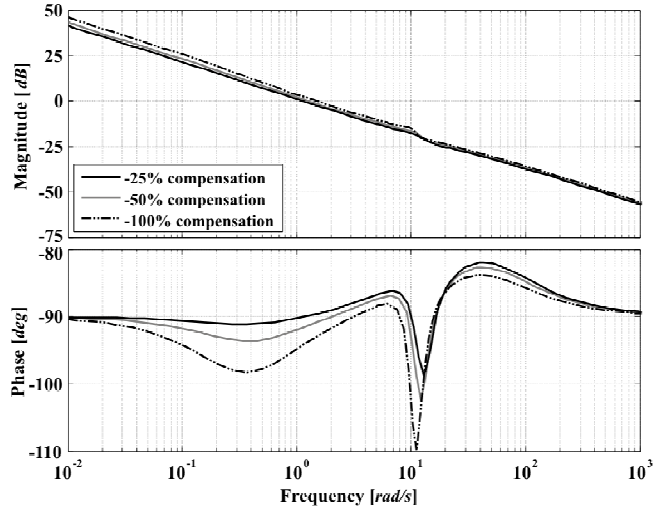

(*b*)

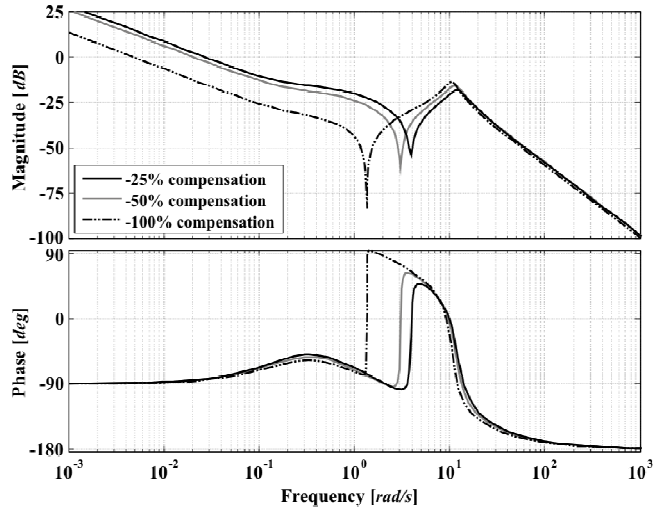

(*c*)

Figure 4.91. Stability robustness assessment. Bode diagrams: (*a*) $k_{11}g_{11}(s)$; (*b*) $k_{22}g_{22}(s)$; (*c*) $k_{33}g_{33}(s)$

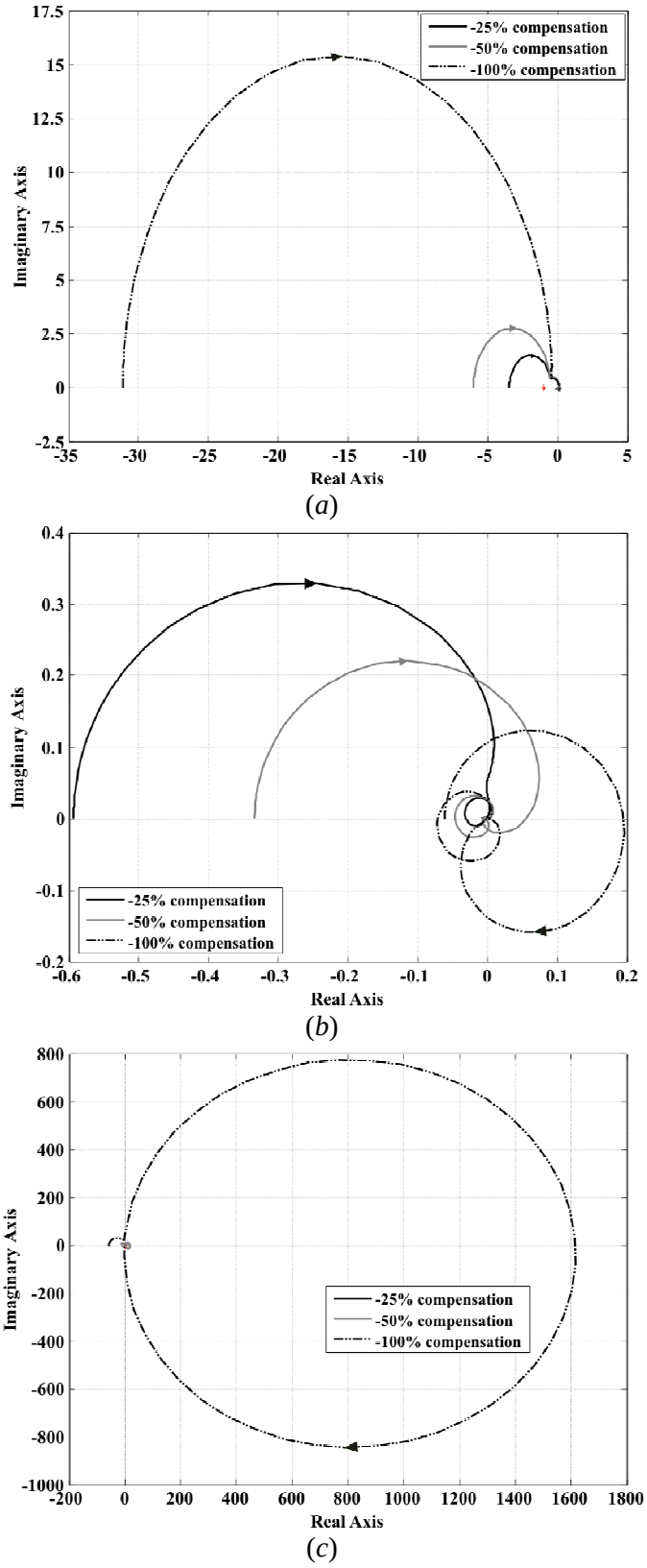

Figure 4.92. Structural robustness assessment. Nyquist diagrams: (*a*) $\gamma_1(s)$; (*b*) $\gamma_2(s)$; (*c*) $\gamma_3(s)$

From the results (Figures 4.89–4.92 and Table 4.22) it can be seen that the synchronous machine – TCSC system can be made to perform adequately with satisfactory robustness measures, although the performance is limited since $C_3(s)$ is non-minimum phase. Therefore, the bandwidth of $C_3(s)$ had to be

reduced below the natural frequency of the channel RHPZs. Relevant information associated to the non-minimum phase characteristic of $C_3(s)$ is given in Table 4.23. The remarks of Study 1 in Section 4.4.3.1 also apply to this study. Nevertheless, there seems to be little interest in using the TCSC in its inductive region of operation owing to the lack of obvious benefit to the transmission system.

Table 4.23. $C_3(s)$ non-minimum phase assessment. Inductive operation.

Condition	**Non-minimum phase term**		**RHPZs** $C_3(s)$	**Damped Natural Freq.** ω_d (*rad/s*)	**Natural Freq.** ω_n (*rad/s*)	**Damping Ratio** ζ	**Bandwidth** $C_3(s)$ (*rad/s*)
	$\gamma_3(s)$	$C_3(s)$					
–25% comp.	$(s^2 – 4.657s + 78.51)$	$(s^2 – 0.962s + 15.22)$	$0.48075 \pm j3.87155$	3.87155	3.901	–0.12323	0.406
–50% comp.	$(s^2 – 7.912s + 79.76)$	$(s^2 – 1.65s + 10.47)$	$0.825 \pm j3.1288$	3.13053	3.236	–0.25497	0.408
–100% comp.	$(s^2 – 12.2s + 86.78)$	$(s^2 – 2.647s + 7.142)$	$1.324 \pm j2.32171$	2.32171	2.672	–0.49524	0.368

Remark: The fact that three SISO channels encapsulate the full MIMO system enables the design of simple controllers with a fixed structure for different operating conditions, providing stability, adequate robustness measures and a satisfactory performance. Moreover, notice that such results are achieved by adjusting a single controller parameter (*i.e.*, k_{TCSC}).

4.5. Comparison between SVC, TCSC and PSS

The main application of an SVC is to provide dynamic reactive power support to enable an effective *voltage regulation* and to enhance *transient stability*; however, it was shown in Section 4.3 that such device is able to damp electromechanical oscillations providing a damping control loop is made available, resulting in increased stability margins. The additional control loop successfully incorporates damping into the system, which eliminates the problematic switch-back characteristic present in the synchronous generators and, therefore, allows the use of high bandwidths in the terminal voltage channel, thus enhancing disturbance rejection. Likewise, the TCSC, a FACTS device whose main application is to maximise active power transfers, is also able to damp electromechanical oscillations by effectively modulating the electrical length of a transmission line, and therefore, reducing the switch-back characteristic, as shown in Section 4.4. Notwithstanding that the primary tasks of the SVC (a shunt controller) and the TCSC (a series controller) differ, their secondary functions, which is their ability to damp electromechanical oscillations, invites a comparison to be made between these two quite distinct devices.

The Power System Stabiliser (PSS) has been the conventional solution used to ameliorate power system oscillations. It is included in the comparative study for completeness owing to its ability to

provide system damping. It should be noticed that the PSS has already been compared with the SVC in previous work [18,21,22]. Some of this work has focused on finding out the best location for such devices in multi-machine systems [21]. In reference [22] it is concluded that the SVC is equally effective as the PSS to damp electromechanical oscillations provided it is correctly placed in the system. In this section, the comparison is extended to include the TCSC where ICAD is used as the framework.

4.5.1. Synchronous generator – PSS system

The basic function of the Power System Stabiliser (PSS) is to provide damping to system oscillations in two different forms: (*i*) to damp local plant mode oscillations in the frequency range of 0.8–2 *Hz*, caused by units at the generating station swinging with respect to the rest of the power system; (*ii*) to damp inter-area oscillations in the range of 0.1–0.7 *Hz*, caused by the swinging of various machines in one part of the system against machines in other parts of the system [13,25,33]. The PSS can be viewed as an additional block of the generator excitation control system or AVR [22].

The synchronous generator – PSS system performance has already been studied and critically examined in the open literature using ICAD [34]. The mathematical model corresponds to a 2×2 system. Figure 4.93 shows a compact block diagram representation of a synchronous generator – PSS system connected to an infinite bus via a tie-line reactance. As in the case of the SVC featuring a damping control loop, the PSS acts as a post-compensator of the speed output; however, in this case its impact occurs directly on the machine's terminal voltage channel. The resulting signal, $\Delta V_{add}(s)$, is added to the terminal voltage control channel reference.

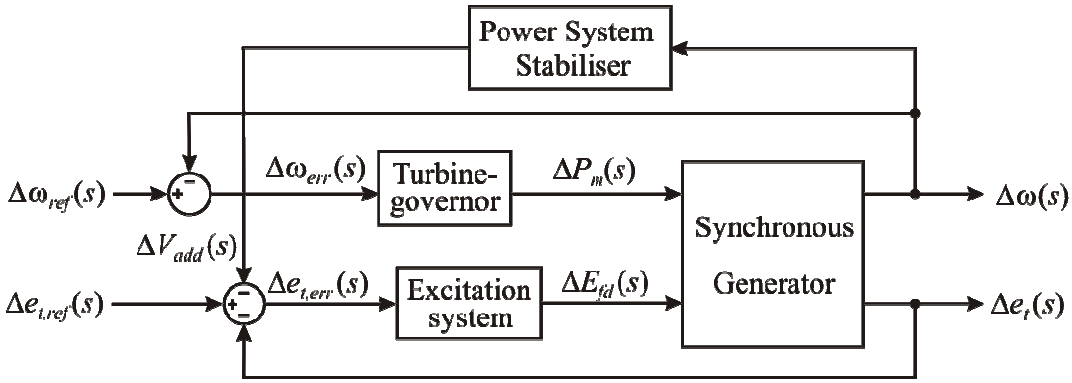

Figure 4.93. Block diagram: synchronous generator – PSS system

4.5.1.1. PSS modelling

The transfer function matrix representation of the synchronous generator is provided by (3.7) and (3.8), where the individual elements of $\mathbf{G}(s)$ are given by (3.9) for a 5th order synchronous generator model (Model 1). From Figure 4.93, it is observed that the system featuring a PSS takes the post-compensated form

$$\begin{aligned}\mathbf{G}'(s) &= \mathbf{P}_{PSS}(s)\mathbf{G}(s) \\ &= \begin{bmatrix} 1 & 0 \\ -K_{PSS}(s) & 1 \end{bmatrix}\begin{bmatrix} g_{11}(s) & g_{12}(s) \\ g_{21}(s) & g_{22}(s) \end{bmatrix}\end{aligned} \tag{4.46}$$

or

$$\mathbf{G}'(s) = \begin{bmatrix} g_{11}(s) & g_{12}(s) \\ g'_{21}(s) & g'_{22}(s) \end{bmatrix} \tag{4.47}$$

where

$$\begin{aligned} g'_{21}(s) &= g_{21}(s) - K_{PSS}(s)\,g_{11}(s) \\ g'_{22}(s) &= g_{22}(s) - K_{PSS}(s)\,g_{12}(s) \end{aligned} \tag{4.48}$$

In the non-diagonal post-compensator matrix $\mathbf{P}_{PSS}(s)$ in (4.46), the cross-coupling element $K_{PSS}(s)$ denotes the transfer function of the PSS, given by

$$K_{PSS}(s) = k_{pss} \cdot \frac{s\tau_w}{1+s\tau_w} \cdot \frac{1+s\tau_1}{1+s\tau_2} \tag{4.49}$$

Similarly to the damping controller of the SVC (4.27), the term $s\tau_w/(1 + s\tau_w)$ is a wash-out filter, the term $(1 + s\tau_1)/(1 + s\tau_2)$ is a phase lead/lag compensator, and k_{pss} is the stabiliser gain. The wash-out filter is a high pass filter which removes DC signals to ensure that steady changes in speed do not modify the terminal voltage. The time constant has values in the range of 1–20 *s* – long enough to let pass stabilising signals at frequencies of interest relatively unchanged, but not so long that it leads to undesirable generator voltage excursions as a result of stabiliser action during system islanding conditions [25]. The damping controller $K_{PSS}(s)$ in (4.49) is a simplified version of the one presented in reference [25], where two phase lead compensators are used. Notice that both, the damping controller of the SVC (4.27) and the PSS (4.49) here studied, have similar structures.

4.5.1.2. PSS in a weak transmission system

The operating condition of a synchronous generator – PSS system connected to an infinite bus via a weak tie-line is given in Table 4.24. The PSS has the following transfer function

$$K_{PSS}(s) = \frac{125s(s+4)}{(s+100)(s+0.1)} \tag{4.50}$$

where $k_{pss} = 5$, $\tau_w = 10$ *s*, $\tau_1 = 0.25$ *s* and $\tau_2 = 0.01$ *s*.

In (4.46), the PSS transfer function $K_{PSS}(s)$ multiplies the benign transfer functions $g_{11}(s)$ and $g_{12}(s)$ which contain no lightly damped LHP zeros, this causing the terminal voltage transfer functions $g_{21}(s)$ and $g_{22}(s)$ to change to $(g_{21} - K_{PSS}g_{11})$ and $(g_{22} - K_{PSS}g_{12})$. Figure 4.94 shows the frequency response of the original transfer functions $g_{21}(s)$ and $g_{22}(s)$ and the amended $g'_{21}(s)$ and $g'_{22}(s)$ for a weak transmission system when using controller (4.50).

Table 4.24. System operating condition for TCSC, SVC and PSS

Variable	No FACTS device	TCSC, 70% compensation	SVC with damping loop	PSS
P_g	0.736 *p.u.*	0.736 *p.u.*	0.736 *p.u.*	0.736 *p.u.*
Q_g	0.26798 *p.u.*	0.77952 *p.u.*	0.08719 *p.u.*	0.26798 *p.u.*
PF	0.93965	0.87667	0.99306	0.93965
Q_{SVC}	-	-	0.32887 *p.u.*	-
P_∞	0.736 *p.u.*	0.736 *p.u.*	0.736 *p.u.*	0.736 *p.u.*
Q_∞	–0.12155 *p.u.*	0.30991 *p.u.*	0.051173 *p.u.*	–0.12155 *p.u.*
δ_0	60°	60°	60°	60°
$\lvert V_{\infty 0}\rvert$	1 *p.u.*	1 *p.u.*	1 *p.u.*	1 *p.u.*
$\angle V_{\infty 0}$	30°	30°	30°	30°
$\lvert e_{t0}\rvert$	1.05 *p.u.*	1.05 *p.u.*	1.05 *p.u.*	1.05 *p.u.*
$\angle e_{t0}$	59.384°	35.922°	57.714°	59.384°
$\lvert I_{\infty 0}\rvert$	0.74597 *p.u.*	0.81906 *p.u.*	0.73778 *p.u.*	0.74597 *p.u.*
$\angle I_{\infty 0}$	39.378°	7.1652°	26.023°	39.378°
$\lvert V_{mid}\rvert / \lvert V_{TCSC0}\rvert / \lvert V_{SVC0}\rvert$	0.99151 *p.u.*	1.3089 *p.u.*	1.05 *p.u.*	0.99151 *p.u.*
$\angle V_{mid} / \angle V_{TCSC0} / \angle V_{SVC0}$	45.059°	53.81°	44.202°	45.059°
E_{fd0}	1.7368 *p.u.*	1.7757 *p.u.*	1.5301 *p.u.*	1.7368 *p.u.*
X_{TCSC}	-	–0.56 *p.u.*	-	-
α_0	-	142.7261°	150°	-
$\partial X_{TCSC} / \partial \alpha_0$	-	162.82	-	-
B_{SVC0}	-	-	0.37734 *p.u.*	-
X_{t1}	-	-	0.35 *p.u.*	-
X_t	0.7 *p.u.*	0.7 *p.u.*	0.7 *p.u.*	0.7 *p.u.*
X_{total}	0.7 *p.u.*	0.14 *p.u.*	0.7 *p.u.*	0.7 *p.u.*

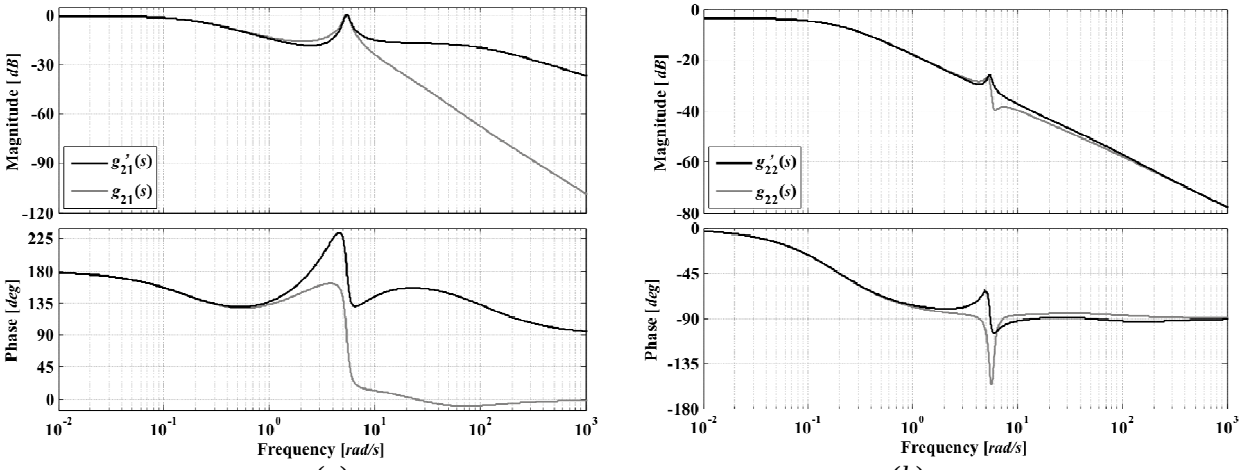

(*a*) (*b*)

Figure 4.94. Bode diagrams of non-compensated and amended subsystems: (*a*) g_{21} vs $g'_{21}(s) = (g_{21} - K_{PSS}\, g_{11})$; (*b*) g_{22} vs $g'_{22}(s) = (g_{22} - K_{PSS}\, g_{12})$.

By comparing the frequency responses of ($g_{21} - K_{PSS}\, g_{11}$) with that of g_{21} and ($g_{22} - K_{PSS}\, g_{12}$) with that of g_{22} in Figures 4.94(*a*) and 4.94(*b*), respectively, it is noticed that the effect of the inverted notch characteristic K_{PSS} (*s*) multiplied by the benign system dynamics $g_{11}(s)$ and $g_{12}(s)$ dominates the problematic switch-back characteristic exhibited by element $g_{22}(s)$ and provides a 90 *deg* phase lead in $g_{11}(s)$. Figure 4.95 shows the MSF associated to the amended transfer function matrix (4.47) when the PSS is used and that of an OMIB system with no PSS.

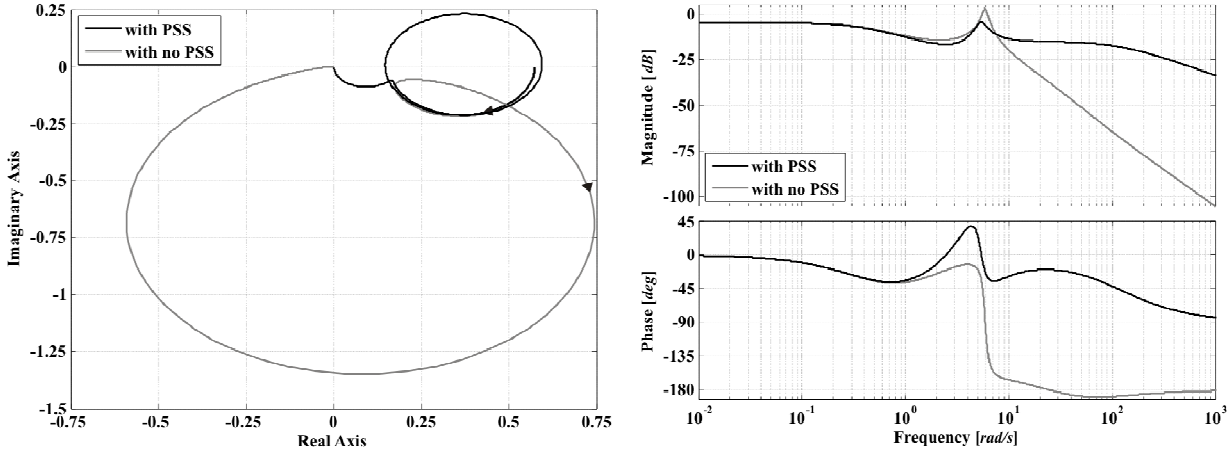

(*a*) (*b*)

Figure 4.95. Assessment of $\gamma_a(s)$ for an OMIB system with and with no PSS:
(*a*) Nyquist plot; (*b*) Bode plot

The results in Figure 4.95 show that use of the PSS reduces coupling considerably around the frequency range where the switch-back characteristic is present (less than –5 *dB*); the plots are for the MSF $\gamma_a(s)$. Notice that a 90 *deg* phase lead is also provided in the MSF of the amended system. The PSS can be considered a device that internally decouples the synchronous generator and dominates the switch-back characteristic. In particular, by working on an amended subsystem ($g_{22} - K_{PSS}\, g_{11}$) instead of the original subsystem $g_{22}(s)$, the damping control loop allows the use of an arbitrary high-bandwidth in the terminal voltage channel without the presence of the switch-back characteristic [34].

Careful examination of the block diagram in Figure 4.93 and K_{PSS} (*s*) in (4.50) reveals that a feedback loop is introduced into the system with the following main effects: (*i*) it reduces the relative degree and magnitude of $g'_{21}(s)$ at about 1–10 *rad/s* (shown in Figure 4.94(*a*)); (*ii*) it preserves the relative degree of $g'_{22}(s)$ (Figure 4.94(*b*)); (*iii*) it preserves the negative gain of $g_{21}(s)$ in $g'_{21}(s)$ (shown in Figure 4.94(*a*)). It can be observed in Figure 4.95 that the MSF of the new system is favourably affected since the ratio $g'_{21}(s)/g'_{22}(s)$ is smaller, decoupling the system. An important conclusion, similar to the one reached in the case of the SVC, can be drawn for the PSS: it successfully exploits the synchronous generator dynamics.

Remark: Although the PSS and the SVC damping loop both act as post-compensators of the speed output, their auxiliary signals $V_{add}(s)$ impact different channels, as shown by the block diagrams of Figures 4.29 and 4.93. While the PSS acts directly on the terminal voltage channel, achieving an internal decoupling of the synchronous generator and elimination of the switch-back characteristic, the SVC damping loop acts on the SVC control loop channel and, therefore, the internal coupling of the synchronous generator remains unchanged, as concluded in Section 4.3. The synchronous generator – TCSC system, as discussed in Section 4.4.2, can be controlled using diagonal controllers.

4.5.2. Control system design comparison

The performance of an SVC featuring a damping control loop, TCSC and PSS are examined to assess their capability to damp electromechanical oscillations in a weak transmission system, comprising a synchronous generator connected to an infinite bus via a tie-line reactance with a value of $X_t = 0.7$ *p.u.* The block diagrams of such systems are given in Figures 4.29, 4.50 and 4.93, respectively. Both the SVC and the TCSC are connected at the mid-point of the transmission line. The operating conditions for these systems are given in Table 4.24. The SVC damping controller and the PSS are given by (4.30) and (4.50), respectively.

It is observed in Table 4.24 that a high voltage at the point of connection of the TCSC and a high demand of reactive power to the synchronous generator exist. In a practical scenario, these problems can be avoided by using shunt reactors [28] and various TCSC modules (as shown in reference [35]).

Assessment of the coupling between the two channels of the synchronous generator (speed and terminal voltage) is carried out by looking at the relevant MSFs associated to the operating conditions of Table 4.24. The MSFs $\Gamma_2(s)$ (considering transfer function matrix $\mathbf{G}_{312}$) in the SVC and TCSC systems and $\gamma_a(s)$ for the system with PSS and with no controlling device, are shown in Figure 4.96.

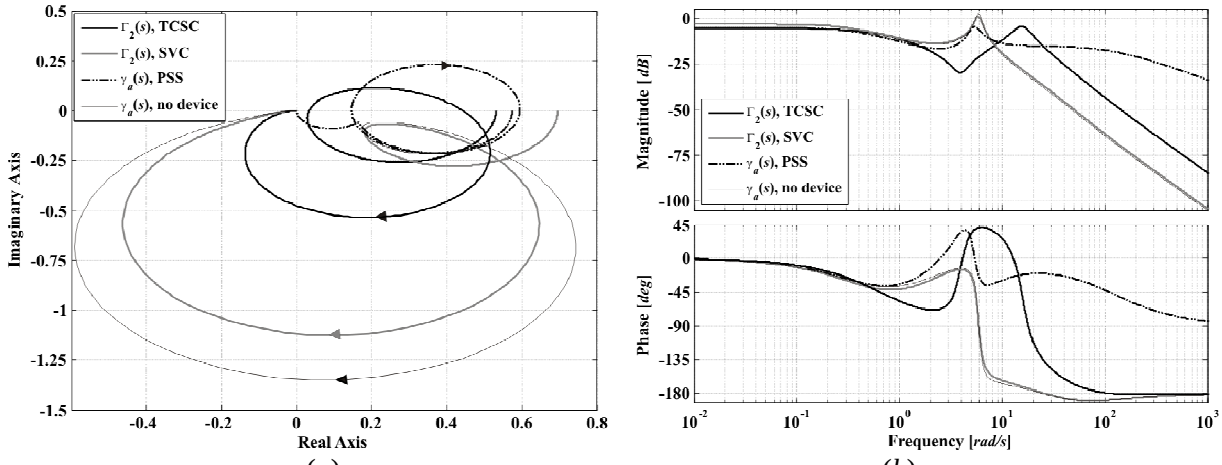

(*a*) (*b*)

Figure 4.96. Assessment of MSFs. (*a*) Nyquist plot; (*b*) Bode plot

It is shown that the coupling in the synchronous generator with no auxiliary devices, given by MSF $\gamma_a(s)$, changes little around the switch-back frequency with respect to that of the system with SVC. The reason is that the effect of the damping control loop of the SVC does not impact directly on the speed or terminal voltage channels, as shown by its MSF $\Gamma_2(s)$.

For the case of the TCSC, its MSF $\Gamma_2(s)$ shows a reduced coupling due to a decreasing electrical distance of the transmission line. The peak moves on to higher frequencies, but it is still quite pronounced. The PSS is very successful in decoupling the synchronous machine, as evidenced by the Nyquist trajectory of the MSF $\gamma_a(s)$ of the PSS-upgraded system in Figure 4.96(*a*) and the small peak around the switch-back frequencies in Figure 4.96(*b*). It should be pointed out that the TCSC has been set to provide a 70% of series compensation for this operating condition.

The performance of the various systems is compared using suitably designed controllers. For the synchronous generator – SVC system featuring a damping control loop, the control pair of (4.29) and (4.30), designed in Section 4.3, is used. The following diagonal multivariable controller is used for the synchronous generator – TCSC system

$$\mathbf{K}_{TCSC}(s)=\begin{bmatrix} k_{11}(s) & 0 & 0 \\ 0 & k_{22}(s) & 0 \\ 0 & 0 & k_{33}(s) \end{bmatrix}$$
$$=\text{diag}\left[\frac{17.3598(s+0.35)(s^2+6.111s+165.5)}{s^2(s+5)(s+0.6)},\quad \frac{75.8019(s+5)(s+1)(s+0.1)}{s(s+3)(s+2)},\quad \frac{-0.046018(s+0.2)}{s(s+7)(s+0.7)}\right] \tag{4.51}$$

For the synchronous generator – PSS system the control pair of (4.50) and

$$\mathbf{K}_{PSS}(s)=\begin{bmatrix} k_{11}(s) & 0 \\ 0 & k_{22}(s) \end{bmatrix}$$
$$=\text{diag}\left[\frac{41.64(s^2+0.6s+26)}{s^2(s+5)},\quad \frac{76.953(s+0.43)}{s}\right] \tag{4.52}$$

is used. The control system performance and robustness indicators for each system are presented in Figures 4.97–4.100. Notice that the PSS-upgraded system does not contain a Channel 3, this being a 2×2 control system. Key information associated to these figures is presented in Table 4.25.

Figure 4.97 shows the step responses of the various control systems. The performance of Channel 1 (speed channel) is adequate for all cases, as shown in Figure 4.97(*a*). Figure 4.97(*b*) illustrates the step response of Channel 2 (terminal voltage channel), and it is noticed that in the case of the PSS the response shows some oscillations. The response of Channel 2 for the system with a TCSC, although adequate, is slower than the rest due to the chosen bandwidth. Notice from Figure 4.97(*c*) that the step response associated to Channel 3 (either SVC voltage control loop or TCSC impedance control loop) is also

adequate. However, the response of the SVC system is slightly oscillatory, not too dissimilar to Channel 2 in a system with PSS. This is not due to a lack of system damping, as evidenced by the phase margins of Table 4.25, but rather due to the presence of complex poles. In the system with a TCSC, the step response of the impedance control loop is slow due to the chosen bandwidth. It should be emphasised that the performances of the control systems are satisfactory regardless of the detrimental effect on the terminal voltage step response (Channel 2) when using the PSS and on the SVC voltage step response (Channel 3) when using the SVC.

Figure 4.98 shows the Bode diagrams of the individual channels. From figure 4.98(*a*) and Table 4.25, it is observed that the chosen bandwidth for Channel 1 is almost the same for the three cases. All control systems offer adequate stability margins for the speed channel, although the SVC offers the best performance. It is clear from Figure 4.98(*b*) that both the SVC damping loop and the PSS successfully eliminate the switch-back characteristic in the terminal voltage channel, and as a consequence, an arbitrary high bandwidth can be achieved for the systems featuring such devices. In the case of the SVC, the effect is passed on indirectly through the existing coupling with Channel 3; on the other hand, when the PSS is used, the switch-back is dominated by the inverted notch characteristic provided by controller (4.50). In the case of the TCSC-upgraded system, and since the amount of series compensation has to be limited to 70% due to its impact on the reactive power generated by the synchronous machine, the switch-back characteristic is not completely eliminated. Therefore, the bandwidth has to be reduced, producing a slow Channel 2. From Figure 4.98(*c*), it can be seen that for the case of the SVC, the inverted notch characteristic is dominant around the frequencies of the switch-back characteristic in Channel 3; therefore, a high bandwidth can be achieved. When the TCSC is in use, the combination of a resonant complex conjugate zero/pole pairs suggests that a bandwidth reduction has to be carried out – however, notice that a 70% of series compensation is sufficient to make Channel 3 minimum phase.

The structural robustness of the control system is assessed in Figures 4.99 and 4.100. Figure 4.99 shows the Bode diagrams of the individual channel subsystems $h_i(s)$. It can be noticed that for the case of the open loop subsystem $h_1(s)$ (that is, $k_{11}g_{11}(s)$ in Figure 4.99(*a*)), the frequency responses are similar for all systems. However, it is observed in Figure 4.99(*b*) that only the PSS eliminates the switch-back characteristic from subsystem $h_2(s)$. The reason for this is that the PSS directly modifies subsystem $g_{22}(s)$. Although the TCSC reduces the switch-back characteristic, it is not completely eliminated. A different situation arises with the SVC damping controller, whose direct influence is only in $g_{33}(s)$ (Figure 4.99(*c*)) – failing to eliminate fully the switch-back characteristic in subsystem $h_2(s)$. As shown in Figure 4.100, all MSFs $\gamma_i(s)$ and $\gamma_a h_i(s)$ start to the left to (1,0).

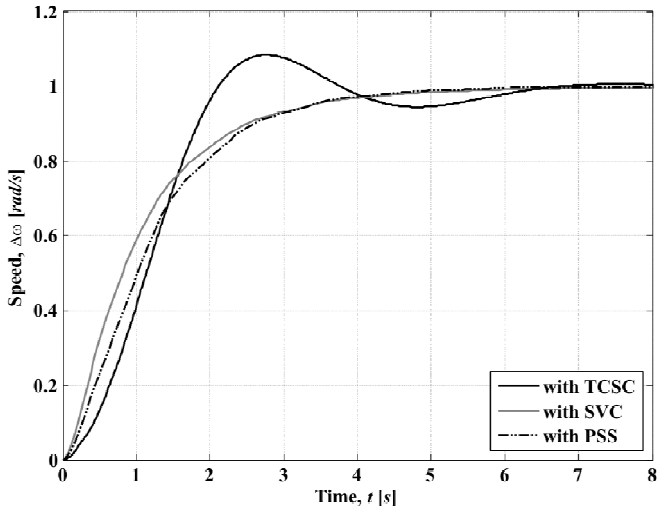

(*a*)

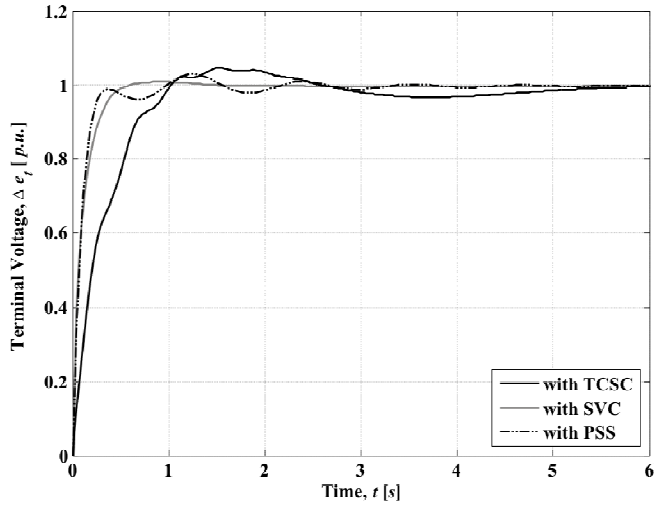

(*b*)

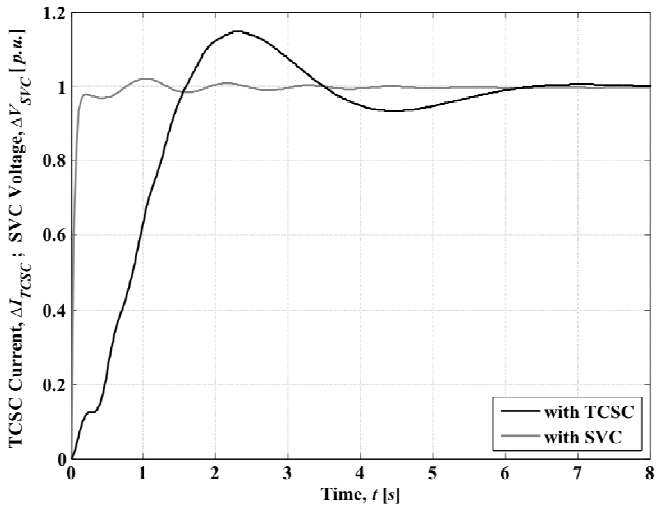

(*c*)

Figure 4.97. System performance. Step response: (*a*) Channel 1 ($T_{c1}(s)$); (*b*) Channel 2 ($T_{c2}(s)$); (*c*) Channel 3 ($T_{c3}(s)$)

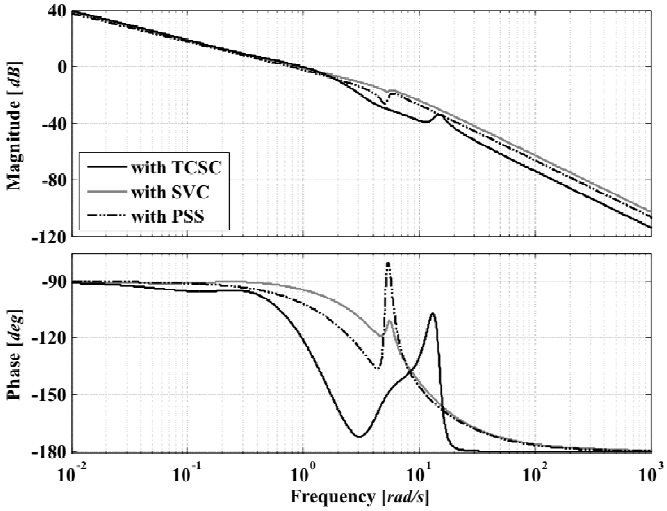

(*a*)

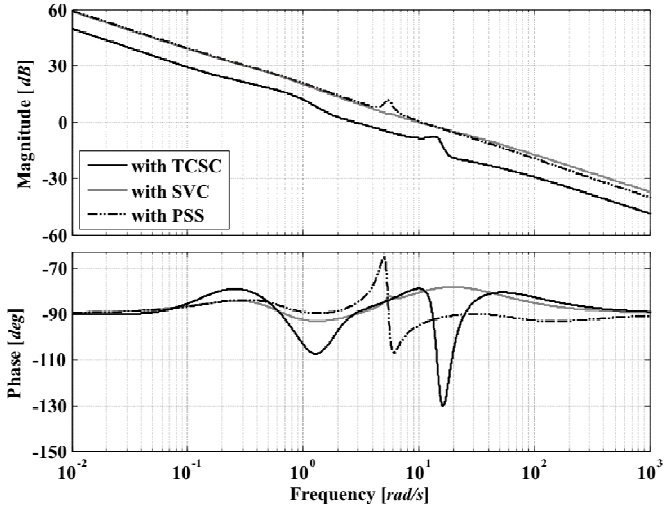

(*b*)

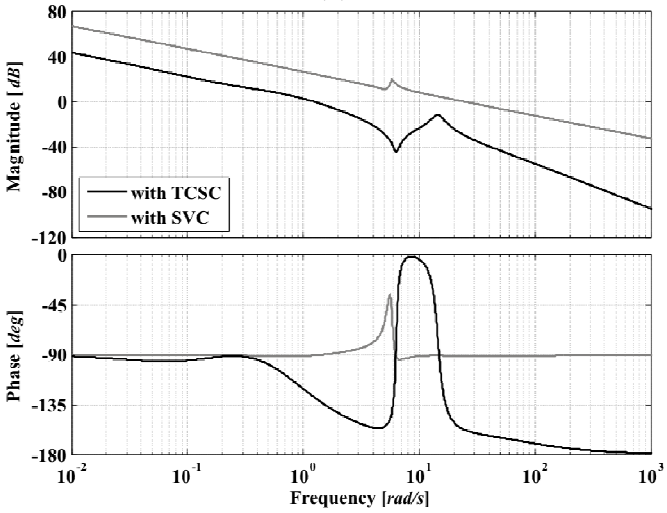

(*c*)

Figure 4.98. System performance and stability robustness assessment. Bode diagrams: (*a*) Channel 1 ($C_1(s)$); (*b*) Channel 2 ($C_2(s)$); (*c*) Channel 3 ($C_3(s)$)

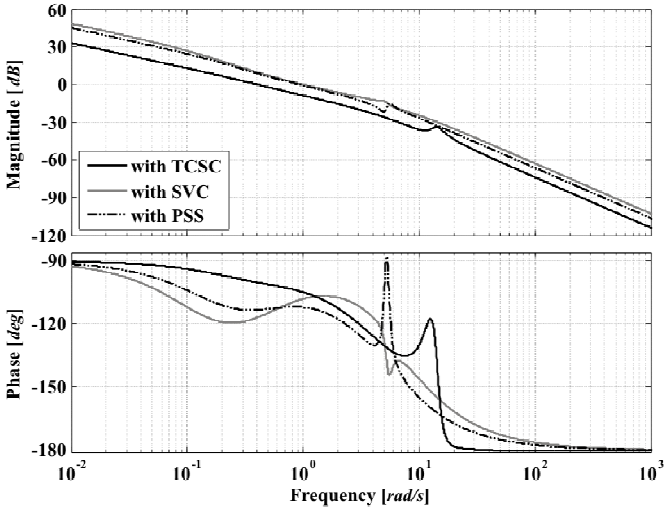

(*a*)

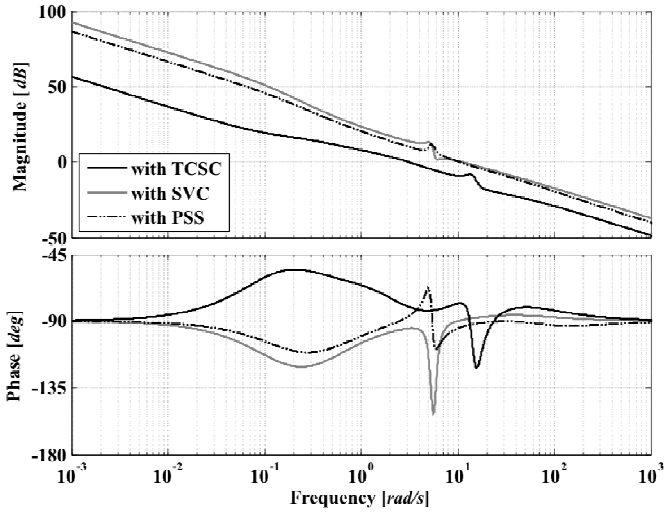

(*b*)

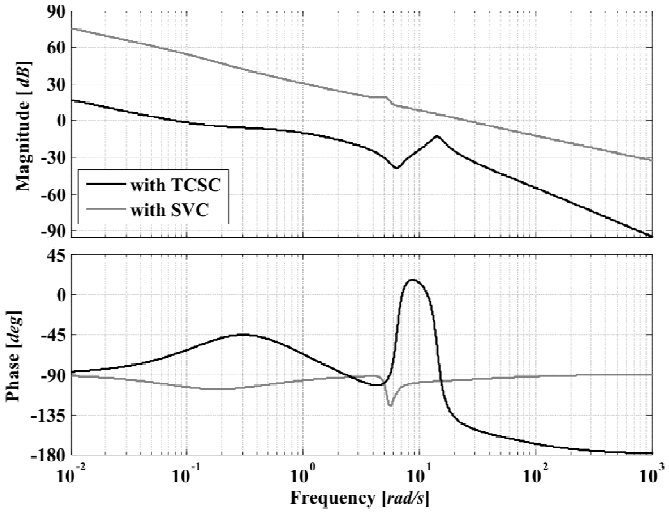

(*c*)

Figure 4.99. Stability robustness assessment. Bode diagrams: (*a*) $k_{11}g_{11}(s)$; (*b*) $k_{22}g_{22}(s)$; (*c*) $k_{33}g_{33}(s)$

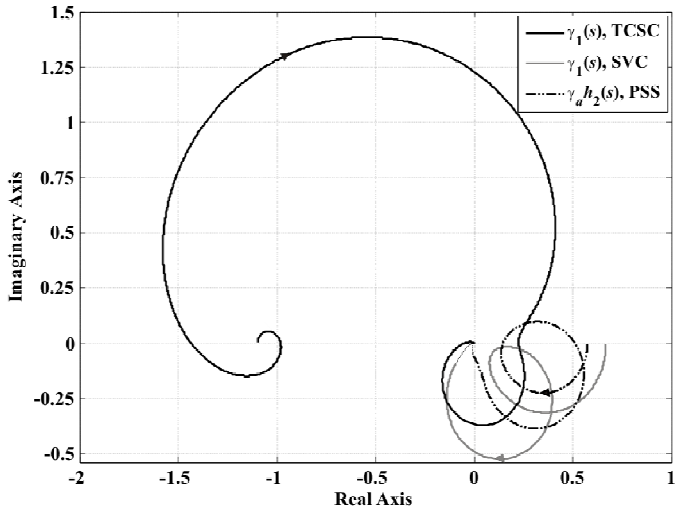

(*a*)

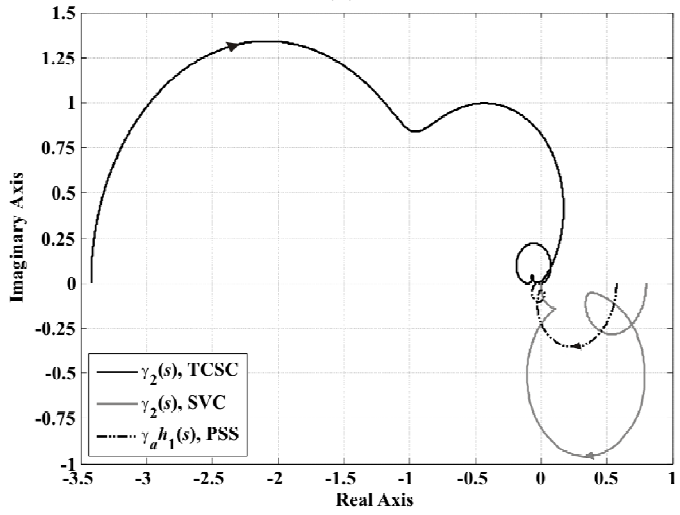

(*b*)

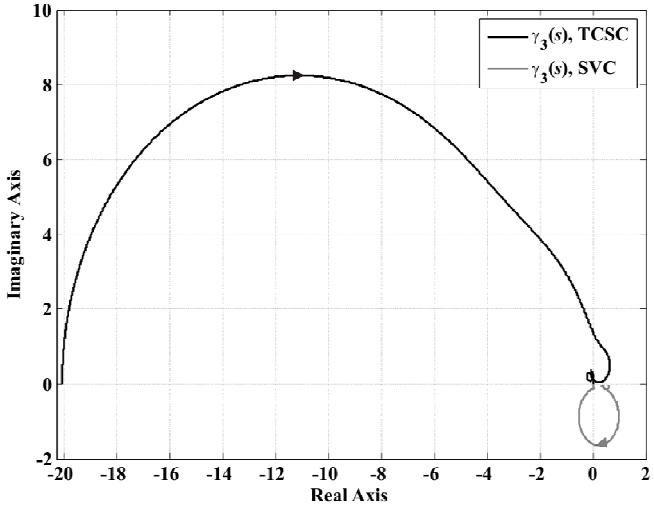

(*c*)

Figure 4.100. Structural robustness assessment. Nyquist diagrams: (*a*) $\gamma_1(s)$ and $\gamma_a h_2(s)$; (*b*) $\gamma_2(s)$ and $\gamma_a h_1(s)$; (*c*) $\gamma_3(s)$

Table 4.25. Structural and stability robustness of the channels and control system featuring an SVC with damping control loop, a TCSC or a PSS for a weak transmission system

Device	Measure	$C_1(s)$	$k_{11}g_{11}(s)$	$\gamma_1(s)$ / $\gamma_6 h_2(s)$	$C_2(s)$	$k_{22}g_{22}(s)$	$\gamma_2(s)$ / $\gamma_6 h_1(s)$	$C_3(s)$	$k_{33}g_{33}(s)$	$\gamma_3(s)$
TCSC	**Bandwidth** (*rad/s*)	1.28	0.557	–	4.17	4.4	–	1.55	0.134	–
	Gain margin (*dB*)	54.8	58	12.9	∞	∞	50.9	∞	∞	∞
	Phase margin (*deg*)	59.7	79.7	74.9	89.9	99.6	104.2	51.3	113	62.1
SVC	**Bandwidth** (*rad/s*)	1.28	1.4	–	15.1	17	–	35.7	35.9	–
	Gain margin (*dB*)	∞	∞	3.51	∞	∞	2	∞	∞	4.15
	Phase margin (*deg*)	86.2	71.8	∞	99.1	90.8	39.5	88.6	84.1	29.2
PSS	**Bandwidth** (*rad/s*)	1.08	1.26	–	15.1	15	–	–	–	–
	Gain margin (*dB*)	∞	∞	4.83	∞	∞	4.83	–	–	–
	Phase margin (*deg*)	81	68	∞	85.5	85.4	∞	–	–	–

In general, an adequate control system performance with satisfactory robustness measures is obtained when including a PSS, a SVC or a TCSC. However, the effectiveness of the TCSC can be constrained by the large amount of reactive power demanded to the synchronous generator and the proximity to the resonant boundary in the TCSC impedance characteristic. Use of either a SVC or a PSS yields a satisfactory behaviour in the synchronous generator channels. Moreover, the switch-back characteristic can be successfully eliminated, and therefore, a higher bandwidth and disturbance rejection can be obtained in the terminal voltage channel. Nonetheless, the most cost effective way to damp electromechanical oscillations is by using PSSs. As discussed in [21], the SVC should only be considered for this task once the PSS option has been exhausted

4.6. Conclusions

Multivariable control system analyses and designs of the synchronous generator – SVC and TCSC systems have been carried out in this chapter using ICAD, aimed at small-signal stability assessments. Fundamental analyses have been carried out to explain the generator dynamic behaviour as affected by these two FACTS devices. Key aspects of the SVC and TCSC operation have been elucidated by application of ICAD, which may not had been revealed, at least not as emphatically, using other form of analysis methods such as block diagrams, eigenanalysis and synchronising and damping coefficients. Simulation results obtained are in agreement with system behaviour observed in practice.

In the first part of this chapter it is formally shown that the addition of the SVC is highly effective in providing dynamic reactive power support, enhancing voltage regulation. The inclusion of the SVC does not impair the dynamical structure of the system; no considerable coupling or adverse dynamics are added to the plant. This is qualified by examining the Bode and Nyquist diagrams of the system – robustness measures are similar in an SVC-upgraded system compared to those of a system with no SVC. It is also shown that the SVC is more effective when used in weak systems.

The performance of a transmission system tends to deteriorate with electrical distance and the use of shunt compensation should be contemplated to improve the operation of the system; some benefits of shunt compensation are voltage regulation and oscillation damping provided by the SVC damping control loop. It has been shown that the SVC damping loop can be modelled as a non-diagonal post-compensator of the shaft speed output. Moreover, its inclusion does not change the dynamical structure of the system. By successfully eliminating the problematic switch-back characteristic, a higher bandwidth can be obtained for the terminal voltage channel, and, as a consequence, a better performance is obtained in weak transmission systems.

If the aim is to reduce the electrical length of the transmission line, series compensation in the form of a TCSC represents a viable option. The dynamic performance of the synchronous generator – TCSC system has been studied using ICAD. The parameters of the TCSC installed in Kayenta have been used in this study. It has been formally shown that the addition of the TCSC, operating in its capacitive region, improves the dynamical performance of the synchronous machine by substantially decreasing the electrical distance, which in turn reduces the switch-back characteristic exhibited by synchronous generators. However, although an effective modulation of the tie-line reactance and with it, an accurate regulation of power flows are available, this is achieved at the expense of introducing fragility on to the system on two counts: (*i*) the system becomes non-minimum phase (except for cases of extreme compensation), limiting the TCSC potential performance; (*ii*) the TCSC impedance control loop introduces adverse dynamics by means of cross-coupling, particularly to the speed channel of the synchronous machine. The minimum phase condition achieved for some cases featuring high compensation levels requires careful and judicious analysis, involving SSR studies, aiming at achieving the best operating point of the TCSC along its impedance characteristic. Also, it is formally shown that inductive operation of the TCSC is prejudicial to the system.

The ability of the TCSC, SVC and PSS to damp electromechanical oscillations has been formally investigated using ICAD. It has been shown that although the primordial task of the SVC is to enhance voltage regulation, an auxiliary signal in the form of a damping control loop enables quite satisfactory performance. Both control structures, the SVC and the PSS, can be modelled as post-compensators of the speed output. Their success is guaranteed since the synchronous generator dynamics are exploited to overcome the switch-back characteristic, and as a consequence, a higher bandwidth can be achieved. The primary task of the TCSC is to reduce the electrical length of the transmission line to maximise active power throughputs; however, the TCSC has also got the capacity to damp power oscillations. The overall control system with a TCSC has a better performance provided a high value of series compensation is used since the system becomes minimum phase and the switch-back characteristic decreases with an increase in tie-line compensation.

4.7. References

[1] Heffron WG, Phillips RA. *Effects of modern Amplidyne voltage regulator in under excited operation of large turbine generators*. Transactions AIEE, **71**, pp. 692–697, 1952.

[2] DeMello FP, Concordia C. *Concepts of synchronous machine stability as affected by excitation control*. IEEE Transactions on Power Apparatus and Systems, **88**, no. 4, pp. 316–329, 1969.

[3] Saidy M, Hughes FM. *Block diagram transfer function model of a generator including damper windings*. IEE Proceedings on Generation, Transmission and Distribution, **141**, no. 6, pp. 599–608, 1994.

[4] Aree P, Acha E. *Block diagram model for fundamental studies of a synchronous generator – static VAR compensator system*. IEE Proceedings on Generation, Transmission and Distribution, **146**, no. 5, pp. 507–514, 1999.

[5] Kundur P, Rogers GJ, Wong DY, Wang L, Lauby MG. *A comprehensive computer program package for small signal stability analysis of power systems*. IEEE Transactions on Power Systems, **5**, no. 4, pp. 1076–1083, 1990.

[6] Leithead WE, O'Reilly J. *M-input m-output feedback control by individual channel design. Part 1. Structural Issues.* International Journal of Control, **56**, no. 6. pp. 1347–1397, 1992.

[7] Hingorani NG. *FACTS – Flexible AC Transmission Systems*. IEE International Conference on AC and DC Power Transmission, pp. 1–7, 1991.

[8] Hingorani NG. *Flexible AC Transmission*. IEEE Spectrum, **30**(4), pp. 40–45, April 1993.

[9] Hingorani NG, Gyugyi L. *Understanding FACTS: Concepts and Technology of Flexible AC Transmission Systems.* USA: IEEE Press; 2000.

[10] Wang HF, Swift FJ. *A unified model for the analysis of FACTS devices in damping power system oscillation Part I: Single-machine infinite-bus power system*. IEEE Transactions on Power Delivery, **12**(2), pp. 941–646, 1997.

[11] Hammons TJ, Winning DJ. *Comparisons of synchronous – machine models in the study of the transient behaviour of electrical power systems*. IEE Proceedings, **118**, no. 10, pp. 1442–1458, 1971.

[12] Aree P. *Small Signal Stability Modelling and Analysis of Power Systems with Electronically Controlled Compensation*. PhD Thesis. Department of Electronics and Electrical Engineering, University of Glasgow, Scotland, UK, 2000.

[13] Kundur P. *Power Systems Stability and Control. The EPRI Power Systems Engineering Series.* USA: McGraw-Hill; 1994.

[14] Licéaga-Castro E, Licéaga-Castro J, Ugalde-Loo CE. *Beyond the Existence of Diagonal Controllers: from the Relative Gain Array to the Multivariable Structure Function*. Proceedings of the Joint 44th IEEE Conference on Decision and Control and the European Control Conference 2005, pp. 7150–7156, 2005.

[15] O'Reilly J, Leithead WE. *Multivariable control by individual channel design*. International Journal of Control, **54**, no. 1, pp. 1–46, 1991.

[16] Angquist L, Lundin B, Samuelson J. *Power Oscillation Damping Using Controlled Reactive Power Compensation: A Comparison between Series and Shunt Approaches*. IEEE Transactions on Power Systems, **8**, no. 2, pp. 687–699, 1993.

[17] Chen J, Milanovic JV, Hughes FM. *Comparison of the Effectiveness of PSS and SVC in Damping of Power System Oscillations.* Proceedings of the International Conference on Electric Power Engineering, pp. 103, 1999.

[18] Chen J, Milanovic JV, Hughes FM. *Selection of Auxiliary Input Signal and Location of a SVC for Damping Electromechanical Oscillations.* Proceedings of the IEEE Power Engineering Society Winter Meeting, **2**, pp. 623–627, 2001.

[19] Hammad AE, El-Sadek M. *Application of a Thyristor Controlled VAr Compensator for Damping Subsynchronous Oscillations in Power Systems*. IEEE Transactions on Power Apparatus and Systems, **103**, no. 1, pp. 198–212, 1984.

[20] Kapoor SC. *Dynamic Stability of Static Compensator – Synchronous Generator Combination*. IEEE Transactions on Power Apparatus and Systems, **100**, no. 4, pp. 1694–1702, 1981.

[21] Martins N, Lima LTG. *Determination of Suitable Locations for Power System Stabilizers and Static VAr Compensators for Damping Electromechanical Oscillations in Large Scale Power Systems*. IEEE Transactions on Power Systems, **5**, no. 4, pp. 1455–1469, 1990.

[22] Mithulananthan N, Canizares CA, Reeve J, Rogers GJ. *Comparison of PSS, SVC, and STATCOM Controllers for Damping Power System Oscillations.* IEEE Transactions on Power Systems, **18**, no. 2, pp. 786–792, 2003.

[23] Wang HF, Swift FJ. *Application of the Phillips-Heffron model in the analysis of the damping torque contribution to power systems by SVC damping control*. International Journal of Electrical Power and Energy Systems, **18**, no. 5, pp. 307–313, 1996.

[24] Wang HF. *Interaction Analysis and Co-ordinatinon of SVC Voltage and Damping Control*. Proceedings of the IEEE International Conference on Electric Utility Deregulation and Restructuring and Power Technologies, pp. 361–365, 2000.

[25] Kundur P, Klein M, Rogers GJ, Zywno MS. *Application of Power System Stabilizers for Enhancement of Overall System Stability*. IEEE Transactions on Power Systems, **4**, no. 2, pp. 614–626, 1989.

[26] IEEE/CIGRE (Institute of Electrical and Electronic Engineers/Conseil International des Grands Reseaux Electriques). *FACTS Overview*, special issue, 95TP108, USA: IEEE Service Centre; 1995.

[27] Jancke G, Fahlen N, Nerf O. *Series Capacitor in Power System*. IEEE Transactions on Power Apparatus and Systems, **94**, pp. 915–925, 1975.

[28] Iliceto F, Cinieri E. *Comparative Analysis of Series and Shunt Compensation Control Schemes for AC Transmission Systems*. IEEE Transactions on Power Apparatus and Systems, **96**, no. 1, pp. 1819–1830, 1977.

[29] Helbing SG, Karady GG. *Investigations of an Advanced Form of Series Compensation*. IEEE Transactions on Power Delivery, **9,** no. 2, pp. 939–947, 1994.

[30] Christl N, Hedin R, Sadek K, Lutzelberger P, Krause PE, McKenna SM, Montoya AH, Togerson D. *Advanced Series Compensation (ASC) with Thyristor Controlled Impedance*. Proceedings of the International Conference of Large High Voltage Electric Systems (CIGRE), paper 14/37/38-05, Paris, Sept. 1992.

[31] Freudenberg JS, Looze D. *Right half plane poles and zeros and design tradeoffs in feedback systems.* IEEE Transactions on Automatic Control, **30**, no.6, pp. 555–565, 1985.

[32] Leithead WE, O'Reilly J. *Uncertain SISO systems with fixed stable minimum-phase controllers: relationship of closed-loop system to RHP poles and zeros.* International Journal of Control, **53**, no.4, pp. 771–798, 1991.

[33] Kundur P, Lee DC, Zeineldin HM. *Power system stabilizers for thermal units: analytical techniques and on-site validations*. IEEE Transactions on Power Apparatus and Systems, **100**, pp. 81–95, 1981.

[34] Fadlalmoula Z, Robertson SS, O'Reilly J, Leithead WE. *Individual channel analysis of the turbogenerator with a power system stabilizer*. International Journal of Control, **69**, no.2, pp. 175–202, 1998.

[35] Hauer JF, Mittelstadt WA, Piwko RJ, Damsky BL, Eden JD. *Test results and initial operating experience for the BPA 500 kV thyristor controlled series capacitor-modulation, SSR and performance monitoring.* Proceedings of the IEEE Technical Applications Conference and Workshops Northcon95, pp. 274–279, 1995.

Chapter 5

TRANSFER FUNCTION MATRIX REPRESENTATION OF MULTI-MACHINE SYSTEMS

5.1. Introduction

The previous chapters have dealt with the very useful case of a synchronous generator and FACTS controllers connected to a very strong system (*i.e.*, infinite bus) via a tie-line reactance. Such a representation was amenable to small-signal stability assessments under the ICAD framework. The impact of the SVC and the TCSC on the generator was examined, with the analyses and control system designs carried out using a two-axis 5^{th} order synchronous generator. Such exercises enabled a fundamental understanding of the synchronous generator plant, its interaction with FACTS devices and the performance of the system with and with no compensation for a range of operating conditions.

The transfer function matrix representations of the OMIB system are indeed very useful in understanding basic concepts, particularly when carried out under the ICAD framework. Nevertheless, a matter of great practical interest is the case when the idealised, constraining assumptions of the infinite busbar are removed. Modern power systems are mostly of an interconnected nature; therefore, it is desirable to obtain a suitable representation of them in order to assess the dynamic behaviour of a multi-machine power system using ICAD.

Multi-machine power system modelling and small-signal stability studies have been a topic of much research activity in power systems for the last two decades [1,2]. Such studies are carried out using eigenanalysis and eigenvectors based techniques. This has been the preferred route of research. Efficient and comprehensive algorithms have been developed to carry out such studies and are well documented in the open literature [2–8]. However, a criticism levelled at such an approach is its lack of physical insight, relying instead on mathematical abstraction [9].

On the quest for a multi-machine representation that yields physical insight, the transfer-function block-diagram models of the OMIB system have been extended to the case of two machines [9]. Good progress was achieved, with FACTS devices [10–12] and higher order machines with damper windings [9,13] being incorporated into the multi-machine block-diagram. Nevertheless, the multi-machine block diagram representations suffer the same weaknesses as the block diagram of the OMIB system, since the individual transfer functions might not be all useful for control system design purposes. Moreover, the physical insight becomes blurred when dealing with several machines.

In order to achieve a multi-machine representation that is amenable to effective control system designs in the same vein of what was achieved for OMIB systems, a generic transfer function matrix representation generated through state-space representations is developed in this chapter. The procedure is carried out as in reference [1] but following the recommendations given in the most recent literature [2,14], *i.e.*, *q*-axis leading *d*-axis by 90°. Such a representation is suitable for the analysis and control system design using the ICAD framework. A multi-machine, multi-order model is arrived at and results are compared with those available in the open literature.

5.2. Modelling considerations

5.2.1. Statement of the problem

In general, the synchronous generator can be mathematically described by the set of differential and algebraic equations (2.2)–(2.18), or more compactly, as

$$\dot{\mathbf{x}} = f\left(\mathbf{x},\mathbf{u},t\right) \tag{5.1}$$

$$\mathbf{y} = h\left(\mathbf{x},t\right) \tag{5.2}$$

where **x** is the vector of state variables and **u** is the vector of control variables. The dimension of **x** is dependent on the model used.

The set of equations (5.1) represents six first-order differential equations per synchronous generator represented by Model 0 (6^{th} order model), with the number of variables increasing to eight when the machine currents are included. For the case of *n* machines in a power system, there is a set of 6*n* differential equations with 8*n* unknowns. A suitable model is established by deriving a relationship between the terminal voltages e_{tdi} and e_{tqi} (or internal voltages), the currents i_{tdi} and i_{tqi} and the internal angles δ_i of each machine, which provide 2*n* additional equations (given by the set (5.2)) required for the complete mathematical description of the multi-machine system [1]. For convenience, the complex notation introduced in Chapter 2 is used below, which for the *i*-th machine is given by

$$\vec{e}_{ti} = e_{tdi} + je_{tqi} \tag{5.3}$$

$$\vec{i}_{ti} = i_{tdi} + ji_{tqi} \tag{5.4}$$

or, in a more explicit form,

$$\bar{\mathbf{e}}_t = \begin{bmatrix} e_{td1} + je_{tq1} \\ e_{td2} + je_{tq2} \\ \vdots \\ e_{tdn} + je_{tqn} \end{bmatrix} = \begin{bmatrix} \vec{e}_{t1} \\ \vec{e}_{t2} \\ \vdots \\ \vec{e}_{tn} \end{bmatrix} \tag{5.5}$$

$$\bar{\mathbf{i}}_t = \begin{bmatrix} i_{td1} + ji_{tq1} \\ i_{td2} + ji_{tq2} \\ \vdots \\ i_{tdn} + ji_{tqn} \end{bmatrix} = \begin{bmatrix} \vec{i}_{t1} \\ \vec{i}_{t2} \\ \vdots \\ \vec{i}_{tn} \end{bmatrix} \tag{5.6}$$

Notice that the terminal voltage and current phasors (5.3) and (5.4) are referred to the *d*- and *q*-axis of machine *i*. Therefore, each machine has its own reference frame and rotates independently from the others in the system. To be able to carry out studies of interactions between the different machines through the network it is essential to obtain a relationship which relates the complex vectors (5.5) and (5.6) while using a common reference frame rotating at synchronous speed.

5.2.2. Conversion of the electrical network and machine coordinates to a common reference frame

Consider the multi-machine system shown in Figure 5.1, consisting of *n* machines, *r* loads and an arbitrary number of nodes *m*.

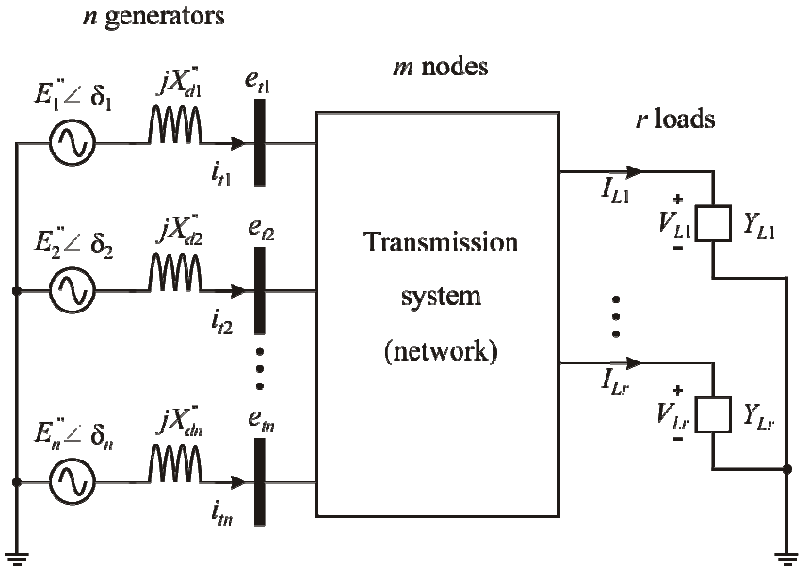

Figure 5.1. Multi-machine system with constant impedance loads

For steady-state purposes, currents and voltages can be represented by phasors referred to a common frame. Recalling from Chapter 2, the matrix form of the network in terms of the nodal admittance matrix including *n* nodes can be written as

$$\begin{bmatrix} \hat{I}_1 \\ \hat{I}_2 \\ \vdots \\ \hat{I}_n \end{bmatrix} = \begin{bmatrix} \overline{Y}_{11} & \overline{Y}_{12} & \cdots & \overline{Y}_{1n} \\ \overline{Y}_{21} & \overline{Y}_{22} & \cdots & \overline{Y}_{2n} \\ \vdots & \vdots & \ddots & \vdots \\ \overline{Y}_{n1} & \overline{Y}_{n2} & \cdots & \overline{Y}_{nn} \end{bmatrix} \begin{bmatrix} \hat{V}_1 \\ \hat{V}_2 \\ \vdots \\ \hat{V}_n \end{bmatrix} \tag{5.7}$$

or

$$\hat{\mathbf{I}} = \overline{\mathbf{Y}}\hat{\mathbf{V}} \tag{5.8}$$

where $\overline{\mathbf{Y}}$ is the nodal admittance matrix, $\hat{\mathbf{V}}$ is the vector of nodal voltage to ground and $\hat{\mathbf{I}}$ is the vector of nodal current injections. Matrix $\overline{\mathbf{Y}}$ is constructed according to (2.40).

Assuming static loads represented by constant impedances, the equivalent shunt admittance is given by

$$\overline{Y}_{Li} = \left(\frac{P_{Li}}{V_{Li}^2}\right) - j\left(\frac{Q_{Li}}{V_{Li}^2}\right) \tag{5.9}$$

where V_{Li} is the voltage magnitude, P_{Li} the active power and Q_{Li} the reactive power at bus *i*. The size of the network is mathematically reduced by elimination of the passive nodes (load nodes) by applying Kron's reduction. As loads are represented by shunt admittances, then all load nodes have zero current injections; hence, for the network with *n* machines and *r* loads,

$$\begin{bmatrix} \vec{I}_{t1} \\ \vdots \\ \vec{I}_{tn} \\ 0 \\ \vdots \\ 0 \end{bmatrix} = \begin{bmatrix} \overline{Y}_{11} & \cdots & \overline{Y}_{1n} & \overline{Y}_{1(n+1)} & \cdots & \overline{Y}_{1r} \\ \vdots & \ddots & \vdots & \vdots & \ddots & \vdots \\ \overline{Y}_{n1} & \cdots & \overline{Y}_{nn} & \overline{Y}_{n(n+1)} & \cdots & \overline{Y}_{nr} \\ \overline{Y}_{(n+1)1} & \cdots & \overline{Y}_{(n+1)n} & \overline{Y}_{(n+1)(n+1)} & \cdots & \overline{Y}_{(n+1)r} \\ \vdots & \ddots & \vdots & \vdots & \ddots & \vdots \\ \overline{Y}_{r1} & \cdots & \overline{Y}_{rn} & \overline{Y}_{r(n+1)} & \cdots & \overline{Y}_{rr} \end{bmatrix} \begin{bmatrix} \vec{E}_{t1} \\ \vdots \\ \vec{E}_{tn} \\ \vec{V}_{(n+1)} \\ \vdots \\ \vec{V}_r \end{bmatrix} \tag{2.43}$$

or, compactly,

$$\begin{bmatrix} \overline{\mathbf{I}}_t \\ \cdots \\ \mathbf{0} \end{bmatrix} = \begin{bmatrix} \overline{\mathbf{Y}}_{nn} & \vdots & \overline{\mathbf{Y}}_{nr} \\ \cdots\cdots & \vdots & \cdots\cdots \\ \overline{\mathbf{Y}}_{rn} & \vdots & \overline{\mathbf{Y}}_{rr} \end{bmatrix} \begin{bmatrix} \overline{\mathbf{E}}_t \\ \cdots \\ \overline{\mathbf{V}}_r \end{bmatrix} \tag{2.44}$$

Eliminating the passive nodes by applying Kron's reduction yields

$$\overline{\mathbf{I}}_t = \left(\overline{\mathbf{Y}}_{nn} - \overline{\mathbf{Y}}_{nr}\overline{\mathbf{Y}}_{rr}^{-1}\overline{\mathbf{Y}}_{rn}\right)\overline{\mathbf{E}}_t \tag{2.47}$$

or

$$\overline{\mathbf{I}}_t = \overline{\mathbf{Y}}_n\overline{\mathbf{E}}_t \tag{2.48}$$

where matrix $\overline{\mathbf{Y}}_n = \left(\overline{\mathbf{Y}}_{nn} - \overline{\mathbf{Y}}_{nr}\overline{\mathbf{Y}}_{rr}^{-1}\overline{\mathbf{Y}}_{rn}\right)$ is the reduced admittance matrix and

$$\bar{\mathbf{E}}_t = \begin{bmatrix} E_{tD1} + jE_{tQ1} \\ E_{tD2} + jE_{tQ2} \\ \vdots \\ E_{tDn} + jE_{tQn} \end{bmatrix} = \begin{bmatrix} \vec{E}_{t1} \\ \vec{E}_{t2} \\ \vdots \\ \vec{E}_{tn} \end{bmatrix} \tag{5.10}$$

$$\bar{\mathbf{I}}_t = \begin{bmatrix} I_{tD1} + jI_{tQ1} \\ I_{tD2} + jI_{tQ2} \\ \vdots \\ I_{tDn} + jI_{tQn} \end{bmatrix} = \begin{bmatrix} \vec{I}_{t1} \\ \vec{I}_{t2} \\ \vdots \\ \vec{I}_{tn} \end{bmatrix} \tag{5.11}$$

It should be emphasised that the current and terminal voltage phasors in the previous equations are expressed in terms of a common system reference frame. The reference is the *q*-axis of an hypothetical rotor *i*-th located at an angle δ_i with respect to a synchronously rotating system reference, as shown in Figure 5.2.

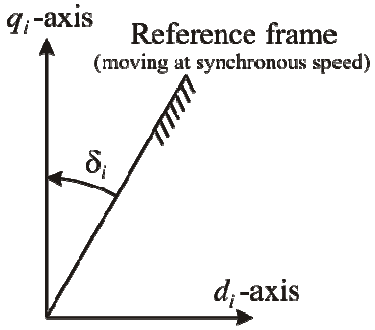

Figure 5.2. Position of axes of rotor *i*-th with respect to reference frame

Recalling from Chapter 2, the terminal voltage of the *i*-th machine (on the machine *dq* frame) can be represented in the *DQ* system reference frame as

$$\vec{E}_{ti} = e^{j\left(\delta_i - \pi/2\right)} \vec{e}_{ti} \tag{5.12}$$

Expression (5.12) is obtained by inspection of Figure 2.8. Similarly,

$$\vec{I}_{ti} = e^{j\left(\delta_i - \pi/2\right)} \vec{i}_{ti} \tag{5.13}$$

can be used to convert the currents to the common reference frame. Equations (5.12) and (5.13) can be generalised to include all *n* nodes. Let

$$\mathbf{T} = \begin{bmatrix} e^{j(\delta_1 - \pi/2)} & 0 & \cdots & 0 \\ 0 & e^{j(\delta_2 - \pi/2)} & \cdots & 0 \\ \vdots & \vdots & \ddots & \vdots \\ 0 & 0 & \cdots & e^{j(\delta_n - \pi/2)} \end{bmatrix} \tag{5.14}$$

From (5.14) it can be seen that **T** is a matrix that transforms *d* and *q* quantities of all machines to the common system frame that rotates at synchronous speed. Transformation (5.14) is orthogonal, thus

$$\mathbf{T}^{-1} = \mathbf{T}^{*} \tag{5.15}$$

Then, from (5.5), (5.6), (5.10), (5.11) (5.14) and (5.15) the following relations are established:

$$\bar{\mathbf{E}}_t = \mathbf{T}\bar{\mathbf{e}}_t \tag{5.16}$$

$$\bar{\mathbf{I}}_t = \mathbf{T}\bar{\mathbf{i}}_t \tag{5.17}$$

and

$$\bar{\mathbf{e}}_t = \mathbf{T}^{-1}\bar{\mathbf{E}}_t \tag{5.18}$$

$$\bar{\mathbf{i}}_t = \mathbf{T}^{-1}\bar{\mathbf{I}}_t \tag{5.19}$$

Using (5.16) and (5.17) in (2.47) yields

$$\mathbf{T}\bar{\mathbf{i}}_t = \bar{\mathbf{Y}}_n\mathbf{T}\bar{\mathbf{e}}_t \tag{5.20}$$

Pre-multiplying (5.20) by $\mathbf{T}^{-1}$ gives

$$\bar{\mathbf{i}}_t = \bar{\mathbf{M}}\bar{\mathbf{e}}_t \tag{5.21}$$

where

$$\bar{\mathbf{M}} = \mathbf{T}^{-1}\bar{\mathbf{Y}}_n\mathbf{T} \tag{5.22}$$

Equation (5.21) relates the terminal voltages and currents of the machines in a new, unified reference frame. In explicit form, for an *n*-machine system, the reduced admittance matrix $\bar{\mathbf{Y}}_n$ of the network is of the form

$$\bar{\mathbf{Y}}_n = \begin{bmatrix} Y_{11}e^{j\theta_{11}} & Y_{12}e^{j\theta_{12}} & \dots & Y_{1n}e^{j\theta_{1n}} \\ Y_{21}e^{j\theta_{21}} & Y_{22}e^{j\theta_{22}} & \dots & Y_{2n}e^{j\theta_{2n}} \\ \vdots & \vdots & \ddots & \vdots \\ Y_{n1}e^{j\theta_{n1}} & Y_{n2}e^{j\theta_{n2}} & \dots & Y_{nn}e^{j\theta_{nn}} \end{bmatrix} \tag{5.23}$$

where Y_{ik} is the impedance magnitude between nodes *i* and *k*. From (5.14) and (5.23),

$$\bar{\mathbf{Y}}_n\mathbf{T} = \begin{bmatrix} Y_{11}e^{j(\theta_{11}+\delta_1-\pi/2)} & Y_{12}e^{j(\theta_{12}+\delta_2-\pi/2)} & \dots & Y_{1n}e^{j(\theta_{1n}+\delta_n-\pi/2)} \\ Y_{21}e^{j(\theta_{21}+\delta_1-\pi/2)} & Y_{22}e^{j(\theta_{22}+\delta_2-\pi/2)} & \dots & Y_{2n}e^{j(\theta_{2n}+\delta_n-\pi/2)} \\ \vdots & \vdots & \ddots & \vdots \\ Y_{n1}e^{j(\theta_{n1}+\delta_1-\pi/2)} & Y_{n2}e^{j(\theta_{n2}+\delta_2-\pi/2)} & \dots & Y_{nn}e^{j(\theta_{nn}+\delta_n-\pi/2)} \end{bmatrix} \tag{5.24}$$

Pre-multiplying (5.24) by $\mathbf{T}^{-1}$ yields

$$\bar{\mathbf{M}} = \mathbf{T}^{-1}\bar{\mathbf{Y}}_n\mathbf{T} = \begin{bmatrix} Y_{11}e^{j\theta_{11}} & Y_{12}e^{j(\theta_{12}+\delta_2-\delta_1)} & \dots & Y_{1n}e^{j(\theta_{1n}+\delta_n-\delta_1)} \\ Y_{21}e^{j(\theta_{21}+\delta_1-\delta_2)} & Y_{22}e^{j\theta_{22}} & \dots & Y_{2n}e^{j(\theta_{2n}+\delta_n-\delta_2)} \\ \vdots & \vdots & \ddots & \vdots \\ Y_{n1}e^{j(\theta_{n1}+\delta_1-\delta_n)} & Y_{n2}e^{j(\theta_{n2}+\delta_2-\delta_n)} & \dots & Y_{nn}e^{j\theta_{nn}} \end{bmatrix} \tag{5.25}$$

Moreover, expression (5.25) may be rewritten as

$$\bar{\mathbf{M}} = \begin{bmatrix} Y_{11}e^{j\theta_{11}} & Y_{12}e^{j(\theta_{12}-\delta_{12})} & \dots & Y_{1n}e^{j(\theta_{1n}-\delta_{1n})} \\ Y_{21}e^{j(\theta_{21}-\delta_{21})} & Y_{22}e^{j\theta_{22}} & \dots & Y_{2n}e^{j(\theta_{2n}-\delta_{2n})} \\ \vdots & \vdots & \ddots & \vdots \\ Y_{n1}e^{j(\theta_{n1}-\delta_{n1})} & Y_{n2}e^{j(\theta_{n2}-\delta_{n2})} & \dots & Y_{nn}e^{j\theta_{nn}} \end{bmatrix} \tag{5.26}$$

where

$$\delta_{ik} = \delta_i - \delta_k \tag{5.27}$$

and

$$\delta_{ki} = -\delta_{ik} \tag{5.28}$$

5.2.3. Linearised model of the network

Linearising (5.21) yields

$$\Delta\bar{\mathbf{i}}_t = \bar{\mathbf{M}}_0 \Delta\bar{\mathbf{e}}_t + \Delta\bar{\mathbf{M}}\bar{\mathbf{e}}_{t0} \tag{5.29}$$

where $\bar{\mathbf{M}}_0$ is evaluated at the initial angles δ_{i0}, i = 1,2,…,n, and $\bar{\mathbf{e}}_{t0}$ is the initial value of vector $\bar{\mathbf{e}}_t$. Let $\delta_i = \delta_{i0} + \Delta\delta_i$. Then the matrix $\bar{\mathbf{M}}$ in (5.26) becomes

$$\bar{\mathbf{M}} = \begin{bmatrix} Y_{11}e^{j\theta_{11}} & Y_{12}e^{j(\theta_{12}-\delta_{120}-\Delta\delta_{12})} & \cdots & Y_{1n}e^{j(\theta_{1n}-\delta_{1n0}-\Delta\delta_{1n})} \\ Y_{21}e^{j(\theta_{21}-\delta_{210}-\Delta\delta_{21})} & Y_{22}e^{j\theta_{22}} & \cdots & Y_{2n}e^{j(\theta_{2n}-\delta_{2n0}-\Delta\delta_{2n})} \\ \vdots & \vdots & \ddots & \vdots \\ Y_{n1}e^{j(\theta_{n1}-\delta_{n10}-\Delta\delta_{n1})} & Y_{n2}e^{j(\theta_{n2}-\delta_{n20}-\Delta\delta_{n2})} & \cdots & Y_{nn}e^{j\theta_{nn}} \end{bmatrix} \tag{5.30}$$

Notice that the general term $\bar{m}_{ik}$ of matrix $\bar{\mathbf{M}}$, with $i \neq k$, is of the form $Y_{ik}e^{j(\theta_{ik}-\delta_{ik0}-\Delta\delta_{ik})}$, thus

$$\bar{m}_{ik} = Y_{ik}e^{j(\theta_{ik}-\delta_{ik0})}e^{-j\Delta\delta_{ik}} \tag{5.31}$$

For small increments, $\cos\Delta\delta_{ik} \cong 1$ and $\sin\Delta\delta_{ik} \cong \Delta\delta_{ik}$, so,

$$\bar{m}_{ik} = Y_{ik}e^{j(\theta_{ik}-\delta_{ik0})}\left(1 - j\Delta\delta_{ik}\right) \tag{5.32}$$

Therefore, the general term in $\Delta\bar{\mathbf{M}}$ is given by

$$\Delta\bar{m}_{ik} = -jY_{ik}e^{j(\theta_{ik}-\delta_{ik0})}\Delta\delta_{ik} \tag{5.33}$$

It should be noticed that $\Delta\bar{\mathbf{M}}$ has off-diagonal terms only, since the diagonal terms in $\bar{\mathbf{M}}$ are constants, *i.e.*, $\Delta\bar{m}_{ii} = 0$. Then

$$\Delta\bar{\mathbf{M}}\bar{\mathbf{e}}_{t0} = -j\begin{bmatrix} 0 & Y_{12}e^{j(\theta_{12}-\delta_{120})}\Delta\delta_{12} & \cdots & Y_{1n}e^{j(\theta_{1n}-\delta_{1n0})}\Delta\delta_{1n} \\ Y_{21}e^{j(\theta_{21}-\delta_{210})}\Delta\delta_{21} & 0 & \cdots & Y_{2n}e^{j(\theta_{2n}-\delta_{2n0})}\Delta\delta_{2n} \\ \vdots & \vdots & \ddots & \vdots \\ Y_{n1}e^{j(\theta_{n1}-\delta_{n10})}\Delta\delta_{n1} & Y_{n2}e^{j(\theta_{n2}-\delta_{n20})}\Delta\delta_{n2} & \cdots & 0 \end{bmatrix}\begin{bmatrix} \vec{e}_{t10} \\ \vec{e}_{t20} \\ \vdots \\ \vec{e}_{tn0} \end{bmatrix} \tag{5.34}$$

or, more compactly,

$$\Delta\bar{\mathbf{M}}\bar{\mathbf{V}}_0 = -j\begin{bmatrix} \sum_{k=2}^{n}\vec{e}_{tk0}Y_{1k}e^{j(\theta_{1k}-\delta_{1k0})}\Delta\delta_{1k} \\ \sum_{\substack{k=1 \\ k\neq 2}}^{n}\vec{e}_{tk0}Y_{2k}e^{j(\theta_{2k}-\delta_{2k0})}\Delta\delta_{2k} \\ \vdots \\ \sum_{k=1}^{n-1}\vec{e}_{tk0}Y_{nk}e^{j(\theta_{nk}-\delta_{nk0})}\Delta\delta_{nk} \end{bmatrix} \tag{5.35}$$

and the linearised equation (5.29) becomes,

$$\begin{bmatrix} \Delta\vec{i}_{t1} \\ \Delta\vec{i}_{t2} \\ \vdots \\ \Delta\vec{i}_{tn} \end{bmatrix} = \begin{bmatrix} Y_{11}e^{j\theta_{11}} & Y_{12}e^{j(\theta_{12}-\delta_{120})} & \cdots & Y_{1n}e^{j(\theta_{1n}-\delta_{1n0})} \\ Y_{21}e^{j(\theta_{21}-\delta_{210})} & Y_{22}e^{j\theta_{22}} & \cdots & Y_{2n}e^{j(\theta_{2n}-\delta_{2n0})} \\ \vdots & \vdots & \ddots & \vdots \\ Y_{n1}e^{j(\theta_{n1}-\delta_{n10})} & Y_{n2}e^{j(\theta_{n2}-\delta_{n20})} & \cdots & Y_{nn}e^{j\theta_{nn}} \end{bmatrix} \begin{bmatrix} \Delta\vec{e}_{t1} \\ \Delta\vec{e}_{t2} \\ \vdots \\ \Delta\vec{e}_{tn} \end{bmatrix} - j \begin{bmatrix} \sum_{k=2}^{n} \vec{e}_{tk0} Y_{1k} e^{j(\theta_{1k}-\delta_{1k0})} \Delta\delta_{1k} \\ \sum_{\substack{k=1 \\ k\neq 2}}^{n} \vec{e}_{tk0} Y_{2k} e^{j(\theta_{2k}-\delta_{2k0})} \Delta\delta_{2k} \\ \vdots \\ \sum_{k=1}^{n-1} \vec{e}_{tk0} Y_{nk} e^{j(\theta_{nk}-\delta_{nk0})} \Delta\delta_{nk} \end{bmatrix} \tag{5.36}$$

5.3. State-space model construction

Suitable combination of the algebraic and differential equations (2.2)–(2.18) provides for different order models for the synchronous machine. In this chapter only the 6th order model (2*d*.2*q*, previously called Model 0) will be used. Notice that lower order models can be obtained by performing some simplifying assumptions in the 6th order model.

Thus, for the *i*-th machine in the *n*-machine system of Figure 5.1, the differential equations describing its behaviour are:

$$\Delta\dot{E}'_{qi} = \frac{1}{\tau'_{di0}}\left[\Delta E_{fdi} - \left(X_{di} - X'_{di}\right)\Delta i_{tdi} - \Delta E'_{qi}\right] \tag{5.37}$$

$$\Delta\dot{E}''_{qi} = \frac{1}{\tau''_{di0}}\left\{\frac{\tau''_{di0}}{\tau'_{di0}}\Delta E_{fdi} - \left[\left(X'_{di} - X''_{di}\right) + \frac{\tau''_{di0}}{\tau'_{di0}}\left(X_{di} - X'_{di}\right)\right]\Delta i_{tdi} + \left[1 - \frac{\tau''_{di0}}{\tau'_{di0}}\right]\Delta E'_{qi} - \Delta E''_{qi}\right\} \tag{5.38}$$

$$\Delta\dot{E}'_{di} = \frac{1}{\tau'_{qi0}}\left[\left(X_{qi} - X'_{qi}\right)\Delta i_{tqi} - \Delta E'_{di}\right] \tag{5.39}$$

$$\Delta\dot{E}''_{di} = \frac{1}{\tau''_{qi0}}\left[\left(X'_{qi} - X''_{qi}\right)\Delta i_{tqi} - \Delta E''_{di}\right] \tag{5.40}$$

$$\Delta\dot{\omega}_i = \frac{1}{2H_i}\left[\Delta P_{mi} - \Delta P_{ei} - D_i\Delta\omega_i\right] \tag{5.41}$$

$$\Delta\dot{\delta}_i = \omega_{i0}\Delta\omega_i \tag{5.42}$$

where

$$\Delta P_{ei} = i_{tdi0}\Delta E''_{di} + i_{tqi0}\Delta E''_{qi} + \left[E''_{di0} + i_{tqi0}\left(X''_{qi} - X''_{di}\right)\right]\Delta i_{tdi} + \left[E''_{qi0} + i_{tdi0}\left(X''_{qi} - X''_{di}\right)\right]\Delta i_{tqi} \tag{5.43}$$

$$\Delta e_{ti} = \left(e_{ti0}\right)^{-1}\left[e_{tdi0}\Delta e_{tdi} + e_{tqi0}\Delta e_{tqi}\right] \tag{5.44}$$

$$\Delta e_{tqi} = \Delta E''_{qi} - X''_{di}\Delta i_{tdi} \tag{5.45}$$

$$\Delta e_{tdi} = \Delta E''_{di} + X''_{qi}\Delta i_{tqi} \tag{5.46}$$

Notice that equations (5.37)–(5.46) are represented in terms of internal voltages. Therefore, the terminal voltages $\vec{e}_{ti}$ are replaced by the sub-transient internal voltages $\vec{E}_i^{"}$ and the sub-transient generator impedances are incorporated in the network impedance matrix $\bar{\mathbf{Y}}$ in the linearised network equation (5.36) prior to its reduction to $\bar{\mathbf{Y}}_n$. Also,

$$\bar{Y}_{ik} = \bar{Y}_{ki} \tag{5.47}$$

$$Y_{ii} e^{j\theta_{ii}} = G_{ii} + jB_{ii} \tag{5.48}$$

$$\Delta\vec{i}_{ti} = \Delta i_{tdi} + j\Delta i_{tqi} \tag{5.49}$$

$$\Delta\vec{E}_i^{"} = \Delta E_{di}^{"} + j\Delta E_{qi}^{"} \tag{5.50}$$

$$\vec{E}_{i0}^{"} = E_{di0}^{"} + jE_{qi0}^{"} \tag{5.51}$$

Provided the appropriate variable substitutions and using (5.27), (5.28), (5.47)–(5.51) into (5.36), the following general current expressions can be deduced for the *i*-th machine:

$$\begin{aligned}
\Delta i_{tdi} = {} & G_{ii}\Delta E_{di}^{"} - B_{ii}\Delta E_{qi}^{"} + \sum_{k=i+1}^{n} Y_{ik}\left[\cos\left(\theta_{ik} - \delta_{ik0}\right)\Delta E_{dk}^{"} - \sin\left(\theta_{ik} - \delta_{ik0}\right)\Delta E_{qk}^{"}\right] + \\
& + \sum_{\substack{k=1 \\ i>k}}^{i-1} Y_{ki}\left[\cos\left(\theta_{ki} + \delta_{ki0}\right)\Delta E_{dk}^{"} - \sin\left(\theta_{ki} + \delta_{ki0}\right)\Delta E_{qk}^{"}\right] + \\
& + \sum_{k=i+1}^{n} Y_{ik}\left[E_{dk0}^{"}\sin\left(\theta_{ik} - \delta_{ik0}\right) + E_{qk0}^{"}\cos\left(\theta_{ik} - \delta_{ik0}\right)\right]\Delta\delta_{ik} + \\
& - \sum_{\substack{k=1 \\ i>k}}^{i-1} Y_{ki}\left[E_{dk0}^{"}\sin\left(\theta_{ki} + \delta_{ki0}\right) + E_{qk0}^{"}\cos\left(\theta_{ki} + \delta_{ki0}\right)\right]\Delta\delta_{ki}
\end{aligned} \tag{5.52}$$

$$\begin{aligned}
\Delta i_{tqi} = {} & B_{ii}\Delta E_{di}^{"} + G_{ii}\Delta E_{qi}^{"} + \sum_{k=i+1}^{n} Y_{ik}\left[\sin\left(\theta_{ik} - \delta_{ik0}\right)\Delta E_{dk}^{"} - \cos\left(\theta_{ik} - \delta_{ik0}\right)\Delta E_{qk}^{"}\right] + \\
& + \sum_{\substack{k=1 \\ i>k}}^{i-1} Y_{ki}\left[\sin\left(\theta_{ki} + \delta_{ki0}\right)\Delta E_{dk}^{"} + \cos\left(\theta_{ki} + \delta_{ki0}\right)\Delta E_{qk}^{"}\right] + \\
& + \sum_{k=i+1}^{n} Y_{ik}\left[-E_{dk0}^{"}\cos\left(\theta_{ik} - \delta_{ik0}\right) + E_{qk0}^{"}\sin\left(\theta_{ik} - \delta_{ik0}\right)\right]\Delta\delta_{ik} + \\
& - \sum_{\substack{k=1 \\ i>k}}^{i-1} Y_{ki}\left[-E_{dk0}^{"}\cos\left(\theta_{ki} + \delta_{ki0}\right) + E_{qk0}^{"}\sin\left(\theta_{ki} + \delta_{ki0}\right)\right]\Delta\delta_{ki}
\end{aligned} \tag{5.53}$$

Substitution of (5.52) and (5.53) for $i = 1,2,\ldots n$ into (5.37)–(5.46) yields the algebraic and differential equations of the multi-machine model. In general, the differential equations of the *i*-th machine can be expressed as

$$\Delta\dot{\omega}_i = \frac{1}{2H_i}\left[\Delta P_{mi} - D_i\Delta\omega_i - \sum_{k=1}^{n}\left(K_{2ik}\Delta E_{qk}^{"} + K_{2dik}\Delta E_{dk}^{"}\right) - \sum_{k=i+1}^{n} K_{1iik}\Delta\delta_{ik} - \sum_{\substack{k=1 \\ i>k}}^{i-1} K_{1iki}\Delta\delta_{ki}\right] \tag{5.54}$$

$$\Delta \dot{E}'_{qi} = \frac{1}{\tau'_{di0}}\left[\Delta E_{fdi} - \Delta E'_{qi}\right] + \sum_{k=1}^{n}\left(C_{2ik}\Delta E''_{qk} + C_{2dik}\Delta E''_{dk}\right) + \sum_{k=i+1}^{n} C_{1iik}\Delta\delta_{ik} + \sum_{\substack{k=1\\ i>k}}^{i-1} C_{1iki}\Delta\delta_{ki} \tag{5.55}$$

$$\Delta \dot{E}''_{qi} = \frac{1}{\tau''_{di0}}\left\{\frac{\tau''_{di0}}{\tau'_{di0}}\Delta E_{fdi} + \left[1 - \frac{\tau''_{di0}}{\tau'_{di0}}\right]\Delta E'_{qi}\right\} + \sum_{k=1}^{n}\left(C_{4ik}\Delta E''_{qk} + C_{4dik}\Delta E''_{dk}\right) + \sum_{k=i+1}^{n} C_{3iik}\Delta\delta_{ik} + \sum_{\substack{k=1\\ i>k}}^{i-1} C_{3iki}\Delta\delta_{ki} \tag{5.56}$$

$$\Delta \dot{E}'_{di} = -\frac{1}{\tau'_{qi0}}\Delta E'_{di} + \sum_{k=1}^{n}\left(C_{6ik}\Delta E''_{qk} + C_{6dik}\Delta E''_{dk}\right) + \sum_{k=i+1}^{n} C_{5iik}\Delta\delta_{ik} + \sum_{\substack{k=1\\ i>k}}^{i-1} C_{5iki}\Delta\delta_{ki} \tag{5.57}$$

$$\Delta \dot{E}''_{di} = \sum_{k=1}^{n}\left(C_{8ik}\Delta E''_{qk} + C_{8dik}\Delta E''_{dk}\right) + \sum_{k=i+1}^{n} C_{7iik}\Delta\delta_{ik} + \sum_{\substack{k=1\\ i>k}}^{i-1} C_{7iki}\Delta\delta_{ki} \tag{5.58}$$

$$\Delta \dot{\delta}_{1i} = \omega_{10}\Delta\omega_1 - \omega_{i0}\Delta\omega_i \qquad i > 1 \tag{5.59}$$

where

$$\Delta P_{ei} = \sum_{k=1}^{n}\left(K_{2ik}\Delta E''_{qk} + K_{2dik}\Delta E''_{dk}\right) + \sum_{k=i+1}^{n} K_{1iik}\Delta\delta_{ik} + \sum_{\substack{k=1\\ i>k}}^{i-1} K_{1iki}\Delta\delta_{ki} \tag{5.60}$$

$$\Delta e_{ti} = \sum_{k=1}^{n}\left(K_{6ik}\Delta E''_{qk} + K_{6dik}\Delta E''_{dk}\right) + \sum_{k=i+1}^{n} K_{5iik}\Delta\delta_{ik} + \sum_{\substack{k=1\\ i>k}}^{i-1} K_{5iki}\Delta\delta_{ki} \tag{5.61}$$

The coefficients of equations (5.54)–(5.61) are:

$$\begin{aligned} K_{1iik} = {} & Y_{ik}\left[E''_{dk0}\sin\left(\theta_{ik} - \delta_{ik0}\right) + E''_{qk0}\cos\left(\theta_{ik} - \delta_{ik0}\right)\right]\left[E''_{di0} + i_{tqi0}\left(X''_{qi} - X''_{di}\right)\right] + \\ & -Y_{ik}\left[E''_{dk0}\cos\left(\theta_{ik} - \delta_{ik0}\right) - E''_{qk0}\sin\left(\theta_{ik} - \delta_{ik0}\right)\right]\left[E''_{qi0} + i_{tdi0}\left(X''_{qi} - X''_{di}\right)\right], \\ & \text{with } \begin{cases} k > i \\ i = 1,2,\ldots,n-1 \\ k = 2,3,\ldots,n \end{cases} \end{aligned} \tag{5.62}$$

$$\begin{aligned} K_{1iki} = {} & -Y_{ki}\left[E''_{dk0}\sin\left(\theta_{ki} + \delta_{ki0}\right) + E''_{qk0}\cos\left(\theta_{ki} + \delta_{ki0}\right)\right]\left[E''_{di0} + i_{tqi0}\left(X''_{qi} - X''_{di}\right)\right] + \\ & +Y_{ki}\left[E''_{dk0}\cos\left(\theta_{ki} + \delta_{ki0}\right) - E''_{qk0}\sin\left(\theta_{ki} + \delta_{ki0}\right)\right]\left[E''_{qi0} + i_{tdi0}\left(X''_{qi} - X''_{di}\right)\right], \\ & \text{with } \begin{cases} i > k \\ i = 2,3,\ldots,n \\ k = 1,2,\ldots,n-1 \end{cases} \end{aligned} \tag{5.63}$$

$$K_{2ii} = \left\{i_{tqi0} - B_{ii}\left[E''_{di0} + i_{tqi0}\left(X''_{qi} - X''_{di}\right)\right] + G_{ii}\left[E''_{qi0} + i_{tdi0}\left(X''_{qi} - X''_{di}\right)\right]\right\}, \quad i = 1,2,\ldots,n \tag{5.64}$$

$$K_{2dii} = \left\{i_{tdi0} + G_{ii}\left[E''_{di0} + i_{tqi0}\left(X''_{qi} - X''_{di}\right)\right] + B_{ii}\left[E''_{qi0} + i_{tdi0}\left(X''_{qi} - X''_{di}\right)\right]\right\}, \quad i = 1,2,\ldots,n \tag{5.65}$$

$$K_{2ik}=\begin{cases}Y_{ik}\left\{-\sin\left(\theta_{ik}-\delta_{ik0}\right)\left[E_{di0}^{"}+i_{tqi0}\left(X_{qi}^{"}-X_{di}^{"}\right)\right]+\cos\left(\theta_{ik}-\delta_{ik0}\right)\left[E_{qi0}^{"}+i_{tdi0}\left(X_{qi}^{"}-X_{di}^{"}\right)\right]\right\}, & \left(k>i\right)\\ Y_{ki}\left\{-\sin\left(\theta_{ki}+\delta_{ki0}\right)\left[E_{di0}^{"}+i_{tqi0}\left(X_{qi}^{"}-X_{di}^{"}\right)\right]+\cos\left(\theta_{ki}+\delta_{ki0}\right)\left[E_{qi0}^{"}+i_{tdi0}\left(X_{qi}^{"}-X_{di}^{"}\right)\right]\right\}, & \left(i>k\right)\end{cases}$$

$$\text{with}\begin{cases}i,k=1,2,\ldots,n\\ i\neq k\end{cases}$$

(5.66)

$$K_{2dik}=\begin{cases}Y_{ik}\left\{\cos\left(\theta_{ik}-\delta_{ik0}\right)\left[E_{di0}^{"}+i_{tqi0}\left(X_{qi}^{"}-X_{di}^{"}\right)\right]+\sin\left(\theta_{ik}-\delta_{ik0}\right)\left[E_{qi0}^{"}+i_{tdi0}\left(X_{qi}^{"}-X_{di}^{"}\right)\right]\right\}, & \left(k>i\right)\\ Y_{ki}\left\{\cos\left(\theta_{ki}+\delta_{ki0}\right)\left[E_{di0}^{"}+i_{tqi0}\left(X_{qi}^{"}-X_{di}^{"}\right)\right]+\sin\left(\theta_{ki}+\delta_{ki0}\right)\left[E_{qi0}^{"}+i_{tdi0}\left(X_{qi}^{"}-X_{di}^{"}\right)\right]\right\}, & \left(i>k\right)\end{cases}$$

$$\text{with}\begin{cases}i,k=1,2,\ldots,n\\ i\neq k\end{cases}$$

(5.67)

$$K_{5iik}=\frac{e_{tdi0}}{e_{ti0}}Y_{ik}\left[-E_{dk0}^{"}\cos\left(\theta_{ik}-\delta_{ik0}\right)+E_{qk0}^{"}\sin\left(\theta_{ik}-\delta_{ik0}\right)\right]X_{qi}^{"}+$$

$$-\frac{e_{tqi0}}{e_{ti0}}Y_{ik}\left[E_{dk0}^{"}\sin\left(\theta_{ik}-\delta_{ik0}\right)+E_{qk0}^{"}\cos\left(\theta_{ik}-\delta_{ik0}\right)\right]X_{di}^{"},\qquad\text{with}\begin{cases}k>i\\ i=1,2,\ldots,n-1\\ k=2,3,\ldots,n\end{cases}\tag{5.68}$$

$$K_{5iki}=-\frac{e_{tdi0}}{e_{ti0}}Y_{ki}\left[-E_{dk0}^{"}\cos\left(\theta_{ki}+\delta_{ki0}\right)+E_{qk0}^{"}\sin\left(\theta_{ki}+\delta_{ki0}\right)\right]X_{qi}^{"}+$$

$$+\frac{e_{tqi0}}{e_{ti0}}Y_{ki}\left[E_{dk0}^{"}\sin\left(\theta_{ki}+\delta_{ki0}\right)+E_{qk0}^{"}\cos\left(\theta_{ki}+\delta_{ki0}\right)\right]X_{di}^{"},\qquad\text{with}\begin{cases}i>k\\ i=2,3,\ldots,n\\ k=1,2,\ldots,n-1\end{cases}\tag{5.69}$$

$$K_{6ii}=\left[\frac{e_{tdi0}}{e_{ti0}}G_{ii}X_{qi}^{"}+\frac{e_{tqi0}}{e_{ti0}}\left(1+B_{ii}X_{di}^{"}\right)\right],\qquad i=1,2,\ldots,n\tag{5.70}$$

$$K_{6dii}=\left[\frac{e_{tdi0}}{e_{ti0}}\left(1+B_{ii}X_{qi}^{"}\right)-\frac{e_{tqi0}}{e_{ti0}}G_{ii}X_{di}^{"}\right],\qquad i=1,2,\ldots,n\tag{5.71}$$

$$K_{6ik}=\begin{cases}Y_{ik}\left[\frac{e_{tdi0}}{e_{ti0}}\cos\left(\theta_{ik}-\delta_{ik0}\right)X_{qi}^{"}+\frac{e_{tqi0}}{e_{ti0}}\sin\left(\theta_{ik}-\delta_{ik0}\right)X_{di}^{"}\right], & \left(k>i\right)\\ Y_{ki}\left[\frac{e_{tdi0}}{e_{ti0}}\cos\left(\theta_{ki}+\delta_{ki0}\right)X_{qi}^{"}+\frac{e_{tqi0}}{e_{ti0}}\sin\left(\theta_{ki}+\delta_{ki0}\right)X_{di}^{"}\right], & \left(i>k\right)\end{cases}\quad\text{with}\begin{cases}i,k=1,2,\ldots,n\\ i\neq k\end{cases}\tag{5.72}$$

$$K_{6dik}=\begin{cases}Y_{ik}\left[\frac{e_{tdi0}}{e_{ti0}}\sin\left(\theta_{ik}-\delta_{ik0}\right)X_{qi}^{"}-\frac{e_{tqi0}}{e_{ti0}}\cos\left(\theta_{ik}-\delta_{ik0}\right)X_{di}^{"}\right], & \left(k>i\right)\\ Y_{ki}\left[\frac{e_{tdi0}}{e_{ti0}}\sin\left(\theta_{ki}+\delta_{ki0}\right)X_{qi}^{"}-\frac{e_{tqi0}}{e_{ti0}}\cos\left(\theta_{ki}+\delta_{ki0}\right)X_{di}^{"}\right], & \left(i>k\right)\end{cases}\quad\text{with}\begin{cases}i,k=1,2,\ldots,n\\ i\neq k\end{cases}\tag{5.73}$$

$$C_{1iik}=-\frac{Y_{ik}}{\tau_{di0}^{'}}\left[E_{dk0}^{"}\sin\left(\theta_{ik}-\delta_{ik0}\right)+E_{qk0}^{"}\cos\left(\theta_{ik}-\delta_{ik0}\right)\right]\left(X_{di}-X_{di}^{'}\right),\quad\text{with}\begin{cases}k>i\\ i=1,2,\ldots,n-1\\ k=2,3,\ldots,n\end{cases}\tag{5.74}$$

$$C_{1iki}=\frac{Y_{ki}}{\tau'_{di0}}\left[E''_{dk0}\sin\left(\theta_{ki}+\delta_{ki0}\right)+E''_{qk0}\cos\left(\theta_{ki}+\delta_{ki0}\right)\right]\left(X_{di}-X'_{di}\right),\quad \text{with}\begin{cases}i>k\\ i=2,3,\ldots,n\\ k=1,2,\ldots,n-1\end{cases} \tag{5.75}$$

$$C_{2ii}=\frac{B_{ii}}{\tau'_{di0}}\left(X_{di}-X'_{di}\right),\qquad i=1,2,\ldots,n \tag{5.76}$$

$$C_{2dii}=-\frac{G_{ii}}{\tau'_{di0}}\left(X_{di}-X'_{di}\right),\qquad i=1,2,\ldots,n \tag{5.77}$$

$$C_{2ik}=\begin{cases}\dfrac{Y_{ik}}{\tau'_{di0}}\sin\left(\theta_{ik}-\delta_{ik0}\right)\left(X_{di}-X'_{di}\right), & (k>i)\\ \dfrac{Y_{ki}}{\tau'_{di0}}\sin\left(\theta_{ki}+\delta_{ki0}\right)\left(X_{di}-X'_{di}\right), & (i>k)\end{cases} \tag{5.78}$$

$$C_{2dik}=\begin{cases}-\dfrac{Y_{ik}}{\tau'_{di0}}\cos\left(\theta_{ik}-\delta_{ik0}\right)\left(X_{di}-X'_{di}\right), & (k>i)\\ -\dfrac{Y_{ki}}{\tau'_{di0}}\cos\left(\theta_{ki}+\delta_{ki0}\right)\left(X_{di}-X'_{di}\right), & (i>k)\end{cases} \tag{5.79}$$

$$C_{3iik}=-\frac{Y_{ik}}{\tau''_{di0}}\left[E''_{dk0}\sin\left(\theta_{ik}-\delta_{ik0}\right)+E''_{qk0}\cos\left(\theta_{ik}-\delta_{ik0}\right)\right]\left[\left(X'_{di}-X''_{di}\right)+\frac{\tau''_{di0}}{\tau'_{di0}}\left(X_{di}-X'_{di}\right)\right],$$
$$\text{with}\begin{cases}k>i\\ i=1,2,\ldots,n-1\\ k=2,3,\ldots,n\end{cases} \tag{5.80}$$

$$C_{3iki}=\frac{Y_{ki}}{\tau''_{di0}}\left[E''_{dk0}\sin\left(\theta_{ki}+\delta_{ki0}\right)+E''_{qk0}\cos\left(\theta_{ki}+\delta_{ki0}\right)\right]\left[\left(X'_{di}-X''_{di}\right)+\frac{\tau''_{di0}}{\tau'_{di0}}\left(X_{di}-X'_{di}\right)\right],$$
$$\text{with}\begin{cases}i>k\\ i=2,3,\ldots,n\\ k=1,2,\ldots,n-1\end{cases} \tag{5.81}$$

$$C_{4ii}=\frac{1}{\tau''_{di0}}\left\{B_{ii}\left[\left(X'_{di}-X''_{di}\right)+\frac{\tau''_{di0}}{\tau'_{di0}}\left(X_{di}-X'_{di}\right)\right]-1\right\},\qquad i=1,2,\ldots,n \tag{5.82}$$

$$C_{4dii}=-\frac{G_{ii}}{\tau''_{di0}}\left[\left(X'_{di}-X''_{di}\right)+\frac{\tau''_{di0}}{\tau'_{di0}}\left(X_{di}-X'_{di}\right)\right],\qquad i=1,2,\ldots,n \tag{5.83}$$

$$C_{4ik}=\begin{cases}\dfrac{Y_{ik}}{\tau''_{di0}}\sin\left(\theta_{ik}-\delta_{ik0}\right)\left[\left(X'_{di}-X''_{di}\right)+\dfrac{\tau''_{di0}}{\tau'_{di0}}\left(X_{di}-X'_{di}\right)\right], & (k>i)\\ \dfrac{Y_{ki}}{\tau''_{di0}}\sin\left(\theta_{ki}+\delta_{ki0}\right)\left[\left(X'_{di}-X''_{di}\right)+\dfrac{\tau''_{di0}}{\tau'_{di0}}\left(X_{di}-X'_{di}\right)\right], & (i>k)\end{cases}\quad \text{with}\begin{cases}i,k=1,2,\ldots,n\\ i\neq k\end{cases} \tag{5.84}$$

$$C_{4dik}=\begin{cases}-\dfrac{Y_{ik}}{\tau''_{di0}}\cos\left(\theta_{ik}-\delta_{ik0}\right)\left[\left(X'_{di}-X''_{di}\right)+\dfrac{\tau''_{di0}}{\tau'_{di0}}\left(X_{di}-X'_{di}\right)\right], & (k>i)\\ -\dfrac{Y_{ki}}{\tau''_{di0}}\cos\left(\theta_{ki}+\delta_{ki0}\right)\left[\left(X'_{di}-X''_{di}\right)+\dfrac{\tau''_{di0}}{\tau'_{di0}}\left(X_{di}-X'_{di}\right)\right], & (i>k)\end{cases}\quad \text{with}\begin{cases}i,k=1,2,\ldots,n\\ i\neq k\end{cases} \tag{5.85}$$

$$C_{5iik}=\frac{Y_{ik}}{\tau_{qi0}^{'}}\left[-E_{dk0}^{''}\cos\left(\theta_{ik}-\delta_{ik0}\right)+E_{qk0}^{''}\sin\left(\theta_{ik}-\delta_{ik0}\right)\right]\left(X_{qi}-X_{qi}^{'}\right),\quad \text{with}\begin{cases}k>i\\ i=1,2,\ldots,n-1\\ k=2,3,\ldots,n\end{cases} \tag{5.86}$$

$$C_{5iki}=-\frac{Y_{ki}}{\tau_{qi0}^{'}}\left[-E_{dk0}^{''}\cos\left(\theta_{ki}+\delta_{ki0}\right)+E_{qk0}^{''}\sin\left(\theta_{ki}+\delta_{ki0}\right)\right]\left(X_{qi}-X_{qi}^{'}\right),\quad \text{with}\begin{cases}i>k\\ i=2,3,\ldots,n\\ k=1,2,\ldots,n-1\end{cases} \tag{5.87}$$

$$C_{6ii}=\frac{G_{ii}}{\tau_{qi0}^{'}}\left(X_{qi}-X_{qi}^{'}\right),\qquad i=1,2,\ldots,n \tag{5.88}$$

$$C_{6dii}=\frac{B_{ii}}{\tau_{qi0}^{'}}\left(X_{qi}-X_{qi}^{'}\right),\qquad i=1,2,\ldots,n \tag{5.89}$$

$$C_{6ik}=\begin{cases}\dfrac{Y_{ik}}{\tau_{qi0}^{'}}\cos\left(\theta_{ik}-\delta_{ik0}\right)\left(X_{qi}-X_{qi}^{'}\right), & (k>i)\\ \dfrac{Y_{ki}}{\tau_{qi0}^{'}}\cos\left(\theta_{ki}+\delta_{ki0}\right)\left(X_{qi}-X_{qi}^{'}\right), & (i>k)\end{cases}\quad \text{with}\begin{cases}i,k=1,2,\ldots,n\\ i\neq k\end{cases} \tag{5.90}$$

$$C_{6dik}=\begin{cases}\dfrac{Y_{ik}}{\tau_{qi0}^{'}}\sin\left(\theta_{ik}-\delta_{ik0}\right)\left(X_{qi}-X_{qi}^{'}\right), & (k>i)\\ \dfrac{Y_{ki}}{\tau_{qi0}^{'}}\sin\left(\theta_{ki}+\delta_{ki0}\right)\left(X_{qi}-X_{qi}^{'}\right), & (i>k)\end{cases}\quad \text{with}\begin{cases}i,k=1,2,\ldots,n\\ i\neq k\end{cases} \tag{5.91}$$

$$C_{7iik}=\frac{Y_{ik}}{\tau_{qi0}^{''}}\left[-E_{dk0}^{''}\cos\left(\theta_{ik}-\delta_{ik0}\right)+E_{qk0}^{''}\sin\left(\theta_{ik}-\delta_{ik0}\right)\right]\left(X_{qi}^{'}-X_{qi}^{''}\right),\quad \text{with}\begin{cases}k>i\\ i=1,2,\ldots,n-1\\ k=2,3,\ldots,n\end{cases} \tag{5.92}$$

$$C_{7iki}=-\frac{Y_{ki}}{\tau_{qi0}^{''}}\left[-E_{dk0}^{''}\cos\left(\theta_{ki}+\delta_{ki0}\right)+E_{qk0}^{''}\sin\left(\theta_{ki}+\delta_{ki0}\right)\right]\left(X_{qi}^{'}-X_{qi}^{''}\right),\quad \text{with}\begin{cases}i>k\\ i=2,3,\ldots,n\\ k=1,2,\ldots,n-1\end{cases} \tag{5.93}$$

$$C_{8ii}=\frac{G_{ii}}{\tau_{qi0}^{''}}\left(X_{qi}^{'}-X_{qi}^{''}\right),\qquad i=1,2,\ldots,n \tag{5.94}$$

$$C_{8dii}=\frac{1}{\tau_{qi0}^{''}}\left[B_{ii}\left(X_{qi}^{'}-X_{qi}^{''}\right)-1\right],\qquad i=1,2,\ldots,n \tag{5.95}$$

$$C_{8ik}=\begin{cases}\dfrac{Y_{ik}}{\tau_{qi0}^{''}}\cos\left(\theta_{ik}-\delta_{ik0}\right)\left(X_{qi}^{'}-X_{qi}^{''}\right), & (k>i)\\ \dfrac{Y_{ki}}{\tau_{qi0}^{''}}\cos\left(\theta_{ki}+\delta_{ki0}\right)\left(X_{qi}^{'}-X_{qi}^{''}\right), & (i>k)\end{cases}\quad \text{with}\begin{cases}i,k=1,2,\ldots,n\\ i\neq k\end{cases} \tag{5.96}$$

$$C_{8dik}=\begin{cases}\dfrac{Y_{ik}}{\tau_{qi0}^{''}}\sin\left(\theta_{ik}-\delta_{ik0}\right)\left(X_{qi}^{'}-X_{qi}^{''}\right), & (k>i)\\ \dfrac{Y_{ki}}{\tau_{qi0}^{''}}\sin\left(\theta_{ki}+\delta_{ki0}\right)\left(X_{qi}^{'}-X_{qi}^{''}\right), & (i>k)\end{cases}\quad \text{with}\begin{cases}i,k=1,2,\ldots,n\\ i\neq k\end{cases} \tag{5.97}$$

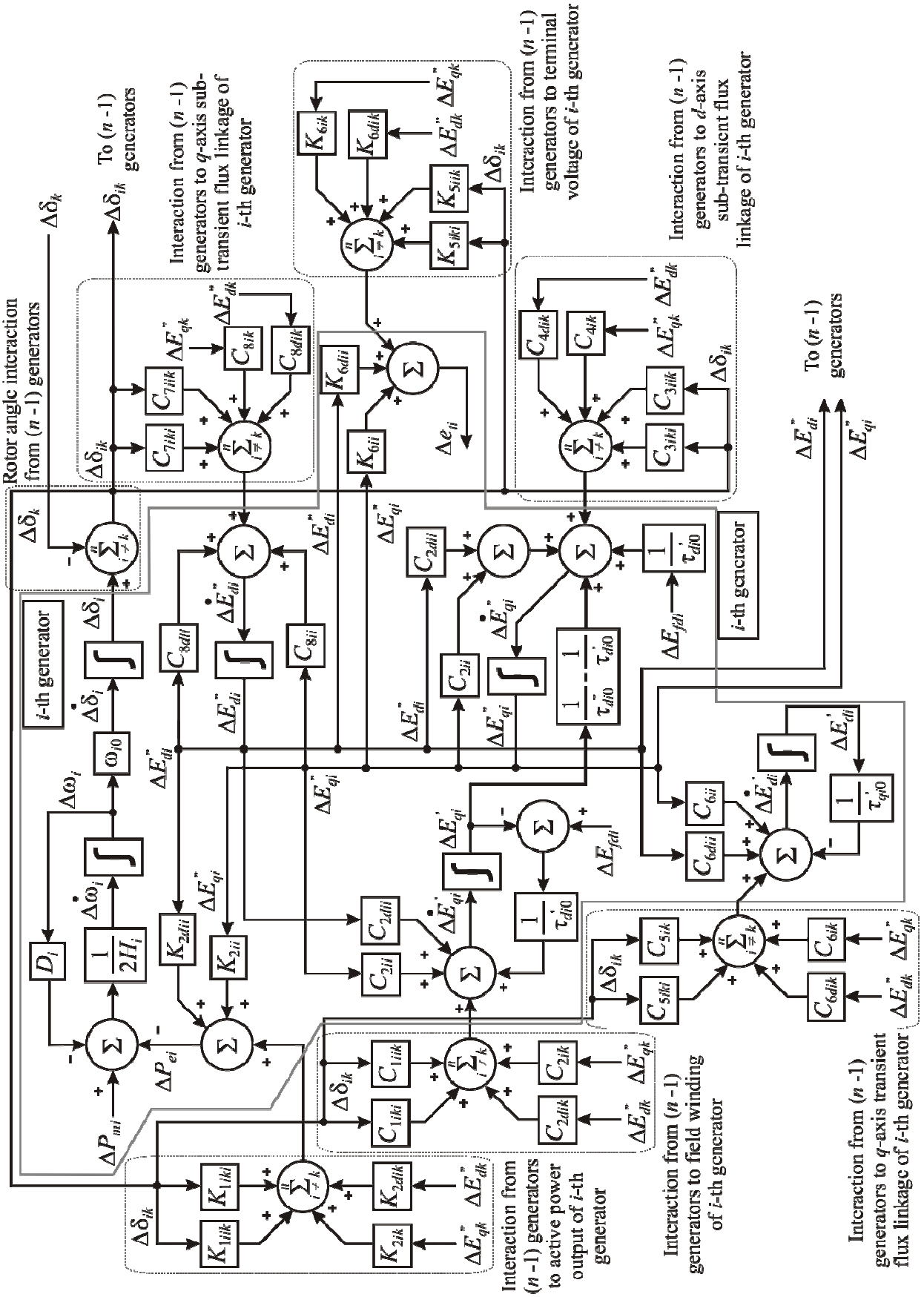

Figure 5.3. Block diagram of the *i*-th machine of a multi-machine system

A block diagram that represents the *i*-th synchronous generator in an *n*-machine system, described by equations (5.54)–(5.61), is shown in Figure 5.3. The *i*-th synchronous generator represents the characteristic of any one generator in the system. The dynamic behaviour of the *i*-th generator (given by a 6^{th} order model) is represented by the incremental change in output power (ΔP_{ei}), output voltage (Δe_{ti}) and voltages proportional to the *d*- and *q*-axis flux linkages ($\Delta E''_{qi}$, $\Delta E'_{qi}$, $\Delta E''_{di}$ and $\Delta E'_{di}$). As it can be appreciated in Figure 5.3, these variables will change in response to $\Delta\delta_{ik}$, $\Delta E''_{q}$ and $\Delta E''_{d}$ changes in the *i*-th generator, as well as in the other $(n-1)$ generators. On the one hand, the solid gray line encloses the coefficients corresponding to the internal change of the main variables of the *i*-th generator. On the other hand, the dotted lines enclose the external dynamical contributions, which consist of a summation of changes in $\Delta\delta_{ik}$, $\Delta E''_{qk}$ and $\Delta E''_{dk}$ from the other $(n-1)$ generators. They influence the *i*-th generator through the coupling coefficients with subscripts *ik*, where $k = 1,\ldots,n$, $k \neq i$. Conversely, the dynamic characteristic of the $(n-1)$ generators will be influenced by changes in $\Delta\delta_{ik}$, $\Delta E''_{qi}$, $\Delta E'_{qi}$, $\Delta E''_{di}$ and $\Delta E'_{di}$ from the *i*-th generator through coefficients with subscripts *ki*, where $k = 1,\ldots,n$, $k \neq i$.

The *n*-machine system comprises $(6n-1)$ linear differential equations with

$$(6n-1)+\sum_{i=1}^{n-2} i$$

variables. In order to obtain an independent set of equations and to eliminate the redundant variables given by the $\Delta\delta_{ik}$ terms, the following relation is required:

$$\Delta\delta_{ik} = \Delta\delta_{1k} - \Delta\delta_{1i}, \qquad i>1, k>i \tag{5.98}$$

Substitution of (5.98) in (5.54)–(5.61) provides the desired multi-machine model, following a straightforward simplification process. A state-space representation of the form

$$\begin{aligned} \dot{\Delta\mathbf{x}} &= \mathbf{A}\Delta\mathbf{x} + \mathbf{B}\Delta\mathbf{u} \\ \Delta\mathbf{y} &= \mathbf{C}\Delta\mathbf{x} + \mathbf{D}\Delta\mathbf{u} \end{aligned} \tag{5.99}$$

may be arrived at, where the state, input and output vectors are given, in general form, as

$$\Delta\mathbf{x} = \begin{bmatrix} \Delta\mathbf{x}_1 & \Delta\mathbf{x}_2 & \cdots & \Delta\mathbf{x}_i & \cdots & \Delta\mathbf{x}_{(n-1)} & \Delta\mathbf{x}_n & \Delta\boldsymbol{\delta} \end{bmatrix}^T \tag{5.100}$$

$$\Delta\mathbf{u} = \begin{bmatrix} \Delta\mathbf{u}_1 & \Delta\mathbf{u}_2 & \cdots & \Delta\mathbf{u}_i & \cdots & \Delta\mathbf{u}_{(n-1)} & \Delta\mathbf{u}_n \end{bmatrix}^T \tag{5.101}$$

$$\Delta\mathbf{y} = \begin{bmatrix} \Delta\mathbf{y}_1 & \Delta\mathbf{y}_2 & \cdots & \Delta\mathbf{y}_i & \cdots & \Delta\mathbf{y}_{(n-1)} & \Delta\mathbf{y}_n \end{bmatrix}^T \tag{5.102}$$

For the particular case of *i* ($i = 1,2,\ldots,n$),

$$\Delta\mathbf{x}_i = \begin{bmatrix} \Delta\omega_i & \Delta E'_{qi} & \Delta E''_{qi} & \Delta E'_{di} & \Delta E''_{di} \end{bmatrix} \tag{5.103}$$

$$\Delta\mathbf{u}_i = \begin{bmatrix} \Delta P_{mi} & \Delta E_{fdi} \end{bmatrix} \tag{5.104}$$

$$\Delta\mathbf{y}_i = \begin{bmatrix} \Delta\omega_i & \Delta e_{ti} \end{bmatrix} \tag{5.105}$$

and vector $\Delta\boldsymbol{\delta}$ in (5.100) being defined as

$$\Delta\boldsymbol{\delta} = \begin{bmatrix} \Delta\delta_{12} & \cdots & \Delta\delta_{1i} & \cdots & \Delta\delta_{1(n-1)} & \Delta\delta_{1n} \end{bmatrix} \tag{5.106}$$

Therefore, the state, input and output vectors have dimensions: $((6n-1)\times 1)$, $(2n\times 1)$ and $(2n\times 1)$, respectively.

System matrix $\mathbf{A}$ in (5.99), a square matrix of dimension $((6n-1)\times(6n-1))$, is given as

$$\mathbf{A} = \begin{bmatrix} \mathbf{A}_n & \mathbf{A}_\delta \\ \mathbf{A}_\omega & \mathbf{A}_0 \end{bmatrix} \tag{5.107}$$

where the sub-matrices of (5.107) are of the form

$$\mathbf{A}_n = \begin{bmatrix} \mathbf{A}_{11} & \mathbf{A}_{12} & \cdots & \mathbf{A}_{1i} & \cdots & \mathbf{A}_{1(n-1)} & \mathbf{A}_{1n} \\ \mathbf{A}_{21} & \mathbf{A}_{22} & \cdots & \mathbf{A}_{2i} & \cdots & \mathbf{A}_{2(n-1)} & \mathbf{A}_{2n} \\ \vdots & \vdots & \ddots & \vdots & \ddots & \vdots & \vdots \\ \mathbf{A}_{i1} & \mathbf{A}_{i2} & \cdots & \mathbf{A}_{ii} & \cdots & \mathbf{A}_{i(n-1)} & \mathbf{A}_{in} \\ \vdots & \vdots & \ddots & \vdots & \ddots & \vdots & \vdots \\ \mathbf{A}_{(n-1)1} & \mathbf{A}_{(n-1)2} & \cdots & \mathbf{A}_{(n-1)i} & \cdots & \mathbf{A}_{(n-1)(n-1)} & \mathbf{A}_{(n-1)n} \\ \mathbf{A}_{n1} & \mathbf{A}_{n2} & \cdots & \mathbf{A}_{ni} & \cdots & \mathbf{A}_{n(n-1)} & \mathbf{A}_{nn} \end{bmatrix} \tag{5.108}$$

$$\mathbf{A}_\delta = \begin{bmatrix} \mathbf{A}_{\delta 12} & \cdots & \mathbf{A}_{\delta 1i} & \cdots & \mathbf{A}_{\delta 1(n-1)} & \mathbf{A}_{\delta 1n} \\ \mathbf{A}_{\delta 22} & \cdots & \mathbf{A}_{\delta 2i} & \cdots & \mathbf{A}_{\delta 2(n-1)} & \mathbf{A}_{\delta 2n} \\ \vdots & \ddots & \vdots & \ddots & \vdots & \vdots \\ \mathbf{A}_{\delta i2} & \cdots & \mathbf{A}_{\delta ii} & \cdots & \mathbf{A}_{\delta i(n-1)} & \mathbf{A}_{\delta in} \\ \vdots & \ddots & \vdots & \ddots & \vdots & \vdots \\ \mathbf{A}_{\delta(n-1)2} & \cdots & \mathbf{A}_{\delta(n-1)i} & \cdots & \mathbf{A}_{\delta(n-1)(n-1)} & \mathbf{A}_{\delta(n-1)n} \\ \mathbf{A}_{\delta n2} & \cdots & \mathbf{A}_{\delta ni} & \cdots & \mathbf{A}_{\delta n(n-1)} & \mathbf{A}_{\delta nn} \end{bmatrix} \tag{5.109}$$

$$\mathbf{A}_\omega = \begin{bmatrix} \mathbf{A}_{\omega 1} & \mathbf{A}_{\omega 2} & \cdots & \mathbf{0}_{1\times 5} & \cdots & \mathbf{0}_{1\times 5} & \mathbf{0}_{1\times 5} \\ \vdots & \vdots & \ddots & \vdots & \ddots & \vdots & \vdots \\ \mathbf{A}_{\omega 1} & \mathbf{0}_{1\times 5} & \cdots & \mathbf{A}_{\omega i} & \cdots & \mathbf{0}_{1\times 5} & \mathbf{0}_{1\times 5} \\ \vdots & \vdots & \ddots & \vdots & \ddots & \vdots & \vdots \\ \mathbf{A}_{\omega 1} & \mathbf{0}_{1\times 5} & \cdots & \mathbf{0}_{1\times 5} & \cdots & \mathbf{A}_{\omega(n-1)} & \mathbf{0}_{1\times 5} \\ \mathbf{A}_{\omega 1} & \mathbf{0}_{1\times 5} & \cdots & \mathbf{0}_{1\times 5} & \cdots & \mathbf{0}_{1\times 5} & \mathbf{A}_{\omega n} \end{bmatrix} \tag{5.110}$$

$$\mathbf{A}_0 = \mathbf{0}_{(n-1)\times(n-1)} \tag{5.111}$$

The diagonal and off-diagonal sub-matrices of $\mathbf{A}_n$ in (5.108) are of the form

$$\mathbf{A}_{ii}=\begin{bmatrix} -\frac{D_i}{2H_i} & 0 & -\frac{K_{2ii}}{2H_i} & 0 & -\frac{K_{2dii}}{2H_i} \\ 0 & -\frac{1}{\tau'_{di0}} & C_{2ii} & 0 & C_{2dii} \\ 0 & \frac{1}{\tau''_{di0}}-\frac{1}{\tau'_{di0}} & C_{4ii} & 0 & C_{4dii} \\ 0 & 0 & C_{6ii} & -\frac{1}{\tau'_{qi0}} & C_{6dii} \\ 0 & 0 & C_{8ii} & 0 & C_{8dii} \end{bmatrix}, \qquad i=1,2,\ldots,n \tag{5.112}$$

$$\mathbf{A}_{ik}=\begin{bmatrix} 0 & 0 & -\frac{K_{2ik}}{2H_i} & 0 & -\frac{K_{2dik}}{2H_i} \\ 0 & 0 & C_{2ik} & 0 & C_{2dik} \\ 0 & 0 & C_{4ik} & 0 & C_{4dik} \\ 0 & 0 & C_{6ik} & 0 & C_{6dik} \\ 0 & 0 & C_{8ik} & 0 & C_{8dik} \end{bmatrix}, \qquad \text{with } \begin{cases} i,k=1,2,\ldots,n \\ i\neq k \end{cases} \tag{5.113}$$

Therefore, $\mathbf{A}_n$ is a ($5n \times 5n$) matrix. Similarly, the sub-matrices (column vectors of matrix $\mathbf{A}_\delta$ in (5.109)) are of the form

$$\mathbf{A}_{\delta ik}=\begin{cases} \begin{bmatrix} -\frac{K_{1iik}}{2H_i} & C_{1iik} & C_{3iik} & C_{5iik} & C_{7iik} \end{bmatrix}^T, & \text{when } \begin{cases} k>i \\ i=1,2,\ldots,n-1 \\ k=2,3,\ldots,n \end{cases} \\ \begin{bmatrix} \frac{K_{1iki}}{2H_i} & -C_{1iki} & -C_{3iki} & -C_{5iki} & -C_{7iki} \end{bmatrix}^T, & \text{when } \begin{cases} i>k \\ i=3,4,\ldots,n \\ k=2,3,\ldots,n-1 \end{cases} \end{cases} \tag{5.114}$$

and

$$\mathbf{A}_{\delta ii}=\begin{bmatrix} -\sum_{k=1}^{i-1}\frac{K_{1iki}}{2H_i}+\sum_{k=i+1}^{n}\frac{K_{1iik}}{2H_i} \\ \sum_{k=1}^{i-1}C_{1iki}-\sum_{k=i+1}^{n}C_{1iik} \\ \sum_{k=1}^{i-1}C_{3iki}-\sum_{k=i+1}^{n}C_{3iik} \\ \sum_{k=1}^{i-1}C_{5iki}-\sum_{k=i+1}^{n}C_{5iik} \\ \sum_{k=1}^{i-1}C_{7iki}-\sum_{k=i+1}^{n}C_{7iik} \end{bmatrix}, \qquad i=3,4,\ldots,n-2 \tag{5.115}$$

Further expressions of $\mathbf{A}_{\delta i}$ not included in (5.115) (i = 2, n – 1, n) are:

$$\mathbf{A}_{\delta 22}=\begin{bmatrix} -\dfrac{K_{1212}}{2H_2}+\sum_{k=3}^{n}\dfrac{K_{122k}}{2H_2} \\ C_{1212}-\sum_{k=3}^{n}C_{122k} \\ C_{3212}-\sum_{k=3}^{n}C_{322k} \\ C_{5212}-\sum_{k=3}^{n}C_{522k} \\ C_{7212}-\sum_{k=3}^{n}C_{722k} \end{bmatrix},\quad \mathbf{A}_{\delta(n-1)(n-1)}=\begin{bmatrix} -\sum_{k=1}^{n-2}\dfrac{K_{1(n-1)k(n-1)}}{2H_{(n-1)}}+\dfrac{K_{1(n-1)(n-1)n}}{2H_{(n-1)}} \\ \sum_{k=1}^{n-2}C_{1(n-1)k(n-1)}-C_{1(n-1)(n-1)n} \\ \sum_{k=1}^{n-2}C_{3(n-1)k(n-1)}-C_{3(n-1)(n-1)n} \\ \sum_{k=1}^{n-2}C_{5(n-1)k(n-1)}-C_{5(n-1)(n-1)n} \\ \sum_{k=1}^{n-2}C_{7(n-1)k(n-1)}-C_{7(n-1)(n-1)n} \end{bmatrix},\quad \mathbf{A}_{\delta nn}=\begin{bmatrix} -\sum_{k=1}^{n-1}\dfrac{K_{1nkn}}{2H_n} \\ \sum_{k=1}^{n-1}C_{1nkn} \\ \sum_{k=1}^{n-1}C_{3nkn} \\ \sum_{k=1}^{n-1}C_{5nkn} \\ \sum_{k=1}^{n-1}C_{7nkn} \end{bmatrix} \tag{5.116}$$

Thus, it can be seen that $\mathbf{A}_{\delta}$ is a $(5n \times (n-1))$ matrix. Similarly, matrix $\mathbf{A}_{\omega}$ is made up of the following vectors:

$$\mathbf{A}_{\omega 1}=\begin{bmatrix}\omega_{10} & 0 & 0 & 0 & 0\end{bmatrix} \tag{5.117}$$

$$\mathbf{A}_{\omega i}=\begin{bmatrix}-\omega_{i0} & 0 & 0 & 0 & 0\end{bmatrix},\qquad i=2,\ldots,n \tag{5.118}$$

and $\mathbf{0}_{1x5}$ is a row vector with zero elements. It can be seen that $\mathbf{A}_{\omega}$ is a $((n-1) \times 5n)$ matrix. Matrix $\mathbf{A}_0$ (5.111) is a $((n-1) \times (n-1))$ matrix with zero entries.

Control matrix $\mathbf{B}$ in (5.99), a matrix of dimension $((6n-1) \times 2n)$, is given as

$$\mathbf{B}=\begin{bmatrix}\mathbf{B}_n \\ \mathbf{B}_0\end{bmatrix} \tag{5.119}$$

with sub-matrices of the form

$$\mathbf{B}_n=\begin{bmatrix} \mathbf{B}_1 & \mathbf{0}_{5\times2} & \cdots & \mathbf{0}_{5\times2} & \cdots & \mathbf{0}_{5\times2} & \mathbf{0}_{5\times2} \\ \mathbf{0}_{5\times2} & \mathbf{B}_2 & \cdots & \mathbf{0}_{5\times2} & \cdots & \mathbf{0}_{5\times2} & \mathbf{0}_{5\times2} \\ \vdots & \vdots & \ddots & \vdots & \ddots & \vdots & \vdots \\ \mathbf{0}_{5\times2} & \mathbf{0}_{5\times2} & \cdots & \mathbf{B}_i & \cdots & \mathbf{0}_{5\times2} & \mathbf{0}_{5\times2} \\ \vdots & \vdots & \ddots & \vdots & \ddots & \vdots & \vdots \\ \mathbf{0}_{5\times2} & \mathbf{0}_{5\times2} & \cdots & \mathbf{0}_{5\times2} & \cdots & \mathbf{B}_{(n-1)} & \mathbf{0}_{5\times2} \\ \mathbf{0}_{5\times2} & \mathbf{0}_{5\times2} & \cdots & \mathbf{0}_{5\times2} & \cdots & \mathbf{0}_{5\times2} & \mathbf{B}_n \end{bmatrix} \tag{5.120}$$

and

$$\mathbf{B}_0=\mathbf{0}_{(n-1)\times2n} \tag{5.121}$$

The diagonal sub-matrices of $\mathbf{B}_n$ in (5.120) are of the form

$$\mathbf{B}_i=\begin{bmatrix} \dfrac{1}{2H_i} & 0 & 0 & 0 & 0 \\ 0 & \dfrac{1}{\tau'_{di0}} & \dfrac{1}{\tau'_{di0}} & 0 & 0 \end{bmatrix}^T,\qquad i=1,2,\ldots,n \tag{5.122}$$

The off-diagonal sub-matrices of $\mathbf{B}_n$ in (5.120) are zero matrices of dimension (5×2). Hence, $\mathbf{B}_n$ has a dimension of $(5n \times 2n)$. Similarly, matrix $\mathbf{B}_0$ (5.121) is a $((n-1) \times 2n)$ matrix of zero elements.

Output matrix **C** in (5.99), is a matrix of dimension ($2n \times (6n-1)$),

$$\mathbf{C} = \begin{bmatrix} \mathbf{C}_n & \mathbf{C}_\delta \end{bmatrix} \tag{5.123}$$

where the sub-matrices of (5.123) are of the form

$$\mathbf{C}_n = \begin{bmatrix} \mathbf{C}_{11} & \mathbf{C}_{12} & \cdots & \mathbf{C}_{1i} & \cdots & \mathbf{C}_{1(n-1)} & \mathbf{C}_{1n} \\ \mathbf{C}_{21} & \mathbf{C}_{22} & \cdots & \mathbf{C}_{2i} & \cdots & \mathbf{C}_{2(n-1)} & \mathbf{C}_{2n} \\ \vdots & \vdots & \ddots & \vdots & \ddots & \vdots & \vdots \\ \mathbf{C}_{i1} & \mathbf{C}_{i2} & \cdots & \mathbf{C}_{ii} & \cdots & \mathbf{C}_{i(n-1)} & \mathbf{C}_{in} \\ \vdots & \vdots & \ddots & \vdots & \ddots & \vdots & \vdots \\ \mathbf{C}_{(n-1)1} & \mathbf{C}_{(n-1)2} & \cdots & \mathbf{C}_{(n-1)i} & \cdots & \mathbf{C}_{(n-1)(n-1)} & \mathbf{C}_{(n-1)n} \\ \mathbf{C}_{n1} & \mathbf{C}_{n2} & \cdots & \mathbf{C}_{ni} & \cdots & \mathbf{C}_{n(n-1)} & \mathbf{C}_{nn} \end{bmatrix} \tag{5.124}$$

$$\mathbf{C}_\delta = \begin{bmatrix} \mathbf{C}_{\delta 12} & \cdots & \mathbf{C}_{\delta 1i} & \cdots & \mathbf{C}_{\delta 1(n-1)} & \mathbf{C}_{\delta 1n} \\ \mathbf{C}_{\delta 22} & \cdots & \mathbf{C}_{\delta 2i} & \cdots & \mathbf{C}_{\delta 2(n-1)} & \mathbf{C}_{\delta 2n} \\ \vdots & \ddots & \vdots & \ddots & \vdots & \vdots \\ \mathbf{C}_{\delta i2} & \cdots & \mathbf{C}_{\delta ii} & \cdots & \mathbf{C}_{\delta i(n-1)} & \mathbf{C}_{\delta in} \\ \vdots & \ddots & \vdots & \ddots & \vdots & \vdots \\ \mathbf{C}_{\delta(n-1)2} & \cdots & \mathbf{C}_{\delta(n-1)i} & \cdots & \mathbf{C}_{\delta(n-1)(n-1)} & \mathbf{C}_{\delta(n-1)n} \\ \mathbf{C}_{\delta n2} & \cdots & \mathbf{C}_{\delta ni} & \cdots & \mathbf{C}_{\delta n(n-1)} & \mathbf{C}_{\delta nn} \end{bmatrix} \tag{5.125}$$

The diagonal and off-diagonal sub-matrices of $\mathbf{C}_n$ in (5.124) are of the form

$$\mathbf{C}_{ii} = \begin{bmatrix} 1 & 0 & 0 & 0 & 0 \\ 0 & 0 & K_{6ii} & 0 & K_{6dii} \end{bmatrix}, \qquad i = 1, 2, \ldots, n \tag{5.126}$$

$$\mathbf{C}_{ik} = \begin{bmatrix} 0 & 0 & 0 & 0 & 0 \\ 0 & 0 & K_{6ik} & 0 & K_{6dik} \end{bmatrix}, \qquad \text{with } \begin{cases} i,k = 1,2,\ldots,n \\ i \neq k \end{cases} \tag{5.127}$$

Therefore, $\mathbf{C}_n$ is a ($2n \times 5n$) matrix. Similarly, sub-matrices (column vectors) of matrix $\mathbf{C}_\delta$ in (5.125) are

$$\mathbf{C}_{\delta ik} = \begin{cases} \begin{bmatrix} 0 \\ K_{5iik} \end{bmatrix}, & \text{when } \begin{cases} k > i \\ i = 1,2,\ldots,n-1 \\ k = 2,3,\ldots,n \end{cases} \\ \begin{bmatrix} 0 \\ -K_{5iki} \end{bmatrix}, & \text{when } \begin{cases} i > k \\ i = 3,4,\ldots,n \\ k = 2,3,\ldots,n-1 \end{cases} \end{cases} \tag{5.128}$$

$$\mathbf{C}_{\delta ii} = \begin{bmatrix} 0 \\ \sum_{k=1}^{i-1} K_{5iki} - \sum_{k=i+1}^{n} K_{5iik} \end{bmatrix}, \qquad i = 3,4,\ldots,n-1 \tag{5.129}$$

Further expressions not included in (5.129) ($i = 2,\ n-1,\ n$) are:

$$\mathbf{C}_{\delta 22} = \begin{bmatrix} 0 \\ K_{5212} - \sum_{k=3}^{n} K_{522k} \end{bmatrix}, \quad \mathbf{C}_{\delta(n-1)(n-1)} = \begin{bmatrix} 0 \\ \sum_{k=1}^{n-2} K_{5(n-1)k(n-1)} - K_{5(n-1)(n-1)n} \end{bmatrix}, \quad \mathbf{C}_{\delta nn} = \begin{bmatrix} 0 \\ \sum_{k=1}^{n-1} K_{5nkn} \end{bmatrix} \tag{5.130}$$

Thus, the dimension of $\mathbf{C}_\delta$ is $(2n \times (n-1))$.

The feed-forward matrix **D** in (5.99) is a square matrix of dimension $(2n \times 2n)$,

$$\mathbf{D} = \mathbf{0}_{2n \times 2n} \tag{5.131}$$

with zero entries.

Remark: Whenever the multi-machine problem formulation is compared to that of the OMIB system, a readily apparent difference can be noticed by inspection of the relevant phasor diagrams. The phasor diagrams of an OMIB system and of the synchronous machine are shown in Appendix C (Figure C.1) and in Figure 2.7, respectively. In is noticed that the internal rotor angle δ_i represents the angle by which the *q*-axis leads the stator terminal voltage phasor $\vec{e}_t$. For a multi-machine system, the model formulation is carried out around this angle, as evidenced by differential equations (5.41) and (5.42) of the *i*-th machine. Nevertheless, in an OMIB system the swing equation, given by (3.5) and (3.6) (in the *s*-domain) is not expressed in terms of the internal rotor angle but through a rotor angle δ, which is the sum of the internal angle and the angle by which $\vec{e}_t$ leads V_∞. The angle δ can be seen as the angle by which the *q*-axis leads the reference V_∞. Such a choice was seen as convenient from the viewpoint of solution of the network equations associated to the OMIB system.

5.4. Order reduction and multi-order models

A multi-machine mathematical model was constructed in the previous section for the case of a detailed machine representation. However, it is highly unlikely that in a practical power system all the machine parameters associated to such a high order model will be available. Furthermore, even if full data were to exist for all machines in the power system, it is a matter of practical interest to conduct dynamic assessments of the power system through highly detailed models (like Models 0 or 1) for those machines near the actual disturbance, whilst representing other machines in a simple form (*e.g.*, Model 3 or Classical Model).

A solution to this very practical requirement is to develop a multi-order representation in which different machines are represented by different kinds of models, using any one of the six kinds of models previously developed, as well as the Classical Model – the one where field flux is assumed to be constant. To this end, the detailed multi-machine model, using Model 0 for all the machines, is judiciously simplified in order to obtain lower order representations. Two modelling scenarios are presented below: (*i*) all the machines in the system are represented by lower order machine representations; (*ii*) the construction of a multi-machine, multi-order model is discussed.

5.4.1. Lower order multi-machine models

The higher order multi-machine model forms the basis on which lower order models may be obtained by applying judicious simplifying assumptions. Such simplifications are in the same vein as the ones used in the OMIB systems. The case when all machines in the system are represented with the same level of detail involves a suitable combination of equations (5.54)–(5.59) together with (5.60) and (5.61) (providing different orders of multi-machine models).

The procedure for each lower order multi-machine model can be thought of as a particular case of the one presented in Section 5.3. The simplifying assumptions to be employed are equivalent to those described in Sections 3.2.2–3.2.5. They will have a direct impact on the differential equations and their coefficients. The state-space constructions may be obtained in an equivalent manner as in Section 5.3; therefore, no further discussion is warranted.

5.4.2. Multi-order multi-machine models

It is very unlikely that full data would be available for a multi-machine power system study in which all synchronous generators are represented with the upmost mathematical detail. In some cases, for instance, no information associated to the sub-transient dynamics may exist. On the other hand, lower order representations can be used for preliminary studies to identify problematic areas of the power system, in which further study might need to be carried out with a higher level of fidelity [1]. Therefore, it makes common sense to have multi-machine system models in which generators can be represented by different mathematical models.

The modelling problem of a truly multi-machine, multi-order representation is not a simple matter and the algebra behind it can be quite cumbersome, as the number of machines increases. Depending on the chosen model for a given machine, several coefficients associated to the differential and algebraic equations may or may not exist depending on the kind of model used for the rest of the machines. In fact, the whole mathematical representation will differ for each study case. Nevertheless, a set of sequential steps can be followed to construct a coherent multi-machine model which takes into account the data available for each generator in the power system and the location of the generator with respect to the study area. Such steps are:

1. Collect the parameters associated to each generator and determine the kind of model to be used that better meets the available data;
2. Choose a system base and convert parameters which are given on a different base to the one selected for the system as a whole;
3. Carry out a power flow study of the network;

4. Determine the initial operating condition of the system. Some initial values will be model dependant; that is, some models require sub-transient information and some others would only require transient information;
5. Convert all loads to equivalent shunt admittances using nodal voltages derived from the power flow solution;
6. Set up the nodal admittance matrix of the network using either transient or sub-transient generator impedances, and carry out a Kron's reduction;
7. Calculate the constants associated to the differential equations of each machine. These are dependent on the order of the mathematical model selected to describe the dynamics of this machine, while the existence of constants describing the interaction with other machines will depend on the models used to represent the other machines. A way to determine the parameters involved in their calculation is through examination of the general current expressions (5.52) and (5.53). Internal voltages in those expressions should conform to the chosen model – with its consequent impact in the calculation of constants.
8. Construct matrices **A**, **B**, **C** and **D** for the state-space representation. Matrices dimensions will depend on the chosen models of the machines. This should be done in connection with the existence of constants from Step 7. Notice that each model has different differential equations describing it, and therefore, different state variables will exist for each model.

The existence of constants and the construction of the state-space representation of a multi-order, multi-machine system can be coded in software by using suitable functions. A full example of a multi-order model published in the open literature will be used in the following section to illustrate the sequence of steps in a numeric fashion.

5.5. Model assessment

The multi-machine models developed in the previous section are here evaluated for effectiveness and accuracy of response. Two test systems available in the open literature are studied. The first system is the three-machine, nine-bus system presented in reference [1] and the second one is the four-machine, eleven-bus system of reference [2]. The output response of the multi-machine system is compared against the eigenvalues of the test systems reported in the open literature.

5.5.1. Three-machine nine-bus system

The nine-bus power system has three generators and three loads [1]. Although the test system is small, it is large enough to be a non-trivial one and entirely suitable to exemplify the construction of a multi-order system. Figure 5.4 shows the one-line diagram, where all impedances shown in the diagram are given in *p.u.* on a 100 *MVA* base. The power flows are shown in Figure 5.5, where the active and reactive power flows are given in *MW* and *MVAr*, respectively. The generator data for the three synchronous machines is given in Appendix B.

The initial operating conditions of the system are provided in Table 5.1, obtained by using equations (2.19)–(2.32). One generator in the system is represented by the classical model (0*d*.0*q*) and the other two generators by the two-axis model 2C (1*d*.1*q*). All the parameters are already given on the system base of 100 *MVA*, and no further conversion is necessary.

Table 5.1. Initial operating conditions for the three-machine, nine-bus system

Variable	Machine 1	Machine 2	Machine 3
Model type	Classic (0*d*.0*q*)	4th C (1*d*.1*q*)	4th C (1*d*.1*q*)
P_G	0.71641 *p.u.*	1.63 *p.u.*	0.85 *p.u.*
Q_G	0.27046 *p.u.*	0.066537 *p.u.*	–0.1086 *p.u.*
PF	0.93555	0.99917	0.99194
δ_0	3.5857 *deg*	55.267 *deg*	44.285 *deg*
$\lvert e_{t0} \rvert$	1.04 *p.u.*	1.025 *p.u.*	1.025 *p.u.*
$\angle e_{t0}$	0 *deg*	9.28 *deg*	4.6648 *deg*
e_{tq0}	1.038 *p.u.*	0.584 *p.u.*	0.73377 *p.u.*
e_{td0}	0.065043 *p.u.*	0.84236 *p.u.*	0.71569 *p.u.*
$\lvert i_{t0} \rvert$	0.73631 *p.u.*	1.5916 *p.u.*	0.83601 *p.u.*
i_{tq0}	0.67124 *p.u.*	0.8527 *p.u.*	0.51967 *p.u.*
i_{td0}	0.30263 *p.u.*	1.3439 *p.u.*	0.65487 *p.u.*
$\lvert E'_0 \rvert$	1.0564 *p.u.*	1.0049 *p.u.*	1.0343 *p.u.*
E'_{q0}	1.0564 *p.u.*	0.74499 *p.u.*	0.8525 *p.u.*
E'_{d0}	0 *p.u.*	0.67446 *p.u.*	0.58577 *p.u.*
E_{fd0}	1.0821 *p.u.*	1.7878 *p.u.*	1.5933 *p.u.*

The power loads are converted into equivalent admittances using voltage information from the power flow study,

$$\overline{Y}_{L5} = 1.26099 - j0.504398 \; p.u.$$
$$\overline{Y}_{L6} = 0.877647 - j0.292549 \; p.u.$$
$$\overline{Y}_{L8} = 0.968976 - j0.339142 \; p.u.$$

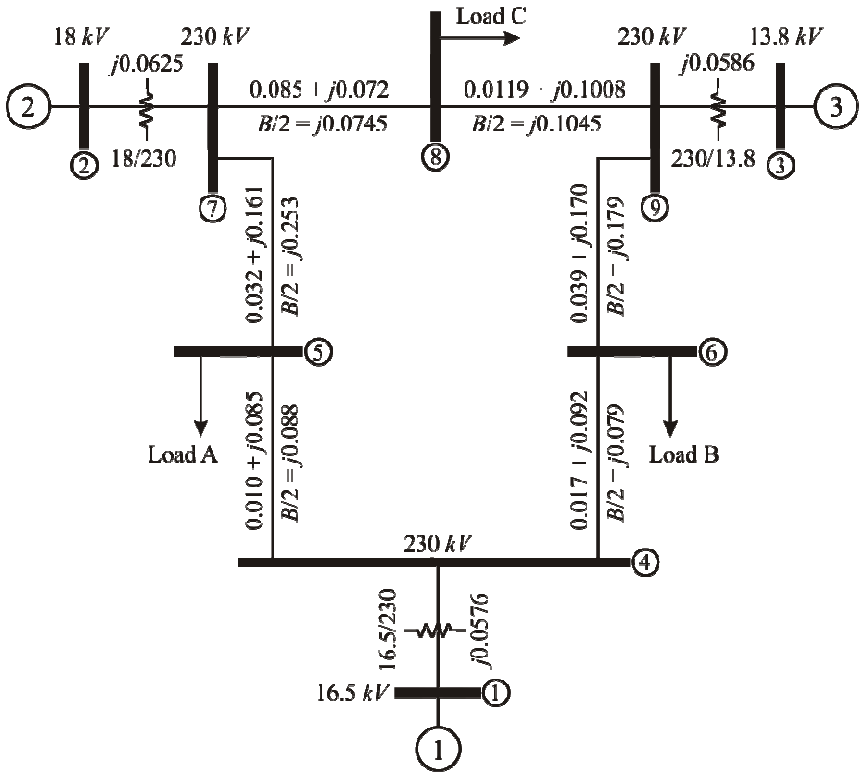

Figure 5.4. Three-machine system impedance diagram

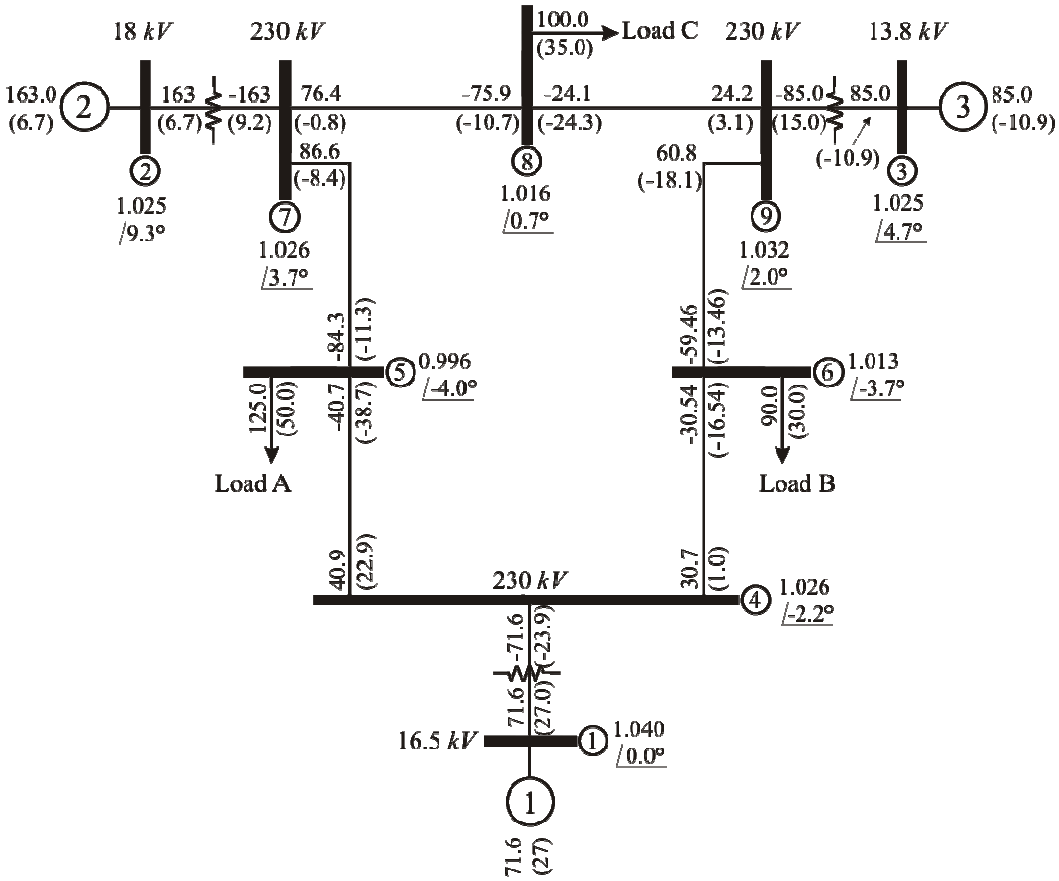

Figure 5.5. Three-machine power flow diagram

Using the equivalent shunt admittances of the load and the branch impedances of Figure 5.4, the network nodal admittance matrix is constructed. Notice that the transient generator impedances should be included in the network nodal admittance matrix $\bar{\mathbf{Y}}$ since the general current equations (5.52) and (5.53) are expressed in terms of machine internal voltages as opposed to the terminal voltages. The system impedance matrix is

$$\bar{\mathbf{Y}} = \begin{bmatrix} -j8.45 & 0 & 0 & j8.45 & 0 & 0 & 0 & 0 & 0 \\ 0 & -j5.49 & 0 & 0 & 0 & 0 & j5.49 & 0 & 0 \\ 0 & 0 & -j4.17 & 0 & 0 & 0 & 0 & 0 & j4.17 \\ j8.45 & 0 & 0 & 3.31-j30.39 & -1.37+j11.60 & -1.94+j10.51 & 0 & 0 & 0 \\ 0 & 0 & 0 & -1.37+j11.60 & 3.81-j17.84 & 0 & -1.19+j5.98 & 0 & 0 \\ 0 & 0 & 0 & -1.94+j10.51 & 0 & 4.10-j16.13 & 0 & 0 & -1.28+j5.59 \\ 0 & j5.49 & 0 & 0 & -1.19+j5.98 & 0 & 2.81-j24.93 & -1.62+j13.70 & 0 \\ 0 & 0 & 0 & 0 & 0 & 0 & -1.62+j13.70 & 3.74-j23.64 & -1.16+j9.78 \\ 0 & 0 & j4.17 & 0 & 0 & -1.28+j5.59 & 0 & -1.16+j9.78 & 2.44-j19.26 \end{bmatrix} \tag{5.132}$$

Eliminating the load buses in (5.132) using a Kron's reduction yields

$$\bar{\mathbf{Y}}_n = \begin{bmatrix} 0.8455-j2.9883 & 0.2871+j1.5129 & 0.2096+j1.2256 \\ 0.2871+j1.5129 & 0.4200-j2.7239 & 0.2133+j1.0880 \\ 0.2096+j1.2256 & 0.2133+j1.0880 & 0.2770-j2.3681 \end{bmatrix} \tag{5.133}$$

The algebraic and differential equations for Machine 1, which is represented by the Classic Model, are given by

$$\Delta\dot{\omega}_1 = \frac{1}{2H_1}\left[\Delta P_{m1} - \Delta P_{e1} - D_1\Delta\omega_1\right] \tag{5.134}$$

$$\Delta\dot{\delta}_1 = \omega_{10}\Delta\omega_1 \tag{5.135}$$

where

$$\Delta P_{e1} = i_{tq10}\left(X'_{q1} - X'_{d1}\right)\Delta i_{td1} + \left[E'_{q10} + i_{td10}\left(X'_{q1} - X'_{d1}\right)\right]\Delta i_{tq1} \tag{5.136}$$

$$\Delta e_{t1} = \left(e_{t10}\right)^{-1}\left[e_{td10}\Delta e_{td1} + e_{tq10}\Delta e_{tq1}\right] \tag{5.137}$$

and

$$\Delta e_{tq1} = -X'_{d1}\Delta i_{td1} \tag{5.138}$$

$$\Delta e_{td1} = X'_{q1}\Delta i_{tq1} \tag{5.139}$$

The algebraic and differential equations for Machine 2 and Machine 3, which are represented by Model 2C (1*d*.1*q*), are given by

$$\Delta\dot{E}'_{qi} = \frac{1}{\tau'_{di0}}\left[\Delta E_{fdi} - \left(X_{di} - X'_{di}\right)\Delta i_{tdi} - \Delta E'_{qi}\right] \tag{5.140}$$

$$\Delta\dot{E}'_{di} = \frac{1}{\tau'_{qi0}}\left[\left(X_{qi} - X'_{qi}\right)\Delta i_{tqi} - \Delta E'_{di}\right] \tag{5.141}$$

$$\Delta\dot{\omega}_i = \frac{1}{2H_i}\left[\Delta P_{mi} - \Delta P_{ei} - D_i\Delta\omega_i\right] \tag{5.142}$$

$$\Delta\dot{\delta}_i = \omega_{i0}\Delta\omega_i \tag{5.143}$$

where i = 2,3 and

$$\Delta P_{ei} = i_{tdi0}\Delta E'_{di} + i_{tqi0}\Delta E'_{qi} + \left[E'_{di0} + i_{tqi0}\left(X'_{qi} - X'_{di} \right) \right]\Delta i_{tdi} + \left[E'_{q30} + i_{tdi0}\left(X'_{qi} - X'_{di} \right) \right]\Delta i_{tqi} \tag{5.144}$$

$$\Delta e_{ti} = \left(e_{ti0} \right)^{-1}\left[e_{tdi0}\Delta e_{tdi} + e_{tqi0}\Delta e_{tqi} \right] \tag{5.145}$$

and

$$\Delta e_{tqi} = \Delta E'_{qi} - X'_{di}\Delta i_{tdi} \tag{5.146}$$

$$\Delta e_{tdi} = \Delta E'_{di} + X'_{qi}\Delta i_{tqi} \tag{5.147}$$

It should be mentioned that in this example, in order to match the results with those of reference [1], all parameters are expressed in *p.u.*, including time constants τ'_{di0} and τ'_{qi0}. Also, $\omega_0 = 1$ *p.u.*, $\omega_b = 2\pi f_0$ and a *p.u.* inertia constant $\tau_{ji} = 2H_i\omega_b$ should be used. Therefore, the swing equation

$$\Delta\dot{\omega}_i = \frac{1}{\tau_{ji}}\left[\Delta P_{mi} - \Delta P_{ei} - D_i\Delta\omega_i \right] \tag{5.148}$$

is used instead of (5.134) or (5.142).

The nodal injection currents are substituted in equations (5.134)–(5.148), which are obtained through the general current expressions (5.36). In this system, the terminal voltages are replaced by the transient internal voltages for Machine 2 and Machine 3 (4th order representations). In the case of Machine 1, represented by the Classical Model, this entry is eliminated. Evaluation of (5.36) yields

$$\begin{aligned}
\Delta i_{td1} + j\Delta i_{tq1} = {} & Y_{12}\left[\cos\left(\theta_{12} - \delta_{120} \right) + j\sin\left(\theta_{12} - \delta_{120} \right) \right]\Delta E'_{d2} + \\
& + jY_{12}\left[\cos\left(\theta_{12} - \delta_{120} \right) + j\sin\left(\theta_{12} - \delta_{120} \right) \right]\Delta E'_{q2} + \\
& + Y_{13}\left[\cos\left(\theta_{13} - \delta_{130} \right) + j\sin\left(\theta_{13} - \delta_{130} \right) \right]\Delta E'_{d3} + \\
& + jY_{13}\left[\cos\left(\theta_{13} - \delta_{130} \right) + j\sin\left(\theta_{13} - \delta_{130} \right) \right]\Delta E'_{q3} + \\
& - jY_{12}\left[\cos\left(\theta_{12} - \delta_{120} \right) + j\sin\left(\theta_{12} - \delta_{120} \right) \right]\left(E'_{d20} + jE'_{q20} \right)\Delta\delta_{12} + \\
& - jY_{13}\left[\cos\left(\theta_{13} - \delta_{130} \right) + j\sin\left(\theta_{13} - \delta_{130} \right) \right]\left(E'_{d30} + jE'_{q30} \right)\Delta\delta_{13}
\end{aligned} \tag{5.149}$$

$$\begin{aligned}
\Delta i_{td2} + j\Delta i_{tq2} = {} & \left(G_{22} + jB_{22} \right)\Delta E'_{d2} + j\left(G_{22} + jB_{22} \right)\Delta E'_{q2} + \\
& + Y_{23}\left[\cos\left(\theta_{23} - \delta_{230} \right) + j\sin\left(\theta_{23} - \delta_{230} \right) \right]\Delta E'_{d3} + \\
& + jY_{23}\left[\cos\left(\theta_{23} - \delta_{230} \right) + j\sin\left(\theta_{23} - \delta_{230} \right) \right]\Delta E'_{q3} + \\
& + jY_{12}\left[\cos\left(\theta_{12} + \delta_{120} \right) + j\sin\left(\theta_{12} + \delta_{120} \right) \right]\left(jE'_{q10} \right)\Delta\delta_{12} + \\
& - jY_{23}\left[\cos\left(\theta_{23} - \delta_{230} \right) + j\sin\left(\theta_{23} - \delta_{230} \right) \right]\left(E'_{d30} + jE'_{q30} \right)\Delta\delta_{23}
\end{aligned} \tag{5.150}$$

$$\begin{aligned}
\Delta i_{td3} + j\Delta i_{tq3} = {} & Y_{23}\left[\cos\left(\theta_{23} + \delta_{230} \right) + j\sin\left(\theta_{23} + \delta_{230} \right) \right]\Delta E'_{d2} + \\
& + jY_{23}\left[\cos\left(\theta_{23} + \delta_{230} \right) + j\sin\left(\theta_{23} + \delta_{230} \right) \right]\Delta E'_{q2} + \\
& + \left(G_{33} + jB_{33} \right)\Delta E'_{d3} + j\left(G_{33} + jB_{33} \right)\Delta E'_{q3} + \\
& + jY_{13}\left[\cos\left(\theta_{13} + \delta_{130} \right) + j\sin\left(\theta_{13} + \delta_{130} \right) \right]\left(jE'_{q10} \right)\Delta\delta_{13} + \\
& + jY_{23}\left[\cos\left(\theta_{23} + \delta_{230} \right) + j\sin\left(\theta_{23} + \delta_{230} \right) \right]\left(E'_{d20} + jE'_{q20} \right)\Delta\delta_{23}
\end{aligned} \tag{5.151}$$

Separating the real and imaginary terms of (5.149)–(5.151) yields

$$\begin{aligned}\Delta i_{td1} &= Y_{12}\cos\left(\theta_{12}-\delta_{120}\right)\Delta E'_{d2} - Y_{12}\sin\left(\theta_{12}-\delta_{120}\right)\Delta E'_{q2} + \\ &+Y_{13}\cos\left(\theta_{13}-\delta_{130}\right)\Delta E'_{d3} - Y_{13}\sin\left(\theta_{13}-\delta_{130}\right)\Delta E'_{q3} + \\ &+Y_{12}\left[E'_{d20}\sin\left(\theta_{12}-\delta_{120}\right)+E'_{q20}\cos\left(\theta_{12}-\delta_{120}\right)\right]\Delta\delta_{12} + \\ &+Y_{13}\left[E'_{d30}\sin\left(\theta_{13}-\delta_{130}\right)+E'_{q30}\cos\left(\theta_{13}-\delta_{130}\right)\right]\Delta\delta_{13}\end{aligned} \tag{5.152}$$

$$\begin{aligned}\Delta i_{tq1} &= Y_{12}\sin\left(\theta_{12}-\delta_{120}\right)\Delta E'_{d2} + Y_{12}\cos\left(\theta_{12}-\delta_{120}\right)\Delta E'_{q2} + \\ &+Y_{13}\sin\left(\theta_{13}-\delta_{130}\right)\Delta E'_{d3} + Y_{12}\cos\left(\theta_{13}-\delta_{130}\right)\Delta E'_{q3} + \\ &+Y_{12}\left[-E'_{d20}\cos\left(\theta_{12}-\delta_{120}\right)+E'_{q20}\sin\left(\theta_{12}-\delta_{120}\right)\right]\Delta\delta_{12} + \\ &+Y_{13}\left[-E'_{d30}\cos\left(\theta_{13}-\delta_{130}\right)+E'_{q30}\sin\left(\theta_{13}-\delta_{130}\right)\right]\Delta\delta_{13}\end{aligned} \tag{5.153}$$

$$\begin{aligned}\Delta i_{td2} &= G_{22}\Delta E'_{d2} - B_{22}\Delta E'_{q2} + Y_{23}\cos\left(\theta_{23}-\delta_{230}\right)\Delta E'_{d3} + \\ &-Y_{23}\sin\left(\theta_{23}-\delta_{230}\right)\Delta E'_{q3} - Y_{12}E'_{q10}\cos\left(\theta_{12}+\delta_{120}\right)\Delta\delta_{12} + \\ &+Y_{23}\left[E'_{d30}\sin\left(\theta_{23}-\delta_{230}\right)+E'_{q30}\cos\left(\theta_{23}-\delta_{230}\right)\right]\Delta\delta_{23}\end{aligned} \tag{5.154}$$

$$\begin{aligned}\Delta i_{tq2} &= B_{22}\Delta E'_{d2} + G_{22}\Delta E'_{q2} + Y_{23}\sin\left(\theta_{23}-\delta_{230}\right)\Delta E'_{d3} + \\ &+Y_{23}\cos\left(\theta_{23}-\delta_{230}\right)\Delta E'_{q3} - Y_{12}E'_{q10}\sin\left(\theta_{12}+\delta_{120}\right)\Delta\delta_{12} + \\ &+Y_{23}\left[-E'_{d30}\cos\left(\theta_{23}-\delta_{230}\right)+E'_{q30}\sin\left(\theta_{23}-\delta_{230}\right)\right]\Delta\delta_{23}\end{aligned} \tag{5.155}$$

$$\begin{aligned}\Delta i_{td3} &= Y_{23}\cos\left(\theta_{23}+\delta_{230}\right)\Delta E'_{d2} - Y_{23}\sin\left(\theta_{23}+\delta_{230}\right)\Delta E'_{q2} + \\ &+G_{33}\Delta E'_{d3} - B_{33}\Delta E'_{q3} - Y_{13}E'_{q10}\cos\left(\theta_{13}+\delta_{130}\right)\Delta\delta_{13} + \\ &-Y_{23}\left[E'_{d20}\sin\left(\theta_{23}+\delta_{230}\right)+E'_{q20}\cos\left(\theta_{23}+\delta_{230}\right)\right]\Delta\delta_{23}\end{aligned} \tag{5.156}$$

$$\begin{aligned}\Delta i_{tq3} &= Y_{23}\sin\left(\theta_{23}+\delta_{230}\right)\Delta E'_{d2} + Y_{23}\cos\left(\theta_{23}+\delta_{230}\right)\Delta E'_{q2} + \\ &+B_{33}\Delta E'_{d3} + G_{33}\Delta E'_{q3} - Y_{13}E'_{q10}\sin\left(\theta_{13}+\delta_{130}\right)\Delta\delta_{13} + \\ &-Y_{23}\left[-E'_{d20}\cos\left(\theta_{23}+\delta_{230}\right)+E'_{q20}\sin\left(\theta_{23}+\delta_{230}\right)\right]\Delta\delta_{23}\end{aligned} \tag{5.157}$$

Substitution of (5.152) and (5.153) into (5.134)–(5.139) and (5.154)–(5.157) into (5.140)–(5.148) yields the differential and algebraic equations of the system.

Machine 1

Substitution of (5.152)–(5.153) into (5.136), provides the electrical power expression for Machine 1,

$$\Delta P_{e1} = K_{1112}\Delta\delta_{12} + K_{1113}\Delta\delta_{13} + K_{212}\Delta E'_{q2} + K_{213}\Delta E'_{q3} + K_{2d12}\Delta E'_{d2} + K_{2d13}\Delta E'_{d3} \tag{5.158}$$

where

$$\begin{aligned}K_{1112} &= Y_{12}\left[E'_{d20}\sin\left(\theta_{12}-\delta_{120}\right)+E'_{q20}\cos\left(\theta_{12}-\delta_{120}\right)\right]\left[i_{tq10}\left(X'_{q1}-X'_{d1}\right)\right] + \\ &+Y_{12}\left[-E'_{d20}\cos\left(\theta_{12}-\delta_{120}\right)+E'_{q20}\sin\left(\theta_{12}-\delta_{120}\right)\right]\left[E'_{q10}+i_{td10}\left(X'_{q1}-X'_{d1}\right)\right] \\ K_{1113} &= Y_{13}\left[E'_{d30}\sin\left(\theta_{13}-\delta_{130}\right)+E'_{q30}\cos\left(\theta_{13}-\delta_{130}\right)\right]\left[i_{tq10}\left(X'_{q1}-X'_{d1}\right)\right] + \\ &+Y_{13}\left[-E'_{d30}\cos\left(\theta_{13}-\delta_{130}\right)+E'_{q30}\sin\left(\theta_{13}-\delta_{130}\right)\right]\left[E'_{q10}+i_{td10}\left(X'_{q1}-X'_{d1}\right)\right]\end{aligned}$$

$$K_{212} = Y_{12}\left\{-\sin\left(\theta_{12}-\delta_{120}\right)\left[i_{tq10}\left(X_{q1}^{'}-X_{d1}^{'}\right)\right]+\cos\left(\theta_{12}-\delta_{120}\right)\left[E_{q10}^{'}+i_{td10}\left(X_{q1}^{'}-X_{d1}^{'}\right)\right]\right\}$$

$$K_{213} = Y_{13}\left\{-\sin\left(\theta_{13}-\delta_{130}\right)\left[i_{tq10}\left(X_{q1}^{'}-X_{d1}^{'}\right)\right]+\cos\left(\theta_{13}-\delta_{130}\right)\left[E_{q10}^{'}+i_{td10}\left(X_{q1}^{'}-X_{d1}^{'}\right)\right]\right\}$$

$$K_{2d12} = Y_{12}\left\{\cos\left(\theta_{12}-\delta_{120}\right)\left[i_{tq10}\left(X_{q1}^{'}-X_{d1}^{'}\right)\right]+\sin\left(\theta_{12}-\delta_{120}\right)\left[E_{q10}^{'}+i_{td10}\left(X_{q1}^{'}-X_{d1}^{'}\right)\right]\right\}$$

$$K_{2d13} = Y_{13}\left\{\cos\left(\theta_{13}-\delta_{130}\right)\left[i_{tq10}\left(X_{q1}^{'}-X_{d1}^{'}\right)\right]+\sin\left(\theta_{13}-\delta_{130}\right)\left[E_{q10}^{'}+i_{td10}\left(X_{q1}^{'}-X_{d1}^{'}\right)\right]\right\}$$

Proceeding in the same way, using terminal voltages expressions (5.137)–(5.139), yields

$$\Delta e_{t1} = K_{5112}\Delta\delta_{12} + K_{5113}\Delta\delta_{13} + K_{612}\Delta E_{q2}^{'} + K_{613}\Delta E_{q3}^{'} + K_{6d12}\Delta E_{d2}^{'} + K_{6d13}\Delta E_{d3}^{'} \tag{5.159}$$

where

$$K_{5112} = \frac{e_{td10}}{e_{t10}}Y_{12}\left[-E_{d20}^{'}\cos\left(\theta_{12}-\delta_{120}\right)+E_{q20}^{'}\sin\left(\theta_{12}-\delta_{120}\right)\right]X_{q1}^{'} +$$
$$-\frac{e_{tq10}}{e_{t10}}Y_{12}\left[E_{d20}^{'}\sin\left(\theta_{12}-\delta_{120}\right)+E_{q20}^{'}\cos\left(\theta_{12}-\delta_{120}\right)\right]X_{d1}^{'}$$

$$K_{5113} = \frac{e_{td10}}{e_{t10}}Y_{13}\left[-E_{d30}^{'}\cos\left(\theta_{13}-\delta_{130}\right)+E_{q30}^{'}\sin\left(\theta_{13}-\delta_{130}\right)\right]X_{q1}^{'} +$$
$$-\frac{e_{tq10}}{e_{t10}}Y_{13}\left[E_{d30}^{'}\sin\left(\theta_{13}-\delta_{130}\right)+E_{q30}^{'}\cos\left(\theta_{13}-\delta_{130}\right)\right]X_{d1}^{'}$$

$$K_{612} = Y_{12}\left[\frac{e_{td10}}{e_{t10}}\cos\left(\theta_{12}-\delta_{120}\right)X_{q1}^{'}+\frac{e_{tq10}}{e_{t10}}\sin\left(\theta_{12}-\delta_{120}\right)X_{d1}^{'}\right]$$

$$K_{613} = Y_{13}\left[\frac{e_{td10}}{e_{t10}}\cos\left(\theta_{13}-\delta_{130}\right)X_{q1}^{'}+\frac{e_{tq10}}{e_{t10}}\sin\left(\theta_{13}-\delta_{130}\right)X_{d1}^{'}\right]$$

$$K_{6d12} = Y_{12}\left[\frac{e_{td10}}{e_{t10}}\sin\left(\theta_{12}-\delta_{120}\right)X_{q1}^{'}-\frac{e_{tq10}}{e_{t10}}\cos\left(\theta_{12}-\delta_{120}\right)X_{d1}^{'}\right]$$

$$K_{6d13} = Y_{13}\left[\frac{e_{td10}}{e_{t10}}\sin\left(\theta_{13}-\delta_{130}\right)X_{q1}^{'}-\frac{e_{tq10}}{e_{t10}}\cos\left(\theta_{13}-\delta_{130}\right)X_{d1}^{'}\right]$$

Substituting the electrical power equation (5.158) into (5.148) gives

$$\Delta\dot{\omega}_1 = -\frac{D_1}{2H_1\omega_b}\Delta\omega_1 - \frac{K_{1112}}{2H_1\omega_b}\Delta\delta_{12} - \frac{K_{1113}}{2H_1\omega_b}\Delta\delta_{13} - \frac{K_{212}}{2H_1\omega_b}\Delta E_{q2}^{'} - \frac{K_{213}}{2H_1\omega_b}\Delta E_{q3}^{'} +$$
$$-\frac{K_{2d12}}{2H_1\omega_b}\Delta E_{d2}^{'} - \frac{K_{2d13}}{2H_1\omega_b}\Delta E_{d3}^{'} + \frac{1}{2H_1\omega_b}\Delta P_{m1} \tag{5.160}$$

Equations (5.158)–(5.160) and (5.135) constitute the expressions for Machine 1.

Machine 2

Following substitution of (5.154)–(5.155) into (5.144), the electrical power expression for Machine 2 is given by

$$\Delta P_{e2} = K_{1212}\Delta\delta_{12} + K_{1223}\Delta\delta_{23} + K_{222}\Delta E_{q2}^{'} + K_{223}\Delta E_{q3}^{'} + K_{2d22}\Delta E_{d2}^{'} + K_{2d23}\Delta E_{d3}^{'} \tag{5.161}$$

where

$$K_{1212} = -Y_{12}E'_{q10}\left\{\cos\left(\theta_{12}+\delta_{120}\right)\left[E'_{d20}+i_{tq20}\left(X'_{q2}-X'_{d2}\right)\right]+\sin\left(\theta_{12}+\delta_{120}\right)\left[E'_{q20}+i_{td20}\left(X'_{q2}-X'_{d2}\right)\right]\right\}$$

$$K_{1223} = Y_{23}\left[E'_{d30}\sin\left(\theta_{23}-\delta_{230}\right)+E'_{q30}\cos\left(\theta_{23}-\delta_{230}\right)\right]\left[E'_{d20}+i_{tq20}\left(X'_{q2}-X'_{d2}\right)\right]+$$
$$+Y_{23}\left[-E'_{d30}\cos\left(\theta_{23}-\delta_{230}\right)+E'_{q30}\sin\left(\theta_{23}-\delta_{230}\right)\right]\left[E'_{q20}+i_{td20}\left(X'_{q2}-X'_{d2}\right)\right]$$

$$K_{222} = i_{tq20}-B_{22}\left[E'_{d20}+i_{tq20}\left(X'_{q2}-X'_{d2}\right)\right]+G_{22}\left[E'_{q20}+i_{td20}\left(X'_{q2}-X'_{d2}\right)\right]$$

$$K_{223} = Y_{23}\left\{-\sin\left(\theta_{23}-\delta_{230}\right)\left[E'_{d20}+i_{tq20}\left(X'_{q2}-X'_{d2}\right)\right]+\cos\left(\theta_{23}-\delta_{230}\right)\left[E'_{q20}+i_{td20}\left(X'_{q2}-X'_{d2}\right)\right]\right\}$$

$$K_{2d22} = i_{td20}+G_{22}\left[E'_{d20}+i_{tq20}\left(X'_{q2}-X'_{d2}\right)\right]+B_{22}\left[E'_{q20}+i_{td20}\left(X'_{q2}-X'_{d2}\right)\right]$$

$$K_{2d23} = Y_{23}\left\{\cos\left(\theta_{23}-\delta_{230}\right)\left[E'_{d20}+i_{tq20}\left(X'_{q2}-X'_{d2}\right)\right]+\sin\left(\theta_{23}-\delta_{230}\right)\left[E'_{q20}+i_{td20}\left(X'_{q2}-X'_{d2}\right)\right]\right\}$$

Using the terminal voltages expressions (5.145)–(5.147),

$$\Delta e_{t2} = K_{5212}\Delta\delta_{12}+K_{5223}\Delta\delta_{23}+K_{622}\Delta E'_{q2}+K_{623}\Delta E'_{q3}+K_{6d22}\Delta E'_{d2}+K_{6d23}\Delta E'_{d3} \tag{5.162}$$

where

$$K_{5212} = -Y_{12}E'_{q10}\left[\frac{e_{td20}}{e_{t20}}\sin\left(\theta_{12}+\delta_{120}\right)X'_{q2}-\frac{e_{tq20}}{e_{t20}}\cos\left(\theta_{12}+\delta_{120}\right)X'_{d2}\right]$$

$$K_{5223} = \frac{e_{td20}}{e_{t20}}Y_{23}\left[-E'_{d30}\cos\left(\theta_{23}-\delta_{230}\right)+E'_{q30}\sin\left(\theta_{23}-\delta_{230}\right)\right]X'_{q2}+$$
$$-\frac{e_{tq20}}{e_{t20}}Y_{23}\left[E'_{d30}\sin\left(\theta_{23}-\delta_{230}\right)+E'_{q30}\cos\left(\theta_{23}-\delta_{230}\right)\right]X'_{d2}$$

$$K_{622} = \left[\frac{e_{td20}}{e_{t20}}G_{22}X'_{q2}+\frac{e_{tq20}}{e_{t20}}\left(1+B_{22}X'_{d2}\right)\right]$$

$$K_{623} = Y_{23}\left[\frac{e_{td10}}{e_{t10}}\cos\left(\theta_{23}-\delta_{230}\right)X'_{q2}+\frac{e_{tq10}}{e_{t10}}\sin\left(\theta_{23}-\delta_{230}\right)X'_{d2}\right]$$

$$K_{6d22} = \left[\frac{e_{td20}}{e_{t20}}\left(1+B_{22}X'_{q2}\right)-\frac{e_{tq20}}{e_{t20}}G_{22}X'_{d2}\right]$$

$$K_{6d23} = Y_{23}\left[\frac{e_{td10}}{e_{t10}}\sin\left(\theta_{23}-\delta_{230}\right)X'_{q2}-\frac{e_{tq10}}{e_{t10}}\cos\left(\theta_{23}-\delta_{230}\right)X'_{d2}\right]$$

Substitution of (5.154) into the *d*-axis flux linkage transient voltage equation (5.140) gives

$$\Delta\dot{E}'_{q2} = \frac{1}{\tau'_{d20}}\Delta E_{fd2}+C_{1212}\Delta\delta_{12}+C_{1223}\Delta\delta_{23}+C_{222}\Delta E'_{q2}+C_{223}\Delta E'_{q3}+C_{2d22}\Delta E'_{d2}+C_{2d23}\Delta E'_{d3} \tag{5.163}$$

where

$$C_{1212} = \frac{Y_{12}}{\tau'_{d20}}E'_{q10}\cos\left(\theta_{12}+\delta_{120}\right)\left(X_{d2}-X'_{d2}\right)$$

$$C_{1223} = -\frac{Y_{23}}{\tau'_{d20}}\left[E'_{d30}\sin\left(\theta_{23}-\delta_{230}\right)+E'_{q30}\cos\left(\theta_{23}-\delta_{230}\right)\right]\left(X_{d2}-X'_{d2}\right)$$

$$C_{222} = \frac{1}{\tau'_{d20}}\left[B_{22}\left(X_{d2}-X'_{d2}\right)-1\right]$$

$$C_{223} = \frac{Y_{23}}{\tau'_{d20}}\sin\left(\theta_{23}-\delta_{230}\right)\left(X_{d2}-X'_{d2}\right)$$

$$C_{2d22} = -\frac{G_{22}}{\tau'_{d20}}\left(X_{d2} - X'_{d2}\right)$$

$$C_{2d23} = -\frac{Y_{23}}{\tau'_{d20}}\cos\left(\theta_{23} - \delta_{230}\right)\left(X_{d2} - X'_{d2}\right)$$

Substitution of (5.155) into the *q*-axis flux linkage transient voltage equation (5.141) yields

$$\Delta \dot{E}'_{d2} = C_{5212}\Delta\delta_{12} + C_{5223}\Delta\delta_{23} + C_{622}\Delta E'_{q2} + C_{623}\Delta E'_{q3} + C_{6d22}\Delta E'_{d2} + C_{6d23}\Delta E'_{d3} \tag{5.164}$$

where

$$C_{5212} = -\frac{Y_{12}}{\tau'_{q20}}E'_{q10}\sin\left(\theta_{12} + \delta_{120}\right)\left(X_{q2} - X'_{q2}\right)$$

$$C_{5223} = \frac{Y_{23}}{\tau'_{q20}}\left[-E'_{d30}\cos\left(\theta_{23} - \delta_{230}\right) + E'_{q30}\sin\left(\theta_{23} - \delta_{230}\right)\right]\left(X_{q2} - X'_{q2}\right)$$

$$C_{622} = \frac{G_{22}}{\tau'_{q20}}\left(X_{q2} - X'_{q2}\right)$$

$$C_{623} = \frac{Y_{23}}{\tau'_{q20}}\cos\left(\theta_{23} - \delta_{230}\right)\left(X_{q2} - X'_{q2}\right)$$

$$C_{6d22} = \frac{1}{\tau'_{q20}}\left[B_{22}\left(X_{q2} - X'_{q2}\right) - 1\right]$$

$$C_{6d23} = \frac{Y_{23}}{\tau'_{q20}}\sin\left(\theta_{23} - \delta_{230}\right)\left(X_{q2} - X'_{q2}\right)$$

Substituting the electrical power equation (5.161) into (5.148) gives

$$\begin{aligned}\Delta\dot{\omega}_2 = &-\frac{D_2}{2H_2\omega_b}\Delta\omega_2 - \frac{K_{1212}}{2H_2\omega_b}\Delta\delta_{12} - \frac{K_{1223}}{2H_2\omega_b}\Delta\delta_{23} - \frac{K_{222}}{2H_2\omega_b}\Delta E'_{q2} - \frac{K_{223}}{2H_2\omega_b}\Delta E'_{q3} + \\ &-\frac{K_{2d22}}{2H_2\omega_b}\Delta E'_{d2} - \frac{K_{2d23}}{2H_2\omega_b}\Delta E'_{d3} + \frac{1}{2H_2\omega_b}\Delta P_{m2}\end{aligned} \tag{5.165}$$

From (5.143),

$$\Delta\dot{\delta}_2 = \omega_{20}\Delta\omega_2 \tag{5.166}$$

Equations (5.161)–(5.166) constitute the set of expressions for Machine 2.

Machine 3

Substitution of (5.156)–(5.157) into (5.144) yields the electrical power expression for Machine 3,

$$\Delta P_{e3} = K_{1313}\Delta\delta_{13} + K_{1323}\Delta\delta_{23} + K_{232}\Delta E'_{q2} + K_{233}\Delta E'_{q3} + K_{2d32}\Delta E'_{d2} + K_{2d33}\Delta E'_{d3} \tag{5.167}$$

where

$$K_{1313} = -Y_{13}E'_{q10}\left\{\cos\left(\theta_{13} + \delta_{130}\right)\left[E'_{d30} + i_{tq30}\left(X'_{q3} - X'_{d3}\right)\right] + \sin\left(\theta_{13} + \delta_{130}\right)\left[E'_{q30} + i_{td30}\left(X'_{q3} - X'_{d3}\right)\right]\right\}$$

$$\begin{aligned}K_{1323} = &-Y_{23}\left[E'_{d20}\sin\left(\theta_{23} + \delta_{230}\right) + E'_{q20}\cos\left(\theta_{23} + \delta_{230}\right)\right]\left[E'_{d30} + i_{tq30}\left(X'_{q3} - X'_{d3}\right)\right] + \\ &-Y_{23}\left[-E'_{d20}\cos\left(\theta_{23} + \delta_{230}\right) + E'_{q20}\sin\left(\theta_{23} + \delta_{230}\right)\right]\left[E'_{q30} + i_{td30}\left(X'_{q3} - X'_{d3}\right)\right]\end{aligned}$$

$$K_{232} = Y_{23}\left\{-\sin\left(\theta_{23} + \delta_{230}\right)\left[E'_{d30} + i_{tq30}\left(X'_{q3} - X'_{d3}\right)\right] + \cos\left(\theta_{23} + \delta_{230}\right)\left[E'_{q30} + i_{td30}\left(X'_{q3} - X'_{d3}\right)\right]\right\}$$

$$K_{233} = i_{tq30} - B_{33}\left[E'_{d30} + i_{tq30}\left(X'_{q3} - X'_{d3}\right)\right] + G_{33}\left[E'_{q30} + i_{td30}\left(X'_{q3} - X'_{d3}\right)\right]$$

$$K_{2d32} = Y_{23}\left\{\cos\left(\theta_{23} + \delta_{230}\right)\left[E'_{d30} + i_{tq30}\left(X'_{q3} - X'_{d3}\right)\right] + \sin\left(\theta_{23} + \delta_{230}\right)\left[E'_{q30} + i_{td30}\left(X'_{q3} - X'_{d3}\right)\right]\right\}$$

$$K_{2d33} = i_{td30} + G_{33}\left[E'_{d30} + i_{tq30}\left(X'_{q3} - X'_{d3}\right)\right] + B_{33}\left[E'_{q30} + i_{td30}\left(X'_{q3} - X'_{d3}\right)\right]$$

Proceeding along the same way with terminal voltages expressions (5.145)–(5.147) yields

$$\Delta e_{t3} = K_{5313}\Delta\delta_{13} + K_{5323}\Delta\delta_{23} + K_{632}\Delta E'_{q2} + K_{633}\Delta E'_{q3} + K_{6d32}\Delta E'_{d2} + K_{6d33}\Delta E'_{d3} \tag{5.168}$$

where

$$K_{5313} = -Y_{13}E'_{q10}\left[\frac{e_{td30}}{e_{t30}}\sin\left(\theta_{13} + \delta_{130}\right)X'_{q3} - \frac{e_{tq30}}{e_{t30}}\cos\left(\theta_{13} + \delta_{130}\right)X'_{d3}\right]$$

$$K_{5323} = -\frac{e_{td30}}{e_{t30}}Y_{23}\left[-E'_{d20}\cos\left(\theta_{23} + \delta_{230}\right) + E'_{q20}\sin\left(\theta_{23} + \delta_{230}\right)\right]X'_{q3} +$$

$$+\frac{e_{tq30}}{e_{t30}}Y_{23}\left[E'_{d20}\sin\left(\theta_{23} + \delta_{230}\right) + E'_{q20}\cos\left(\theta_{23} + \delta_{230}\right)\right]X'_{d3}$$

$$K_{632} = Y_{23}\left[\frac{e_{td30}}{e_{t30}}\cos\left(\theta_{23} + \delta_{230}\right)X'_{q3} + \frac{e_{tq30}}{e_{t30}}\sin\left(\theta_{23} + \delta_{230}\right)X'_{d3}\right]$$

$$K_{633} = \left[\frac{e_{td30}}{e_{t30}}G_{33}X'_{q3} + \frac{e_{tq30}}{e_{t30}}\left(1 + B_{33}X'_{d3}\right)\right]$$

$$K_{6d32} = Y_{23}\left[\frac{e_{td30}}{e_{t30}}\sin\left(\theta_{23} + \delta_{230}\right)X'_{q3} - \frac{e_{tq30}}{e_{t30}}\cos\left(\theta_{23} + \delta_{230}\right)X'_{d3}\right]$$

$$K_{6d33} = \left[\frac{e_{td30}}{e_{t30}}\left(1 + B_{33}X'_{q3}\right) - \frac{e_{tq30}}{e_{t30}}G_{33}X'_{d3}\right]$$

Substitution of (5.156) into the *d*-axis flux linkage transient voltage equation (5.140) provides

$$\Delta\dot{E}'_{q3} = \frac{1}{\tau'_{d30}}\Delta E_{fd3} + C_{1313}\Delta\delta_{13} + C_{1323}\Delta\delta_{23} + C_{232}\Delta E'_{q2} + C_{233}\Delta E'_{q3} + C_{2d32}\Delta E'_{d2} + C_{2d33}\Delta E'_{d3} \tag{5.169}$$

where

$$C_{1313} = \frac{Y_{13}}{\tau'_{d30}}E'_{q10}\cos\left(\theta_{13} + \delta_{130}\right)\left(X_{d3} - X'_{d3}\right)$$

$$C_{1323} = \frac{Y_{23}}{\tau'_{d30}}\left[E'_{d20}\sin\left(\theta_{23} + \delta_{230}\right) + E'_{q20}\cos\left(\theta_{23} + \delta_{230}\right)\right]\left(X_{d3} - X'_{d3}\right)$$

$$C_{232} = \frac{Y_{23}}{\tau'_{d30}}\sin\left(\theta_{23} + \delta_{230}\right)\left(X_{d3} - X'_{d3}\right)$$

$$C_{233} = \frac{1}{\tau'_{d30}}\left[B_{33}\left(X_{d3} - X'_{d3}\right) - 1\right]$$

$$C_{2d32} = -\frac{Y_{23}}{\tau'_{d30}}\cos\left(\theta_{23} + \delta_{230}\right)\left(X_{d3} - X'_{d3}\right)$$

$$C_{2d33} = -\frac{G_{33}}{\tau'_{d30}}\left(X_{d3} - X'_{d3}\right)$$

Also, substitution of (5.157) into the *q*-axis flux linkage transient voltage equation (5.141) provides

$$\Delta \dot{E}'_{d3} = C_{5313}\Delta\delta_{13} + C_{5323}\Delta\delta_{23} + C_{632}\Delta E'_{q2} + C_{633}\Delta E'_{q3} + C_{6d32}\Delta E'_{d2} + C_{6d33}\Delta E'_{d3} \tag{5.170}$$

where

$$C_{5313} = -\frac{Y_{13}}{\tau'_{q30}} E'_{q10} \sin\left(\theta_{13} + \delta_{130}\right)\left(X_{q3} - X'_{q3}\right)$$

$$C_{5223} = -\frac{Y_{23}}{\tau'_{q30}}\left[-E'_{d20}\cos\left(\theta_{23} + \delta_{230}\right) + E'_{q20}\sin\left(\theta_{23} + \delta_{230}\right)\right]\left(X_{q3} - X'_{q3}\right)$$

$$C_{632} = \frac{Y_{23}}{\tau'_{q30}}\cos\left(\theta_{23} + \delta_{230}\right)\left(X_{q3} - X'_{q3}\right)$$

$$C_{633} = \frac{G_{33}}{\tau'_{q30}}\left(X_{q3} - X'_{q3}\right)$$

$$C_{6d32} = \frac{Y_{23}}{\tau'_{q30}}\sin\left(\theta_{23} + \delta_{230}\right)\left(X_{q3} - X'_{q3}\right)$$

$$C_{6d33} = \frac{1}{\tau'_{q30}}\left[B_{33}\left(X_{q3} - X'_{q3}\right) - 1\right]$$

Substituting electrical power equation (5.161) into (5.148) gives

$$\begin{aligned}\Delta \dot{\omega}_3 = &-\frac{D_3}{2H_3\omega_b}\Delta\omega_3 - \frac{K_{1313}}{2H_3\omega_b}\Delta\delta_{13} - \frac{K_{1323}}{2H_3\omega_b}\Delta\delta_{23} - \frac{K_{232}}{2H_3\omega_b}\Delta E'_{q2} - \frac{K_{233}}{2H_3\omega_b}\Delta E'_{q3} + \\ &-\frac{K_{2d32}}{2H_3\omega_b}\Delta E'_{d2} - \frac{K_{2d33}}{2H_3\omega_b}\Delta E'_{d3} + \frac{1}{2H_3\omega_b}\Delta P_{m3}\end{aligned} \tag{5.171}$$

From (5.143),

$$\Delta \dot{\delta}_3 = \omega_{30}\Delta\omega_3 \tag{5.172}$$

Equations (5.167)–(5.172) constitute the set of expressions for Machine 3.

Differential and algebraic equations (5.158)–(5.172) and (5.135) provide the mathematical model for the three-machine system. Notice that the system is not a 10th order one since the equations are not independent; in fact, the system is a 9th order system. In order to obtain an independent set and to eliminate redundant variables given by the $\Delta\delta_{ik}$ terms, (5.98) is used with (5.135), (5.166) and (5.172) as

$$\Delta \dot{\delta}_{12} = \omega_{10}\Delta\omega_1 - \omega_{20}\Delta\omega_2 \tag{5.173}$$

$$\Delta \dot{\delta}_{13} = \omega_{10}\Delta\omega_1 - \omega_{30}\Delta\omega_3 \tag{5.174}$$

Also, the following substitution is required:

$$\Delta\delta_{23} = \Delta\delta_{13} - \Delta\delta_{12} \tag{5.175}$$

Once the independent system of equations is obtained, the state-space representation

$$\begin{aligned}\Delta\dot{\mathbf{x}} &= \mathbf{A}\Delta\mathbf{x} + \mathbf{B}\Delta\mathbf{u} \\ \Delta\mathbf{y} &= \mathbf{C}\Delta\mathbf{x} + \mathbf{D}\Delta\mathbf{u}\end{aligned} \tag{5.99}$$

is constructed as in section 5.3. The state, input and output vectors are given, respectively, as

$$\Delta\mathbf{x} = \begin{bmatrix} \Delta\mathbf{x}_1 & \Delta\mathbf{x}_2 & \Delta\mathbf{x}_3 & \Delta\boldsymbol{\delta} \end{bmatrix}^T \tag{5.176}$$

$$\Delta\mathbf{u} = \begin{bmatrix} \Delta P_{m1} & \Delta P_{m2} & \Delta E_{fd2} & \Delta P_{m3} & \Delta E_{fd3} \end{bmatrix}^T \tag{5.177}$$

$$\Delta\mathbf{y} = \begin{bmatrix} \Delta\omega_1 & \Delta e_{t1} & \Delta\omega_2 & \Delta e_{t2} & \Delta\omega_3 & \Delta e_{t3} \end{bmatrix}^T \tag{5.178}$$

where

$$\Delta\mathbf{x}_1 = \Delta\omega_1 \tag{5.179}$$

$$\Delta\mathbf{x}_2 = \begin{bmatrix} \Delta\omega_2 & \Delta E'_{q2} & \Delta E'_{d2} \end{bmatrix} \tag{5.180}$$

$$\Delta\mathbf{x}_3 = \begin{bmatrix} \Delta\omega_3 & \Delta E'_{q3} & \Delta E'_{d3} \end{bmatrix} \tag{5.181}$$

$$\Delta\boldsymbol{\delta} = \begin{bmatrix} \Delta\delta_{12} & \Delta\delta_{13} \end{bmatrix} \tag{5.182}$$

The three-machine model gives rise to a 5-input 6-output system, since Machine 1 is represented by the classical model with constant field voltage. System matrix **A** in (5.99), a square matrix of dimension (7 × 7), is given by

$$\mathbf{A} = \begin{bmatrix} \mathbf{A}_n & \mathbf{A}_\delta \\ \mathbf{A}_\omega & \mathbf{A}_0 \end{bmatrix} \tag{5.107}$$

where

$$\mathbf{A}_n = \begin{bmatrix} -\frac{D_1}{2H_1\omega_b} & 0 & -\frac{K_{212}}{2H_1\omega_b} & -\frac{K_{2d12}}{2H_1\omega_b} & 0 & -\frac{K_{213}}{2H_1\omega_b} & -\frac{K_{2d13}}{2H_1\omega_b} \\ 0 & -\frac{D_2}{2H_2\omega_b} & -\frac{K_{222}}{2H_2\omega_b} & -\frac{K_{2d22}}{2H_2\omega_b} & 0 & -\frac{K_{223}}{2H_2\omega_b} & -\frac{K_{2d23}}{2H_2\omega_b} \\ 0 & 0 & C_{222} & C_{2d22} & 0 & C_{223} & C_{2d23} \\ 0 & 0 & C_{622} & C_{6d22} & 0 & C_{623} & C_{6d23} \\ 0 & 0 & -\frac{K_{232}}{2H_3\omega_b} & -\frac{K_{2d32}}{2H_3\omega_b} & -\frac{D_3}{2H_3\omega_b} & -\frac{K_{233}}{2H_3\omega_b} & -\frac{K_{2d33}}{2H_3\omega_b} \\ 0 & 0 & C_{232} & C_{2d32} & 0 & C_{233} & C_{2d33} \\ 0 & 0 & C_{632} & C_{6d32} & 0 & C_{633} & C_{6d33} \end{bmatrix} \tag{5.183}$$

or, more compactly,

$$\mathbf{A}_n = \begin{bmatrix} \mathbf{A}_{11} & \mathbf{A}_{12} & \mathbf{A}_{13} \\ \mathbf{A}_{21} & \mathbf{A}_{22} & \mathbf{A}_{23} \\ \mathbf{A}_{31} & \mathbf{A}_{32} & \mathbf{A}_{33} \end{bmatrix} \tag{5.184}$$

where diagonal sub-matrices $\mathbf{A}_{ii}$ correspond to square self-matrices of the *i*-th machine and off-diagonal non-square sub-matrices $\mathbf{A}_{ik}$ correspond to the interaction of the *i*-th and *k*-th machines. For off-diagonal matrices, the number of rows depends on the order of the *i*-th machine (*i.e.*, number of states in $\Delta\mathbf{x}_i$), whereas the number of columns depends on the order of the *k*-th machine (*i.e.*, number of states in $\Delta\mathbf{x}_k$). Although for Machine 1, the lower order machine, some self-coefficients are not defined, it is noticed that the interactions from the higher order Machines 2 and 3 with Machine 1 do appear. Sub-matrix A_δ in (5.107) is of the form

$$\mathbf{A}_{\delta} = \begin{bmatrix} -\dfrac{K_{1112}}{2H_1\omega_b} & -\dfrac{K_{1113}}{2H_1\omega_b} \\ -\dfrac{K_{1212}}{2H_2\omega_b} + \dfrac{K_{1223}}{2H_2\omega_b} & -\dfrac{K_{1223}}{2H_2\omega_b} \\ C_{1212} - C_{1223} & C_{1223} \\ C_{5212} - C_{5223} & C_{5223} \\ \dfrac{K_{1323}}{2H_3\omega_b} & -\dfrac{K_{1313}}{2H_3\omega_b} - \dfrac{K_{1323}}{2H_3\omega_b} \\ -C_{1323} & C_{1313} + C_{1323} \\ -C_{5323} & C_{5313} + C_{5323} \end{bmatrix} \tag{5.185}$$

or, more compactly,

$$\mathbf{A}_{\delta} = \begin{bmatrix} \mathbf{A}_{\delta 12} & \mathbf{A}_{\delta 13} \\ \mathbf{A}_{\delta 22} & \mathbf{A}_{\delta 23} \\ \mathbf{A}_{\delta 32} & \mathbf{A}_{\delta 33} \end{bmatrix} \tag{5.186}$$

where the dimensions of column vectors $\mathbf{A}_{\delta k}$ depend on the order of the *i*-th machine. Sub-matrix A_{ω} in (5.107) takes the form

$$\mathbf{A}_{\omega} = \begin{bmatrix} \omega_{10} & -\omega_{20} & 0 & 0 & 0 & 0 & 0 \\ \omega_{10} & 0 & 0 & 0 & -\omega_{30} & 0 & 0 \end{bmatrix} \tag{5.187}$$

or, more compactly,

$$\mathbf{A}_{\omega} = \begin{bmatrix} \mathbf{A}_{\omega 1} & \mathbf{A}_{\omega 2} & \mathbf{0}_{1\times 3} \\ \mathbf{A}_{\omega 1} & \mathbf{0}_{1\times 3} & \mathbf{A}_{\omega 3} \end{bmatrix} \tag{5.188}$$

Notice that row vector $\mathbf{A}_{\omega 1}$ has a dimension that depends on the order of the 1st machine (in this case, $\mathbf{A}_{\omega 1}$ is a scalar since $\Delta\mathbf{x}_1$ is a scalar), vectors $\mathbf{A}_{\omega k}$, with $k \neq 1$, have dimensions depending on the order of the *k*-th machine (given by dimensions of $\Delta\mathbf{x}_2$ and $\Delta\mathbf{x}_3$) and $\mathbf{0}_{1\times 3}$ are row vectors with 3 zero elements. Sub-matrix $\mathbf{A}_0$ in (5.107) is of the form

$$\mathbf{A}_0 = \mathbf{0}_{2\times 2} \tag{5.189}$$

Control matrix **B** in (5.99), a matrix of dimension (9 × 5), is given by

$$\mathbf{B} = \begin{bmatrix} \mathbf{B}_n \\ \mathbf{B}_0 \end{bmatrix} \tag{5.119}$$

where sub-matrix $\mathbf{B}_n$ of (5.119) is given by

$$\mathbf{B}_n = \begin{bmatrix} \frac{1}{2H_1\omega_b} & 0 & 0 & 0 & 0 \\ 0 & \frac{1}{2H_2\omega_b} & 0 & 0 & 0 \\ 0 & 0 & \frac{1}{\tau'_{d20}} & 0 & 0 \\ 0 & 0 & 0 & 0 & 0 \\ 0 & 0 & 0 & \frac{1}{2H_3\omega_b} & 0 \\ 0 & 0 & 0 & 0 & \frac{1}{\tau'_{d30}} \\ 0 & 0 & 0 & 0 & 0 \end{bmatrix} \tag{5.190}$$

or, more compactly,

$$\mathbf{B}_n = \begin{bmatrix} \mathbf{B}_1 & \mathbf{0}_{1\times2} & \mathbf{0}_{1\times2} \\ \mathbf{0}_{3\times1} & \mathbf{B}_2 & \mathbf{0}_{3\times2} \\ \mathbf{0}_{3\times1} & \mathbf{0}_{3\times2} & \mathbf{B}_3 \end{bmatrix} \tag{5.191}$$

where, in general, diagonal sub-matrices $\mathbf{B}_i$ correspond to self-matrices of the *i*-th machine having a dimension ($n_i \times 2$), where n_i stands for the order of vector $\Delta\mathbf{x}_i$. In the particular case of Machine 1, as it is represented by the Classical Model, it has just one input and therefore $\mathbf{B}_1$ has dimension (1 × 1). Off-diagonal matrices $\mathbf{0}_{i\times m}$ are filled in with zeros depending on the order *i* of vector $\Delta\mathbf{x}_i$ and the number of *m* inputs of the *i*-th machine. Sub-matrix $\mathbf{B}_0$ in (5.107) is of the form

$$\mathbf{B}_0 = \mathbf{0}_{2\times5} \tag{5.192}$$

Control matrix **C** in (5.99), a matrix of dimension (6 × 9), is given as

$$\mathbf{C} = \begin{bmatrix} \mathbf{C}_n & \mathbf{C}_\delta \end{bmatrix} \tag{5.123}$$

where sub-matrix $\mathbf{C}_n$ of (5.123) is given as

$$\mathbf{C}_n = \begin{bmatrix} 1 & 0 & 0 & 0 & 0 & 0 & 0 \\ 0 & 0 & K_{612} & K_{6d12} & 0 & K_{613} & K_{6d13} \\ 0 & 1 & 0 & 0 & 0 & 0 & 0 \\ 0 & 0 & K_{622} & K_{6d22} & 0 & K_{623} & K_{6d23} \\ 0 & 0 & 0 & 0 & 1 & 0 & 0 \\ 0 & 0 & K_{632} & K_{6d32} & 0 & K_{633} & K_{6d33} \end{bmatrix} \tag{5.193}$$

or, more compactly,

$$\mathbf{C}_n = \begin{bmatrix} \mathbf{C}_{11} & \mathbf{C}_{12} & \mathbf{C}_{13} \\ \mathbf{C}_{21} & \mathbf{C}_{22} & \mathbf{C}_{23} \\ \mathbf{C}_{31} & \mathbf{C}_{32} & \mathbf{C}_{33} \end{bmatrix} \tag{5.194}$$

where diagonal sub-matrices $\mathbf{C}_{ii}$ correspond to self-matrices of the *i*-th machine of dimension ($2 \times n_i$), where n_i stands for the order of vector $\Delta\mathbf{x}_i$. Off-diagonal matrices $\mathbf{C}_{ik}$ are of dimension ($2 \times n_k$) and n_k stands for the order of vector $\Delta\mathbf{x}_k$. Sub-matrix C_δ in (5.123) is of the form

$$\mathbf{C}_{\delta} = \begin{bmatrix} 0 & 0 \\ K_{5112} & K_{5113} \\ 0 & 0 \\ K_{5212} - K_{5223} & K_{5223} \\ 0 & 0 \\ -K_{5323} & K_{5313} + K_{5323} \end{bmatrix} \tag{5.195}$$

or, more compactly,

$$\mathbf{C}_{\delta} = \begin{bmatrix} \mathbf{C}_{\delta 12} & \mathbf{C}_{\delta 13} \\ \mathbf{C}_{\delta 22} & \mathbf{C}_{\delta 23} \\ \mathbf{C}_{\delta 32} & \mathbf{C}_{\delta 33} \end{bmatrix} \tag{5.196}$$

where column vectors $\mathbf{C}_{\delta ik}$ have a dimension of (1 × 2). Finally, feed-forward matrix **D** in (5.99), a matrix of dimensions (6 × 5), is given as

$$\mathbf{D} = \mathbf{0}_{6\times 5} \tag{5.197}$$

where all its entries are zero.

For the three-machine system, calculation of the constants associated to the partitioned matrices (5.183)–(5.196) allows the numerical construction of (5.107), (5.119), (5.123) and (5.197), which become

$$\mathbf{A} = \begin{bmatrix} 0 & 0 & 0.0000598 & -0.0000689 & 0 & 0.0000379 & -0.0000632 & -0.0000917 & -0.0000761 \\ 0 & 0 & -0.000622 & 0.0000833 & 0 & 0.0000793 & -0.000213 & 0.000549 & -0.000231 \\ 0 & 0 & -0.00138 & -0.000144 & 0 & 0.000352 & -0.000143 & 0.000823 & -0.000328 \\ 0 & 0 & 0.00139 & -0.0140 & 0 & 0.00138 & 0.00340 & -0.00458 & 0.00209 \\ 0 & 0 & 0.000285 & -0.000417 & 0 & -0.000944 & 0.000530 & -0.000503 & 0.00108 \\ 0 & 0 & 0.000565 & -0.00000108 & 0 & -0.00166 & -0.000141 & -0.000382 & 0.000897 \\ 0 & 0 & 0.00000946 & 0.00494 & 0 & 0.00123 & -0.0150 & 0.00367 & -0.00740 \\ 1 & -1 & 0 & 0 & 0 & 0 & 0 & 0 & 0 \\ 1 & 0 & 0 & 0 & -1 & 0 & 0 & 0 & 0 \end{bmatrix} \tag{5.198}$$

$$\mathbf{B} = 1\times 10^{-3} \cdot \begin{bmatrix} 0.05610 & 0 & 0 & 0 & 0 & 0 & 0 & 0 & 0 \\ 0 & 0.2072 & 0 & 0 & 0 & 0 & 0 & 0 & 0 \\ 0 & 0 & 0.4421 & 0 & 0 & 0 & 0 & 0 & 0 \\ 0 & 0 & 0 & 0 & 0.4406 & 0 & 0 & 0 & 0 \\ 0 & 0 & 0 & 0 & 0 & 0.4504 & 0 & 0 & 0 \end{bmatrix}^{T} \tag{5.199}$$

$$\mathbf{C} = \begin{bmatrix} 1 & 0 & 0 & 0 & 0 & 0 & 0 & 0 & 0 \\ 0 & 0 & 0.06448 & 0.06828 & 0 & 0.06080 & 0.04531 & 0.007378 & 0.003017 \\ 0 & 1 & 0 & 0 & 0 & 0 & 0 & 0 & 0 \\ 0 & 0 & 0.4518 & 0.3524 & 0 & 0.1375 & 0.1378 & -0.06034 & 0.03692 \\ 0 & 0 & 0 & 0 & 1 & 0 & 0 & 0 & 0 \\ 0 & 0 & 0.1443 & 0.1932 & 0 & 0.4569 & 0.2489 & 0.04667 & -0.06145 \end{bmatrix} \tag{5.200}$$

$$\mathbf{D} = \mathbf{0}_{6\times 5} \tag{5.201}$$

The model assessment may be carried out by obtaining the eigenvalues of system matrix **A** (5.198). Recalling from Chapter 3, the complex pairs of eigenvalues are given as:

$$\lambda = \sigma \pm j\omega \tag{3.33}$$

where the frequency of oscillation (in *Hz*) is given by

$$f = \frac{\omega}{2\pi}\omega_b \tag{5.202}$$

which represents the actual or damped frequency. The product times base ω_b in (5.202) is required as $\omega_0 = 1$ *p.u.* and $\omega_b = 2\pi f_0$ for this example. The damping ratio is given by

$$\zeta = \frac{-\sigma}{\sqrt{\sigma^2 + \omega^2}} \tag{3.35}$$

which determines the rate of decay of the amplitude of the oscillation. The time constant of amplitude decay is $1/|\sigma|$, *i.e.*, the amplitude decays to $1/e$ or 37% of the initial amplitude in $1/|\sigma|$ seconds.

Tables 5.2 summarises the eigenvalues of the three-machine system alongside those reported in [1] for a system with slightly different conditions than those used in this study, which will be pointed out below. A case for D_i = 1 *p.u.* is also included for completeness. The frequencies of oscillation and damping ratios of the complex eigenvalues found in Table 5.2 are shown in Table 5.3.

Table 5.2. Eigenvalues of the three-machine, nine-bus system

Eigenvalue	**Case 1** $D_i = 0$ *p.u.* Multi-order model	**Case 1** $D_i = 0$ *p.u.* Multi-order model with $X'_{qi} \cong X'_{di}$	**Case 1** $D_i = 0$ *p.u.* Literature [1]	**Case 2** $D_i = 1$ *p.u.* Multi-order model	**Case 2** $D_i = 1$ *p.u.* Multi-order model with $X'_{qi} \cong X'_{di}$	**Case 2** $D_i = 1$ *p.u.* Literature [1]
λ_1	0	0	0	–0.000208	–0.000243 + *j*0.000029	–0.000199 + *j*0.000129
λ_2	–0.000375	–0.000370	–0.000281	–0.000283	–0.000243 + –*j*0.000029	–0.000199 + –*j*0.000129
λ_3	–0.000649	–0.000643	–0.000458	–0.000640	–0.000634	–0.000455
λ_4	–0.009650	–0.009706	–0.010366	–0.009659	–0.009716	–0.010373
λ_5	–0.01481	–0.015030	–0.016659	–0.014800	–0.015017	–0.016644
λ_6	–0.000519 + *j*0.024000	–0.000474 + *j*0.023128	–0.000529 + *j*0.022983	–0.000615 + *j*0.024002	–0.000567 + *j*0.023129	–0.000622 + *j*0.022984
λ_7	–0.000519 + –*j*0.024000	–0.000474 + –*j*0.023128	–0.000529 + –*j*0.022983	–0.000615 + –*j*0.024002	–0.000567 + –*j*0.023129	–0.000622 + –*j*0.022984
λ_8	–0.002728 + *j*0.035780	–0.002642 + *j*0.034636	–0.002459 + *j*0.034636	–0.002932 + *j*0.035794	–0.002848 + *j*0.034650	–0.002664 + *j*0.034648
λ_9	–0.002728 + –*j*0.035780	–0.002642 + –*j*0.034636	–0.002459 + –*j*0.034636	–0.002932 + –*j*0.035794	–0.002848 + –*j*0.034650	–0.002664 + –*j*0.034648

Table 5.3. Frequencies and damping ratios of the complex eigenvalues (three-machine, nine-bus system)

Complex Eigenvalue Pair	**Case 1** $D_i = 0$ *p.u.* Multi-order model	**Case 1** $D_i = 0$ *p.u.* Multi-order model with $X'_{qi} \cong X'_{di}$	**Case 1** $D_i = 0$ *p.u.* Literature [1]	**Case 2** $D_i = 1$ *p.u.* Multi-order model	**Case 2** $D_i = 1$ *p.u.* Multi-order model with $X'_{qi} \cong X'_{di}$	**Case 2** $D_i = 1$ *p.u.* Literature [1]
λ_1, λ_2	—	—	—	—	$f = 0.002$ *Hz* $\zeta = 0.993$	$f = 0.008$ *Hz* $\zeta = 0.839$
λ_6, λ_7	$f = 1.440$ *Hz* $\zeta = 0.022$	$f = 1.388$ *Hz* $\zeta = 0.020$	$f = 1.379$ *Hz* $\zeta = 0.023$	$f = 1.440$ *Hz* $\zeta = 0.026$	$f = 1.388$ *Hz* $\zeta = 0.024$	$f = 1.379$ *Hz* $\zeta = 0.027$
λ_8, λ_9	$f = 2.147$ *Hz* $\zeta = 0.076$	$f = 2.078$ *Hz* $\zeta = 0.076$	$f = 2.078$ *Hz* $\zeta = 0.071$	$f = 2.148$ *Hz* $\zeta = 0.082$	$f = 2.079$ *Hz* $\zeta = 0.082$	$f = 2.079$ *Hz* $\zeta = 0.077$

From Table 5.2, it is noticed that the system is stable in all cases. It can be concluded that the mathematical model here presented renders reliable results for the case when the "*complete*" model (multi-order with no transient saliency) is used. It should be noted that if transient saliency is assumed, as it was the case in [1], the eigenvalues match is even closer – in particular, it is observed in Table 5.3 that the frequencies of oscillation of the complex pairs are nearly the same. It should be emphasised that the mathematical model presented in this chapter is not exactly the same model as the one used in [1], even though they are equivalent. A major difference is that in this work the machine *q*-axis is assumed to lead the *d*-axis by 90 *deg*, whereas in reference [1] the *d*-axis is taken to lead the *q*-axis by 90 *deg*. Moreover, the procedure for obtaining the initial operating conditions is again different. In particular, the rotor angle (2.22) (the angle by which the *q*-axis leads the stator terminal voltage phasor $\vec{e}_t$) is calculated in a different but equivalent fashion.

Remark: Case 1, where $D_i = 0$ *p.u.*, is a special case of uniform damping ($D_i / \tau_{ji} = 0$). In this situation, a zero eigenvalue (λ_1) is present, which can be interpreted as a system order reduction [1]. Nevertheless, the frequencies corresponding to the electromechanical oscillations, given by eigenvalues 6–9, are almost unchanged regardless of the value of D_i.

The results presented in this section were obtained with a computer program written in MATLAB. The software executes sequentially all the steps involved in the study. The user introduces the parameters of the machines and the transmission network. The program starts by running a power flow, converts parameters to the system base, calculates initial conditions, forms the reduced nodal admittance matrix, calculates all constants associated to the differential and algebraic equations, forms the state-space representation, obtains the equivalent transfer function matrix representation (which will be described later on) and presents the results on the Command Window screen. Moreover, the state-space and transfer function matrix multi-machine, multi-order models are presented with a high degree of flexibility; the

user chooses the desired order model for each machine in the system, where seven possible options are available. A more complex system, with an even higher order machine representation, is presented below, where results are compared to those obtained against industrial-grade power system simulation tools [17].

5.5.2. Four-machine eleven-bus system

The two-area system shown in Figure 5.6 consists of four generators and two loads [2,15,16]. It may be seen to be made up of two similar areas connected by a weak tie link. Each area comprises two coupled generating units, each having a rating of 900 *MVA* and 20 *kV*. The data for the synchronous machines is given in Appendix B. It should be mentioned that a damping coefficient $D = 0$ *p.u.* is used for all machines.

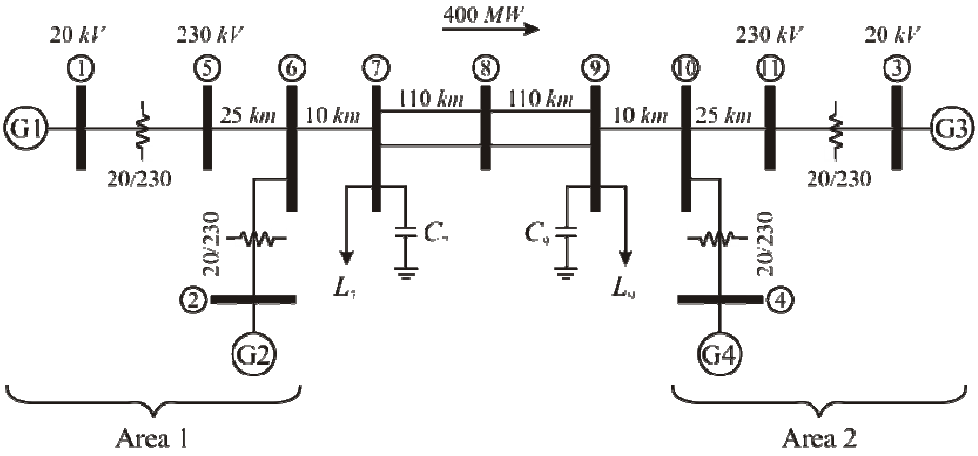

Figure 5.6. Four-machine system impedance diagram

Each step-up transformer has an impedance of $0 + j0.15$ *p.u.* on a 900 *MVA* and 20/230 *kV* base. The transmission system nominal voltage is 230 *kV*. The line lengths are shown in Figure 5.6. The parameters of the lines on a 100 *MVA* and 230 *kV* base are:

$$R = 0.0001 \ p.u./km \qquad X_L = 0.0001 \ p.u./km \qquad B_C = 0.00175 \ p.u./km$$

The power flow results in *MW* and *MVAr* are shown in Figure 5.7. The system is operating with area 1 exporting 400 MW to area 2, as it can be seen from the active flows leaving bus 7 towards bus 8.

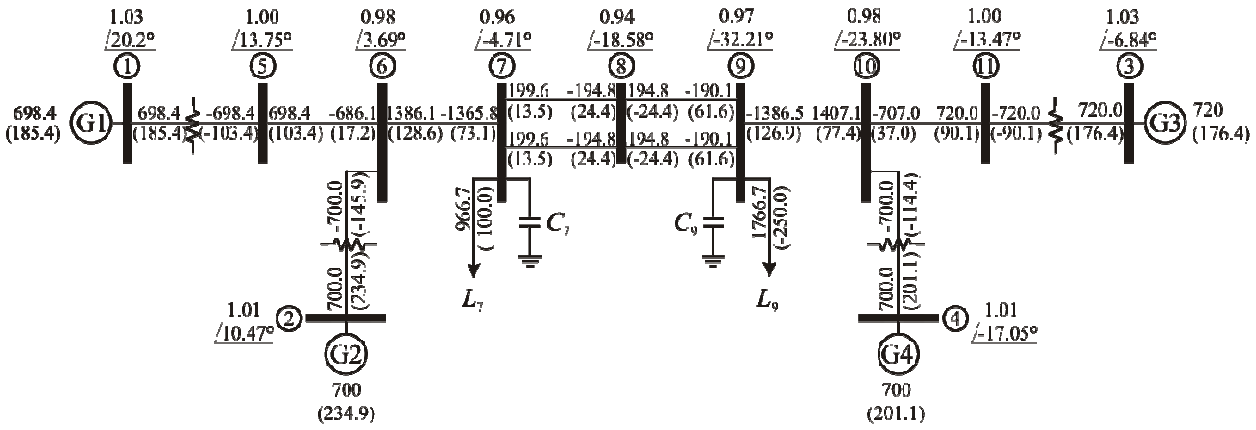

Figure 5.7. Four-machine power flow diagram

In order to match the loading given to the generators in [2,15,16], a modified transmission line susceptance value of $B_C = 0.001\ p.u./km$ is used. The loads and reactive power Q_C supplied by the shunt capacitors at buses 7 and 9 are given as

Bus 7: $P_L = 967\ MW$ $Q_L = 100\ MVAr$ $Q_C = 200\ MVAr$

Bus 9: $P_L = 1,767\ MW$ $Q_L = 100\ MVAr$ $Q_C = 350\ MVAr$

The initial operating condition of the system is provided in Table 5.4 and is obtained by using equations (2.19)–(2.32) and considering a system base of 100 *MVA*. Full parameters are available for all four synchronous generators; thus, each machine can be represented by using any of the previously presented models ranging from a 6th order to a 2nd order model.

Table 5.4. Initial operating condition for the four-machine, eleven-bus system

Variable	Machine 1	Machine 2	Machine 3	Machine 4
P_G	6.9841 *p.u.*	7 *p.u.*	7.2 *p.u.*	7 *p.u.*
Q_G	1.8538 *p.u.*	2.3495 *p.u.*	1.7641 *p.u.*	2.0107 *p.u.*
PF	0.96653	0.94803	0.97127	0.96114
δ_0	51.346 *deg*	46.127 *deg*	41.608 *deg*	36.999 *deg*
$\lvert e_{t0} \rvert$	1.03 *p.u.*	1.01 *p.u.*	1.03 *p.u.*	1.01 *p.u.*
$\angle e_{t0}$	20.2 *deg*	10.472 *deg*	–6.8381 *deg*	–17.053 *deg*
e_{tq0}	0.64336 *p.u.*	0.7 *p.u.*	0.77013 *p.u.*	0.80664 *p.u.*
e_{td0}	0.80436 *p.u.*	0.72808 *p.u.*	0.68396 *p.u.*	0.60781 *p.u.*
$\lvert i_{t0} \rvert$	7.0154 *p.u.*	7.3107 *p.u.*	7.1971 *p.u.*	7.2109 *p.u.*
i_{tq0}	2.8298 *p.u.*	3.1265 *p.u.*	4.0893 *p.u.*	4.3372 *p.u.*
i_{td0}	6.4194 *p.u.*	6.6084 *p.u.*	5.9224 *p.u.*	5.7608 *p.u.*
$\lvert E_0^{''} \rvert$	1.0981 *p.u.*	1.0935 *p.u.*	1.0968 *p.u.*	1.0844 *p.u.*
$E_{q0}^{''}$	0.82246 *p.u.*	0.88443 *p.u.*	0.93578 *p.u.*	0.96786 *p.u.*
$E_{d0}^{''}$	0.72753 *p.u.*	0.64307 *p.u.*	0.57201 *p.u.*	0.48894 *p.u.*
$\lvert E_0^{'} \rvert$	1.0665 *p.u.*	1.0672 *p.u.*	1.0622 *p.u.*	1.0575 *p.u.*
$E_{q0}^{'}$	0.85813 *p.u.*	0.92114 *p.u.*	0.96868 *p.u.*	0.99987 *p.u.*
$E_{d0}^{'}$	0.63321 *p.u.*	0.53885 *p.u.*	0.4357 *p.u.*	0.34436 *p.u.*
E_{fd0}	1.9272 *p.u.*	2.0217 *p.u.*	1.9546 *p.u.*	1.9588 *p.u.*

In order to convert loads into equivalent admittances, the nodal voltages from the power flow study are used in (2.41) and (2.42), giving

$$\bar{Y}_{L7} = 10.4668 + j1.08277 \; p.u.$$
$$\bar{Y}_{L9} = 18.7042 + j2.64681 \; p.u.$$

The network admittance matrix $\bar{\mathbf{Y}}$ is:

$$\bar{\mathbf{Y}} = \begin{bmatrix}
14.1 - j22.5 & 0 & 0 & 0 & -14.1 + j22.5 & 0 & 0 & 0 & 0 & 0 \\
0 & 14.1 - j22.5 & 0 & 0 & 0 & -14.1 + j22.5 & 0 & 0 & 0 & 0 \\
0 & 0 & 14.1 - j22.5 & 0 & 0 & 0 & 0 & 0 & 0 & -14.1 + j22.5 \\
0 & 0 & 0 & 14.1 - j22.5 & 0 & 0 & 0 & 0 & -14.1 + j22.5 & 0 \\
-14.1 + j22.5 & 0 & 0 & 0 & 4.10 - j62.1 & -3.96 + j39.6 & 0 & 0 & 0 & 0 \\
0 & -14.1 + j22.5 & 0 & 0 & -3.96 + j39.6 & 14 - j161.1 & -9.9 + j99.01 & 0 & 0 & 0 \\
0 & 0 & 0 & 0 & 0 & -9.9 + j99.01 & 22.17 - j115.8 & -1.8 + j18 & 0 & 0 \\
0 & 0 & 0 & 0 & 0 & 0 & -1.8 + j18 & 3.6 - j35.8 & -1.8 + j18 & 0 \\
0 & 0 & 0 & 0 & 0 & 0 & 0 & -1.8 + j18 & 30.41 - j114.25 & -9.9 + j99.01 \\
0 & 0 & 0 & -14.1 + j22.5 & 0 & 0 & 0 & 0 & -9.9 + j99.01 & 14 - j161.1 \\
0 & 0 & -14.1 + j22.5 & 0 & 0 & 0 & 0 & 0 & 0 & -3.96 + j39.6 \\
\end{bmatrix}$$

$$\begin{bmatrix}
-3.96 + j39.6 & 4.1 - j62.1
\end{bmatrix} \quad (5.203)$$

Kron's reduction of (5.132) is achieved by means of (2.43)–(2.47), yielding

$$\bar{\mathbf{Y}}_n = \begin{bmatrix}
1.3825 - j9.8279 & 1.5009 + j7.0630 & 0.4830 + j0.5486 & 0.7836 + j0.8318 \\
1.5009 + j7.0630 & 2.8581 - j11.5422 & 0.7836 + j0.8318 & 1.2682 + j1.2584 \\
0.4830 + j0.5486 & 0.7836 + j0.8318 & 1.9253 - j10.2264 & 2.3281 + j6.4117 \\
0.7836 + j0.8318 & 1.2682 + j1.2584 & 2.3281 + j6.4117 & 4.1163 - j12.6034
\end{bmatrix} \quad (5.204)$$

Having calculated all the preliminary data, it proceeds to construct the state-space model for the four-machine system. For instance, if all generators are represented by 6th order models, their algebraic and differential equations are given by (5.54)–(5.61) and matrices **A**, **B**, **C** and **D** are arrived at (not shown). Notice that the system is of 23rd order. It is needless to say that multi-machine models with generators represented by lower order models can be obtained quite straightforwardly. For the cases where a multi-order model is desired, the construction has to be carried out as in the example of the three-machine system presented in previous section. Table 5.5 gives the eigenvalues of system matrix **A** for this system. The frequencies of oscillation and damping ratios of the complex eigenvalues are provided in Table 5.6. The order of the eigenvalues is arbitrary.

From Table 5.5, it can be observed that $\lambda_1 = 0$ for all multi-machine models. As in the three-machine model, these are cases of uniform damping ($D_i = 0$) and the zero eigenvalue is interpreted as a system order reduction [1]. Whenever detailed high-order Models 0 and 1 are used for every machine, the system is unstable, as evidenced by the positive values of λ_8. An important conclusion arises from this observation: the mathematical models which do not feature a damping winding representation in both *d*- and *q*-axis for every machine, render stable systems, *i.e.*, all eigenvalues are negative. For instance, even though Models 2A and 2C are two-axis models, they do not possess a damping winding in the *d*-axis. An examination of the eigenvalues for these models suggests stable systems. For this test system, the use of lower order representations for all machines (4th to 2nd order) renders stable systems.

Table 5.5. Eigenvalues of the four-machine eleven-bus system

Eigen-value	Equal machine representations							Multi-order models		
	Model 0	Model 1	Model 2A	Model 2B	Model 2C	Model 3	Classic	Models 0,1,2C,3	Models 1,1,0,1	Models 2C,2C,2C,0
λ_1	0	0	0	0	0	0	0	0	0	0
λ_2	–0.137 + *j*3.583	–0.14 + *j*3.633	–0.124 + *j*3.80	–0.058 + *j*4.958	–0.095 + *j*3.75	–0.053 + *j*4.9	*j*3.782	–0.094 + *j*3.935	–0.139 + *j*3.616	–0.103 + *j*3.692
λ_3	–0.137 + –*j*3.583	–0.14 + –*j*3.633	–0.124 + –*j*3.80	–0.058 + –*j*4.958	–0.095 + –*j*3.75	–0.053 + –*j*4.9	–*j*3.782	–0.094 + –*j*3.935	–0.139 + –*j*3.616	–0.103 + –*j*3.692
λ_4	–0.265 + *j*7.218	–0.268 + *j*6.788	–0.234 + *j*7.093	–0.050 ± *j*10.134	–0.632 + *j*7.361	–0.034 + *j*9.784	*j*7.788	–0.606 + *j*8.517	–0.267 + *j*6.788	–0.626 + *j*7.351
λ_5	–0.265 + –*j*7.218	–0.268 + –*j*6.788	–0.234 + –*j*7.093	–0.050 ± –*j*10.134	–0.632 + –*j*7.361	–0.034 + –*j*9.784	–*j*7.788	–0.606 + –*j*8.517	–0.267 + –*j*6.788	–0.626 + –*j*7.351
λ_6	–0.29 + *j*6.902	–0.296 + *j*6.272	–0.269 + *j*6.537	–0.029 + *j*9.589	–0.817 + *j*7.027	–0.021 + *j*9.276	*j*7.716	–0.268 + *j*6.941	–0.292 + *j*6.482	–0.482 + *j*6.989
λ_7	–0.29 + –*j*6.902	–0.296 + –*j*6.272	–0.269 + –*j*6.537	–0.029 + –*j*9.589	–0.817 + –*j*7.027	–0.021 + –*j*9.276	–*j*7.716	–0.268 + –*j*6.941	–0.292 + –*j*6.482	–0.482 + –*j*6.989
λ_8	0.0016	0.005	–0.002	–0.405	–0.021	–0.153		–0.038	0.005	–0.012
λ_9	–0.207 + *j*0.004	–0.171	–0.177	–0.165 + *j*0.010	–0.205	–0.173		–0.203	–0.180	–0.225 + *j*0.025
λ_{10}	–0.207 + –*j*0.004	–0.180	–0.186	–0.165 + –*j*0.010	–0.207	–0.395		–0.234	–0.193	–0.225 + –*j*0.025
λ_{11}	–0.216	–0.262	–0.268	–0.425	–0.258	–0.419		–0.242	–0.244	–0.204
λ_{12}	–2.5	–35.733	–27.943	–33.797	–3.276			–2.5	–2.5	–2.5
λ_{13}	–2.5	–36.511	–39.314	–34.429	–4.405			–4.527	–24.261	–3.53
λ_{14}	–2.5	–31.08 + *j*3.391	–76.864	–36.614	–6.329			–23.587	–32.66 + *j*2.685	–4.918
λ_{15}	–2.5	–31.08 + –*j*3.391	–77.837	–36.664	–6.665			–33.968	–32.66 + –*j*2.685	–6.675
λ_{16}	–21.997	–37.14 + *j*0.631						–36.584	–34.4	–28.704
λ_{17}	–24.145	–37.14 + –*j*0.631						–59.983	–36.516	–35.285
λ_{18}	–31.719	–76.841							–36.636	
λ_{19}	–31.872	–77.827							–62.879	
λ_{20}	–33.260								–77.199	
λ_{21}	–34.289									
λ_{22}	–36.523									
λ_{23}	–36.590									

Table 5.6. Frequencies and damping ratios of the complex eigenvalues (four-machine eleven-bus system)

Complex Eigen-value	**Equal machine representations**							**Multi-order models**		
	Model 0	Model 1	Model 2A	Model 2B	Model 2C	Model 3	Classic	Models 0,1,2C,3	Models 1,1,0,1	Models 2C,2C,2C,0
λ_2, λ_3	f = 0.57 *Hz* ζ = 0.038	f = 0.58 *Hz* ζ = 0.039	f = 0.6 *Hz* ζ = 0.033	f = 0.79 *Hz* ζ = 0.012	f = 0.6 *Hz* ζ = 0.025	f = 0.78 *Hz* ζ = 0.011	f = 0.60 *Hz*	f = 0.63 *Hz* ζ = 0.024	f = 0.58 *Hz* ζ = 0.038	f = 0.59 *Hz* ζ = 0.028
λ_4, λ_5	f = 1.15 *Hz* ζ = 0.037	f = 1.08 *Hz* ζ = 0.039	f = 1.13 *Hz* ζ = 0.033	f = 1.61 *Hz* ζ = 0.005	f = 1.17 *Hz* ζ = 0.086	f = 1.56 *Hz* ζ = 0.003	f = 1.24 *Hz*	f = 1.36 *Hz* ζ = 0.071	f = 1.08 *Hz* ζ = 0.039	f = 1.17 *Hz* ζ = 0.085
λ_6, λ_7	f = 1.1 *Hz* ζ = 0.042	f = 1.0 *Hz* ζ = 0.047	f = 1.04 *Hz* ζ = 0.041	f = 1.53 *Hz* ζ = 0.003	f = 1.12 *Hz* ζ = 0.116	f = 1.48 *Hz* ζ = 0.002	f = 1.23 *Hz*	f = 1.1 *Hz* ζ = 0.039	f = 1.03 *Hz* ζ = 0.045	f = 1.11 *Hz* ζ = 0.069
λ_9, λ_{10}	f = 0.007 *Hz* ζ = 1.0	—	—	f = 0.002 *Hz* ζ = 1.0	—	—		—	—	f = 0.004 *Hz* ζ = 0.994
λ_{14}, λ_{15}	—	f = 0.54 *Hz* ζ = 1.0	—	—	—			—	f = 0.43 *Hz* ζ = 1.0	—
λ_{16}, λ_{17}	—	f = 0.1 *Hz* ζ = 1.0						—	—	—

Notice that for the particular study case, three rotor angle modes of oscillation exist. They can be observed through an examination of eigenvalues λ_2 to λ_7 in Table 5.5, with their frequencies and damping ratios shown in Table 5.6. Borrowing from the discussion of reference [2], an inter-area mode of around f = 0.545 *Hz* exists, where generators 1 and 2 swing against generators 3 and 4. An area 1 local mode of around f = 1.087 *Hz* also exists, where generators 1 and 2 swing against each other. Moreover, an area 2 local mode of around f = 1.117 *Hz* causes that generator 3 swings against generator 4. In this study, the inter-area, the area 1 and the area 2 modes are associated to the complex eigenvalue pairs λ_2–λ_3, λ_6–λ_7 and λ_4–λ_5, respectively. It is noticed in Table 5.6 that these oscillatory modes are clearly present in the responses given by the various models here presented and are quite similar in the two-axis representations, *i.e.*, Models 0, 1, 2A and 2C. The use of multi-order representations preserves relevant information of the system if a combination of two-axis models is used.

Tables 5.7 shows a comparison of results for the two-area system using industrial-grade power system software [17]; the oscillation frequencies and damping ratios of the complex eigenvalues from Table 5.7 are provided in Table 5.8. The order of the eigenvalues is arbitrary. In this exercise, results available from the packages PSS/E, DIgSILENT, EUROSTAG and PST are employed. These are based on 6^{th} order representations for all generators. From Table 5.7 it can be observed that the software presented in this chapter and the package PST have a real unstable eigenvalue (λ_2), while PSS/E features an unstable complex pair (λ_1 and λ_2). The packages DIgSILENT and EUROSTAG produce stable eigenvalues. Zero eigenvalues are present in the developed software, in DIgSILENT and in EUROSTAG (given by λ_1), with a complex pair quite close to zero in [2] (λ_1 and λ_2). Reference [17] suggests that the presence of the zero eigenvalue may be due to the use of absolute deviations of rotor speed and angle as state variables in the formation of system matrices, which is similar to the explanation provided in [2].

The assumption that the generator torques are independent of speed deviation arises from the lack of modelling of speed governors and that $D_i = 0$ [2]; the latter being consistent with reference [1].

Table 5.7. Eigenvalues of the four-machine system. Comparison with industrial-grade software

	Software with 6th order models					
Eigenvalue	Developed software	PSS/E [17]	DIgSILENT [17]	EUROSTAG [17]	PST [17]	Literature [2]
λ_1	0	0.187 + *j*0.163	0	0	–0.019	–0.00076 + *j*0.0022
λ_2	0.0016	0.187 + –*j*0.163	–0.031	–0.026	0.027	–0.00076 + –*j*0.0022
λ_3	–0.207 + *j*0.0045	–0.149 + *j*0.067	–0.069	–0.0998 + *j*0.030	–0.075 + *j*0.020	–0.096
λ_4	–0.207 + –*j*0.0045	–0.149 + –*j*0.067	–0.219	–0.0998 + –*j*0.030	–0.075 + –*j*0.020	–0.117
λ_5	–0.137 + *j*3.583	–0.155 + *j*3.41	–0.140 + *j*3.41	–0.115 + *j*3.42	–0.123 + *j*3.42	–0.111 + *j*3.43
λ_6	–0.137 + –*j*3.583	–0.155 + –*j*3.41	–0.140 + –*j*3.41	–0.115 + –*j*3.42	–0.123 + –*j*3.42	–0.111 + –*j*3.43
λ_7	–0.216	–0.233	–0.226	–0.204	–0.214	–0.265
λ_8	–2.5	–0.572	–0.396	–0.218	–0.231	–0.276
λ_9	–0.29 + *j*6.902	–0.613 + *j*6.76	–0.626 + *j*6.67	–0.558 + *j*6.58	–0.581 + *j*6.79	–0.492 + *j*6.82
λ_{10}	–0.29 + –*j*6.902	–0.613 + –*j*6.76	–0.626 + –*j*6.67	–0.558 + –*j*6.58	–0.581 + –*j*6.79	–0.492 + –*j*6.82
λ_{11}	–0.265 + *j*7.218	–0.631 + *j*6.94	–0.636 + *j*6.90	–0.570 + *j*6.77	–0.589 + *j*6.98	–0.506 + *j*7.02
λ_{12}	–0.265 + –*j*7.218	–0.631 + –*j*6.94	–0.636 + –*j*6.90	–0.570 + –*j*6.77	–0.589 + –*j*6.98	–0.506 + –*j*7.02
λ_{13}	–2.5	–2.967	–3.523	–3.812	–2.362	–3.428
λ_{14}	–2.5	–3.860	–4.254	–4.706	–3.280	–4.139
λ_{15}	–2.5	–5.183	–5.546	–5.964	–4.656	–5.287
λ_{16}	–21.997	–5.190	–5.582	–5.992	–4.697	–5.303
λ_{17}	–24.145	–28.45	–25.66	–22.35	–28.89	–31.03
λ_{18}	–31.719	–29.94	–26.89	–24.22	–30.39	–32.45
λ_{19}	–31.872	–33.33	–32.99	–31.20	–33.41	–34.07
λ_{20}	–33.260	–34.70	–33.11	–31.37	–34.80	–35.53
λ_{21}	–34.289	–35.67	–34.35	–33.13	–36.03	–37.89 + *j*0.142
λ_{22}	–36.523	–35.85	–35.15	–34.61	–36.19	–37.89 + –*j*0.142
λ_{23}	–36.590	–37.08	–37.28	–37.01	–37.15	–38.01 + *j*0.038
λ_{24}		–37.17	–37.34	–37.10	–37.23	–38.01 + –*j*0.038

Table 5.8. Frequencies and damping ratios. Comparison with industrial-grade software

Complex Eigenvalue Pair	**Software with 6th order models**					
	Developed software	PSS/E [17]	DIgSILENT [17]	EUROSTAG [17]	PST [17]	Literature [2]
λ_1, λ_2	–	f = 0.026 *Hz* ζ = –0.754	–	–	–	f = 0.0003 *Hz* ζ = 0.331
λ_3, λ_4	f = 0.007 *Hz* ζ = 1.0	f = 0.011 *Hz* ζ = 0.912	–	f = 0.005 *Hz* ζ = 0.957	f = 0.003 *Hz* ζ = 0.965	–
λ_5, λ_6	f = 0.57 *Hz* ζ = 0.038	f = 0.543 *Hz* ζ = 0.045	f = 0.542 *Hz* ζ = 0.041	f = 0.544 *Hz* ζ = 0.034	f = 0.544 *Hz* ζ = 0.036	f = 0.545 *Hz* ζ = 0.032
λ_9, λ_{10}	f = 1.1 *Hz* ζ = 0.042	f = 1.075 *Hz* ζ = 0.090	f = 1.062 *Hz* ζ = 0.093	f = 1.047 *Hz* ζ = 0.085	f = 1.080 *Hz* ζ = 0.085	f = 1.087 *Hz* ζ = 0.072
$\lambda_{11}, \lambda_{12}$	f = 1.149 *Hz* ζ = 0.037	f = 1.105 *Hz* ζ = 0.090	f = 1.097 *Hz* ζ = 0.092	f = 1.077 *Hz* ζ = 0.084	f = 1.111 *Hz* ζ = 0.084	f = 1.117 *Hz* ζ = 0.072
$\lambda_{21}, \lambda_{22}$	–	–	–	–	–	f = 0.023 *Hz* ζ = 1.0
$\lambda_{23}, \lambda_{24}$	–	–	–	–	–	f = 0.006 *Hz* ζ = 1.0

From Table 5.8, it is noticed that the oscillatory pairs (inter-area, area 1 local and area 2 local modes, represented by the complex eigenvalue pairs λ_5–λ_6, λ_9–λ_{10} and λ_{11}–λ_{12}, respectively) obtained with the developed software agree on well with those obtained using the various commercial tools and the results reported in [2]. Although the frequencies are nearly the same, the main difference appears in the damping ratio of the local modes, with the developed software offering less damping than any of the packages. The differences are attributable to modelling variations and the solution methodology used by the commercial tools [17]. For instance, the linearised model presented in this chapter does not take into account the effects of generator magnetic saturation. In spite of such differences, it can be concluded that these results are close enough for the purpose of small signal-stability assessments.

5.6. Transfer function matrix representation

The transfer function matrix representation a multi-machine power system is not only necessary but essential for analysis under ICAD. Consider the state-space representation of an arbitrary multi-machine system, given by

$$\begin{aligned} \dot{\Delta\mathbf{x}} &= \mathbf{A}\Delta\mathbf{x} + \mathbf{B}\Delta\mathbf{u} \\ \Delta\mathbf{y} &= \mathbf{C}\Delta\mathbf{x} + \mathbf{D}\Delta\mathbf{u} \end{aligned} \tag{5.99}$$

The Laplace transform of the linearised multi-machine system is given by

$$s\Delta\mathbf{x}(s) - \Delta\mathbf{x}(0) = \mathbf{A}\Delta\mathbf{x}(s) + \mathbf{B}\Delta\mathbf{u}(s) \tag{3.19}$$

$$\Delta\mathbf{y}(s) = \mathbf{C}\Delta\mathbf{x}(s) + \mathbf{D}\Delta\mathbf{u}(s) \tag{3.20}$$

Solving for $\Delta\mathbf{x}(s)$ in the state equation (3.19) and substituting into the output equation (3.20) yields

$$\Delta\mathbf{y}(s) = \mathbf{C}(s\mathbf{I} - \mathbf{A})^{-1}\Delta\mathbf{x}(0) + \left[\mathbf{C}(s\mathbf{I} - \mathbf{A})^{-1}\mathbf{B} + \mathbf{D}\right]\Delta\mathbf{u}(s) \tag{3.22}$$

If $\Delta\mathbf{x}(0) = 0$,

$$\Delta\mathbf{y}(s) = \mathbf{G}(s)\Delta\mathbf{u}(s) \tag{3.23}$$

where

$$\mathbf{G}(s) = \mathbf{C}(s\mathbf{I} - \mathbf{A})^{-1}\mathbf{B} + \mathbf{D} \tag{3.24}$$

is the desired transfer function matrix of the system. In general, for a multi-machine system consisting of n machines, the input and output vectors $\Delta\mathbf{u}(s)$ and $\Delta\mathbf{y}(s)$ are given by

$$\Delta\mathbf{u} = \begin{bmatrix} \Delta\mathbf{u}_1 & \Delta\mathbf{u}_2 & \cdots & \Delta\mathbf{u}_i & \cdots & \Delta\mathbf{u}_{(n-1)} & \Delta\mathbf{u}_n \end{bmatrix}^T \tag{5.101}$$

$$\Delta\mathbf{y} = \begin{bmatrix} \Delta\mathbf{y}_1 & \Delta\mathbf{y}_2 & \cdots & \Delta\mathbf{y}_i & \cdots & \Delta\mathbf{y}_{(n-1)} & \Delta\mathbf{y}_n \end{bmatrix}^T \tag{5.102}$$

where, for a particular case of i,

$$\Delta\mathbf{u}_i = \begin{bmatrix} \Delta P_{mi} & \Delta E_{fdi} \end{bmatrix} \tag{5.104}$$

$$\Delta\mathbf{y}_i = \begin{bmatrix} \Delta\omega_i & \Delta e_{ti} \end{bmatrix} \tag{5.105}$$

where (i = 1,2,…,n). Apart from the Classical Model, all representations render multi-machine models with 2n inputs and 2n outputs. Therefore, $\mathbf{G}(s)$ has a dimension of ($2n \times 2n$). When considering machines represented by the Classical Model, the number of inputs will be ($2n - m$), where m is the number of machines represented by the contrived Classical Model. In those cases, $\mathbf{G}(s)$ will have a dimension of (($2n - m$) × 2n).

Recalling from Chapter 3, transfer function matrix (3.24) can be rewritten as

$$\mathbf{G}(s) = \frac{1}{\det(s\mathbf{I} - \mathbf{A})}\mathbf{C}\mathrm{Adj}(s\mathbf{I} - \mathbf{A})\mathbf{B} + \mathbf{D} \tag{3.28}$$

The calculation of (3.28) is not straightforward and the problem complexity grows very considerably with the size of the multi-machine system. While considerable efforts have been made to develop efficient algorithms to calculate eigenvalues and eigenvectors for large systems [2–8], the determination of the zeros of the transfer function matrix in power systems applications has not received the same attention. For lower order systems, the use of Leverrier-Faddeev algorithm provides a simple to understand and implement tool for the determination of the transfer function matrix $\mathbf{G}(s)$; however, due to its recursive nature, it is susceptible to the accumulation of round-off errors [18]. It requires a massive number of multiplications and additions [19], a fact that impacts negatively when dealing with large multi-machine systems. In reference [20], an algorithm is provided for the calculation of the transfer function zeros of

linearised models for large interconnected power systems, reformulating the AESOPS (Analysis of Essentially Spontaneous Oscillations in Power System) algorithm given in [3] as a zero finding problem. It should be mentioned that the implementation of a suitable algorithm for the calculation of the transfer function matrix of large power systems is beyond the scope of this thesis. Therefore, the transfer function matrix is obtained using available subroutines found in the MATLAB Control Toolbox.

For control system design purposes, the calculation of the transfer function matrix offers an additional advantage to purely eigenvalue-based solutions, which provide only the poles of the systems; as the knowledge of unstable zeros allows for a more effective control system design. It is well known that the right hand plane zeros (RHPZs) have adverse effects in the control system performance and sensitivity [21,22]. Within the ICAD framework, the potential restrictions in performance due to non-minimum phase behaviour can be established from the RHPZs or purely imaginary zeros of $(1 - \Gamma_i(s))$. Notice that the RHPZs of $(1 - \Gamma_i(s))$ are the transmission zeros in the multivariable right hand plane.

An additional aspect to be addressed is that the individual elements $g_{ik}(s)$ of the transfer function matrix $\mathbf{G}(s)$ (3.28) will be of high-order in systems featuring a large number of machines. This fact should be taken into consideration since it complicates the analysis. However, not all the eigenvalues/poles will be dominant in the system and therefore some simplifications should be possible. For instance, an order reduction may be performed so that the frequency response of an arbitrary element $g_{ik}(s)$ preserves an adequate behaviour around the significant frequency range of 0.1–10 *Hz* when compared to the original transfer function. To achieve such a reduction, it is useful to obtain a scaled system realization to enhance numerical stability [23]. Then, uncontrollable or unobservable state dynamics (or stable zero/pole pairs) could be cancelled out. The last step is to eliminate states with a weak effect on the input/output map of the system. This can be done through balanced realizations, obtained by means of similarity transformations. Small Hankel singular values associated to the balanced representation are associated to states that can be discarded since they have a negligible contribution to the input-output response [24].

5.7. Conclusions

In this chapter a general multi-machine mathematical model was obtained. The modelling process was carried out for systems featuring machines with higher order representations (6^{th} order), from which lower order models can be obtained after applying suitable simplifying assumptions. A guideline for obtaining multi-machine, multi-order models was shown; that is, those in which machines are represented by arbitrary models of different complexity. The construction of a three-machine system model was carried out in order to show in full detail how a state-space representation is arrived at and to evaluate the model itself. The results are in close agreement with those found in the open literature. A high-order, four-

machine system available in the open literature was also studied. Results are adequate as they considerably match those obtained through commercial industrial-grade software. The use of the higher order representations is highly recommended in order to avoid misleading information associated to the lack of a *d*-axis damping winding in the lower order models.

The transfer function matrix representation of the multi-machine system, suitable for ICAD small-signal stability assessments, has been established, as it will be made apparent in the next chapter. It should be emphasised that all results presented in this chapter were obtained through generic software programmed in MATLAB. It can be concluded that the developed mathematical models and software are suitable for multi-order, multi-machine power system studies.

5.8. References

[1] Anderson PM, Fouad AA. *Power System Control and Stability*. IEEE Press, USA; 1994.

[2] Kundur P. *Power System Stability and Control*. USA: McGraw-Hill; 1994.

[3] Kundur P, Rogers GJ, Wong DY, Wang L, Lauby MG. *A Comprehensive Computer Program Package for Small Signal Stability Analysis of Power Systems.* IEEE Transactions on Power Systems, **5**, no. 4, pp. 1076–1083, 1990.

[4] Martins N. *Efficient Eigenvalue and Frequency Response Methods Applied to Power System Small-Signal Stability Studies*. IEEE Transactions on Power Systems, **1**, pp. 217–225, 1986.

[5] Wang L, Semlyen A. *Application of Sparse Eigenvalue Techniques to the Small Signal Stability Analysis of Large Power Systems.* IEEE Transactions on Power Systems, **6**, pp. 635–642, 1990.

[6] Uchida N, Nagao T. *A New Eigen-Analysis Method of Steady-State Stability Studies for Large Power Systems: S Matrix Method*. IEEE Transactions on Power Systems, **3**, pp. 706–714, 1988.

[7] Arnoldi WE. *The Principle of Minimized Iterations in the Solution of the Matrix Eigenvalue Problem.* Quarterly of Applied Mathematics, **9**, pp. 17–29, 1951.

[8] Saad Y. *Variations on Arnoldi's Method for Computing Eigenelements of Large Unsymmetric Matrices.* Linear Algebra and its Applications, **34**, pp. 184–198, 1981.

[9] Aree P. *Small Signal Stability Modelling and Analysis of Power Systems with Electronically Controlled Compensation*. PhD Thesis. Department of Electronics and Electrical Engineering, University of Glasgow, Scotland, UK, 2000.

[10] Wang HF, Swift FJ, Li M. *A Unified Model for the Analysis of FACTS Devices in Damping Power System Oscillation. Part II: Multi-Machine Power System*. IEEE Transactions on Power Delivery, **13**, no. 4, pp. 1355–1360, 1998.

[11] Wang HF. *Selection of Robust Installing Locations and Feedback Signals of FACTS-based Stabilizers in Multi-Machine Power System.* IEEE Transactions on Power Systems, **14**, no. 2, pp. 569–574, 1999.

[12] Wang HF, Swift FJ, Li M. *Selection of Installing Locations and Feedback Signals of FACTS-based Stabilisers in Multimachine Power Systems by Reduced-Order Modal Analysis*. IEE Proceedings on Generation, Transmission and Distribution, **144**, part C, no. 3, pp. 306–312, 1999.

[13] Aree P, Acha E. *Block diagram model for fundamental studies of a synchronous generator – static VAR compensator system*. IEE Proceedings on Generation, Transmission and Distribution, **146**, no. 5, pp. 507–514, 1999.

[14] ANSI/IEEE Standard 100-1997. IEEE Standard Dictionary of Electrical and Electronic Terms, 1997.

[15] Klein M, Rogers GJ, Kundur P. *A Fundamental Study of Inter-Area Oscillations*. IEEE Transactions on Power Systems, **6**, no. 3, pp. 914–921, 1991.

[16] Klein M, Rogers GJ, Moorty S, Kundur P. *Analytical Investigation of Factors Influencing Power System Stabilizers Performance*. 92WM016-6EC, IEEE PES Winter Meeting, 1992.

[17] Kaberere KK, Folly KA, Ntombela M, Petroianu AI. *Comparative Analysis and Numerical Validation of Industrial-Grade Power System Simulation Tools: Application to Small-Signal Stability*. Proceedings of the 15th Power Systems Computation Conference (PSCC), Liege, Belgium, 2005.

[18] Bingulac S, Van Landingham HF. *Algorithms for Computer-aided Design of Multivariable Systems*. CRC Press, USA; 1993.

[19] Perry RJ, Sun HH, Berger WA. *Determination of a Transfer Function Matrix in Multivariable Systems*. IEEE Transactions on Automatic Control, **33**, no. 3, pp. 305–307, 1988.

[20] Martins N, Pinto HJCP, Lima LTG. *Efficient Methods for Finding Transfer Function Zeros of Power Systems*. IEEE Transactions on Power Systems, **7**, no. 3, pp. 1350–1361, 1992.

[21] Freudenberg JS, Looze D. *Right half plane poles and zeros and design tradeoffs in feedback systems.* IEEE Transactions on Automatic Control, **30**, no. 6, pp. 555–565, 1985.

[22] Leithead WE, O'Reilly J. *Uncertain SISO systems with fixed stable minimum-phase controllers: relationship of closed-loop systems to plant RHP poles and zeros.* International Journal of Control, **53**, no. 4, pp. 771–798, 1991.

[23] Moore BC. *Principal Component Analysis in Linear Systems: Controllability, Observability, and Model Reduction*. IEEE Transactions on Automatic Control, **26**, no. 1, pp. 17–32, 1981.

[24] Laub AJ, Heath MT, Paige CC, Ward RC. *Computation of System Balancing Transformations and Other Applications of Simultaneous Diagonalization Algorithms.* IEEE Transactions on Automatic Control, **32**, no. 2, pp. 115–122, 1987.

Chapter 6

INDIVIDUAL CHANNEL ANALYSIS AND DESIGN OF MULTI-MACHINE SYSTEMS

6.1. Introduction

A general state-space multi-machine model and its equivalent transfer function matrix representation have been presented in Chapter 5. Their use in small-signal stability assessments was evaluated using conventional eigenvalue techniques in two multi-machine test systems available in the open literature [1,2]. In this chapter the individual channel analysis and design of a two-machine system is carried out, including fundamental analyses of the dynamic interactions existing between the two generators. Two different studies are presented: the first one assesses the effect of the transmission line length; the second study evaluates the effect of a changing system load. In these studies, special attention is paid to the multivariable structure functions. A control system design with robustness assessment is included.

The test system under study is a relatively simple and yet realistic transmission system consisting of only two synchronous generators. The study of complex power systems involving a larger number of machines is beyond the scope of the present research work. It may be argued that a network with a small number of elements is better placed for carrying out fundamental analysis than a network with a large number of elements where key effects could be meshed. However, it should be noticed that the previously introduced multi-machine model is general enough to study large power networks; therefore, the results presented throughout this chapter provide a reliable starting basis for the use the ICAD framework into more complex systems.

Recent research in multi-machine systems has been directed towards the examination of the AVR and the PSS performance using individual channels [3]. The dynamical models are generated using the commercial power system package PSS/E, with a good representation of the electrical dynamics but with no representation of the mechanical dynamics on grounds of bandwidth separation between the AVR and the turbine-governor. It is noticed that this may be a valid assumption in the application pursued in this paper where the thrust is to assess the dynamic interactions between the AVR and the PSS. The effect of the PSS is incorporated by taking the output speed deviation of one generator in the system at the time.

The analysis shows that both devices are dynamically inter-linked and that performance improvement in one device comes at the expense of a reduced performance in the other device.

The research reported in this chapter is more general, in the sense that it is not application specific and the electrical and mechanical channels are both fully represented within the ICAD context. Fundamental studies are carried for the case of high-order two-machine system, arising from the generic multi-machine model presented in Chapter 5. The emphasis is on the dynamical interactions between the electrical and mechanical channels of the two machines at various transmission line lengths and system loading. It should be noticed that the two-machine system may represent the most onerous scenario in terms of coupling that may exist in a multi-machine system, since coupling between the two machines may not be channelled to any other element in the system.

6.2. Multi-machine system under study

In order to out carry fundamental studies of the dynamic interactions between synchronous generators, the two-machine system shown in Figure 6.1 is used. It consists of two identical synchronous generators connected through a two-section transmission line, three nodes, and three loads. The parameters of the machines are given in Appendix B, corresponding to Generator 1, where a value of $D \neq 0$ is used. Depending on the study, the values of the tie-line impedances and the load at nodes will vary. The quantities given in the figure are all in *p.u.* on a 100 *MVA* base.

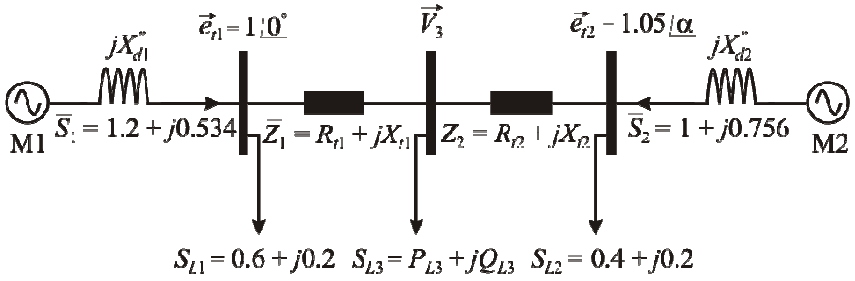

Figure 6.1. System under study (two-generator system)

6.2.1. Block diagram representation

The small-signal model that represents the two-machine system is derived from the generic multi-machine model presented in the previous chapter. In this case, a 5th order model (Model 1) is used for both synchronous generators. Therefore, equations (5.54)–(5.61) are employed to build up the two-machine system, bearing in mind that $n = 2$ and $i,k = 1,2$, with $i \neq k$. The block diagram representation can be obtained from Figure 5.3 (after suitable simplification to 5th order models of the synchronous generator), where, for Machine 1, $i = 1$ and $k = 2$. A similar structure is considered for the construction of the blocks representing Machine 2, *i.e.*, using $i = 2$ and $k = 1$.

The block diagram representation gives a detailed account of the many dynamic interactions that may exist in the generator two-machine system and yields a visual understanding as to how one machine impacts on the other machine and vice-versa. However, caution needs to be exercised because not all interactions between variables are required for control system design purposes. Moreover, the block diagram representation becomes increasingly complex, and therefore, the physical picture afforded by such a model in the case of the OMIB system becomes blurred. Also, it should be emphasised that it is not possible to assess the stability of a system through block diagram representations. The stability of a multivariable system is determined by the eigenvalues of its system matrix **A** (*i.e.*, the roots of the characteristic equation of **A**, $|s\mathbf{I} - \mathbf{A}| = 0$) or by all the poles of its transfer function matrix $\mathbf{G}(s)$ [4]. The individual transfer functions in block diagram representations do not appear in the transfer function matrix and their poles do not provide the complete set of eigenvalues of the system.

6.2.2. Transfer function matrix representation

The transfer function matrix representation of the two-machine system shown in Figure 6.1 is obtained directly from matrices **A**, **B**, **C, D**, as stated in section 5.6, but bearing in mind that both machines are represented by 5th order models. In general, the transfer function matrix representation of the two-machine system is given by

$$\begin{bmatrix} \Delta\omega_1(s) \\ \Delta e_{t1}(s) \\ \Delta\omega_2(s) \\ \Delta e_{t2}(s) \end{bmatrix} = \begin{bmatrix} g_{11}(s) & g_{12}(s) & g_{13}(s) & g_{14}(s) \\ g_{21}(s) & g_{22}(s) & g_{23}(s) & g_{24}(s) \\ g_{31}(s) & g_{32}(s) & g_{33}(s) & g_{34}(s) \\ g_{41}(s) & g_{42}(s) & g_{43}(s) & g_{44}(s) \end{bmatrix} \begin{bmatrix} \Delta P_{m1}(s) \\ \Delta E_{fd1}(s) \\ \Delta P_{m2}(s) \\ \Delta E_{fd2}(s) \end{bmatrix} \tag{6.1}$$

or in compact form

$$\mathbf{y}(s) = \mathbf{G}(s)\mathbf{u}(s) \tag{6.2}$$

where $\mathbf{G}(s)$ is the transfer function matrix of the 4×4 linearised model of the two-machine system. Subscripts 1 and 2 in the input and output vectors **u** and **y**, correspond to signals of Machine 1 and 2, respectively. The individual elements of $\mathbf{G}(s)$ are dependent on the system initial conditions, derived from a power flow solution. For control system analysis purposes and considering a diagonal controller, the closed-loop diagram of the system is shown in Figure 6.2.

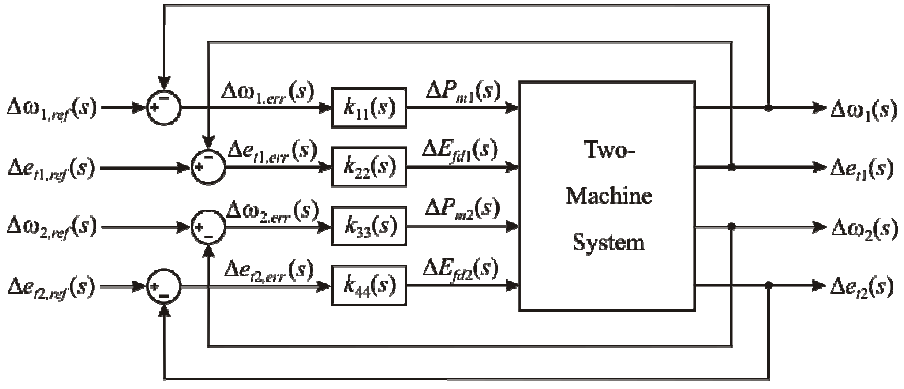

Figure 6.2. Block diagram for control system analysis

Table 6.1. System operating conditions. Study 1

	Parameter	Case 1	Case 2	Case 3	Case 4	Case 5	Case 6
Machine 1	P_{g1}	1.2 *p.u.*	1.2 *p.u.*	1.2 *p.u.*	1.228 *p.u.*	1.2 *p.u.*	1.211 *p.u.*
	Q_{g1}	0.699 *p.u.*	0.586 *p.u.*	0.534 *p.u.*	0.54 *p.u.*	0.3 *p.u.*	0.299 *p.u.*
	PF_1	0.864	0.899	0.914	0.915	0.97	0.971
	δ_{10}	34.56 °	36.38 °	37.277 °	37.81 °	41.818 °	42.061 °
	$\lvert e_{t10}\rvert$	1.0 *p.u.*	1.0 *p.u.*	1.0 *p.u.*	1.0 *p.u.*	1.0 *p.u.*	1.0 *p.u.*
	$\angle e_{t10}$	0 °	0 °	0 °	0 °	0 °	0 °
	$\lvert i_{t10}\rvert$	1.389 *p.u.*	1.336 *p.u.*	1.313 *p.u.*	1.342 *p.u.*	1.237 *p.u.*	1.247 *p.u.*
	i_{tq10}	0.592 *p.u.*	0.619 *p.u.*	0.632 *p.u.*	0.639 *p.u.*	0.695 *p.u.*	0.699 *p.u.*
	i_{td10}	1.257 *p.u.*	1.184 *p.u.*	1.152 *p.u.*	1.179 *p.u.*	1.023 *p.u.*	1.033 *p.u.*
	$\lvert E''_{10}\rvert$	1.15 *p.u.*	1.13 *p.u.*	1.121 *p.u.*	1.123 *p.u.*	1.081 *p.u.*	1.082 *p.u.*
	E''_{q10}	1.049 *p.u.*	1.017 *p.u.*	1.002 *p.u.*	1.001 *p.u.*	0.928 *p.u.*	0.927 *p.u.*
	E''_{d10}	0.471 *p.u.*	0.493 *p.u.*	0.503 *p.u.*	0.509 *p.u.*	0.554 *p.u.*	0.557 *p.u.*
	$\lvert E'_{10}\rvert$	1.221 *p.u.*	1.179 *p.u.*	1.16 *p.u.*	1.163 *p.u.*	1.068 *p.u.*	1.069 *p.u.*
	E'_{q10}	1.221 *p.u.*	1.179 *p.u.*	1.16 *p.u.*	1.163 *p.u.*	1.068 *p.u.*	1.069 *p.u.*
	E'_{d10}	0 *p.u.*	0 *p.u.*	0 *p.u.*	0 *p.u.*	0 *p.u.*	0 *p.u.*
	E_{fd10}	2.639 *p.u.*	2.515 *p.u.*	2.46 *p.u.*	2.494 *p.u.*	2.223 *p.u.*	2.225 *p.u.*
Machine 2	P_{g2}	1.0 *p.u.*	1.0 *p.u.*	1.0 *p.u.*	1.0 *p.u.*	1.0 *p.u.*	1.0 *p.u.*
	Q_{g2}	0.847 *p.u.*	0.774 *p.u.*	0.756 *p.u.*	0.76 *p.u.*	0.827 *p.u.*	0.828 *p.u.*
	PF_2	0.763	0.791	0.798	0.796	0.771	0.77
	δ_{20}	26.23 °	27.202 °	27.481 °	27.063 °	26.762 °	26.587 °
	$\lvert e_{t20}\rvert$	1.05 *p.u.*	1.05 *p.u.*	1.05 *p.u.*	1.05 *p.u.*	1.05 *p.u.*	1.05 *p.u.*
	$\angle e_{t20}$	–0.817 °	–0.555 °	–0.446 °	–1.208 °	–0.165 °	–0.519 °
	$\lvert i_{t20}\rvert$	1.248 *p.u.*	1.205 *p.u.*	1.194 *p.u.*	1.197 *p.u.*	1.236 *p.u.*	1.236 *p.u.*
	i_{tq20}	0.498 *p.u.*	0.51 *p.u.*	0.513 *p.u.*	0.519 *p.u.*	0.496 *p.u.*	0.499 *p.u.*
	i_{td20}	1.144 *p.u.*	1.091 *p.u.*	1.078 *p.u.*	1.078 *p.u.*	1.132 *p.u.*	1.131 *p.u.*
	$\lvert E''_{20}\rvert$	1.209 *p.u.*	1.197 *p.u.*	1.194 *p.u.*	1.195 *p.u.*	1.206 *p.u.*	1.206 *p.u.*
	E''_{q20}	1.147 *p.u.*	1.129 *p.u.*	1.125 *p.u.*	1.128 *p.u.*	1.14 *p.u.*	1.142 *p.u.*
	E''_{d20}	0.383 *p.u.*	0.397 *p.u.*	0.401 *p.u.*	0.394 *p.u.*	0.392 *p.u.*	0.389 *p.u.*
	$\lvert E'_{20}\rvert$	1.304 *p.u.*	1.279 *p.u.*	1.272 *p.u.*	1.276 *p.u.*	1.295 *p.u.*	1.297 *p.u.*
	E'_{q20}	1.3035 *p.u.*	1.279 *p.u.*	1.272 *p.u.*	1.276 *p.u.*	1.295 *p.u.*	1.297 *p.u.*
	E'_{d20}	–0.013 *p.u.*	–0.009 *p.u.*	–0.007 *p.u.*	–0.02 *p.u.*	–0.003 *p.u.*	–0.008 *p.u.*
	E_{fd20}	2.596 *p.u.*	2.511 *p.u.*	2.489 *p.u.*	2.493 *p.u.*	2.573 *p.u.*	2.574 *p.u.*
Network	P_{mid}	–1.2 *p.u.*	–1.2 *p.u.*	–1.2 *p.u.*	–1.2 *p.u.*	–1.2 *p.u.*	–1.2 *p.u.*
	Q_{mid}	–0.62 *p.u.*	–0.62 *p.u.*	–0.62 *p.u.*	–0.62 *p.u.*	–0.62 *p.u.*	–0.62 *p.u.*
	$\lvert V_{mid}\rvert$	0.835 *p.u.*	0.902 *p.u.*	0.929 *p.u.*	0.912 *p.u.*	0.992 *p.u.*	0.986 *p.u.*
	$\angle V_{mid}$	–16.694 °	–11.507 °	–9.294 °	–9.377 °	–3.468 °	–3.494 °
	R_{t1}, R_{t2}	0 *p.u.*	0 *p.u.*	0 *p.u.*	0.025 *p.u.*	0 *p.u.*	0.01 *p.u.*
	X_{t1}, X_{t2}	0.4 *p.u.*	0.3 *p.u.*	0.25 *p.u.*	0.25 *p.u.*	0.1 *p.u.*	0.1 *p.u.*

Table 6.2. System operating conditions. Study 2

	Parameter	Case A	Case B	Case C	Case D
Machine 1	P_{g1}	1.5 *p.u.*	1.2 *p.u.*	0.9 *p.u.*	0.6 *p.u.*
	Q_{g1}	0.74 *p.u.*	0.534 *p.u.*	0.384 *p.u.*	0.281 *p.u.*
	PF_1	0.897	0.914	0.92	0.906
	δ_{10}	40.075 °	37.277 °	32.236 °	24.389 °
	$\lvert e_{t10}\rvert$	1.0 *p.u.*	1.0 *p.u.*	1.0 *p.u.*	1.0 *p.u.*
	$\angle e_{t10}$	0 °	0 °	0 °	0 °
	$\lvert i_{t10}\rvert$	1.673 *p.u.*	1.313 *p.u.*	0.979 *p.u.*	0.662 *p.u.*
	i_{tq10}	0.671 *p.u.*	0.632 *p.u.*	0.556 *p.u.*	0.431 *p.u.*
	i_{td10}	1.532 *p.u.*	1.152 *p.u.*	0.805 *p.u.*	0.503 *p.u.*
	$\lvert E''_{10}\rvert$	1.169 *p.u.*	1.121 *p.u.*	1.085 *p.u.*	1.058 *p.u.*
	E''_{q10}	1.039 *p.u.*	1.002 *p.u.*	0.99 *p.u.*	1 *p.u.*
	E''_{d10}	0.535 *p.u.*	0.503 *p.u.*	0.443 *p.u.*	0.343 *p.u.*
	$\lvert E'_{10}\rvert$	1.249 *p.u.*	1.16 *p.u.*	1.1 *p.u.*	1.07 *p.u.*
	E'_{q10}	1.249 *p.u.*	1.16 *p.u.*	1.1 *p.u.*	1.07 *p.u.*
	E'_{d10}	0 *p.u.*	0 *p.u.*	0 *p.u.*	0 *p.u.*
	E_{fd10}	2.979 *p.u.*	2.46 *p.u.*	2.01 *p.u.*	1.638 *p.u.*
Machine 2	P_{g2}	1.0 *p.u.*	1.0 *p.u.*	1.0 *p.u.*	1.0 *p.u.*
	Q_{g2}	0.904 *p.u.*	0.756 *p.u.*	0.636 *p.u.*	0.539 *p.u.*
	PF_2	0.742	0.798	0.845	0.88
	δ_{20}	23.528 °	27.481 °	31.251 °	34.864 °
	$\lvert e_{t20}\rvert$	1.05 *p.u.*	1.05 *p.u.*	1.05 *p.u.*	1.05 *p.u.*
	$\angle e_{t20}$	–5.383 °	–0.446 °	4.091 °	8.383 °
	$\lvert i_{t20}\rvert$	1.284 *p.u.*	1.194 *p.u.*	1.129 *p.u.*	1.082 *p.u.*
	i_{tq20}	0.529 *p.u.*	0.513 *p.u.*	0.5 *p.u.*	0.488 *p.u.*
	i_{td20}	1.17 *p.u.*	1.078 *p.u.*	1.012 *p.u.*	0.965 *p.u.*
	$\lvert E''_{20}\rvert$	1.219 *p.u.*	1.194 *p.u.*	1.174 *p.u.*	1.158 *p.u.*
	E''_{q20}	1.172 *p.u.*	1.125 *p.u.*	1.079 *p.u.*	1.034 *p.u.*
	E''_{d20}	0.333 *p.u.*	0.401 *p.u.*	0.464 *p.u.*	0.521 *p.u.*
	$\lvert E'_{20}\rvert$	1.335 *p.u.*	1.272 *p.u.*	1.219 *p.u.*	1.174 *p.u.*
	E'_{q20}	1.332 *p.u.*	1.272 *p.u.*	1.218 *p.u.*	1.167 *p.u.*
	E'_{d20}	–0.089 *p.u.*	–0.007 *p.u.*	0.065 *p.u.*	0.132 *p.u.*
	E_{fd20}	2.653 *p.u.*	2.489 *p.u.*	2.36 *p.u.*	2.256 *p.u.*
Network	P_{mid}	–1.5 *p.u.*	–1.2 *p.u.*	–0.9 *p.u.*	–0.6 *p.u.*
	Q_{mid}	–0.775 *p.u.*	–0.62 *p.u.*	–0.465 *p.u.*	–0.31 *p.u.*
	$\lvert V_{mid}\rvert$	0.894 *p.u.*	0.929 *p.u.*	0.957 *p.u.*	0.98 *p.u.*
	$\angle V_{mid}$	–14.581 °	–9.294 °	–4.496 °	0 °
	R_{t1}, R_{t2}	0 *p.u.*	0 *p.u.*	0 *p.u.*	0 *p.u.*
	X_{t1}, X_{t2}	0.25 *p.u.*	0.25 *p.u.*	0.25 *p.u.*	0.25 *p.u.*

Two different study cases are carried out below. The first one assesses the influence that the length of the transmission line exerts on the dynamic characteristics of the two generators; the tie-line impedance is varied while keeping the loads constant. The second study evaluates the performance of the system under different loading conditions. The initial operating conditions for both studies are provided in Tables 6.1 and 6.2, respectively. A numerical inspection shows that all the transfer functions $g_{jj}(s)$ of $\mathbf{G}(s)$ (not shown) are stable for both study cases.

6.3. Multivariable analysis

In the framework afforded by ICAD, the dynamical structure of plant (6.1) is determined by input-output channels resulting from pairing each input to each output by means of diagonal controllers, in much the same way as it was done with OMIB systems in previous chapters. For the case of the two-machine system, the traditional pairing of inputs to outputs is given as

$$\mathbf{K}(s)=\begin{bmatrix} k_{11}(s) & 0 & 0 & 0 \\ 0 & k_{22}(s) & 0 & 0 \\ 0 & 0 & k_{33}(s) & 0 \\ 0 & 0 & 0 & k_{44}(s) \end{bmatrix} \Rightarrow \begin{cases} C_1(s):\Delta P_{m1}(s)\rightarrow \Delta\omega_1(s) \\ C_2(s):\Delta E_{fd1}(s)\rightarrow \Delta e_{t1}(s) \\ C_3(s):\Delta P_{m2}(s)\rightarrow \Delta\omega_2(s) \\ C_4(s):\Delta E_{fd2}(s)\rightarrow \Delta e_{t2}(s) \end{cases} \tag{6.3}$$

Notice that in (6.3) the Individual Channels $C_1(s)$ and $C_2(s)$ correspond to the pairing of inputs and outputs associated to Machine 1 whereas $C_3(s)$ and $C_4(s)$ are associated to Machine 2. Figure 6.3 shows the individual channel representation for the two-machine system.

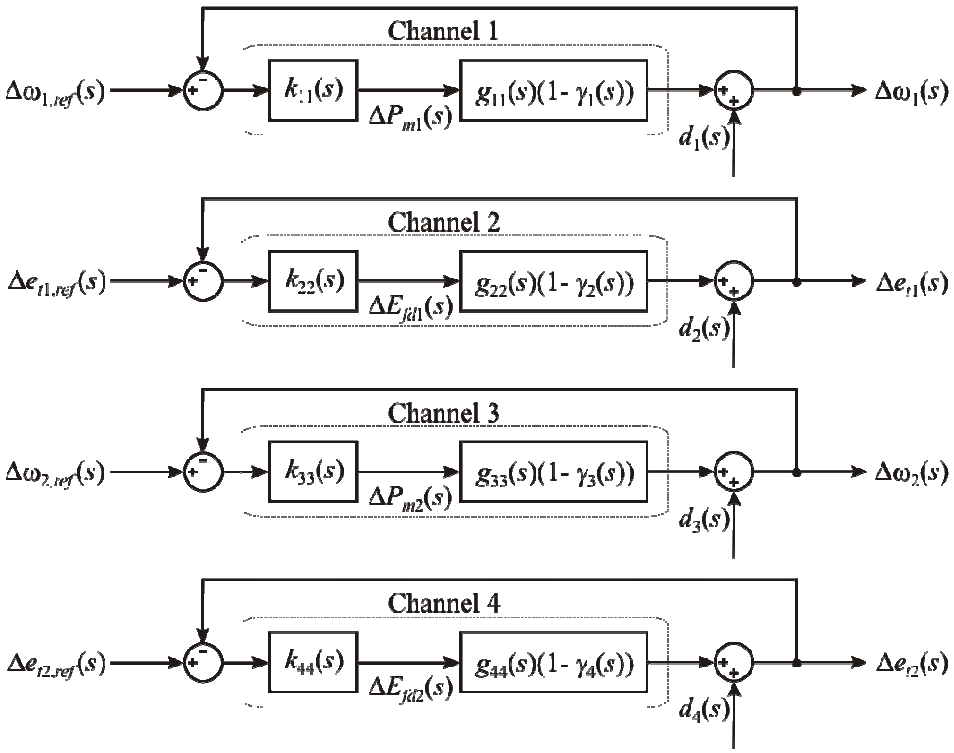

Figure 6.3. Two-machine system with conventional controllers represented in individual channels

From Figure 6.3, it can be appreciated that the multivariable system can be re-formulated as four SISO channels, where each channel comprises a feedback loop and its controller. Each controller can be designed to comply with the specifications associated to each individual channel. Notice that every channel is subject to a disturbance $d_i(s)$ – representing the effect of the other channel references. Thus, the behaviour of an individual channel will not be only affected by its controller but also by the other individual channels. It should be emphasised that the representation of Figure 6.3 is fully equivalent to the original two-machine system of Figure 6.2 and that no information is lost. The multivariable character of the plant is suitably contained and quantified -in the frequency domain- by the MSFs.

An assessment of coupling between channels, which is determined by means of the Multivariable Structure Functions (MSF) $\Gamma_i(s)$, is a pre-condition for an effective control system design. In this case, the system is 4×4 and the MSFs $\Gamma_i(s)$ are defined as [5,6]

$$\Gamma_i(s) = -\left|\mathbf{G}_i^{12\ldots(i-1)}\right| / g_{ii} \left|\mathbf{G}^{12\ldots(i-1)i}\right| \tag{A.58}$$

where $\Gamma_4 = 0$ and $i = 1,2,3$. Moreover,

$$\begin{aligned}\Gamma_1(s) &= -\left|\mathbf{G}_1\right| / g_{11}\left|\mathbf{G}^1\right| \\ &= -\begin{vmatrix} 0 & g_{12} & g_{13} & g_{14} \\ g_{21} & g_{22} & g_{23} & g_{24} \\ g_{31} & g_{32} & g_{33} & g_{34} \\ g_{41} & g_{42} & g_{43} & g_{44} \end{vmatrix} / g_{11} \begin{vmatrix} g_{22} & g_{23} & g_{24} \\ g_{32} & g_{33} & g_{34} \\ g_{42} & g_{43} & g_{44} \end{vmatrix} \\ &= \frac{-\left[-g_{12}\begin{vmatrix} g_{21} & g_{23} & g_{24} \\ g_{31} & g_{33} & g_{34} \\ g_{41} & g_{43} & g_{44} \end{vmatrix} + g_{13}\begin{vmatrix} g_{21} & g_{22} & g_{24} \\ g_{31} & g_{32} & g_{34} \\ g_{41} & g_{42} & g_{44} \end{vmatrix} - g_{14}\begin{vmatrix} g_{21} & g_{22} & g_{23} \\ g_{31} & g_{32} & g_{33} \\ g_{41} & g_{42} & g_{43} \end{vmatrix} \right]}{g_{11}\left[g_{22}\left(g_{33}g_{44} - g_{34}g_{43}\right) - g_{23}\left(g_{32}g_{44} - g_{34}g_{42}\right) + g_{24}\left(g_{32}g_{43} - g_{33}g_{42}\right)\right]}\end{aligned} \tag{6.4}$$

$$\begin{aligned}\Gamma_2(s) &= -\left|\mathbf{G}_2^1\right| / g_{22}\left|\mathbf{G}^{12}\right| \\ &= -\begin{vmatrix} 0 & g_{23} & g_{24} \\ g_{32} & g_{33} & g_{34} \\ g_{42} & g_{43} & g_{44} \end{vmatrix} / g_{22} \begin{vmatrix} g_{33} & g_{34} \\ g_{43} & g_{44} \end{vmatrix} \\ &= \frac{-\left[-g_{23}\left(g_{32}g_{44} - g_{34}g_{42}\right) + g_{24}\left(g_{32}g_{43} - g_{33}g_{42}\right)\right]}{g_{22}\left(g_{33}g_{44} - g_{34}g_{43}\right)}\end{aligned} \tag{6.5}$$

$$\begin{aligned}\Gamma_3(s) &= -\left|\mathbf{G}_3^{12}\right| / g_{33}\left|\mathbf{G}^{123}\right| \\ &= -\begin{vmatrix} 0 & g_{34} \\ g_{43} & g_{44} \end{vmatrix} / g_{33}\left|g_{44}\right| \\ &= \frac{g_{34}g_{43}}{g_{33}g_{44}}\end{aligned} \tag{6.6}$$

In the assessment of the MSFs $\Gamma_i(s)$ of the two-machine system, the transfer function matrix in (6.1) will be called $\mathbf{G}_{1234}$, where the subscripts indicate that the individual transfer functions associated to

the output of $C_1(s)$ occupy the first row, those to $C_2(s)$ the second row, and so on. When analysing $\mathbf{G}_{1234}$, $\Gamma_1(s)$ in (6.4) provides a measure of coupling between Individual Channel $C_1(s)$ and Multiple Channel $\mathbf{M}_{234}(s)$. Similarly, $\Gamma_2(s)$ in (6.5) quantifies coupling between Individual Channel $C_2(s)$ and Multiple Channel $\mathbf{M}_{34}(s)$. Lastly, $\Gamma_3(s)$ in (6.6) provides the coupling measure between Individual Channels $C_3(s)$ and $C_4(s)$. If the aim is to assess the coupling involving other channels, either individual or multiple, then expressions (6.4)–(6.6) are suitably modified, as discussed in Chapter 4. It should be noticed that some degree of information redundancy exists in the analysis and that a number of transfer function matrices should yield identical information, *e.g.*, $\mathbf{G}_{1234}$ and $\mathbf{G}_{1243}$. Hence, redundant cases are grouped together under the following notation: $\mathbf{G}_{xxik}$ and $\mathbf{G}_{xxki}$, where $\Gamma_3(s)$ provides the coupling between Individual Channels $C_i(s)$ and $C_k(s)$, for a given value of x ($x \neq i,k$; $i \neq k$); and $\mathbf{G}_{xxxi}$, where $\Gamma_1(s)$ provides the coupling measure between an Individual Channel $C_i(s)$ and any other Multiple Channel $\mathbf{M}_{xxx}(s)$ (with $x \neq i$).

6.3.1. Study 1. Impact of the transmission line length

In this study the impact that the length of the transmission line has in the two-machine system of Figure 6.1, is evaluated. The system operating conditions for both machines are provided in Table 6.1, where the transmission system ranges from a weak (X_t = 0.8 *p.u.*) to a strong system (X_t = 0.2 *p.u.*). The effect of increasing the resistance of the tie-line impedance is also considered. The loads connected to the machine terminals are given in Figure 6.1 and kept constant in all studies. The load at the mid-point of the transmission line is given a value of 1.2 + *j*1.62 *p.u.*

Figures 6.4–6.9 show the Nyquist and Bode diagrams of the various $\Gamma_3(s)$ of the two-machine system. Coupling between an individual channel and a multiple channel, formed by any two individual channels, can be evaluated by assessing MSFs $\Gamma_2(s)$, whose Bode and Nyquist diagrams are provided in Figures 6.10–6.21. Figures 6.22–6.25 show the Nyquist and Bode diagrams of $\Gamma_1(s)$, which provide the coupling between an individual channel and a multiple channel formed by three individual channels.

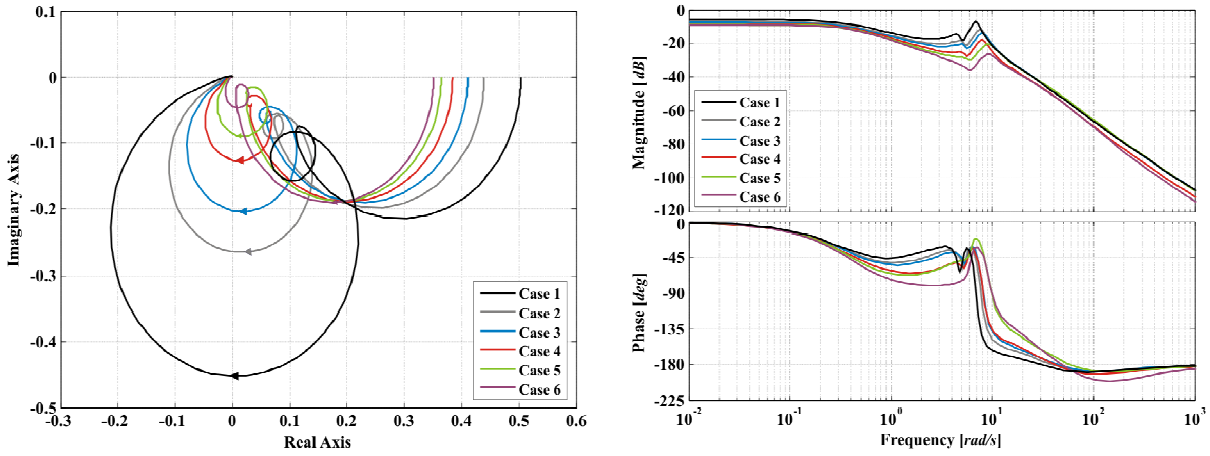

(*a*) (*b*)

Figure 6.4. Assessment of $\Gamma_3(s)$. Coupling between Individual Channels $C_1(s)$ and $C_2(s)$ from systems $\mathbf{G}_{xx12}(s)$ and $\mathbf{G}_{xx21}(s)$ (Study 1): (*a*) Nyquist plot; (*b*) Bode plot

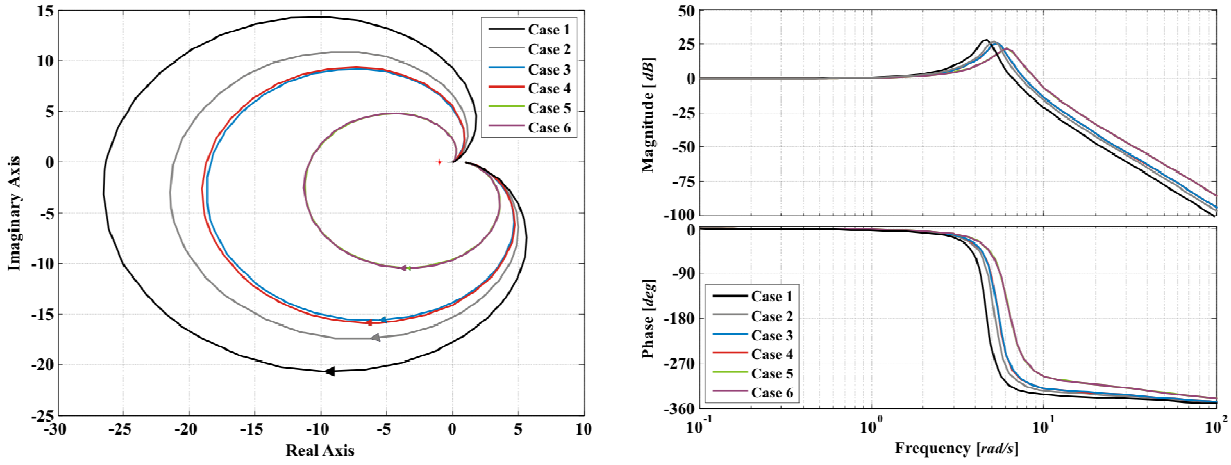

(*a*) (*b*)

Figure 6.5. Assessment of $\Gamma_3(s)$. Coupling between Individual Channels $C_1(s)$ and $C_3(s)$ from systems $\mathbf{G}_{xx13}(s)$ and $\mathbf{G}_{xx31}(s)$ (Study 1): (*a*) Nyquist plot; (*b*) Bode plot

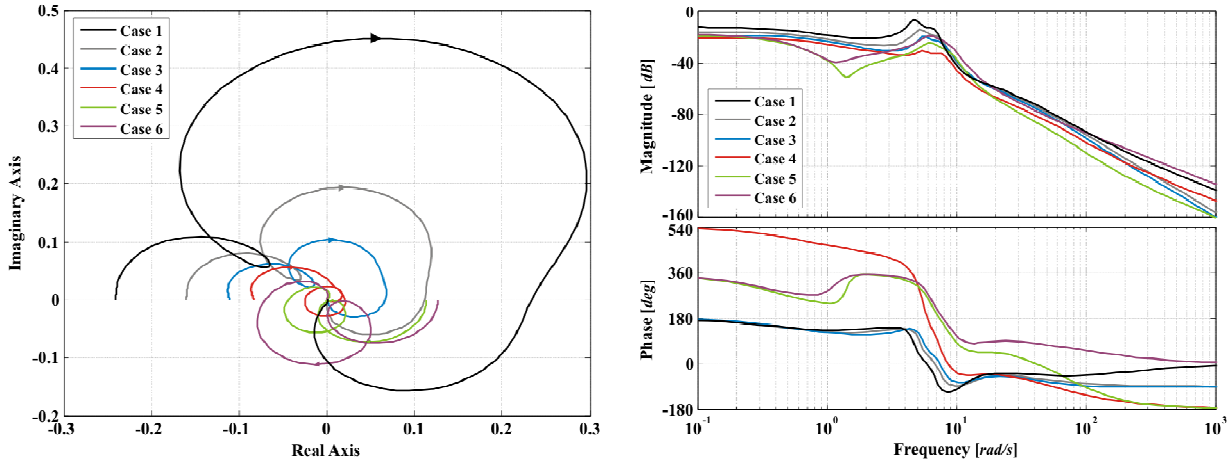

(*a*) (*b*)

Figure 6.6. Assessment of $\Gamma_3(s)$. Coupling between Individual Channels $C_1(s)$ and $C_4(s)$ from systems $\mathbf{G}_{xx14}(s)$ and $\mathbf{G}_{xx41}(s)$ (Study 1): (*a*) Nyquist plot; (*b*) Bode plot

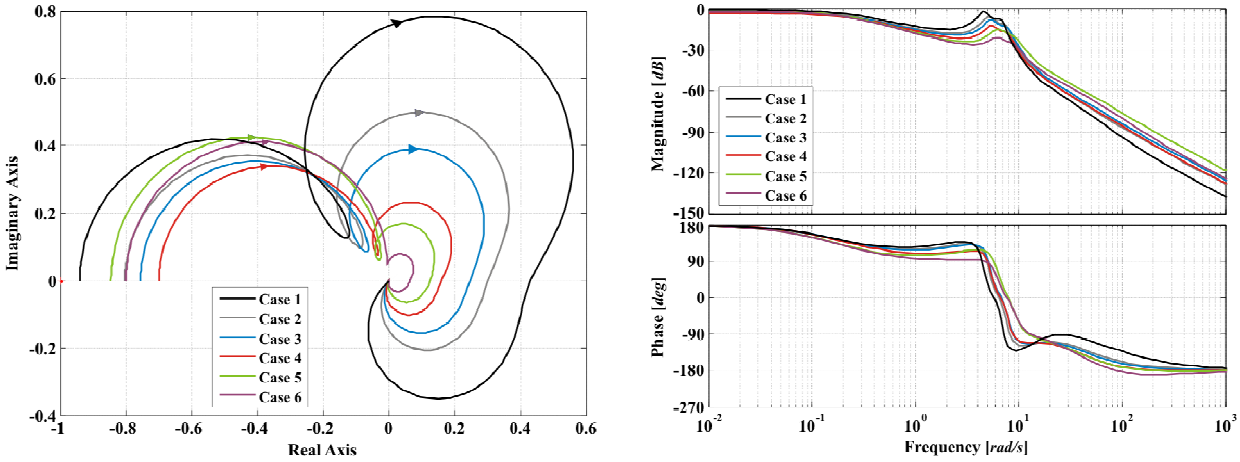

(*a*) (*b*)

Figure 6.7. Assessment of $\Gamma_3(s)$. Coupling between Individual Channels $C_2(s)$ and $C_3(s)$ from systems $\mathbf{G}_{xx23}(s)$ and $\mathbf{G}_{xx32}(s)$ (Study 1): (*a*) Nyquist plot; (*b*) Bode plot

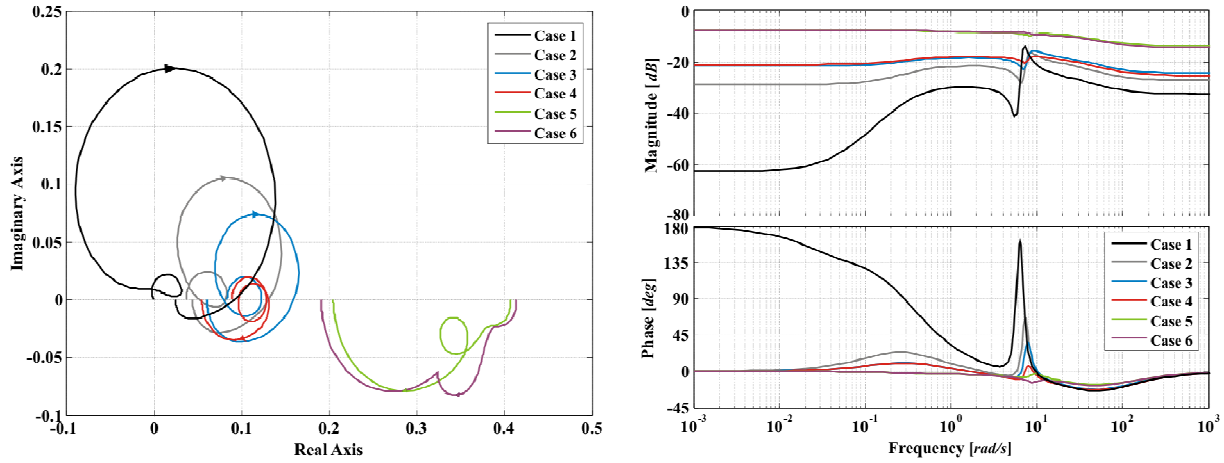

(*a*) (*b*)

Figure 6.8. Assessment of $\Gamma_3(s)$. Coupling between Individual Channels $C_2(s)$ and $C_4(s)$ from systems $\mathbf{G}_{xx24}(s)$ and $\mathbf{G}_{xx42}(s)$ (Study 1): (*a*) Nyquist plot; (*b*) Bode plot

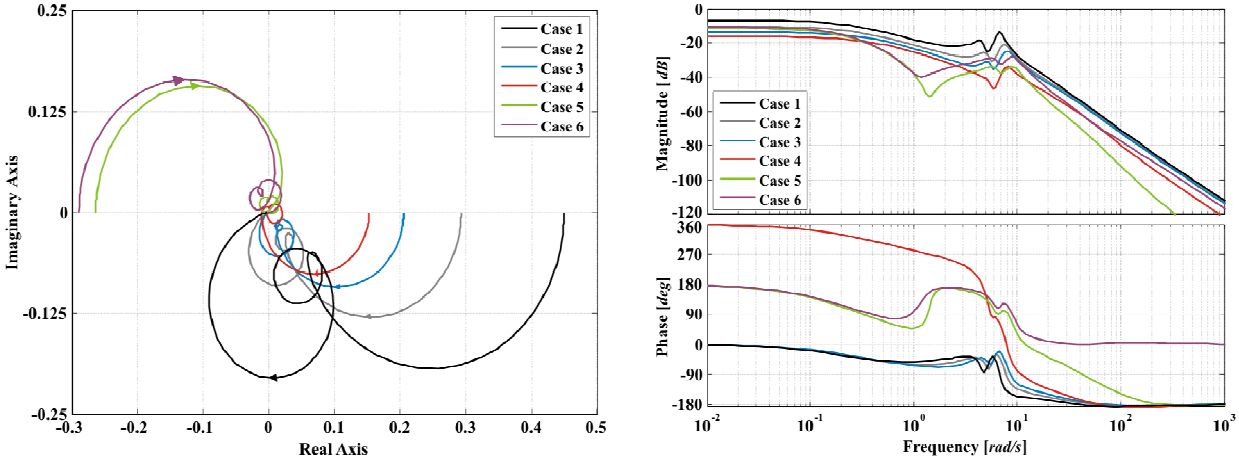

(*a*) (*b*)

Figure 6.9. Assessment of $\Gamma_3(s)$. Coupling between Individual Channels $C_3(s)$ and $C_4(s)$ from systems $\mathbf{G}_{xx34}(s)$ and $\mathbf{G}_{xx43}(s)$ (Study 1): (*a*) Nyquist plot; (*b*) Bode plot

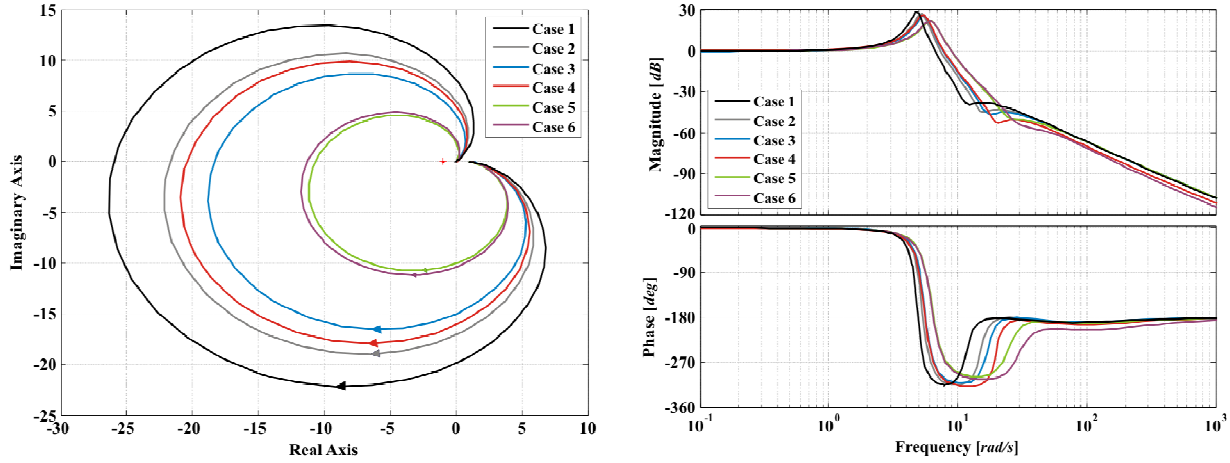

(*a*) (*b*)

Figure 6.10. Assessment of $\Gamma_2(s)$. Coupling between Individual Channel $C_1(s)$ and Multiple Channel $\mathbf{M}_{23}(s)$ from systems $\mathbf{G}_{4123}(s)$ and $\mathbf{G}_{4132}(s)$ (Study 1): (*a*) Nyquist plot; (*b*) Bode plot

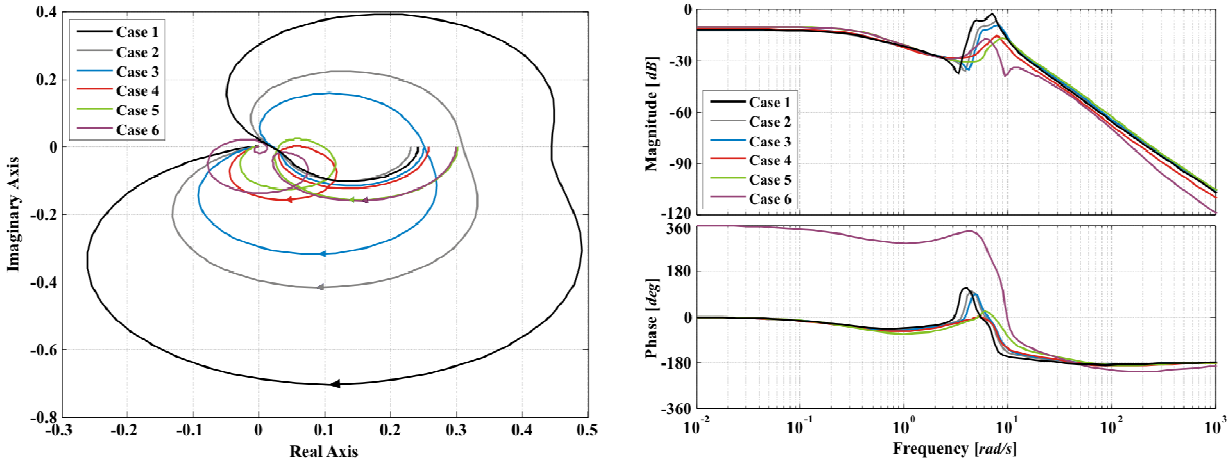

(*a*) (*b*)

Figure 6.11. Assessment of $\Gamma_2(s)$. Coupling between Individual Channel $C_1(s)$ and Multiple Channel $\mathbf{M}_{24}(s)$ from systems $\mathbf{G}_{3124}(s)$ and $\mathbf{G}_{3142}(s)$ (Study 1): (*a*) Nyquist plot; (*b*) Bode plot

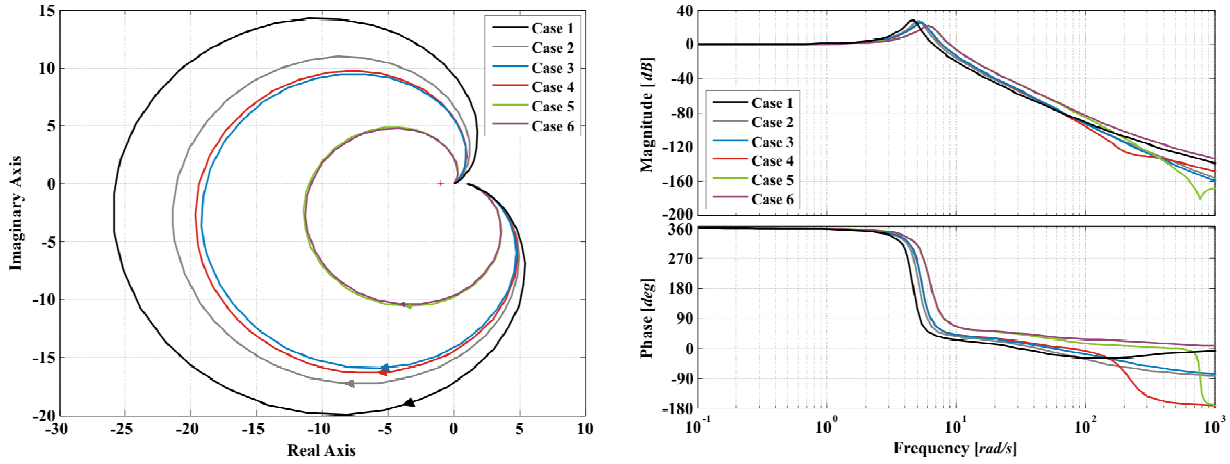

(*a*) (*b*)

Figure 6.12. Assessment of $\Gamma_2(s)$. Coupling between Individual Channel $C_1(s)$ and Multiple Channel $\mathbf{M}_{34}(s)$ from systems $\mathbf{G}_{2134}(s)$ and $\mathbf{G}_{2143}(s)$ (Study 1): (*a*) Nyquist plot; (*b*) Bode plot

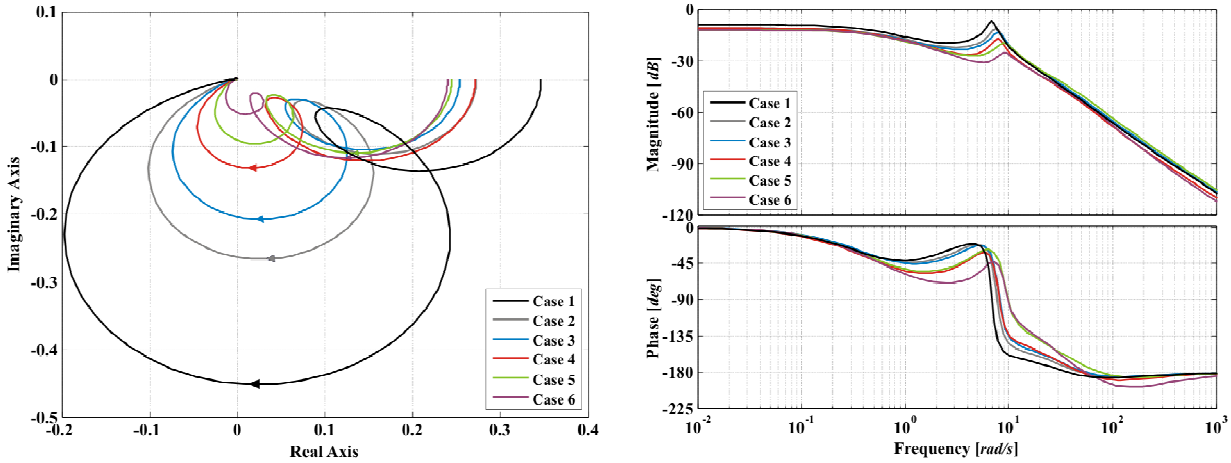

(*a*) (*b*)

Figure 6.13. Assessment of $\Gamma_2(s)$. Coupling between Individual Channel $C_2(s)$ and Multiple Channel $\mathbf{M}_{13}(s)$ from systems $\mathbf{G}_{4213}(s)$ and $\mathbf{G}_{4231}(s)$ (Study 1): (*a*) Nyquist plot; (*b*) Bode plot

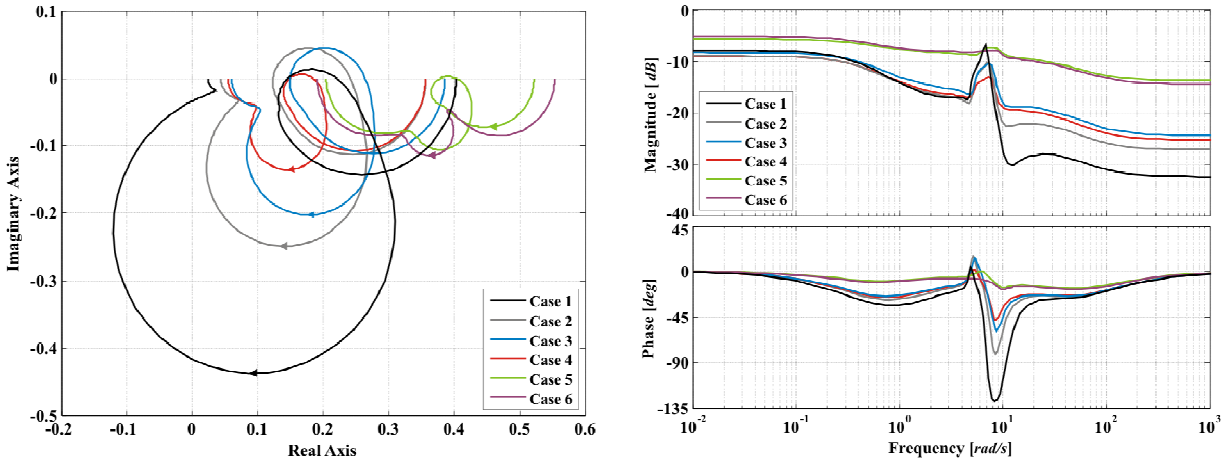

(*a*) (*b*)

Figure 6.14. Assessment of $\Gamma_2(s)$. Coupling between Individual Channel $C_2(s)$ and Multiple Channel $\mathbf{M}_{14}(s)$ from systems $\mathbf{G}_{3214}(s)$ and $\mathbf{G}_{3241}(s)$ (Study 1): (*a*) Nyquist plot; (*b*) Bode plot

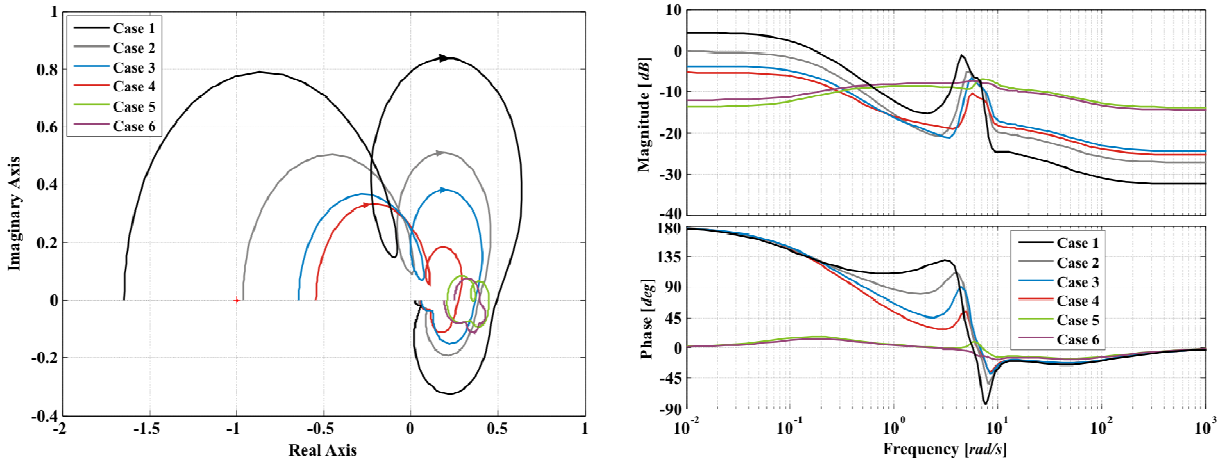

(*a*) (*b*)

Figure 6.15. Assessment of $\Gamma_2(s)$. Coupling between Individual Channel $C_2(s)$ and Multiple Channel $\mathbf{M}_{34}(s)$ from systems $\mathbf{G}_{1234}(s)$ and $\mathbf{G}_{1243}(s)$ (Study 1): (*a*) Nyquist plot; (*b*) Bode plot

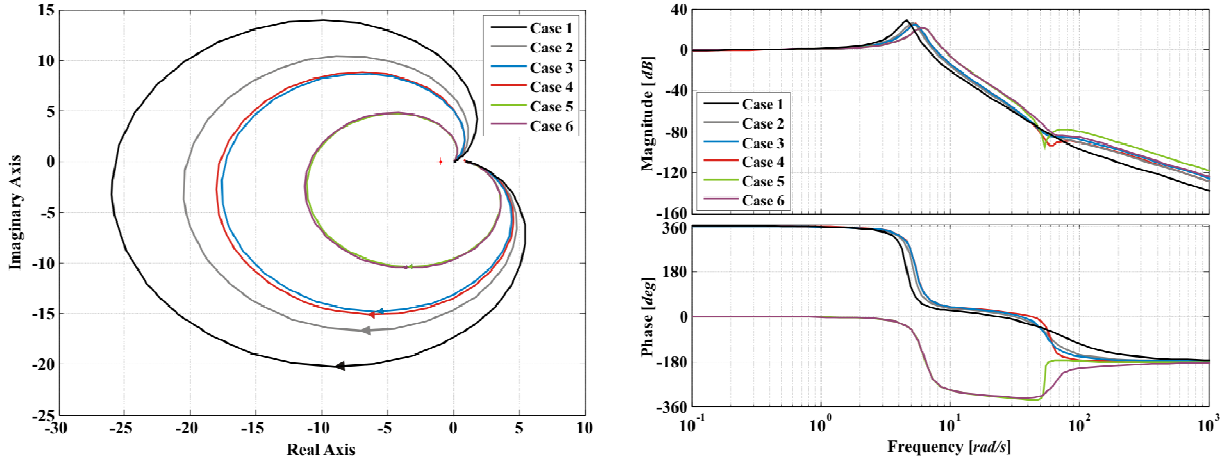

(*a*) (*b*)

Figure 6.16. Assessment of $\Gamma_2(s)$. Coupling between Individual Channel $C_3(s)$ and Multiple Channel $\mathbf{M}_{12}(s)$ from systems $\mathbf{G}_{4312}(s)$ and $\mathbf{G}_{4321}(s)$ (Study 1): (*a*) Nyquist plot; (*b*) Bode plot

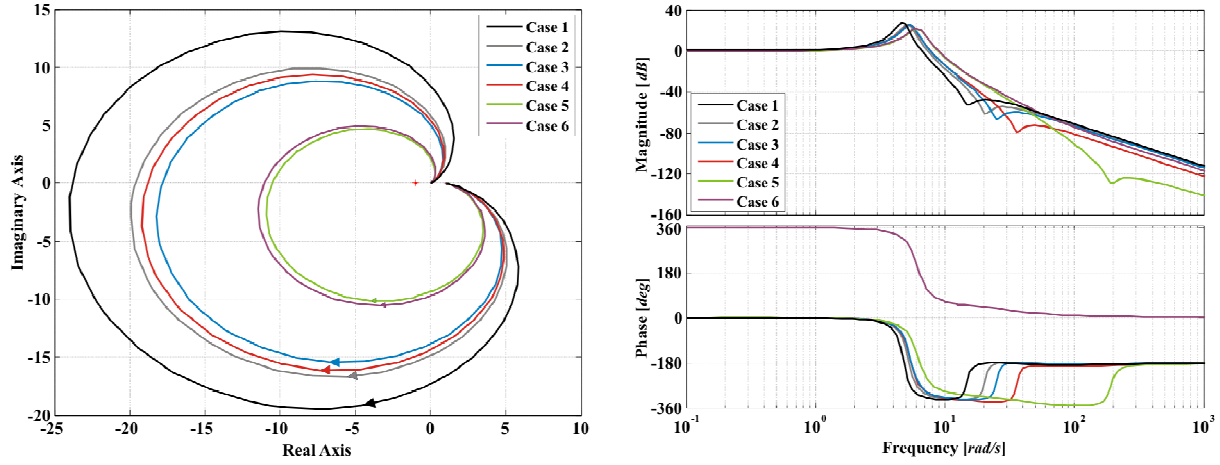

(*a*) (*b*)

Figure 6.17. Assessment of $\Gamma_2(s)$. Coupling between Individual Channel $C_3(s)$ and Multiple Channel $\mathbf{M}_{14}(s)$ from systems $\mathbf{G}_{2314}(s)$ and $\mathbf{G}_{2341}(s)$ (Study 1): (*a*) Nyquist plot; (*b*) Bode plot

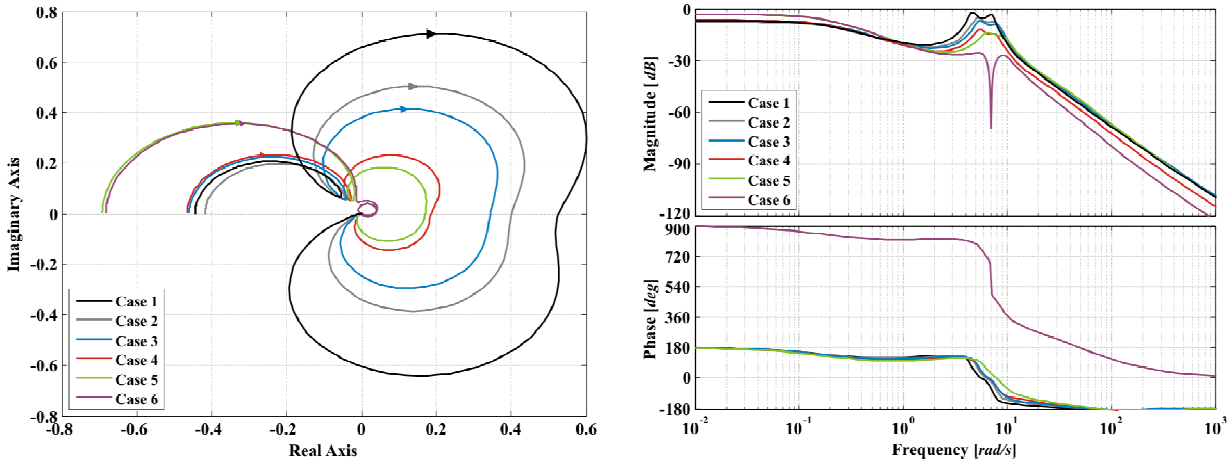

(*a*) (*b*)

Figure 6.18. Assessment of $\Gamma_2(s)$. Coupling between Individual Channel $C_3(s)$ and Multiple Channel $\mathbf{M}_{24}(s)$ from systems $\mathbf{G}_{1324}(s)$ and $\mathbf{G}_{1342}(s)$ (Study 1): (*a*) Nyquist plot; (*b*) Bode plot

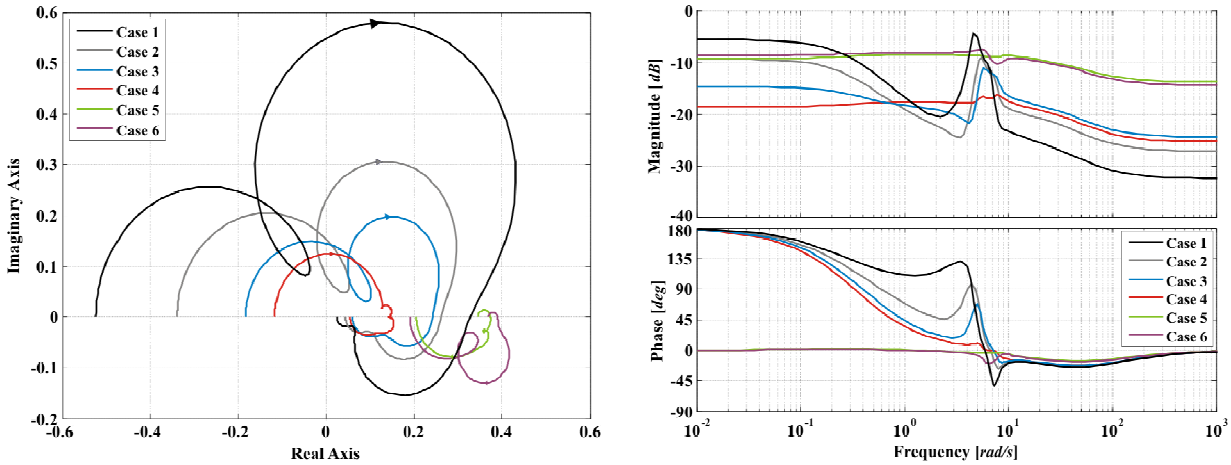

(*a*) (*b*)

Figure 6.19. Assessment of $\Gamma_2(s)$. Coupling between Individual Channel $C_4(s)$ and Multiple Channel $\mathbf{M}_{12}(s)$ from systems $\mathbf{G}_{3412}(s)$ and $\mathbf{G}_{3421}(s)$ (Study 1): (*a*) Nyquist plot; (*b*) Bode plot

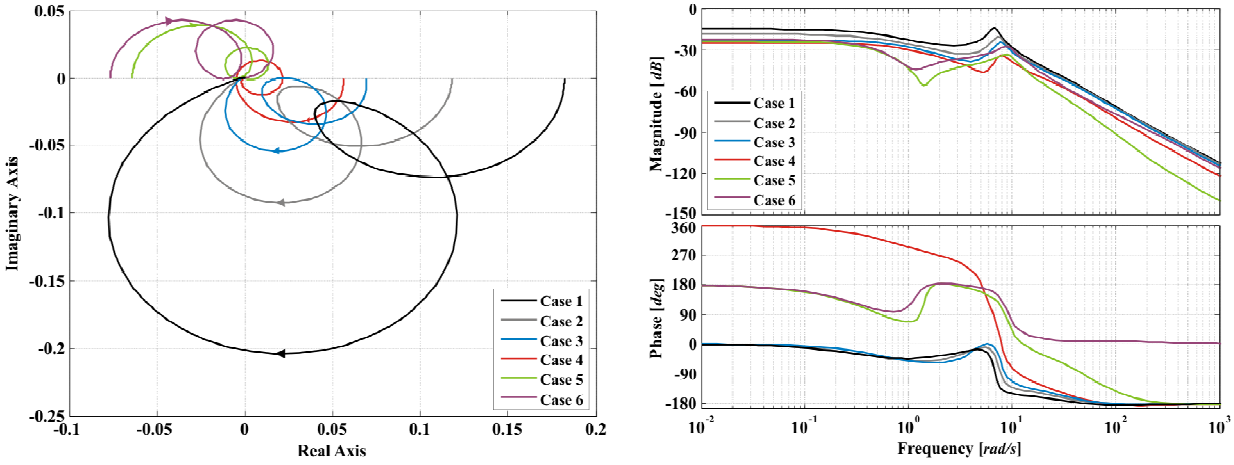

(*a*) (*b*)

Figure 6.20. Assessment of $\Gamma_2(s)$. Coupling between Individual Channel $C_4(s)$ and Multiple Channel $\mathbf{M}_{13}(s)$ from systems $\mathbf{G}_{2413}(s)$ and $\mathbf{G}_{2431}(s)$ (Study 1): (*a*) Nyquist plot; (*b*) Bode plot

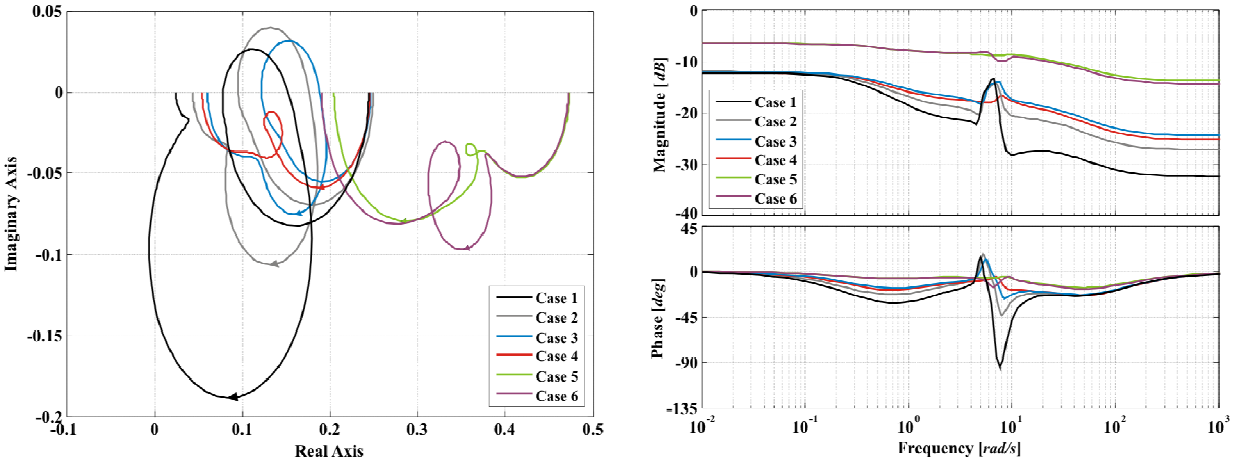

(*a*) (*b*)

Figure 6.21. Assessment of $\Gamma_2(s)$. Coupling between Individual Channel $C_4(s)$ and Multiple Channel $\mathbf{M}_{23}(s)$ from systems $\mathbf{G}_{1423}(s)$ and $\mathbf{G}_{1432}(s)$ (Study 1): (*a*) Nyquist plot; (*b*) Bode plot

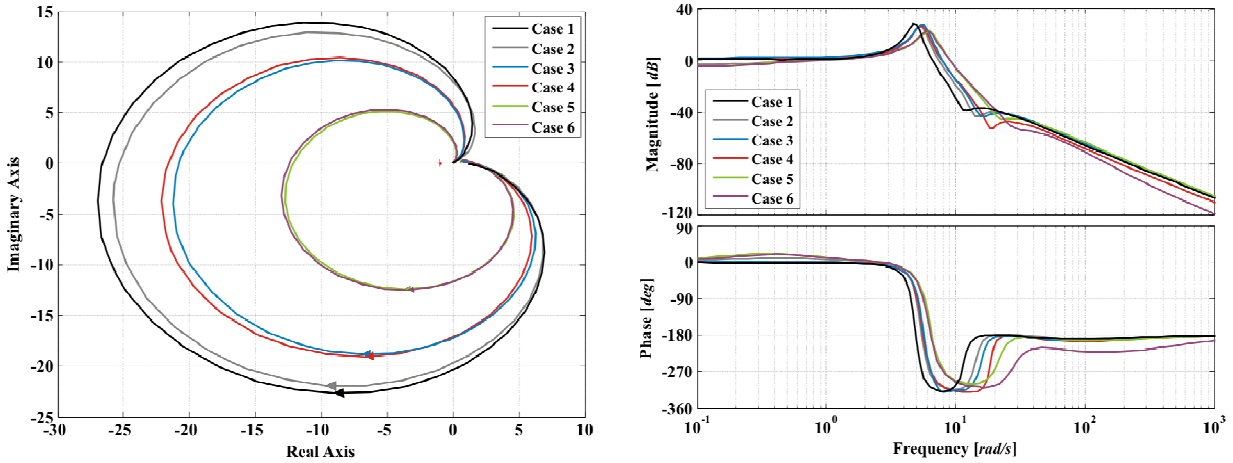

(*a*) (*b*)

Figure 6.22. Assessment of $\Gamma_1(s)$. Coupling between Individual Channel $C_1(s)$ and Multiple Channel $\mathbf{M}_{234}(s)$ from systems $\mathbf{G}_{1xxx}(s)$ (Study 1): (*a*) Nyquist plot; (*b*) Bode plot

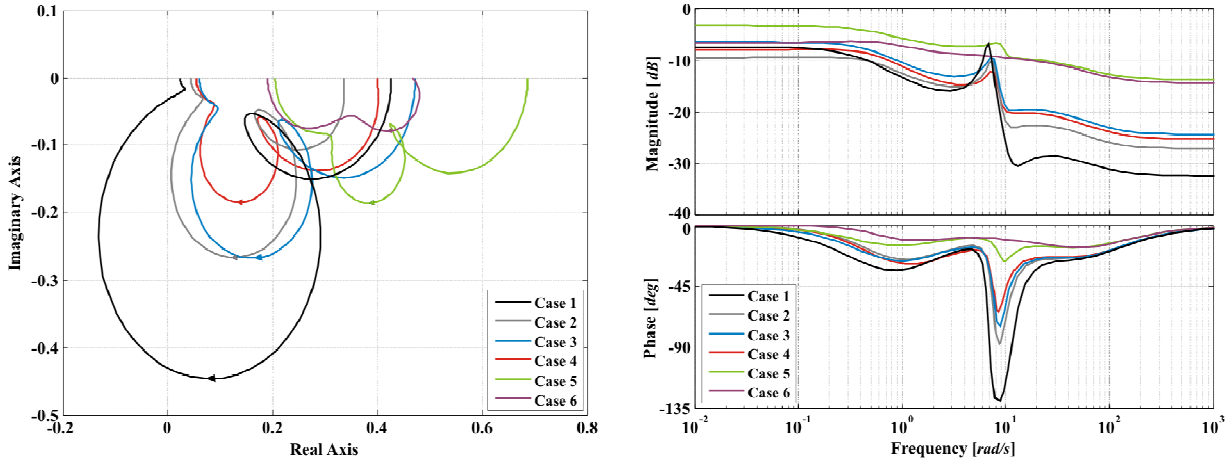

(*a*) (*b*)

Figure 6.23. Assessment of $\Gamma_1(s)$. Coupling between Individual Channel $C_2(s)$ and Multiple Channel $\mathbf{M}_{134}(s)$ from systems $\mathbf{G}_{2xxx}(s)$ (Study 1): (*a*) Nyquist plot; (*b*) Bode plot

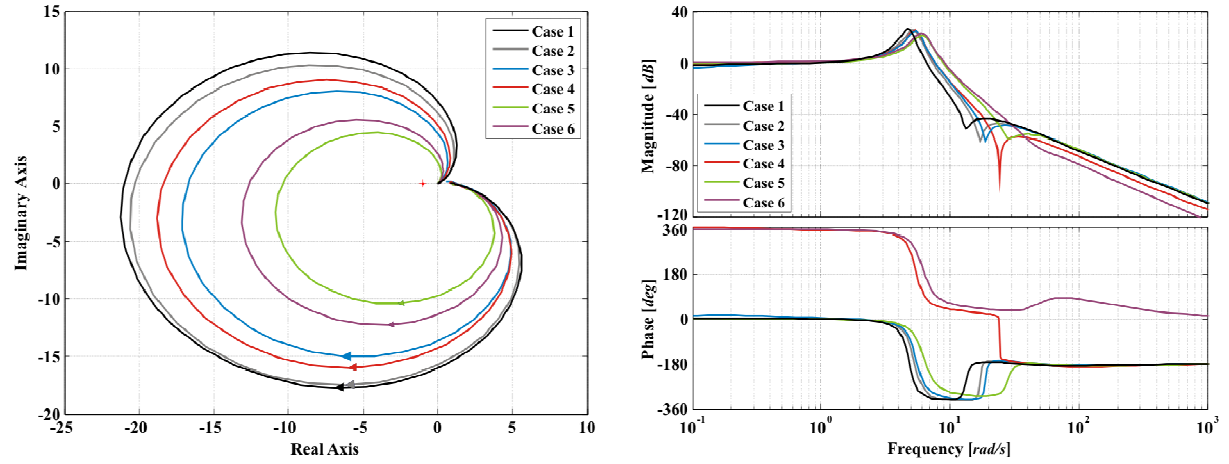

(*a*) (*b*)

Figure 6.24. Assessment of $\Gamma_1(s)$. Coupling between Individual Channel $C_3(s)$ and Multiple Channel $\mathbf{M}_{124}(s)$ from systems $\mathbf{G}_{3xxx}(s)$ (Study 1): (*a*) Nyquist plot; (*b*) Bode plot

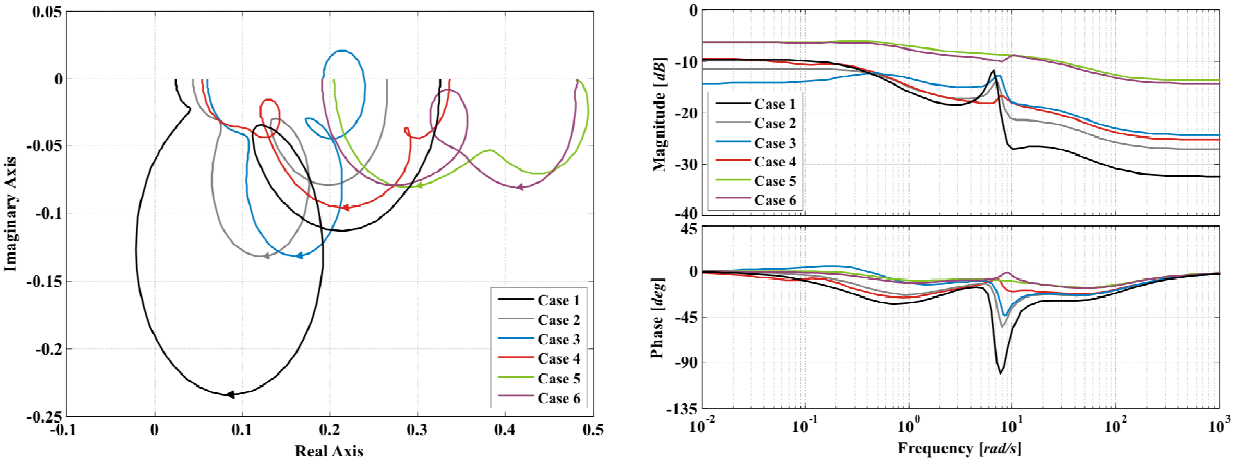

(*a*) (*b*)

Figure 6.25. Assessment of $\Gamma_1(s)$. Coupling between Individual Channel $C_4(s)$ and Multiple Channel $\mathbf{M}_{123}(s)$ from systems $\mathbf{G}_{4xxx}(s)$ (Study 1): (*a*) Nyquist plot; (*b*) Bode plot

The following remarks can be made with reference to the MSFs $\Gamma_3(s)$ of Figures 6.4–6.9:

- Coupling between $C_1(s)$ and $C_2(s)$, *i.e.*, electrical and mechanical individual channels of Machine 1, and $C_3(s)$ and $C_4(s)$, *i.e.*, electrical and mechanical individual channels of Machine 2, is relatively low (less than –5 *dB*) and decreases with the tie-line reactance value, as shown by Figures 6.4 and 6.9. In other words, the inner coupling is low for both machines.
- Coupling between the electrical individual channel of either machine with the mechanical individual channel of the other machine is also low (less than 0 *dB*); the coupling decreases with the electrical distance, as evidenced from Figures 6.6 and 6.7.
- Coupling between the electrical individual channels, *i.e.*, $C_2(s)$ and $C_4(s)$, of the machines is low; however, it increases with the reduction of the electrical distance, as shown in Figure 6.8.
- Coupling between the mechanical individual channels ($C_1(s)$ and $C_3(s)$) of the machines is high, particularly at frequencies in the range 2–8 *rad/s* (rising up to 20 *dB*); it reduces with decreasing electrical distances, as shown in Figure 6.5. It should be observed that the MSFs start close to the point (1,0), indicating high coupling at static-stationary-state; moreover, $\mathbf{G}(s)$ at $s = 0$ is singular.

Similarly, the following conclusions can be arrived at from the analysis of MSFs $\Gamma_2(s)$ of Figures 6.10–6.21:

- Coupling between a mechanical individual channel, either $C_1(s)$ or $C_3(s)$, and any of the multiple channels made up by one mechanical and one electric channel, involving the same or different machines, is high at frequencies in the range 2–8 *rad/s* (for instance between $C_1(s)$ and $\mathbf{M}_{23}(s)$ or $\mathbf{M}_{34}(s)$). However, the coupling decreases with a reduction of the electrical distance, as shown in Figures 6.10, 6.12, 6.16 and 6.17. It is noticed that for these cases the MSFs start close to the point (1,0), indicating high coupling at static-stationary-state; moreover, $\mathbf{G}(s)$ at $s = 0$ is singular.
- The coupling between an electrical individual channel, either $C_2(s)$ or $C_4(s)$, and a multiple channel formed by one mechanical and one electric channel, involving one machine or the two machines, is relatively low (*e.g.*, between $C_2(s)$ and $\mathbf{M}_{14}(s)$ or $\mathbf{M}_{34}(s)$, always below 0 *dB*) – except for Case 1 at low frequencies as shown in Figure 6.15. However, the coupling increases considerably, particularly at high frequencies, with a decrease of the electrical distance, as shown in Figures 6.14, 6.15, 6.19 and 6.21.
- The coupling between any mechanical individual channel, $C_1(s)$ or $C_3(s)$, and a multiple channel formed by the electrical individual channels $C_2(s)$ and $C_4(s)$ is small at low frequencies, but grows around the switch-back frequency range; the coupling increases with an increase of the electrical distance, as evidenced by Figures 6.11 and 6.18.
- The coupling between any electrical individual channel, $C_2(s)$ or $C_4(s)$, and a multiple channel formed by the mechanical individual channels $C_1(s)$ and $C_3(s)$ is relatively low (lower than –7 *dB*), and decreases with a decrease of the line length, as shown in Figures 6.13 and 6.20.

Following careful examination of the MSFs $\Gamma_1(s)$ in Figures 6.22–6.25, the following two points are worth mentioning:

- The coupling between any electrical individual channel, $C_2(s)$ or $C_4(s)$, and the multiple channel made up by the three other remaining channels, is low; the coupling increases with a decrease of the electrical distance, as shown in Figures 6.23 and 6.25.
- The coupling between a mechanical individual channel, $C_1(s)$ or $C_3(s)$, and the multiple channel comprised of the three other remaining channels is high at frequencies in the range 2–8 *rad/s*; the coupling decreases with decreasing electrical distances, as shown in Figures 6.22 and 6.24. It can be observed that these MSFs start close to the point (1,0), indicating high coupling at static-stationary-state; moreover, $\mathbf{G}(s)$ at $s = 0$ is singular.

From the previous analysis, it can be observed that the two-machine system is a highly coupled multivariable system, regardless of the strength of the tie-line system – particularly at low frequencies, over the range of interest of 1–10 *rad/s*. The mechanical individual channels are strongly coupled between them, whereas the coupling between the electrical individual channels is weak and so is the coupling with the mechanical subsystems. One cannot fail to notice the resonant response, typical of a pair of complex conjugate poles, in the frequency range 2–8 *rad/s* for most of the MSFs; however, the resonant peak tends to decrease with a reduction in the electrical distance.

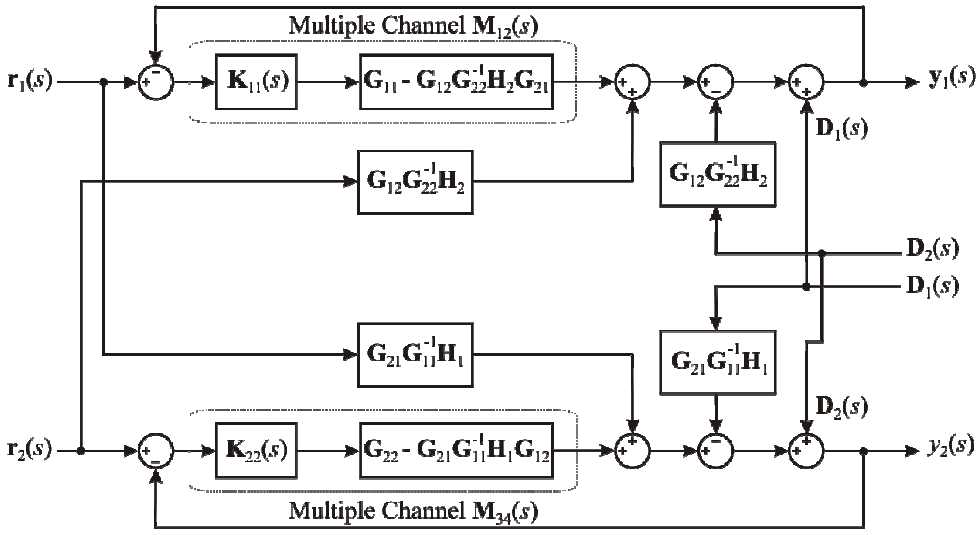

Figure 6.26. Two-machine system represented as two multiple channels

Within the context of the ICAD framework, the actual dynamics of synchronous generator 1 as affected by the influence of generator 2, are fully described by the Multiple Channel $\mathbf{M}_{12}(s)$. Similarly, the dynamics of synchronous generator 2 as affected by the influence of generator 1, are fully described by the Multiple Channel $\mathbf{M}_{34}(s)$. The interaction between the two machines, each one represented as a multiple channel, can be graphically seen in Figure 6.26. Notice from Figure 6.12 that the mechanical channel of generator 1 ($C_1(s)$) is strongly coupled to the multiple channel that represents generator 2

($\mathbf{M}_{34}(s)$). As observed in the results presented in Figure 6.16, the mechanical channel of generator 2 ($C_3(s)$) is strongly coupled to the multiple channel that represents generator 1 ($\mathbf{M}_{12}(s)$). Further to the results presented in Figures 6.4–6.25, careful assessment of the coupling characteristics between Multiple Channels $\mathbf{M}_{12}(s)$ and $\mathbf{M}_{34}(s)$ is required in order to carry out an effective control system design strategy for the two-machine system. To this end, the following procedure is offered [5]:

Consider an m-input m-output plant partitioned into m_1-input m_1-output Multiple Channel $\mathbf{M}_1(s)$ and m_2-input m_2-output Multiple Channel $\mathbf{M}_2(s)$ as given in Appendix A by equations (A.32) and (A.35):

$$\mathbf{M}_1(s) = \left[\mathbf{I} - \mathbf{G}_{12}(s)\mathbf{G}_{22}^{-1}(s)\mathbf{H}_2(s)\mathbf{G}_{21}(s)\mathbf{G}_{11}^{-1}(s)\right]\mathbf{G}_{11}(s)\mathbf{K}_{11}(s) \tag{A.32}$$

$$\mathbf{M}_2(s) = \left[\mathbf{I} - \mathbf{G}_{21}(s)\mathbf{G}_{11}^{-1}(s)\mathbf{H}_1(s)\mathbf{G}_{12}(s)\mathbf{G}_{22}^{-1}(s)\right]\mathbf{G}_{22}(s)\mathbf{K}_{22}(s) \tag{A.35}$$

The following transfer function matrix is constructed

$$\mathbf{G}_{11}^{*}(s) = \left[\mathbf{I} - \mathbf{G}_{12}(s)\mathbf{G}_{22}^{-1}(s)\mathbf{G}_{21}(s)\mathbf{G}_{11}^{-1}(s)\right]\mathbf{G}_{11}(s) \tag{6.7}$$

Then, the two multiple channels exhibit a weak coupling and Multiple Channel $\mathbf{M}_1(s)$ can be designed on the basis of $\mathbf{G}_{11}(s)$ alone, provided the following is fulfilled:

1. The diagonal elements of $\mathbf{G}_{11}^{*}(s)$ do not differ significantly from those of $\mathbf{G}_{11}(s)$;
2. The MSFs $\Gamma_i(s)$ of the m_1-input m_1-output system $\mathbf{G}_{11}^{*}(s)$ do not differ significantly from those of $\mathbf{G}_{11}(s)$;
3. The structure (RHPPs and RHPZs) of $\mathbf{G}_{11}^{*}(s)$ does not differ significantly from that of $\mathbf{G}_{11}(s)$.

It should be beared in mind that decoupling of the system so that Multiple Channel $\mathbf{M}_1(s)$ can be designed on the basis of $\mathbf{G}_{11}(s)$ alone, does not necessarily mean that Multiple Channel $\mathbf{M}_2(s)$ can be designed on the basis of $\mathbf{G}_{22}(s)$ alone [5]. For that case, construct the following transfer function matrix

$$\mathbf{G}_{22}^{*}(s) = \left[\mathbf{I} - \mathbf{G}_{21}(s)\mathbf{G}_{11}^{-1}(s)\mathbf{G}_{12}(s)\mathbf{G}_{22}^{-1}(s)\right]\mathbf{G}_{22}(s) \tag{6.8}$$

The two multiple channels have weak coupling and Multiple Channel $\mathbf{M}_2(s)$ can be designed on the basis of $\mathbf{G}_{22}(s)$ alone, provided the following is fulfilled:

1. The diagonal elements of $\mathbf{G}_{22}^{*}(s)$ do not differ significantly from those of $\mathbf{G}_{22}(s)$;
2. The MSFs $\Gamma_i(s)$ of the m_2-input m_2-output system $\mathbf{G}_{22}^{*}(s)$ do not differ significantly from those of $\mathbf{G}_{22}(s)$;
3. The structure (RHPPs and RHPZs) of $\mathbf{G}_{22}^{*}(s)$ does not differ significantly from that of $\mathbf{G}_{22}(s)$.

Consider the 4-input 4-output two-machine system given by (6.1), where transfer function matrix $\mathbf{G}(s)$ will be referred to as $\mathbf{G}_{1234}$. In order to assess the coupling characteristics between the two synchronous generators, the system is decomposed into Multiple Channels $\mathbf{M}_{12}(s)$ and $\mathbf{M}_{34}(s)$ as shown in Figure 6.26, where Multiple Channel $\mathbf{M}_{12}$ contains 2 inputs and 2 outputs and Multiple Channel $\mathbf{M}_{34}$ contains 2 inputs and 2 outputs. The partitioning of the system is such that:

$$\mathbf{G}_{1234}(s)=\begin{bmatrix}\mathbf{G}_{11}(s) & \mathbf{G}_{12}(s)\\ \mathbf{G}_{21}(s) & \mathbf{G}_{22}(s)\end{bmatrix} \tag{6.9}$$

where

$$\mathbf{G}_{11}(s)=\begin{bmatrix}g_{11}(s) & g_{12}(s)\\ g_{21}(s) & g_{22}(s)\end{bmatrix} \tag{6.10}$$

$$\mathbf{G}_{12}(s)=\begin{bmatrix}g_{13}(s) & g_{14}(s)\\ g_{23}(s) & g_{24}(s)\end{bmatrix} \tag{6.11}$$

$$\mathbf{G}_{21}(s)=\begin{bmatrix}g_{31}(s) & g_{32}(s)\\ g_{41}(s) & g_{42}(s)\end{bmatrix} \tag{6.12}$$

$$\mathbf{G}_{22}(s)=\begin{bmatrix}g_{33}(s) & g_{34}(s)\\ g_{43}(s) & g_{44}(s)\end{bmatrix} \tag{6.13}$$

The coupling characteristics between Multiple Channels $\mathbf{M}_{12}(s)$ and $\mathbf{M}_{34}(s)$ are evaluated by means of the constructs $\mathbf{G}^*_{11}(s)$ and $\mathbf{G}^*_{22}(s)$ given by (6.7) and (6.8), respectively, bearing in mind the partitioned matrices (6.9)–(6.13). The relevant Bode and Nyquist plots of the diagonal elements of subsystems $\mathbf{G}_{11}(s)$, $\mathbf{G}_{22}(s)$, $\mathbf{G}^*_{11}(s)$, $\mathbf{G}^*_{22}(s)$ and their MSFs are provided in Figures 6.27–6.30, where the system operating conditions for Case 1, given in Table 6.1, are considered.

By examining Figure 6.27(*a*), it can be seen that the Bode plot of diagonal element $g_{11}(s)$ of $\mathbf{G}_{11}(s)$ is considerably different from that of $g^*_{11}(s)$ of $\mathbf{G}^*_{11}(s)$ (defined in (6.7)), particularly for frequencies below 10 *rad/s*. On the other hand, the Bode plot of diagonal element $g_{22}(s)$ of $\mathbf{G}_{11}(s)$ is reasonably similar when compared to that of $g^*_{22}(s)$ of $\mathbf{G}^*_{11}(s)$, as evidenced by Figure 6.27(*b*). However, notice that the switch-back characteristic increases in subsystem $g^*_{22}(s)$ and that it shifts towards the lower frequencies. Figure 6.28 shows the Bode and Nyquist plots of the MSF of subsystems $\mathbf{G}_{11}(s)$ and $\mathbf{G}^*_{11}(s)$. Notice that the behaviour of both $\gamma(s)$ and $\gamma^*(s)$ is similar; nevertheless, coupling is stronger for $\mathbf{G}^*_{11}(s)$.

Figure 6.29 shows the Bode plots of the diagonal elements of $\mathbf{G}_{22}(s)$ and $\mathbf{G}^*_{22}(s)$ (as defined in (6.8)). Notice that the frequency response plot of element $g_{33}(s)$ of $\mathbf{G}_{22}(s)$ is considerably different from that of $g^*_{33}(s)$ of $\mathbf{G}^*_{22}(s)$, particularly at frequencies below 10 *rad/s*, as it can be seen in Figure 6.29(*a*). Figure 6.29(*b*) shows that the Bode plot of element $g_{44}(s)$ of $\mathbf{G}_{22}(s)$ is similar to that of $g^*_{44}(s)$ of $\mathbf{G}^*_{22}(s)$, but the switch-back characteristic increases in subsystem $g^*_{44}(s)$ and shifts towards the lower frequencies. Figure 6.30 illustrates the Bode and Nyquist plots of the MSF of subsystems $\mathbf{G}_{22}(s)$ and $\mathbf{G}^*_{22}(s)$. The behaviour of MSFs $\gamma(s)$ and $\gamma^*(s)$ is similar; however, coupling is stronger in the latter case.

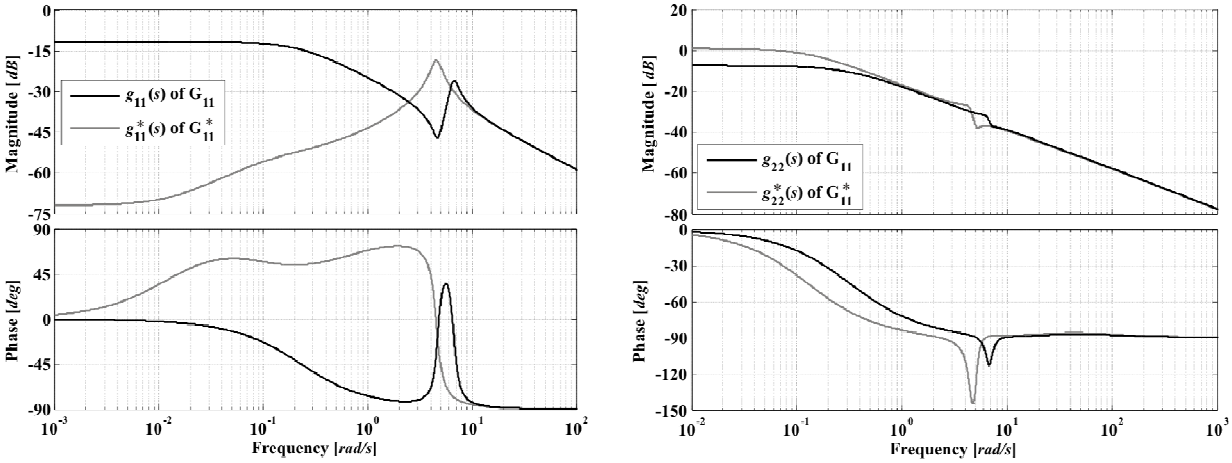

(*a*) (*b*)

Figure 6.27. Coupling assessment between Multiple Channels $\mathbf{M}_{12}(s)$ and $\mathbf{M}_{34}(s)$ (Case 1, Study 1). Bode diagrams of diagonal elements of $\mathbf{G}_{11}(s)$ and $\mathbf{G}_{11}^*(s)$: (*a*) $g_{11}(s)$ and $g_{11}^*(s)$; (*b*) $g_{22}(s)$ and $g_{22}^*(s)$

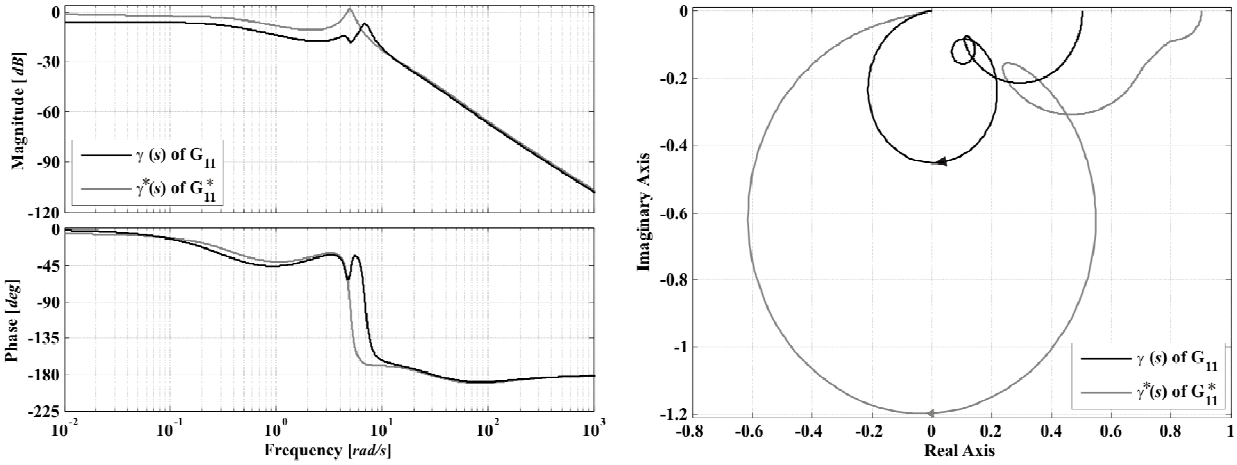

(*a*) (*b*)

Figure 6.28. Coupling assessment between Multiple Channels $\mathbf{M}_{12}(s)$ and $\mathbf{M}_{34}(s)$ (Case 1, Study 1). Assessment of MSFs $\gamma(s)$ of $\mathbf{G}_{11}(s)$ and $\gamma^*(s)$ of $\mathbf{G}_{11}^*(s)$: (*a*) Bode diagrams; (*b*) Nyquist diagrams

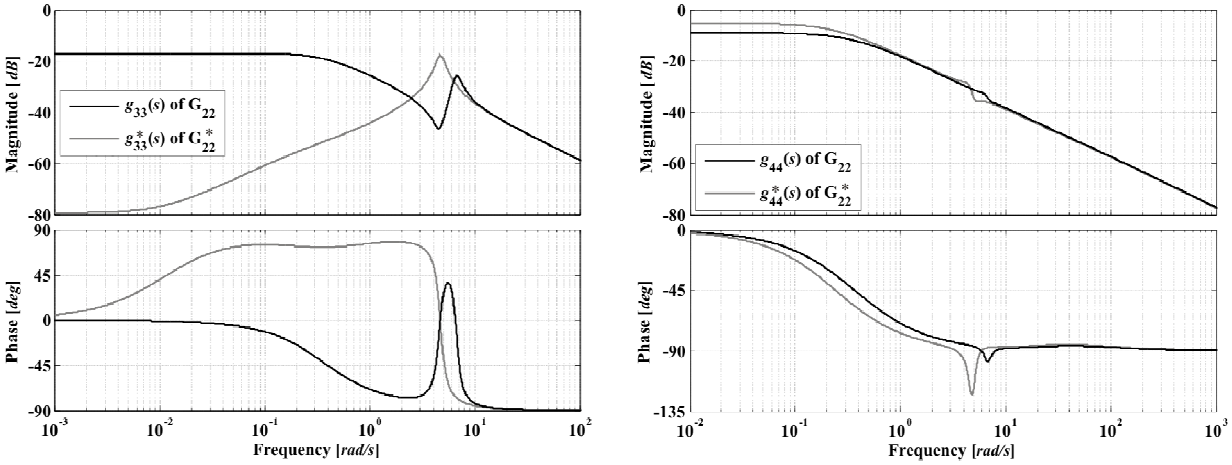

(*a*) (*b*)

Figure 6.29. Coupling assessment between Multiple Channels $\mathbf{M}_{12}(s)$ and $\mathbf{M}_{34}(s)$ (Case 1, Study 1). Bode diagrams of diagonal elements of $\mathbf{G}_{22}(s)$ and $\mathbf{G}_{22}^*(s)$: (*a*) $g_{33}(s)$ and $g_{33}^*(s)$; (*b*) $g_{44}(s)$ and $g_{44}^*(s)$

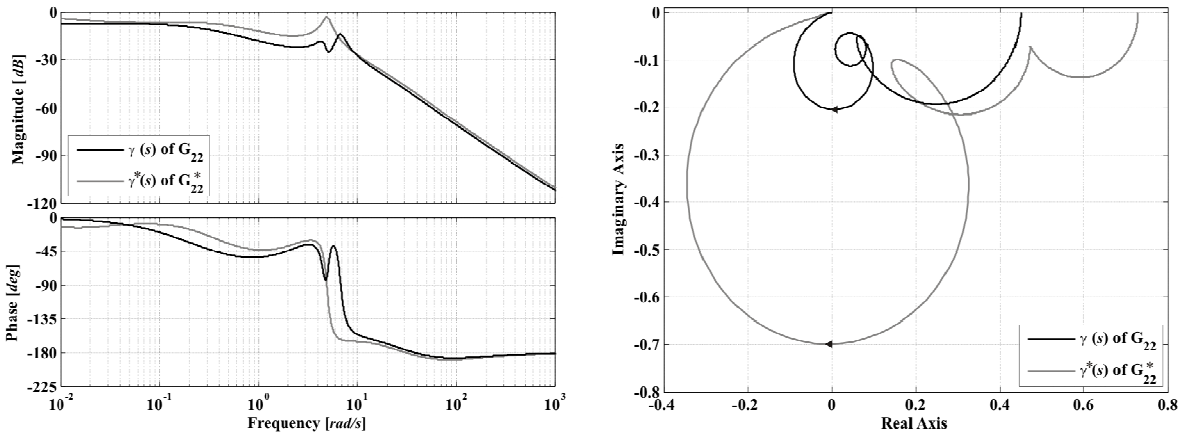

(*a*) (*b*)

Figure 6.30. Coupling assessment between Multiple Channels $\mathbf{M}_{12}(s)$ and $\mathbf{M}_{34}(s)$ (Case 1, Study 1). Assessment of MSFs $\gamma(s)$ of $\mathbf{G}_{22}(s)$ and $\gamma^*(s)$ of $\mathbf{G}_{22}^*(s)$: (*a*) Bode diagrams; (*b*) Nyquist diagrams

A similar set of results can be arrived at for all other operating conditions provided in Table 6.1, where the relevant Bode and Nyquist plots (not shown) feature a similar behaviour to that shown in Figures 6.27–6.30. In summary:

- Elements $g_{11}(s)$ and $g_{33}(s)$ are quite different at low frequencies from $g_{11}^*(s)$ and $g_{33}^*(s)$.
- Elements $g_{22}(s)$ and $g_{44}(s)$ are quite similar to $g_{22}^*(s)$ and $g_{44}^*(s)$ except for the region around their switch-back characteristics, associated with the electrical channels of the synchronous machines, which are shifted towards the lower frequencies and are more pronounced in $g_{22}^*(s)$ and $g_{44}^*(s)$.
- MSFs $\gamma(s)$ associated to $\mathbf{G}_{11}(s)$ and $\mathbf{G}_{22}(s)$ are similar to those $\gamma^*(s)$ of $\mathbf{G}_{11}^*(s)$ and $\mathbf{G}_{22}^*(s)$.

Based on these results, it can be concluded that Multiple Channel $\mathbf{M}_{12}(s)$ cannot be designed on the basis of $\mathbf{G}_{11}^*(s)$ alone. Similarly, Multiple Channel $\mathbf{M}_{34}(s)$ cannot be designed on the basis of $\mathbf{G}_{22}^*(s)$ alone. Both the multiple channels representing the two machines ought to be designed by including the multiple channel representing the other machine, regardless of transmission line length. These findings support previous results obtained when analysing the MSFs $\Gamma_i(s)$ shown in Figures 6.4–6.25.

Remark: The fact that the Nyquist trajectory of several MSFs $\Gamma_i(s)$ passes close to or through the point (1,0) is a matter of great importance. Those MSFs are given in Figures 6.5, 6.10, 6.12, 6.16, 6.17, 6.22 and 6.24. Their common characteristic is that they encapsulate the coupling between the mechanical individual channels or between a mechanical individual channel of one machine and a multiple channel including the mechanical individual channel of the other machine. In general, a system possesses purely imaginary transmission zeros at the frequency $s = s_0$ if $\Gamma(s_0) = 1$ [6,7]. In such a case, the transfer function matrix $\mathbf{G}(s)$ loses rank [8]. This kind of system has low structural robustness or excessive structural sensitivity since the number of encirclements to the point (1,0) in the Nyquist plot could change due to disturbances or non-modelled dynamics [6] – therefore changing the nature of the zeros of the individual channels. For instance, the transfer function matrix $\mathbf{G}(s)$ in (6.1) has the following set of transmission zeros:

$$T_Z = \left\{-44.8, -38.5, -35.7, -17.1, -15.5, -11.7, -10.7, -0.78 \pm j6.62, -0.59, -0.41, -0.28, 1.5\times10^{-13}\right\}$$

where the system operating conditions for Case 1, given in Table 6.1, are considered. Notice that the transmission zero 1.5×10^{-13}, is practically zero. A similar situation occurs for the rest of the operating conditions (not included). Therefore, special attention must be paid to the structural robustness of the system at low frequencies. Since some $\Gamma_i(s)$ are very close to the point (1,0) at nearly 0 *rad/s*, the system lacks robustness due to excessive structural sensitivity. The physical consequence of this condition in the two-machine system is that the mechanical channels of both machines cannot act independently and the system cannot be decoupled. They can be thought of as forming a single system; therefore, the mechanical subsystems should be manipulated simultaneously. This can be related to the fact that every synchronous generator connected to the electrical grid will rotate at near synchronous speed, which is proportional to the nominal frequency of the power system.

The following control system design strategy is proposed based on the results given in Figures 6.4–6.25, 6.27–6.30 and the previous remark:

1. Design controller $k_{22}(s)$ for Individual Channel $C_2(s)$ as a separate SISO subsystem, since the electrical subsystem of Machine 1 is weakly coupled to either of the mechanical subsystems of either machine (assume that $\gamma_2(s) = 0$). Provide adequate robustness measures to completely decouple the subsystem from the rest of the plant. As in the case of OMIB systems from Chapter 3, a bandwidth limitation is a sensible option to avoid the application of active control at the frequencies where the switch-back characteristic is present.
2. Calculate subsystem $h_2(s)$ using the previously designed $k_{22}(s)$.
3. Design controller $k_{44}(s)$ for the Individual Channel $C_4(s)$ as a separate SISO subsystem, since the electrical subsystem of Machine 2 is weakly coupled to either of the mechanical subsystem of either machine (assume that $\gamma_4(s) = 0$). Provide adequate robustness measures to completely decouple the subsystem from the rest of the plant.
4. Calculate subsystem $h_4(s)$ using the already available $k_{44}(s)$.
5. Design controller $k_{11}(s)$ for the Individual Channel $C_1(s)$, using equations (A.55) and (A.56). Assume $h_3(s) = 1$ and use the already calculated $h_2(s)$ and $h_4(s)$ for the construction of $\bar{\mathbf{G}}$, $\bar{\mathbf{G}}^1$ and $\bar{\mathbf{G}}_1$.
6. Calculate subsystem $h_1(s)$ using the already available $k_{11}(s)$.
7. Design of controller $k_{33}(s)$ for the Individual Channel $C_3(s)$, using equations (A.55) and (A.56) together with $h_1(s)$, $h_2(s)$ and $h_4(s)$ for the construction of matrices $\bar{\mathbf{G}}$, $\bar{\mathbf{G}}^1$ and $\bar{\mathbf{G}}_1$ and MSF $\gamma_3(s)$. Notice that matrix $\bar{\mathbf{G}}$ calculated in Step 5, becomes updated.
8. Calculation of subsystem $h_3(s)$ using $k_{33}(s)$.
9. Re-design of controller $k_{11}(s)$ for Individual Channel $C_1(s)$ taking into account the impact of $h_2(s)$, $h_3(s)$ and $h_4(s)$ in the construction of matrices $\bar{\mathbf{G}}$, $\bar{\mathbf{G}}^1$ and $\bar{\mathbf{G}}_1$ and MSF $\gamma_1(s)$.

10. Calculation of matrices $\bar{\mathbf{G}}^2$, $\bar{\mathbf{G}}^4$, $\bar{\mathbf{G}}_2$ and $\bar{\mathbf{G}}_4$ to obtain MSFs $\gamma_2(s)$ and $\gamma_4(s)$.

11. Repeat Steps 7–10 until a successful controller is achieved and robustness is assured in each individual channel, subsystems $h_i(s)$, and multivariable structure functions $\gamma_i(s)$.

It should be noticed that the design process above exploits the fact that coupling in the two-machine system arises mainly because of the interaction between the two mechanical channels; that the electrical channels exhibit weak coupling both between themselves and also with the mechanical subsystems. The only major concern relating to the controller design of the electrical channels relates to the presence of the switch-back characteristic. Even though this was the most problematic dynamic when assessing the OMIB system performance, an issue dealt with in Chapter 3, this is a problem which is overshadowed by the strong coupling exhibited by the two mechanical channels. The fact that each synchronous machine has a low internal coupling (between its mechanical and electric subsystems) is consistent with the results obtained for the OMIB systems in Chapter 3.

6.3.2. Study 2. Impact of the system loading

This study assesses the effect that the system loading has in the two-machine system of Figure 6.1. To this end, consider the system operating conditions provided in Table 6.2 for both machines of the system. The transmission system is purely reactive, with a total tie-line reactance X_t = 0.5 *p.u.* Loads 1 and 2, which are connected to the terminals of synchronous generators 1 and 2, respectively, are kept constant; while the load is connected at the mid-point of the transmission line taking the values given in Table 6.3. It is seen from the table that in Case A, the load increases by 25% when compared to case B. In case C, in contrast, it decreases by 25%, and in case D it decreases by 50%. It should be noticed that Case B corresponds to Case 3 of Study 1.

Table 6.3. Load values at the mid-point of transmission line for Study 2

	Load at node 3	
Case	P_{L3}	Q_{L3}
A	1.5 *p.u.*	0.775 *p.u.*
B	1.2 *p.u.*	0.62 *p.u.*
C	0.9 *p.u.*	0.465 *p.u.*
D	0.6 *p.u.*	0.31 *p.u.*

The MSFs of the two-machine system are given in Figures 6.31–6.52. Coupling between any two individual channels will be given by MSFs $\Gamma_3(s)$. Figures 6.31–6.36 show the Nyquist and Bode diagrams for the various $\Gamma_3(s)$ of the two-machine system. Coupling between an individual channel and a multiple channel (formed by any two individual channels) can be evaluated through MSFs $\Gamma_2(s)$, whose Bode and Nyquist diagrams are provided in Figures 6.37–6.48. Figures 6.49–6.52 show the Nyquist and Bode diagrams of the different $\Gamma_1(s)$, which provide the coupling between an individual channel and a multiple

channel formed by three individual channels.

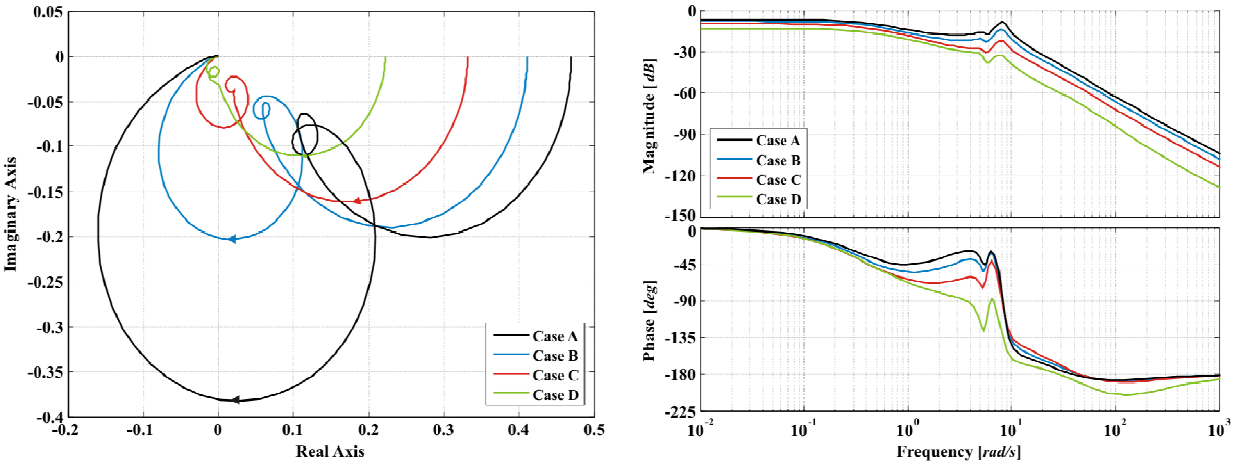

(*a*) (*b*)

Figure 6.31. Assessment of $\Gamma_3(s)$. Coupling between Individual Channels $C_1(s)$ and $C_2(s)$ from systems $\mathbf{G}_{xx12}(s)$ and $\mathbf{G}_{xx21}(s)$ (Study 2): (*a*) Nyquist plot; (*b*) Bode plot

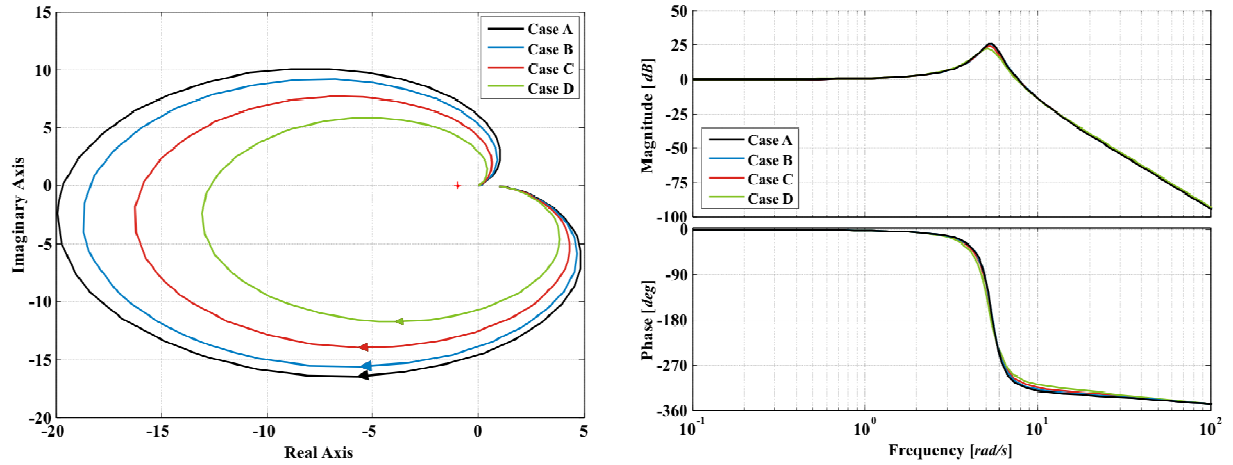

(*a*) (*b*)

Figure 6.32. Assessment of $\Gamma_3(s)$. Coupling between Individual Channels $C_1(s)$ and $C_3(s)$ from systems $\mathbf{G}_{xx13}(s)$ and $\mathbf{G}_{xx31}(s)$ (Study 2): (*a*) Nyquist plot; (*b*) Bode plot

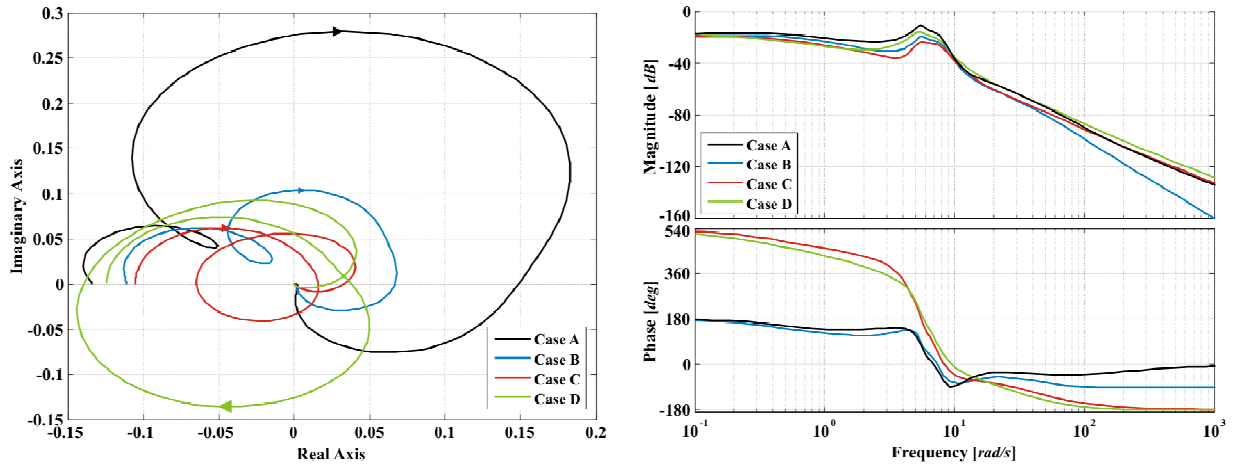

(*a*) (*b*)

Figure 6.33. Assessment of $\Gamma_3(s)$. Coupling between Individual Channels $C_1(s)$ and $C_4(s)$ from systems $\mathbf{G}_{xx14}(s)$ and $\mathbf{G}_{xx41}(s)$ (Study 2): (*a*) Nyquist plot; (*b*) Bode plot

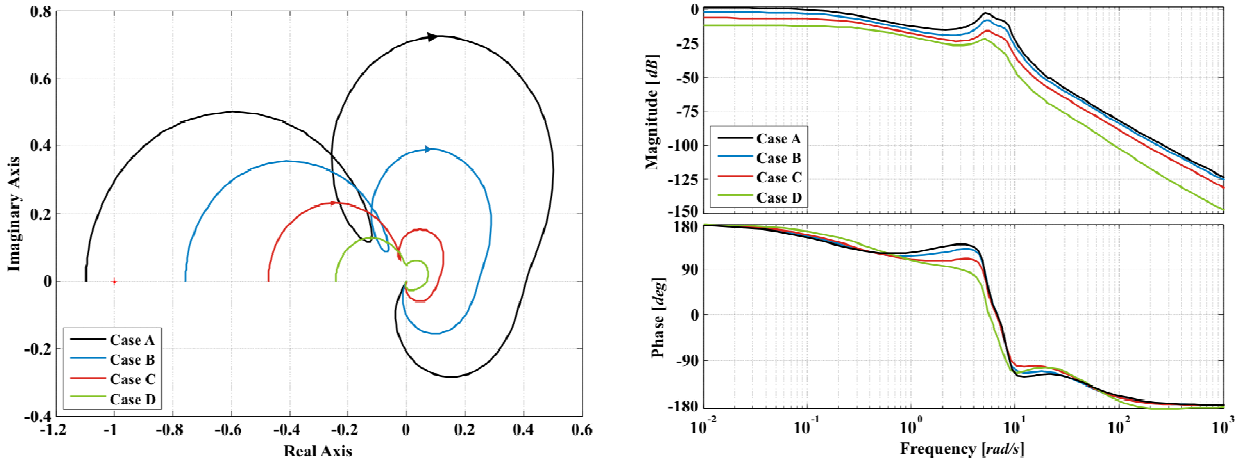

(*a*) (*b*)

Figure 6.34. Assessment of $\Gamma_3(s)$. Coupling between Individual Channels $C_2(s)$ and $C_3(s)$ from systems $\mathbf{G}_{xx23}(s)$ and $\mathbf{G}_{xx32}(s)$ (Study 2): (*a*) Nyquist plot; (*b*) Bode plot

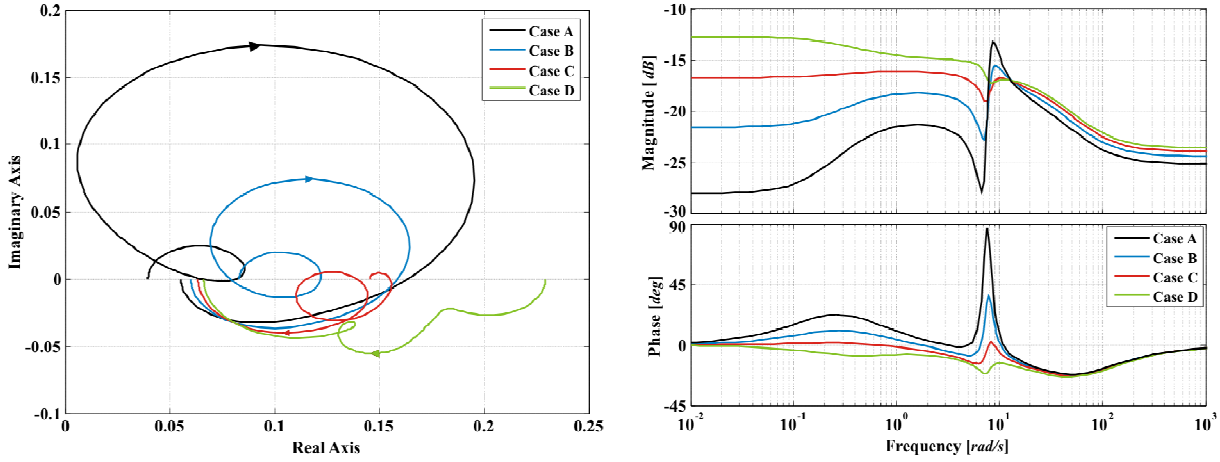

(*a*) (*b*)

Figure 6.35. Assessment of $\Gamma_3(s)$. Coupling between Individual Channels $C_2(s)$ and $C_4(s)$ from systems $\mathbf{G}_{xx24}(s)$ and $\mathbf{G}_{xx42}(s)$ (Study 2): (*a*) Nyquist plot; (*b*) Bode plot

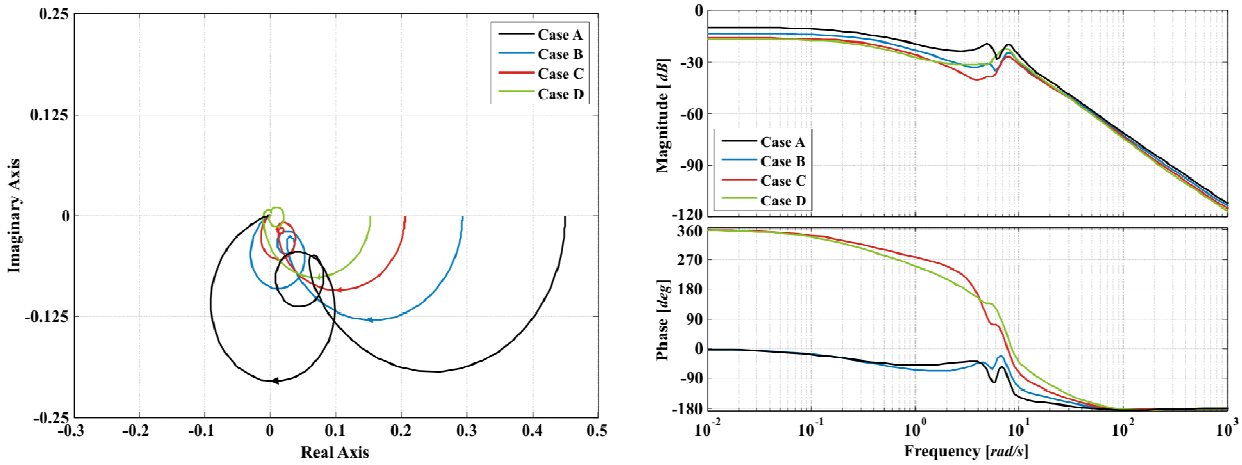

(*a*) (*b*)

Figure 6.36. Assessment of $\Gamma_3(s)$. Coupling between Individual Channels $C_3(s)$ and $C_4(s)$ from systems $\mathbf{G}_{xx34}(s)$ and $\mathbf{G}_{xx43}(s)$ (Study 2): (*a*) Nyquist plot; (*b*) Bode plot

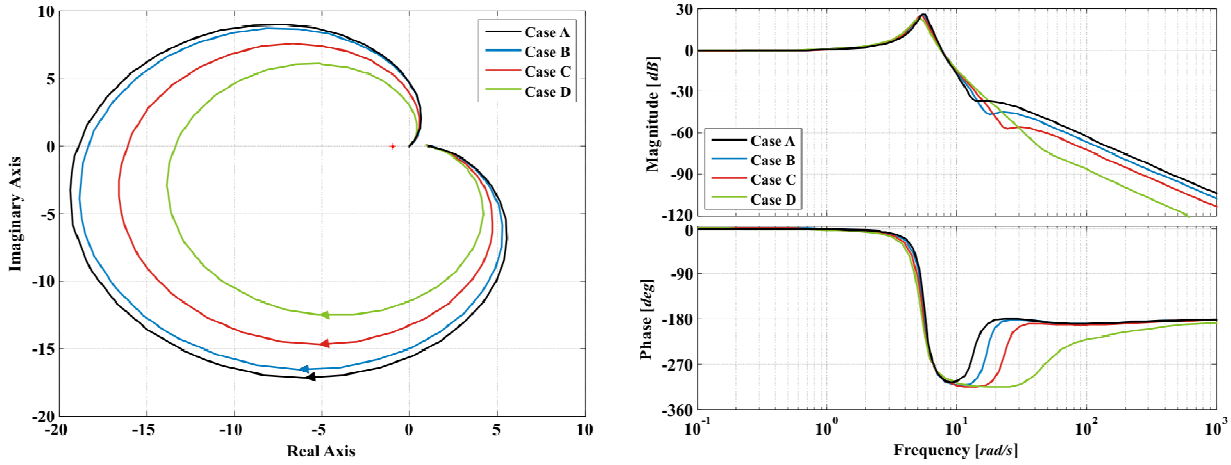

(*a*) (*b*)

Figure 6.37. Assessment of $\Gamma_2(s)$. Coupling between Individual Channel $C_1(s)$ and Multiple Channel $\mathbf{M}_{23}(s)$ from systems $\mathbf{G}_{4123}(s)$ and $\mathbf{G}_{4132}(s)$ (Study 2): (*a*) Nyquist plot; (*b*) Bode plot

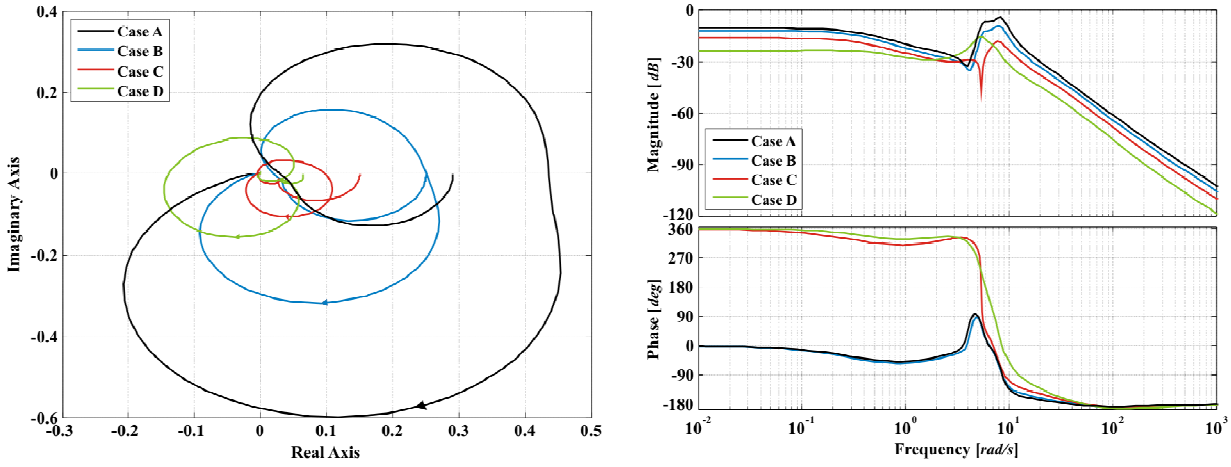

(*a*) (*b*)

Figure 6.38. Assessment of $\Gamma_2(s)$. Coupling between Individual Channel $C_1(s)$ and Multiple Channel $\mathbf{M}_{24}(s)$ from systems $\mathbf{G}_{3124}(s)$ and $\mathbf{G}_{3142}(s)$ (Study 2): (*a*) Nyquist plot; (*b*) Bode plot

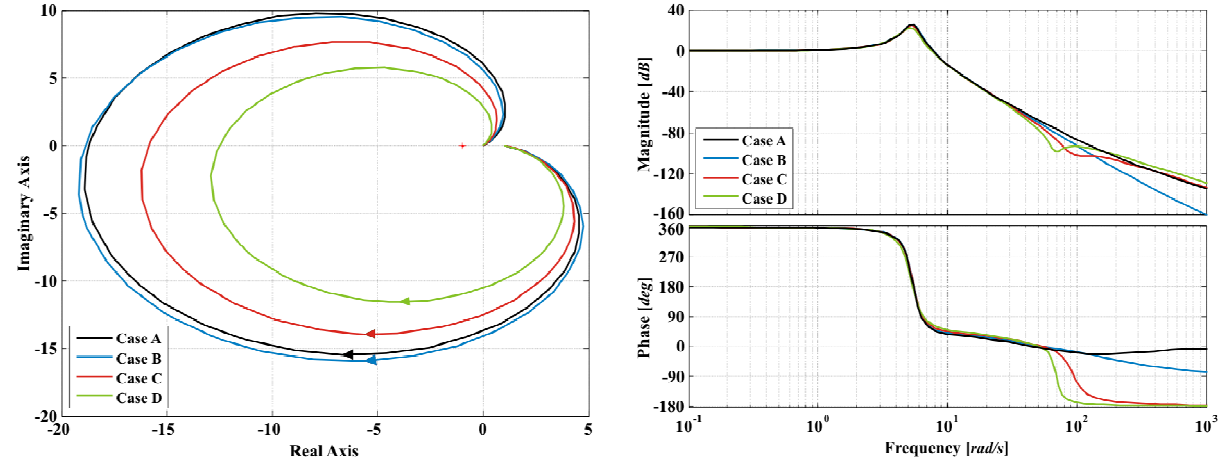

(*a*) (*b*)

Figure 6.39. Assessment of $\Gamma_2(s)$. Coupling between Individual Channel $C_1(s)$ and Multiple Channel $\mathbf{M}_{34}(s)$ from systems $\mathbf{G}_{2134}(s)$ and $\mathbf{G}_{2143}(s)$ (Study 2): (*a*) Nyquist plot; (*b*) Bode plot

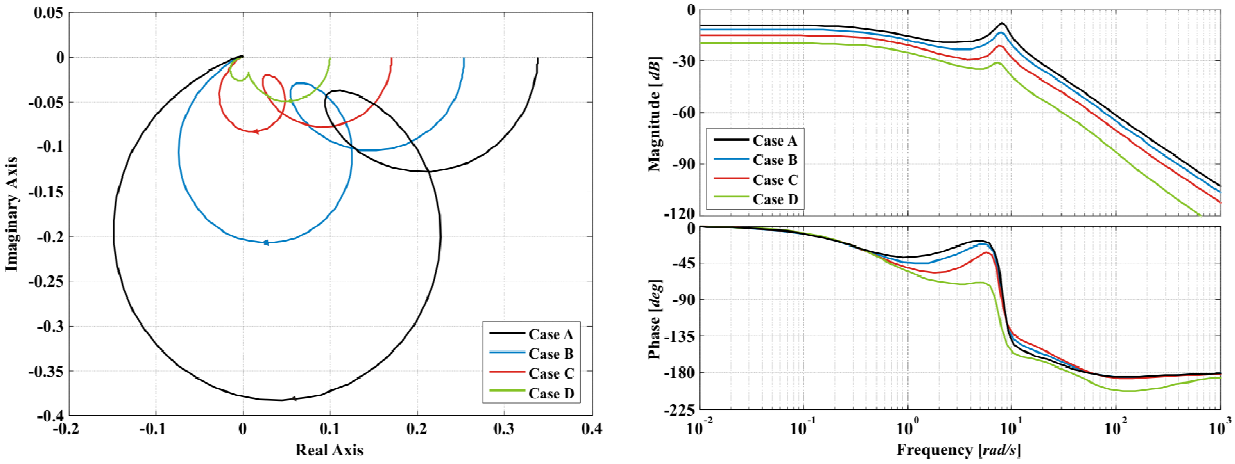

(*a*) (*b*)

Figure 6.40. Assessment of $\Gamma_2(s)$. Coupling between Individual Channel $C_2(s)$ and Multiple Channel $\mathbf{M}_{13}(s)$ from systems $\mathbf{G}_{4213}(s)$ and $\mathbf{G}_{4231}(s)$ (Study 2): (*a*) Nyquist plot; (*b*) Bode plot

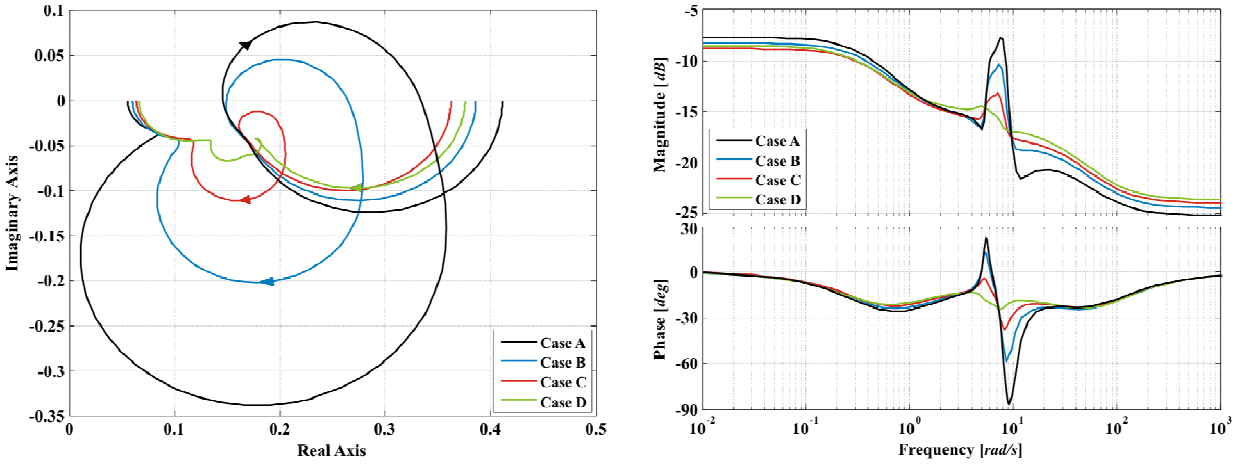

(*a*) (*b*)

Figure 6.41. Assessment of $\Gamma_2(s)$. Coupling between Individual Channel $C_2(s)$ and Multiple Channel $\mathbf{M}_{14}(s)$ from systems $\mathbf{G}_{3214}(s)$ and $\mathbf{G}_{3241}(s)$ (Study 2): (*a*) Nyquist plot; (*b*) Bode plot

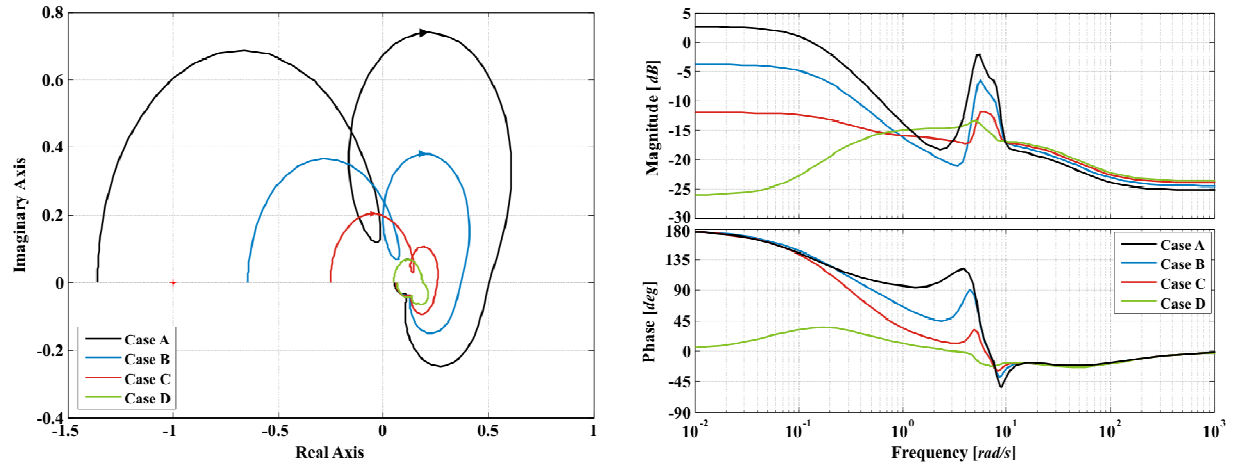

(*a*) (*b*)

Figure 6.42. Assessment of $\Gamma_2(s)$. Coupling between Individual Channel $C_2(s)$ and Multiple Channel $\mathbf{M}_{34}(s)$ from systems $\mathbf{G}_{1234}(s)$ and $\mathbf{G}_{1243}(s)$ (Study 2): (*a*) Nyquist plot; (*b*) Bode plot

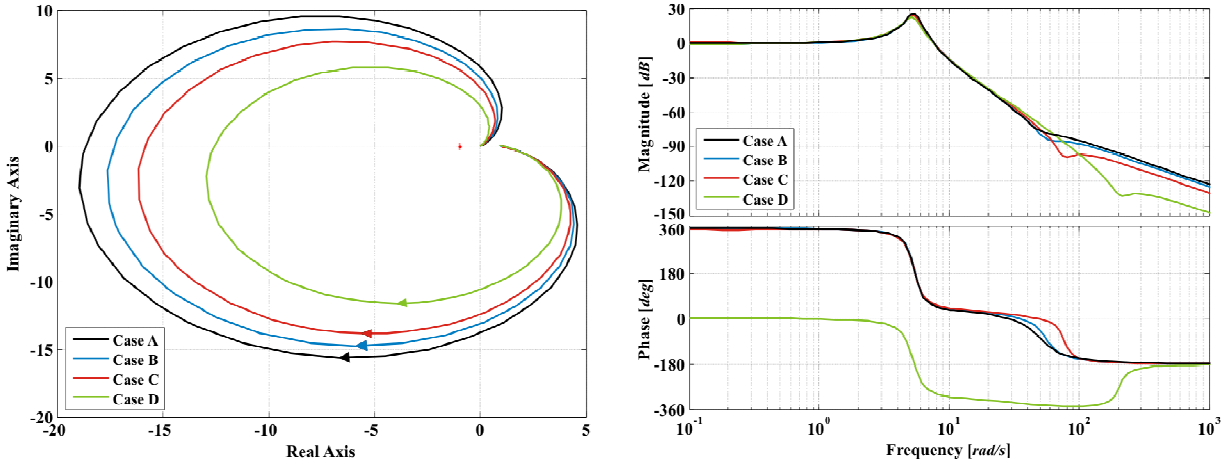

(*a*) (*b*)

Figure 6.43. Assessment of $\Gamma_2(s)$. Coupling between Individual Channel $C_3(s)$ and Multiple Channel $\mathbf{M}_{12}(s)$ from systems $\mathbf{G}_{4312}(s)$ and $\mathbf{G}_{4321}(s)$ (Study 2): (*a*) Nyquist plot; (*b*) Bode plot

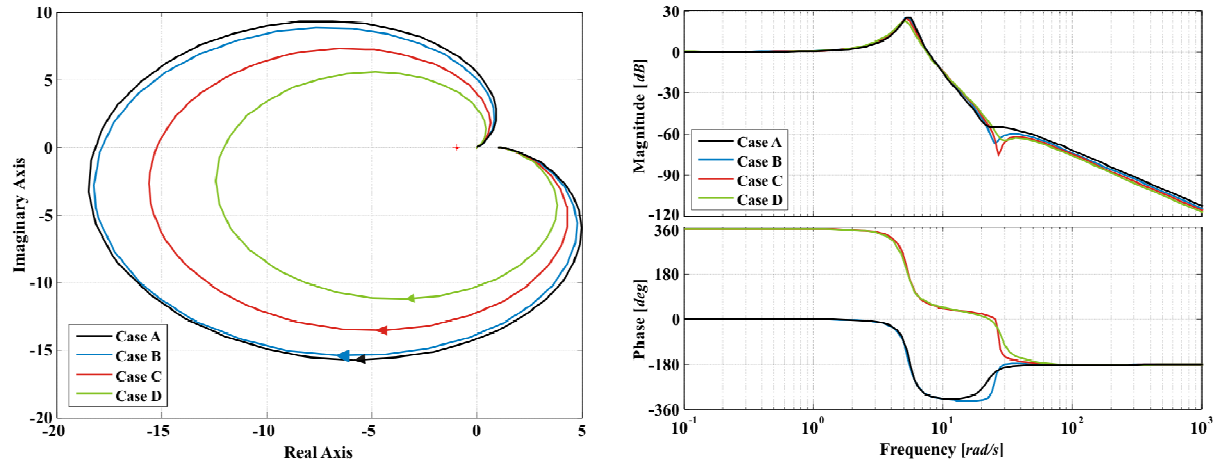

(*a*) (*b*)

Figure 6.44. Assessment of $\Gamma_2(s)$. Coupling between Individual Channel $C_3(s)$ and Multiple Channel $\mathbf{M}_{14}(s)$ from systems $\mathbf{G}_{2314}(s)$ and $\mathbf{G}_{2341}(s)$ (Study 2): (*a*) Nyquist plot; (*b*) Bode plot

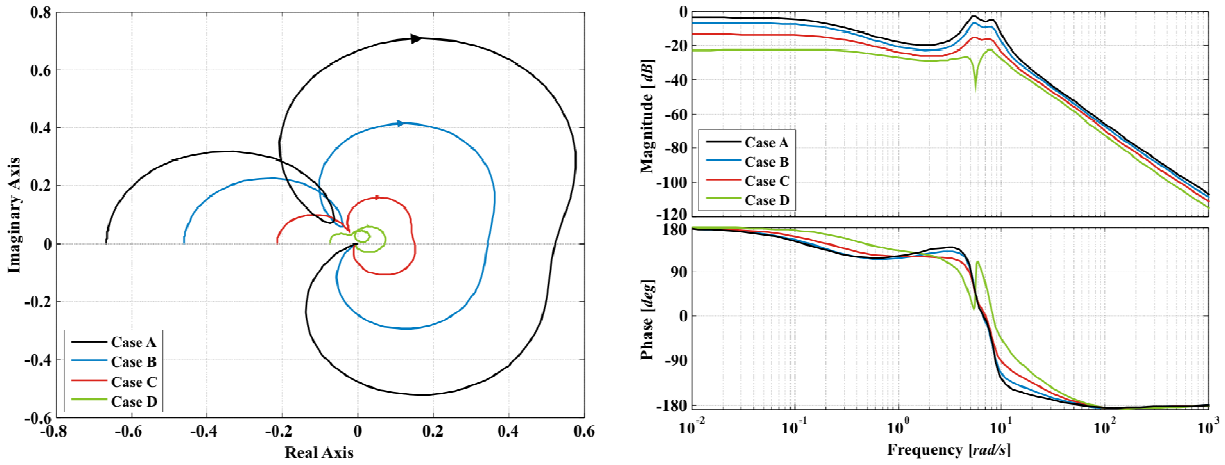

(*a*) (*b*)

Figure 6.45. Assessment of $\Gamma_2(s)$. Coupling between Individual Channel $C_3(s)$ and Multiple Channel $\mathbf{M}_{24}(s)$ from systems $\mathbf{G}_{1324}(s)$ and $\mathbf{G}_{1342}(s)$ (Study 2): (*a*) Nyquist plot; (*b*) Bode plot

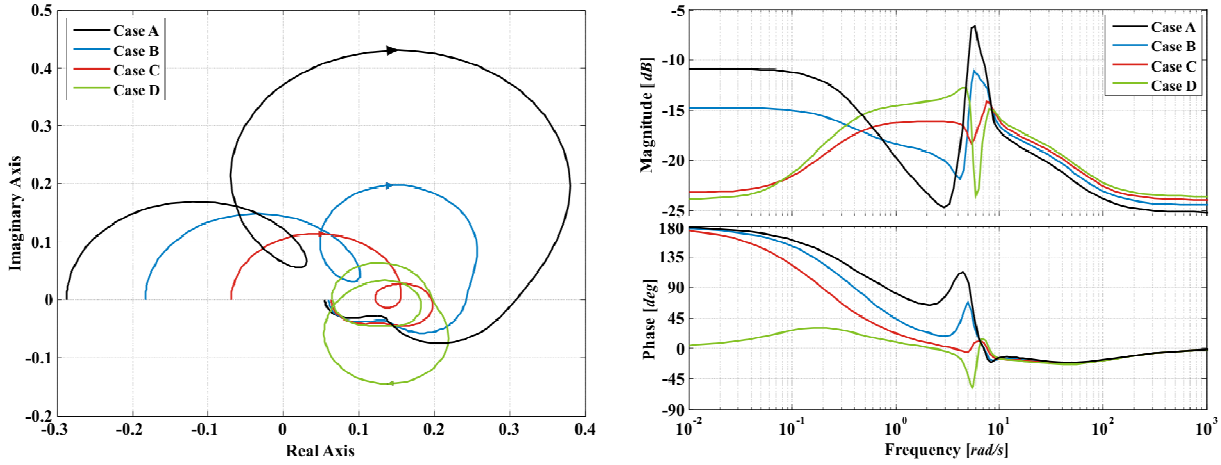

(*a*) (*b*)

Figure 6.46. Assessment of $\Gamma_2(s)$. Coupling between Individual Channel $C_4(s)$ and Multiple Channel $\mathbf{M}_{12}(s)$ from systems $\mathbf{G}_{3412}(s)$ and $\mathbf{G}_{3421}(s)$ (Study 2): (*a*) Nyquist plot; (*b*) Bode plot

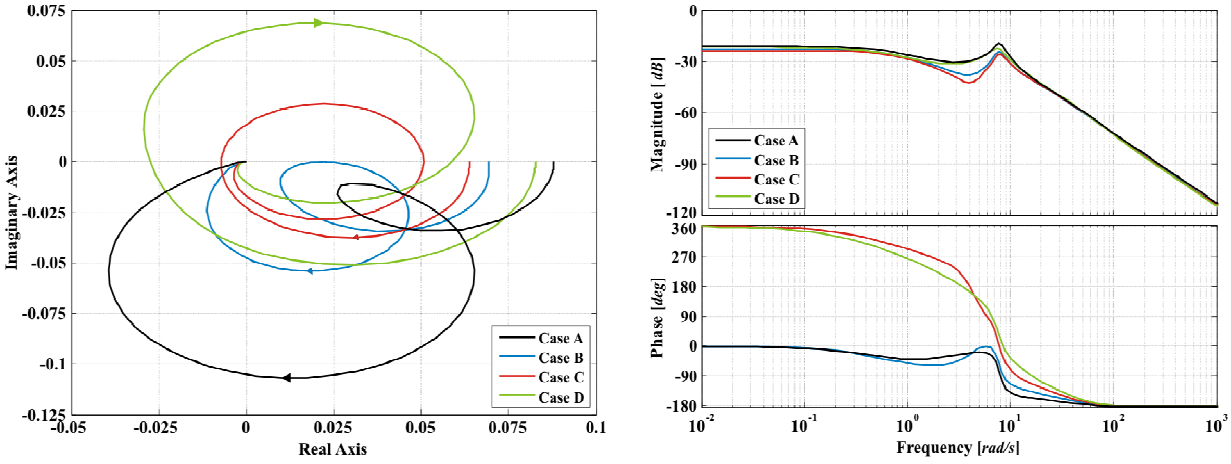

(*a*) (*b*)

Figure 6.47. Assessment of $\Gamma_2(s)$. Coupling between Individual Channel $C_4(s)$ and Multiple Channel $\mathbf{M}_{13}(s)$ from systems $\mathbf{G}_{2413}(s)$ and $\mathbf{G}_{2431}(s)$ (Study 2): (*a*) Nyquist plot; (*b*) Bode plot

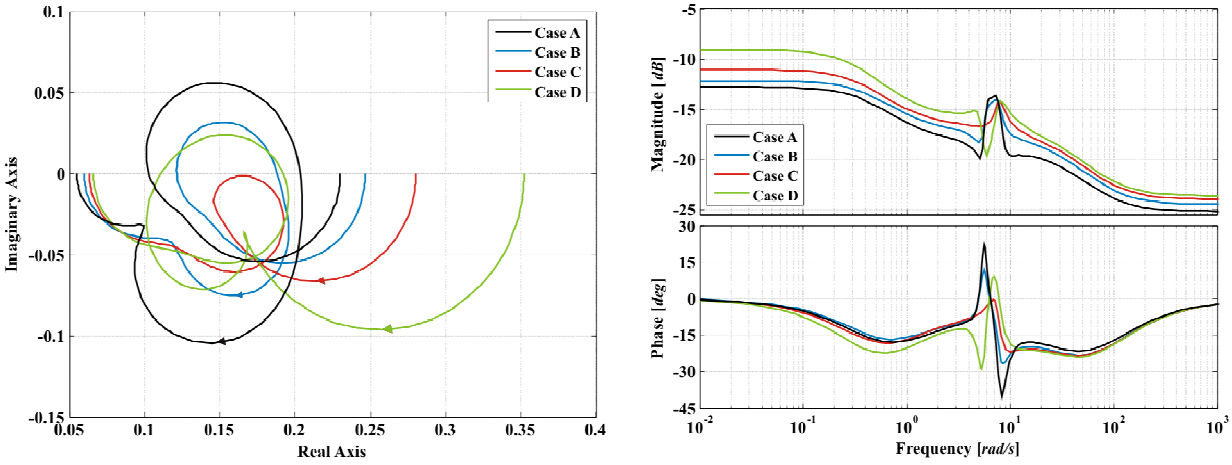

(*a*) (*b*)

Figure 6.48. Assessment of $\Gamma_2(s)$. Coupling between Individual Channel $C_4(s)$ and Multiple Channel $\mathbf{M}_{23}(s)$ from systems $\mathbf{G}_{1423}(s)$ and $\mathbf{G}_{1432}(s)$ (Study 2): (*a*) Nyquist plot; (*b*) Bode plot

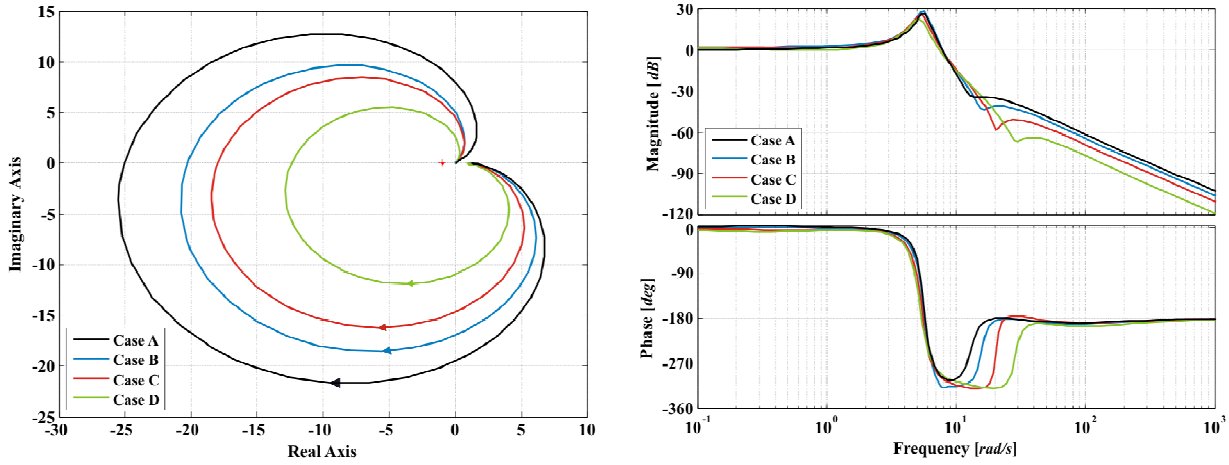

(*a*) (*b*)

Figure 6.49. Assessment of $\Gamma_1(s)$. Coupling between Individual Channel $C_1(s)$ and Multiple Channel $\mathbf{M}_{234}(s)$ from systems $\mathbf{G}_{1xxx}(s)$ (Study 2): (*a*) Nyquist plot; (*b*) Bode plot

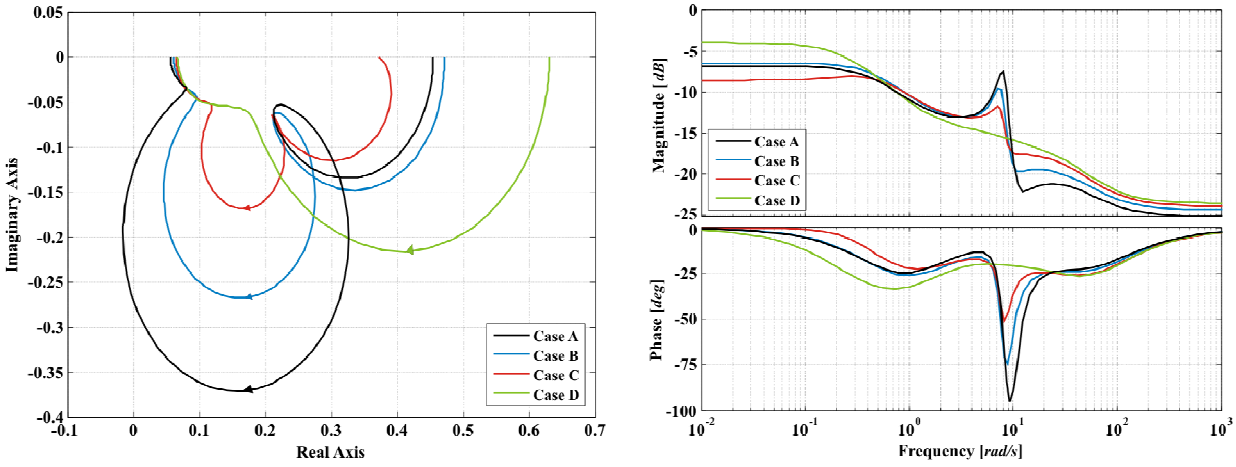

(*a*) (*b*)

Figure 6.50. Assessment of $\Gamma_1(s)$. Coupling between Individual Channel $C_2(s)$ and Multiple Channel $\mathbf{M}_{134}(s)$ from systems $\mathbf{G}_{2xxx}(s)$ (Study 2): (*a*) Nyquist plot; (*b*) Bode plot

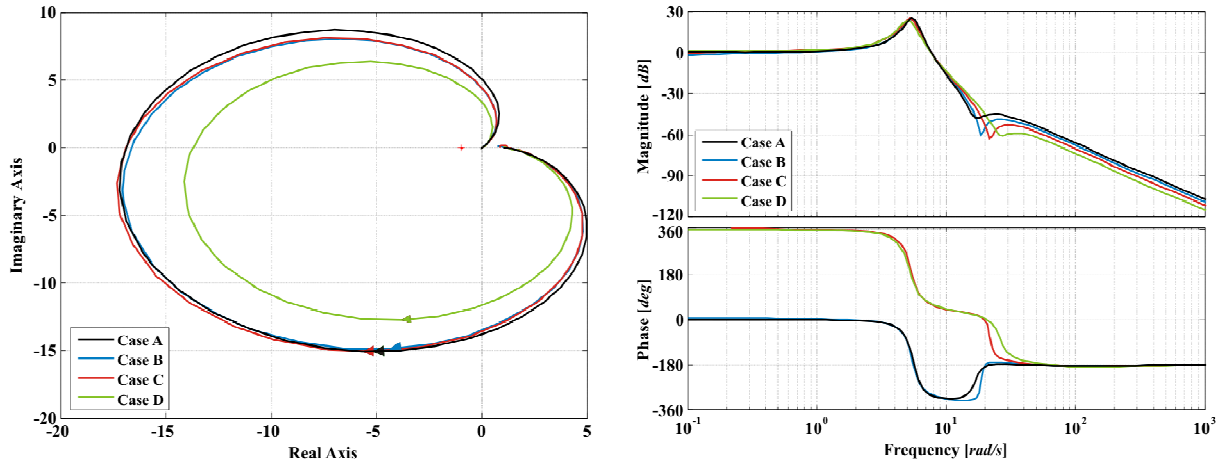

(*a*) (*b*)

Figure 6.51. Assessment of $\Gamma_1(s)$. Coupling between Individual Channel $C_3(s)$ and Multiple Channel $\mathbf{M}_{124}(s)$ from systems $\mathbf{G}_{3xxx}(s)$ (Study 2): (*a*) Nyquist plot; (*b*) Bode plot

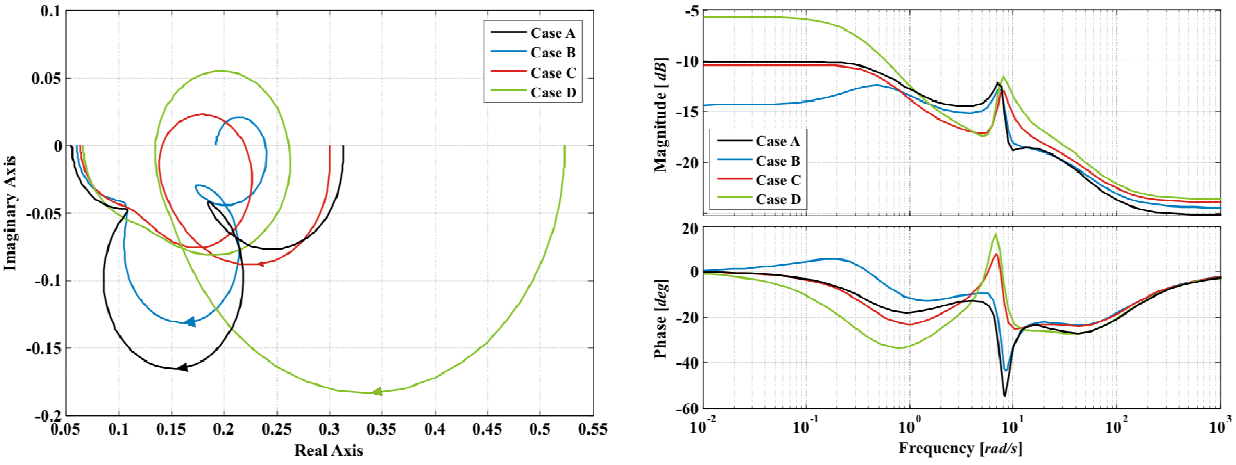

(*a*) (*b*)

Figure 6.52. Assessment of $\Gamma_1(s)$. Coupling between Individual Channel $C_4(s)$ and Multiple Channel $\mathbf{M}_{123}(s)$ from systems $\mathbf{G}_{4xxx}(s)$ (Study 2): (*a*) Nyquist plot; (*b*) Bode plot

The following remarks can be made after analysing MSFs $\Gamma_3(s)$ of Figures 6.31–6.36:

- Coupling between the electrical ($C_1(s)$) and mechanical ($C_2(s)$) individual channels of Machine 1 and the electrical ($C_3(s)$) and mechanical ($C_4(s)$) individual channels of Machine 2 is relatively low (below –5 *dB*) and decreases with a reduction in system loading, as shown by Figures 6.31 and 6.36.
- Coupling between the electrical individual channel of one machine with the mechanical individual channel of the other machine is relatively low (less than 0 *dB*); it decreases further with a decrease in system loading (that is $C_1(s)$ and $C_4(s)$ or $C_2(s)$ and $C_3(s)$), as evidenced by Figures 6.33 and 6.34. Notice that the exception is Case A in Figure 6.34, which shows considerable coupling at low frequencies.
- Coupling between the electrical individual channels ($C_2(s)$ and $C_4(s)$) of the two machines is low (below –12 *dB*); however, it increases with a reduction in system loading, as shown in Figure 6.35.
- Coupling between the mechanical individual channels ($C_1(s)$ and $C_3(s)$) of the two machines is high particularly at frequencies in the range 2–8 *rad/s* (up to 25 *dB*); however, it decreases with a reduction in system loading, as shown in Figure 6.32. It can be observed that these MSFs start close to the point (1,0), indicating high coupling at static-stationary-state; moreover, $\mathbf{G}(s)$ at $s = 0$ is singular.

The following conclusions are arrived at from the analysis of MSFs $\Gamma_2(s)$ of Figures 6.37–6.48:

- Coupling between any of the mechanical individual channels (that is, $C_1(s)$ or $C_3(s)$) and any multiple channel formed by a mechanical and an electric channel, either from the same or different machine, is high at frequencies in the range 2–8 *rad/s* (let say, between $C_1(s)$ and $\mathbf{M}_{23}(s)$ or $\mathbf{M}_{34}(s)$). However, coupling decreases with a reduction in system loading, as shown in Figures

6.37, 6.39, 6.43 and 6.44. In such cases, it is noticed that the MSFs start close to the point (1,0), indicating high coupling at static-stationary-state; moreover, $\mathbf{G}(s)$ at $s = 0$ is singular.

- Coupling between any of the electrical individual channels (that is, $C_2(s)$ or $C_4(s)$) and any multiple channel formed by a mechanical and an electric channel, either from the same or different machine, remains relatively low (less than –3 *dB*) for different loading conditions (*e.g.*, between $C_2(s)$ and $\mathbf{M}_{14}(s)$ or $\mathbf{M}_{34}(s)$), as it can be appreciated in Figures 6.41, 6.42, 6.46 and 6.48.
- Coupling between any of the mechanical individual channels ($C_1(s)$ or $C_3(s)$) and a multiple channel formed by the electrical individual channels ($C_2(s)$ and $C_4(s)$) is relatively small –below 0 dB–; coupling decreases as the system loading decreases, as evidenced by Figures 6.38 and 6.45.
- Coupling between any of the electrical individual channels ($C_2(s)$ or $C_4(s)$) and a multiple channel formed by the mechanical individual channels ($C_1(s)$ and $C_3(s)$) is relatively low (below –5 *dB*), and decreases with a reduction in system loading, as observed in Figures 6.40 and 6.47.

Careful scrutiny of the MSFs $\Gamma_1(s)$ of Figures 6.49–6.52 shows that

- Coupling between any of the electrical individual channels ($C_2(s)$ or $C_4(s)$) and the multiple channel formed by the remaining three other channels is relatively small for all system loading conditions, with higher values at low frequencies, as shown by Figures 6.50 and 6.52.
- Coupling between any of the mechanical individual channels ($C_1(s)$ or $C_3(s)$) and the multiple channel formed by the remaining three other channels is high at frequencies in the range 2–8 *rad/s* (up to 30 *dB*); coupling decreases with a decrease in system loading, as shown by Figures 6.49 and 6.51. It can be observed that these MSFs start close to the point (1,0), indicating high coupling at static-stationary-state; moreover, $\mathbf{G}(s)$ at $s = 0$ is singular.

From the previous analysis, it can be observed that the two-machine system is a highly coupled multivariable system regardless of system loading – particularly at low frequencies over the range of interest of 1–10 *rad/s*; with a decrease of coupling for small system loads. As in Study 1, the coupling between mechanical individual channels is strong, whereas the coupling between electrical subsystems is weak and so it is its coupling with the mechanical subsystems. A resonant response typical of a pair of complex conjugate poles is present in most of the MSFs in the frequency range 2–8 *rad/s*, which decreases with a reduction in system loading.

The coupling characteristics between Multiple Channels $\mathbf{M}_{12}(s)$ (representing the dynamics of generator 1 under the influence of generator 2) and $\mathbf{M}_{34}(s)$ (representing the dynamics of generator 2 under the influence of generator 1) under load changes can be evaluated by the construction of matrices $\mathbf{G}^*_{11}(s)$ and $\mathbf{G}^*_{22}(s)$, as established by equations (6.7) and (6.8). A similar procedure to that followed in Study 1 is adopted, where the two-machine system (6.1) is partitioned using (6.9)–(6.13). The Bode and Nyquist plots of the diagonal elements of subsystems $\mathbf{G}_{11}(s)$, $\mathbf{G}_{22}(s)$, $\mathbf{G}^*_{11}(s)$, $\mathbf{G}^*_{22}(s)$ and their MSFs are

provided in Figures 6.53–6.56, where the system operating conditions for Case D, given in Table 6.2, are considered.

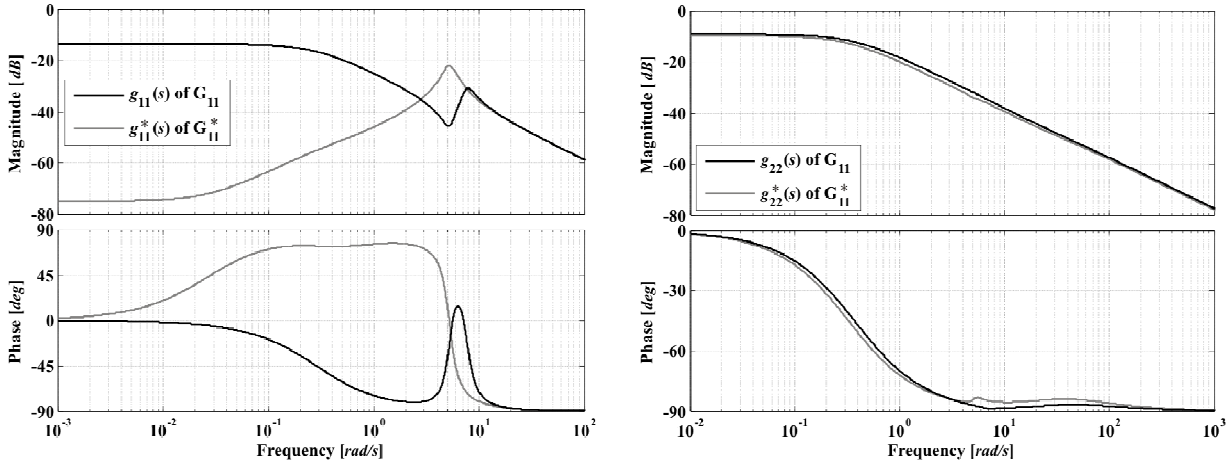

(*a*) (*b*)

Figure 6.53. Coupling assessment between Multiple Channels $\mathbf{M}_{12}(s)$ and $\mathbf{M}_{34}(s)$ (Case D, Study 2). Bode diagrams of diagonal elements of $\mathbf{G}_{11}(s)$ and $\mathbf{G}_{11}^*(s)$: (*a*) $g_{11}(s)$ and $g_{11}^*(s)$; (*b*) $g_{22}(s)$ and $g_{22}^*(s)$

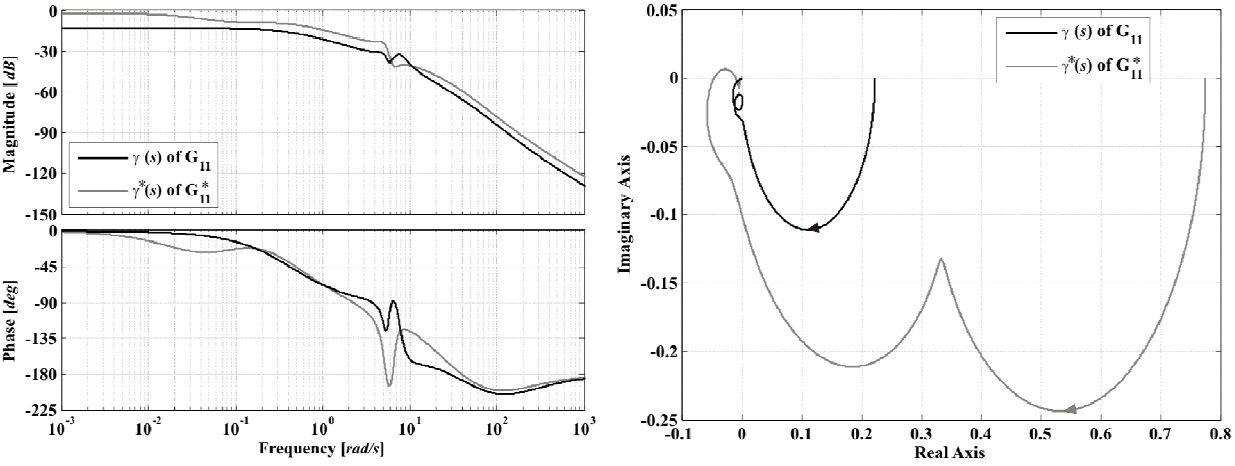

(*a*) (*b*)

Figure 6.54. Coupling assessment between Multiple Channels $\mathbf{M}_{12}(s)$ and $\mathbf{M}_{34}(s)$ (Case D, Study 2). Assessment of MSFs $\gamma(s)$ of $\mathbf{G}_{11}(s)$ and $\gamma^*(s)$ of $\mathbf{G}_{11}^*(s)$: (*a*) Bode diagrams; (*b*) Nyquist diagrams

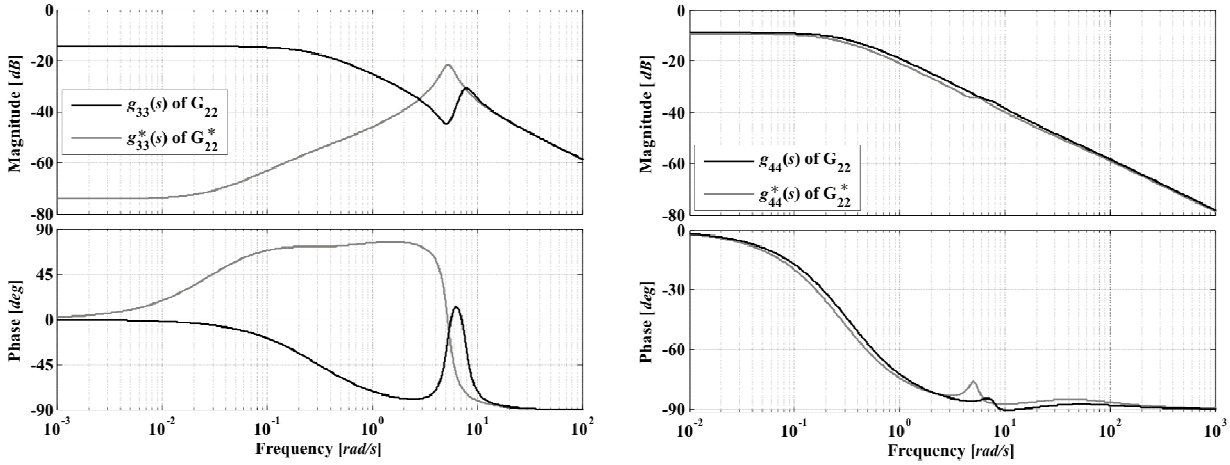

(*a*) (*b*)

Figure 6.55. Coupling assessment between Multiple Channels $\mathbf{M}_{12}(s)$ and $\mathbf{M}_{34}(s)$ (Case D, Study 2). Bode diagrams of diagonal elements of $\mathbf{G}_{22}(s)$ and $\mathbf{G}_{22}^*(s)$: (*a*) $g_{33}(s)$ and $g_{33}^*(s)$; (*b*) $g_{44}(s)$ and $g_{44}^*(s)$

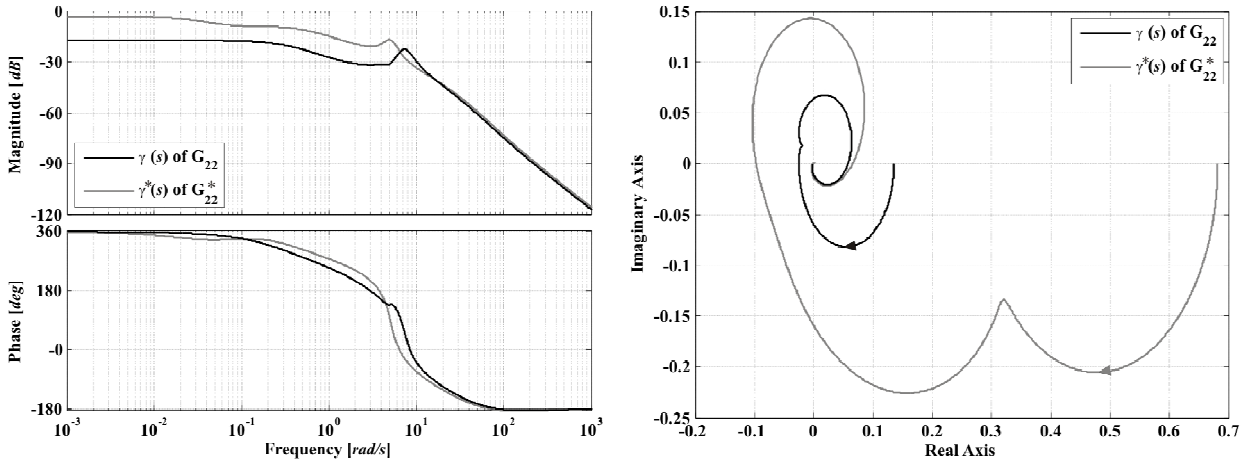

(*a*) (*b*)

Figure 6.56. Coupling assessment between Multiple Channels $\mathbf{M}_{12}(s)$ and $\mathbf{M}_{34}(s)$ (Case D, Study 2). Assessment of MSFs $\gamma(s)$ of $\mathbf{G}_{22}(s)$ and $\gamma^*(s)$ of $\mathbf{G}_{22}^*(s)$: (*a*) Bode diagrams; (*b*) Nyquist diagrams

Notice that the plots of Figures 6.53–6.56 are quite similar to those of Case 1 of Study 1 (featuring a long transmission line) given by Figures 6.27–6.30. Similar Bode and Nyquist diagrams (not shown) can be obtained for the rest of the operating conditions provided in Table 6.2. Regardless of load variations, the following points can be stated:

- Elements $g_{11}(s)$ and $g_{33}(s)$ are quite different at low frequencies from $g_{11}^*(s)$ and $g_{33}^*(s)$.
- Elements $g_{22}(s)$ and $g_{44}(s)$ are quite similar to $g_{22}^*(s)$ and $g_{44}^*(s)$; however, a distinctive difference is reflected in the switch-back characteristic associated to each of these mechanical channels of the synchronous machines, which shifts towards the lower frequencies, a fact which is more apparent in $g_{22}^*(s)$ and $g_{44}^*(s)$.
- MSFs $\gamma(s)$ associated to $\mathbf{G}_{11}(s)$ and $\mathbf{G}_{22}(s)$ are similar to those $\gamma^*(s)$ of $\mathbf{G}_{11}^*(s)$ and $\mathbf{G}_{22}^*(s)$.

Based on the previous results, it can be concluded that Multiple Channel $\mathbf{M}_{12}(s)$ cannot be designed on the basis of $\mathbf{G}_{11}^*(s)$ alone and, likewise, Multiple Channel $\mathbf{M}_{34}(s)$ cannot be designed on the basis of $\mathbf{G}_{22}^*(s)$ alone. As in Study 1, these findings support previous results obtained when analysing the MSFs $\Gamma_i(s)$ shown in Figures 6.31–6.52. The discussion in Study 1 concerning the proximity of some Nyquist trajectories of $\Gamma_i(s)$ to the point (1,0), involving the interaction of the mechanical channels (observed in Figures 6.32, 6.37, 6.39, 6.43, 6.44, 6.49 and 6.51), also applies in the current study.

It should be remarked that the results arrived at in this study are fully compatible with those obtained in Study 1. As the load decreases, the electrical subsystems tend to decouple. However, the interaction between the mechanical individual channels or any multiple channel featuring two mechanical individual channels is high. Therefore, the control system design strategy proposed previously for Study 1 also applies for Study 2.

6.4. Control system design example

The control system design of the two-machine system, given by (6.3), is made up of the following elements of the diagonal controller matrix: the turbine-governor control and the excitation control of Machine 1 corresponding to $k_{11}(s)$ and $k_{22}(s)$, respectively; and the turbine-governor control and the excitation control of Machine 2 corresponding to $k_{33}(s)$ and $k_{44}(s)$, respectively.

Following analysis of the MSFs resulting from the operating conditions given in Tables 6.1 and 6.2 and taken account of the control system design strategy described in Section 6.3.1, the diagonal controller

$$\begin{aligned}\mathbf{K_1}(s) &= \begin{bmatrix} k_{11}(s) & 0 & 0 & 0 \\ 0 & k_{22}(s) & 0 & 0 \\ 0 & 0 & k_{33}(s) & 0 \\ 0 & 0 & 0 & k_{44}(s) \end{bmatrix} \\ &= \text{diag}\left[\frac{k_{\omega 1}(s+1)}{s(s+10)}, \quad \frac{k_{et1}(s+0.4)(s+0.3)}{s(s+5)(s+0.5)}, \quad \frac{k_{\omega 2}(s+1)}{s(s+10)}, \quad \frac{k_{et2}(s+0.375)(s+0.3)}{s(s+5)(s+0.45)} \right]\end{aligned} \tag{6.14}$$

is proposed. Notice that the structure of both controllers for the mechanical channels, that is, $k_{11}(s)$ and $k_{33}(s)$, is exactly the same. On the other hand, the controllers for the electrical channels, that is, $k_{22}(s)$ and $k_{44}(s)$, differ only in the location of a zero/pole lead term. The various constants of the controller matrix are selected to meet a desired bandwidth.

Remark: The pure derivative term appearing in the transfer function matrix elements $g_{1k}(s)$ (with k = 1,2) of OMIB systems, explicitly shown in equation (3.9), disappears for multi-machine systems. This can be noticed by inspection of the transfer functions $g_{1k}(s)$ and $g_{3k}(s)$ in (6.1), with k = 1,2,3,4, for all the operating conditions given in Tables 6.1 and 6.2 (not shown). This detail has significant implications in control system design. For instance, an extra integral term had to be included in $k_{11}(s)$ of the controller (3.45) in order to counteract the derivative effect of $g_{11}(s)$, while still providing zero steady-state error. As opposed to OMIB systems, a double integral action in the controllers of the mechanical channels will destabilise the multi-machine system. In fact, the only situation where pure derivative terms could appear in a multi-machine system occurs when one machine has an infinite inertia constant H (resembling, in a way, a machine being modelled as an infinite bus), which is never the case for a practical scenario.

6.4.1. Study 1. Impact of the transmission line length

The control system design is assessed for different length values of the transmission line linking the two machines. The operating conditions for this study are given in Table 6.1. For this case, the scalar gains of the multivariable controller (6.14) are taken to be: $k_{\omega 1} = k_{\omega 2} = 100$ and $k_{et1} = k_{et2} = 90.75$. The control

system performance and stability robustness indicators are presented in Figures 6.57–6.59. The time responses shown in Figure 6.60 were obtained through a closed-loop simulation using Simulink. Key information relating to the control system design is summarised in Table 6.4.

Figure 6.57 shows the Bode diagrams of the four individual channels of the two-machine system. From Figures 6.57(*a*) and 6.57(*c*), it can be seen that the mechanical channels $C_1(s)$ and $C_3(s)$ exhibit a similar behaviour for all the operating conditions under study. A resonant characteristic of around 7 *rad/s* (after the roll-off) is present both in magnitude and phase; with the response becoming smoother with a reduction of the transmission line length. In order to achieve a successful performance featuring adequate robustness margins, this characteristic should be avoided by reducing the bandwidth of both mechanical channels to values of around 1 *rad/s*. Figures 6.57(*b*) and 6.57(*d*), give the frequency response of the electrical channels $C_2(s)$ and $C_4(s)$. It is noticed that the performance is adequate regardless of the operating condition, affording satisfactory gain and phase margins. For smaller transmission line lengths the bandwidth falls slightly. Notice that the bandwidths of the electrical subsystems could have been chosen to be higher; however, they were deliberately curtailed to avoid the frequency range where the switch-back characteristic is more pronounced.

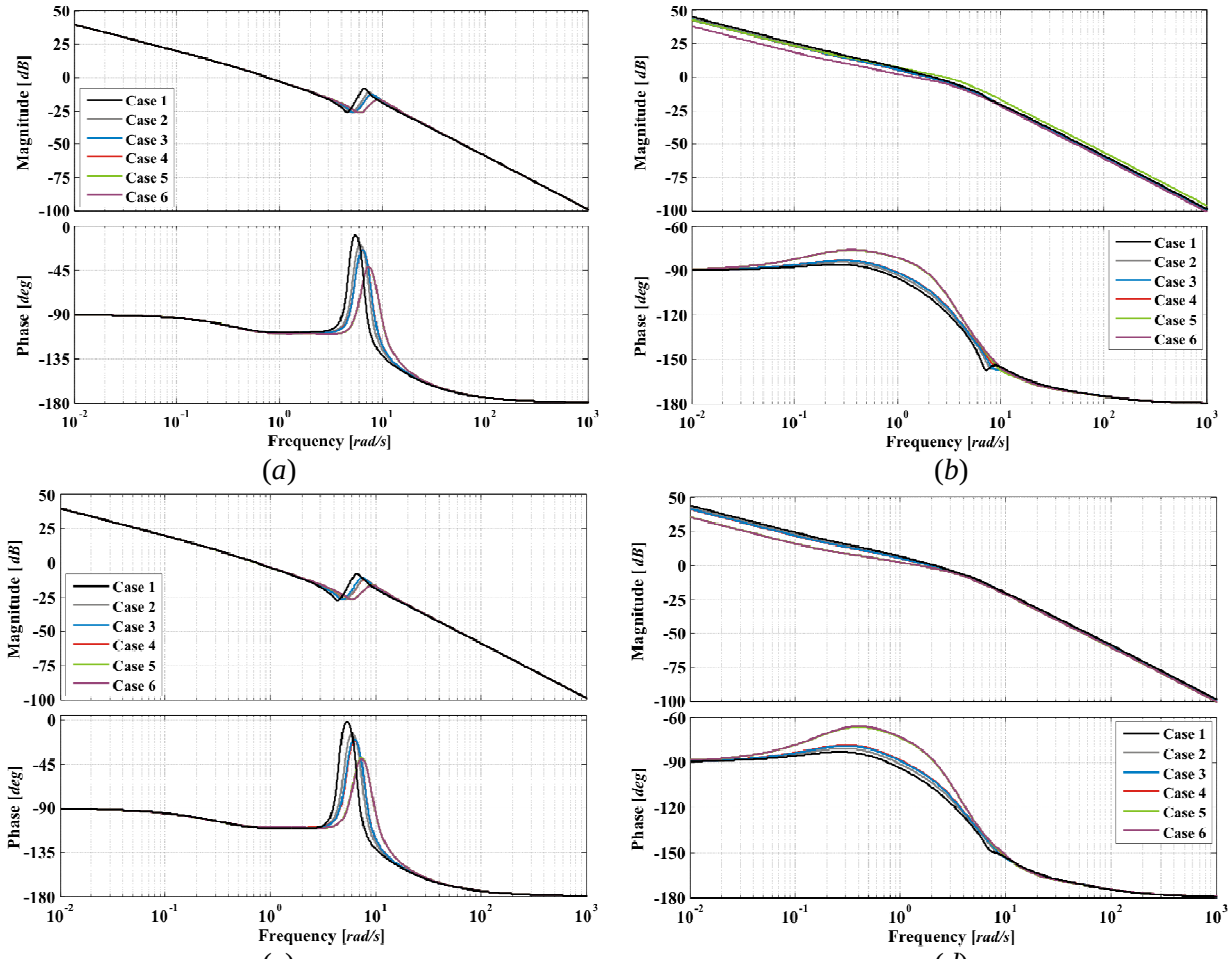

Figure 6.57. System performance and stability robustness assessment (Study 1). Bode diagrams: (*a*) Channel 1 ($C_1(s)$); (*b*) Channel 2 ($C_2(s)$); (*c*) Channel 3 ($C_3(s)$); (*d*) Channel 4 ($C_4(s)$)

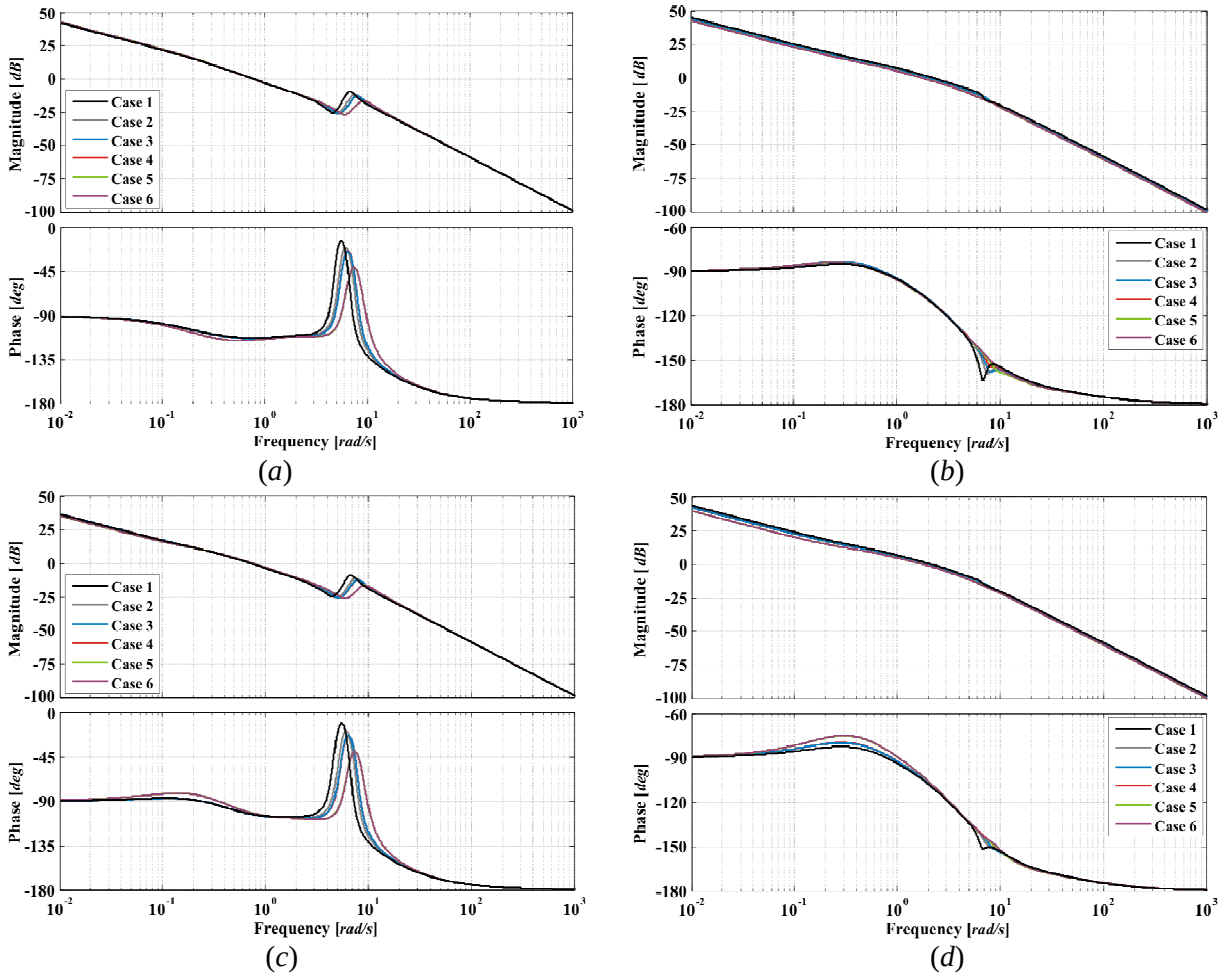

Figure 6.58. Stability robustness assessment (Study 1). Bode diagrams: (*a*) $k_{11}g_{11}(s)$; (*b*) $k_{22}g_{22}(s)$; (*c*) $k_{33}g_{33}(s)$; (*d*) $k_{44}g_{44}(s)$

Table 6.4. Structural and stability robustness of the channels and control system. Study 1.

Case	Measure	C_1	$k_{11}g_{11}$	γ_1	C_2	$k_{22}g_{22}$	γ_2	C_3	$k_{33}g_{33}$	γ_3	C_4	$k_{44}g_{44}$	γ_4
1	**Bandwidth** (*rad/s*)	1	1.02	–	3	3.04	–	0.97	0.95	–	2.87	2.91	–
	Gain margin (*dB*)	∞	∞	11.64	∞	∞	29.8	∞	∞	12.7	∞	∞	29.7
	Phase margin (*deg*)	71.9	66.8	∞	70	68.1	∞	70.3	76.9	∞	72	70.2	∞
2	**Bandwidth** (*rad/s*)	1	1.01	–	2.83	2.88	–	0.97	0.96	–	2.74	2.78	–
	Gain margin (*dB*)	∞	∞	12.35	∞	∞	21.9	∞	∞	18	∞	∞	22.6
	Phase margin (*deg*)	71.7	66.6	∞	74.3	69.6	∞	70.4	76.7	∞	76.6	72.2	∞
3	**Bandwidth** (*rad/s*)	1	1.01	–	2.73	2.79	–	0.97	0.97	–	2.66	2.71	–
	Gain margin (*dB*)	∞	∞	12.06	∞	∞	17.73	∞	∞	20.47	∞	∞	18.03
	Phase margin (*deg*)	71.7	66.4	∞	77.3	70.5	∞	70.5	76.7	∞	79.8	72.8	∞
4	**Bandwidth** (*rad/s*)	1	1.01	–	2.7	2.76	–	0.98	0.98	–	2.65	2.71	–
	Gain margin (*dB*)	∞	∞	13	∞	∞	17.56	∞	∞	24.01	∞	∞	17.41
	Phase margin (*deg*)	71.5	66.4	∞	77.9	70.8	∞	70.6	76.6	∞	80.3	72.9	∞
5	**Bandwidth** (*rad/s*)	1.01	1	–	2.27	2.41	–	0.98	0.99	–	2.36	2.43	–
	Gain margin (*dB*)	∞	∞	10.34	∞	∞	7.83	∞	∞	27.94	∞	∞	7.87
	Phase margin (*deg*)	71.2	64.7	∞	94	73.4	∞	70.8	77.9	∞	99.8	77.2	∞
6	**Bandwidth** (*rad/s*)	1.01	1	–	2.24	2.39	–	0.98	1	–	2.37	2.43	–
	Gain margin (*dB*)	∞	∞	10.44	∞	∞	7.78	∞	∞	31.37	∞	∞	7.75
	Phase margin (*deg*)	71.1	64.7	∞	94.5	73.6	∞	70.9	77.7	∞	100	77.3	∞

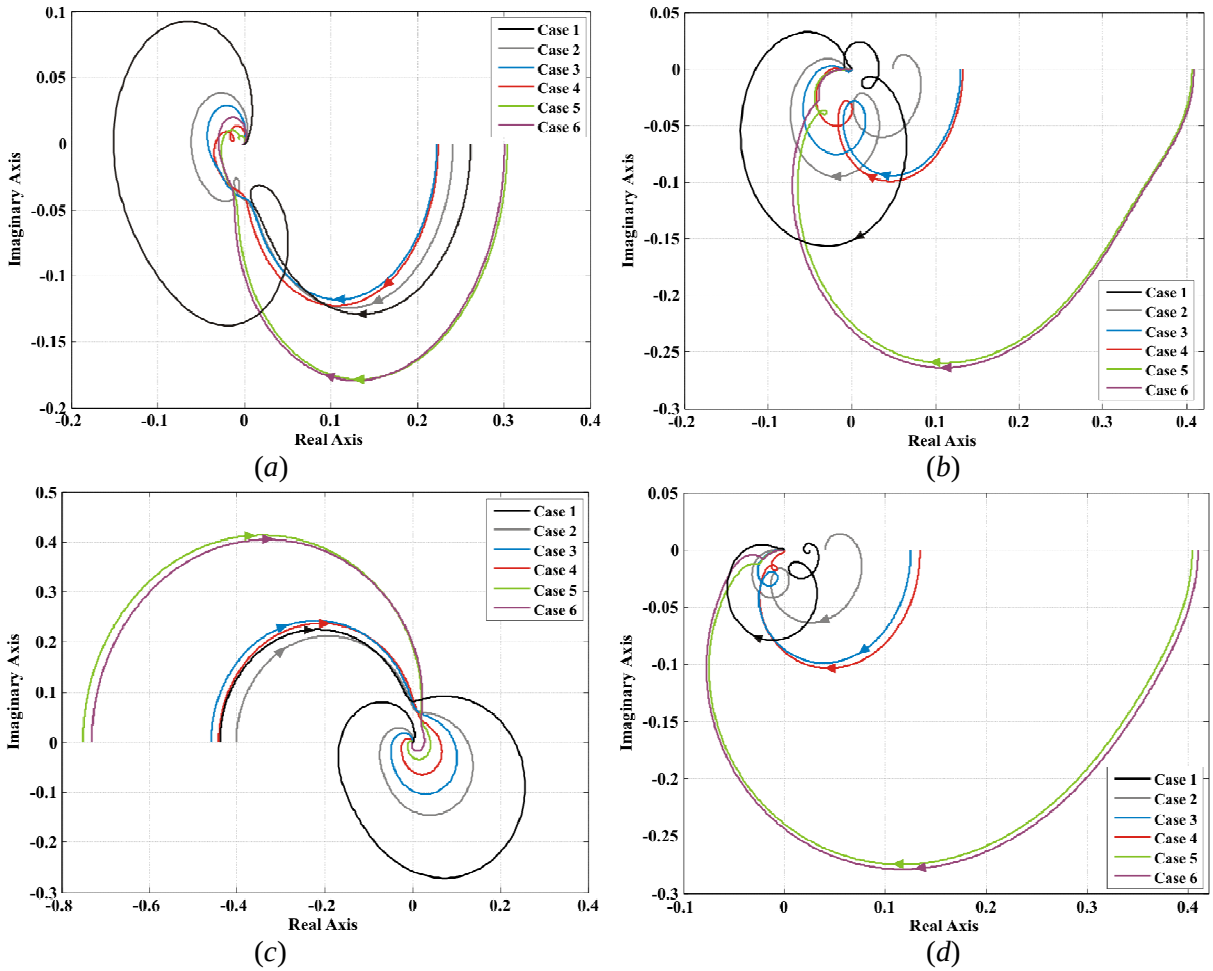

Figure 6.59. Structural robustness assessment (Study 1). Nyquist diagrams: (*a*) $\gamma_1(s)$; (*b*) $\gamma_2(s)$; (*c*) $\gamma_3(s)$; (*d*) $\gamma_4(s)$;

The structural robustness of the control system is assessed in Figures 6.58 and 6.59. Figure 6.58 shows the Bode diagrams of the individual channel subsystems $h_i(s)$. Notice that all open loop subsystems $k_{ii}g_{ii}(s)$ have similar frequency responses, with little influence from their operating points. From Figure 6.59, it can be seen that MSFs $\gamma_i(s)$ start to the left of (1,0) and do not encircle it. However, the gain margin decreases when the transmission line is shortened.

From the previous set of results it can be seen that the overall performance of the control system using the multivariable controller (6.14) is adequate, offering satisfactory robustness measures, *i.e.*, gain and phase margins over 6 *dB* and 40 *deg*, respectively [9]. This can be explored further with a closed-loop time domain simulation. Figure 6.60 shows the rotor speed and terminal voltage responses of the two synchronous generators to changes in their references. Starting from the steady-state, a step change of 0.05 *p.u.* at a time t = 10 *s* is applied to the terminal voltage Δe_{t1} of Machine 1, as shown in Figure 6.60(*b*). As it can be seen, the terminal voltage Δe_{t2} of Machine 2 undergoes a small transient but returns to the original steady-state value, as shown in Figure 6.60(*d*). Then, at a time t = 30 *s*, a step change of 0.05 *p.u.* takes place in the terminal voltage Δe_{t2}, producing a similar transient effect in Δe_{t1}. The little influence that a step change in one terminal voltage has in the other electrical channel is consistent with

the information provided by the MSFs $\Gamma_3(s)$ of Figure 6.8. It can be noticed that the step changes in the electrical channels have practically no effect in the mechanical channels, as it can be observed in Figures 6.60(*a*) and 6.60(*c*); this behaviour is consistent with the information arising from the analysis of the MSFs $\Gamma_3(s)$ of Figures 6.4, 6.6, 6.7 and 6.9. To complete the test, a step change of 0.1 *Hz* is applied at a time t = 50 *s* in both of the speed references $\Delta\omega_1$ and $\Delta\omega_2$ – since both mechanical channels are strongly coupled (as evidenced by the MSFs $\Gamma_3(s)$ in Figure 6.5), an equal response takes place in both channels. It can be observed in Figures 6.60(*b*) and 6.60(*d*) that the step changes in the mechanical channels have no discerning effect in the electrical channels. Moreover, the time responses of the mechanical channels are quite similar for all the operating conditions considered in Study 1. On the other hand, the time responses of the electrical channels are marginally better for higher values of transmission line lengths.

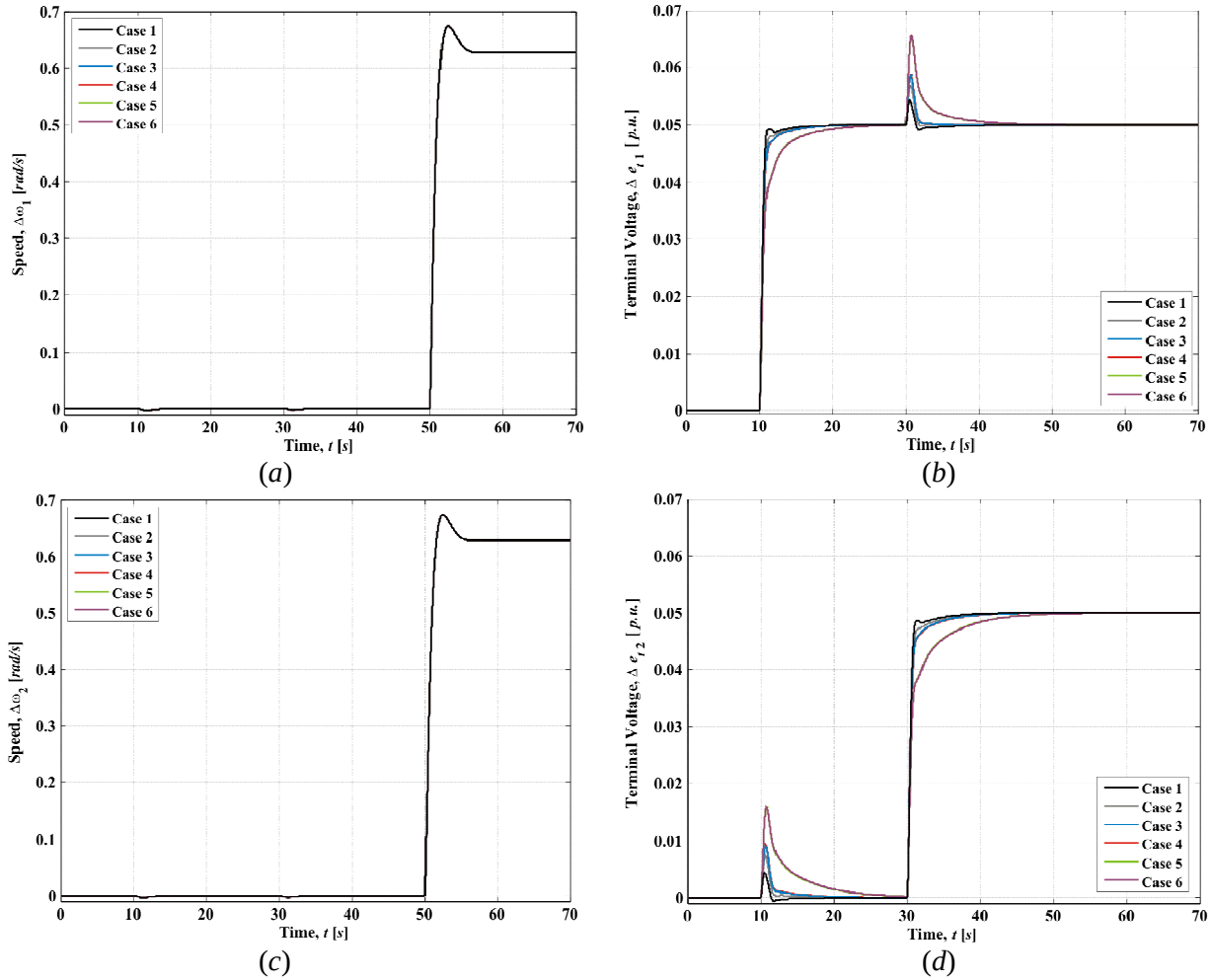

Figure 6.60. System performance (Study 1). Time response: (*a*) Channel 1 ($\Delta\omega_1$); (*b*) Channel 2 (Δe_{t1}); (*c*) Channel 3 ($\Delta\omega_2$); (*d*) Channel 4 (Δe_{t2})

In summary, the results obtained in Figure 6.60 are consistent with the multivariable analysis presented in Section 6.3: coupling between the electric channels is weak and increases with a decrease of the transmission line impedance; coupling between the electrical and the mechanical channels is weak; and coupling between the mechanical channels is strong.

Figure 6.61 shows a complementary closed-loop simulation, in which step changes to the speed references occur at different times. The gray solid line shows the desired reference for each individual channel. The references of both electrical channels remain unchanged at zero during the whole of the simulation.

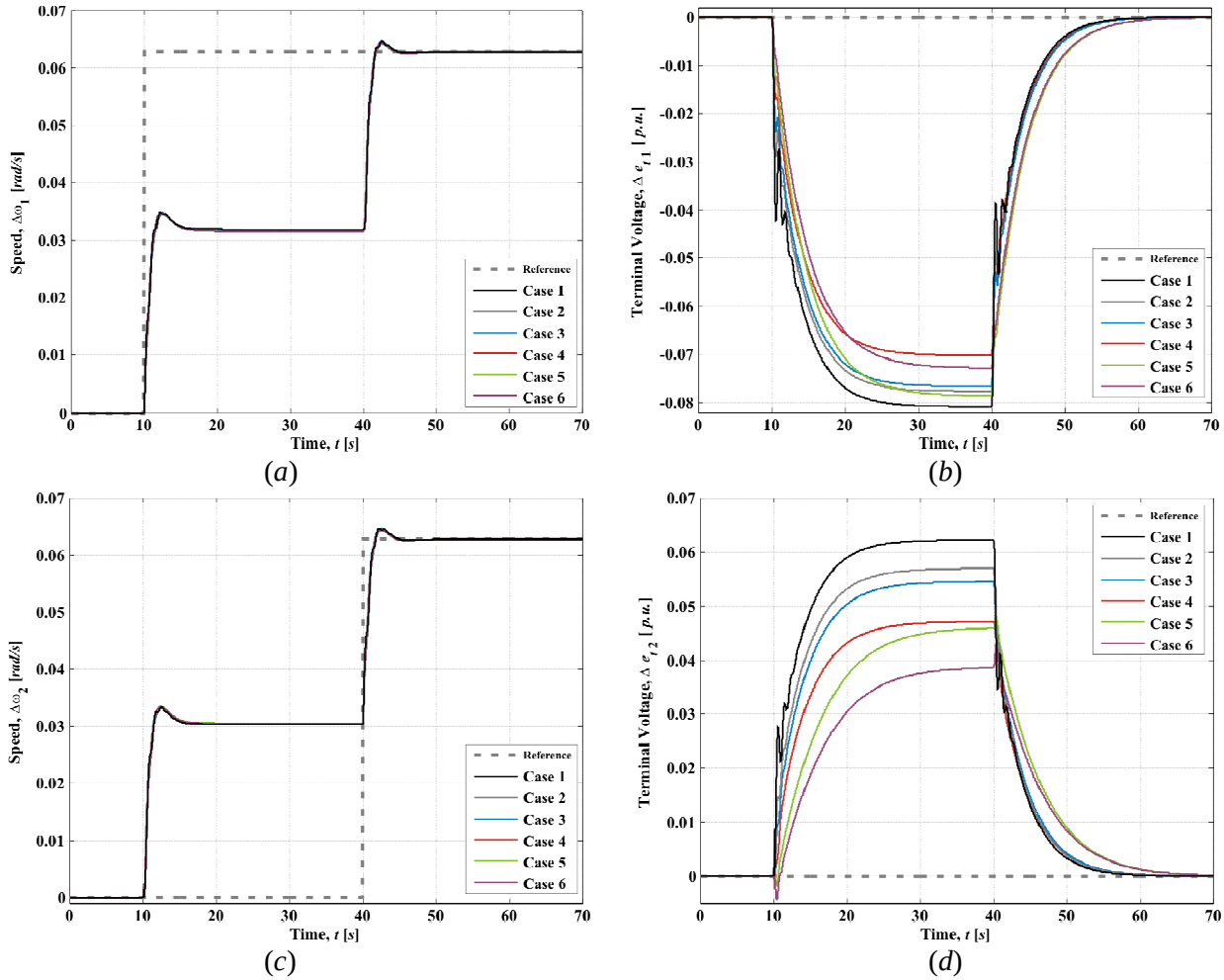

Figure 6.61. System performance 2 (Study 1). Time response: (*a*) Channel 1 ($\Delta\omega_1$); (*b*) Channel 2 (Δe_{t1}); (*c*) Channel 3 ($\Delta\omega_2$); (*d*) Channel 4 (Δe_{t2})

Starting from the steady-state, a step change of 0.01 *Hz* at a time t = 10 *s* is applied to the speed reference $\Delta\omega_1$ of Machine 1 (as shown in Figure 6.61(*a*)), while keeping the speed reference $\Delta\omega_2$ of Machine 2 unchanged (Figure 6.61(*c*)). It can be noticed that the output speed of both machines is modified and reaches a steady-state, but does not match the given references. Moreover, the terminal voltages Δe_{t1} of Machine 1 and Δe_{t2} of Machine 2, shown in Figure 6.61(*b*) and Figure 6.61(*d*), respectively, undergo a transient response causing terminal voltages different from the original zero reference. The mismatch in the terminal voltages decreases with a reduction in the tie-line length. Then, at a time t = 40 *s*, a step change of 0.01 *Hz* takes place in the speed reference $\Delta\omega_2$, matching the reference value of $\Delta\omega_1$, as shown in Figures 6.61(*a*) and 6.61(*c*). It is seen that all channels follow correctly their given references after a transient period. The plant response is due to the occurrence of transmission zeros

near the origin and the fact that several MSFs $\Gamma_i(s)$ (given in Figures 6.5, 6.10, 6.12, 6.16, 6.17, 6.22 and 6.24) pass close to the point (1,0). It can be seen that step changes in speed should happen simultaneously and equally, enabling the overall control system to reach the desired references.

6.4.2. Study 2. Impact of the system loading

In this section, the control system design of the two-machine system is evaluated for different system loading conditions. All data pertaining to this study is provided in Tables 6.2 and 6.3 and the scalar gains of the multivariable controller (6.14) are similar to those of Study 1, *i.e.*, $k_{\omega 1} = k_{\omega 2} = 100$ and $k_{et1} = k_{et2} = 90.75$. The control system performance and stability robustness indicators are given in Figures 6.62–6.64 and the closed-loop time-domain simulation results are provided in Figures 6.65 and 6.66. All relevant information associated to the control system design is summarised in Table 6.5.

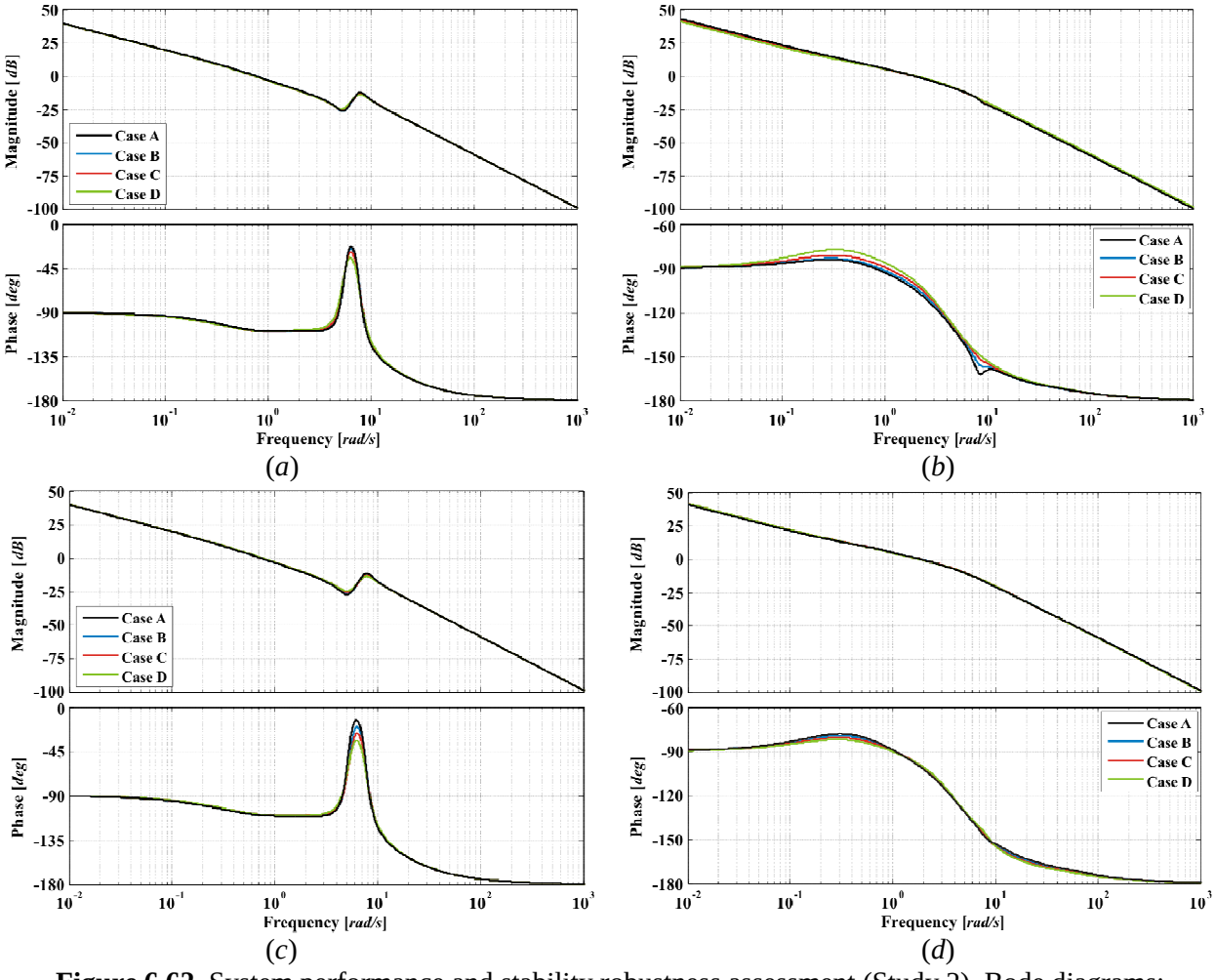

Figure 6.62. System performance and stability robustness assessment (Study 2). Bode diagrams: (*a*) Channel 1 ($C_1(s)$); (*b*) Channel 2 ($C_2(s)$); (*c*) Channel 3 ($C_3(s)$); (*d*) Channel 4 ($C_4(s)$)

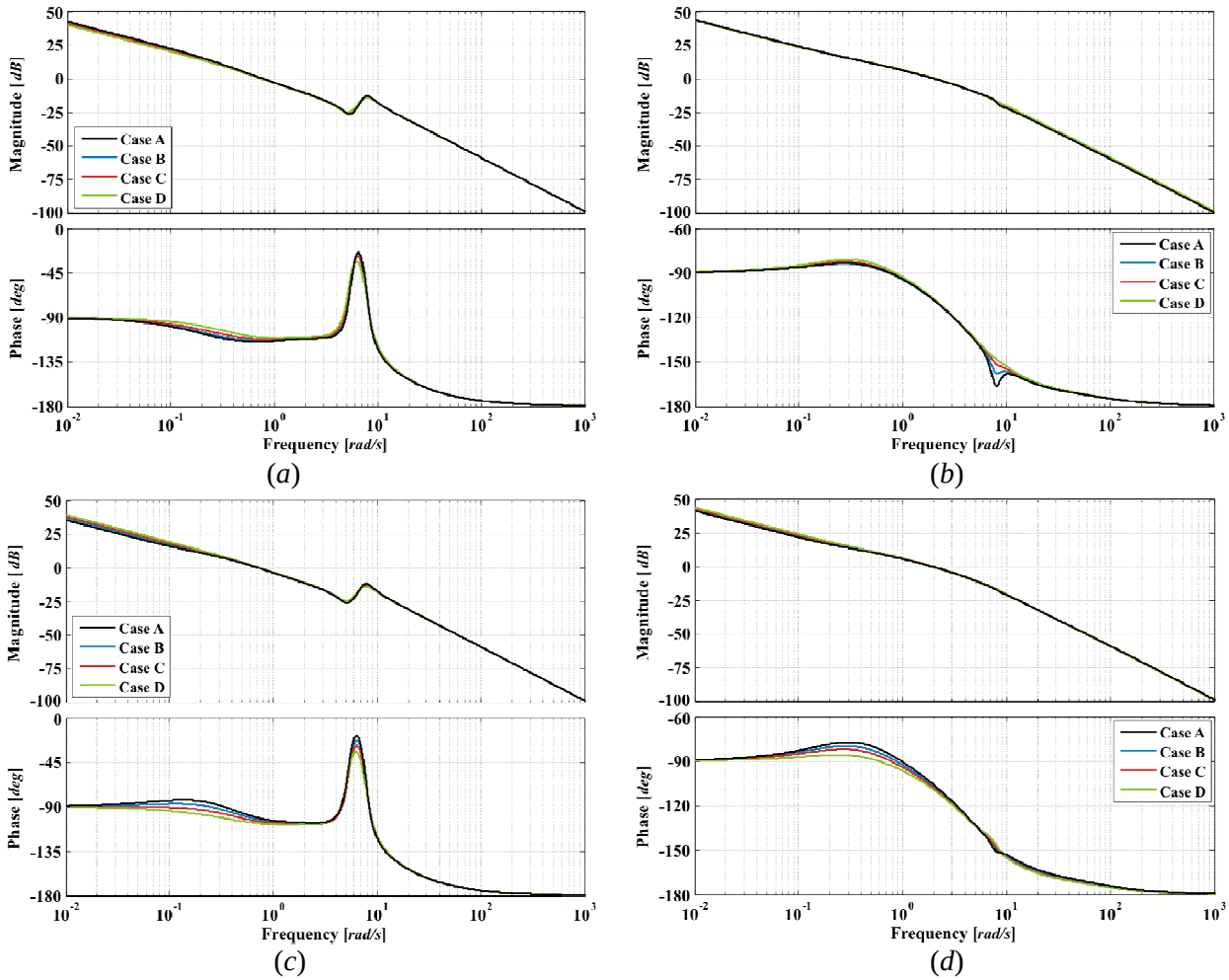

Figure 6.63. Stability robustness assessment (Study 2). Bode diagrams: (*a*) $k_{11}g_{11}(s)$; (*b*) $k_{22}g_{22}(s)$; (*c*) $k_{33}g_{33}(s)$; (*d*) $k_{44}g_{44}(s)$

Table 6.5. Structural and stability robustness of the channels and control system. Study 2.

Case	Measure	C_1	$k_{11}g_{11}$	γ_1	C_2	$k_{22}g_{22}$	γ_2	C_3	$k_{33}g_{33}$	γ_3	C_4	$k_{44}g_{44}$	γ_4
A	**Bandwidth** (*rad/s*)	1.02	1.04	–	2.73	2.79	–	0.96	0.95	–	2.61	2.68	–
	Gain margin (*dB*)	∞	∞	10.63	∞	∞	21.93	∞	∞	15.96	∞	∞	21.81
	Phase margin (*deg*)	71.8	65.2	∞	75.2	70.8	∞	70.1	78.7	∞	79.3	74.4	∞
B	**Bandwidth** (*rad/s*)	1	1.01	–	2.73	2.79	–	0.97	0.97	–	2.66	2.71	–
	Gain margin (*dB*)	∞	∞	12.06	∞	∞	17.73	∞	∞	20.47	∞	∞	18.03
	Phase margin (*deg*)	71.7	66.4	∞	77.3	70.5	∞	70.5	76.7	∞	79.8	72.8	∞
C	**Bandwidth** (*rad/s*)	0.99	1	–	2.77	2.82	–	0.99	0.98	–	2.65	2.71	–
	Gain margin (*dB*)	∞	∞	15.72	∞	∞	16.53	∞	∞	26.07	∞	∞	16.59
	Phase margin (*deg*)	71.5	67.8	∞	79.2	70.7	∞	70.7	74.9	∞	80.4	71.7	∞
D	**Bandwidth** (*rad/s*)	0.98	1	–	2.86	2.86	–	1	0.98	–	2.58	2.64	–
	Gain margin (*dB*)	∞	∞	24.63	∞	∞	13.58	∞	∞	29.45	∞	∞	12.59
	Phase margin (*deg*)	71.8	69.6	∞	80.7	70.8	∞	70.6	73	∞	81.2	71.1	∞

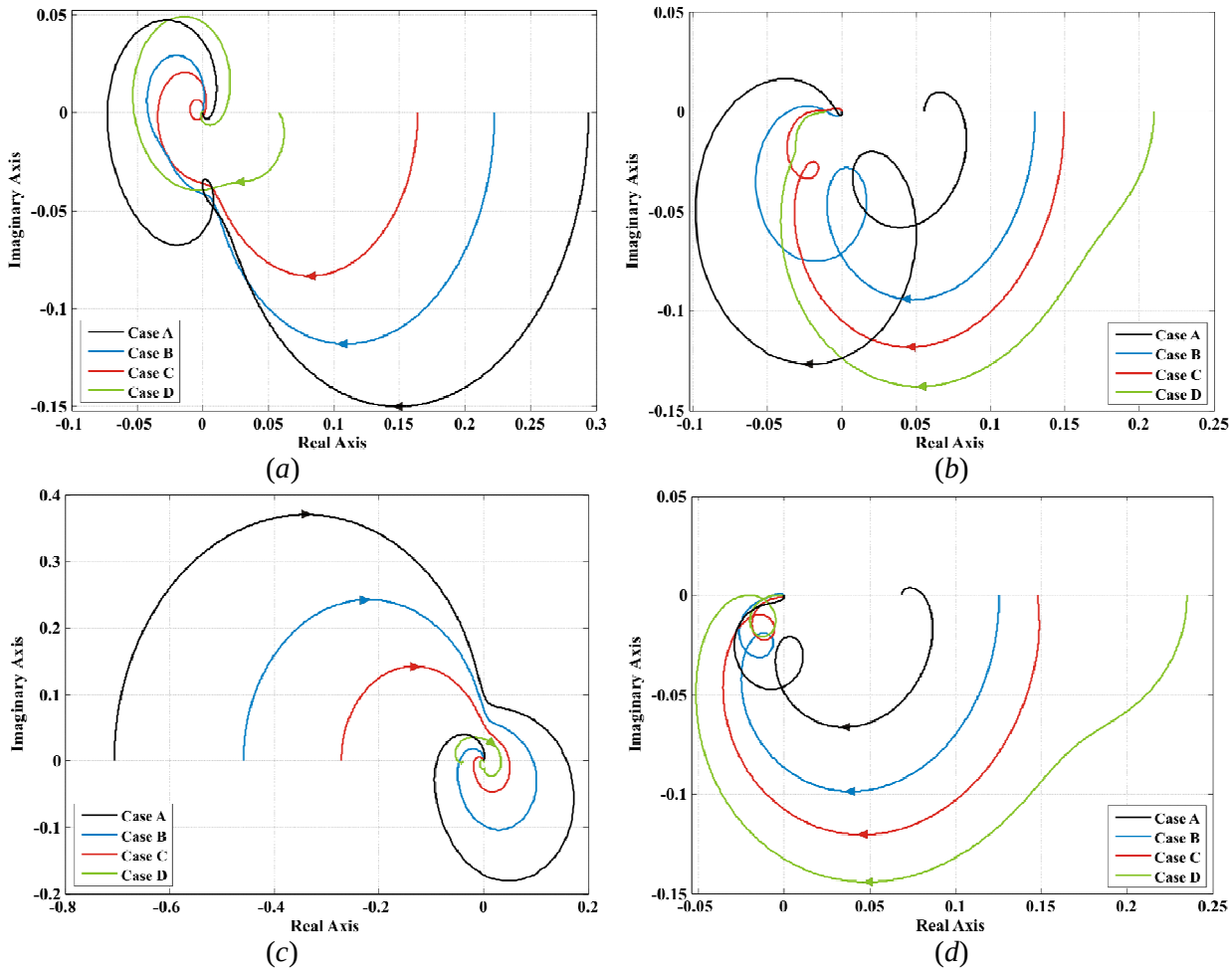

Figure 6.64. Structural robustness assessment (Study 2). Nyquist diagrams: (*a*) $\gamma_1(s)$; (*b*) $\gamma_2(s)$; (*c*) $\gamma_3(s)$; (*d*) $\gamma_4(s)$;

Figure 6.62 shows the Bode diagrams of the four individual channels of the two-machine system. It is observed that the performance of the system is adequate for all operating conditions; the mechanical channels $C_1(s)$ and $C_3(s)$ behave similarly at all loading conditions, as evidenced by Figures 6.62(*a*) and 6.62(*c*). The same can be said about the response of the electrical channels $C_2(s)$ and $C_4(s)$, as shown in Figures 6.62(*b*) and 6.62(*d*). Robustness measures for all channels are adequate, as seen in Table 6.5.

Figures 6.63 and 6.64 illustrate the robustness of the control system. Figure 6.63 shows that the subsystems $k_{ii}g_{ii}(s)$ have adequate gain and phase margins, regardless of system loading. As in Study 1, the MSFs $\gamma_i(s)$ start to the left of (1,0) and do not encircle it. However, it is seen in Table 6.5 that the gain margins of the MSFs associated to the electrical channels decrease when the system loading is reduced; whereas those associated to the mechanical channels decrease when the system loading increases.

The previous results show that the performance of the control system design is satisfactory. This analysis can be further expanded by carrying out closed-loop time domain simulations. For instance, the simulation results shown in Figure 6.65 start from a steady-state operating condition and step changes in the voltage references are applied at different times and changes in the speed references are applied

simultaneously. The sequence of step changes is the same as that of Simulation 1 of Study 1 (Figure 6.60). It can be seen in Figures 6.65(*b*) and 6.65(*d*) that a step change in one terminal voltage channel has little influence in the other electrical channel, which is consistent with the information provided by the MSFs $\Gamma_3(s)$ of Figure 6.35. From Figures 6.65(*a*) and 6.65(*c*) it is noticed that step changes in the terminal voltages have practically no effect in the mechanical channels; such behaviour is consistent with the information provided the MSFs $\Gamma_3(s)$ of Figures 6.31, 6.33, 6.34 and 6.36. Moreover, simultaneous step changes in the mechanical channels have no effect in the electrical channels, with all time responses of the mechanical channels being quite similar for all the operating conditions considered in Study 2. The time responses of the electrical channels are marginally better for higher values of system loading. The results are similar to those of Simulation 1 of Study 1, regardless of system loading, and are consistent with the multivariable analysis presented in Section 6.3.

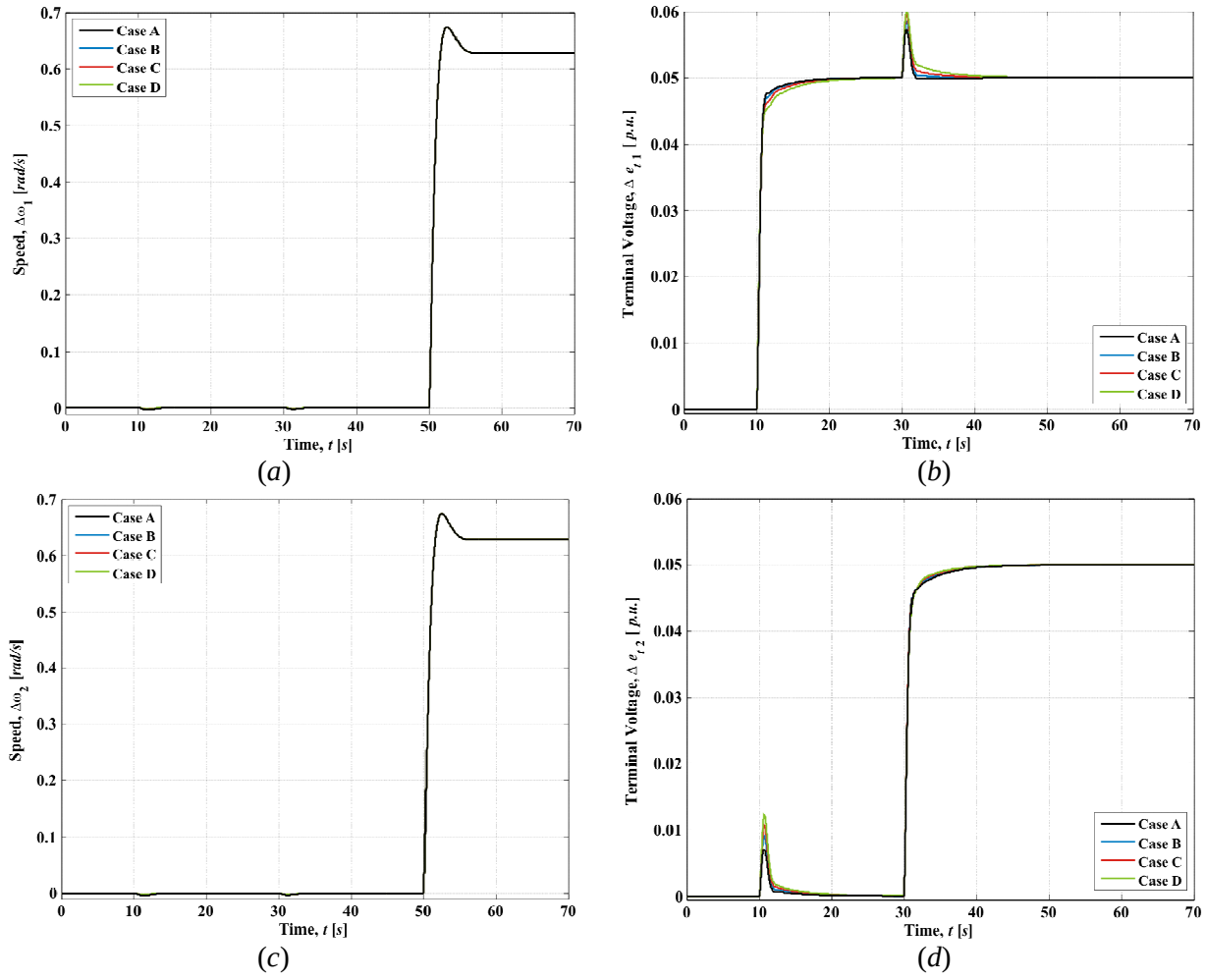

Figure 6.65. System performance (Study 2). Time response: (*a*) Channel 1 ($\Delta\omega_1$); (*b*) Channel 2 (Δe_{t1}); (*c*) Channel 3 ($\Delta\omega_2$); (*d*) Channel 4 (Δe_{t2})

The simulation results in Figure 6.66 correspond to step changes to the speed references at different times, while keeping the same reference in terminal voltages during the whole simulation. The sequence of step changes is the same as that of Simulation 2 of Study 1 (Figure 6.61). It can be seen that whenever the speed reference of one machine changes while leaving the speed reference of the other

machine unchanged, neither the speed nor the terminal voltage outputs reach their given references. The mismatch in the terminal voltages decreases with a reduction in system loading. Only when both speed references match all channels follow their references. As in Study 1, the plant response is due to the occurrence of transmission zeros near the origin and the fact that several MSFs $\Gamma_i(s)$ (given in Figures 6.32, 6.37, 6.39, 6.43, 6.44, 6.49 and 6.51) pass close to the point (1,0), a fact that causes the mechanical channels to be strongly coupled.

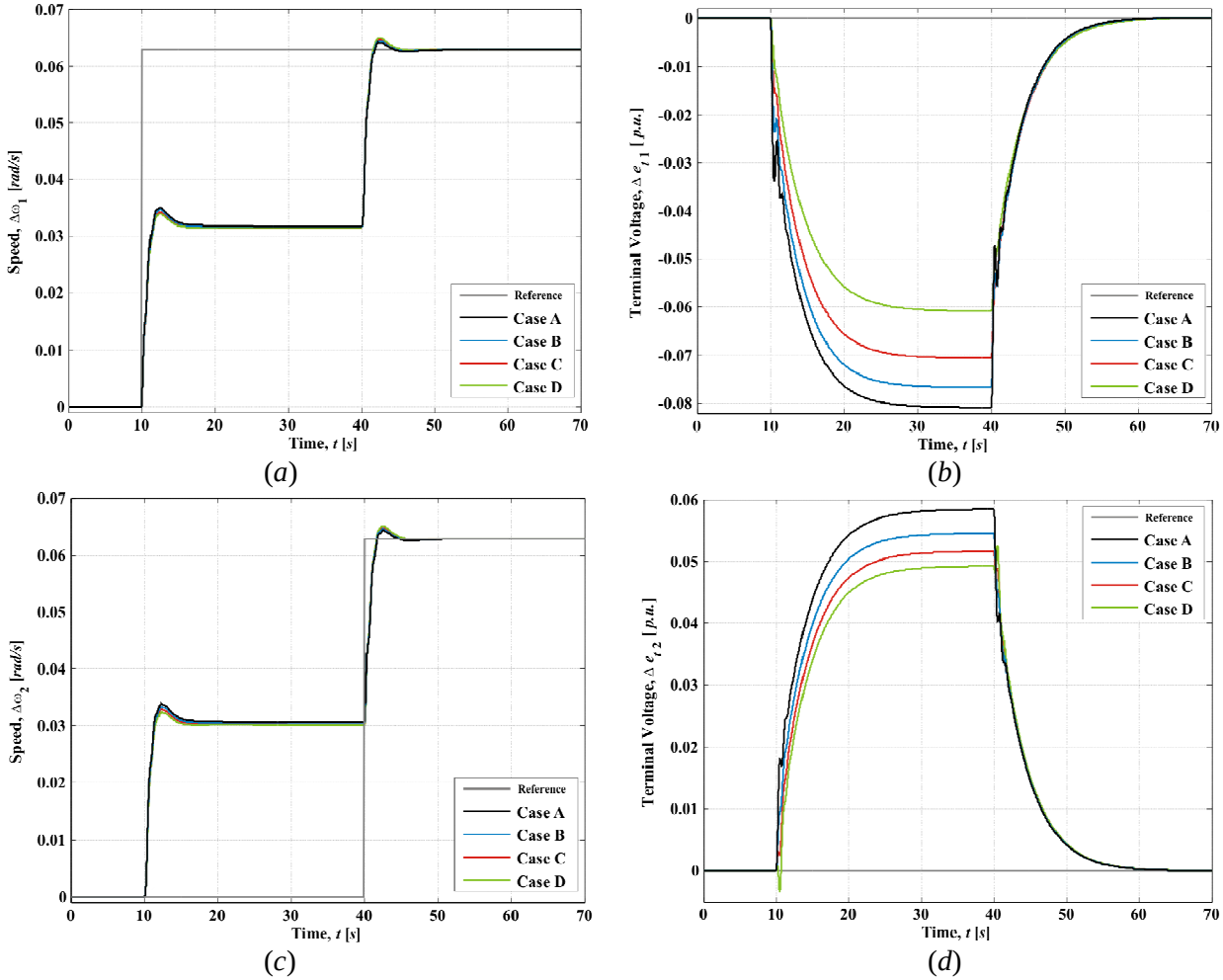

Figure 6.66. System performance 2 (Study 2). Time response: (*a*) Channel 1 ($\Delta\omega_1$); (*b*) Channel 2 (Δe_{t1}); (*c*) Channel 3 ($\Delta\omega_2$); (*d*) Channel 4 (Δe_{t2})

Remark: It should be emphasised that although the proposed control system design has a satisfactory performance in terms of robustness measures, the controller does not decouple the two mechanical subsystems for the frequency range of interest. Moreover, the presence of transmission zeros close to the imaginary axis and the closeness of some MSFs to the point (1,0) require a control system strategy in which the two machines are treated as a single system. Nevertheless, a further exploration of such a scheme is beyond the scope of this thesis. The problems faced in the two-machine system arise from the nature of the plant. As discussed by Leithead and O'Reilly [10], these issues cannot be removed by feedback control.

6.4.3. A note on numerical errors in MATLAB

Results obtained for Studies 1 and 2 in previous sub-sections show that the control system performance is adequate, offering satisfactory robustness measures, and consistent with the multivariable analysis carried out earlier in this chapter. However, it should be mentioned that for some operating conditions the frequency response plots of the individual channels resembled those of an unstable system when using equation (A.55). Hence, an alternative avenue to obtain the channels information had to be realised. Even though time simulations offered satisfactory results for all cases, the Bode and Nyquist plots of the associated MSFs and individual channels yielded characteristics that did not match at all the closed-loop behaviour of the control system. It is clear that the reason for this anomalous set of results was not a bad control system design or an incorrect multivariable analysis, as evidenced by the results presented in the previous section, but due to numerical instabilities present in the frequency domain calculation tools of the MATLAB package. The *i*-th Individual Channel $C_i(s)$ expression is given by

$$C_i(s) = k_{ii} g_{ii} (1 - \gamma_i) \tag{A.55}$$

and its associated MSF by

$$\gamma_i(s) = -\left|\bar{\mathbf{G}}_i\right| / g_{ii} \left|\bar{\mathbf{G}}^i\right| \tag{A.56}$$

It should be noticed that for the case of 4-input 4-output systems, as it is the case of the two-machine system, the MSFs $\gamma_i(s)$ are obtained by calculating the determinant of a 4th order matrix divided, by the determinant of a 3rd order matrix, where each individual element is a transfer function with a polynomial of 9th degree in its denominator for the case of the 5th order synchronous generator model. This common denominator corresponds to the characteristic polynomial, with roots equal to the eigenvalues of the system matrix **A** of the two-machine plant for a given operating condition. The calculation of the MSFs in (A.56) involves several algebraic operations and exact pole/zero cancellations. However, severe problems arise in the form of numerical error propagation if such cancellations are not carried out to a very high degree of accuracy: the error increases with the number of operations, leading to numerical instabilities. This problem did not surface in the analysis of 3-input 3-output plants, such as in the synchronous generator – SVC or the synchronous generator – TCSC systems, but became all too apparent in 4×4 systems. It is surmised that this problem would increase exponentially with system size and that larger systems such as an SVC connected at some point of the transmission line between the two synchronous machines would not be possible to be carried out with the current version of MATLAB.

The cure of such numerical problems using MATLAB and the programming of effective functions, although highly desirable, are out of the scope of this thesis. Although such numerical problems were not present in all cases, it was deemed necessary to develop an alternative and reliable way to construct the frequency domain responses for all the cases studied in this chapter. The aim is to enable a reliable and effective assessment of the control system design, with the controller itself having been obtained following a rigorous set of analyses.

A simple and effective way to circumvent the numerical instabilities shown by MATLAB when calculating the MSFs and the individual channels of high-order systems, was to use built-in functions from the Control Systems Toolbox of MATLAB into a Simulink model. The mathematical representation of the multi-machine system can be implemented in Simulink either as a set of differential equations using gains, additions and integrators; or as a state-space realization using calculated matrices **A**, **B**, **C** and **D**; or as a set of transfer functions using elements $g_{ik}(s)$ of the transfer function matrix $\mathbf{G}(s)$. Since the two-machine system is a linear model, the open loop transmittance between one input and one output pairing (*i.e.*, an individual channel) can be obtained through the MATLAB command *linmod* and by using a set of logical rules to close the loops associated to the remaining input-output channels. The basic function of *linmod* is to extract the state-space linear model described in a block diagram when the inputs and outputs are explicitly specified in the block diagram. The result is a transfer function which would be fully equivalent to that obtained when the individual channel (A.55) is calculated correctly, *i.e.*, with no numerical instabilities.

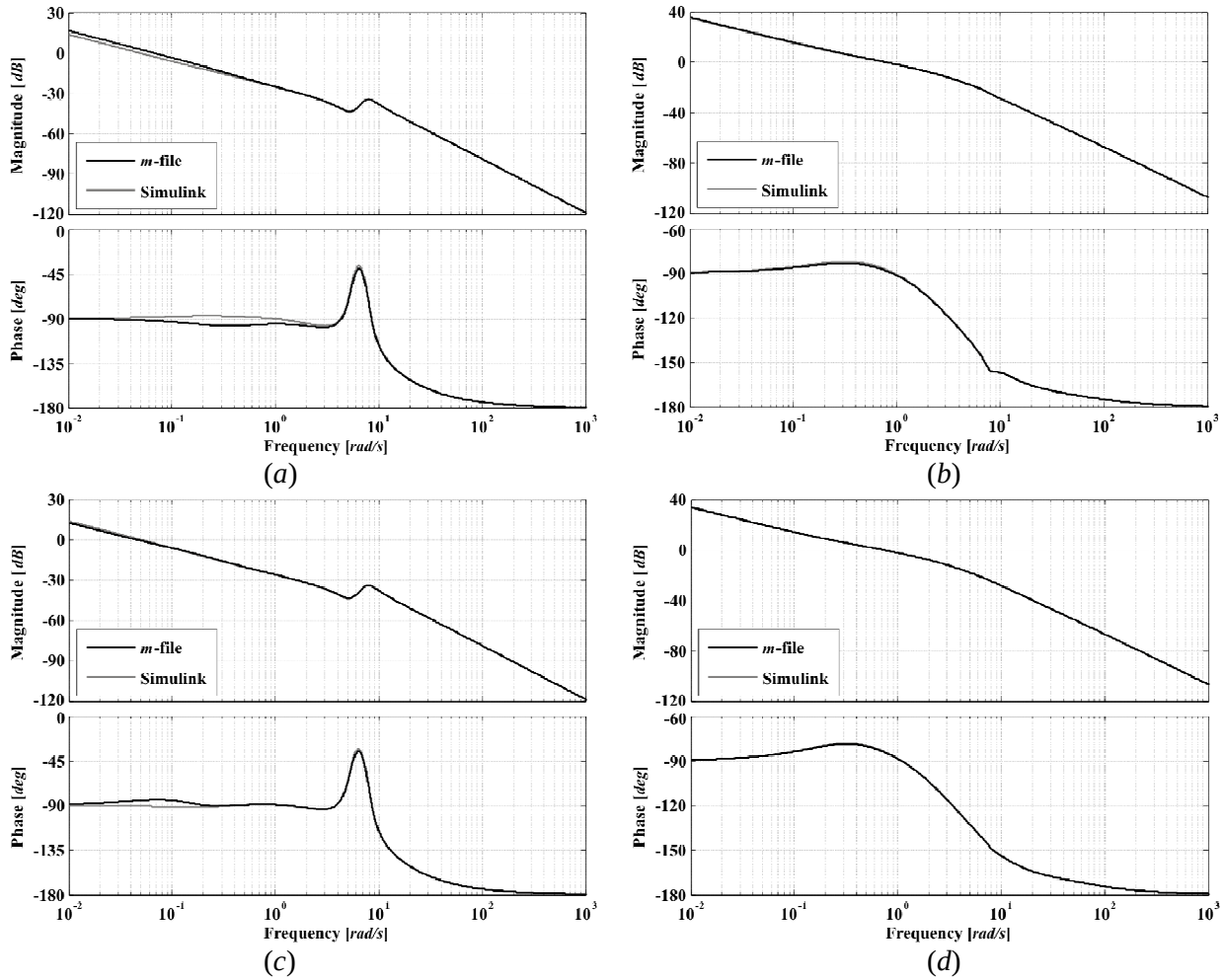

Figure 6.67. Bode diagrams of individual channels using (A.55) and built-in function *linmod*: (*a*) Channel 1 ($C_1(s)$); (*b*) Channel 2 ($C_2(s)$); (*c*) Channel 3 ($C_3(s)$); (*d*) Channel 4 ($C_4(s)$)

To show the effectiveness of the procedure based on function *linmod* to calculate the MSFs and the individual channels, take Case 3 of Study 1, provided in Table 6.1. In this example, controller (6.14) is used, with the following gains: $k_{\omega 1} = k_{\omega 2} = 10$ and $k_{et1} = k_{et2} = 36.3$. A damping term of $D = 10$ *p.u.* is used for both synchronous generators. Figure 6.67 shows the Bode plots of the individual channels obtained using equation (A.55) (legend "*m*-file") and by using *linmod* in the Simulink model (legend "Simulink").

The electrical individual channels $C_2(s)$ and $C_4(s)$, shown in Figures 6.67(*b*) and (*d*), have the same frequency response plots, and only minor differences are observed in the mechanical individual channels $C_1(s)$ and $C_3(s)$, shown in Figures 6.67(*a*) and (*c*), around the cut-off frequency. As a corollary to this discussion, it should be said that whenever the construction of the individual channels becomes thwarted due to intrinsic numeric instabilities in the MATLAB engine calculation, the use of the alternative method introduced in this thesis renders adequate results.

6.5. Conclusions

In this chapter, small-signal stability assessments and multivariable control system analysis and design of a two-machine system have been carried out using the ICAD framework. Two study cases have been carried out: the first study assesses the system behaviour under a change of transmission line length, while the second study evaluates the consequence of changes in system loading. Simulation results obtained are in agreement with system behaviour observed in practice.

The two-machine system is a highly coupled multivariable system in which the most significant interactions are those of the mechanical subsystems of the two synchronous generators. The electrical subsystems are weakly coupled with the mechanical subsystems of the two machines. These characteristics are well preserved regardless of system loading and transmission line length. A low internal coupling exists between the electrical and mechanical channels within a machine and this is consistent with results obtained in OMIB systems. The strong coupling between the two machines is due to the nature of plant: there are transmission zeros very close to the imaginary axis and several MSFs are near the point (1,0) at low frequencies. As a consequence of this, the mechanical channels of both machines have to act upon simultaneously as if they were a single system.

Difficulties were encountered with the computational software used to carry out this research, namely, MATLAB. Its numerical performance becomes impaired whenever ICAD is employed for 4-input 4-output and more complex systems. The main problem arises from incorrect pole/zero cancellations in the frequency domain. Such effects were not present in 3-input 3-output plants. The additional input-output pairing in the two-machine system causes a considerable increase in complexity

when calculating the individual channel expressions and their associated MSFs. In order to assess properly the control system design performance and robustness, such a problem was circumvented by using some in-built functions of the Control Systems Toolbox and Simulink. The effectiveness of the proposed solution was tested and proved to be satisfactory as an alternative MSF and individual channel computing method.

6.6. References

[1] Anderson PM, Fouad AA. *Power System Control and Stability*. IEEE Press, USA; 1994.

[2] Kundur P. *Power System Stability and Control*. USA: McGraw-Hill; 1994.

[3] Dudgeon GJW, Leithead WE, Dysko A, O'Reilly J, McDonald JR. *The Effective Role of AVR and PSS in Power Systems: Frequency Response Analysis*. IEEE Transactions on Power Systems, **22**, no. 4, pp. 1986–1994, 2007.

[4] Chen CT. *Linear System Theory and Design*. USA: Saunders College Publishing; 1984.

[5] Leithead WE, O'Reilly J. *M-input m-output feedback control by individual channel design. Part 1. Structural Issues.* International Journal of Control, **56**, no. 6, pp. 1347–1397, 1992.

[6] O'Reilly J, Leithead WE. *Multivariable control by individual channel design*. International Journal of Control, **54**, no. 1, pp. 1–46, 1991.

[7] Licéaga–Castro E, Licéaga–Castro J, Ugalde–Loo CE. *Beyond the existence of diagonal controllers: from the relative gain array to the multivariable structure function*. Proc. Joint 44th IEEE Conference on Decision and Control - European Control Conference, pp.7150–7156, 2005.

[8] Maciejowski JM. *Multivariable Feedback Design*. UK: Addison–Wesley; 1989.

[9] Kundur P. *Power System Stability and Control*. USA: McGraw-Hill; 1994.

[10] Leithead WE, O'Reilly J. *Performance Issues in the Individual Channel 2–input 2–output Systems. Part 1: Structural issues.* International Journal of Control, **54**, no. 1, pp. 47–82, 1991.

Chapter 7

CONCLUSIONS

7.1. General

In this research work, the mathematical modelling, analysis, control system design and simulation of electrical power systems with FACTS devices have been addressed. The analysis and control system design have been carried out using classical control and Nyquist/Bode methodology, in a multivariable context, by exploiting the Individual Channel Analysis and Design framework, together with an in-depth analysis of the Multivariable Structure Function. The research has shown that ICAD is well suited to the task of carrying out small-signal stability assessments of multi-machine power systems taking full account of electrical and mechanical subsystems.

The motivation driving this research has been the realisation of comprehensive power system models with which to conduct small-signal stability assessments where physical insight is favoured over mathematical abstraction, aiming at effective evaluations of control system performance and robustness. The FACTS technology is a relatively recent development in power systems engineering and its widespread integration into the power network is affecting power generation, transmission, distribution, utilisation and equipment manufacturing. The use of ICAD to carry out fundamental dynamical studies allows the understanding of the dynamic interactions taking place between different power system components, including FACTS devices, in a transparent manner. The role FACTS equipment in the provision of electromechanical oscillations damping has been revised, with the analysis carried out using the framework of ICAD, where a clear picture of the dynamical structure of the system becomes readily available. Moreover, information of the system's multivariable structure functions is all that is needed for a complete control system design. The analysis and control of both the single-machine, infinite-bus and multi-machine system were carried out successfully; synchronous generator representation involved varying degrees of modelling complexity.

The research work has shown that the framework afforded by ICAD is an effective and insightful alternative for the analysis and control system design of OMIB systems with FACTS equipment representation, from the vantage of small-signal perturbation. The many advantages that the ICAD framework has over the block diagram method when carrying out small-signal stability assessments, have been expounded. ICAD enables full multivariable analyses which are a pre-requisite for robust control system designs applicable that cover a wide range of system operating conditions. It has been found that information emanating from ICAD provides formal proof as to why some system operating conditions are more critical than others; a fact that is further validated by examining the closed-loop performance of the control system design. ICAD analysis corroborates the fact that the most critical operating condition is when the synchronous generator is made to absorb VARs, *i.e.*, it operates with a leading power factor. A scalar MSF encapsulates fully the dynamical structure of the OMIB system, providing an effective measure of coupling between the OMIB input-output channels. Careful inspection of the MSF reveals that the electrical and mechanical channels become more tightly coupled as the electrical distance increases; a fact that relates to a long-distance transmission system impaired by excessive power loss and angular stability issues. By way of example, a simple control system design, using ICAD, was carried out for the excitation and turbine-governor controllers; exhibiting a far superior performance when compared to the two corresponding controllers given in the open literature for generic power system stability studies. A family of synchronous generator models with a varying degree of complexity was derived within the context of ICAD, and it was categorically concluded that higher order models should be used as long as system parameters are available. It is worth mentioning that an idealised zero damping coefficient D was assumed in order to assess a more critical condition. In practice, although the value of D can be small, it is always non-zero. However, the methods and analyses presented throughout this research work are valid for any value of D.

The prowess shown by ICAD in the conduction of multivariable control system analyses and designs in OMIB systems encouraged its use in more complex transmission systems. FACTS equipment is used to regulate key power system parameters. ICAD has led to a formal understanding of the complex dynamic interactions that take place between synchronous generators and electronically-controlled compensation devices such as the SVC and the TCSC. The analyses show that the dynamic performance of the OMIB system is much improved by the addition of an SVC; a highly effective VAR compensation whose primary task is to yield dynamic voltage regulation at the point of connection. ICAD analyses have revealed that the dynamical structure of the system is well preserved and that no adverse dynamics are introduced into the plant. The research has also shed new light into the long-established claim that added functionality is achieved when an ancillary control loop is fitted into the SVC to enable damping capabilities. An immediate benefit of using ICAD to assess the impact of supplementary signals in the SVC control loop is that the dynamical structure of the system is preserved. The ensuing frequency response analyses visually show that the unwanted switch-back characteristic, which is intrinsic to

synchronous generator operation, is smoothed out. This is reflected in much improved dynamic performances even in cases of weak transmission systems, with no need to curtail the bandwidth. Concerning the dynamical evaluation of the TCSC from the ICAD vantage, it is observed that the TCSC decreases the switch-back characteristic of the synchronous generator through an effective modulation of the tie-line reactance and a tight power flow regulation, leading to an improved performance of the TCSC-upgraded transmission system. On the negative side, ICAD has revealed that the TCSC inclusion brings fragility on to the system, it introduces cross-coupling between channels and makes the system non-minimum phase, limiting the potential performance of the TCSC in the operating capacitive region, which is the customary region of operation. An interesting observation is that for very high levels of capacitive compensation, say 80% for a long transmission line length of 0.8 *p.u.*, the system reverts to being minimum phase. However, the practical significance of this fact is debatable since such high levels of compensation are achieved at close proximity to the resonant point – a forbidden area of operation, with the potential to cause equipment permanent damage and lethal injury to personnel. There appears to be little incentive in operating the TCSC in its inductive region since this effectively increases the electrical length of the transmission systems. Moreover, ICAD analysis has formally corroborated that the inductive region of operation of the TCSC is problematic and brings no obvious benefits to the system due to an increment both in the internal coupling of the machine and the electrical distance of the transmission line.

The damping of electromechanical oscillations remains an area of much research interest in power systems. The classical solution used to ameliorate electromechanical oscillations has been the fitting of PSS in large synchronous generators identified as troublesome, to overcome their switch-back characteristics. Theory and practice have shown the PSS to be quite an effective remedy to prevent the oscillations since the corrective signals are applied at the same physical location where the synchronous generator is. In this research the damping capabilities observed in the SVC and the TCSC have been compared using ICAD, and for completeness, owing to its widespread acceptability within the industry, the PSS was also brought into the comparative analysis. To this end, existing work on PSS representation using ICAD proved to be very useful, as it was found that the PSS and SVC ancillary damping loops share a great deal of similarity – both control structures are modelled as post-compensators of the speed output. The research has shown that the SVC ancillary loop is just as effective as the PSS in damping electromechanical oscillations. Both controllers exploit very effectively the synchronous generator dynamics to overcome its switch-back characteristic. However, it should be kept in mind that the primary function of the SVC is to provide dynamic VARs support, and that their installation is likely to take place in locations far away from where the large synchronous generators sit. In that respect, they should be viewed as complementary, as opposed to competing, technical solutions to the problem posed by electromechanical oscillations. Recent research work carried out using non-ICAD modelling and analysis tools are very much in line with the findings of this research, and recommends that PSSs be given priority

over SVCs in the application of electromechanical oscillations damping. This recommendation seems to make sense but newer information has emerged, using ICAD, on the conflicting requirements of high-gain AVRs and PSSs, both controllers located within the generating plant – it is argued that the un-impeding action of the AVR should takes precedence over that of the PSS. This research has also shown that although at least in theory, the TCSC has the ability to damp electromechanical oscillations, in practice this is severely impaired by the TCSC dynamic structure being non-minimum phase for most of its operating range. It is only when large amounts of series compensation are applied that the system becomes minimum phase and that the switch-back characteristic decreases sufficiently. This may be a non-practical solution, since a substantial increase in series compensation comes together with other issues, such as an increment in the reactive power supplied by the generator, high fault currents, possible difficulties of power flow control, and resonance implications.

The positive experience gained with the OMIB system representation using ICAD, where multi-order synchronous machine models were developed using first principles, provided the motivation for moving on to the multi-machine representation using ICAD, taking proper care of the electrical and mechanical channels and the various synchronous machine models. The first leg of this mammoth task was to develop the state-space representation of a multi-machine, multi-order power system model, which incidentally may be used for carrying out small-signal stability assessments using eigenvalue-based analysis. The second leg consists of the actual representation of the multi-machine system in the framework afforded by ICAD. The software, coded in MATLAB, enables the solution of an arbitrary number of synchronous generators in the network, limited only by the numerical capability range of MATLAB; where each generator is represented by a pre-defined model. The model choice tailored to fit the available data for that generator and its likely impact on the overall dynamic study – the generator may be at the centre of the disturbance or it may be located at a quite a considerable electrical distance from the epicentre. The software is comprehensive; it has provisions for conducting power flow solutions and the calculation of the initial state that the generators keep prior to the disturbance. The state-space representation and the equivalent transfer function matrix of the system are generated automatically following the formation of the reduced nodal admittance matrix using Kron's reduction. Eigenvalue analysis is carried out using the standard MATLAB functionality. Two text-book networks were used to check on the sanity of the results given by the new software. They are a three-machine and a four-machine test systems; they are sufficiently small to allow for a meaningful comparison and yet large enough to provide sufficient realism into the study. The results were also compared with available results generated with commercial industrial-grade software.

The mathematical model of the multi-machine system in state-space form is used as the starting point for conducting analysis and control system design of a multi-machine system using the full ICAD framework, taking proper account of the electrical and mechanical channels. A test system made up by

two synchronous generators linked by a transmission line is singled out for analysis using the ICAD framework. The ensuing multivariable analysis reveals that, contrary to the performance of the OMIB systems, the two-machine system is strongly coupled; where very significant interactions exist between the two mechanical subsystems. On the other hand, interactions between the two electrical subsystems are relatively weak. The loose coupling that exists between the electrical and mechanical channels of the synchronous generator in the OMIB system is very much preserved in the internal channels of the two synchronous generators in the two-machine system. By extension, the coupling between the electrical channel of one generator and the mechanical channel of the other generator has been found to be weak. In a nutshell, the only significant coupling is between the two mechanical subsystems. Such coupling characteristic seems to be independent of transmission line length and system loading conditions. This is not altogether an unexpected result since the electrical channel in a synchronous machine is closely linked to reactive power and it is well known that reactive power does not travel easily and tends to be largely, a local phenomenon. On the other hand, the mechanical channel is closely associated with active power, which travels in the power network with little difficulty. Hence, owing to the nature of the plant, which is a two-machine system, it is not possible to achieve a complete decoupling of the mechanical subsystems using feedback control – it is quite plausible that the two-machine system represents the worst scenario, in terms of coupling, that may exist in a multi-machine system. As a result, the control system design of one machine is carried out taking into consideration the dynamics of the other machine and vice-versa. Nevertheless, the closed-loop performance of the two-machine system is adequate, offering satisfactory robustness measures.

7.2. Suggestions for further research work

This research work has contributed new knowledge to the theory of electrical power systems, with particular reference to the dynamical modelling of FACTS equipment representation in the control-oriented systems framework of ICAD. The impact of the SVC and the TCSC on the unwanted switch-back characteristic of the synchronous generator has been assessed using ICAD, and comparisons have been drawn with the PSS, the current standard bearer in the provision of electromechanical oscillations damping. A major contribution has been made on the representation of a two-machine system in the control-oriented framework of ICAD, where a full representation of the mechanical and electrical channels has been made. Notwithstanding the great research value of these new contributions represent, it is fair to say that these are only a small portion of the vast wealth of knowledge that the use of a formal control-oriented framework such as ICAD can bring into the study area of dynamical power systems. The list below provides a number of research items which ought to be undertaken in the not too distant future as a way of furthering the research findings of the present research work:

- Individual Channel Analysis of multi-machine systems with more than two machines. A natural step forward will be to conduct the study of a three-machine system and the two-area (four-machine) systems studies in Chapter 5 of this thesis using eigenvalue-based methods. This should be followed by a research on dynamic equivalents using ICAD to enable the study of large-scale power networks under the framework of ICAD. An issue of high priority in the research list is a deeper analysis of the high coupling that exists between the mechanical subsystems of synchronous machines; to examine alternative control structures, such as feed-forward controllers, and to explore alternative control design methods.

- The multi-machine, multi-order power system representation in ICAD with dynamic equivalents provision, would benefit from the inclusion of a wide range of FACTS equipment models; using a similar level representation as those of the SVC and the TCSC in the OMIB system in Chapter 3 of this thesis. This would enable an in-depth assessment of the electromechanical oscillation damping capabilities of FACTS controllers in a multi-machine environment.

- It is a matter of paramount importance to develop mathematical models of induction generators, double-fed induction generators and permanent magnet synchronous generators suitable for ICAD representation. The aim is to study the dynamical effects of wind farms in the power grid under the framework of ICAD.

- Concerning software development of ICAD, the creation of an efficient $m \times m$ Toolbox should receive urgent attention. At present, a 2×2 Toolbox is available in MATLAB, which allows control system analysis and design of 2-input 2-output. A generalisation to the m-input m-output is mandatory for the more complex systems resulting from multi-machine systems with more than two synchronous generators. This issue does not seem to be a trivial programming matter. Owing to fundamental numerical errors associated to standard MATLAB functions when dealing with 4×4 systems, it is envisaged that fundamental mathematical work would need to be carried out if an alternative software engine different from MATLAB, such EASY5, were to incur the same failings as the MATLAB software when calculating the roots of polynomials, convolutions and exact pole/zero cancellations.

Appendix A

INDIVIDUAL CHANNEL ANALYSIS AND DESIGN FORMULATIONS

A.1. Representation of 2×2 systems in individual channels

The individual channel representation for a 2-input 2-output plant, originally introduced in [1], is here presented since the synchronous generator plant considered in this thesis corresponds to a 2×2 plant. Moreover, its proper assessment will ease the understanding of *m*-input *m*-output systems – *e.g.*, the multi-machine system or models including FACTS controllers.

A.1.1. Individual channel formulation

Consider the standard multivariable feedback control system of Figure 2.25. Assume the plant **G**(*s*) is a 2-input 2-output system and **K**(*s*) is a diagonal controller matrix. Such configuration can be described by

$$\mathbf{Y}(s) = \mathbf{G}(s)\mathbf{u}(s) \tag{A.1}$$

or in more detail by

$$\begin{bmatrix} y_1(s) \\ y_2(s) \end{bmatrix} = \begin{bmatrix} g_{11}(s) & g_{12}(s) \\ g_{21}(s) & g_{22}(s) \end{bmatrix} \begin{bmatrix} u_1(s) \\ u_2(s) \end{bmatrix} \tag{A.2}$$

where $g_{ij}(s)$ represents scalar transfer functions, $y_i(s)$ the outputs, and $u_i(s)$ the inputs of the system, with $i,j = 1,2$. If a diagonal controller is assumed, that is

$$\mathbf{u}(s) = \mathbf{K}(s)\mathbf{e}(s) \tag{A.3}$$

$$\begin{bmatrix} u_1(s) \\ u_2(s) \end{bmatrix} = \begin{bmatrix} k_{11}(s) & 0 \\ 0 & k_{22}(s) \end{bmatrix} \begin{bmatrix} e_1(s) \\ e_2(s) \end{bmatrix} \tag{A.4}$$

with $e_i(s) = r_i(s) - y_i(s)$, where $r_i(s)$ represents the plant references. The feedback system can be redrawn as in Figure A.1, where $k_{ii}(s)$ are the diagonal elements of the controller matrix **K**(*s*) in (A.4) and $g_{ij}(s)$ are the elements of the plant matrix **G**(*s*) in (A.2).

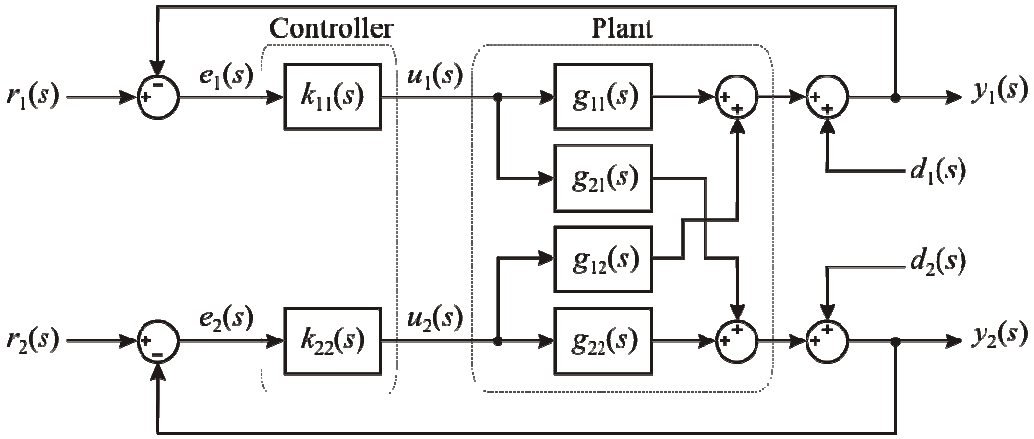

Figure A.1. 2-input 2-output multivariable control system with diagonal controller

Without considering external disturbances $d_i(s)$, the signal transmission from $r_1(s)$ to its associated output $y_1(s)$ in Figure A.1 has two parallel paths; one directly through $g_{11}(s)$; and the other via $g_{21}(s)$, the bottom feedback system and $g_{12}(s)$. Also, the forward cross-signal transmission from the second reference $r_2(s)$ to $y_1(s)$ is via the bottom feedback subsystem and $g_{12}(s)$. These signal transmission from $r_1(s)$ to $y_1(s)$ and $r_2(s)$ to $y_1(s)$ can be described as in Figure A.2. The same applies to output $y_2(s)$, shown in Figure A.3.

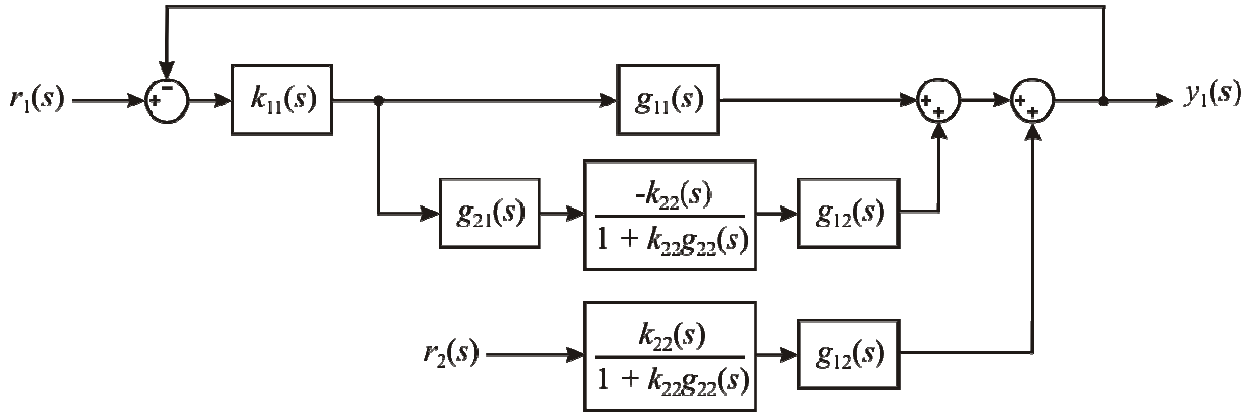

Figure A.2. Signal transmission to output y_1

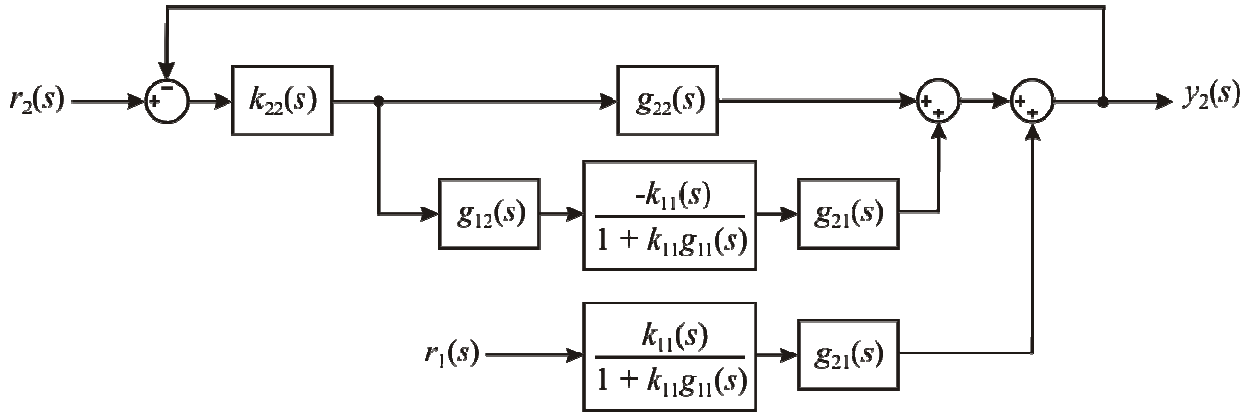

Figure A.3. Signal transmission to output y_2

More generally, the previous result in a feedback multivariable loop where an input $u_i(s)$ and a reference $r_i(s)$ can be assigned to each of the outputs $y_i(s)$ (i = 1,2) of the process. Each controller $k_{ii}(s)$ uses the information of the output $y_i(s)$ and the reference value $r_i(s)$ to provide the control signal $u_i(s)$. Notice that the plant is subject to the external disturbance $d_i(s)$. Under these suppositions, after performing some algebraic manipulation it is possible to represent the multivariable control loop (in a more compact form) in two SISO systems, each one formed of a channel $C_i(s)$. For the multivariable system described by (A.1)–(A.4), the response of the closed-loop system of the channel with respect to the references is given by

$$\mathbf{y} = (\mathbf{I} + \mathbf{GK})^{-1}\mathbf{GKr} = \begin{bmatrix} y_1(s) \\ y_2(s) \end{bmatrix} = \begin{bmatrix} \dfrac{C_1(s)}{1+C_1(s)} & \dfrac{g_{12}(s)}{g_{22}(s)}\dfrac{h_2(s)}{1+C_1(s)} \\ \dfrac{g_{21}(s)}{g_{11}(s)}\dfrac{h_1(s)}{1+C_2(s)} & \dfrac{C_2(s)}{1+C_2(s)} \end{bmatrix} \begin{bmatrix} r_1(s) \\ r_2(s) \end{bmatrix} \tag{A.5}$$

Equation (A.5) can be illustrated with the block diagram representations shown in Figure A.4.

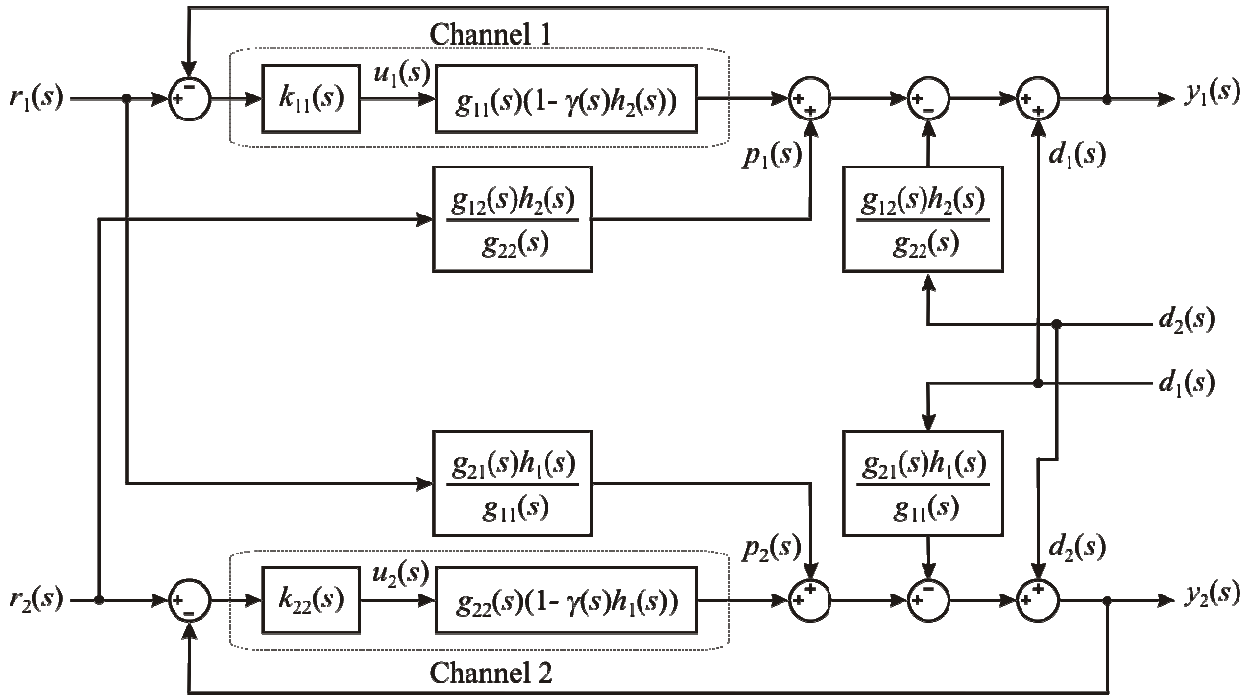

Figure A.4. 2×2 system with diagonal controller represented in individual channels

From Figure A.4, Individual Channel $C_1(s)$ has an open-loop SISO transmittance

$$\begin{aligned} C_1(s) &= k_{11}g_{11}\left(1 - g_{12}g_{22}^{-1}H_2g_{21}g_{11}^{-1}\right) \\ &= k_{11}g_{11}(1-\gamma_1) \\ &= k_{11}g_{11}(1-\gamma h_2) \end{aligned} \tag{A.6}$$

where the multivariable structure function (MSF) $\gamma_1(s)$ is defined by

$$\gamma_1(s) = -\frac{\begin{vmatrix} 0 & g_{12} \\ g_{21} & g_{22}/h_2 \end{vmatrix}}{g_{11}(g_{22}/h_2)} = \frac{g_{12}g_{21}}{g_{11}g_{22}} \cdot h_2 = \gamma h_2 \tag{A.7}$$

$$\gamma = \frac{g_{12}g_{21}}{g_{11}g_{22}} \tag{A.8}$$

and the subsystem transfer functions $h_2(s)$ and $H_2(s)$ are defined by

$$h_2(s) = H_2(s) = k_{22}g_{22}(1 + k_{22}g_{22})^{-1} \tag{A.9}$$

and is subject to the disturbance

$$d_1(s) = g_{12}g_{22}^{-1}H_2 r_2(s) \tag{A.10}$$

Similarly, Individual Channel $C_2(s)$ has an open-loop signal transmittance

$$\begin{aligned} C_2(s) &= k_{22}g_{22}(1 - g_{21}g_{11}^{-1}H_1 g_{12}g_{22}^{-1}) \\ &= k_{22}g_{22}(1 - \gamma_2) \\ &= k_{22}g_{22}(1 - \gamma h_1) \end{aligned} \tag{A.11}$$

where MSF $\gamma_2(s)$ is defined by

$$\gamma_2(s) = -\frac{\begin{vmatrix} g_{11}/h_1 & g_{12} \\ g_{21} & 0 \end{vmatrix}}{g_{22}(g_{11}/h_1)} = \frac{g_{12}g_{21}}{g_{11}g_{22}} \cdot h_1 = \gamma h_1 \tag{A.12}$$

and the system transfer functions $h_1(s)$ and $H_1(s)$ are defined by

$$h_1(s) = H_1(s) = k_{11}g_{11}(1 + k_{11}g_{11})^{-1} \tag{A.13}$$

Likewise, Individual Channel $C_2(s)$ is subject to the disturbance

$$d_2(s) = g_{21}g_{11}^{-1}H_1 r_1(s) \tag{A.14}$$

No assumptions are made as regards the nature of any of the transfer functions $g_{ij}(s)$, $h_i(s)$ or $H_i(s)$; *i.e.*, they need not be stable or minimum phase.

Thus, using (A.5)–(A.14), the closed-loop response of $C_1(s)$ in Figure A.4 is described by

$$y_1(s) = T_1(s)r_1(s) + D_1(s)r_2(s) \tag{A.15}$$

where

$$\begin{aligned} T_1(s) &= \left[1 + k_{11}g_{11}(1 - \gamma_1)\right]^{-1} k_{11}g_{11}(1 - \gamma_1) \\ &= (1 - h_1\gamma_1)^{-1} h_1(1 - \gamma_1) \end{aligned} \tag{A.16}$$

and

$$\begin{aligned} D_1(s) &= \left[1+k_{11}g_{11}(1-\gamma_1)\right]^{-1} g_{12}g_{22}^{-1}H_2 \\ &= (1-h_1\gamma_1)^{-1}(1-h_1)\,g_{12}g_{22}^{-1}H_2 \end{aligned} \tag{A.17}$$

Similarly, the closed-loop response of $C_2(s)$ in Figure A.4 is described by

$$y_2(s) = T_2(s)r_2(s) + D_2(s)r_1(s) \tag{A.18}$$

where

$$\begin{aligned} T_2(s) &= \left[1+k_{22}g_{22}(1-\gamma_2)\right]^{-1} k_2 g_{22}(1-\gamma_2) \\ &= (1-h_2\gamma_2)^{-1} h_2(1-\gamma_2) \end{aligned} \tag{A.19}$$

and

$$\begin{aligned} D_2(s) &= \left[1+k_{22}g_{22}(1-\gamma_2)\right]^{-1} g_{21}g_{11}^{-1}H_1 \\ &= (1-h_2\gamma_2)^{-1}(1-h_2)\,g_{21}g_{11}^{-1}H_1 \end{aligned} \tag{A.20}$$

In a broad sense, $C_i(s)$ represents the open-loop SISO transfer function, $h_i(s)$ describes the impact of controller $k_{jj}(s)$ in the i-th control loop, $\gamma_i(s)$ describes the internal coupling of the plant, and $d_i(s)$ represents the influence of the j-th channel in the i-th channel, or in other words, the interaction or coupling between channels.

Similarly, from Figure A.4 it can be seen that the closed-loop system response of the channels with respect to external disturbances is given by

$$\begin{bmatrix} y_1(s) \\ y_2(s) \end{bmatrix} = \begin{bmatrix} \dfrac{1}{1+C_1(s)} & -\dfrac{g_{12}(s)}{g_{22}(s)}\dfrac{h_2(s)}{1+C_1(s)} \\ -\dfrac{g_{21}(s)}{g_{11}(s)}\dfrac{h_1(s)}{1+C_2(s)} & \dfrac{1}{1+C_2(s)} \end{bmatrix} \begin{bmatrix} d_1(s) \\ d_2(s) \end{bmatrix} \tag{A.21}$$

Both equations (A.5) and (A.21) can be arrived at after performing some algebraic manipulations.

It can be noticed that the multivariable problem is reduced to two SISO channels, each one contained in a feedback loop with a controller. Such controller should be designed to comply with the specifications associated to each channel. Nevertheless, each channel is subject to disturbances $d_i(s)$, $d_j(s)$, and to the coupling $p_i(s)$. Therefore the behaviour will be not only affected by the channel controller but also by the behaviour of the other channel. In this way, it is clear and should be emphasised that the previous representation is equivalent to the original multivariable system and that it entails no loss of information. The multivariable character and cross coupling of the plant are contained in the MSF and the cross coupling terms. That is, the transfer function matrix in (A.5) is equivalent to the closed-loop matrix function [1,2,3]

$$\mathbf{G_{cl}}(s) = \left(\mathbf{I}+\mathbf{G}(s)\mathbf{K}(s)\right)^{-1}\mathbf{G}(s)\mathbf{K}(s) \tag{A.22}$$

It is possible to prove that in order to stabilise the closed-loop response (A.5) it is only necessary to stabilise channels $C_i(s)$ [1,4]. In other words, if $k_{ii}(s)$ stabilises channels (A.6) and (A.11), it will also stabilise the closed-loop response (A.5); that is, if $k_{ii}(s)$ is a stabilising controller for $C_i(s)$ and the reference signals r_i and r_j are stable, then the response y_i is stable. Hence $d_i(s)$ in Figure A.4 can be treated as a normal disturbance acting on the SISO system representing $C_i(s)$.

Assuming that the plant is genuinely multivariable, *i.e.*, $\gamma_a(s) \neq 0$, and accordingly with equations (A.5), (A.21), and with the previous statement, the dynamical performance and disturbance rejection of output $y_i(s)$ can be characterised entirely by the transmittance (or channel) $C_i(s)$. In other words [3]:

- For stable reference inputs and disturbances, $y_i(s)$ is stable if $C_i(s)/(1+C_i(s))$ is stable;
- For the reference $r_i(s)$, the tracking performance of $y_i(s)$ is indicated by $C_i(s)/(1+C_i(s))$;
- For the reference $r_j(s)$, $i \neq j$, (due to $g_{ij}(s)h_j(s)/g_{jj}(s)$, $i \neq j$), coupling rejection $p_i(s)$ in $y_i(s)$ is indicated by $1/(1+C_i(s))$;
- For the disturbance $d_i(s)$, disturbance rejection in $y_i(s)$ is indicated by $1/(1+C_i(s))$;
- For the disturbance $d_j(s)$, $i \neq j$, (due to $g_{ij}(s)h_j(s)/g_{jj}(s)$, $i \neq j$), disturbance rejection in $y_i(s)$ is indicated by $1/(1+C_i(s))$;

Thus, given a diagonal controller, the transmittances $C_i(s)$, $i = 1,2$, can be used to assess the dynamical performance achieved by the controller, where the parameters in the frequency domain as well as the cut-off frequencies of $C_i(s)$ and the bandwidths of $C_i(s)/(1+C_i(s))$ preserve their meanings. In order to have a design rejecting external disturbances and coupling from one channel to the other, it is necessary to maintain the sensitivity function $1/(1+C_i(s))$ small over a wide range of frequencies, especially those in which the disturbances and the coupling are dominant [5,6].

Notice that $C_i(s)$ is only the open loop transmittance of channel i; that is, the transmittance between input i and output i with the feedback loop between output i and input i opened but the other feedback loops closed. By analysing the open loop channels given by (A.6) and (A.11) it is possible to assess the requirements in the controller gains.

A.1.2. The dynamical structure

In a stable and minimum phase SISO system, the only existent restrictions in the closed-loop system dynamical performance are those arising from plant uncertainty and the actuator capability. When the plant possesses RHPPs and RHPZs, the closed-loop system performance is dramatically limited. The open loop gain of the system should be bigger than one in the frequency regions of the RHHPs but less than one in the frequency regions of the RHPZs. Therefore, the controller nature and the closed-loop system dynamical behaviour are invariably influenced by the plant structure [2].

In the multivariable case, the nature of the diagonal controller gains, $k_{ii}(s)$, are influenced by the structure of the scalar channel transmittances $C_i(s)$ given in (A.6) and (A.11) by the same way as in a SISO case [1,3]. Consider the open-loop transmittance $g_{11}(1 - g_{12}g_{22}^{-1}H_2g_{21}g_{11}^{-1})$ in Channel $C_1(s)$ and the open-loop transmittance $g_{22}(1-g_{21}g_{11}^{-1}H_1g_{12}g_{22}^{-1})$ in Channel $C_2(s)$ respectively. The pole–zero structures, or dynamical structure of the open loop channels, assuming a diagonal controller are summarised by Table A.1, provided that no pole-zero cancellation occurs.

Table A.1. Dynamical structure of open loop individual channel

	Zeros	**Poles**
Channel $C_1(s)$	Zeros of $(1 - g_{12}g_{22}^{-1}H_2g_{21}g_{11}^{-1})$	Poles of g_{11}, g_{12} , g_{21}, H_2
Channel $C_2(s)$	Zeros of $(1 - g_{21}g_{11}^{-1}H_1g_{12}g_{22}^{-1})$	Poles of g_{22}, g_{12}, g_{21}, H_1

Derivation of Table A.1 is obtained from (A.6)–(A.9) and (A.11)–(A.13). From (A.8) it can be seen that the poles of $g_{12}(s)$ and $g_{21}(s)$ and the zeros of $g_{11}(s)$ and $g_{22}(s)$ are the poles of $\gamma(s)$. However, in the case of $C_1(s)$, the zeros of $h_2(s)$ in (A.9) include the zeros of $g_{22}(s)$ but not the zeros of $g_{11}(s)$, which in this case are the poles of $(1–\gamma(s)h_2(s))$ and will cancel the zeros of $g_{11}(s)$ before the parenthesis. Therefore, the zeros of $g_{11}(s)(1–\gamma(s)h_2(s))$ are the zeros of $(1– \gamma(s)h_2(s))$ and the poles of $g_{11}(s)(1–\gamma(s)h_2(s))$ are the poles of $g_{11}(s)$, $g_{12}(s)$, $g_{21}(s)$, and $h_2(s)$. The structure of $C_2(s)$ is found in a similar manner.

In some circumstances, not all the zeros and poles indicated in Table A.1 are present for an open-loop channel since pole–zero cancellation within $\gamma_i(s)$ of (A.7) and (A.12) or cancellation between channel zeros and poles within $(1 - \gamma_i)$ of (A.6) and (A.11) may occur. If pole-zero cancellations occur, the poles and zeros are subsets of those indicated by Table A.1. Naturally, the cancellation of poles with zeros in the left hand plane (LHPP and LHPZ) has no consequence. Also, it is observed that the zeros of $C_1(s)$ and $C_2(s)$ are different from the multivariable system transmission zeros defined as the zeros of $|\mathbf{G}|$ and which are the same as the zeros of $(1 - \gamma)$, where γ is defined as in (A.8).

The set of closed-loop poles for Channel C_1 and Channel C_2 are the same since the closed-loop poles of Channels C_1 and C_2 are the zeros of $(1 - \gamma h_2)$ and $(1 - \gamma h_1)$ respectively and these two set of poles are the same since $\gamma h_1 + \gamma h_2 = \gamma h_2 h_1$, where h_1, h_2 and γ are defined by (A.13), (A.9) and (A.8) respectively. When the bandwidth of Channel C_2 and the structure of γ_1 is the same as the structure of γ, the RHPZs of the open-loop transfer function for Channel C_2 are essentially the RHPPs of the closed-loop transfer function for Channel C_1.

An important aspect that should be considered is that no particular characteristics are assumed for the transfer functions $g_{ij}(s)$, $g_{ii}(s)$, and $h_i(s)$ (i,j = 1,2 with $i \neq j$). It should be noticed that the RHPPs of the channels are at the same time RHPPs of individual transfer functions, as established in Table A.1.

The possible closed-loop dynamical performance and control system design of the individual channels are adversely affected by the presence of channel RHPZs and is related to the behaviour of the multivariable structure functions $\gamma(s)$ and $\gamma_i(s)$, i = 1,2. For instance, whenever $\mathbf{G}(s)$ is obtained from a state-space representation, the number of RHPZs of $(1 - \gamma_i)$ is given by [7].

$$Z = N + P - Q \tag{A.23}$$

where Z is the number of RHPZs of $(1 - \gamma_i)$, P is the number of RHPPs of $\gamma_i(s)$, N is the number of clockwise encirclements to the (1,0) point in the Nyquist plot of $\gamma_i(s)$, and Q is the number of eigenvalues in the right hand plane of the state-space representation. Whenever $\mathbf{G}(s)$ is obtained differently, Q = 0 in (A.23). Notice that (A.23) is an application of the Nyquist Stability Criterion [7]. It is readily apparent that if the system itself does not possess RHPPs, the channel's RHPZs are the RHPZs of $(1 - \gamma_i)$.

A.1.3. The multivariable structure function

The Multivariable Structure Function (MSF) introduced in (A.8) is a function defined in the frequency domain. Its correct interpretation is of great importance since [8]:

- It determines the dynamical characteristics of each input-output configuration;
- It has an interpretation in the frequency domain;
- Its magnitude quantifies the coupling between the channels;
- It is related to the plant transmission zeros (zeros of $(1 - \gamma)$, $|\mathbf{G}(s)| = g_{11}g_{22} - g_{12}g_{21} = 0$);
- $\gamma = 1$ determines the non-minimum phase condition;
- Its closeness to (1,0) in the Nyquist plot indicates to what extent the plant is sensitive to uncertainty in terms of gain and phase margins. This characteristic plays a key role in the design of robust controllers.

From (A.6) and (A.11) it is clear that the characteristics of the controller performance are determined by the MSF and that the channel interaction can be treated as a disturbance [3]. When the magnitude of $\gamma(s)$ is a lot less than one the interaction is very small; on the other hand, the interaction is high. A system which MSF has a magnitude much smaller than one for every frequency the channels can be represented by $(1 - \gamma_i)$

$$C_i'(s) = k_{ii}(s)\, g_{ii}(s) \tag{A.24}$$

Coupling between channels is defined by the term $\gamma_i(s)$ ($\gamma(s)h_i(s)$) and can be expressed in *dB* directly from the channels (A.6) and (A.11). Notice that a system is ill-conditioned when the value of $\gamma(s)$ tends to 1. If $\gamma(s) = 1$, $\mathbf{G}(s)$ is non-minimum phase, as previously stated.

The reason to call $\gamma(s)$ as Multivariable Structure Function is justified from the fact that from this function the dynamical structure of the multivariable system can be determined, as summarised by Table

A.1 and (A.23). In fact, the transmission zeros of the transfer function matrix $\mathbf{G}(s)$, given a state-space representation, are the zeros of $(1 - \gamma)$ that are not the poles of $\mathbf{G}(s)$ [7], as stated by (A.23). If the system has no RHPPs, then the transmission zeros of the system are the zeros of $(1 - \gamma)$. In general, the poles of $g_{ij}(s)$ are known and the poles of $h_i(s)$ are determined as part of the control design process. On the other hand, the zeros of the channels should be checked to determine if any of them is or becomes non-minimum phase. The contribution of the reference of $C_i(s)$ in the response of $C_j(s)$ can be studied from the closed-loop system response.

It is well known that the RHPZs have adverse effects in the performance and sensitivity of the control system [9,10]. The potential restrictions in performance due to non-minimum phase behaviour can be established through the RHPZs or purely imaginary zeros of $(1 - \gamma)$. Notice that the RHPZs of $(1 - \gamma)$ are the transmission zeros in the right hand plane of the multivariable system. Moreover, if the system possesses purely imaginary transmission zeros at the frequency $s = s_0$ if $\gamma(s_0) = 1$. Clearly, function $\gamma(s)$ determines the necessary restrictions in $C_i(s)$ and therefore in the controller $k_{ii}(s)$. However, in a more general case, it is required that $(1 - \gamma(s)h_i(s))$ has no RHPZs and not only $(1 - \gamma(s))$. The existence of stabilising controllers for a particular system is determined by its MSF, $\gamma(s)$, and the design specifications reflected by $h_i(s)$. Thus, a general pattern that establishes a design process does not exist [3,8,11].

A preliminary analysis can be carried out assuming that the bandwidth of one of the channels, for instance $C_2(s)$, is higher than the one of the other channel, $C_1(s)$ [3]. Then, the gain of controller $k_{22}(s)$ is high over the frequency range that includes the dynamics of $C_1(s)$. That is, $h_2(s)$ is close to one over the bandwidth required by $C_1(s)$. Under these circumstances $C_1(s)$ can be simplified to

$$C_1(s) = k_{11}(s)\, g_{11}(s)\big(1 - \gamma(s)\big) \tag{A.25}$$

As it was previously mentioned, it is clear from (A.6) and (A.11) that the performance characteristics of the controllers are determined by $\gamma(s)$. If the transfer function matrix $\mathbf{G}(s)$ possesses a non-minimum phase transmission zero, some problems to stabilise the plant will arise especially if the value of the zero is less than the cut-off frequency required for the system [8,10]. Moreover, the robustness of the channels can be established in terms of gain and phase margins as long as the Nyquist paths of the functions $\gamma(s)h_i(s)$ pass far away from (1,0). Thus, the design of $k_{ii}(s)$, which should provide adequate gain and phase margins for $k_{ii}g_{ii}(s)$, can be found using an iterative process [11] that will discussed soon.

It is possible to argue that the gain and phase margins are not good robustness measures. In fact, it is possible to find a system with good stability margins but with an undesirable nominal sensitivity function [12]. Considering that the Nyquist/Bode approach is a graphical tool, the appropriate interpretation of gain and phase margins requires a corresponding Bode diagram [13]. That is, if the trajectory during the *roll-off* has borders or it is curly the information provided by the stability is useless.

Therefore, when it said that the *Nyquist diagram should not pass near the critical point*, this should be interpreted as good roll-off behaviour as well. This is a part of the design process (*Bode shaping*). Thus, the gain and phase margins should be considered jointly with their corresponding Bode and Nyquist diagrams.

Finally, another characteristic particular to the MSF that has not been mentioned yet exists. A technique based in the Relative Gain Array (RGA), originally introduced in [14] and that was limited to zero frequency is used to determine if it is possible to design decentralised control systems (*i.e.*, with diagonal controllers) [5,12]. In [5] it is stated that the method is effective for the whole frequency range. The RGA matrix can be expressed in terms of the MSF, fact that confirms the previous proposition and proves that both have the same information [8]. In accordance with the characteristics of the RGA matrix it is possible to determine in a somewhat *empirical* way how the input-output pairing of multivariable systems should be done [12]. Nevertheless, the correct interpretation of the MSF goes far beyond of an empirical result. In fact, the appropriate analysis of the MSF (at low and high frequency) provides a complete and effective framework, the ICAD, to design multivariable control systems even for highly coupled and pathological plants [8]. The MSF clarifies the possibilities to meet design specifications and satisfying robustness conditions. Moreover, it is possible to determine the existence and perform the analysis and design of diagonal controllers that stabilise the input-output chosen configuration for a given multivariable plant [8].

A.1.4. The design process

As it was previously mentioned, the dynamical structure of the 2×2 plant is determined by the input-output channels defined after pairing each input to each output. In fact, for the 2-input 2-output case two different possibilities exist:

(*a*) $C_1(s) \rightarrow u_1(s) - y_1(s)$ with $\gamma_a(s) = g_{12}(s)g_{21}(s)/g_{11}(s)g_{22}(s)$
$C_2(s) \rightarrow u_2(s) - y_2(s)$

(*b*) $C_1(s) \rightarrow u_1(s) - y_2(s)$ with $\gamma_b(s) = g_{11}(s)g_{22}(s)/g_{12}(s)g_{21}(s)$
$C_2(s) \rightarrow u_2(s) - y_1(s)$

The coupling characteristic of each configuration is determined by $\gamma_a(s)$ and $\gamma_b(s)$ – its associated MSF.

Although a general pattern dictating the design process does not exist, it is possible to be carried out in the following iterative way [11]:

1. Define a state-space representation and obtain its transfer function matrix.
2. Analyse both possible MSFs and determine the existence of the controller for the chosen case.
3. Define the control matrix by choosing the input-output pairing associated to the desired MSF:

(*a*) $\mathbf{K}(s) = \begin{bmatrix} k_{11}(s) & 0 \\ 0 & k_{22}(s) \end{bmatrix} \Rightarrow \begin{matrix} u_1(s) \rightarrow y_1(s) \\ u_2(s) \rightarrow y_2(s) \end{matrix} \Rightarrow \gamma_a(s)$

(*b*) $\mathbf{K}(s)=\begin{bmatrix} 0 & k_{12}(s) \\ k_{21}(s) & 0 \end{bmatrix} \Rightarrow \begin{matrix} u_1(s)\to y_2(s) \\ u_2(s)\to y_1(s) \end{matrix} \Rightarrow \gamma_b(s)$

If the configuration (*a*) is chosen, equations (A.6) through (A.14) hold. Otherwise, the channels are defined as

$$C_i(s)=k_{ij}g_{ji}\left(1-\gamma_b(s)h_j(s)\right) \tag{A.26}$$

where $i,j = 1,2$ with $i \neq j$ and

$$\gamma_b(s)=\frac{g_{11}(s)g_{22}(s)}{g_{12}(s)g_{21}(s)} \tag{A.27}$$

$$h_j(s)=\frac{k_{ji}(s)g_{ij}(s)}{1+k_{ji}(s)g_{ij}(s)} \tag{A.28}$$

$$p_i(s)=\frac{g_{jj}(s)}{g_{ij}(s)}h_j(s)r_j(s) \tag{A.29}$$

4. First approximation in $C_i(s)$ ($h_j(s) = 1$); $i \neq j$.
5. Channel $C_i(s)$ controller design.
6. Interaction with channel $C_j(s)$ defined ($h_i(s)$ is defined).
7. Structural robustness assessment ($\gamma_k(s)h_i(s)$, $k = a$ or b).
8. Channel $C_j(s)$ controller design.
9. Interaction with channel $C_i(s)$ defined ($h_j(s)$ is defined).
10. Structural robustness assessment ($\gamma_k(s)h_j(s)$).
11. Channel $C_i(s)$ controller redesign.
12. The process is repeated until an adequate controller for both channels is designed and robustness in $C_i(s)$, $k_{ii}(s)g_{ii}(s)$ (or $k_{ij}(s)g_{ji}(s)$), and $\gamma_k(s)h_i(s)$ is guaranteed ($i \neq j$, $i,j = 1,2$, $k = a$ or b).

A.2. Representation of *m*×*m* systems in individual channels

The individual channel representation for *m*×*m* is included next for completeness, as previously shown in [4]. Particular example designs of 3×3 and 4×4 control systems can be found in [15] and [16], respectively.

A.2.1. Structural analysis of *m*×*m* systems. Multiple channel structure

The general *m*-input *m*-output system is decomposed into two multiple channels $\mathbf{M}_1$ and $\mathbf{M}_2$ as in Figure A.5, where Multiple Channel $\mathbf{M}_1$ contains m_1 inputs and m_1 outputs whereas Multiple Channel $\mathbf{M}_2$ contains m_2 inputs and m_2 outputs, and $m_1 + m_2 = m$.

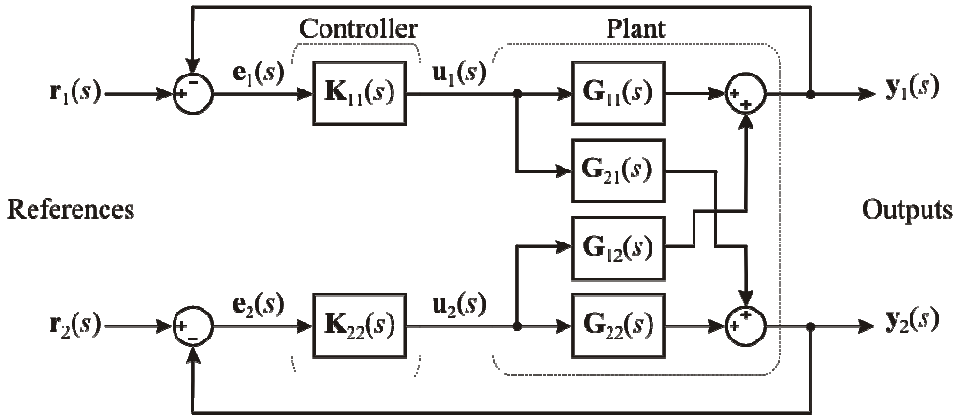

Figure A.5. Partitioned *m*-input *m*-output multivariable system with diagonal controller

The partitioning of the system is such that:

$$\mathbf{G}(s)=\begin{bmatrix}\mathbf{G}_{11}(s) & \mathbf{G}_{12}(s)\\ \mathbf{G}_{21}(s) & \mathbf{G}_{22}(s)\end{bmatrix} \qquad \mathbf{K}(s)=\begin{bmatrix}\mathbf{K}_{11}(s) & \mathbf{0}\\ \mathbf{0} & \mathbf{K}_{22}(s)\end{bmatrix} \tag{A.30}$$

$$\mathbf{r}(s)=\begin{bmatrix}\mathbf{r}_1(s)\\ \mathbf{r}_2(s)\end{bmatrix} \qquad \mathbf{y}(s)=\begin{bmatrix}\mathbf{y}_1(s)\\ \mathbf{y}_2(s)\end{bmatrix} \tag{A.31}$$

where $\mathbf{G}(s)$ is the plant matrix transfer function and $\mathbf{K}(s)$ is the controller. As $\mathbf{K}(s)$ is assumed a diagonal controller, both $\mathbf{K}_{11}(s)$ and $\mathbf{K}_{22}(s)$ are diagonal controllers.

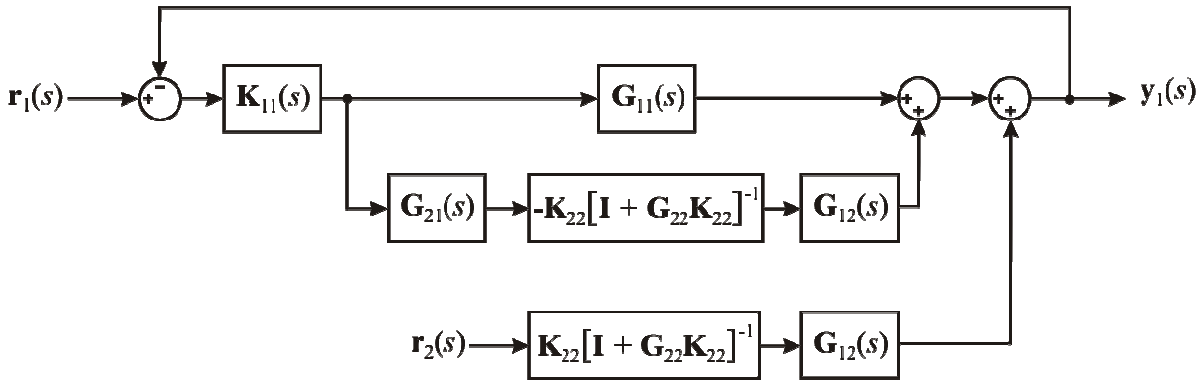

Figure A.6. Signal transmissions to output $\mathbf{y}_1$

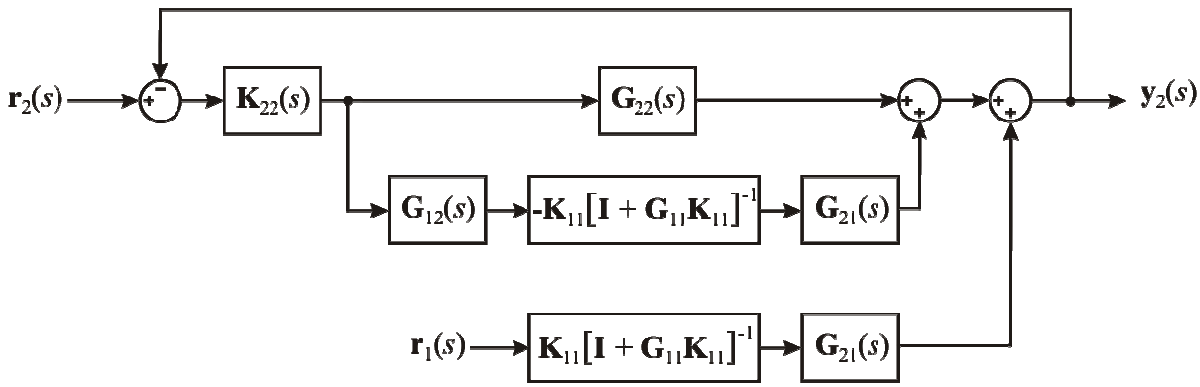

Figure A.7. Signal transmissions to output $\mathbf{y}_2$

Consider the forward signal transmission from the reference m_1-vector $\mathbf{r}_1$ to its associated output m_1-vector $\mathbf{y}_1$. As in the 2-input 2-output case, this transmission follows two paths: one directly through $\mathbf{G}_{11}(s)$; and another via $\mathbf{G}_{12}(s)$, the bottom of the system (multiple feedback), and $\mathbf{G}_{12}(s)$, as shown in Figure A.6. The same applies when considering the forward signal transmission from the reference m_2-vector $\mathbf{r}_2$ to its associated output m_2-vector $\mathbf{y}_2$, as shown in Figure A.7. Therefore, the block diagram of Figure A.5 can be decomposed into two equivalent multiple channels. Such situation is depicted in Figure A.8.

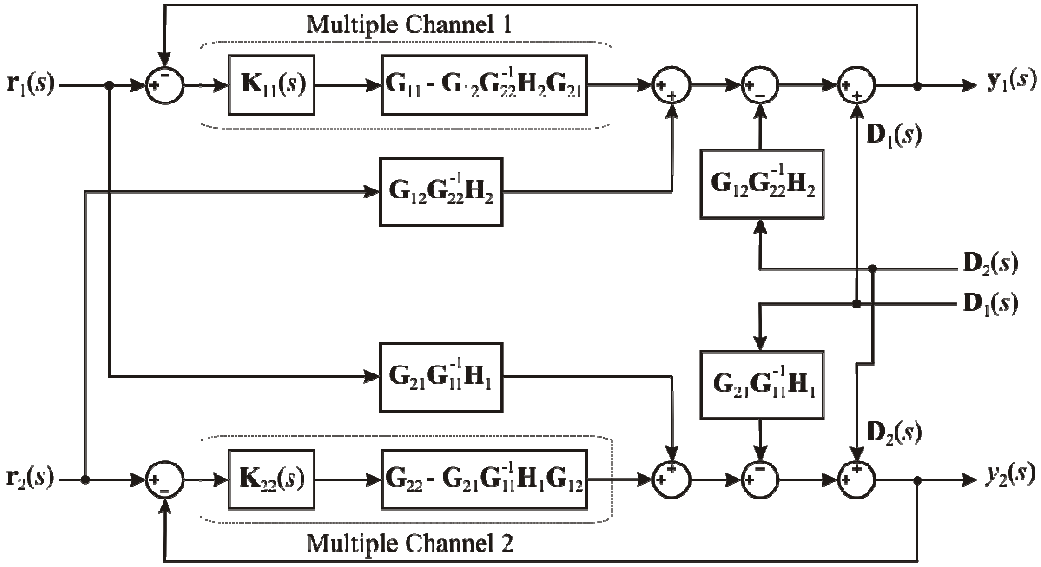

Figure A.8. Multiple channel representation

Multiple Channel $\mathbf{M}_1$ has the forward path m_1-input m_1-output transmittance matrix

$$\mathbf{M}_1(s)=\left[\mathbf{I}-\mathbf{G}_{12}(s)\mathbf{G}_{22}^{-1}(s)\mathbf{H}_2(s)\mathbf{G}_{21}(s)\mathbf{G}_{11}^{-1}(s)\right]\mathbf{G}_{11}(s)\mathbf{K}_{11}(s) \tag{A.32}$$

where the multiple subsystem transfer function matrix $\mathbf{H}_2(s)$ is given by

$$\mathbf{H}_2(s)=\mathbf{G}_{22}(s)\mathbf{K}_2(s)\left[\mathbf{I}+\mathbf{G}_{22}(s)\mathbf{K}_2(s)\right]^{-1} \tag{A.33}$$

and is subjected to the cross-reference disturbance

$$\mathbf{D}_1(s)=\mathbf{G}_{12}(s)\mathbf{G}_{22}^{-1}(s)\mathbf{H}_2(s) \tag{A.34}$$

Similarly, Multiple Channel $\mathbf{M}_2$ has the forward path m_2-input m_2-output transmittance matrix

$$\mathbf{M}_2(s)=\left[\mathbf{I}-\mathbf{G}_{21}(s)\mathbf{G}_{11}^{-1}(s)\mathbf{H}_1(s)\mathbf{G}_{12}(s)\mathbf{G}_{22}^{-1}(s)\right]\mathbf{G}_{22}(s)\mathbf{K}_{22}(s) \tag{A.35}$$

where the multiple subsystem transfer function matrix $\mathbf{H}_2(s)$ is given by

$$\mathbf{H}_1(s)=\mathbf{G}_{11}(s)\mathbf{K}_{11}(s)\left[\mathbf{I}+\mathbf{G}_{11}(s)\mathbf{K}_{11}(s)\right]^{-1} \tag{A.36}$$

and is subjected to the cross-reference disturbance

$$\mathbf{D}_2(s)=\mathbf{G}_{21}(s)\mathbf{G}_{11}^{-1}(s)\mathbf{H}_1(s) \tag{A.37}$$

The multiple channels pole-zero structure can be obtained through an extension of the 2-input 2-output case summarised in Table A.1 [4].

A.2.2. Individual channel structure for *m*-input *m*-output systems

The structure of individual channels for *m*-input *m*-output systems is a particular case of the multiple channels. Consider the Individual Channel C_1 (Channel C_1 for brevity); *i.e.*, the channel defined by choosing $\mathbf{r}_1$ to be a scalar comprising reference input one only and $\mathbf{y}_1$ to be a scalar comprising output one only with feedback loop one open but all other feedback loops closed. Channel C_1 can be interpreted as the Multiple Channel $\mathbf{M}_1$ with the partitioning (A.30) chosen as:

$$\mathbf{G}(s)=\begin{bmatrix} g_{11} & g_{12} & \cdots & g_{1m} \\ g_{21} & g_{22} & \cdots & g_{2m} \\ \vdots & \vdots & & \vdots \\ g_{m1} & g_{m2} & \cdots & g_{mm} \end{bmatrix} \qquad \mathbf{K}(s)=\begin{bmatrix} k_{11} & 0 & \cdots & 0 \\ 0 & k_{22} & \cdots & 0 \\ \vdots & \vdots & & \vdots \\ 0 & 0 & \cdots & k_{mm} \end{bmatrix} \tag{A.38}$$

with

$$\mathbf{G}_{11}(s)=g_{11}(s) \qquad \mathbf{G}_{12}(s)=\begin{bmatrix} g_{12}(s) & \cdots & g_{1m}(s) \end{bmatrix} \qquad \mathbf{K}_{11}(s)=k_{11}(s) \tag{A.39}$$

$$\mathbf{G}_{21}(s)=\begin{bmatrix} g_{21} \\ \vdots \\ g_{m1} \end{bmatrix} \qquad \mathbf{G}_{22}(s)=\begin{bmatrix} g_{22} & \cdots & g_{2m} \\ \vdots & & \vdots \\ g_{m2} & \cdots & g_{mm} \end{bmatrix} \tag{A.40}$$

$$\mathbf{K}_{22}(s)=\begin{bmatrix} k_{22} & \cdots & 0 \\ \vdots & & \vdots \\ 0 & \cdots & k_{mm} \end{bmatrix} \tag{A.41}$$

Some definitions are required prior to the Individual Channel derivation. Define

$$\bar{\mathbf{G}}(s)=\left[\mathbf{K}^{-1}+\mathbf{G}\right]=\begin{bmatrix} \left(k_{11}^{-1}+g_{11}\right) & g_{12} & \cdots & g_{1m} \\ g_{21} & \left(k_{22}^{-1}+g_{22}\right) & \cdots & g_{2m} \\ \vdots & \vdots & & \vdots \\ g_{m1} & g_{m2} & \cdots & \left(k_{mm}^{-1}+g_{mm}\right) \end{bmatrix} \tag{A.42}$$

possible since $\mathbf{K}$ is an $m\times m$ diagonal controller matrix. However,

$$k_{ii}^{-1}+g_{ii}=g_{ii}\left(1+k_{ii}g_{ii}\right)/\left(k_{ii}g_{ii}\right)=g_{ii}/h_i \tag{A.43}$$

where $i = 1,\ldots,m$ and the individual subsystem transfer function, $h_i(s)$, is

$$h_i(s)=k_{ii}g_{ii}/\left(1+k_{ii}g_{ii}\right) \tag{A.44}$$

Hence, by substituting (A.43) into (A.42), we have

$$\bar{\mathbf{G}}(s)=\begin{bmatrix} g_{11}/h_1 & g_{12} & \cdots & g_{1m} \\ g_{21} & g_{22}/h_2 & \cdots & g_{2m} \\ \vdots & \vdots & & \vdots \\ g_{m1} & g_{m2} & \cdots & g_{mm}/h_m \end{bmatrix} \tag{A.45}$$

From (A.32), Channel $C_1(s)$ has the open-loop SISO transmittance

$$C_1(s) = k_{11} g_{11} (1 - \gamma_1) \tag{A.46}$$

where

$$\gamma_1(s) = \mathbf{G}_{12}\mathbf{G}_{22}^{-1}\mathbf{H}_2\mathbf{G}_{21}\mathbf{G}_{11}^{-1} \tag{A.47}$$

Also,

$$\gamma_1(s) = \mathbf{G}_{12}\mathbf{G}_{22}^{-1}\mathbf{H}_2\mathbf{G}_{21}\mathbf{G}_{11}^{-1} = -\begin{vmatrix} \mathbf{0} & \mathbf{G}_{12} \\ \mathbf{G}_{21} & \bar{\mathbf{G}}_{22} \end{vmatrix} / g_{11} \left| \bar{\mathbf{G}}_{22} \right| \tag{A.48}$$

where

$$\bar{\mathbf{G}}_{22} = \mathbf{H}_2^{-1}\mathbf{G}_{22} = \left[\mathbf{K}_{22}^{-1} + \mathbf{G}_{22} \right] \tag{A.49}$$

Therefore, considering (A.38) and (A.49), (A.48) becomes

$$\gamma_1(s) = -\begin{vmatrix} 0 & g_{12} & \cdots & g_{1m} \\ g_{21} & g_{22}/h_2 & \cdots & g_{2m} \\ \vdots & \vdots & & \vdots \\ g_{m1} & g_{m2} & \cdots & g_{mm}/h_m \end{vmatrix} / g_{11} \begin{vmatrix} g_{22}/h_2 & \cdots & g_{2m} \\ \vdots & & \vdots \\ g_{m2} & \cdots & g_{mm}/h_m \end{vmatrix} \tag{A.50}$$

Channel C_1 is subject to the scalar disturbance

$$\begin{aligned} d_1(s) &= \mathbf{G}_{12}\mathbf{G}_{22}^{-1}\mathbf{H}_2 \cdot \mathbf{r}_2 \\ &= -\begin{vmatrix} \mathbf{0} & \mathbf{G}_{12} \\ \mathbf{r}_2 & \bar{\mathbf{G}}_{22} \end{vmatrix} / \left| \bar{\mathbf{G}}_{22} \right| \end{aligned} \tag{A.51}$$

i.e., using (A.48) and (A.50)

$$d_1(s) = -\begin{vmatrix} 0 & g_{12} & \cdots & g_{1m} \\ r_2 & g_{22}/h_2 & \cdots & g_{2m} \\ \vdots & \vdots & & \vdots \\ r_m & g_{m2} & \cdots & g_{mm}/h_m \end{vmatrix} / \begin{vmatrix} g_{22}/h_2 & \cdots & g_{2m} \\ \vdots & & \vdots \\ g_{m2} & \cdots & g_{mm}/h_m \end{vmatrix} \tag{A.52}$$

In order to simplify equations (A.46), (A.50) and (A.52), and to generalise this procedure to the other (m – 1) individual channels, some definitions are required.

Let matrix $\bar{\mathbf{G}}^{i_1 i_2 \ldots i_r}$ be defined as the matrix obtained from $\bar{\mathbf{G}}$ in (A.45) by eliminating the i_1-th row and column, the i_2-th row and column and so on up to the i_r-th row and column. Define the matrix $\bar{\mathbf{G}}_j^{i_1 i_2 \ldots i_r}$ as the matrix obtained by setting diagonal element g_{jj}/h_j of $\bar{\mathbf{G}}$ to zero before eliminating the rows and columns as in the definition of $\bar{\mathbf{G}}^{i_1 i_2 \ldots i_r}$. Define $\mathbf{R}_j$ as the matrix obtained by replacing the j-th column of $\bar{\mathbf{G}}$ by $\mathbf{r}$ and setting r_j to zero. With these definitions the multivariable structure function of (A.50), $\gamma_1(s)$, for Channel C_1 is

$$\gamma_1(s) = -\left| \bar{\mathbf{G}}_1 \right| / g_{11} \left| \bar{\mathbf{G}}^1 \right| \tag{A.53}$$

and Channel C_1 is subject to the disturbance (A.51), rewritten as

$$d_1(s) = -\left| \mathbf{R}_1 \right| / \left| \bar{\mathbf{G}}^1 \right| \tag{A.54}$$

Therefore, by allocating the assignment of input-output pairs to the Multiple Channel $\mathbf{M}_1$ and Multiple Channel $\mathbf{M}_2$, it follows in the same manner that the m individual channels $C_m(s)$ have the open-loop SISO transmittance

$$C_i(s) = k_{ii} g_{ii} (1 - \gamma_i) \tag{A.55}$$

where $i = 1,\ldots,m$, and

$$\gamma_i(s) = -\left|\bar{\mathbf{G}}_i\right| / g_{ii} \left|\bar{\mathbf{G}}^i\right| \tag{A.56}$$

and are subjected to the disturbances

$$d_i(s) = -\left|\mathbf{R}_i\right| / \left|\bar{\mathbf{G}}^i\right| \tag{A.57}$$

The multivariable design task is thus replaced by the set of SISO design tasks shown in Figure A.9. No assumptions are made as regards the nature of any of the transfer functions $g_{ij}(s)$ or $h_i(s)$; *i.e.*, they need not to be stable or minimum-phase.

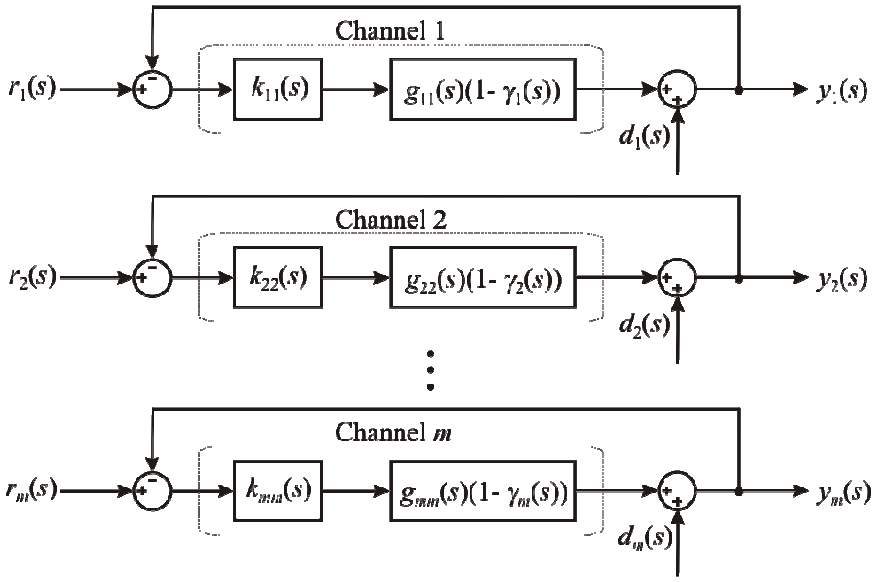

Figure A.9. m-input m-output ICAD structures

Fundamental indicators of the potential performance and coupling of the multivariable system, equivalent to the MSF $\gamma(s)$ for 2-input 2-output systems, are provided by MSFs $\Gamma_i(s)$. MSFs $\Gamma_i(s)$ ($i = 1,2,\ldots,m$ are defined as [4]

$$\Gamma_i(s) = -\left|\mathbf{G}_i^{12\ldots(i-1)}\right| / \left(g_{ii} \left|\mathbf{G}^{12\ldots(i-1)i}\right|\right) \tag{A.58}$$

where $\mathbf{G}^{i_1 i_2 \ldots i_r}$ is the transfer function matrix obtained from the plant matrix $\mathbf{G}(s)$ by eliminating rows and columns of elements $i_1, i_2, \ldots, i_r$; and matrix $\mathbf{G}_j^{i_1 i_2 \ldots i_r}$ is the transfer function matrix obtained from $\mathbf{G}(s)$ by setting diagonal element g_{jj} of $\mathbf{G}(s)$ to zero before eliminating the rows and columns as in the definition of $\mathbf{G}^{i_1 i_2 \ldots i_r}$. By definition (A.58), $\Gamma_m(s) = 0$. Alternatively, $\Gamma_i(s)$ can be defined as

$$\Gamma_i(s) = \gamma(s)_{12\ldots i|h(i+1)=h(i+2)=\cdots=h_m=1} = \gamma_i(s)\Big|_{\substack{h_1=h_2=\cdots=h_{(i-1)}=0 \\ h_{(i+1)}=h_{(i+2)}=\cdots=h_m=1}} \quad \text{(A.59)}$$

A.3. References

[1] Leithead WE, O'Reilly J. *Performance Issues in the Individual Channel 2–input 2–output Systems. Part 1: Structural issues.* International Journal of Control, **54**, no. 1, pp. 47–82, 1991.

[2] O'Reilly J, Leithead WE. *Multivariable Control by Individual Channel Design*. International Journal of Control, **54**, no. 1, pp. 1–46, 1991.

[3] Leithead WE. *What is Individual Channel Analysis and Design?* Department of Electronic and Electrical Engineering, University of Strathclyde, Scotland; University of Glasgow, Scotland, 1993.

[4] Leithead WE, O'Reilly J. *M-input m-output Feedback Control by Individual Channel Design. Part 1. Structural Issues.* International Journal of Control, **56**, no. 6. pp. 1347–1397, 1992.

[5] Skogestad S, Postlethwaite I. *Multivariable feedback control. Analysis and design*. UK: John Wiley & Sons; 1996.

[6] Zhou K, Doyle J. *Essentials of Robust Control*. USA: Prentice–Hall; 1998.

[7] Leithead WE, O'Reilly J. *Investigation of the ICD Structure of Systems Defined by State Space Models.* International Journal of Control, **60**, pp. 71–89, 1994.

[8] Licéaga–Castro E, Licéaga–Castro J, Ugalde–Loo CE. *Beyond the Existence of Diagonal Controllers: from the Relative Gain Array to the Multivariable Structure Function*. Proceedings of the Joint 44th IEEE Conference on Decision and Control and European Control Conference, pp. 7150–7156, 2005.

[9] Freudenberg JS, Looze D. *Right Half Plane Poles and Zeros and Design Tradeoffs in Feedback Systems*. IEEE Transactions on Automatic Control, pp. 555–565, 1985.

[10] Leithead WE, O'Reilly J. *Uncertain SISO Systems with Fixed Stable Minimum–Phase Controllers: Relationship of Closed–Loop Systems to Plant RHP Poles and Zeros*. International Journal of Control, **53**, pp. 771–798, 1991.

[11] Ugalde–Loo CE, Licéaga–Castro E, Licéaga–Castro J. *2x2 Individual Channel Design MATLAB® Toolbox*. Proceedings of the Joint 44th IEEE Conference on Decision and Control and European Control Conference, pp. 7603–7608, 2005.

[12] Goodwin G, Graebe SF, Salgado ME. *Control System Design*. USA: Prentice–Hall; 2001.

[13] Zames G. *Feedback and Optimal Sensitivity: Model Reference Transformations, Multiplicative Seminorms, and Approximate Inverse.* IEEE Transactions on Automatic Control, **AC–26**, pp. 301–320, 1981.

[14] Bristol EH. *On a New Measure of Interaction for Multivariable Process Control*. IEEE Transactions on Automatic Control, **AC–11**, pp. 133–134, 1966.

[15] Akbar MA, Leithead WE, O'Reilly J, Robertson SS. *Design of Robust Controllers for 3–input 3–output Supersonic Aircraft Power Plant using ICD.* Proceedings of the 3rd IEEE Conference on Control Applications, **1**, pp. 95–99, 1994.

[16] Licéaga–Castro J, Verde C, O'Reilly J, Leithead WE. *Helicopter Control using Individual Channel Design.* IEE Proceedings – Control Theory and Applications, **142,** pp. 58–72, 1995.

Appendix B

SYSTEM PARAMETERS

GENERATOR 1

The following synchronous generator parameters are used in the OMIB studies carried out in Chapters 3 and 4 and in the multi-machine studies of Chapter 6.

Base power	$S_{Base} = 100\ MVA$
Base voltage	$V_{Base} = 20\ kV$
Nominal frequency	$f_0 = 50\ Hz$
Inertia constant	$H = 4.27\ s$
Damping coefficient	$D = 0$ (unless stated otherwise)
Stator resistance	$R_a = 0\ p.u.$
Direct axis:	
Synchronous reactance	$X_d = 1.445\ p.u.$
Transient reactance	$X_d^{'} = 0.316\ p.u.$
Sub-transient reactance	$X_d^{''} = 0.179\ p.u.$
Transient time constant	$\tau_{d0}^{'} = 5.26\ s$
Sub-transient time constant	$\tau_{d0}^{''} = 0.028\ s$
Quadrature axis:	
Synchronous reactance	$X_q = 0.959\ p.u.$
Sub-transient reactance	$X_q^{''} = 0.162\ p.u.$
Sub-transient time constant	$\tau_{q0}^{''} = 0.159\ s$

GENERATOR 2

The following generator parameters are used in the model comparison performed in section 3.6.6.

Base power	$S_{Base} = 2220\ MVA$
Base voltage	$V_{Base} = 24\ kV$
Nominal frequency	$f_0 = 60\ Hz$
Inertia constant	$H = 3.5\ s$
Damping coefficient	$D = 0\ p.u.$
Stator resistance	$R_a = 0.003\ p.u.$
Direct axis:	
Synchronous reactance	$X_d = 1.81\ p.u.$
Transient reactance	$X_d^{'} = 0.3\ p.u.$
Sub-transient reactance	$X_d^{''} = 0.23\ p.u.$
Transient time constant	$\tau_{d0}^{'} = 8\ s$
Sub-transient time constant	$\tau_{d0}^{''} = 0.03\ s$
Quadrature axis:	
Synchronous reactance	$X_q = 1.76\ p.u.$
Transient reactance	$X_q^{'} = 0.65\ p.u.$
Sub-transient reactance	$X_q^{''} = 0.25\ p.u.$
Transient time constant	$\tau_{q0}^{'} = 1\ s$
Sub-transient time constant	$\tau_{q0}^{''} = 0.07\ s$

STATIC VAR COMPENSATOR

The following SVC parameters are used in Chapter 4:

Inductive reactance	$X_L = 2.5\ p.u.$
Capacitive reactance	$X_C = 2.5\ p.u.$

THYRISTOR-CONTROLLED SERIES COMPENSATOR

The following TCSC parameters are used in Chapter 4:

Inductive reactance	$X_L = 1.625 \times 10^{-3}\ p.u.$
Capacitive reactance	$X_C = 9.375 \times 10^{-3}\ p.u.$

MULTI-MACHINE SYSTEM 1: 3 machines, 9 buses

The following parameters are used in the multi-machine model assessment of Chapter 5, section 5.5.1.

Base power $S_{Base} = 100\ MVA$

Number of machines $n = 3$

Table B.1. Parameters of multi-machine system 1 (3 machines, 9 buses)

	Value		
Variable	**Machine 1**	**Machine 2**	**Machine 3**
Model type	Classic (0*d*.0*q*)	4th C (1*d*.1*q*)	4th C (1*d*.1*q*)
Base power, $S_{G,Base}$	100 *MVA*	100 *MVA*	100 *MVA*
Base voltage, $V_{G,Base}$	16.5 *kV*	18 *kV*	13.8 *kV*
Nominal frequency, f_0	60 *Hz*	60 *Hz*	60 *Hz*
Inertia constant, H	23.64 *s*	6.4 *s*	3.01 *s*
Damping coefficient, D	0 *p.u.*	0 *p.u.*	0 *p.u.*
Stator resistance, R_a	0 *p.u.*	0 *p.u.*	0 *p.u.*
Direct axis:			
Synchronous reactance, X_d	0.1460 *p.u.*	0.8958 *p.u.*	1.3125 *p.u.*
Transient reactance, $X_d^{'}$	0.0608 *p.u.*	0.1198 *p.u.*	0.1813 *p.u.*
Transient time constant, $\tau_{d0}^{'}$	8.96 *s* 3377.84 *p.u.*	6 *s* 2261.95 *p.u.*	5.89 *s* 2220.48 *p.u.*
Quadrature axis:			
Synchronous reactance, X_q	0.0969 *p.u.*	0.8645 *p.u.*	1.2578 *p.u.*
Transient reactance, $X_q^{'}$	0.0969 *p.u.*	0.1969 *p.u.*	0.25 *p.u.*
Transient time constant, $\tau_{q0}^{'}$	0 *s* 0 *p.u.*	0.535 *s* 201.69 *p.u.*	0.6 *s* 226.19 *p.u.*
Transformer:			
Base power, $S_{T,Base}$	100 *MVA*	100 *MVA*	100 *MVA*
Base voltage, $V_{T,Base}$	230 *kV*	230 *kV*	230 *kV*
Reactance, X_{Trans}	0.0576 *p.u.*	0.0625 *p.u.*	0.0586 *p.u.*

MULTI-MACHINE SYSTEM 2: 4 machines, 11 buses

The following parameters are used in the multi-machine model assessment of Chapter 5, section 5.5.2.

Base power $S_{Base} = 100\ MVA$

Number of machines $n = 4$

Table B.2. Parameters of multi-machine system 2 (4 machines, 11 buses)

	Value			
Variable	**Machine 1**	**Machine 2**	**Machine 3**	**Machine 4**
Model type	6^{th} (2*d*.2*q*)	6^{th} (2*d*.2*q*)	6^{th} (2*d*.2*q*)	6^{th} (2*d*.2*q*)
Base power, $S_{G,Base}$	900 *MVA*	900 *MVA*	900 *MVA*	900 *MVA*
Base voltage, $V_{G,Base}$	20 *kV*	20 *kV*	20 *kV*	20 *kV*
Nominal frequency, f_0	60 *Hz*	60 *Hz*	60 *Hz*	60 *Hz*
Inertia constant, H	6.5 *s*	6.5 *s*	6.175 *s*	6.175 *s*
Damping coefficient, D	0 *p.u.*	0 *p.u.*	0 *p.u.*	0 *p.u.*
Stator resistance, R_a	0.0025 *p.u.*	0.0025 *p.u.*	0.0025 *p.u.*	0.0025 *p.u.*
Direct axis:				
Synchronous reactance, X_d	1.8 *p.u.*	1.8 *p.u.*	1.8 *p.u.*	1.8 *p.u.*
Transient reactance, $X_d^{'}$	0.3 *p.u.*	0.3 *p.u.*	0.3 *p.u.*	0.3 *p.u.*
Sub-transient reactance, $X_d^{''}$	0.25 *p.u.*	0.25 *p.u.*	0.25 *p.u.*	0.25 *p.u.*
Transient time constant, $\tau_{d0}^{'}$	8 *s*	8 *s*	8 *s*	8 *s*
Sub-transient time constant, $\tau_{d0}^{''}$	0.03 *s*	0.03 *s*	0.03 *s*	0.03 *s*
Quadrature axis:				
Synchronous reactance, X_q	1.7 *p.u.*	1.7 *p.u.*	1.7 *p.u.*	1.7 *p.u.*
Transient reactance, $X_q^{'}$	0.55 *p.u.*	0.55 *p.u.*	0.55 *p.u.*	0.55 *p.u.*
Sub-transient reactance, $X_q^{''}$	0.25 *p.u.*	0.25 *p.u.*	0.25 *p.u.*	0.25 *p.u.*
Transient time constant, $\tau_{q0}^{'}$	0.4 *s*	0.4 *s*	0.4 *s*	0.4 *s*
Sub-transient time constant, $\tau_{q0}^{''}$	0.05 *s*	0.05 *s*	0.05 *s*	0.05 *s*
Transformer:				
Base power, $S_{T,Base}$	900 *MVA*	900 *MVA*	900 *MVA*	900 *MVA*
Base voltage, $V_{T,Base}$	230 *kV*	230 *kV*	230 *kV*	230 *kV*
Reactance, X_{Trans}	0.15 *p.u.*	0.15 *p.u.*	0.15 *p.u.*	0.15 *p.u.*

Appendix C

DERIVATION OF THE SMALL-SIGNAL TRANSFER FUNCTION MATRIX AND STATE-SPACE MODELS OF THE SYNCHRONOUS GENERATOR

C.1. General considerations

The small-signal models of the OMIB representations used in this thesis can be derived from the algebraic and differential equations (2.2)–(2.18), which describe the synchronous generator. Suitable combination of those equations, as described in Chapter 2, provides various orders of generator models. For small variations, the differential equations are given as

$$\Delta\dot{\delta} = \omega_0 \Delta\omega \tag{C.1}$$

$$\Delta\dot{\omega} = \frac{1}{2H}\left[\Delta P_m - \Delta P_e - D\Delta\omega\right] \tag{C.2}$$

$$\Delta\dot{E}_q' = \frac{1}{\tau_{d0}'}\left[\Delta E_{fd} - \left(X_d - X_d'\right)\Delta i_{td} - \Delta E_q'\right] \tag{C.3}$$

$$\begin{aligned}\Delta\dot{E}_q'' &= \frac{1}{\tau_{d0}''}\left[\Delta E_q' - \left(X_d' - X_d''\right)\Delta i_{td} - \Delta E_q''\right] + \Delta\dot{E}_q' \\ &= \frac{1}{\tau_{d0}''}\left\{\frac{\tau_{d0}''}{\tau_{d0}'}\Delta E_{fd} - \left[\left(X_d' - X_d''\right) + \frac{\tau_{d0}''}{\tau_{d0}'}\left(X_d - X_d'\right)\right]\Delta i_{td} + \left[1 - \frac{\tau_{d0}''}{\tau_{d0}'}\right]\Delta E_q' - \Delta E_q''\right\}\end{aligned} \tag{C.4}$$

$$\Delta\dot{E}_d' = \frac{1}{\tau_{q0}'}\left[\left(X_q - X_q'\right)\Delta i_{tq} - \Delta E_d'\right] \tag{C.5}$$

$$\Delta\dot{E}_d'' = \frac{1}{\tau_{q0}''}\left[\left(X_q' - X_q''\right)\Delta i_{tq} - \Delta E_d''\right] \tag{C.6}$$

The phasor diagram of the system under study is given in Figure B.1. With the rotor position taken as the reference, it can be seen that the components of the infinite bus voltage are given by

$$V_{\infty q} = V_\infty \cos\delta \tag{C.7}$$

$$V_{\infty d} = V_\infty \sin\delta \tag{C.8}$$

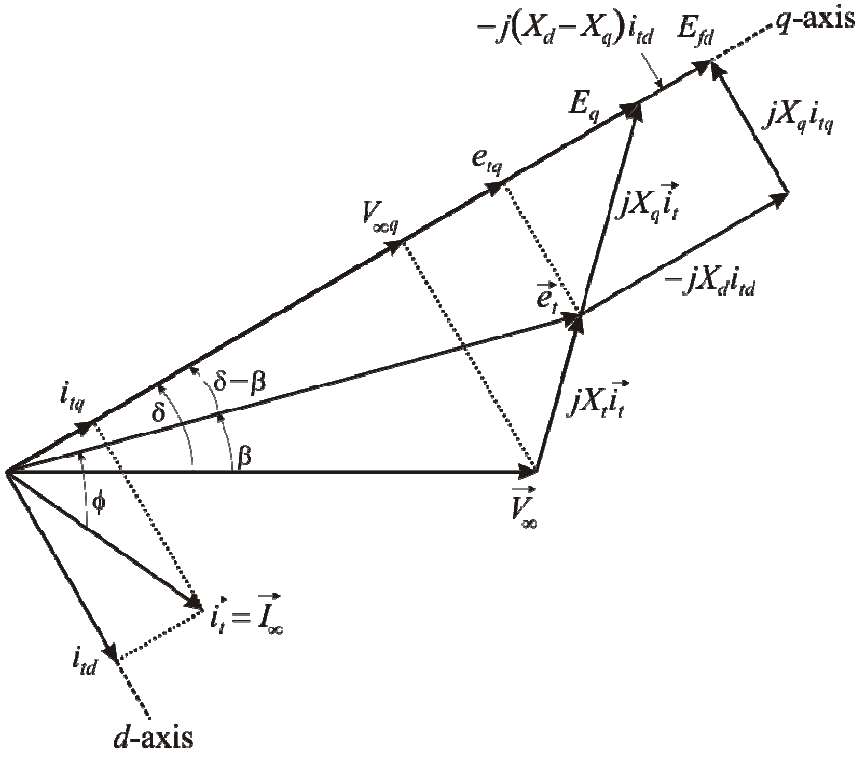

Figure C.1. Phasor diagram of an OMIB system

For small variations, an incremental change of the infinite bus voltage can be stated as

$$\Delta V_{\infty q} = -V_{\infty 0}\sin\delta_0\Delta\delta = -V_{\infty d0}\Delta\delta \tag{C.9}$$

$$\Delta V_{\infty d} = V_{\infty 0}\cos\delta_0\Delta\delta = V_{\infty q0}\Delta\delta \tag{C.10}$$

From Figure C.1, the terminal current can be expressed as

$$\vec{i}_t = \frac{\vec{e}_t - \vec{V}_\infty}{jX_t} \tag{C.11}$$

Notice that

$$\vec{i}_t = \vec{I}_\infty \tag{C.12}$$

Separating into real and imaginary parts,

$$i_{td}X_t = e_{tq} - V_{\infty q} \tag{C.13}$$

$$i_{tq}X_t = V_{\infty d} - e_{td} \tag{C.14}$$

Rearranging (C.13) and (C.14) by making use of the sub-transient equations (2.8) and (2.9) gives

$$i_{tq} = \frac{V_{\infty d} + R_a i_{td} - E_d^{"}}{X_q^{"} + X_t} \tag{C.15}$$

$$i_{td} = \frac{E_q^{"} - R_a i_{tq} - V_{\infty q}}{X_d^{"} + X_t} \tag{C.16}$$

For small variations and by neglecting the armature resistance, (C.15) and (C.16) become

$$\Delta i_{tq} = \frac{\Delta V_{\infty d} - \Delta E_d^{"}}{X_q^{"} + X_t} \tag{C.17}$$

$$\Delta i_{td} = \frac{\Delta E_q^{"} - \Delta V_{\infty q}}{X_d^{"} + X_t} \tag{C.18}$$

Therefore, using (C.10) in (C.17) and (C.9) in (C.18) provides

$$\Delta i_{tq} = \frac{V_{\infty q0}\Delta\delta - \Delta E_d^{"}}{X_q^{"} + X_t} \tag{C.19}$$

$$\Delta i_{td} = \frac{\Delta E_q^{"} + V_{\infty d0}\Delta\delta}{X_d^{"} + X_t} \tag{C.20}$$

The generator terminal voltage equation (2.3) can be expressed in terms of *d*- and *q*-axis components as

$$e_t^2 = e_{td}^2 + e_{tq}^2 \tag{C.21}$$

which, for small variations, becomes

$$\Delta e_t = \left(e_{t0}\right)^{-1}\left[e_{td0}\Delta e_{td} + e_{tq0}\Delta e_{tq}\right] \tag{C.22}$$

where

$$\Delta e_{tq} = \Delta E_q^{"} - X_d^{"}\Delta i_{td} \tag{C.23}$$

$$\Delta e_{td} = \Delta E_d^{"} + X_q^{"}\Delta i_{tq} \tag{C.24}$$

Equations (C.23) and (C.24) can be obtained from (2.8) and (2.9) for small variations and by neglecting the stator resistance. The synchronous generator active power equation (2.14) can be written as

$$P_e = V_{\infty d} I_{\infty d} + V_{\infty q} I_{\infty q} \tag{C.25}$$

or

$$P_e = V_{\infty d} i_{td} + V_{\infty q} i_{tq} \tag{C.26}$$

which for small variations becomes

$$\Delta P_e = V_{\infty d0}\Delta i_{td} + i_{td0}\Delta V_{\infty d} + V_{\infty q0}\Delta i_{tq} + i_{tq0}\Delta V_{\infty q} \tag{C.27}$$

Substitution of (C.9), (C.10), (C.19) and (C.20) into (C.27) yields

$$\Delta P_e = \left(\frac{V_{\infty d0}^2}{X_d^{"} + X_t} + \frac{V_{\infty q0}^2}{X_q^{"} + X_t} + i_{td0}V_{\infty q0} - i_{tq0}V_{\infty d0}\right)\Delta\delta + \frac{V_{\infty d0}}{X_d^{"} + X_t}\Delta E_q^{"} - \frac{V_{\infty q0}}{X_d^{"} + X_t}\Delta E_d^{"} \tag{C.28}$$

Similarly, substitution of (C.19) and (C.20) into (C.23) and (C.24) gives

$$\Delta e_{tq} = -\frac{V_{\infty d0}X_d^{"}}{X_d^{"} + X_t}\Delta\delta + \frac{X_t}{X_d^{"} + X_t}\Delta E_q^{"} \tag{C.29}$$

$$\Delta e_{td} = \frac{V_{\infty q0}X_q^{"}}{X_q^{"} + X_t}\Delta\delta + \frac{X_t}{X_q^{"} + X_t}\Delta E_d^{"} \tag{C.30}$$

By making use of (C.29) and (C.30) in (C.22), the generator terminal voltage equation can be expressed as

$$\Delta e_t = \left[\frac{e_{td0}}{e_{t0}}\cdot\frac{V_{\infty q0}X_q^{"}}{X_q^{"}+X_t} - \frac{e_{tq0}}{e_{t0}}\cdot\frac{V_{\infty d0}X_d^{"}}{X_d^{"}+X_t}\right]\Delta\delta + \left[\frac{e_{tq0}}{e_{t0}}\cdot\frac{X_t}{X_d^{"}+X_t}\right]\Delta E_q^{"} + \left[\frac{e_{td0}}{e_{t0}}\cdot\frac{X_t}{X_q^{"}+X_t}\right]\Delta E_d^{"} \quad \text{(C.31)}$$

For convenience, (C.28) and (C.31) are rewritten as

$$\Delta P_e = K_1\Delta\delta + K_2\Delta E_q^{"} - K_{2d}\Delta E_d^{"} \quad \text{(C.32)}$$

$$\Delta e_t = K_5\Delta\delta + K_6\Delta E_q^{"} + K_{6d}\Delta E_d^{"} \quad \text{(C.33)}$$

where

$$K_1 = \frac{V_{\infty d0}^2}{X_d^{"}+X_t} + \frac{V_{\infty q0}^2}{X_q^{"}+X_t} + i_{td0}V_{\infty q0} - i_{tq0}V_{\infty d0} \quad \text{(C.34)}$$

$$K_2 = \frac{V_{\infty d0}}{X_d^{"}+X_t} \quad \text{(C.35)}$$

$$K_{2d} = \frac{V_{\infty q0}}{X_d^{"}+X_t} \quad \text{(C.36)}$$

$$K_5 = \frac{e_{td0}}{e_{t0}}\cdot\frac{V_{\infty q0}X_q^{"}}{X_q^{"}+X_t} - \frac{e_{tq0}}{e_{t0}}\cdot\frac{V_{\infty d0}X_d^{"}}{X_d^{"}+X_t} \quad \text{(C.37)}$$

$$K_6 = \frac{e_{tq0}}{e_{t0}}\cdot\frac{X_t}{X_d^{"}+X_t} \quad \text{(C.38)}$$

$$K_{6d} = \frac{e_{td0}}{e_{t0}}\cdot\frac{X_t}{X_q^{"}+X_t} \quad \text{(C.39)}$$

Substitution of terminal current equations (C.19) and (C.20) into (C.3)–(C.6) provides

$$\Delta\dot{E}_q^{'} = \frac{1}{\tau_{d0}^{'}}\Delta E_{fd} - \frac{V_{\infty d0}\left(X_d - X_d^{'}\right)}{\tau_{d0}^{'}\left(X_d^{"}+X_t\right)}\Delta\delta - \frac{1}{\tau_{d0}^{'}}\Delta E_q^{'} - \frac{\left(X_d - X_d^{'}\right)}{\tau_{d0}^{'}\left(X_d^{"}+X_t\right)}\Delta E_q^{"} \quad \text{(C.40)}$$

$$\begin{aligned}\Delta\dot{E}_q^{"} = {} & \frac{1}{\tau_{d0}^{'}}\Delta E_{fd} - V_{\infty d0}\left[\frac{\tau_{d0}^{'}\left(X_d^{'}-X_d^{"}\right)+\tau_{d0}^{"}\left(X_d-X_d^{'}\right)}{\tau_{d0}^{"}\tau_{d0}^{'}\left(X_d^{"}+X_t\right)}\right]\Delta\delta + \left(\frac{1}{\tau_{d0}^{"}} - \frac{1}{\tau_{d0}^{'}}\right)\Delta E_q^{'} + \\ & - \left[\frac{\tau_{d0}^{'}\left(X_d^{'}+X_t\right)+\tau_{d0}^{"}\left(X_d-X_d^{'}\right)}{\tau_{d0}^{"}\tau_{d0}^{'}\left(X_d^{"}+X_t\right)}\right]\Delta E_q^{"}\end{aligned} \quad \text{(C.41)}$$

$$\Delta\dot{E}_d^{'} = \frac{V_{\infty q0}\left(X_q - X_q^{'}\right)}{\tau_{q0}^{'}\left(X_q^{"}+X_t\right)}\Delta\delta - \frac{1}{\tau_{q0}^{'}}\Delta E_d^{'} - \frac{\left(X_q - X_q^{'}\right)}{\tau_{q0}^{'}\left(X_q^{"}+X_t\right)}\Delta E_d^{"} \quad \text{(C.42)}$$

$$\Delta\dot{E}_d^{"} = \frac{V_{\infty q0}\left(X_q^{'} - X_q^{"}\right)}{\tau_{q0}^{"}\left(X_q^{"}+X_t\right)}\Delta\delta - \frac{\left(X_q^{'}+X_t\right)}{\tau_{q0}^{"}\left(X_q^{"}+X_t\right)}\Delta E_d^{"} \quad \text{(C.43)}$$

Suitable combination of differential equations (C.1), (C.2), (C.40)–(C.43) while considering the generator power and terminal voltage equations (C.32) and (C.33), respectively, produces different OMIB models. Procedures are carried out for both transfer function matrix and state-space representations in the next sections.

C.2. Transfer function matrix representation

The synchronous generator connected to an infinite bus via a tie-line reactance has the following generic representation in frequency domain

$$\begin{bmatrix} \Delta\omega(s) \\ \Delta e_t(s) \end{bmatrix} = \begin{bmatrix} g_{11}(s) & g_{12}(s) \\ g_{21}(s) & g_{22}(s) \end{bmatrix} \begin{bmatrix} \Delta P_m(s) \\ \Delta E_{fd}(s) \end{bmatrix} \tag{C.44}$$

$$\mathbf{y}(s) = \mathbf{G}(s)\mathbf{u}(s) \tag{C.45}$$

where $\mathbf{G}(s)$ is the transfer function matrix of the linearised models of the synchronous generator connected to an infinite bus via a tie-line reactance. In order to obtain $\mathbf{G}(s)$ for the different models, some previous algebraic manipulations are required. In the frequency domain, equations (C.1), (C.2), (C.40)–(C.43) can be given as

$$\Delta\delta(s) = \frac{\omega_0}{s}\Delta\omega(s) \tag{C.46}$$

$$\Delta\omega(s) = \frac{1}{2Hs}\left[\Delta P_m(s) - \Delta P_e(s) - D\Delta\omega(s)\right] \tag{C.47}$$

$$\Delta E_q^{'}(s) = \frac{1}{1+\tau_{d0}^{'}s}\Delta E_{fd}(s) - \frac{V_{\infty d0}\left(X_d - X_d^{'}\right)}{\left(X_d^{''} + X_t\right)\left(1+\tau_{d0}^{'}s\right)}\Delta\delta(s) - \frac{\left(X_d - X_d^{'}\right)}{\left(X_d^{''} + X_t\right)\left(1+\tau_{d0}^{'}s\right)}\Delta E_q^{''}(s) \tag{C.48}$$

$$\Delta E_q^{''}(s) = \frac{\left(1+\tau_{d0}^{''}s\right)\left(X_d^{''} + X_t\right)\Delta E_{fd}(s) - V_{\infty d0}\left\{\left(X_d - X_d^{''}\right) + \left[\tau_{d0}^{'}\left(X_d^{'} - X_d^{''}\right) + \tau_{d0}^{''}\left(X_d - X_d^{'}\right)\right]s\right\}\Delta\delta(s)}{\tau_{d0}^{'}\tau_{d0}^{''}\left(X_d^{''} + X_t\right)s^2 + \left[\tau_{d0}^{''}\left\{\left(X_d^{''} + X_t\right) + \left(X_d - X_d^{'}\right)\right\} + \tau_{d0}^{'}\left(X_d^{'} + X_t\right)\right]s + \left(X_d + X_t\right)} \tag{C.49}$$

$$\Delta E_d^{'}(s) = \frac{V_{\infty q0}\left(X_q - X_q^{'}\right)}{\left(X_q^{''} + X_t\right)\left(1+\tau_{q0}^{'}s\right)}\Delta\delta(s) - \frac{\left(X_q - X_q^{'}\right)}{\left(X_q^{''} + X_t\right)\left(1+\tau_{q0}^{'}s\right)}\Delta E_d^{''}(s) \tag{C.50}$$

$$\Delta E_d^{''}(s) = \frac{V_{\infty q0}\left(X_q^{'} - X_q^{''}\right)}{\left(X_q^{'} + X_t\right)\left[1+\tau_{q0}^{''}\left(\dfrac{X_q^{''} + X_t}{X_q^{'} + X_t}\right)s\right]}\Delta\delta(s) \tag{C.51}$$

where (C.49) is obtained by using equation (C.48) in the Laplace transformation of (C.41). For convenience, (C.49) and (C.51) are rewritten as

$$\Delta E_q^{''}(s) = K_3(s)\Delta E_{fd}(s) - K_4(s)\Delta\delta(s) \tag{C.52}$$

$$\Delta E_d^{''}(s) = K_{4d}(s)\Delta\delta(s) \tag{C.53}$$

where

$$K_3(s) = \frac{\left(X_d^{''} + X_t\right)\left(1+\tau_{d0}^{''}s\right)}{\tau_{d0}^{'}\tau_{d0}^{''}\left(X_d^{''} + X_t\right)s^2 + \left[\tau_{d0}^{''}\left\{\left(X_d^{''} + X_t\right) + \left(X_d - X_d^{'}\right)\right\} + \tau_{d0}^{'}\left(X_d^{'} + X_t\right)\right]s + \left(X_d + X_t\right)} \tag{C.54}$$

$$K_4(s)=\frac{V_{\infty d0}\left\{\left(X_d-X_d^{"}\right)+\left[\tau_{d0}^{'}\left(X_d^{'}-X_d^{"}\right)+\tau_{d0}^{"}\left(X_d-X_d^{'}\right)\right]s\right\}}{\tau_{d0}^{'}\tau_{d0}^{"}\left(X_d^{"}+X_t\right)s^2+\left[\tau_{d0}^{"}\left\{\left(X_d^{"}+X_t\right)+\left(X_d-X_d^{'}\right)\right\}+\tau_{d0}^{'}\left(X_d^{'}+X_t\right)\right]s+\left(X_d+X_t\right)} \tag{C.55}$$

$$K_{4d}(s)=\frac{C_{4d}}{1+\tau_q^{"}s} \tag{C.56}$$

$$C_{4d}=V_{\infty q0}\left(\frac{X_q^{'}-X_q^{"}}{X_q^{'}+X_t}\right) \tag{C.57}$$

$$\tau_q^{"}=\tau_{q0}^{"}\left(\frac{X_q^{"}+X_t}{X_q^{'}+X_t}\right) \tag{C.58}$$

In the frequency domain, the generator power and terminal voltages expressions (C.32) and (C.33), respectively, are given as

$$\Delta P_e(s)=K_1\Delta\delta(s)+K_2\Delta E_q^{"}(s)-K_{2d}\Delta E_d^{"}(s) \tag{C.59}$$

$$\Delta e_t(s)=K_5\Delta\delta(s)+K_6\Delta E_q^{"}(s)+K_{6d}\Delta E_d^{"}(s) \tag{C.60}$$

with coefficients defined by (C.34)–(C.39).

C.2.1. Model 1 (2*d*.1*q*, 5th order, two-axis)

The model is described by equations (C.46), (C.47), (C.52), (C.53), (C.59) and (C.60) while considering the following simplifying assumption

$$X_{qi}^{'}=X_{qi} \tag{C.61}$$

Therefore, constants associated to transfer function (C.56) in equation (C.53) become

$$C_{4d}=V_{\infty q0}\left(\frac{X_q-X_q^{"}}{X_q+X_t}\right) \tag{C.62}$$

$$\tau_q^{"}=\tau_{q0}^{"}\left(\frac{X_q^{"}+X_t}{X_q+X_t}\right) \tag{C.63}$$

The transfer function matrix representation given by (C.44) is obtained by substituting (C.46) into (C.52), (C.53), (C.59) and (C.60) to obtain expressions in terms of $\Delta\omega(s)$:

$$\Delta P_e(s)=K_1\frac{\omega_0}{s}\Delta\omega(s)+K_2\Delta E_q^{"}(s)-K_{2d}\Delta E_d^{"}(s) \tag{C.64}$$

$$\Delta e_t(s)=K_5\frac{\omega_0}{s}\Delta\omega(s)+K_6\Delta E_q^{"}(s)+K_{6d}\Delta E_d^{"}(s) \tag{C.65}$$

$$\Delta E_q^{"}(s)=K_3(s)\Delta E_{fd}(s)-K_4(s)\frac{\omega_0}{s}\Delta\omega(s) \tag{C.66}$$

$$\Delta E_d^{"}(s)=K_{4d}(s)\frac{\omega_0}{s}\Delta\omega(s) \tag{C.67}$$

To simplify the procedure, transfer functions (C.54) and (C.55) are rewritten as

$$K_3(s) = \frac{A\left(1+\tau_{d0}^{"}s\right)}{Es^2+Fs+G} \tag{C.68}$$

$$K_4(s) = \frac{B+Cs}{Es^2+Fs+G} \tag{C.69}$$

where

$$A = X_d^{"} + X_t \tag{C.70}$$

$$B = V_{\infty d0}\left(X_d - X_d^{"}\right) \tag{C.71}$$

$$C = V_{\infty d0}\left[\tau_{d0}^{'}\left(X_d^{'} - X_d^{"}\right) + \tau_{d0}^{"}\left(X_d - X_d^{'}\right)\right] \tag{C.72}$$

$$E = \tau_{d0}^{'}\tau_{d0}^{"}\left(X_d^{"} + X_t\right) \tag{C.73}$$

$$F = \tau_{d0}^{"}\left[\left(X_d^{"} + X_t\right) + \left(X_d - X_d^{'}\right)\right] + \tau_{d0}^{'}\left(X_d^{'} + X_t\right) \tag{C.74}$$

$$G = X_d + X_t \tag{C.75}$$

Substituting (C.68) and (C.69) in (C.66) and (C.56) in (C.67) renders

$$\Delta E_q^{"}(s) = \frac{A\left(1+\tau_{d0}^{"}s\right)}{Es^2+Fs+G}\Delta E_{fd}(s) - \frac{B+Cs}{Es^2+Fs+G}\cdot\frac{\omega_0}{s}\Delta\omega(s) \tag{C.76}$$

$$\Delta E_d^{"}(s) = \frac{C_{4d}}{1+\tau_q^{"}s}\cdot\frac{\omega_0}{s}\Delta\omega(s) \tag{C.77}$$

Using (C.76) and (C.77) in (C.64) and (C.65) gives the following intermediate result:

$$\Delta P_e(s) = \left[K_1 - \frac{K_2(B+Cs)}{Es^2+Fs+G} - \frac{K_{2d}C_{4d}}{1+\tau_q^{"}s}\right]\frac{\omega_0}{s}\Delta\omega(s) + \frac{K_2A\left(1+\tau_{d0}^{"}s\right)}{Es^2+Fs+G}\Delta E_{fd}(s) \tag{C.78}$$

$$\Delta e_t(s) = \left[K_5 - \frac{K_6(B+Cs)}{Es^2+Fs+G} + \frac{K_{6d}C_{4d}}{1+\tau_q^{"}s}\right]\frac{\omega_0}{s}\Delta\omega(s) + \frac{K_6A\left(1+\tau_{d0}^{"}s\right)}{Es^2+Fs+G}\Delta E_{fd}(s) \tag{C.79}$$

Substituting (C.78) in (C.47), and with slight rearrangement, gives

$$2Hs\Delta\omega(s) + D\Delta\omega(s) = \Delta P_m(s) - \Delta P_e(s)$$

$$\Downarrow$$

$$(2Hs+D)\Delta\omega(s) + \left[K_1 - \frac{K_2(B+Cs)}{Es^2+Fs+G} - \frac{K_{2d}C_{4d}}{1+\tau_q^{"}s}\right]\cdot\frac{\omega_0}{s}\Delta\omega(s) = \Delta P_m(s) - \frac{K_2A\left(1+\tau_{d0}^{"}s\right)}{Es^2+Fs+G}\Delta E_{fd}(s)$$

$$\Downarrow$$

$$\Delta\omega(s) = \frac{\left(Es^2+Fs+G\right)\left(1+\tau_q^{"}s\right)s}{\Pi(s)}\Delta P_m(s) - \frac{K_2A\left(1+\tau_{d0}^{"}s\right)\left(1+\tau_q^{"}s\right)s}{\Pi(s)}\Delta E_{fd}(s) \tag{C.80}$$

where

$$\begin{aligned}\Pi(s) = {} & (2Hs+D)\left(Es^2+Fs+G\right)\left(1+\tau_q^{"}s\right)s + K_1\omega_0\left(Es^2+Fs+G\right)\left(1+\tau_q^{"}s\right)+ \\ & -K_2\omega_0\left(B+Cs\right)\left(1+\tau_q^{"}s\right) - K_{2d}C_{4d}\omega_0\left(Es^2+Fs+G\right)\end{aligned} \tag{C.81}$$

In (C.80), speed is given in terms of the mechanical power and the field voltage, as required by (C.44). The equation for the terminal voltage is found by substituting (C.80) in (C.79), yielding

$$\begin{aligned}\Delta e_t(s) = {} & \omega_0\left[\frac{K_5\left(Es^2+Fs+G\right)\left(1+\tau_q^{"}s\right) - K_6\left(B+Cs\right)\left(1+\tau_q^{"}s\right) + K_{6d}C_{4d}\left(Es^2+Fs+G\right)}{\Pi(s)}\right]\Delta P_m(s) + \\ & + F(s)\Delta E_{fd}(s)\end{aligned} \tag{C.82}$$

where

$$\begin{aligned}F(s) = {} & \frac{A\left(1+\tau_{d0}^{"}s\right)}{\Pi(s)}\cdot \\ & \left\{K_6\left(1+\tau_q^{"}s\right)\left(2Hs+D\right)s + \left(K_6\left[\left(1+\tau_q^{"}s\right)K_1 - K_{2d}C_{4d}\right] - K_2\left[\left(1+\tau_q^{"}s\right)K_5 + K_{6d}C_{4d}\right]\right)\omega_0\right\}\end{aligned} \tag{C.83}$$

Notice that equations (C.80) and (C.82) have the form of (C.44), provided that

$$\begin{aligned}g_{11}(s) = {} & \frac{\left(1+\tau_q^{"}s\right)\left(Es^2+Fs+G\right)s}{\Pi(s)} \\ g_{12}(s) = {} & -\frac{K_2A\left(1+\tau_{d0}^{"}s\right)\left(1+\tau_q^{"}s\right)s}{\Pi(s)} \\ g_{21}(s) = {} & \omega_0\left[\frac{K_5\left(Es^2+Fs+G\right)\left(1+\tau_q^{"}s\right) - K_6\left(B+Cs\right)\left(1+\tau_q^{"}s\right) + K_{6d}C_{4d}\left(Es^2+Fs+G\right)}{\Pi(s)}\right] \\ g_{22}(s) = {} & \frac{A\left(1+\tau_{d0}^{"}s\right)}{\Pi(s)}\cdot\left[K_6\left(1+\tau_q^{"}s\right)\left(2Hs+D\right)s\right]+ \\ & + \frac{A\left(1+\tau_{d0}^{"}s\right)}{\Pi(s)}\cdot\left(K_6\left[\left(1+\tau_q^{"}s\right)K_1 - K_{2d}C_{4d}\right] - K_2\left[\left(1+\tau_q^{"}s\right)K_5 + K_{6d}C_{4d}\right]\right)\omega_0\end{aligned} \tag{C.84}$$

C.2.2. Model 2A (1*d*.1*q*, 4th order, two-axis)

The following simplifying assumptions

$$\tau_{d0}^{"} \to 0, X_d^{"} = X_d^{'}, E_q^{"} = E_q^{'} \tag{C.85}$$

are made in Model 1 to yield Model 2A. Constants and transfer functions (C.34)–(C.39), (C.54)–(C.56), (C.62), (C.63) and (C.70)–(C.75) become

$$K_1 = \frac{V_{\infty d0}^2}{X_d^{'} + X_t} + \frac{V_{\infty q0}^2}{X_q^{"} + X_t} - i_{tq0}V_{\infty d0} + i_{td0}V_{\infty q0} \tag{C.86}$$

$$K_2 = \frac{V_{\infty d0}}{X_d^{'} + X_t} \tag{C.87}$$

$$K_{2d} = \frac{V_{\infty q0}}{X_q^{"} + X_t} \tag{C.88}$$

$$K_5 = \frac{e_{td0}}{e_{t0}} \cdot \frac{X_q^{"} V_{\infty q0}}{X_q^{"} + X_t} - \frac{e_{tq0}}{e_{t0}} \cdot \frac{X_d^{'} V_{\infty d0}}{X_d^{'} + X_t} \tag{C.89}$$

$$K_6 = \frac{e_{tq0}}{e_{t0}} \cdot \frac{X_t}{X_d^{'} + X_t} \tag{C.90}$$

$$K_{6d} = \frac{e_{td0}}{e_{t0}} \cdot \frac{X_t}{X_q^{"} + X_t} \tag{C.91}$$

$$K_3(s) = \frac{X_d^{'} + X_t}{\tau_{d0}^{'}\left(X_d^{'} + X_t\right)s + \left(X_d + X_t\right)} \tag{C.92}$$

$$K_4(s) = \frac{V_{\infty d0}\left(X_d - X_d^{'}\right)}{\tau_{d0}^{'}\left(X_d^{'} + X_t\right)s + \left(X_d + X_t\right)} \tag{C.93}$$

$$K_{4d}(s) = \frac{C_{4d}}{1 + \tau_q^{"} s} \tag{C.94}$$

$$C_{4d} = V_{\infty q0}\left(\frac{X_q - X_q^{"}}{X_q + X_t}\right) \tag{C.95}$$

$$\tau_q^{"} = \tau_{q0}^{"}\left(\frac{X_q^{"} + X_t}{X_q + X_t}\right) \tag{C.96}$$

$$A = X_d^{'} + X_t \tag{C.97}$$

$$B = V_{\infty d0}\left(X_d - X_d^{'}\right) \tag{C.98}$$

$$C = E = 0 \tag{C.99}$$

$$F = \tau_{d0}^{'}\left(X_d^{'} + X_t\right) = A\tau_{d0}^{'} \tag{C.100}$$

$$G = X_d + X_t \tag{C.101}$$

Considering (C.86)–(C.101) the transfer function matrix elements given by (C.84) become

$$\begin{aligned}
g_{11}(s) &= \frac{\left(1 + \tau_q^{"} s\right)\left(G + A\tau_{d0}^{'} s\right)s}{\Pi(s)} \\
g_{12}(s) &= -\frac{K_2 A\left(1 + \tau_q^{"} s\right)s}{\Pi(s)} \\
g_{21}(s) &= \omega_0\left[\frac{K_5\left(G + A\tau_{d0}^{'} s\right)\left(1 + \tau_q^{"} s\right) - K_6 B\left(1 + \tau_q^{"} s\right) + K_{6d} C_{4d}\left(G + A\tau_{d0}^{'} s\right)}{\Pi(s)}\right] \\
g_{22}(s) &= \frac{A\left\{K_6\left(1 + \tau_q^{"} s\right)(2Hs + D)s + \left(K_6\left[\left(1 + \tau_q^{"} s\right)K_1 - K_{2d} C_{4d}\right] - K_2\left[\left(1 + \tau_q^{"} s\right)K_5 + K_{6d} C_{4d}\right]\right)\omega_0\right\}}{\Pi(s)}
\end{aligned} \tag{C.102}$$

where

$$\Pi(s)=(2Hs+D)\left(G+A\tau_{d0}^{'}s\right)\left(1+\tau_{q}^{"}s\right)s+K_1\omega_0\left(G+A\tau_{d0}^{'}s\right)\left(1+\tau_{q}^{"}s\right)-K_2B\omega_0\left(1+\tau_{q}^{"}s\right)+ \\ -K_{2d}C_{4d}\omega_0\left(G+A\tau_{d0}^{'}s\right) \tag{C.103}$$

The individual elements of the transfer function matrix **G**(*s*) in (C.44) for the 2×2 linearised Model 2A of the synchronous generator connected to an infinite bus via a tie-line reactance are given by (C.102).

C.2.3. Model 2B (2*d*.0*q*, 4th order, one-axis)

With reference to Model 1, the following simplifying assumptions are made to yield Model 2B:

$$\tau_{q0}^{"}\to 0, X_q^{"}=X_q, E_d^{"}=0 \tag{C.104}$$

Constants and transfer functions (C.34)–(C.39), (C.54)–(C.56), (C.62), (C.63) and (C.70)–(C.75) become

$$K_1=\frac{V_{\infty d0}^2}{X_d^{"}+X_t}+\frac{V_{\infty q0}^2}{X_q+X_t}-i_{tq0}V_{\infty d0}+i_{td0}V_{\infty q0} \tag{C.105}$$

$$K_2=\frac{V_{\infty d0}}{X_d^{"}+X_t} \tag{C.106}$$

$$K_{2d}=\frac{V_{\infty q0}}{X_q+X_t} \tag{C.107}$$

$$K_5=\frac{e_{td0}}{e_{t0}}\cdot\frac{X_qV_{\infty q0}}{X_q+X_t}-\frac{e_{tq0}}{e_{t0}}\cdot\frac{X_d^{"}V_{\infty d0}}{X_d^{"}+X_t} \tag{C.108}$$

$$K_6=\frac{e_{tq0}}{e_{t0}}\cdot\frac{X_t}{X_d^{"}+X_t} \tag{C.109}$$

$$K_{6d}=\frac{e_{td0}}{e_{t0}}\cdot\frac{X_t}{X_q+X_t} \tag{C.110}$$

$$K_3(s)=\frac{\left(X_d^{"}+X_t\right)\left(1+\tau_{d0}^{"}s\right)}{\tau_{d0}^{'}\tau_{d0}^{"}\left(X_d^{"}+X_t\right)s^2+\left[\tau_{d0}^{"}\left\{\left(X_d^{"}+X_t\right)+\left(X_d-X_d^{'}\right)\right\}+\tau_{d0}^{'}\left(X_d^{'}+X_t\right)\right]s+\left(X_d+X_t\right)} \tag{C.111}$$

$$K_4(s)=\frac{V_{\infty d0}\left[\left(X_d-X_d^{"}\right)+\left\{\left(X_d^{'}-X_d^{"}\right)\tau_{d0}^{'}+\left(X_d-X_d^{'}\right)\tau_{d0}^{"}\right\}s\right]}{\tau_{d0}^{'}\tau_{d0}^{"}\left(X_d^{"}+X_t\right)s^2+\left[\tau_{d0}^{"}\left\{\left(X_d^{"}+X_t\right)+\left(X_d-X_d^{'}\right)\right\}+\tau_{d0}^{'}\left(X_d^{'}+X_t\right)\right]s+\left(X_d+X_t\right)} \tag{C.112}$$

$$K_{4d}(s)=C_{4d}=\tau_q^{"}=0 \tag{C.113}$$

$$A=X_d^{"}+X_t \tag{C.114}$$

$$B=V_{\infty d0}\left(X_d-X_d^{"}\right) \tag{C.115}$$

$$C=V_{\infty d0}\left[\tau_{d0}^{'}\left(X_d^{'}-X_d^{"}\right)+\tau_{d0}^{"}\left(X_d-X_d^{'}\right)\right] \tag{C.116}$$

$$E=\tau_{d0}^{'}\tau_{d0}^{"}\left(X_d^{"}+X_t\right) \tag{C.117}$$

$$F = \tau_{d0}^{"}\left\{\left(X_d^{"} + X_t\right) + \left(X_d - X_d^{'}\right)\right\} + \tau_{d0}^{'}\left(X_d^{'} + X_t\right) \tag{C.118}$$

$$G = X_d + X_t \tag{C.119}$$

Considering (C.105)–(C.119), the transfer function matrix elements given by (C.84) become

$$\begin{aligned}
g_{11}(s) &= \frac{\left(Es^2 + Fs + G\right)s}{\Pi(s)} \\
g_{12}(s) &= -\frac{K_2 A\left(1 + \tau_{d0}^{"}s\right)s}{\Pi(s)} \\
g_{21}(s) &= \omega_0\left[\frac{K_5\left(Es^2 + Fs + G\right) - K_6\left(B + Cs\right)}{\Pi(s)}\right] \\
g_{22}(s) &= \frac{A\left(1 + \tau_{d0}^{"}s\right)\left[K_6\left(2Hs + D\right)s + \left(K_1K_6 - K_2K_5\right)\omega_0\right]}{\Pi(s)}
\end{aligned} \tag{C.120}$$

where

$$\Pi(s) = \left(2Hs + D\right)\left(Es^2 + Fs + G\right)s + K_1\omega_0\left(Es^2 + Fs + G\right) - K_2\omega_0\left(B + Cs\right) \tag{C.121}$$

The individual elements of the transfer function matrix **G**(*s*) in (C.44) for the 2×2 linearised Model 2B of the synchronous generator connected to an infinite bus via a tie-line reactance are given by (C.120).

C.2.4. Model 3 (1*d*.0*q*, 3rd order, one-axis)

Consider Model 2A described by (C.44) and (C.86)–(C.103). The following simplifying assumptions are made to yield Model 3

$$\tau_{q0}^{"} \to 0, X_q^{"} = X_q, E_d^{"} = 0 \tag{C.122}$$

Constants and transfer functions (C.86)–(C.101) become

$$K_1 = \frac{V_{\infty d0}^2}{X_d^{'} + X_t} + \frac{V_{\infty q0}^2}{X_q + X_t} - i_{tq0}V_{\infty d0} + i_{td0}V_{\infty q0} \tag{C.123}$$

$$K_2 = \frac{V_{\infty d0}}{X_d^{'} + X_t} \tag{C.124}$$

$$K_{2d} = \frac{V_{\infty q0}}{X_q + X_t} \tag{C.125}$$

$$K_5 = \frac{e_{td0}}{e_{t0}} \cdot \frac{X_q V_{\infty q0}}{X_q + X_t} - \frac{e_{tq0}}{e_{t0}} \cdot \frac{X_d^{'} V_{\infty d0}}{X_d^{'} + X_t} \tag{C.126}$$

$$K_6 = \frac{e_{tq0}}{e_{t0}} \cdot \frac{X_t}{X_d^{'} + X_t} \tag{C.127}$$

$$K_{6d} = \frac{e_{td0}}{e_{t0}} \cdot \frac{X_t}{X_q + X_t} \tag{C.128}$$

$$K_3(s)=\frac{X_d^{'}+X_t}{\tau_{d0}^{'}\left(X_d^{'}+X_t\right)s+\left(X_d+X_t\right)} \tag{C.129}$$

$$K_4(s)=\frac{V_{\infty d0}\left(X_d-X_d^{'}\right)}{\tau_{d0}^{'}\left(X_d^{'}+X_t\right)s+\left(X_d+X_t\right)} \tag{C.130}$$

$$K_{4d}(s)=C_{4d}=\tau_q^{''}=0 \tag{C.131}$$

$$A=X_d^{'}+X_t \tag{C.132}$$

$$B=V_{\infty d0}\left(X_d-X_d^{'}\right) \tag{C.133}$$

$$C=E=0 \tag{C.134}$$

$$F=\tau_{d0}^{'}\left(X_d^{'}+X_t\right)=A\tau_{d0}^{'} \tag{C.135}$$

$$G=X_d+X_t \tag{C.136}$$

Considering (C.123)–(C.136), (C.102) becomes

$$\begin{aligned}
g_{11}(s)&=\frac{\left(G+A\tau_{d0}^{'}s\right)s}{\Pi(s)}\\
g_{12}(s)&=-\frac{K_2As}{\Pi(s)}\\
g_{21}(s)&=\omega_0\left[\frac{K_5\left(G+A\tau_{d0}^{'}s\right)-K_6B}{\Pi(s)}\right]\\
g_{22}(s)&=\frac{A\left\{K_6\left(2Hs+D\right)s+\left(K_1K_6-K_2K_5\right)\omega_0\right\}}{\Pi(s)}
\end{aligned} \tag{C.137}$$

where

$$\Pi(s)=\left(2Hs+D\right)\left(G+A\tau_{d0}^{'}s\right)s+K_1\omega_0\left(G+A\tau_{d0}^{'}s\right)-K_2B\omega_0 \tag{C.138}$$

The individual elements of the transfer function matrix **G**(*s*) in (C.44) for the 2×2 linearised Model 3 of the synchronous generator connected to an infinite bus via a tie-line reactance are given by (C.137). The same results can be obtained if the assumptions

$$\tau_{d0}^{''}\to 0, X_d^{''}=X_d^{'}, E_q^{''}=E_q^{'}$$

are made in Model 2B, which is described by (C.44) and (C.105)–(C.121).

C.2.5. Model 2C (1*d*.1*q*, 4th order, two-axis)

This 4th order model is obtained in a slightly different way than Models 4A and 4B – no assumptions are used, but a set of different equations are used. In this case, the differential equations to be considered are (C.1)–(C.3) and (C.5). Let the terminal current be defined by (C.11), where the infinite voltage components are given by (C.7) and (C.8). The terminal current components, provided by (C.13) and (C.14), are rearranged by making use of the transient equations (2.4) and (2.5), yielding

$$i_{tq} = \frac{V_{\infty d} + R_a i_{td} - E_d^{'}}{X_q^{'} + X_t} \tag{C.139}$$

$$i_{td} = \frac{E_q^{'} - R_a i_{tq} - V_{\infty q}}{X_d^{'} + X_t} \tag{C.140}$$

For small variations and by neglecting the armature resistance, (C.139) and (C.140) become

$$\Delta i_{tq} = \frac{\Delta V_{\infty d} - \Delta E_d^{'}}{X_q^{'} + X_t} \tag{C.141}$$

$$\Delta i_{td} = \frac{\Delta E_q^{'} - \Delta V_{\infty q}}{X_d^{'} + X_t} \tag{C.142}$$

Using (C.10) in (C.141) and (C.9) in (C.142) provides

$$\Delta i_{tq} = \frac{V_{\infty q0}\Delta\delta - \Delta E_d^{'}}{X_q^{'} + X_t} \tag{C.143}$$

$$\Delta i_{td} = \frac{\Delta E_q^{'} + V_{\infty d0}\Delta\delta}{X_d^{'} + X_t} \tag{C.144}$$

The generator terminal voltage equation (2.3) for small variations is given by

$$\Delta e_t = \left(e_{t0}\right)^{-1}\left[e_{td0}\Delta e_{td} + e_{tq0}\Delta e_{tq}\right] \tag{C.22}$$

where

$$\Delta e_{tq} = \Delta E_q^{'} - X_d^{'}\Delta i_{td} \tag{C.145}$$

$$\Delta e_{td} = \Delta E_d^{'} + X_q^{'}\Delta i_{tq} \tag{C.146}$$

Equations (C.145) and (C.146) can be obtained from (2.4) and (2.5) for small variations and by neglecting the stator resistance. The synchronous generator active power equation, for small variations is given by

$$\Delta P_e = V_{\infty d0}\Delta i_{td} + i_{td0}\Delta V_{\infty d} + V_{\infty q0}\Delta i_{tq} + i_{tq0}\Delta V_{\infty q} \tag{C.27}$$

Substitution of (C.9), (C.10), (C.143) and (C.144) into (C.27) yields

$$\Delta P_e = \left(\frac{V_{\infty d0}^2}{X_d^{'} + X_t} + \frac{V_{\infty q0}^2}{X_q^{'} + X_t} + i_{td0}V_{\infty q0} - i_{tq0}V_{\infty d0}\right)\Delta\delta + \frac{V_{\infty d0}}{X_d^{'} + X_t}\Delta E_q^{'} - \frac{V_{\infty q0}}{X_d^{'} + X_t}\Delta E_d^{'} \tag{C.147}$$

Similarly, substitution of (C.143) and (C.144) into (C.145) and (C.146) gives

$$\Delta e_{tq} = -\frac{V_{\infty d0}X_d^{'}}{X_d^{'} + X_t}\Delta\delta + \frac{X_t}{X_d^{'} + X_t}\Delta E_q^{'} \tag{C.148}$$

$$\Delta e_{td} = \frac{V_{\infty q0}X_q^{'}}{X_q^{'} + X_t}\Delta\delta + \frac{X_t}{X_q^{'} + X_t}\Delta E_d^{'} \tag{C.149}$$

By making use of (C.148) and (C.149) in (C.22), the generator terminal voltage can be expressed as

$$\Delta e_t = \left[\frac{e_{td0}}{e_{t0}}\cdot\frac{V_{\infty q0}X_q^{'}}{X_q^{'} + X_t} - \frac{e_{tq0}}{e_{t0}}\cdot\frac{V_{\infty d0}X_d^{'}}{X_d^{'} + X_t}\right]\Delta\delta + \left[\frac{e_{tq0}}{e_{t0}}\cdot\frac{X_t}{X_d^{'} + X_t}\right]\Delta E_q^{'} + \left[\frac{e_{td0}}{e_{t0}}\cdot\frac{X_t}{X_q^{'} + X_t}\right]\Delta E_d^{'} \tag{C.150}$$

For convenience, (C.147) and (C.150) are rewritten as

$$\Delta P_e = K_1 \Delta\delta + K_2 \Delta E_q^{'} - K_{2d} \Delta E_d^{'} \tag{C.151}$$

$$\Delta e_t = K_5 \Delta\delta + K_6 \Delta E_q^{'} + K_{6d} \Delta E_d^{'} \tag{C.152}$$

where

$$K_1 = \frac{V_{\infty d0}^2}{X_d^{'} + X_t} + \frac{V_{\infty q0}^2}{X_q^{'} + X_t} + i_{td0} V_{\infty q0} - i_{tq0} V_{\infty d0} \tag{C.153}$$

$$K_2 = \frac{V_{\infty d0}}{X_d^{'} + X_t} \tag{C.154}$$

$$K_{2d} = \frac{V_{\infty q0}}{X_d^{'} + X_t} \tag{C.155}$$

$$K_5 = \frac{e_{td0}}{e_{t0}} \cdot \frac{V_{\infty q0} X_q^{'}}{X_q^{'} + X_t} - \frac{e_{tq0}}{e_{t0}} \cdot \frac{V_{\infty d0} X_d^{'}}{X_d^{'} + X_t} \tag{C.156}$$

$$K_6 = \frac{e_{tq0}}{e_{t0}} \cdot \frac{X_t}{X_d^{'} + X_t} \tag{C.157}$$

$$K_{6d} = \frac{e_{td0}}{e_{t0}} \cdot \frac{X_t}{X_q^{'} + X_t} \tag{C.158}$$

Substitution of terminal current equations (C.143) and (C.144) into (C.3) and (C.5) provides

$$\Delta \dot{E}_q^{'} = \frac{1}{\tau_{d0}^{'}} \Delta E_{fd} - \frac{V_{\infty d0}\left(X_d - X_d^{'}\right)}{\tau_{d0}^{'}\left(X_d^{'} + X_t\right)} \Delta\delta - \frac{\left(X_d + X_t\right)}{\tau_{d0}^{'}\left(X_d^{'} + X_t\right)} \Delta E_q^{'} \tag{C.159}$$

$$\Delta \dot{E}_d^{'} = \frac{V_{\infty q0}\left(X_q - X_q^{'}\right)}{\tau_{q0}^{'}\left(X_q^{'} + X_t\right)} \Delta\delta - \frac{\left(X_q + X_t\right)}{\tau_{q0}^{'}\left(X_q^{'} + X_t\right)} \Delta E_d^{'} \tag{C.160}$$

All preliminary manipulations in time domain have been carried out. In the frequency domain, equations (C.1), (C.2), (C.159) and (C.160) are given by

$$\Delta\delta(s) = \frac{\omega_0}{s} \Delta\omega(s) \tag{C.46}$$

$$\Delta\omega(s) = \frac{1}{2Hs}\left[\Delta P_m(s) - \Delta P_e(s) - D\Delta\omega(s)\right] \tag{C.47}$$

$$\Delta E_q^{'}(s) = \frac{\left(X_d^{'} + X_t\right)}{\left(X_d + X_t\right)\left[1 + \tau_{d0}^{'}\left(\frac{X_d^{'} + X_t}{X_d + X_t}\right)s\right]} \Delta E_{fd}(s) - \frac{V_{\infty d0}\left(X_d - X_d^{'}\right)}{\left(X_d + X_t\right)\left[1 + \tau_{d0}^{'}\left(\frac{X_d^{'} + X_t}{X_d + X_t}\right)s\right]} \Delta\delta(s) \tag{C.161}$$

$$\Delta E_d^{'}(s) = \frac{V_{\infty q0}\left(X_q - X_q^{'}\right)}{\left(X_q + X_t\right)\left[1 + \tau_{q0}^{'}\left(\frac{X_q^{'} + X_t}{X_q + X_t}\right)s\right]} \Delta\delta(s) \tag{C.162}$$

Equations (C.161) and (C.162) are rewritten as

$$\Delta E_q^{'}(s) = K_3(s)\Delta E_{fd}(s) - K_4(s)\Delta\delta(s) \tag{C.163}$$

$$\Delta E_d^{'}(s) = K_{4d}(s)\Delta\delta(s) \tag{C.164}$$

where

$$K_3(s) = \frac{A}{1+\tau_d^{'}s} \tag{C.165}$$

$$K_4(s) = \frac{B}{1+\tau_d^{'}s} \tag{C.166}$$

$$K_{4d}(s) = \frac{C}{1+\tau_q^{'}s} \tag{C.167}$$

$$\tau_d^{'} = \tau_{d0}^{'}\left(\frac{X_d^{'}+X_t}{X_d+X_t}\right) \tag{C.168}$$

$$\tau_q^{'} = \tau_{q0}^{'}\left(\frac{X_q^{'}+X_t}{X_q+X_t}\right) \tag{C.169}$$

$$A = \frac{X_d^{'}+X_t}{X_d+X_t} \tag{C.170}$$

$$B = \frac{V_{\infty d0}\left(X_d - X_d^{'}\right)}{X_d+X_t} \tag{C.171}$$

$$C = \frac{V_{\infty q0}\left(X_q - X_q^{'}\right)}{X_q+X_t} \tag{C.172}$$

The generator power and terminal voltage equations (C.151) and (C.152), in the frequency domain, are given as

$$\Delta P_e(s) = K_1\Delta\delta(s) + K_2\Delta E_q^{'}(s) - K_{2d}\Delta E_d^{'}(s) \tag{C.173}$$

$$\Delta e_t(s) = K_5\Delta\delta(s) + K_6\Delta E_q^{'}(s) + K_{6d}\Delta E_d^{'}(s) \tag{C.174}$$

The transfer function matrix representation given by (C.44) is obtained by using (C.46) in (C.163), (C.164), (C.173) and (C.174) to obtain expressions in terms of $\Delta\omega(s)$:

$$\Delta P_e(s) = K_1\frac{\omega_0}{s}\Delta\omega(s) + K_2\Delta E_q^{'}(s) - K_{2d}\Delta E_d^{'}(s) \tag{C.175}$$

$$\Delta e_t(s) = K_5\frac{\omega_0}{s}\Delta\omega(s) + K_6\Delta E_q^{'}(s) + K_{6d}\Delta E_d^{'}(s) \tag{C.176}$$

$$\Delta E_q^{'}(s) = \frac{A}{1+\tau_d^{'}s}\Delta E_{fd}(s) - \frac{B\omega_0}{\left(1+\tau_d^{'}s\right)s}\Delta\omega(s) \tag{C.177}$$

$$\Delta E_d^{'}(s) = \frac{C\omega_0}{\left(1+\tau_q^{'}s\right)s}\Delta\omega(s) \tag{C.178}$$

Using (C.177) and (C.178) in (C.175) and (C.176) gives the following intermediate result:

$$\Delta P_e(s)=\left[K_1-\frac{K_2B}{1+\tau_d^{'}s}-\frac{K_{2d}C}{1+\tau_q^{'}s}\right]\frac{\omega_0}{s}\Delta\omega(s)+\frac{K_2A}{1+\tau_d^{'}s}\Delta E_{fd}(s) \tag{C.179}$$

$$\Delta e_t(s)=\left[K_5-\frac{K_6B}{1+\tau_d^{'}s}+\frac{K_{6d}C}{1+\tau_q^{'}s}\right]\frac{\omega_0}{s}\Delta\omega(s)+\frac{K_6A}{1+\tau_d^{'}s}\Delta E_{fd}(s) \tag{C.180}$$

Substituting (C.179) in (C.47), and with slight re-arrangement, gives

$$2Hs\Delta\omega(s)+D\Delta\omega(s)=\Delta P_m(s)-\Delta P_e(s)$$

$$\Downarrow$$

$$(2Hs+D)\Delta\omega(s)+\left[K_1-\frac{K_2B}{1+\tau_d^{'}s}-\frac{K_{2d}C}{1+\tau_q^{'}s}\right]\cdot\frac{\omega_0}{s}\Delta\omega(s)=\Delta P_m(s)-\frac{K_2A}{1+\tau_d^{'}s}\Delta E_{fd}(s)$$

$$\Downarrow$$

$$\Delta\omega(s)=\frac{\left(1+\tau_d^{'}s\right)\left(1+\tau_q^{'}s\right)s}{\Pi(s)}\Delta P_m(s)-\frac{K_2A\left(1+\tau_q^{'}s\right)s}{\Pi(s)}\Delta E_{fd}(s) \tag{C.181}$$

where

$$\begin{aligned}\Pi(s)=&(2Hs+D)\left(1+\tau_d^{'}s\right)\left(1+\tau_q^{'}s\right)s+K_1\omega_0\left(1+\tau_d^{'}s\right)\left(1+\tau_q^{'}s\right)-K_2B\omega_0\left(1+\tau_q^{'}s\right)+\\&-K_{2d}C\omega_0\left(1+\tau_d^{'}s\right)\end{aligned} \tag{C.182}$$

The equation for the terminal voltage is found by substituting (C.181) in (C.180), yielding

$$\Delta e_t(s)=\omega_0\left[\frac{K_5\left(1+\tau_d^{'}s\right)\left(1+\tau_q^{'}s\right)-K_6B\left(1+\tau_q^{'}s\right)+K_{6d}C\left(1+\tau_d^{'}s\right)}{\Pi(s)}\right]\Delta P_m(s)+F(s)\Delta E_{fd}(s) \tag{C.183}$$

where

$$F(s)=\frac{A\left\{K_6\left(1+\tau_q^{'}s\right)(2Hs+D)s+\left(K_6\left[\left(1+\tau_q^{'}s\right)K_1-K_{2d}C\right]-K_2\left[\left(1+\tau_q^{'}s\right)K_5+K_{6d}C\right]\right)\omega_0\right\}}{\Pi(s)} \tag{C.184}$$

Notice that equations (C.181) and (C.183) can be written as (C.44), provided that

$$\begin{aligned}g_{11}(s)&=\frac{\left(1+\tau_d^{'}s\right)\left(1+\tau_q^{'}s\right)s}{\Pi(s)}\\g_{12}(s)&=-\frac{K_2A\left(1+\tau_q^{'}s\right)s}{\Pi(s)}\\g_{21}(s)&=\omega_0\left[\frac{K_5\left(1+\tau_d^{'}s\right)\left(1+\tau_q^{'}s\right)-K_6B\left(1+\tau_q^{'}s\right)+K_{6d}C\left(1+\tau_d^{'}s\right)}{\Pi(s)}\right]\\g_{22}(s)&=\frac{A\left\{K_6\left(1+\tau_q^{'}s\right)(2Hs+D)s+\left(K_6\left[\left(1+\tau_q^{'}s\right)K_1-K_{2d}C\right]-K_2\left[\left(1+\tau_q^{'}s\right)K_5+K_{6d}C\right]\right)\omega_0\right\}}{\Pi(s)}\end{aligned} \tag{C.185}$$

C.3. State-space representation

Suitable combination of differential equations (C.1), (C.2), (C.40)–(C.43) while considering the generator power and terminal voltage equations (C.32) and (C.33), provides for different order models of the synchronous generator. A state-space representation

$$\begin{aligned}\dot{\Delta\mathbf{x}} &= \mathbf{A}\Delta\mathbf{x} + \mathbf{B}\Delta\mathbf{u} \\ \Delta\mathbf{y} &= \mathbf{C}\Delta\mathbf{x} + \mathbf{D}\Delta\mathbf{u}\end{aligned} \tag{C.186}$$

can be arrived at, where the output, input, and state vectors are given, respectively, as

$$\Delta\mathbf{y} = \begin{bmatrix}\Delta\omega & \Delta e_t\end{bmatrix}^T \tag{C.187}$$

$$\Delta\mathbf{u} = \begin{bmatrix}\Delta P_m & \Delta E_{fd}\end{bmatrix}^T \tag{C.188}$$

$$\Delta\mathbf{x} = \begin{bmatrix}\Delta\omega & \Delta\mathbf{E} & \Delta\delta\end{bmatrix}^T \tag{C.189}$$

Vector $\Delta\mathbf{E}$ of state vector $\Delta\mathbf{x}$ in (C.189) has a variable size depending on the synchronous generator model to be used.

C.3.1. Model 0 (2*d*.2*q*, 6th order, two-axis)

Let the 6th order model be defined by differential equations (C.1), (C.2), (C.40)–(C.43) and algebraic equations (C.32) and (C.33):

$$\Delta\dot{\delta} = \omega_0\Delta\omega \tag{C.1}$$

$$\Delta\dot{\omega} = \frac{1}{2H}\left[\Delta P_m - \Delta P_e - D\Delta\omega\right] \tag{C.2}$$

$$\Delta\dot{E}_q' = \frac{1}{\tau_{d0}'}\Delta E_{fd} - \frac{V_{\infty d0}\left(X_d - X_d'\right)}{\tau_{d0}'\left(X_d'' + X_t\right)}\Delta\delta - \frac{1}{\tau_{d0}'}\Delta E_q' - \frac{\left(X_d - X_d'\right)}{\tau_{d0}'\left(X_d'' + X_t\right)}\Delta E_q'' \tag{C.40}$$

$$\begin{aligned}\Delta\dot{E}_q'' = {} & \frac{1}{\tau_{d0}'}\Delta E_{fd} - V_{\infty d0}\left[\frac{\tau_{d0}'\left(X_d' - X_d''\right) + \tau_{d0}''\left(X_d - X_d'\right)}{\tau_{d0}''\tau_{d0}'\left(X_d'' + X_t\right)}\right]\Delta\delta + \left(\frac{1}{\tau_{d0}''} - \frac{1}{\tau_{d0}'}\right)\Delta E_q' + \\ & - \left[\frac{\tau_{d0}'\left(X_d' + X_t\right) + \tau_{d0}''\left(X_d - X_d'\right)}{\tau_{d0}''\tau_{d0}'\left(X_d'' + X_t\right)}\right]\Delta E_q''\end{aligned} \tag{C.41}$$

$$\Delta\dot{E}_d' = \frac{V_{\infty q0}\left(X_q - X_q'\right)}{\tau_{q0}'\left(X_q'' + X_t\right)}\Delta\delta - \frac{1}{\tau_{q0}'}\Delta E_d' - \frac{\left(X_q - X_q'\right)}{\tau_{q0}'\left(X_q'' + X_t\right)}\Delta E_d'' \tag{C.42}$$

$$\Delta\dot{E}_d'' = \frac{V_{\infty q0}\left(X_q' - X_q''\right)}{\tau_{q0}''\left(X_q'' + X_t\right)}\Delta\delta - \frac{\left(X_q' + X_t\right)}{\tau_{q0}''\left(X_q'' + X_t\right)}\Delta E_d'' \tag{C.43}$$

$$\Delta P_e = K_1\Delta\delta + K_2\Delta E_q'' - K_{2d}\Delta E_d'' \tag{C.32}$$

$$\Delta e_t = K_5 \Delta\delta + K_6 \Delta E_q^{"} + K_{6d} \Delta E_d^{"} \tag{C.33}$$

where the coefficients in (C.32) and (C.33) are given by (C.34)–(C.39). Substitution of (C.32) in (C.2) yields

$$\Delta\dot{\omega} = -\frac{K_1}{2H}\Delta\delta - \frac{D}{2H}\Delta\omega - \frac{K_2}{2H}\Delta E_q^{"} + \frac{K_{2d}}{2H}\Delta E_d^{"} + \frac{1}{2H}\Delta P_m \tag{C.190}$$

Considering differential equations (C.1), (C.40)–(C.43) and (C.190), and the terminal voltage equation (C.33), the state-space representation (C.186) is constructed, where

$$\Delta\mathbf{y} = \begin{bmatrix} \Delta\omega & \Delta e_t \end{bmatrix}^T \tag{C.187}$$

$$\Delta\mathbf{u} = \begin{bmatrix} \Delta P_m & \Delta E_{fd} \end{bmatrix}^T \tag{C.188}$$

$$\Delta\mathbf{x} = \begin{bmatrix} \Delta\omega & \Delta E_q^{'} & \Delta E_q^{"} & \Delta E_d^{'} & \Delta E_d^{"} & \Delta\delta \end{bmatrix}^T \tag{C.191}$$

System, control, output and feed-forward matrices **A**, **B, C** and **D,** respectively, are given as

$$\mathbf{A} = \begin{bmatrix} -\frac{D}{2H} & 0 & -\frac{K_2}{2H} & 0 & \frac{K_{2d}}{2H} & -\frac{K_1}{2H} \\ 0 & -\frac{1}{\tau_{d0}^{'}} & a_{23} & 0 & 0 & a_{26} \\ 0 & \frac{1}{\tau_{d0}^{"}} - \frac{1}{\tau_{d0}^{'}} & a_{33} & 0 & 0 & a_{36} \\ 0 & 0 & 0 & -\frac{1}{\tau_{q0}^{'}} & a_{45} & a_{46} \\ 0 & 0 & 0 & 0 & a_{55} & a_{56} \\ \omega_0 & 0 & 0 & 0 & 0 & 0 \end{bmatrix} \tag{C.192}$$

$$\mathbf{B} = \begin{bmatrix} \frac{1}{2H} & 0 & 0 & 0 & 0 & 0 \\ 0 & \frac{1}{\tau_{d0}^{'}} & \frac{1}{\tau_{d0}^{'}} & 0 & 0 & 0 \end{bmatrix}^T \tag{C.193}$$

$$\mathbf{C} = \begin{bmatrix} 1 & 0 & 0 & 0 & 0 & 0 \\ 0 & 0 & K_6 & 0 & K_{6d} & K_5 \end{bmatrix} \tag{C.194}$$

$$\mathbf{D} = \mathbf{0}_{2\times 2} = \begin{bmatrix} 0 & 0 \\ 0 & 0 \end{bmatrix} \tag{C.195}$$

where the coefficients in (C.192) and (C.194) are given by (C.34)–(C.39) and

$$a_{23} = -\frac{\left(X_d - X_d^{'}\right)}{\tau_{d0}^{'}\left(X_d^{"} + X_t\right)} \tag{C.196}$$

$$a_{26} = -\frac{V_{\infty d0}\left(X_d - X_d^{'}\right)}{\tau_{d0}^{'}\left(X_d^{"} + X_t\right)} \tag{C.197}$$

$$a_{33} = -\left[\frac{\tau_{d0}^{'}\left(X_d^{'} + X_t\right) + \tau_{d0}^{''}\left(X_d - X_d^{'}\right)}{\tau_{d0}^{''}\tau_{d0}^{'}\left(X_d^{''} + X_t\right)}\right] \tag{C.198}$$

$$a_{36} = V_{\infty d0}\left[\frac{\tau_{d0}^{'}\left(X_d^{'} - X_d^{''}\right) + \tau_{d0}^{''}\left(X_d - X_d^{'}\right)}{\tau_{d0}^{''}\tau_{d0}^{'}\left(X_d^{''} + X_t\right)}\right] \tag{C.199}$$

$$a_{45} = -\frac{\left(X_q - X_q^{'}\right)}{\tau_{q0}^{'}\left(X_q^{''} + X_t\right)} \tag{C.200}$$

$$a_{46} = \frac{V_{\infty q0}\left(X_q - X_q^{'}\right)}{\tau_{q0}^{'}\left(X_q^{''} + X_t\right)} \tag{C.201}$$

$$a_{55} = -\frac{\left(X_q^{'} + X_t\right)}{\tau_{q0}^{''}\left(X_q^{''} + X_t\right)} \tag{C.202}$$

$$a_{56} = \frac{V_{\infty q0}\left(X_q^{'} - X_q^{''}\right)}{\tau_{q0}^{''}\left(X_q^{''} + X_t\right)} \tag{C.203}$$

C.3.2. Model 1 (2*d*.1*q*, 5th order, two-axis)

This model can be arrived at by considering Model 0 and the following simplifying assumptions:

$$X_q^{'} = X_q, E_d^{'} = 0 \tag{C.204}$$

Therefore, the differential and algebraic equations that define this model are given as

$$\Delta\dot{\delta} = \omega_0\Delta\omega \tag{C.1}$$

$$\Delta\dot{\omega} = \frac{1}{2H}\left[\Delta P_m - \Delta P_e - D\Delta\omega\right] \tag{C.2}$$

$$\Delta\dot{E}_q^{'} = \frac{1}{\tau_{d0}^{'}}\Delta E_{fd} - \frac{V_{\infty d0}\left(X_d - X_d^{'}\right)}{\tau_{d0}^{'}\left(X_d^{''} + X_t\right)}\Delta\delta - \frac{1}{\tau_{d0}^{'}}\Delta E_q^{'} - \frac{\left(X_d - X_d^{'}\right)}{\tau_{d0}^{'}\left(X_d^{''} + X_t\right)}\Delta E_q^{''} \tag{C.40}$$

$$\begin{aligned}\Delta\dot{E}_q^{''} = {} & \frac{1}{\tau_{d0}^{'}}\Delta E_{fd} - V_{\infty d0}\left[\frac{\tau_{d0}^{'}\left(X_d^{'} - X_d^{''}\right) + \tau_{d0}^{''}\left(X_d - X_d^{'}\right)}{\tau_{d0}^{''}\tau_{d0}^{'}\left(X_d^{''} + X_t\right)}\right]\Delta\delta + \left(\frac{1}{\tau_{d0}^{''}} - \frac{1}{\tau_{d0}^{'}}\right)\Delta E_q^{'} + \\ & - \left[\frac{\tau_{d0}^{'}\left(X_d^{'} + X_t\right) + \tau_{d0}^{''}\left(X_d - X_d^{'}\right)}{\tau_{d0}^{''}\tau_{d0}^{'}\left(X_d^{''} + X_t\right)}\right]\Delta E_q^{''}\end{aligned} \tag{C.41}$$

$$\Delta\dot{E}_d^{''} = \frac{V_{\infty q0}\left(X_q - X_q^{''}\right)}{\tau_{q0}^{''}\left(X_q^{''} + X_t\right)}\Delta\delta - \frac{\left(X_q + X_t\right)}{\tau_{q0}^{''}\left(X_q^{''} + X_t\right)}\Delta E_d^{''} \tag{C.205}$$

$$\Delta P_e = K_1\Delta\delta + K_2\Delta E_q^{''} - K_{2d}\Delta E_d^{''} \tag{C.32}$$

$$\Delta e_t = K_5\Delta\delta + K_6\Delta E_q^{''} + K_{6d}\Delta E_d^{''} \tag{C.33}$$

where the coefficients in (C.32) and (C.33) are given by (C.34)–(C.39) – exactly as in Model 0. Substitution of (C.32) in (C.2) yields

$$\Delta\dot{\omega} = -\frac{K_1}{2H}\Delta\delta - \frac{D}{2H}\Delta\omega - \frac{K_2}{2H}\Delta E_q^{"} + \frac{K_{2d}}{2H}\Delta E_d^{"} + \frac{1}{2H}\Delta P_m \tag{C.190}$$

Considering differential equations (C.1), (C.40), (C.41), (C.190) and (C.205), and the terminal voltage equation (C.33), the state-space representation (C.186) is constructed, where

$$\Delta\mathbf{y} = \begin{bmatrix}\Delta\omega & \Delta e_t\end{bmatrix}^T \tag{C.187}$$

$$\Delta\mathbf{u} = \begin{bmatrix}\Delta P_m & \Delta E_{fd}\end{bmatrix}^T \tag{C.188}$$

$$\Delta\mathbf{x} = \begin{bmatrix}\Delta\omega & \Delta E_q^{'} & \Delta E_q^{"} & \Delta E_d^{"} & \Delta\delta\end{bmatrix}^T \tag{C.206}$$

System, control, output and feed-forward matrices **A**, **B, C** and **D,** respectively, are given as

$$\mathbf{A} = \begin{bmatrix} -\frac{D}{2H} & 0 & -\frac{K_2}{2H} & \frac{K_{2d}}{2H} & -\frac{K_1}{2H} \\ 0 & -\frac{1}{\tau_{d0}^{'}} & a_{23} & 0 & a_{25} \\ 0 & \frac{1}{\tau_{d0}^{"}} - \frac{1}{\tau_{d0}^{'}} & a_{33} & 0 & a_{35} \\ 0 & 0 & 0 & a_{44} & a_{45} \\ \omega_0 & 0 & 0 & 0 & 0 \end{bmatrix} \tag{C.207}$$

$$\mathbf{B} = \begin{bmatrix} \frac{1}{2H} & 0 & 0 & 0 & 0 \\ 0 & \frac{1}{\tau_{d0}^{'}} & \frac{1}{\tau_{d0}^{'}} & 0 & 0 \end{bmatrix}^T \tag{C.208}$$

$$\mathbf{C} = \begin{bmatrix} 1 & 0 & 0 & 0 & 0 \\ 0 & 0 & K_6 & K_{6d} & K_5 \end{bmatrix} \tag{C.209}$$

$$\mathbf{D} = \mathbf{0}_{2\times 2} = \begin{bmatrix} 0 & 0 \\ 0 & 0 \end{bmatrix} \tag{C.210}$$

where coefficients in (C.207) and (C.209) are given by (C.34)–(C.39) and

$$a_{23} = -\frac{\left(X_d - X_d^{'}\right)}{\tau_{d0}^{'}\left(X_d^{"} + X_t\right)} \tag{C.211}$$

$$a_{25} = -\frac{V_{\infty d0}\left(X_d - X_d^{'}\right)}{\tau_{d0}^{'}\left(X_d^{"} + X_t\right)} \tag{C.212}$$

$$a_{33} = -\left[\frac{\tau_{d0}^{'}\left(X_d^{'} + X_t\right) + \tau_{d0}^{"}\left(X_d - X_d^{'}\right)}{\tau_{d0}^{"}\tau_{d0}^{'}\left(X_d^{"} + X_t\right)}\right] \tag{C.213}$$

$$a_{35} = V_{\infty d0}\left[\frac{\tau_{d0}^{'}\left(X_d^{'} - X_d^{"}\right) + \tau_{d0}^{"}\left(X_d - X_d^{'}\right)}{\tau_{d0}^{"}\tau_{d0}^{'}\left(X_d^{"} + X_t\right)}\right] \tag{C.214}$$

$$a_{44} = -\frac{\left(X_q + X_t\right)}{\tau_{q0}^{"}\left(X_q^{"} + X_t\right)} \tag{C.215}$$

$$a_{45} = \frac{V_{\infty q0}\left(X_q - X_q^{"}\right)}{\tau_{q0}^{"}\left(X_q^{"} + X_t\right)} \tag{C.216}$$

C.3.3. Model 2A (1*d*.1*q*, 4th order, two-axis)

This model can be arrived at by considering Model 1 and the following simplifying assumptions:

$$\tau_{d0}^{"} \to 0, X_d^{"} = X_d^{'}, E_q^{"} = E_q^{'} \tag{C.85}$$

Therefore, the differential and algebraic equations that define this model are given as

$$\Delta\dot{\delta} = \omega_0\Delta\omega \tag{C.1}$$

$$\Delta\dot{\omega} = \frac{1}{2H}\left[\Delta P_m - \Delta P_e - D\Delta\omega\right] \tag{C.2}$$

$$\Delta\dot{E}_q^{'} = \frac{1}{\tau_{d0}^{'}}\Delta E_{fd} - \frac{V_{\infty d0}\left(X_d - X_d^{'}\right)}{\tau_{d0}^{'}\left(X_d^{'} + X_t\right)}\Delta\delta - \frac{\left(X_d + X_t\right)}{\tau_{d0}^{'}\left(X_d^{'} + X_t\right)}\Delta E_q^{"} \tag{C.217}$$

$$\Delta\dot{E}_d^{"} = \frac{V_{\infty q0}\left(X_q - X_q^{"}\right)}{\tau_{q0}^{"}\left(X_q^{"} + X_t\right)}\Delta\delta - \frac{\left(X_q + X_t\right)}{\tau_{q0}^{"}\left(X_q^{"} + X_t\right)}\Delta E_d^{"} \tag{C.205}$$

$$\Delta P_e = K_1\Delta\delta + K_2\Delta E_q^{'} - K_{2d}\Delta E_d^{"} \tag{C.218}$$

$$\Delta e_t = K_5\Delta\delta + K_6\Delta E_q^{'} + K_{6d}\Delta E_d^{"} \tag{C.219}$$

where the coefficients in (C.218) and (C.219) are given by (C.86)–(C.91). Substitution of (C.218) in (C.2) yields

$$\Delta\dot{\omega} = -\frac{K_1}{2H}\Delta\delta - \frac{D}{2H}\Delta\omega - \frac{K_2}{2H}\Delta E_q^{'} + \frac{K_{2d}}{2H}\Delta E_d^{"} + \frac{1}{2H}\Delta P_m \tag{C.220}$$

Considering differential equations (C.1), (C.205), (C.217) and (C.220), and the terminal voltage equation (C.219), the state-space representation (C.186) is constructed, where

$$\Delta\mathbf{y} = \begin{bmatrix}\Delta\omega & \Delta e_t\end{bmatrix}^T \tag{C.187}$$

$$\Delta\mathbf{u} = \begin{bmatrix}\Delta P_m & \Delta E_{fd}\end{bmatrix}^T \tag{C.188}$$

$$\Delta\mathbf{x} = \begin{bmatrix}\Delta\omega & \Delta E_q^{'} & \Delta E_d^{"} & \Delta\delta\end{bmatrix}^T \tag{C.221}$$

System, control, output and feed-forward matrices **A**, **B, C** and **D,** respectively, are given as

$$\mathbf{A}=\begin{bmatrix} -\frac{D}{2H} & -\frac{K_2}{2H} & \frac{K_{2d}}{2H} & -\frac{K_1}{2H} \\ 0 & a_{22} & 0 & a_{24} \\ 0 & 0 & a_{33} & a_{34} \\ \omega_0 & 0 & 0 & 0 \end{bmatrix} \tag{C.222}$$

$$\mathbf{B}=\begin{bmatrix} \frac{1}{2H} & 0 & 0 & 0 \\ 0 & \frac{1}{\tau_{d0}^{'}} & 0 & 0 \end{bmatrix}^T \tag{C.223}$$

$$\mathbf{C}=\begin{bmatrix} 1 & 0 & 0 & 0 \\ 0 & K_6 & K_{6d} & K_5 \end{bmatrix} \tag{C.224}$$

$$\mathbf{D}=\mathbf{0}_{2\times 2}=\begin{bmatrix} 0 & 0 \\ 0 & 0 \end{bmatrix} \tag{C.225}$$

where coefficients in (C.222) and (C.224) are given by (C.86)–(C.91) and

$$a_{22}=-\frac{\left(X_d+X_t\right)}{\tau_{d0}^{'}\left(X_d^{'}+X_t\right)} \tag{C.226}$$

$$a_{24}=-\frac{V_{\infty d0}\left(X_d-X_d^{'}\right)}{\tau_{d0}^{'}\left(X_d^{'}+X_t\right)} \tag{C.227}$$

$$a_{33}=-\frac{\left(X_q+X_t\right)}{\tau_{q0}^{''}\left(X_q^{''}+X_t\right)} \tag{C.228}$$

$$a_{34}=\frac{V_{\infty q0}\left(X_q-X_q^{''}\right)}{\tau_{q0}^{''}\left(X_q^{''}+X_t\right)} \tag{C.229}$$

C.3.4. Model 2B (1*d*.0*q*, 4th order, one-axis)

This model can be arrived at by considering Model 1 and the following simplifying assumptions:

$$\tau_{q0}^{''}\to 0, X_q^{''}=X_q, E_d^{''}=0 \tag{C.104}$$

Therefore, the differential and algebraic equations that define this model are given as

$$\Delta\dot{\delta}=\omega_0\Delta\omega \tag{C.1}$$

$$\Delta\dot{\omega}=\frac{1}{2H}\left[\Delta P_m-\Delta P_e-D\Delta\omega\right] \tag{C.2}$$

$$\Delta\dot{E}_q^{'}=\frac{1}{\tau_{d0}^{'}}\Delta E_{fd}-\frac{V_{\infty d0}\left(X_d-X_d^{'}\right)}{\tau_{d0}^{'}\left(X_d^{''}+X_t\right)}\Delta\delta-\frac{1}{\tau_{d0}^{'}}\Delta E_q^{'}-\frac{\left(X_d-X_d^{'}\right)}{\tau_{d0}^{'}\left(X_d^{''}+X_t\right)}\Delta E_q^{''} \tag{C.40}$$

$$\Delta \dot{E}_q^{"} = \frac{1}{\tau_{d0}^{'}}\Delta E_{fd} - V_{\infty d0}\left[\frac{\tau_{d0}^{'}\left(X_d^{'} - X_d^{"}\right) + \tau_{d0}^{"}\left(X_d - X_d^{'}\right)}{\tau_{d0}^{"}\tau_{d0}^{'}\left(X_d^{"} + X_t\right)}\right]\Delta\delta + \left(\frac{1}{\tau_{d0}^{"}} - \frac{1}{\tau_{d0}^{'}}\right)\Delta E_q^{'} + \\ -\left[\frac{\tau_{d0}^{'}\left(X_d^{'} + X_t\right) + \tau_{d0}^{"}\left(X_d - X_d^{'}\right)}{\tau_{d0}^{"}\tau_{d0}^{'}\left(X_d^{"} + X_t\right)}\right]\Delta E_q^{"} \tag{C.41}$$

$$\Delta P_e = K_1\Delta\delta + K_2\Delta E_q^{"} \tag{C.230}$$

$$\Delta e_t = K_5\Delta\delta + K_6\Delta E_q^{"} \tag{C.231}$$

where the coefficients in (C.230) and (C.231) are given by (C.105), (C.106), (C.108) and (C.109). Substitution of (C.230) in (C.2) yields

$$\Delta\dot{\omega} = -\frac{K_1}{2H}\Delta\delta - \frac{D}{2H}\Delta\omega - \frac{K_2}{2H}\Delta E_q^{"} + \frac{1}{2H}\Delta P_m \tag{C.232}$$

Considering differential equations (C.1), (C.40), (C.41) and (C.232), and the terminal voltage equation (C.231), the state-space representation (C.186) is constructed, where

$$\Delta\mathbf{y} = \begin{bmatrix}\Delta\omega & \Delta e_t\end{bmatrix}^T \tag{C.187}$$

$$\Delta\mathbf{u} = \begin{bmatrix}\Delta P_m & \Delta E_{fd}\end{bmatrix}^T \tag{C.188}$$

$$\Delta\mathbf{x} = \begin{bmatrix}\Delta\omega & \Delta E_q^{'} & \Delta E_q^{"} & \Delta\delta\end{bmatrix}^T \tag{C.233}$$

System, control, output and feed-forward matrices **A**, **B, C** and **D,** respectively, are given as

$$\mathbf{A} = \begin{bmatrix} -\frac{D}{2H} & 0 & -\frac{K_2}{2H} & -\frac{K_1}{2H} \\ 0 & -\frac{1}{\tau_{d0}^{'}} & a_{23} & a_{24} \\ 0 & \frac{1}{\tau_{d0}^{"}} - \frac{1}{\tau_{d0}^{'}} & a_{33} & a_{34} \\ \omega_0 & 0 & 0 & 0 \end{bmatrix} \tag{C.234}$$

$$\mathbf{B} = \begin{bmatrix} \frac{1}{2H} & 0 & 0 & 0 \\ 0 & \frac{1}{\tau_{d0}^{'}} & \frac{1}{\tau_{d0}^{'}} & 0 \end{bmatrix}^T \tag{C.235}$$

$$\mathbf{C} = \begin{bmatrix} 1 & 0 & 0 & 0 \\ 0 & 0 & K_6 & K_5 \end{bmatrix} \tag{C.236}$$

$$\mathbf{D} = \mathbf{0}_{2\times 2} = \begin{bmatrix} 0 & 0 \\ 0 & 0 \end{bmatrix} \tag{C.237}$$

where coefficients in (C.234) and (C.236) are given by (C.105), (C.106), (C.108), (C.109) and

$$a_{23} = -\frac{\left(X_d - X_d^{'}\right)}{\tau_{d0}^{'}\left(X_d^{"} + X_t\right)} \tag{C.238}$$

$$a_{24} = -\frac{V_{\infty d0}\left(X_d - X_d^{'}\right)}{\tau_{d0}^{'}\left(X_d^{''} + X_t\right)} \tag{C.239}$$

$$a_{33} = -\frac{\left[\tau_{d0}^{'}\left(X_d^{'} + X_t\right) + \tau_{d0}^{''}\left(X_d - X_d^{'}\right)\right]}{\tau_{d0}^{''}\tau_{d0}^{'}\left(X_d^{''} + X_t\right)} \tag{C.240}$$

$$a_{34} = -\frac{V_{\infty d0}\left[\tau_{d0}^{'}\left(X_d^{'} - X_d^{''}\right) + \tau_{d0}^{''}\left(X_d - X_d^{'}\right)\right]}{\tau_{d0}^{''}\tau_{d0}^{'}\left(X_d^{''} + X_t\right)} \tag{C.241}$$

C.3.5. Model 2C (1*d*.1*q*, 4th order, two-axis)

This model can be arrived at by considering Model 0 and the following simplifying assumptions:

$$\tau_{d0}^{''} \to 0, X_d^{''} = X_d^{'}, E_q^{''} = E_q^{'} \tag{C.85}$$

$$\tau_{q0}^{''} \to 0, X_q^{''} = X_q^{'}, E_d^{''} = E_d^{'} \tag{C.242}$$

Therefore, the differential and algebraic equations that define this model are given as

$$\Delta\dot{\delta} = \omega_0 \Delta\omega \tag{C.1}$$

$$\Delta\dot{\omega} = \frac{1}{2H}\left[\Delta P_m - \Delta P_e - D\Delta\omega\right] \tag{C.2}$$

$$\Delta\dot{E}_q^{'} = \frac{1}{\tau_{d0}^{'}}\Delta E_{fd} - \frac{V_{\infty d0}\left(X_d - X_d^{'}\right)}{\tau_{d0}^{'}\left(X_d^{'} + X_t\right)}\Delta\delta - \frac{\left(X_d + X_t\right)}{\tau_{d0}^{'}\left(X_d^{'} + X_t\right)}\Delta E_q^{'} \tag{C.159}$$

$$\Delta\dot{E}_d^{'} = \frac{V_{\infty q0}\left(X_q - X_q^{'}\right)}{\tau_{q0}^{'}\left(X_q^{'} + X_t\right)}\Delta\delta - \frac{\left(X_q + X_t\right)}{\tau_{q0}^{'}\left(X_q^{'} + X_t\right)}\Delta E_d^{'} \tag{C.160}$$

$$\Delta P_e = K_1\Delta\delta + K_2\Delta E_q^{'} - K_{2d}\Delta E_d^{'} \tag{C.151}$$

$$\Delta e_t = K_5\Delta\delta + K_6\Delta E_q^{'} + K_{6d}\Delta E_d^{'} \tag{C.152}$$

where the coefficients in (C.151) and (C.152) are given by (C.153)–(C.158). Substitution of (C.151) in (C.2) yields

$$\Delta\dot{\omega} = -\frac{K_1}{2H}\Delta\delta - \frac{D}{2H}\Delta\omega - \frac{K_2}{2H}\Delta E_q^{'} + \frac{K_{2d}}{2H}\Delta E_d^{'} + \frac{1}{2H}\Delta P_m \tag{C.243}$$

Considering differential equations (C.1), (C.159), (C.160) and (C.243), and the terminal voltage equation (C.152), the state-space representation (C.186) is constructed, where

$$\Delta\mathbf{y} = \begin{bmatrix}\Delta\omega & \Delta e_t\end{bmatrix}^T \tag{C.187}$$

$$\Delta\mathbf{u} = \begin{bmatrix}\Delta P_m & \Delta E_{fd}\end{bmatrix}^T \tag{C.188}$$

$$\Delta\mathbf{x} = \begin{bmatrix}\Delta\omega & \Delta E_q^{'} & \Delta E_d^{'} & \Delta\delta\end{bmatrix}^T \tag{C.244}$$

System, control, output and feed-forward matrices **A**, **B, C** and **D,** respectively, are given as

$$\mathbf{A}=\begin{bmatrix} -\frac{D}{2H} & -\frac{K_2}{2H} & \frac{K_{2d}}{2H} & -\frac{K_1}{2H} \\ 0 & a_{22} & 0 & a_{24} \\ 0 & 0 & a_{33} & a_{34} \\ \omega_0 & 0 & 0 & 0 \end{bmatrix} \tag{C.245}$$

$$\mathbf{B}=\begin{bmatrix} \frac{1}{2H} & 0 & 0 & 0 \\ 0 & \frac{1}{\tau_{d0}^{'}} & 0 & 0 \end{bmatrix}^T \tag{C.246}$$

$$\mathbf{C}=\begin{bmatrix} 1 & 0 & 0 & 0 \\ 0 & K_6 & K_{6d} & K_5 \end{bmatrix} \tag{C.247}$$

$$\mathbf{D}=\mathbf{0}_{2\times 2}=\begin{bmatrix} 0 & 0 \\ 0 & 0 \end{bmatrix} \tag{C.248}$$

where coefficients in (C.245) and (C.247) are given by (C.153)–(C.158) and

$$a_{22}=-\frac{\left(X_d+X_t\right)}{\tau_{d0}^{'}\left(X_d^{'}+X_t\right)} \tag{C.249}$$

$$a_{24}=-\frac{V_{\infty d0}\left(X_d-X_d^{'}\right)}{\tau_{d0}^{'}\left(X_d^{'}+X_t\right)} \tag{C.250}$$

$$a_{33}=-\frac{\left(X_q+X_t\right)}{\tau_{q0}^{'}\left(X_q^{'}+X_t\right)} \tag{C.251}$$

$$a_{34}=\frac{V_{\infty q0}\left(X_q-X_q^{'}\right)}{\tau_{q0}^{'}\left(X_q^{'}+X_t\right)} \tag{C.252}$$

C.3.6. Model 3 (1*d*.0*q*, 3rd order, one-axis)

This model can be arrived at by considering Model 2A and the following simplifying assumptions:

$$\tau_{q0}^{''}\to 0, X_q^{''}\to X_q, E_d^{''}\to 0 \tag{C.122}$$

Therefore, the differential and algebraic equations that define this model are given as

$$\Delta\dot{\delta}=\omega_0\Delta\omega \tag{C.1}$$

$$\Delta\dot{\omega}=\frac{1}{2H}\left[\Delta P_m-\Delta P_e-D\Delta\omega\right] \tag{C.2}$$

$$\Delta\dot{E}_q^{'}=\frac{1}{\tau_{d0}^{'}}\Delta E_{fd}-\frac{V_{\infty d0}\left(X_d-X_d^{'}\right)}{\tau_{d0}^{'}\left(X_d^{'}+X_t\right)}\Delta\delta-\frac{\left(X_d+X_t\right)}{\tau_{d0}^{'}\left(X_d^{'}+X_t\right)}\Delta E_q^{'} \tag{C.217}$$

$$\Delta P_e=K_1\Delta\delta+K_2\Delta E_q^{'} \tag{C.253}$$

$$\Delta e_t = K_5 \Delta\delta + K_6 \Delta E_q^{'} \tag{C.254}$$

where the coefficients in (C.253) and (C.254) are given by (C.123), (C.124), (C.126) and (C.127). Substitution of (C.253) in (C.2) yields

$$\Delta \dot{\omega} = -\frac{K_1}{2H}\Delta\delta - \frac{D}{2H}\Delta\omega - \frac{K_2}{2H}\Delta E_q^{'} + \frac{1}{2H}\Delta P_m \tag{C.255}$$

Considering differential equations (C.1), (C.217) and (C.255), and the terminal voltage equation (C.254), the state-space representation (C.186) is constructed, where

$$\Delta\mathbf{y} = \begin{bmatrix} \Delta\omega & \Delta e_t \end{bmatrix}^T \tag{C.187}$$

$$\Delta\mathbf{u} = \begin{bmatrix} \Delta P_m & \Delta E_{fd} \end{bmatrix}^T \tag{C.188}$$

$$\Delta\mathbf{x} = \begin{bmatrix} \Delta\omega & \Delta E_q^{'} & \Delta\delta \end{bmatrix}^T \tag{C.256}$$

System, control, output and feedf-orward matrices **A**, **B, C** and **D,** respectively, are given as

$$\mathbf{A} = \begin{bmatrix} -\frac{D}{2H} & -\frac{K_2}{2H} & -\frac{K_1}{2H} \\ 0 & a_{22} & a_{23} \\ \omega_0 & 0 & 0 \end{bmatrix} \tag{C.257}$$

$$\mathbf{B} = \begin{bmatrix} \frac{1}{2H} & 0 & 0 \\ 0 & \frac{1}{\tau_{d0}^{'}} & 0 \end{bmatrix}^T \tag{C.258}$$

$$\mathbf{C} = \begin{bmatrix} 1 & 0 & 0 \\ 0 & K_6 & K_5 \end{bmatrix} \tag{C.259}$$

$$\mathbf{D} = \mathbf{0}_{2\times 2} = \begin{bmatrix} 0 & 0 \\ 0 & 0 \end{bmatrix} \tag{C.260}$$

where coefficients in (C.257) and (C.259) are given by (C.123), (C.124), (C.126), (C.127) and

$$a_{22} = -\frac{\left(X_d + X_t\right)}{\tau_{d0}^{'}\left(X_d^{'} + X_t\right)} \tag{C.261}$$

$$a_{23} = -\frac{V_{\infty d0}\left(X_d - X_d^{'}\right)}{\tau_{d0}^{'}\left(X_d^{'} + X_t\right)} \tag{C.262}$$

Appendix D

DERIVATION OF THE SMALL-SIGNAL TRANSFER FUNCTION MATRIX AND STATE-SPACE MODELS OF THE SYNCHRONOUS GENERATOR – SVC SYSTEM

D.1. General considerations

The small-signal model of the synchronous generator – SVC system used in this thesis can be derived from the algebraic and differential equations (2.2)–(2.18), which describe the synchronous generator, and from those equations associated to the system phasor diagram and the SVC itself. Suitable combination of those equations, as described in Chapter 2, provides various orders of generator models. However, only Model 1 (5^{th} order, two-axis) is considered. For small variations, the synchronous generator differential equations are given as

$$\Delta\dot{\delta} = \omega_0 \Delta\omega \tag{D.1}$$

$$\Delta\dot{\omega} = \frac{1}{2H}\left[\Delta P_m - \Delta P_e - D\Delta\omega\right] \tag{D.2}$$

$$\Delta\dot{E}_q^{'} = \frac{1}{\tau_{d0}^{'}}\left[\Delta E_{fd} - \left(X_d - X_d^{'}\right)\Delta i_{td} - \Delta E_q^{'}\right] \tag{D.3}$$

$$\begin{aligned}\Delta\dot{E}_q^{''} &= \frac{1}{\tau_{d0}^{''}}\left[\Delta E_q^{'} - \left(X_d^{'} - X_d^{''}\right)\Delta i_{td} - \Delta E_q^{''}\right] + \Delta\dot{E}_q^{'} \\ &= \frac{1}{\tau_{d0}^{'}}\left\{\frac{\tau_{d0}^{''}}{\tau_{d0}^{'}}\Delta E_{fd} - \left[\left(X_d^{'} - X_d^{''}\right) + \frac{\tau_{d0}^{''}}{\tau_{d0}^{'}}\left(X_d - X_d^{'}\right)\right]\Delta i_{td} + \left[1 - \frac{\tau_{d0}^{''}}{\tau_{d0}^{'}}\right]\Delta E_q^{'} - \Delta E_q^{''}\right\}\end{aligned} \tag{D.4}$$

$$\Delta\dot{E}_d^{''} = \frac{1}{\tau_{q0}^{''}}\left[\left(X_q - X_q^{''}\right)\Delta i_{tq} - \Delta E_d^{''}\right] \tag{D.5}$$

Notice that equations (D.3)–(D.5) are given in terms of the terminal current of the machine. Therefore, it is necessary to obtain suitable expressions for the terminal current components in terms of the SVC and infinite bus parameters. To this end, consider the phasor diagram of the synchronous generator – SVC

system provided in Figure D.1. With the rotor position taken as the reference, it can be seen that the components of the infinite bus voltage are given by

$$V_{\infty q} = V_{\infty} \cos\delta \tag{D.6}$$

$$V_{\infty d} = V_{\infty} \sin\delta \tag{D.7}$$

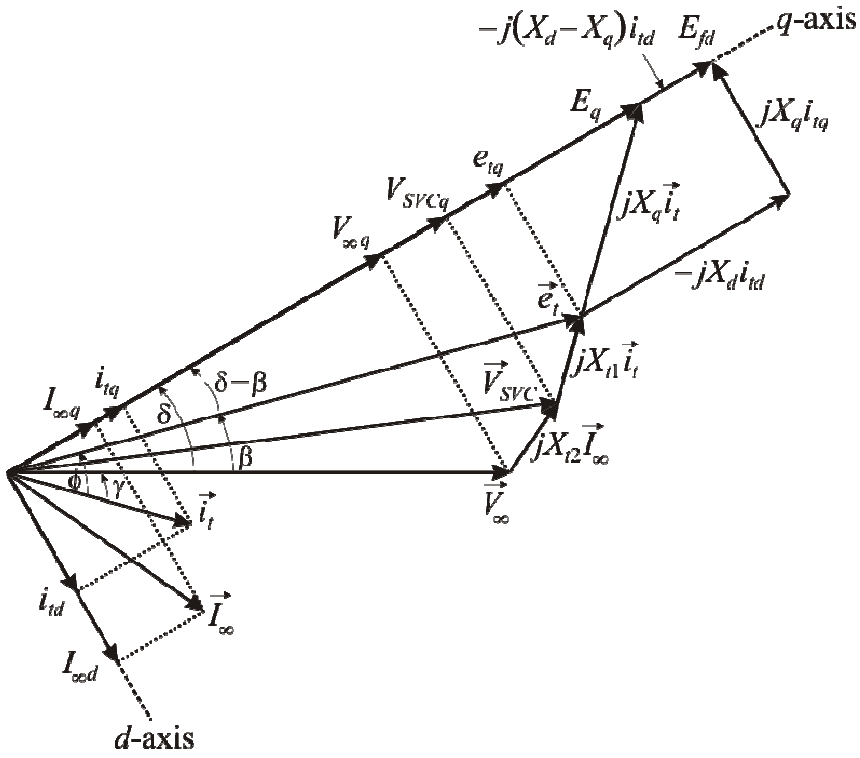

Figure D.1. Phasor diagram of a synchronous generator – SVC system

For small variations, an incremental change of the infinite bus voltage can be stated as

$$\Delta V_{\infty q} = -V_{\infty 0} \sin\delta_0 \Delta\delta = -V_{\infty d0}\Delta\delta \tag{D.8}$$

$$\Delta V_{\infty d} = V_{\infty 0} \cos\delta_0 \Delta\delta = V_{\infty q0}\Delta\delta \tag{D.9}$$

From Figure C.1, the terminal current can be expressed as

$$\vec{i}_t = \vec{I}_{SVC} + \vec{I}_{\infty} \tag{D.10}$$

Separating (D.10) into real and imaginary parts,

$$i_{tq} = I_{SVCq} + I_{\infty q} \tag{D.11}$$

$$i_{td} = I_{SVCd} + I_{\infty d} \tag{D.12}$$

For small variations, (D.11) and (D.12) are given as

$$\Delta i_{tq} = \Delta I_{SVCq} + \Delta I_{\infty q} \tag{D.13}$$

$$\Delta i_{td} = \Delta I_{SVCd} + \Delta I_{\infty d} \tag{D.14}$$

Equation (D.10) can be written also as

$$\vec{i}_t = \vec{Y}_{SVC}\vec{V}_{SVC} + \frac{\left(\vec{V}_{SVC} - \vec{V}_\infty\right)}{jX_{t2}} \tag{D.15}$$

where

$$\vec{I}_{SVC} = \vec{Y}_{SVC}\vec{V}_{SVC} \tag{D.16}$$

$$\vec{I}_\infty = \frac{\vec{V}_{SVC} - \vec{V}_\infty}{jX_{t2}} \tag{D.17}$$

Using (2.49) from Chapter 2, notice that

$$\vec{Y}_{SVC} = j\left(B_C - B_L(\alpha)\right) = jB_{SVC} \tag{D.18}$$

For a given operating condition, $B_{SVC0} = (B_C - B_{L0}(\alpha))$. Recalling (2.50) and (2.51) in Chapter 2:

$$B_C = 2\pi fC \tag{2.50}$$

$$B_L(\alpha) = \frac{2}{\pi X_L}\left\{(\pi - \alpha) + \frac{1}{2}\sin 2\alpha\right\} \tag{2.51}$$

Notice that for small variations, (2.49) is given as

$$\Delta B_{SVC} = -\Delta B_L(\alpha) = F(\alpha)\Delta\alpha \tag{D.19}$$

where

$$F(\alpha) = \frac{2}{\pi X_L} - \frac{2}{\pi X_L}\cos(2\alpha) \tag{D.20}$$

It can be seen from (D.20) that $F(\alpha)$ is a nonlinear function. However, for modelling purposes, a linearised block in the SVC model is considered and

$$F(\alpha) \cong \frac{2}{\pi X_L} \tag{D.21}$$

Separating (D.16) into its components using (D.18) yields

$$I_{SVCq} = B_{SVC}V_{SVCd} \tag{D.22}$$

$$I_{SVCd} = -B_{SVC}V_{SVCq} \tag{D.23}$$

For small variations, (D.22) and (D.23) become

$$\Delta I_{SVCq} = B_{SVC0}\Delta V_{SVCd} + V_{SVCd0}\Delta B_{SVC} \tag{D.24}$$

$$\Delta I_{SVCd} = -\left(B_{SVC0}\Delta V_{SVCq} + V_{SVCq0}\Delta B_{SVC}\right) \tag{D.25}$$

Substituting (D.19) and (D.21) into (D.24) and (D.25) yields

$$\Delta I_{SVCq} = B_{SVC0}\Delta V_{SVCd} + \frac{2}{\pi X_L}V_{SVCd0}\Delta\alpha \tag{D.26}$$

$$\Delta I_{SVCd} = -\left(B_{SVC0}\Delta V_{SVCq} + \frac{2}{\pi X_L}V_{SVCq0}\Delta\alpha\right) \tag{D.27}$$

From Figure D.1, terminal current can be expressed as

$$\vec{i}_t = \frac{\vec{e}_t - \vec{V}_{SVC}}{jX_{t1}} \tag{D.28}$$

Separating (D.28) into real and imaginary parts,

$$i_{td} X_{t1} = e_{tq} - V_{SVCq} \tag{D.29}$$

$$i_{tq} X_{t1} = V_{SVCd} - e_{td} \tag{D.30}$$

Separating the current at the infinite bus (D.17) into real and imaginary parts,

$$I_{\infty d} X_{t2} = V_{SVCq} - V_{\infty q} \tag{D.31}$$

$$I_{\infty q} X_{t2} = V_{\infty d} - V_{SVCd} \tag{D.32}$$

Equations (D.31) and (D.32) are rewritten in terms of (D.12) and (D.11), respectively, as

$$V_{SVCq} = \left(i_{td} - I_{SVCd}\right) X_{t2} + V_{\infty q} \tag{D.33}$$

$$V_{SVCd} = V_{\infty d} - \left(i_{tq} - I_{SVCq}\right) X_{t2} \tag{D.34}$$

Rearranging (D.29) and (D.30) by making use of (D.33) and (D.34), respectively, and solving for the terminal voltage components yields

$$e_{tq} = i_{td}\left(X_{t1} + X_{t2}\right) - I_{SVCd} X_{t2} + V_{\infty q} \tag{D.35}$$

$$e_{td} = V_{\infty d} - i_{tq}\left(X_{t1} + X_{t2}\right) + I_{SVCq} X_{t2} \tag{D.36}$$

Rearranging (D.35) and (D.36) by making use of the sub-transient equations (2.8) and (2.9) while neglecting the stator resistance gives

$$i_{tq} = \frac{V_{\infty d} - E_d^{"} + I_{SVCq} X_{t2}}{X_q^{"} + X_{t1} + X_{t2}} \tag{D.37}$$

$$i_{td} = \frac{E_q^{"} - V_{\infty q} + I_{SVCd} X_{t2}}{X_d^{"} + X_{t1} + X_{t2}} \tag{D.38}$$

For small variations, (D.37) and (D.38) can be written as

$$\Delta i_{tq} = \frac{\Delta V_{\infty d} - \Delta E_d^{"} + X_{t2} \Delta I_{SVCq}}{X_q^{"} + X_{t1} + X_{t2}} \tag{D.39}$$

$$\Delta i_{td} = \frac{\Delta E_q^{"} - \Delta V_{\infty q} + X_{t2} \Delta I_{SVCd}}{X_d^{"} + X_{t1} + X_{t2}} \tag{D.40}$$

Substituting (D.8) into (D.40) and (D.9) into (D.39) in yields the following intermediate result:

$$\Delta i_{tq} = \frac{V_{\infty q0} \Delta\delta - \Delta E_d^{"} + X_{t2} \Delta I_{SVCq}}{X_q^{"} + X_{t1} + X_{t2}} \tag{D.41}$$

$$\Delta i_{td} = \frac{\Delta E_q^{"} + V_{\infty d0} \Delta\delta + X_{t2} \Delta I_{SVCd}}{X_d^{"} + X_{t1} + X_{t2}} \tag{D.42}$$

Separating (D.15) into real and imaginary parts by making use of (D.18) yields

$$i_{tq}X_{t2} = V_{\infty d} - (1 - X_{t2}B_{SVC})V_{SVCd} \tag{D.43}$$

$$i_{td}X_{t2} = (1 - X_{t2}B_{SVC})V_{SVCq} - V_{\infty q} \tag{D.44}$$

Substituting (D.29) into (2.9) and (D.30) into (2.8) and solving for the generator terminal currents provides

$$i_{tq} = \frac{V_{SVCd} - E_d^{"}}{X_q^{"} + X_{t1}} \tag{D.45}$$

$$i_{td} = \frac{E_q^{"} - V_{SVCq}}{X_d^{"} + X_{t1}} \tag{D.46}$$

where the stator resistance is neglected. Substituting (D.45) into (D.43) and (D.46) into (D.44) gives

$$\left[X_{t2} + \left(X_d^{"} + X_{t1}\right)\left(1 - X_{t2}B_{SVC}\right)\right] \cdot V_{SVCq} = X_{t2}E_q^{"} + \left(X_d^{"} + X_{t1}\right)V_{\infty q} \tag{D.47}$$

$$\left[X_{t2} + \left(X_q^{"} + X_{t1}\right)\left(1 - X_{t2}B_{SVC}\right)\right] \cdot V_{SVCd} = X_{t2}E_d^{"} + \left(X_q^{"} + X_{t1}\right)V_{\infty d} \tag{D.48}$$

For small variations, (D.47) and (D.48) can be written as

$$\Delta V_{SVCq} = \frac{X_{t2}\Delta E_q^{"} + \left(X_d^{"} + X_{t1}\right)\Delta V_{\infty q} + X_{t2}\left(X_d^{"} + X_{t1}\right)V_{SVCq0}\Delta B_{SVC}}{X_{t2} + \left(X_d^{"} + X_{t1}\right)\left(1 - X_{t2}B_{SVC0}\right)} \tag{D.49}$$

$$\Delta V_{SVCd} = \frac{X_{t2}\Delta E_d^{"} + \left(X_q^{"} + X_{t1}\right)\Delta V_{\infty d} + X_{t2}\left(X_q^{"} + X_{t1}\right)V_{SVCd0}\Delta B_{SVC}}{X_{t2} + \left(X_q^{"} + X_{t1}\right)\left(1 - X_{t2}B_{SVC0}\right)} \tag{D.50}$$

Substituting (D.8), (D.9), (D.19) and (D.21) into (D.49) and (D.50) yields

$$\Delta V_{SVCq} = \left[\frac{X_{t2}}{\Delta_d^{"}}\right]\Delta E_q^{"} - \left[\frac{\left(X_d^{"} + X_{t1}\right)V_{\infty d0}}{\Delta_d^{"}}\right]\Delta\delta + \left[\frac{2}{\pi X_L} \cdot \frac{X_{t2}\left(X_d^{"} + X_{t1}\right)V_{SVCq0}}{\Delta_d^{"}}\right]\Delta\alpha \tag{D.51}$$

$$\Delta V_{SVCd} = \left[\frac{X_{t2}}{\Delta_q^{"}}\right]\Delta E_d^{"} + \left[\frac{\left(X_q^{"} + X_{t1}\right)V_{\infty q0}}{\Delta_q^{"}}\right]\Delta\delta + \left[\frac{2}{\pi X_L} \cdot \frac{X_{t2}\left(X_q^{"} + X_{t1}\right)V_{SVCd0}}{\Delta_q^{"}}\right]\Delta\alpha \tag{D.52}$$

where

$$\Delta_d^{"} = X_{t2} + \left(X_d^{"} + X_{t1}\right)\left(1 - X_{t2}B_{SVC0}\right) \tag{D.53}$$

$$\Delta_q^{"} = X_{t2} + \left(X_q^{"} + X_{t1}\right)\left(1 - X_{t2}B_{SVC0}\right) \tag{D.54}$$

Rearranging (D.41) and (D.42) by making use of (D.26), (D.27), (D.51)–(D.54) gives

$$\Delta i_{tq} = \left[\frac{V_{\infty q0}}{\Delta_q^{"}}\right]\Delta\delta - \left[\frac{1 - X_{t2}B_{SVC0}}{\Delta_q^{"}}\right]\Delta E_d^{"} + \left[\frac{2}{\pi X_L} \cdot \frac{X_{t2}V_{SVCd0}}{\Delta_q^{"}}\right]\Delta\alpha \tag{D.55}$$

$$\Delta i_{td} = \left[\frac{1 - X_{t2}B_{SVC0}}{\Delta_d^{"}}\right]\Delta E_q^{"} + \left[\frac{V_{\infty d0}}{\Delta_d^{"}}\right]\Delta\delta - \left[\frac{2}{\pi X_L} \cdot \frac{X_{t2}V_{SVCq0}}{\Delta_d^{"}}\right]\Delta\alpha \tag{D.56}$$

which are the necessary expressions for the generator currents.

The synchronous generator active power equation (2.14) can be written as

$$P_e = V_{\infty d} I_{\infty d} + V_{\infty q} I_{\infty q} \tag{D.57}$$

which for small variations becomes

$$\Delta P_e = V_{\infty d0} \Delta I_{\infty d} + I_{\infty d0} \Delta V_{\infty d} + V_{\infty q0} \Delta I_{\infty q} + I_{\infty q0} \Delta V_{\infty q} \tag{D.58}$$

Rearrangement of (D.13) by making use of (D.26), (D.52), (D.54) and (D.55) renders

$$\Delta I_{\infty q} = \left[\frac{\left(1 - \left(X_q^{"} + X_{t1}\right) B_{SVC0}\right) V_{\infty q0}}{\Delta_q^{"}} \right] \Delta\delta - \left[\frac{1}{\Delta_q^{"}} \right] \Delta E_d^{"} - \left[\frac{2}{\pi X_L} \cdot \frac{\left(X_q^{"} + X_{t1}\right) V_{SVCd0}}{\Delta_q^{"}} \right] \Delta\alpha \tag{D.59}$$

Rearrangement of (D.14) by making use of (D.27), (D.51), (D.53) and (D.56) renders

$$\Delta I_{\infty d} = \left[\frac{1}{\Delta_d^{"}} \right] \Delta E_q^{"} + \left[\frac{\left(1 - \left(X_d^{"} + X_{t1}\right) B_{SVC0}\right) V_{\infty d0}}{\Delta_d^{"}} \right] \Delta\delta + \left[\frac{2}{\pi X_L} \cdot \frac{\left(X_d^{"} + X_{t1}\right) V_{SVCq0}}{\Delta_d^{"}} \right] \Delta\alpha \tag{D.60}$$

Substitution of (D.8), (D.9), (D.59) and (D.60) into (D.58) yields

$$\begin{aligned} \Delta P_e = & \left[\frac{\left(1 - \left(X_d^{"} + X_{t1}\right) B_{SVC0}\right) V_{\infty d0}^2}{\Delta_d^{"}} + \frac{\left(1 - \left(X_q^{"} + X_{t1}\right) B_{SVC0}\right) V_{\infty q0}^2}{\Delta_q^{"}} + I_{\infty d0} V_{\infty q0} - I_{\infty q0} V_{\infty d0} \right] \Delta\delta + \\ & + \left[\frac{V_{\infty d0}}{\Delta_d^{"}} \right] \Delta E_q^{"} - \left[\frac{V_{\infty q0}}{\Delta_q^{"}} \right] \Delta E_d^{"} + \frac{2}{\pi X_L} \left[\frac{\left(X_d^{"} + X_{t1}\right) V_{SVCq0} V_{\infty d0}}{\Delta_d^{"}} - \frac{\left(X_q^{"} + X_{t1}\right) V_{SVCd0} V_{\infty q0}}{\Delta_q^{"}} \right] \Delta\alpha \end{aligned} \tag{D.61}$$

The generator terminal voltage equation (2.3) can be expressed in terms of *d*- and *q*-axis components as

$$e_t^2 = e_{td}^2 + e_{tq}^2 \tag{D.62}$$

which, for small variations, becomes

$$\Delta e_t = \left(e_{t0}\right)^{-1} \left[e_{td0} \Delta e_{td} + e_{tq0} \Delta e_{tq} \right] \tag{D.63}$$

where

$$\Delta e_{tq} = \Delta E_q^{"} - X_d^{"} \Delta i_{td} \tag{D.64}$$

$$\Delta e_{td} = \Delta E_d^{"} + X_q^{"} \Delta i_{tq} \tag{D.65}$$

Equations (D.64) and (D.65) can be obtained from (2.8) and (2.9) for small variations and by neglecting the stator resistance. Rearrangement of (D.64) by making use (D.53) and (D.56) gives

$$\Delta e_{tq} = \left[\frac{X_{t2} + X_{t1}\left(1 - X_{t2} B_{SVC0}\right)}{\Delta_d^{"}} \right] \Delta E_q^{"} - \left[\frac{X_d^{"} V_{\infty d0}}{\Delta_d^{"}} \right] \Delta\delta + \left[\frac{2}{\pi X_L} \cdot \frac{X_d^{"} X_{t2} V_{SVCq0}}{\Delta_d^{"}} \right] \Delta\alpha \tag{D.66}$$

Similarly, rearrangement of (D.65) by making use of (D.54) and (D.55) and

$$\Delta e_{td} = \left[\frac{X_{t2} + X_{t1}\left(1 - X_{t2} B_{SVC0}\right)}{\Delta_q^{"}} \right] \Delta E_d^{"} + \left[\frac{X_q^{"} V_{\infty q0}}{\Delta_q^{"}} \right] \Delta\delta + \left[\frac{2}{\pi X_L} \cdot \frac{X_q^{"} X_{t2} V_{SVCd0}}{\Delta_q^{"}} \right] \Delta\alpha \tag{D.67}$$

By substituting (D.66) and (D.67) into (D.63), the generator terminal voltage equation can be expressed as

$$\Delta e_t = \left[\frac{e_{td0}}{e_{t0}}\cdot\frac{X_q^{"}V_{\infty q0}}{\Delta_q^{"}} - \frac{e_{tq0}}{e_{t0}}\cdot\frac{X_d^{"}V_{\infty d0}}{\Delta_d^{"}}\right]\Delta\delta + \left[\frac{e_{tq0}}{e_{t0}}\cdot\frac{X_{t2}+X_{t1}\left(1-X_{t2}B_{SVC0}\right)}{\Delta_d^{"}}\right]\Delta E_q^{"} + \\ + \left[\frac{e_{td0}}{e_{t0}}\cdot\frac{X_{t2}+X_{t1}\left(1-X_{t2}B_{SVC0}\right)}{\Delta_q^{"}}\right]\Delta E_d^{"} + \frac{2}{\pi X_L}\left[\frac{e_{td0}}{e_{t0}}\cdot\frac{X_q^{"}X_{t2}V_{SVCd0}}{\Delta_q^{"}} + \frac{e_{tq0}}{e_{t0}}\cdot\frac{X_d^{"}X_{t2}V_{SVCq0}}{\Delta_d^{"}}\right]\Delta\alpha \tag{D.68}$$

Similarly to the generator terminal voltage, the SVC terminal voltage can be expressed in terms of *d*- and *q*-axis components as

$$V_{SVC}^2 = V_{SVCd}^2 + V_{SVCq}^2 \tag{D.69}$$

which, for small variations, becomes

$$\Delta V_{SVC} = \left(V_{SVC0}\right)^{-1}\left[V_{SVCd0}\Delta V_{SVCd} + V_{SVCq0}\Delta V_{SVCq}\right] \tag{D.70}$$

Rearranging (D.70) by making use of (D.51) and (D.52) yields

$$\Delta V_{SVC} = \left[\frac{V_{SVCd0}}{V_{SVC0}}\cdot\frac{\left(X_q^{"}+X_{t1}\right)V_{\infty q0}}{\Delta_q^{"}} - \frac{V_{SVCq0}}{V_{SVC0}}\cdot\frac{\left(X_d^{"}+X_{t1}\right)V_{\infty d0}}{\Delta_d^{"}}\right]\Delta\delta + \left[\frac{V_{SVCq0}}{V_{SVC0}}\cdot\frac{X_{t2}}{\Delta_d^{"}}\right]\Delta E_q^{"} + \\ + \left[\frac{V_{SVCd0}}{V_{SVC0}}\cdot\frac{X_{t2}}{\Delta_q^{"}}\right]\Delta E_d^{"} + \frac{2}{\pi X_L}\left[\frac{V_{SVCd0}^2}{V_{SVC0}}\cdot\frac{X_{t2}\left(X_q^{"}+X_{t1}\right)}{\Delta_q^{"}} + \frac{V_{SVCq0}^2}{V_{SVC0}}\cdot\frac{X_{t2}\left(X_d^{"}+X_{t1}\right)}{\Delta_d^{"}}\right]\Delta\alpha \tag{D.71}$$

For convenience, (D.61), (D.68) and (D.71) are rewritten as

$$\Delta P_e = K_1\Delta\delta + K_2\Delta E_q^{"} - K_{2d}\Delta E_d^{"} + K_{SVC1}\Delta\alpha \tag{D.72}$$

$$\Delta e_t = K_5\Delta\delta + K_6\Delta E_q^{"} + K_{6d}\Delta E_d^{"} + K_{SVC3}\Delta\alpha \tag{D.73}$$

$$\Delta V_{SVC} = K_{5n}\Delta\delta + K_{6n}\Delta E_q^{"} + K_{6dn}\Delta E_d^{"} + K_{SVC3n}\Delta\alpha \tag{D.74}$$

where

$$K_1 = \frac{\left(1-\left(X_d^{"}+X_{t1}\right)B_{SVC0}\right)V_{\infty d0}^2}{\Delta_d^{"}} + \frac{\left(1-\left(X_q^{"}+X_{t1}\right)B_{SVC0}\right)V_{\infty q0}^2}{\Delta_q^{"}} + I_{\infty d0}V_{\infty q0} - I_{\infty q0}V_{\infty d0} \tag{D.75}$$

$$K_2 = \frac{V_{\infty d0}}{\Delta_d^{"}} \tag{D.76}$$

$$K_{2d} = \frac{V_{\infty q0}}{\Delta_q^{"}} \tag{D.77}$$

$$K_{SVC1} = \frac{2}{\pi X_L}\left[\frac{\left(X_d^{"}+X_{t1}\right)V_{SVCq0}V_{\infty d0}}{\Delta_d^{"}} - \frac{\left(X_q^{"}+X_{t1}\right)V_{SVCd0}V_{\infty q0}}{\Delta_q^{"}}\right] \tag{D.78}$$

$$K_5 = \frac{e_{td0}}{e_{t0}}\cdot\frac{X_q^{"}V_{\infty q0}}{\Delta_q^{"}} - \frac{e_{tq0}}{e_{t0}}\cdot\frac{X_d^{"}V_{\infty d0}}{\Delta_d^{"}} \tag{D.79}$$

$$K_6 = \frac{e_{tq0}}{e_{t0}}\cdot\frac{X_{t2}+X_{t1}\left(1-X_{t2}B_{SVC0}\right)}{\Delta_d^{"}} \tag{D.80}$$

$$K_{6d} = \frac{e_{td0}}{e_{t0}} \cdot \frac{X_{t2} + X_{t1}\left(1 - X_{t2}B_{SVC0}\right)}{\Delta_q^{"}} \tag{D.81}$$

$$K_{SVC3} = \frac{2}{\pi X_L}\left[\frac{e_{td0}}{e_{t0}} \cdot \frac{X_q^{"} X_{t2} V_{SVCd0}}{\Delta_q^{"}} + \frac{e_{tq0}}{e_{t0}} \cdot \frac{X_d^{"} X_{t2} V_{SVCq0}}{\Delta_d^{"}}\right] \tag{D.82}$$

$$K_{5n} = \frac{V_{SVCd0}}{V_{SVC0}} \cdot \frac{\left(X_q^{"} + X_{t1}\right)V_{\infty q0}}{\Delta_q^{"}} - \frac{V_{SVCq0}}{V_{SVC0}} \cdot \frac{\left(X_d^{"} + X_{t1}\right)V_{\infty d0}}{\Delta_d^{"}} \tag{D.83}$$

$$K_{6n} = \frac{V_{SVCq0}}{V_{SVC0}} \cdot \frac{X_{t2}}{\Delta_d^{"}} \tag{D.84}$$

$$K_{6dn} = \frac{V_{SVCd0}}{V_{SVC0}} \cdot \frac{X_{t2}}{\Delta_q^{"}} \tag{D.85}$$

$$K_{SVC3n} = \frac{2}{\pi X_L}\left[\frac{V_{SVCd0}^2}{V_{SVC0}} \cdot \frac{X_{t2}\left(X_q^{"} + X_{t1}\right)}{\Delta_q^{"}} + \frac{V_{SVCq0}^2}{V_{SVC0}} \cdot \frac{X_{t2}\left(X_d^{"} + X_{t1}\right)}{\Delta_d^{"}}\right]\Delta\alpha \tag{D.86}$$

Substitution of terminal current equations (D.55) and (D.56) into (D.3)–(D.5) provides

$$\begin{aligned}\Delta\dot{E}_q^{'} = {} & \frac{1}{\tau_{d0}^{'}}\Delta E_{fd} - \frac{1}{\tau_{d0}^{'}}\Delta E_q^{'} - \frac{1}{\tau_{d0}^{'}}\left[\frac{\left(X_d - X_d^{'}\right)\left(1 - X_{t2}B_{SVC0}\right)}{\Delta_d^{"}}\right]\Delta E_q^{"} - \frac{1}{\tau_{d0}^{'}}\left[\frac{\left(X_d - X_d^{'}\right)V_{\infty d0}}{\Delta_d^{"}}\right]\Delta\delta + \\ & + \frac{1}{\tau_{d0}^{'}}\left[\frac{2}{\pi X_L} \cdot \frac{X_{t2}\left(X_d - X_d^{'}\right)V_{SVCq0}}{\Delta_d^{"}}\right]\Delta\alpha\end{aligned} \tag{D.87}$$

$$\begin{aligned}\Delta\dot{E}_q^{"} = {} & \frac{1}{\tau_{d0}^{'}}\Delta E_{fd} + \left[\frac{1}{\tau_{d0}^{"}} - \frac{1}{\tau_{d0}^{'}}\right]\Delta E_q^{'} - \frac{V_{\infty d0}\left[\tau_{d0}^{'}\left(X_d^{'} - X_d^{"}\right) + \tau_{d0}^{"}\left(X_d - X_d^{'}\right)\right]}{\tau_{d0}^{"}\tau_{d0}^{'}\Delta_d^{"}}\Delta\delta + \\ & - \left\{\frac{\left(1 - X_{t2}B_{SVC0}\right)\left[\tau_{d0}^{'}\left(X_d^{'} + X_{t1}\right) + \tau_{d0}^{"}\left(X_d - X_d^{'}\right)\right] + \tau_{d0}^{'}X_{t2}}{\tau_{d0}^{"}\tau_{d0}^{'}\Delta_d^{"}}\right\}\Delta E_q^{"} + \\ & + \frac{2}{\pi X_L} \cdot \frac{X_{t2}V_{SVCq0}\left[\tau_{d0}^{'}\left(X_d^{'} - X_d^{"}\right) + \tau_{d0}^{"}\left(X_d - X_d^{'}\right)\right]}{\tau_{d0}^{"}\tau_{d0}^{'}\Delta_d^{"}}\Delta\alpha\end{aligned} \tag{D.88}$$

$$\Delta\dot{E}_d^{"} = -\frac{1}{\tau_{q0}^{"}}\left[\frac{\Delta_q}{\Delta_q^{"}}\right]\Delta E_d^{"} + \frac{1}{\tau_{q0}^{"}}\left[\frac{2}{\pi X_L} \cdot \frac{X_{t2}\left(X_q - X_q^{"}\right)V_{SVCd0}}{\Delta_q^{"}}\right]\Delta\alpha + \frac{1}{\tau_{q0}^{"}}\left[\frac{\left(X_q - X_q^{"}\right)V_{\infty q0}}{\Delta_q^{"}}\right]\Delta\delta \tag{D.89}$$

where

$$\Delta_q = X_{t2} + \left(X_q + X_{t1}\right)\left(1 - X_{t2}B_{SVC0}\right) \tag{D.90}$$

Equations (D.1), (D.2), (D.87)–(D.89) while considering the generator power and terminal voltage equations (D.72) and (D.73), respectively, and the SVC terminal voltage equation (D.74) construct the synchronous generator – SVC model. Procedures are carried out for both transfer function matrix and state-space representations in the next sections.

D.2. Transfer function matrix representation

The synchronous generator – SVC system connected to an infinite bus via a tie-line reactance has the following generic representation in frequency domain

$$\begin{bmatrix} \Delta\omega(s) \\ \Delta e_t(s) \\ \Delta V_{SVC}(s) \end{bmatrix} = \begin{bmatrix} g_{11}(s) & g_{12}(s) & g_{13}(s) \\ g_{21}(s) & g_{22}(s) & g_{23}(s) \\ g_{31}(s) & g_{32}(s) & g_{33}(s) \end{bmatrix} \begin{bmatrix} \Delta P_m(s) \\ \Delta E_{fd}(s) \\ \Delta\alpha(s) \end{bmatrix} \tag{D.91}$$

$$\mathbf{y}(s) = \mathbf{G}(s)\mathbf{u}(s) \tag{D.92}$$

where **G**(*s*) is the transfer function matrix of the linearised model of the synchronous generator – SVC system connected to an infinite bus via a tie-line reactance. In order to obtain **G**(*s*), some previous algebraic manipulations are required. In the frequency domain, equations (D.1), (D.2), (D.87)–(D.89) can be given as

$$\Delta\delta(s) = \frac{\omega_0}{s}\Delta\omega(s) \tag{D.93}$$

$$\Delta\omega(s) = \frac{1}{2Hs}\left[\Delta P_m(s) - \Delta P_e(s) - D\Delta\omega(s)\right] \tag{D.94}$$

$$\begin{aligned} \Delta E_q^{'}(s) = {} & \frac{1}{1+\tau_{d0}^{'}s}\Delta E_{fd}(s) - \frac{V_{\infty d0}\left(X_d - X_d^{'}\right)}{\Delta_d^{"}\left(1+\tau_{d0}^{'}s\right)}\Delta\delta(s) - \frac{\left(X_d - X_d^{'}\right)\left(1 - X_{t2}B_{SVC0}\right)}{\Delta_d^{"}\left(1+\tau_{d0}^{'}s\right)}\Delta E_q^{"}(s) + \\ & + \frac{2}{\pi X_L}\cdot\frac{X_{t2}\left(X_d - X_d^{'}\right)V_{SVCq0}}{\Delta_d^{"}\left(1+\tau_{d0}^{'}s\right)}\Delta\alpha(s) \end{aligned} \tag{D.95}$$

$$\begin{aligned} \Delta E_q^{"}(s) = {} & \frac{\Delta_d^{"}\left(1+\tau_{d0}^{"}s\right)\Delta E_{fd}(s) - V_{\infty d0}\left\{\left(X_d - X_d^{"}\right) + \left[\tau_{d0}^{'}\left(X_d^{'} - X_d^{"}\right) + \tau_{d0}^{"}\left(X_d - X_d^{'}\right)\right]s\right\}\Delta\delta(s)}{\tau_{d0}^{'}\tau_{d0}^{"}\Delta_d^{"}s^2 + \left[\tau_{d0}^{"}\Delta_d^{"} + \tau_{d0}^{'}\Delta_d^{'} + \tau_{d0}^{"}\left(X_d - X_d^{'}\right)\left(1 - X_{t2}B_{SVC0}\right)\right]s + \Delta_d} + \\ & + \frac{2}{\pi X_L}\cdot\frac{X_{t2}V_{SVCq0}\left\{\left(X_d - X_d^{"}\right) + \left[\tau_{d0}^{'}\left(X_d^{'} - X_d^{"}\right) + \tau_{d0}^{"}\left(X_d - X_d^{'}\right)\right]s\right\}}{\tau_{d0}^{'}\tau_{d0}^{"}\Delta_d^{"}s^2 + \left[\tau_{d0}^{"}\Delta_d^{"} + \tau_{d0}^{'}\Delta_d^{'} + \tau_{d0}^{"}\left(X_d - X_d^{'}\right)\left(1 - X_{t2}B_{SVC0}\right)\right]s + \Delta_d}\Delta\alpha(s) \end{aligned} \tag{D.96}$$

$$\Delta E_d^{"}(s) = \frac{2}{\pi X_L}\cdot\frac{X_{t2}\left(X_q - X_q^{"}\right)V_{SVCd0}}{\Delta_q\left[1+\tau_{q0}^{"}\left(\frac{\Delta_q^{"}}{\Delta_q}\right)s\right]}\Delta\alpha(s) + \frac{\left(X_q - X_q^{"}\right)V_{\infty q0}}{\Delta_q\left[1+\tau_{q0}^{"}\left(\frac{\Delta_q^{"}}{\Delta_q}\right)s\right]}\Delta\delta(s) \tag{D.97}$$

where

$$\Delta_d^{'} = X_{t2} + \left(X_d^{'} + X_{t1}\right)\left(1 - X_{t2}B_{SVC0}\right) \tag{D.98}$$

$$\Delta_d = X_{t2} + \left(X_d + X_{t1}\right)\left(1 - X_{t2}B_{SVC0}\right) \tag{D.99}$$

Equation (D.96) is obtained by using equation (D.95) in the resultant Laplace transformation of (D.88). For convenience, (D.96) and (D.97) are rewritten as

$$\Delta E_q^{"}(s) = K_3(s)\Delta E_{fd}(s) - K_4(s)\Delta\delta(s) + K_{SVC2}(s)\Delta\alpha(s) \tag{D.100}$$

$$\Delta E_d^{"}(s) = K_{4d}(s)\Delta\delta(s) + K_{SVC2d}(s)\Delta\alpha(s) \tag{D.101}$$

where

$$K_3(s) = \frac{\Delta_d^{"}\left(1+\tau_{d0}^{"}s\right)}{\tau_{d0}^{'}\tau_{d0}^{"}\Delta_d^{"}s^2 + \left[\tau_{d0}^{"}\Delta_d^{"} + \tau_{d0}^{'}\Delta_d^{'} + \tau_{d0}^{"}\left(X_d - X_d^{'}\right)\left(1 - X_{t2}B_{SVC0}\right)\right]s + \Delta_d} \tag{D.102}$$

$$K_4(s) = \frac{V_{\infty d0}\left\{\left(X_d - X_d^{"}\right) + \left[\tau_{d0}^{'}\left(X_d^{'} - X_d^{"}\right) + \tau_{d0}^{"}\left(X_d - X_d^{'}\right)\right]s\right\}}{\tau_{d0}^{'}\tau_{d0}^{"}\Delta_d^{"}s^2 + \left[\tau_{d0}^{"}\Delta_d^{"} + \tau_{d0}^{'}\Delta_d^{'} + \tau_{d0}^{"}\left(X_d - X_d^{'}\right)\left(1 - X_{t2}B_{SVC0}\right)\right]s + \Delta_d} \tag{D.103}$$

$$K_{SVC2}(s) = \frac{2}{\pi X_L}\cdot\frac{X_{t2}V_{SVCq0}\left\{\left(X_d - X_d^{"}\right) + \left[\tau_{d0}^{'}\left(X_d^{'} - X_d^{"}\right) + \tau_{d0}^{"}\left(X_d - X_d^{'}\right)\right]s\right\}}{\tau_{d0}^{'}\tau_{d0}^{"}\Delta_d^{"}s^2 + \left[\tau_{d0}^{"}\Delta_d^{"} + \tau_{d0}^{'}\Delta_d^{'} + \tau_{d0}^{"}\left(X_d - X_d^{'}\right)\left(1 - X_{t2}B_{SVC0}\right)\right]s + \Delta_d} \tag{D.104}$$

$$K_{4d}(s) = \frac{C_{4d}}{1+\tau_q^{"}s} \tag{D.105}$$

$$K_{SVC2d}(s) = \frac{C_{SVC2d}}{1+\tau_q^{"}s} \tag{D.106}$$

$$C_{4d} = V_{\infty q0}\left(\frac{X_q - X_q^{"}}{\Delta_q}\right) \tag{D.107}$$

$$C_{SVC2d} = \frac{2}{\pi X_L}\cdot\left[\frac{X_{t2}\left(X_q - X_q^{"}\right)V_{SVCd0}}{\Delta_q}\right] \tag{D.108}$$

$$\tau_q^{"} = \tau_{q0}^{"}\left(\frac{\Delta_q^{"}}{\Delta_q}\right) \tag{D.109}$$

In the frequency domain, the generator power and terminal voltages expressions (D.72) and (D.73), respectively, and the SVC terminal voltage expression (D.74) are given as

$$\Delta P_e(s) = K_1\Delta\delta(s) + K_2\Delta E_q^{"}(s) - K_{2d}\Delta E_d^{"}(s) + K_{SVC1}\Delta\alpha(s) \tag{D.110}$$

$$\Delta e_t(s) = K_5\Delta\delta(s) + K_6\Delta E_q^{"}(s) + K_{6d}\Delta E_d^{"}(s) + K_{SVC3}\Delta\alpha(s) \tag{D.111}$$

$$\Delta V_{SVC}(s) = K_{5n}\Delta\delta(s) + K_{6n}\Delta E_q^{"}(s) + K_{6dn}\Delta E_d^{"}(s) + K_{SVC3n}\Delta\alpha(s) \tag{D.112}$$

with coefficients defined by (D.75)–(D.86).

The transfer function matrix representation given by (D.91) is obtained by substituting (D.93) into equations (D.100), (D.101), (D.110)–(D.112) to obtain expressions in terms of $\Delta\omega(s)$:

$$\Delta P_e(s) = K_1\frac{\omega_0}{s}\Delta\omega(s) + K_2\Delta E_q^{"}(s) - K_{2d}\Delta E_d^{"}(s) + K_{SVC1}\Delta\alpha(s) \tag{D.113}$$

$$\Delta e_t(s) = K_5\frac{\omega_0}{s}\Delta\omega(s) + K_6\Delta E_q^{"}(s) + K_{6d}\Delta E_d^{"}(s) + K_{SVC3}\Delta\alpha(s) \tag{D.114}$$

$$\Delta V_{SVC}(s) = K_{5n}\frac{\omega_0}{s}\Delta\omega(s) + K_{6n}\Delta E_q^{"}(s) + K_{6dn}\Delta E_d^{"}(s) + K_{SVC3n}\Delta\alpha(s) \tag{D.115}$$

$$\Delta E_q^{"}(s) = K_3(s)\Delta E_{fd}(s) - K_4(s)\frac{\omega_0}{s}\Delta\omega(s) + K_{SVC2}(s)\Delta\alpha(s) \tag{D.116}$$

$$\Delta E_d^{"}(s) = K_{4d}(s)\frac{\omega_0}{s}\Delta\omega(s) + K_{SVC2d}(s)\Delta\alpha(s) \tag{D.117}$$

To simplify the procedure, transfer functions (D.102)–(D.104) are rewritten as

$$K_3(s) = \frac{\Delta_d^{"}\left(1+\tau_{d0}^{"}s\right)}{Es^2+Fs+\Delta_d} \tag{D.118}$$

$$K_4(s) = \frac{V_{\infty d0}(B+Cs)}{Es^2+Fs+\Delta_d} \tag{D.119}$$

$$K_{SVC2}(s) = \frac{I(B+Cs)}{Es^2+Fs+\Delta_d} \tag{D.120}$$

where

$$B = \left(X_d - X_d^{"}\right) \tag{D.121}$$

$$C = \tau_{d0}^{'}\left(X_d^{'} - X_d^{"}\right) + \tau_{d0}^{"}\left(X_d - X_d^{'}\right) \tag{D.122}$$

$$E = \tau_{d0}^{'}\tau_{d0}^{"}\Delta_d^{"} \tag{D.123}$$

$$F = \tau_{d0}^{"}\Delta_d^{"} + \tau_{d0}^{'}\Delta_d^{'} + \tau_{d0}^{"}\left(X_d - X_d^{'}\right)\left(1 - X_{t2}B_{SVC0}\right) \tag{D.124}$$

$$I = \frac{2}{\pi X_L}\cdot X_{t2}V_{SVCq0} \tag{D.125}$$

Substituting (D.118)–(D.120) into (D.116) and (D.105)–(D.106) into (D.117) renders

$$\Delta E_q^{"}(s) = \frac{\Delta_d^{"}\left(1+\tau_{d0}^{"}s\right)}{Es^2+Fs+\Delta_d}\Delta E_{fd}(s) - \frac{V_{\infty d0}(B+Cs)}{Es^2+Fs+\Delta_d}\frac{\omega_0}{s}\Delta\omega(s) + \frac{I(B+Cs)}{Es^2+Fs+\Delta_d}\Delta\alpha(s) \tag{D.126}$$

$$\Delta E_d^{"}(s) = \frac{C_{4d}}{1+\tau_q^{"}s}\cdot\frac{\omega_0}{s}\Delta\omega(s) + \frac{C_{SVC2d}}{1+\tau_q^{"}s}\Delta\alpha(s) \tag{D.127}$$

Using (D.126) and (D.127) in (D.113)–(D.115) gives the following intermediate result after some algebraic manipulations:

$$\begin{aligned}\Delta P_e(s) = &\left[K_1 - \frac{K_2V_{\infty d0}(B+Cs)}{Es^2+Fs+\Delta_d} - \frac{K_{2d}C_{4d}}{1+\tau_q^{"}s}\right]\frac{\omega_0}{s}\Delta\omega(s) + \frac{K_2\Delta_d^{"}\left(1+\tau_{d0}^{"}s\right)}{Es^2+Fs+\Delta_d}\Delta E_{fd}(s) + \\ &+\left[\frac{K_2I(B+Cs)}{Es^2+Fs+\Delta_d} - \frac{K_{2d}C_{SVC2d}}{1+\tau_q^{"}s} + K_{SVC1}\right]\Delta\alpha(s)\end{aligned} \tag{D.128}$$

$$\Delta e_t(s)=\left[K_5-\frac{K_6V_{\infty d0}(B+Cs)}{Es^2+Fs+\Delta_d}+\frac{K_{6d}C_{4d}}{1+\tau_q^{"}s}\right]\frac{\omega_0}{s}\Delta\omega(s)+\frac{K_6\Delta_d^{"}\left(1+\tau_{d0}^{"}s\right)}{Es^2+Fs+\Delta_d}\Delta E_{fd}(s)+$$
$$+\left[\frac{K_6I(B+Cs)}{Es^2+Fs+\Delta_d}+\frac{K_{6d}C_{SVC2d}}{1+\tau_q^{"}s}+K_{SVC3}\right]\Delta\alpha(s) \tag{D.129}$$

$$\Delta V_{SVC}(s)=\left[K_{5n}-\frac{K_{6n}V_{\infty d0}(B+Cs)}{Es^2+Fs+\Delta_d}+\frac{K_{6dn}C_{4d}}{1+\tau_q^{"}s}\right]\frac{\omega_0}{s}\Delta\omega(s)+\frac{K_{6n}\Delta_d^{"}\left(1+\tau_{d0}^{"}s\right)}{Es^2+Fs+\Delta_d}\Delta E_{fd}(s)+$$
$$+\left[\frac{K_{6n}I(B+Cs)}{Es^2+Fs+\Delta_d}+\frac{K_{6dn}C_{SVC2d}}{1+\tau_q^{"}s}+K_{SVC3n}\right]\Delta\alpha(s) \tag{D.130}$$

Substituting (D.128) in (D.94), gives, after some algebraic manipulations

$$2Hs\Delta\omega(s)+D\Delta\omega(s)=\Delta P_m(s)-\Delta P_e(s)$$
$$\Downarrow$$
$$\left\{(2Hs+D)+\left[K_1-\frac{K_2V_{\infty d0}(B+Cs)}{Es^2+Fs+\Delta_d}-\frac{K_{2d}C_{4d}}{1+\tau_q^{"}s}\right]\frac{\omega_0}{s}\right\}\Delta\omega(s)=\Delta P_m(s)-\frac{K_2\Delta_d^{"}\left(1+\tau_{d0}^{"}s\right)}{Es^2+Fs+\Delta_d}\Delta E_{fd}(s)$$
$$-\left[\frac{K_2I(B+Cs)}{Es^2+Fs+\Delta_d}-\frac{K_{2d}C_{SVC2d}}{1+\tau_q^{"}s}+K_{SVC1}\right]\Delta\alpha(s)$$
$$\Downarrow$$
$$\Delta\omega(s)=g_{11}(s)\Delta P_m(s)+g_{12}(s)\Delta E_{fd}(s)+g_{13}(s)\Delta\alpha(s) \tag{D.131}$$

where

$$den(s)=(2Hs+D)\left(Es^2+Fs+\Delta_d\right)\left(1+\tau_q^{"}s\right)s+K_1\omega_0\left(Es^2+Fs+\Delta_d\right)\left(1+\tau_q^{"}s\right)+$$
$$-K_2V_{\infty d0}\omega_0(B+Cs)\left(1+\tau_q^{"}s\right)-K_{2d}C_{4d}\omega_0\left(Es^2+Fs+\Delta_d\right) \tag{D.132}$$

$$g_{11}(s)=\frac{\left(Es^2+Fs+\Delta_d\right)\left(1+\tau_q^{"}s\right)s}{den(s)} \tag{D.133}$$

$$g_{12}(s)=-\frac{K_2\Delta_d^{"}\left(1+\tau_{d0}^{"}s\right)\left(1+\tau_q^{"}s\right)s}{den(s)} \tag{D.134}$$

$$g_{13}(s)=-\frac{\left[K_2I(B+Cs)\left(1+\tau_q^{"}s\right)-K_{2d}C_{SVC2d}\left(Es^2+Fs+\Delta_d\right)+K_{SVC1}\left(Es^2+Fs+\Delta_d\right)\left(1+\tau_q^{"}s\right)\right]s}{den(s)} \tag{D.135}$$

In (D.131), speed is given in terms of the mechanical power, field voltage and SVC firing angle, as required by (D.91). The equation for the synchronous generator terminal voltage is found by substituting (D.131) into (D.129). After a cumbersome algebraic manipulation, it can be expressed as

$$\Delta e_t(s)=g_{21}(s)\Delta P_m(s)+g_{22}(s)\Delta E_{fd}(s)+g_{23}(s)\Delta\alpha(s) \tag{D.136}$$

where

$$g_{21}(s)=\frac{\omega_0\left[K_5\left(Es^2+Fs+\Delta_d\right)\left(1+\tau_q^{"}s\right)-K_6V_{\infty d0}(B+Cs)\left(1+\tau_q^{"}s\right)+K_{6d}C_{4d}\left(Es^2+Fs+\Delta_d\right)\right]}{den(s)} \tag{D.137}$$

$$g_{22}(s)=\frac{\Delta_d^{"}\left(1+\tau_{d0}^{"}s\right)\left\{K_6\left(1+\tau_q^{"}s\right)(2Hs+D)s+\left(K_6\left[\left(1+\tau_q^{"}s\right)K_1-K_{2d}C_{4d}\right]-K_2\left[\left(1+\tau_q^{"}s\right)K_5+K_{6d}C_{4d}\right]\right)\omega_0\right\}}{den(s)} \tag{D.138}$$

$$\begin{aligned}g_{23}(s)=&\frac{(2Hs+D)\left\{K_6I(B+Cs)\left(1+\tau_q^{"}s\right)+\left(Es^2+Fs+\Delta_d\right)\left[\left(1+\tau_q^{"}s\right)K_{SVC3}+K_{6d}C_{SVC2d}\right]\right\}s}{den(s)}+\\&+\frac{\omega_0\left\{\left(Es^2+Fs+\Delta_d\right)\left[K_{6d}\left(K_1C_{SVC2d}-C_{4d}K_{SVC1}\right)+K_{2d}\left(K_5C_{SVC2d}-C_{4d}K_{SVC3}\right)+\left(1+\tau_q^{"}s\right)\left(K_1K_{SVC3}-K_5K_{SVC1}\right)\right]\right\}}{den(s)}+\\&+\frac{\omega_0\left\{(B+Cs)\left[\left(1+\tau_q^{"}s\right)\left[I\left(K_1K_6-K_2K_5\right)+V_{\infty d0}\left(K_6K_{SVC1}-K_2K_{SVC3}\right)\right]-\left(IC_{4d}+C_{SVC2d}V_{\infty d0}\right)\left(K_2K_{6d}+K_{2d}K_6\right)\right]\right\}}{den(s)}\end{aligned} \tag{D.139}$$

In (D.136), the terminal voltage expression is given in terms of the mechanical power, field voltage and SVC firing angle, as required by (D.91). The equation for the SVC terminal voltage is found by substituting (D.131) into (D.130). After a cumbersome algebraic manipulation, it can be expressed as

$$\Delta V_{SVC}(s)=g_{31}(s)\Delta P_m(s)+g_{32}(s)\Delta E_{fd}(s)+g_{33}(s)\Delta\alpha(s) \tag{D.140}$$

where

$$g_{31}(s)=\frac{\omega_0\left[K_{5n}\left(Es^2+Fs+\Delta_d\right)\left(1+\tau_q^{"}s\right)-K_{6n}V_{\infty d0}(B+Cs)\left(1+\tau_q^{"}s\right)+K_{6dn}C_{4d}\left(Es^2+Fs+\Delta_d\right)\right]}{den(s)} \tag{D.141}$$

$$g_{32}(s)=\frac{\Delta_d^{"}\left(1+\tau_{d0}^{"}s\right)\left\{K_{6n}\left(1+\tau_q^{"}s\right)(2Hs+D)s+\left(K_{6n}\left[\left(1+\tau_q^{"}s\right)K_1-K_{2d}C_{4d}\right]-K_2\left[\left(1+\tau_q^{"}s\right)K_{5n}+K_{6dn}C_{4d}\right]\right)\omega_0\right\}}{den(s)} \tag{D.142}$$

$$\begin{aligned}g_{33}(s)=&\frac{(2Hs+D)\left\{K_{6n}I(B+Cs)\left(1+\tau_q^{"}s\right)+\left(Es^2+Fs+\Delta_d\right)\left[\left(1+\tau_q^{"}s\right)K_{SVC3n}+K_{6dn}C_{SVC2d}\right]\right\}s}{den(s)}+\\&+\frac{\omega_0\left\{\left(Es^2+Fs+\Delta_d\right)\left[K_{6dn}\left(K_1C_{SVC2d}-C_{4d}K_{SVC1}\right)+K_{2d}\left(K_{5n}C_{SVC2d}-C_{4d}K_{SVC3n}\right)+\left(1+\tau_q^{"}s\right)\left(K_1K_{SVC3n}-K_{5n}K_{SVC1}\right)\right]\right\}}{den(s)}+\\&+\frac{\omega_0\left\{(B+Cs)\left[\left(1+\tau_q^{"}s\right)\left[I\left(K_1K_{6n}-K_2K_{5n}\right)+V_{\infty d0}\left(K_{6n}K_{SVC1}-K_2K_{SVC3n}\right)\right]-\left(IC_{4d}+C_{SVC2d}V_{\infty d0}\right)\left(K_2K_{6dn}+K_{2d}K_{6n}\right)\right]\right\}}{den(s)}\end{aligned} \tag{D.143}$$

In (D.140), the SVC terminal voltage is given in terms of the mechanical power, field voltage and SVC firing angle, as required by (D.91). Notice that equations (D.131), (D.136) and (D.140) have the form of (D.91), where the transfer function matrix individual transfer functions are given by (D.133)–(D.135), (D.137)–(D.139) and (D.141)–(D.143).

D.3. State-space representation

Consider the synchronous generator – SVC system model, given by differential equations (D.1), (D.2), (D.87)–(D.89) while considering the generator power and terminal voltage equations (D.72) and (D.73), respectively, and the SVC terminal voltage equation (D.74):

$$\Delta\dot{\delta} = \omega_0 \Delta\omega \tag{D.1}$$

$$\Delta\dot{\omega} = \frac{1}{2H}\left[\Delta P_m - \Delta P_e - D\Delta\omega\right] \tag{D.2}$$

$$\begin{aligned}\Delta\dot{E}_q^{'} = {} & \frac{1}{\tau_{d0}^{'}}\Delta E_{fd} - \frac{1}{\tau_{d0}^{'}}\Delta E_q^{'} - \frac{1}{\tau_{d0}^{'}}\left[\frac{\left(X_d - X_d^{'}\right)\left(1 - X_{t2}B_{SVC0}\right)}{\Delta_d^{''}}\right]\Delta E_q^{''} - \frac{1}{\tau_{d0}^{'}}\left[\frac{\left(X_d - X_d^{'}\right)V_{\infty d0}}{\Delta_d^{''}}\right]\Delta\delta + \\ & + \frac{1}{\tau_{d0}^{'}}\left[\frac{2}{\pi X_L}\cdot\frac{X_{t2}\left(X_d - X_d^{'}\right)V_{SVCq0}}{\Delta_d^{''}}\right]\Delta\alpha\end{aligned} \tag{D.87}$$

$$\begin{aligned}\Delta\dot{E}_q^{''} = {} & \frac{1}{\tau_{d0}^{'}}\Delta E_{fd} + \left[\frac{1}{\tau_{d0}^{''}} - \frac{1}{\tau_{d0}^{'}}\right]\Delta E_q^{'} - \frac{V_{\infty d0}\left[\tau_{d0}^{'}\left(X_d^{'} - X_d^{''}\right) + \tau_{d0}^{''}\left(X_d - X_d^{'}\right)\right]}{\tau_{d0}^{''}\tau_{d0}^{'}\Delta_d^{''}}\Delta\delta + \\ & - \left\{\frac{\left(1 - X_{t2}B_{SVC0}\right)\left[\tau_{d0}^{'}\left(X_d^{'} + X_{t1}\right) + \tau_{d0}^{''}\left(X_d - X_d^{'}\right)\right] + \tau_{d0}^{'}X_{t2}}{\tau_{d0}^{''}\tau_{d0}^{'}\Delta_d^{''}}\right\}\Delta E_q^{''} + \\ & + \frac{2}{\pi X_L}\cdot\frac{X_{t2}V_{SVCq0}\left[\tau_{d0}^{'}\left(X_d^{'} - X_d^{''}\right) + \tau_{d0}^{''}\left(X_d - X_d^{'}\right)\right]}{\tau_{d0}^{''}\tau_{d0}^{'}\Delta_d^{''}}\Delta\alpha\end{aligned} \tag{D.88}$$

$$\Delta\dot{E}_d^{''} = -\frac{1}{\tau_{q0}^{''}}\left[\frac{\Delta_q}{\Delta_q^{''}}\right]\Delta E_d^{''} + \frac{1}{\tau_{q0}^{''}}\left[\frac{2}{\pi X_L}\cdot\frac{X_{t2}\left(X_q - X_q^{''}\right)V_{SVCd0}}{\Delta_q^{''}}\right]\Delta\alpha + \frac{1}{\tau_{q0}^{''}}\left[\frac{\left(X_q - X_q^{''}\right)V_{\infty q0}}{\Delta_q^{''}}\right]\Delta\delta \tag{D.89}$$

$$\Delta P_e = K_1\Delta\delta + K_2\Delta E_q^{''} - K_{2d}\Delta E_d^{''} + K_{SVC1}\Delta\alpha \tag{D.72}$$

$$\Delta e_t = K_5\Delta\delta + K_6\Delta E_q^{''} + K_{6d}\Delta E_d^{''} + K_{SVC3}\Delta\alpha \tag{D.73}$$

$$\Delta V_{SVC} = K_{5n}\Delta\delta + K_{6n}\Delta E_q^{''} + K_{6dn}\Delta E_d^{''} + K_{SVC3n}\Delta\alpha \tag{D.74}$$

where the coefficients in (D.72)–(D.74) are given by (D.75)–(D.86). Substitution of (D.72) in (D.2) yields

$$\Delta\dot{\omega} = -\frac{K_1}{2H}\Delta\delta - \frac{D}{2H}\Delta\omega - \frac{K_2}{2H}\Delta E_q^{''} + \frac{K_{2d}}{2H}\Delta E_d^{''} - \frac{K_{SVC1}}{2H}\Delta\alpha + \frac{1}{2H}\Delta P_m \tag{D.144}$$

Considering differential equations (D.1), (D.87)–(D.89) and (D.144), and the generator and SVC terminal voltage equations (D.73) and (D.74), respectively, the state-space representation

$$\begin{aligned}\Delta\dot{\mathbf{x}} &= \mathbf{A}\Delta\mathbf{x} + \mathbf{B}\Delta\mathbf{u} \\ \Delta\mathbf{y} &= \mathbf{C}\Delta\mathbf{x} + \mathbf{D}\Delta\mathbf{u}\end{aligned} \tag{D.145}$$

can be constructed, where the output, input, and state vectors are given, respectively, as

$$\Delta\mathbf{y} = \begin{bmatrix}\Delta\omega & \Delta e_t & \Delta V_{SVC}\end{bmatrix}^T \tag{D.146}$$

$$\Delta\mathbf{u} = \begin{bmatrix} \Delta P_m & \Delta E_{fd} & \Delta\alpha \end{bmatrix}^T \tag{D.147}$$

$$\Delta\mathbf{x} = \begin{bmatrix} \Delta\omega & \Delta E_q^{'} & \Delta E_q^{''} & \Delta E_d^{''} & \Delta\delta \end{bmatrix}^T \tag{D.148}$$

System, control, output and feed-forward matrices **A**, **B, C** and **D,** respectively, are given as

$$\mathbf{A} = \begin{bmatrix} -\frac{D}{2H} & 0 & -\frac{K_2}{2H} & \frac{K_{2d}}{2H} & -\frac{K_1}{2H} \\ 0 & -\frac{1}{\tau_{d0}^{'}} & a_{23} & 0 & a_{25} \\ 0 & \frac{1}{\tau_{d0}^{''}} - \frac{1}{\tau_{d0}^{'}} & a_{33} & 0 & a_{35} \\ 0 & 0 & 0 & a_{44} & a_{45} \\ \omega_0 & 0 & 0 & 0 & 0 \end{bmatrix} \tag{D.149}$$

$$\mathbf{B} = \begin{bmatrix} \frac{1}{2H} & 0 & -\frac{K_{SVC1}}{2H} \\ 0 & \frac{1}{\tau_{d0}^{'}} & b_{23} \\ 0 & \frac{1}{\tau_{d0}^{'}} & b_{33} \\ 0 & 0 & b_{43} \\ 0 & 0 & 0 \end{bmatrix} \tag{D.150}$$

$$\mathbf{C} = \begin{bmatrix} 1 & 0 & 0 & 0 & 0 \\ 0 & 0 & K_6 & K_{6d} & K_5 \\ 0 & 0 & K_{6n} & K_{6dn} & K_{5n} \end{bmatrix} \tag{D.151}$$

$$\mathbf{D} = \begin{bmatrix} 0 & 0 & 0 \\ 0 & 0 & K_{SVC3} \\ 0 & 0 & K_{SVC3n} \end{bmatrix} \tag{D.152}$$

where the coefficients in (D.149)–(D.152) are given by (D.75)–(D.86) and

$$a_{23} = -\frac{\left(X_d - X_d^{'}\right)\left(1 - X_{t2}B_{SVC0}\right)}{\tau_{d0}^{'}\Delta_d^{''}} \tag{D.153}$$

$$a_{25} = -\frac{V_{\infty d0}\left(X_d - X_d^{'}\right)}{\tau_{d0}^{'}\Delta_d^{''}} \tag{D.154}$$

$$a_{33} = -\frac{\left(1 - X_{t2}B_{SVC0}\right)\left[\tau_{d0}^{'}\left(X_d^{'} + X_{t1}\right) + \tau_{d0}^{''}\left(X_d - X_d^{'}\right)\right] + \tau_{d0}^{'}X_{t2}}{\tau_{d0}^{''}\tau_{d0}^{'}\Delta_d^{''}} \tag{D.155}$$

$$a_{35} = -\frac{V_{\infty d0}\left[\tau_{d0}^{'}\left(X_d^{'} - X_d^{''}\right) + \tau_{d0}^{''}\left(X_d - X_d^{'}\right)\right]}{\tau_{d0}^{''}\tau_{d0}^{'}\Delta_d^{''}} \tag{D.156}$$

$$a_{44} = -\frac{\Delta_q}{\tau_{q0}^{''}\Delta_q^{''}} \tag{D.157}$$

$$a_{45} = \frac{V_{\infty q0}\left(X_q - X_q^{"}\right)}{\tau_{q0}^{"}\Delta_q^{"}} \tag{D.158}$$

$$b_{23} = \frac{2}{\pi X_L} \cdot \frac{X_{t2}\left(X_d - X_d^{'}\right)V_{SVCq0}}{\tau_{d0}^{'}\Delta_d^{"}} \tag{D.159}$$

$$b_{33} = \frac{2}{\pi X_L} \cdot \frac{X_{t2}V_{SVCq0}\left[\tau_{d0}^{'}\left(X_d^{'} - X_d^{"}\right) + \tau_{d0}^{"}\left(X_d - X_d^{'}\right)\right]}{\tau_{d0}^{"}\tau_{d0}^{'}\Delta_d^{"}} \tag{D.160}$$

$$b_{43} = \frac{2}{\pi X_L} \cdot \frac{X_{t2}\left(X_q - X_q^{"}\right)V_{SVCd0}}{\tau_{q0}^{"}\Delta_d^{"}} \tag{D.161}$$

Appendix E

DERIVATION OF THE SMALL-SIGNAL TRANSFER FUNCTION MATRIX AND STATE-SPACE MODELS OF THE SYNCHRONOUS GENERATOR – TCSC SYSTEM

E.1. General considerations

The small-signal model of the synchronous generator – TCSC system used in this thesis can be derived from the algebraic and differential equations (2.2)–(2.18), which describe the synchronous generator, and from those equations associated to the system phasor diagram and the TCSC itself. As in the case of the SVC system, only synchronous generator Model 1 (5^{th} order, two-axis) is considered. For small variations, the synchronous generator differential equations are given as

$$\Delta\dot{\delta} = \omega_0 \Delta\omega \tag{E.1}$$

$$\Delta\dot{\omega} = \frac{1}{2H}\left[\Delta P_m - \Delta P_e - D\Delta\omega\right] \tag{E.2}$$

$$\Delta\dot{E}_q^{'} = \frac{1}{\tau_{d0}^{'}}\left[\Delta E_{fd} - \left(X_d - X_d^{'}\right)\Delta i_{td} - \Delta E_q^{'}\right] \tag{E.3}$$

$$\begin{aligned}\Delta\dot{E}_q^{''} &= \frac{1}{\tau_{d0}^{''}}\left[\Delta E_q^{'} - \left(X_d^{'} - X_d^{''}\right)\Delta i_{td} - \Delta E_q^{''}\right] + \Delta\dot{E}_q^{'} \\ &= \frac{1}{\tau_{d0}^{''}}\left\{\frac{\tau_{d0}^{''}}{\tau_{d0}^{'}}\Delta E_{fd} - \left[\left(X_d^{'} - X_d^{''}\right) + \frac{\tau_{d0}^{''}}{\tau_{d0}^{'}}\left(X_d - X_d^{'}\right)\right]\Delta i_{td} + \left[1 - \frac{\tau_{d0}^{''}}{\tau_{d0}^{'}}\right]\Delta E_q^{'} - \Delta E_q^{''}\right\}\end{aligned} \tag{E.4}$$

$$\Delta\dot{E}_d^{''} = \frac{1}{\tau_{q0}^{''}}\left[\left(X_q - X_q^{''}\right)\Delta i_{tq} - \Delta E_d^{''}\right] \tag{E.5}$$

Notice that equations (E.3)–(E.5) are given in terms of the terminal current of the machine. Therefore, it is necessary to obtain suitable expressions for the terminal current components in terms of the TCSC and infinite bus parameters. To this end, consider the phasor diagram of the synchronous generator – TCSC system provided in Figure E.1.

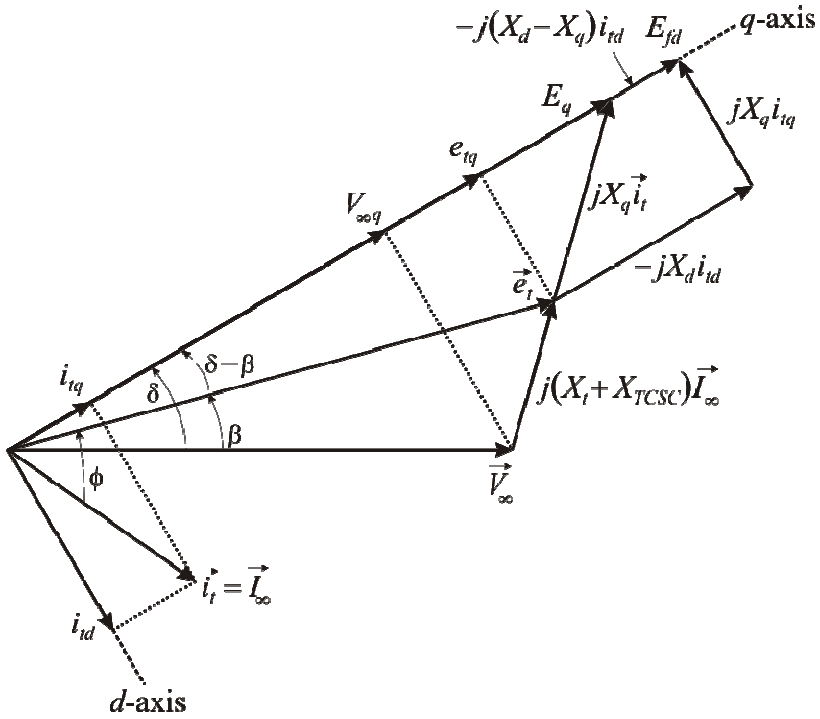

Figure E.1. Phasor diagram of a synchronous generator – TCSC system

With the rotor position taken as the reference, it can be seen that the components of the infinite bus voltage are given by

$$V_{\infty q} = V_\infty \cos\delta \tag{E.6}$$

$$V_{\infty d} = V_\infty \sin\delta \tag{E.7}$$

For small variations, an incremental change of the infinite bus voltage can be stated as

$$\Delta V_{\infty q} = -V_{\infty 0} \sin\delta_0 \Delta\delta = -V_{\infty d0}\Delta\delta \tag{E.8}$$

$$\Delta V_{\infty d} = V_{\infty 0} \cos\delta_0 \Delta\delta = V_{\infty q0}\Delta\delta \tag{E.9}$$

From Figure E.1, the terminal current can be expressed as

$$\vec{i}_t = \frac{\vec{e}_t - \vec{V}_\infty}{j\left(X_t + X_{TCSC}\right)} \tag{E.10}$$

Separating (E.10) into real and imaginary parts,

$$i_{tq}\left(X_t + X_{TCSC}\right) = V_{\infty d} - e_{td} \tag{E.11}$$

$$i_{td}\left(X_t + X_{TCSC}\right) = e_{tq} - V_{\infty q} \tag{E.12}$$

Rearranging (E.11) and (E.12) by making use of the sub-transient equations (2.8) and (2.9) while neglecting the stator resistance gives

$$i_{tq} = \frac{V_{\infty d} - E_d^{"}}{X_q^{"} + X_t + X_{TCSC}} \tag{E.13}$$

$$i_{td} = \frac{E_q^{"} - V_{\infty q}}{X_d^{"} + X_t + X_{TCSC}} \tag{E.14}$$

For small variations, (E.13) and (E.14) can be written as

$$\left(X_q^{"} + X_t + X_{TCSC}\right)\Delta i_{tq} + i_{tq0}\Delta X_{TCSC} = -\Delta E_d^{"} + \Delta V_{\infty d} \tag{E.15}$$

$$\left(X_d^{"} + X_t + X_{TCSC}\right)\Delta i_{td} + i_{td0}\Delta X_{TCSC} = \Delta E_q^{"} - \Delta V_{\infty q} \tag{E.16}$$

Substituting (E.8) into (E.16) and (E.9) into (E.15) gives, after some rearrangement,

$$\Delta i_{tq} = -\left[\frac{1}{\Lambda_q^{"}}\right]\Delta E_d^{"} + \left[\frac{V_{\infty q0}}{\Lambda_q^{"}}\right]\Delta\delta - \left[\frac{i_{tq0}}{\Lambda_q^{"}}\right]\Delta X_{TCSC} \tag{E.17}$$

$$\Delta i_{td} = \left[\frac{1}{\Lambda_d^{"}}\right]\Delta E_q^{"} + \left[\frac{V_{\infty d0}}{\Lambda_d^{"}}\right]\Delta\delta - \left[\frac{i_{td0}}{\Lambda_d^{"}}\right]\Delta X_{TCSC} \tag{E.18}$$

where

$$\Lambda_q^{"} = X_q^{"} + X_t + X_{TCSC} \tag{E.19}$$

$$\Lambda_d^{"} = X_d^{"} + X_t + X_{TCSC} \tag{E.20}$$

Recalling from Chapter 2, the total reactance (X_{TCSC}) of the TCSC can be expressed as a function of the thyristor's firing angle

$$X_{TCSC} = -X_C + C_1\left\{2(\pi-\alpha) + \sin\left[2(\pi-\alpha)\right]\right\} - C_2\cos^2(\pi-\alpha)\left\{\lambda\tan\left[\lambda(\pi-\alpha)\right] - \tan(\pi-\alpha)\right\} \tag{2.52}$$

where

$$C_1 = \frac{X_C + X_{LC}}{\pi} \tag{2.53}$$

$$C_2 = \frac{4X_{LC}^2}{\pi X_L} \tag{2.54}$$

$$\lambda = \frac{\omega_0}{\omega} = \sqrt{\frac{X_C}{X_L}} \tag{2.55}$$

$$X_{LC} = \frac{X_C X_L}{X_C - X_L} \tag{2.56}$$

$$\omega_0^2 = \frac{1}{LC} = \omega^2\frac{X_C}{X_L} \tag{2.57}$$

For small perturbations, variations in the TCSC total reactance (2.52) are given by

$$\Delta X_{TCSC} = \left[-2C_1(1+\cos 2\alpha) + C_2\left\{\frac{\lambda^2\cos^2(\pi-\alpha)}{\cos^2\left[\lambda(\pi-\alpha)\right]} - 1\right\} + C_2\sin 2\alpha\left\{\lambda\tan\left[\lambda(\pi-\alpha)\right] - \tan(\pi-\alpha)\right\}\right]\Delta\alpha \tag{E.21}$$

For convenience, (E.21) is rewritten as

$$\Delta X_{TCSC} = F(\alpha)\Delta\alpha \tag{E.22}$$

where

$$F(\alpha) = -2C_1(1+\cos 2\alpha) + C_2\left\{\frac{\lambda^2\cos^2(\pi-\alpha)}{\cos^2\left[\lambda(\pi-\alpha)\right]} - 1\right\} + C_2\sin 2\alpha\left\{\lambda\tan\left[\lambda(\pi-\alpha)\right] - \tan(\pi-\alpha)\right\} \quad \text{(E.23)}$$

Substituting (E.22) into (E.17) and (E.18) gives

$$\Delta i_{tq} = -\left[\frac{1}{\Lambda_q^{"}}\right]\Delta E_d^{"} + \left[\frac{V_{\infty q0}}{\Lambda_q^{"}}\right]\Delta\delta - F(\alpha)\cdot\left[\frac{i_{tq0}}{\Lambda_q^{"}}\right]\Delta\alpha \quad \text{(E.24)}$$

$$\Delta i_{td} = \left[\frac{1}{\Lambda_d^{"}}\right]\Delta E_q^{"} + \left[\frac{V_{\infty d0}}{\Lambda_d^{"}}\right]\Delta\delta - F(\alpha)\cdot\left[\frac{i_{td0}}{\Lambda_d^{"}}\right]\Delta\alpha \quad \text{(E.25)}$$

which are the necessary expressions for the generator currents.

The synchronous generator active power equation (2.14) can be written as

$$P_e = V_{\infty d}I_{\infty d} + V_{\infty q}I_{\infty q} \quad \text{(E.26)}$$

or

$$P_e = V_{\infty d}i_{td} + V_{\infty q}i_{tq} \quad \text{(E.27)}$$

which for small variations becomes

$$\Delta P_e = V_{\infty d0}\Delta i_{td} + i_{td0}\Delta V_{\infty d} + V_{\infty q0}\Delta i_{tq} + i_{tq0}\Delta V_{\infty q} \quad \text{(E.28)}$$

Substitution of (E.8), (E.9), (E.24) and (E.25) into (E.28) yields

$$\Delta P_e = \left[\frac{V_{\infty d0}^2}{\Lambda_d^{"}} + \frac{V_{\infty q0}^2}{\Lambda_q^{"}} + i_{td0}V_{\infty q0} - i_{tq0}V_{\infty d0}\right]\Delta\delta + \left[\frac{V_{\infty d0}}{\Lambda_d^{"}}\right]\Delta E_q^{"} - \left[\frac{V_{\infty q0}}{\Lambda_q^{"}}\right]\Delta E_d^{"} - F(\alpha)\cdot\left[\frac{i_{td0}V_{\infty d0}}{\Lambda_d^{"}} + \frac{i_{tq0}V_{\infty q0}}{\Lambda_q^{"}}\right]\Delta\alpha \quad \text{(E.29)}$$

The generator terminal voltage equation (2.3) can be expressed in terms of *d*- and *q*-axis components as

$$e_t^2 = e_{td}^2 + e_{tq}^2 \quad \text{(E.30)}$$

which, for small variations, becomes

$$\Delta e_t = (e_{t0})^{-1}\left[e_{td0}\Delta e_{td} + e_{tq0}\Delta e_{tq}\right] \quad \text{(E.31)}$$

where

$$\Delta e_{tq} = \Delta E_q^{"} - X_d^{"}\Delta i_{td} \quad \text{(E.32)}$$

$$\Delta e_{td} = \Delta E_d^{"} + X_q^{"}\Delta i_{tq} \quad \text{(E.33)}$$

Equations (E.32) and (E.33) can be obtained from (2.8) and (2.9) for small variations and by neglecting the stator resistance. Rearrangement of (E.32) by making use of (E.20) and (E.25) gives

$$\Delta e_{tq} = \left[\frac{X_t + X_{TCSC}}{\Lambda_d^{"}}\right]\Delta E_q^{"} - \left[\frac{X_d^{"}V_{\infty d0}}{\Lambda_d^{"}}\right]\Delta\delta + F(\alpha)\cdot\left[\frac{X_d^{"}i_{td0}}{\Lambda_d^{"}}\right]\Delta\alpha \quad \text{(E.34)}$$

Similarly, rearrangement of (E.33) by making use of (E.19) and (E.24) and

$$\Delta e_{td} = \left[\frac{X_t + X_{TCSC}}{\Lambda_q^{"}}\right]\Delta E_d^{"} + \left[\frac{X_q^{"}V_{\infty q0}}{\Lambda_q^{"}}\right]\Delta\delta - F(\alpha)\cdot\left[\frac{X_q^{"}i_{tq0}}{\Lambda_q^{"}}\right]\Delta\alpha \quad \text{(E.35)}$$

By substituting (E.34) and (E.35) into (E.31), the generator terminal voltage equation can be expressed as

$$\Delta e_t = \left[\frac{e_{td0}}{e_{t0}}\cdot\frac{X_q^{"}V_{\infty q0}}{\Lambda_q^{"}} - \frac{e_{tq0}}{e_{t0}}\cdot\frac{X_d^{"}V_{\infty d0}}{\Lambda_d^{"}}\right]\Delta\delta + \left[\frac{e_{tq0}}{e_{t0}}\cdot\frac{X_t + X_{TCSC}}{\Lambda_d^{"}}\right]\Delta E_q^{"} + \left[\frac{e_{td0}}{e_{t0}}\cdot\frac{X_t + X_{TCSC}}{\Lambda_q^{"}}\right]\Delta E_d^{"} + \\ -F(\alpha)\cdot\left[\frac{e_{td0}}{e_{t0}}\cdot\frac{X_q^{"}i_{tq0}}{\Lambda_q^{"}} - \frac{e_{tq0}}{e_{t0}}\cdot\frac{X_d^{"}i_{td0}}{\Lambda_d^{"}}\right]\Delta\alpha \tag{E.36}$$

Similarly to the generator terminal voltage, the TCSC current (in this case, the same as the synchronous generator terminal current) can be expressed in terms of *d*- and *q*-axis components as

$$I_{TCSC}^2 = i_{td}^2 + i_{tq}^2 \tag{E.37}$$

which, for small variations, becomes

$$\Delta I_{TCSC} = (i_{t0})^{-1}\left[i_{td0}\Delta i_{td} + i_{tq0}\Delta i_{tq}\right] \tag{E.38}$$

Rearranging (E.38) by making use of (E.24) and (E.25) yields

$$\Delta I_{TCSC} = \left[\frac{i_{td0}}{i_{t0}}\cdot\frac{V_{\infty d0}}{\Lambda_d^{"}} + \frac{i_{tq0}}{i_{t0}}\cdot\frac{V_{\infty q0}}{\Lambda_q^{"}}\right]\Delta\delta + \left[\frac{i_{td0}}{i_{t0}}\cdot\frac{1}{\Lambda_d^{"}}\right]\Delta E_q^{"} - \left[\frac{i_{tq0}}{i_{t0}}\cdot\frac{1}{\Lambda_q^{"}}\right]\Delta E_d^{"} + \\ -F(\alpha)\cdot\left[\frac{i_{td0}^2}{i_{t0}}\cdot\frac{1}{\Lambda_d^{"}} + \frac{i_{tq0}^2}{i_{t0}}\cdot\frac{1}{\Lambda_q^{"}}\right]\Delta\alpha \tag{E.39}$$

For convenience, (E.29), (E.36) and (E.39) are rewritten as

$$\Delta P_e = K_1\Delta\delta + K_2\Delta E_q^{"} - K_{2d}\Delta E_d^{"} + K_{TCSC1}\Delta\alpha \tag{E.40}$$

$$\Delta e_t = K_5\Delta\delta + K_6\Delta E_q^{"} + K_{6d}\Delta E_d^{"} + K_{TCSC3}\Delta\alpha \tag{E.41}$$

$$\Delta I_{TCSC} = K_{5n}\Delta\delta + K_{6n}\Delta E_q^{"} - K_{6dn}\Delta E_d^{"} + K_{TCSC3n}\Delta\alpha \tag{E.42}$$

where

$$K_1 = \frac{V_{\infty d0}^2}{\Lambda_d^{"}} + \frac{V_{\infty q0}^2}{\Lambda_q^{"}} + i_{td0}V_{\infty q0} - i_{tq0}V_{\infty d0} \tag{E.43}$$

$$K_2 = \frac{V_{\infty d0}}{\Lambda_d^{"}} \tag{E.44}$$

$$K_{2d} = \frac{V_{\infty q0}}{\Lambda_q^{"}} \tag{E.45}$$

$$K_{TCSC1} = -F(\alpha)\cdot\left[\frac{i_{td0}V_{\infty d0}}{\Lambda_d^{"}} + \frac{i_{tq0}V_{\infty q0}}{\Lambda_q^{"}}\right] \tag{E.46}$$

$$K_5 = \frac{e_{td0}}{e_{t0}}\cdot\frac{X_q^{"}V_{\infty q0}}{\Lambda_q^{"}} - \frac{e_{tq0}}{e_{t0}}\cdot\frac{X_d^{"}V_{\infty d0}}{\Lambda_d^{"}} \tag{E.47}$$

$$K_6 = \frac{e_{tq0}}{e_{t0}}\cdot\frac{X_t + X_{TCSC}}{\Lambda_d^{"}} \tag{E.48}$$

$$K_{6d} = \frac{e_{td0}}{e_{t0}} \cdot \frac{X_t + X_{TCSC}}{\Lambda_q^{"}} \tag{E.49}$$

$$K_{TCSC3} = -F(\alpha) \cdot \left[\frac{e_{td0}}{e_{t0}} \cdot \frac{X_q^{"} i_{tq0}}{\Lambda_q^{"}} - \frac{e_{tq0}}{e_{t0}} \cdot \frac{X_d^{"} i_{td0}}{\Lambda_d^{"}} \right] \tag{E.50}$$

$$K_{5n} = \frac{i_{td0}}{i_{t0}} \cdot \frac{V_{\infty d0}}{\Lambda_d^{"}} + \frac{i_{tq0}}{i_{t0}} \cdot \frac{V_{\infty q0}}{\Lambda_q^{"}} \tag{E.51}$$

$$K_{6n} = \frac{i_{td0}}{i_{t0}} \cdot \frac{1}{\Lambda_d^{"}} \tag{E.52}$$

$$K_{6dn} = \frac{i_{tq0}}{i_{t0}} \cdot \frac{1}{\Lambda_q^{"}} \tag{E.53}$$

$$K_{TCSC3n} = -F(\alpha) \cdot \left[\frac{i_{td0}^2}{i_{t0}} \cdot \frac{1}{\Lambda_d^{"}} + \frac{i_{tq0}^2}{i_{t0}} \cdot \frac{1}{\Lambda_q^{"}} \right] \tag{E.54}$$

Substitution of terminal current equations (E.24) and (E.25) into (E.3)–(E.5) provides

$$\begin{aligned} \Delta \dot{E}_q^{'} = {} & \frac{1}{\tau_{d0}^{'}} \Delta E_{fd} - \frac{1}{\tau_{d0}^{'}} \Delta E_q^{'} - \frac{1}{\tau_{d0}^{'}} \left[\frac{\left(X_d - X_d^{'} \right)}{\Lambda_d^{"}} \right] \Delta E_q^{"} - \frac{1}{\tau_{d0}^{'}} \left[\frac{\left(X_d - X_d^{'} \right) V_{\infty d0}}{\Lambda_d^{"}} \right] \Delta \delta + \\ & + \frac{1}{\tau_{d0}^{'}} \left[F(\alpha) \cdot \frac{\left(X_d - X_d^{'} \right) i_{td0}}{\Lambda_d^{"}} \right] \Delta \alpha \end{aligned} \tag{E.55}$$

$$\begin{aligned} \Delta \dot{E}_q^{"} = {} & \frac{1}{\tau_{d0}^{'}} \Delta E_{fd} + \left[\frac{1}{\tau_{d0}^{"}} - \frac{1}{\tau_{d0}^{'}} \right] \Delta E_q^{'} - \frac{V_{\infty d0} \left[\tau_{d0}^{'} \left(X_d^{'} - X_d^{"} \right) + \tau_{d0}^{"} \left(X_d - X_d^{'} \right) \right]}{\tau_{d0}^{"} \tau_{d0}^{'} \Lambda_d^{"}} \Delta \delta + \\ & - \frac{\left[\tau_{d0}^{'} \Lambda_d^{'} + \tau_{d0}^{"} \left(X_d - X_d^{'} \right) \right]}{\tau_{d0}^{"} \tau_{d0}^{'} \Lambda_d^{"}} \Delta E_q^{"} + F(\alpha) \cdot \frac{i_{td0} \left[\tau_{d0}^{'} \left(X_d^{'} - X_d^{"} \right) + \tau_{d0}^{"} \left(X_d - X_d^{'} \right) \right]}{\tau_{d0}^{"} \tau_{d0}^{'} \Lambda_d^{"}} \Delta \alpha \end{aligned} \tag{E.56}$$

$$\Delta \dot{E}_d^{"} = -\frac{1}{\tau_{q0}^{"}} \left[\frac{\Lambda_q}{\Lambda_q^{"}} \right] \Delta E_d^{"} + \frac{1}{\tau_{q0}^{"}} \left[\frac{\left(X_q - X_q^{"} \right) V_{\infty q0}}{\Lambda_q^{"}} \right] \Delta \delta - \frac{1}{\tau_{q0}^{"}} \left[F(\alpha) \cdot \frac{\left(X_q - X_q^{"} \right) i_{tq0}}{\Lambda_q^{"}} \right] \Delta \alpha \tag{E.57}$$

where

$$\Lambda_q = X_q + X_t + X_{TCSC} \tag{E.58}$$

$$\Lambda_d^{'} = X_d^{'} + X_t + X_{TCSC} \tag{E.59}$$

Equations (E.1), (E.2), (E.55)–(E.57) while considering the generator power and terminal voltage equations (E.40) and (E.41), respectively, and the TCSC current equation (E.42) construct the synchronous generator – TCSC model. Procedures are carried out for both transfer function matrix and state-space representations in the next sections.

E.2. Transfer function matrix representation

The synchronous generator – TCSC system connected to an infinite bus via a tie-line reactance has the following generic representation in frequency domain

$$\begin{bmatrix} \Delta\omega(s) \\ \Delta e_t(s) \\ \Delta I_{TCSC}(s) \end{bmatrix} = \begin{bmatrix} g_{11}(s) & g_{12}(s) & g_{13}(s) \\ g_{21}(s) & g_{22}(s) & g_{23}(s) \\ g_{31}(s) & g_{32}(s) & g_{33}(s) \end{bmatrix} \begin{bmatrix} \Delta P_m(s) \\ \Delta E_{fd}(s) \\ \Delta\alpha(s) \end{bmatrix} \tag{E.60}$$

$$\mathbf{y}(s) = \mathbf{G}(s)\mathbf{u}(s) \tag{E.61}$$

where **G**(*s*) is the transfer function matrix of the linearised model of the synchronous generator – SVC system connected to an infinite bus via a tie-line reactance. In order to obtain **G**(*s*), some previous algebraic manipulations are required. In the frequency domain, equations (E.1), (E.2), (E.55)–(E.57) can be given as

$$\Delta\delta(s) = \frac{\omega_0}{s}\Delta\omega(s) \tag{E.62}$$

$$\Delta\omega(s) = \frac{1}{2Hs}\left[\Delta P_m(s) - \Delta P_e(s) - D\Delta\omega(s)\right] \tag{E.63}$$

$$\begin{aligned} \Delta E_q'(s) = {} & \frac{1}{1+\tau_{d0}'s}\Delta E_{fd}(s) - \frac{V_{\infty d0}\left(X_d - X_d'\right)}{\Lambda_d''\left(1+\tau_{d0}'s\right)}\Delta\delta(s) - \frac{\left(X_d - X_d'\right)}{\Lambda_d''\left(1+\tau_{d0}'s\right)}\Delta E_q''(s) + \\ & + F(\alpha)\cdot\frac{\left(X_d - X_d'\right)i_{td0}}{\Lambda_d''\left(1+\tau_{d0}'s\right)}\Delta\alpha(s) \end{aligned} \tag{E.64}$$

$$\begin{aligned} \Delta E_q''(s) = {} & \frac{\Lambda_d''\left(1+\tau_{d0}''s\right)\Delta E_{fd}(s) - V_{\infty d0}\left\{\left(X_d - X_d''\right) + \left[\tau_{d0}'\left(X_d' - X_d''\right) + \tau_{d0}''\left(X_d - X_d'\right)\right]s\right\}\Delta\delta(s)}{\tau_{d0}'\tau_{d0}''\Lambda_d''s^2 + \left[\tau_{d0}''\Lambda_d'' + \tau_{d0}'\Lambda_d' + \tau_{d0}''\left(X_d - X_d'\right)\right]s + \Lambda_d} + \\ & + \frac{F(\alpha)\cdot i_{td0}\left\{\left(X_d - X_d''\right) + \left[\tau_{d0}'\left(X_d' - X_d''\right) + \tau_{d0}''\left(X_d - X_d'\right)\right]s\right\}}{\tau_{d0}'\tau_{d0}''\Lambda_d''s^2 + \left[\tau_{d0}''\Lambda_d'' + \tau_{d0}'\Lambda_d' + \tau_{d0}''\left(X_d - X_d'\right)\right]s + \Lambda_d}\Delta\alpha(s) + \end{aligned} \tag{E.65}$$

$$\Delta E_d''(s) = \frac{\left(X_q - X_q''\right)V_{\infty q0}}{\Lambda_q\left[1+\tau_{q0}''\left(\frac{\Lambda_q''}{\Lambda_q}\right)s\right]}\Delta\delta(s) - F(\alpha)\cdot\frac{\left(X_q - X_q''\right)i_{tq0}}{\Lambda_q\left[1+\tau_{q0}''\left(\frac{\Lambda_q''}{\Lambda_q}\right)s\right]}\Delta\alpha(s) \tag{E.66}$$

where

$$\Lambda_d = X_d + X_t + X_{TCSC} \tag{E.67}$$

Equation (E.65) is obtained by using equation (E.64) in the resultant Laplace transformation of (E.56). For convenience, (E.65) and (E.66) are rewritten as

$$\Delta E_q''(s) = K_3(s)\Delta E_{fd}(s) - K_4(s)\Delta\delta(s) - K_{TCSC2}(s)\Delta\alpha(s) \tag{E.68}$$

$$\Delta E_d''(s) = K_{4d}(s)\Delta\delta(s) + K_{TCSC2d}(s)\Delta\alpha(s) \tag{E.69}$$

where

$$K_3(s)=\frac{\Lambda_d^{"}\left(1+\tau_{d0}^{"}s\right)}{\tau_{d0}^{'}\tau_{d0}^{"}\Lambda_d^{"}s^2+\left[\tau_{d0}^{"}\Lambda_d^{"}+\tau_{d0}^{'}\Lambda_d^{'}+\tau_{d0}^{"}\left(X_d-X_d^{'}\right)\right]s+\Lambda_d} \tag{E.70}$$

$$K_4(s)=\frac{V_{\infty d0}\left\{\left(X_d-X_d^{"}\right)+\left[\tau_{d0}^{'}\left(X_d^{'}-X_d^{"}\right)+\tau_{d0}^{"}\left(X_d-X_d^{'}\right)\right]s\right\}}{\tau_{d0}^{'}\tau_{d0}^{"}\Lambda_d^{"}s^2+\left[\tau_{d0}^{"}\Lambda_d^{"}+\tau_{d0}^{'}\Lambda_d^{'}+\tau_{d0}^{"}\left(X_d-X_d^{'}\right)\right]s+\Lambda_d} \tag{E.71}$$

$$K_{TCSC2}(s)=-F(\alpha)\cdot\frac{i_{td0}\left\{\left(X_d-X_d^{"}\right)+\left[\tau_{d0}^{'}\left(X_d^{'}-X_d^{"}\right)+\tau_{d0}^{"}\left(X_d-X_d^{'}\right)\right]s\right\}}{\tau_{d0}^{'}\tau_{d0}^{"}\Lambda_d^{"}s^2+\left[\tau_{d0}^{"}\Lambda_d^{"}+\tau_{d0}^{'}\Lambda_d^{'}+\tau_{d0}^{"}\left(X_d-X_d^{'}\right)\right]s+\Lambda_d} \tag{E.72}$$

$$K_{4d}(s)=\frac{C_{4d}}{1+\tau_q^{"}s} \tag{E.73}$$

$$K_{TCSC2d}(s)=\frac{C_{TCSC2d}}{1+\tau_q^{"}s} \tag{E.74}$$

$$C_{4d}=V_{\infty q0}\left(\frac{X_q-X_q^{"}}{\Lambda_q}\right) \tag{E.75}$$

$$C_{TCSC2d}=-F(\alpha)\cdot\left[\frac{\left(X_q-X_q^{"}\right)i_{tq0}}{\Lambda_q}\right] \tag{E.76}$$

$$\tau_q^{"}=\tau_{q0}^{"}\left(\frac{\Lambda_q^{"}}{\Lambda_q}\right) \tag{E.77}$$

In the frequency domain, the generator power and terminal voltage expressions (E.40) and (E.41), respectively, and the TCSC current equation (E.42) are given as

$$\Delta P_e(s)=K_1\Delta\delta(s)+K_2\Delta E_q^{"}(s)-K_{2d}\Delta E_d^{"}(s)+K_{TCSC1}\Delta\alpha(s) \tag{E.78}$$

$$\Delta e_t(s)=K_5\Delta\delta(s)+K_6\Delta E_q^{"}(s)+K_{6d}\Delta E_d^{"}(s)+K_{TCSC3}\Delta\alpha(s) \tag{E.79}$$

$$\Delta I_{TCSC}(s)=K_{5n}\Delta\delta(s)+K_{6n}\Delta E_q^{"}(s)-K_{6dn}\Delta E_d^{"}(s)+K_{TCSC3n}\Delta\alpha(s) \tag{E.80}$$

with coefficients defined by (E.43)–(E.54).

The transfer function matrix representation given by (E.60) is obtained by substituting (E.62) into (E.68), (E.69), (E.78)–(E.80) to obtain expressions in terms of $\Delta\omega(s)$:

$$\Delta P_e(s)=K_1\frac{\omega_0}{s}\Delta\omega(s)+K_2\Delta E_q^{"}(s)-K_{2d}\Delta E_d^{"}(s)+K_{TCSC1}\Delta\alpha(s) \tag{E.81}$$

$$\Delta e_t(s)=K_5\frac{\omega_0}{s}\Delta\omega(s)+K_6\Delta E_q^{"}(s)+K_{6d}\Delta E_d^{"}(s)+K_{TCSC3}\Delta\alpha(s) \tag{E.82}$$

$$\Delta I_{TCSC}(s)=K_{5n}\frac{\omega_0}{s}\Delta\omega(s)+K_{6n}\Delta E_q^{"}(s)-K_{6dn}\Delta E_d^{"}(s)+K_{TCSC3n}\Delta\alpha(s) \tag{E.83}$$

$$\Delta E_q^{"}(s) = K_3(s)\Delta E_{fd}(s) - K_4(s)\frac{\omega_0}{s}\Delta\omega(s) - K_{TCSC2}(s)\Delta\alpha(s) \tag{E.84}$$

$$\Delta E_d^{"}(s) = K_{4d}(s)\frac{\omega_0}{s}\Delta\omega(s) + K_{TCSC2d}(s)\Delta\alpha(s) \tag{E.85}$$

To simplify the procedure, transfer functions (E.70)–(E.72) are rewritten as

$$K_3(s) = \frac{\Lambda_d^{"}\left(1+\tau_{d0}^{"}s\right)}{Es^2+Fs+\Lambda_d} \tag{E.86}$$

$$K_4(s) = \frac{V_{\infty d0}(B+Cs)}{Es^2+Fs+\Lambda_d} \tag{E.87}$$

$$K_{TCSC2}(s) = \frac{I(B+Cs)}{Es^2+Fs+\Lambda_d} \tag{E.88}$$

where

$$B = X_d - X_d^{"} \tag{E.89}$$

$$C = \tau_{d0}^{'}\left(X_d^{'} - X_d^{"}\right) + \tau_{d0}^{"}\left(X_d - X_d^{'}\right) \tag{E.90}$$

$$E = \tau_{d0}^{'}\tau_{d0}^{"}\Lambda_d^{"} \tag{E.91}$$

$$F = \tau_{d0}^{"}\Lambda_d^{"} + \tau_{d0}^{'}\Lambda_d^{'} + \tau_{d0}^{"}\left(X_d - X_d^{'}\right) \tag{E.92}$$

$$I = -i_{td0}F(\alpha) \tag{E.93}$$

Substituting (E.86)–(E.88) into (E.84) and (E.73)–(E.74) into (E.85) renders

$$\Delta E_q^{"}(s) = \frac{\Lambda_d^{"}\left(1+\tau_{d0}^{"}s\right)}{Es^2+Fs+\Lambda_d}\Delta E_{fd}(s) - \frac{V_{\infty d0}(B+Cs)}{Es^2+Fs+\Lambda_d}\cdot\frac{\omega_0}{s}\Delta\omega(s) - \frac{I(B+Cs)}{Es^2+Fs+\Lambda_d}\Delta\alpha(s) \tag{E.94}$$

$$\Delta E_d^{"}(s) = \frac{C_{4d}}{1+\tau_q^{"}s}\cdot\frac{\omega_0}{s}\Delta\omega(s) + \frac{C_{TCSC2d}}{1+\tau_q^{"}s}\Delta\alpha(s) \tag{E.95}$$

Using (E.94) and (E.95) in (E.81)–(E.83) gives the following intermediate result after some algebraic manipulations:

$$\begin{aligned}\Delta P_e(s) = &\left[K_1 - \frac{K_2V_{\infty d0}(B+Cs)}{Es^2+Fs+\Lambda_d} - \frac{K_{2d}C_{4d}}{1+\tau_q^{"}s}\right]\frac{\omega_0}{s}\Delta\omega(s) + \frac{K_2\Lambda_d^{"}\left(1+\tau_{d0}^{"}s\right)}{Es^2+Fs+\Lambda_d}\Delta E_{fd}(s) + \\ &+\left[K_{TCSC1} - \frac{K_2I(B+Cs)}{Es^2+Fs+\Lambda_d} - \frac{K_{2d}C_{TCSC2d}}{1+\tau_q^{"}s}\right]\Delta\alpha(s)\end{aligned} \tag{E.96}$$

$$\begin{aligned}\Delta e_t(s) = &\left[K_5 - \frac{K_6V_{\infty d0}(B+Cs)}{Es^2+Fs+\Lambda_d} + \frac{K_{6d}C_{4d}}{1+\tau_q^{"}s}\right]\frac{\omega_0}{s}\Delta\omega(s) + \frac{K_6\Lambda_d^{"}\left(1+\tau_{d0}^{"}s\right)}{Es^2+Fs+\Lambda_d}\Delta E_{fd}(s) + \\ &+\left[K_{TCSC3} - \frac{K_6I(B+Cs)}{Es^2+Fs+\Lambda_d} + \frac{K_{6d}C_{TCSC2d}}{1+\tau_q^{"}s}\right]\Delta\alpha(s)\end{aligned} \tag{E.97}$$

$$\Delta I_{TCSC}(s)=\left[K_{5n}-\frac{K_{6n}V_{\infty d0}(B+Cs)}{Es^2+Fs+\Lambda_d}-\frac{K_{6dn}C_{4d}}{1+\tau_q^{"}s}\right]\frac{\omega_0}{s}\Delta\omega(s)+\frac{K_{6n}\Lambda_d^{"}(1+\tau_{d0}^{"}s)}{Es^2+Fs+\Lambda_d}\Delta E_{fd}(s)+$$
$$+\left[K_{TCSC3n}-\frac{K_{6n}I(B+Cs)}{Es^2+Fs+\Lambda_d}-\frac{K_{6dn}C_{TCSC2d}}{1+\tau_q^{"}s}\right]\Delta\alpha(s) \tag{E.98}$$

Substituting (E.96) in (E.63), gives, after some algebraic manipulations

$$2Hs\Delta\omega(s)+D\Delta\omega(s)=\Delta P_m(s)-\Delta P_e(s)$$
$$\Downarrow$$
$$\left\{(2Hs+D)+\left[K_1-\frac{K_2V_{\infty d0}(B+Cs)}{Es^2+Fs+\Lambda_d}-\frac{K_{2d}C_{4d}}{1+\tau_q^{"}s}\right]\frac{\omega_0}{s}\right\}\Delta\omega(s)=\Delta P_m(s)-\frac{K_2\Lambda_d^{"}(1+\tau_{d0}^{"}s)}{Es^2+Fs+\Lambda_d}\Delta E_{fd}(s)$$
$$-\left[K_{TCSC1}-\frac{K_2I(B+Cs)}{Es^2+Fs+\Lambda_d}-\frac{K_{2d}C_{TCSC2d}}{1+\tau_q^{"}s}\right]\Delta\alpha(s)$$
$$\Downarrow$$
$$\Delta\omega(s)=g_{11}(s)\Delta P_m(s)+g_{12}(s)\Delta E_{fd}(s)+g_{13}(s)\Delta\alpha(s) \tag{E.99}$$

where

$$den(s)=(2Hs+D)\left(Es^2+Fs+\Lambda_d\right)\left(1+\tau_q^{"}s\right)s+K_1\omega_0\left(Es^2+Fs+\Lambda_d\right)\left(1+\tau_q^{"}s\right)+$$
$$-K_2V_{\infty d0}\omega_0(B+Cs)\left(1+\tau_q^{"}s\right)-K_{2d}C_{4d}\omega_0\left(Es^2+Fs+\Lambda_d\right) \tag{E.100}$$

$$g_{11}(s)=\frac{\left(Es^2+Fs+\Lambda_d\right)\left(1+\tau_q^{"}s\right)s}{den(s)} \tag{E.101}$$

$$g_{12}(s)=-\frac{K_2\Delta_d^{"}\left(1+\tau_{d0}^{"}s\right)\left(1+\tau_q^{"}s\right)s}{den(s)} \tag{E.102}$$

$$g_{13}(s)=-\frac{\left[K_{TCSC1}\left(Es^2+Fs+\Lambda_d\right)\left(1+\tau_q^{"}s\right)-K_2I(B+Cs)\left(1+\tau_q^{"}s\right)-K_{2d}C_{TCSC2d}\left(Es^2+Fs+\Lambda_d\right)\right]s}{den(s)} \tag{E.103}$$

In (E.99), speed is given in terms of the mechanical power, field voltage and SVC firing angle, as required by (E.60). The equation for the synchronous generator terminal voltage is found by substituting (E.99) into (E.97). After a cumbersome algebraic manipulation, it can be expressed as

$$\Delta e_t(s)=g_{21}(s)\Delta P_m(s)+g_{22}(s)\Delta E_{fd}(s)+g_{23}(s)\Delta\alpha(s) \tag{E.104}$$

where

$$g_{21}(s)=\frac{\omega_0\left[K_5\left(Es^2+Fs+\Lambda_d\right)\left(1+\tau_q^{"}s\right)-K_6V_{\infty d0}(B+Cs)\left(1+\tau_q^{"}s\right)+K_{6d}C_{4d}\left(Es^2+Fs+\Lambda_d\right)\right]}{den(s)} \tag{E.105}$$

$$g_{22}(s)=\frac{\Lambda_d^{"}\left(1+\tau_{d0}^{"}s\right)\left\{K_6\left(1+\tau_q^{"}s\right)(2Hs+D)s+\left(K_6\left[\left(1+\tau_q^{"}s\right)K_1-K_{2d}C_{4d}\right]-K_2\left[\left(1+\tau_q^{"}s\right)K_5+K_{6d}C_{4d}\right]\right)\omega_0\right\}}{den(s)} \tag{E.106}$$

$$g_{23}(s)=\frac{(2Hs+D)\left\{\left(Es^2+Fs+\Lambda_d\right)\left[\left(1+\tau_q^{"}s\right)K_{TCSC3}+K_{6d}C_{TCSC2d}\right]-K_6I\left(B+Cs\right)\left(1+\tau_q^{"}s\right)\right\}s}{den(s)}+$$
$$+\frac{\omega_0\left\{\left(Es^2+Fs+\Lambda_d\right)\left[K_{6d}\left(K_1C_{TCSC2d}-C_{4d}K_{TCSC1}\right)+K_{2d}\left(K_5C_{TCSC2d}-C_{4d}K_{TCSC3}\right)+\left(1+\tau_q^{"}s\right)\left(K_1K_{TCSC3}-K_5K_{TCSC1}\right)\right]\right\}}{den(s)}+$$
$$+\frac{\omega_0\left\{\left(B+Cs\right)\left[\left(1+\tau_q^{"}s\right)\left[I\left(K_2K_5-K_1K_6\right)+V_{\infty d0}\left(K_6K_{TCSC1}-K_2K_{TCSC3}\right)\right]+\left(IC_{4d}-C_{TCSC2d}V_{\infty d0}\right)\left(K_2K_{6d}+K_{2d}K_6\right)\right]\right\}}{den(s)} \quad \text{(E.107)}$$

In (E.104), the terminal voltage expression is given in terms of the mechanical power, field voltage and SVC firing angle, as required by (E.60). The equation for the TCSC current voltage is found by substituting (E.99) into (E.98). After a cumbersome algebraic manipulation, it can be expressed as

$$\Delta V_{SVC}(s)=g_{31}(s)\Delta P_m(s)+g_{32}(s)\Delta E_{fd}(s)+g_{33}(s)\Delta\alpha(s) \quad \text{(E.108)}$$

where

$$g_{31}(s)=\frac{\omega_0\left[K_{5n}\left(Es^2+Fs+\Lambda_d\right)\left(1+\tau_q^{"}s\right)-K_{6n}V_{\infty d0}\left(B+Cs\right)\left(1+\tau_q^{"}s\right)-K_{6dn}C_{4d}\left(Es^2+Fs+\Lambda_d\right)\right]}{den(s)} \quad \text{(E.109)}$$

$$g_{32}(s)=\frac{\Lambda_d^{"}\left(1+\tau_{d0}^{"}s\right)\left\{K_{6n}\left(1+\tau_q^{"}s\right)(2Hs+D)s+\left(K_{6n}\left[\left(1+\tau_q^{"}s\right)K_1-K_{2d}C_{4d}\right]-K_2\left[\left(1+\tau_q^{"}s\right)K_{5n}-K_{6dn}C_{4d}\right]\right)\omega_0\right\}}{den(s)} \quad \text{(E.110)}$$

$$g_{33}(s)=\frac{(2Hs+D)\left\{\left(Es^2+Fs+\Lambda_d\right)\left[\left(1+\tau_q^{"}s\right)K_{TCSC3n}-K_{6dn}C_{TCSC2d}\right]-K_{6n}I\left(B+Cs\right)\left(1+\tau_q^{"}s\right)\right\}s}{den(s)}+$$
$$+\frac{\omega_0\left\{\left(Es^2+Fs+\Lambda_d\right)\left[K_{6dn}\left(C_{4d}K_{TCSC1}-K_1C_{TCSC2d}\right)+K_{2d}\left(K_{5n}C_{TCSC2d}-C_{4d}K_{TCSC3n}\right)+\left(1+\tau_q^{"}s\right)\left(K_1K_{TCSC3n}-K_{5n}K_{TCSC1}\right)\right]\right\}}{den(s)}+$$
$$+\frac{\omega_0\left\{\left(B+Cs\right)\left[\left(1+\tau_q^{"}s\right)\left[I\left(K_2K_{5n}-K_1K_{6n}\right)+V_{\infty d0}\left(K_{6n}K_{TCSC1}-K_2K_{TCSC3n}\right)\right]+\left(IC_{4d}-C_{TCSC2d}V_{\infty d0}\right)\left(K_{2d}K_{6n}-K_2K_{6dn}\right)\right]\right\}}{den(s)} \quad \text{(E.111)}$$

In (E.108), the SVC terminal voltage is given in terms of the mechanical power, field voltage and SVC firing angle, as required by (E.60). Notice that equations (E.99), (E.104) and (E.111) have the form of (E.60), where the transfer function matrix individual transfer functions are given by (E.101)–(E.103), (E.105)–(E.107) and (E.109)–(E.111).

E.3. State-space representation

Consider the synchronous generator – TCSC system model, given by differential equations (E.1), (E.2), (E.55)–(E.57) while considering the generator power and terminal voltage equations (E.40) and (E.41), respectively, and the SVC terminal voltage equation (E.42):

$$\Delta\dot{\delta}=\omega_0\Delta\omega \quad \text{(E.1)}$$

$$\Delta\dot{\omega} = \frac{1}{2H}\left[\Delta P_m - \Delta P_e - D\Delta\omega\right] \tag{E.2}$$

$$\begin{aligned}\Delta\dot{E}_q^{'} = {} & \frac{1}{\tau_{d0}^{'}}\Delta E_{fd} - \frac{1}{\tau_{d0}^{'}}\Delta E_q^{'} - \frac{1}{\tau_{d0}^{'}}\left[\frac{\left(X_d - X_d^{'}\right)}{\Lambda_d^{''}}\right]\Delta E_q^{''} - \frac{1}{\tau_{d0}^{'}}\left[\frac{\left(X_d - X_d^{'}\right)V_{\infty d0}}{\Lambda_d^{''}}\right]\Delta\delta + \\ & + \frac{1}{\tau_{d0}^{'}}\left[F(\alpha)\cdot\frac{\left(X_d - X_d^{'}\right)i_{td0}}{\Lambda_d^{''}}\right]\Delta\alpha\end{aligned} \tag{E.55}$$

$$\begin{aligned}\Delta\dot{E}_q^{''} = {} & \frac{1}{\tau_{d0}^{'}}\Delta E_{fd} + \left[\frac{1}{\tau_{d0}^{''}} - \frac{1}{\tau_{d0}^{'}}\right]\Delta E_q^{'} - \frac{V_{\infty d0}\left[\tau_{d0}^{'}\left(X_d^{'} - X_d^{''}\right) + \tau_{d0}^{''}\left(X_d - X_d^{'}\right)\right]}{\tau_{d0}^{''}\tau_{d0}^{'}\Lambda_d^{''}}\Delta\delta + \\ & - \frac{\left[\tau_{d0}^{'}\Lambda_d^{'} + \tau_{d0}^{''}\left(X_d - X_d^{'}\right)\right]}{\tau_{d0}^{''}\tau_{d0}^{'}\Lambda_d^{''}}\Delta E_q^{''} + F(\alpha)\cdot\frac{i_{td0}\left[\tau_{d0}^{'}\left(X_d^{'} - X_d^{''}\right) + \tau_{d0}^{''}\left(X_d - X_d^{'}\right)\right]}{\tau_{d0}^{''}\tau_{d0}^{'}\Lambda_d^{''}}\Delta\alpha\end{aligned} \tag{E.56}$$

$$\Delta\dot{E}_d^{''} = -\frac{1}{\tau_{q0}^{''}}\left[\frac{\Lambda_q}{\Lambda_q^{''}}\right]\Delta E_d^{''} + \frac{1}{\tau_{q0}^{''}}\left[\frac{\left(X_q - X_q^{''}\right)V_{\infty q0}}{\Lambda_q^{''}}\right]\Delta\delta - \frac{1}{\tau_{q0}^{''}}\left[F(\alpha)\cdot\frac{\left(X_q - X_q^{''}\right)i_{tq0}}{\Lambda_q^{''}}\right]\Delta\alpha \tag{E.57}$$

$$\Delta P_e = K_1\Delta\delta + K_2\Delta E_q^{''} - K_{2d}\Delta E_d^{''} + K_{TCSC1}\Delta\alpha \tag{E.40}$$

$$\Delta e_t = K_5\Delta\delta + K_6\Delta E_q^{''} + K_{6d}\Delta E_d^{''} + K_{TCSC3}\Delta\alpha \tag{E.41}$$

$$\Delta I_{TCSC} = K_{5n}\Delta\delta + K_{6n}\Delta E_q^{''} - K_{6dn}\Delta E_d^{''} + K_{TCSC3n}\Delta\alpha \tag{E.42}$$

where the coefficients in (E.40)–(E.42) are given by (E.43)–(E.54). Substitution of (E.40) in (E.2) yields

$$\Delta\dot{\omega} = -\frac{K_1}{2H}\Delta\delta - \frac{D}{2H}\Delta\omega - \frac{K_2}{2H}\Delta E_q^{''} + \frac{K_{2d}}{2H}\Delta E_d^{''} - \frac{K_{TCSC1}}{2H}\Delta\alpha + \frac{1}{2H}\Delta P_m \tag{E.112}$$

Considering differential equations (E.1), (E.55)–(E.57) and (E.112), and the generator terminal voltage and TCSC current equations (E.41) and (E.42), respectively, the state-space representation

$$\begin{aligned}\Delta\dot{\mathbf{x}} &= \mathbf{A}\Delta\mathbf{x} + \mathbf{B}\Delta\mathbf{u} \\ \Delta\mathbf{y} &= \mathbf{C}\Delta\mathbf{x} + \mathbf{D}\Delta\mathbf{u}\end{aligned} \tag{E.113}$$

can be constructed, where the output, input, and state vectors are given, respectively, as

$$\Delta\mathbf{y} = \left[\Delta\omega \quad \Delta e_t \quad \Delta I_{TCSC}\right]^T \tag{E.114}$$

$$\Delta\mathbf{u} = \left[\Delta P_m \quad \Delta E_{fd} \quad \Delta\alpha\right]^T \tag{E.115}$$

$$\Delta\mathbf{x} = \left[\Delta\omega \quad \Delta E_q^{'} \quad \Delta E_q^{''} \quad \Delta E_d^{''} \quad \Delta\delta\right]^T \tag{E.116}$$

System, control, output and feed-forward matrices **A**, **B, C** and **D,** respectively, are given as

$$\mathbf{A}=\begin{bmatrix} -\frac{D}{2H} & 0 & -\frac{K_2}{2H} & \frac{K_{2d}}{2H} & -\frac{K_1}{2H} \\ 0 & -\frac{1}{\tau_{d0}^{'}} & a_{23} & 0 & a_{25} \\ 0 & \frac{1}{\tau_{d0}^{''}}-\frac{1}{\tau_{d0}^{'}} & a_{33} & 0 & a_{35} \\ 0 & 0 & 0 & a_{44} & a_{45} \\ \omega_0 & 0 & 0 & 0 & 0 \end{bmatrix} \tag{E.117}$$

$$\mathbf{B}=\begin{bmatrix} \frac{1}{2H} & 0 & -\frac{K_{TCSC1}}{2H} \\ 0 & \frac{1}{\tau_{d0}^{'}} & b_{23} \\ 0 & \frac{1}{\tau_{d0}^{'}} & b_{33} \\ 0 & 0 & b_{43} \\ 0 & 0 & 0 \end{bmatrix} \tag{E.118}$$

$$\mathbf{C}=\begin{bmatrix} 1 & 0 & 0 & 0 & 0 \\ 0 & 0 & K_6 & K_{6d} & K_5 \\ 0 & 0 & K_{6n} & K_{6dn} & K_{5n} \end{bmatrix} \tag{E.119}$$

$$\mathbf{D}=\begin{bmatrix} 0 & 0 & 0 \\ 0 & 0 & K_{TCSC3} \\ 0 & 0 & K_{TCSC3n} \end{bmatrix} \tag{E.120}$$

where the coefficients in (E.117)–(E.120) are given by (E.43)–(E.54) and

$$a_{23}=-\frac{X_d-X_d^{'}}{\tau_{d0}^{'}\Lambda_d^{''}} \tag{E.121}$$

$$a_{25}=-\frac{V_{\infty d0}\left(X_d-X_d^{'}\right)}{\tau_{d0}^{'}\Lambda_d^{''}} \tag{E.122}$$

$$a_{33}=-\frac{\tau_{d0}^{'}\Lambda_d^{'}+\tau_{d0}^{''}\left(X_d-X_d^{'}\right)}{\tau_{d0}^{''}\tau_{d0}^{'}\Lambda_d^{''}} \tag{E.123}$$

$$a_{35}=-\frac{V_{\infty d0}\left[\tau_{d0}^{'}\left(X_d^{'}-X_d^{''}\right)+\tau_{d0}^{''}\left(X_d-X_d^{'}\right)\right]}{\tau_{d0}^{''}\tau_{d0}^{'}\Lambda_d^{''}} \tag{E.124}$$

$$a_{44}=-\frac{\Lambda_q}{\tau_{q0}^{''}\Lambda_q^{''}} \tag{E.125}$$

$$a_{45}=\frac{V_{\infty q0}\left(X_q-X_q^{''}\right)}{\tau_{q0}^{''}\Lambda_q^{''}} \tag{E.126}$$

$$b_{23}=F\left(\alpha\right)\cdot\frac{i_{td0}\left(X_d-X_d^{'}\right)}{\tau_{d0}^{'}\Lambda_d^{''}} \tag{E.127}$$

$$b_{33} = F(\alpha) \cdot \frac{i_{td0}\left[\tau'_{d0}\left(X'_d - X''_d\right) + \tau''_{d0}\left(X_d - X'_d\right)\right]}{\tau''_{d0}\tau'_{d0}\Lambda''_d} \tag{E.128}$$

$$b_{43} = -F(\alpha) \cdot \frac{i_{tq0}\left(X_q - X''_q\right)}{\tau''_{q0}\Lambda''_q} \tag{E.129}$$